Dissertation zur Erlangung des Doktorgrades
der Fakultät für Chemie und Pharmazie
der Ludwig-Maximilians-Universität München

Smart DNA Origami Biosensors and Nanorobots with Allosteric Information Transfer

Von Martina Pfeiffer

aus
München, Deutschland

2024

Erklärung

Diese Dissertation wurde im Sinne von § 7 der Promotionsordnung vom 28. November 2011 von Herrn Prof. Dr. Philip Tinnefeld betreut.

Eidesstattliche Versicherung

Diese Dissertation wurde eigenständig und ohne unerlaubte Hilfe erarbeitet.

München, den 27.02.2024

_____

Martina Pfeiffer

Dissertation eingereicht am	09.01.2024
1. Gutachter:	*Prof. Dr. Philip Tinnefeld*
2. Gutachterin:	*Prof. Dr. Alena Khmelinskaia*
Mündliche Prüfung am	20.02.2024

Summary

DNA-based biosensors and nanorobots aim to mimic cellular functions in a rationally controlled manner. They play key roles in the development of new diagnostic methods and therapeutics. For their large scale application in commercial technologies, however, there are several key challenges that have to be overcome. These challenges, amongst others, include strategies to generate output signals with good signal contrast, simple adaptability to new inputs, strategies to tune the responsive window to relevant input concentration ranges, computing strategies to generate responses to different input combinations, and to enable temporal control on the performance of output operations.

Nature has developed an effective strategy for tackling all of these challenges in a single approach – transferring information by allostery. The ability to include and precisely control allosteric information transfer in nanodevices, would therefore be a milestone in the development of smart DNA-based biosensors and nanorobots. This thesis developed strategies to implement allosteric information transfer in DNA origami nanostructures, helping to overcome the aforementioned challenges and thus marking a significant stride in the evolution of smart DNA origami biosensors and nanorobots. Guiding through the (further) development of three different DNA origami biosensors and nanorobots, it progresses from a static structure over a dynamic two-state structure to a two dimensional network of two-state systems. In each step, the structural complexity of the used DNA origami structures was increased, resulting in advanced capabilities and functionalities of the developed biosensors and nanorobots provided by allostery through information transfer.

DNA origami nanoantennas can be used as fluorescence biosensors with physical signal enhancement. I demonstrated that the incorporation of an allosteric nanoswitch system into DNA origami nanoantennas enables extending their input spectrum from nucleic acids to antibodies. The nanoswitch contained two antigens that were displaced by antibody binding, thereby eliciting a fluorescence signal. In this system, the input receiving unit and the output operation unit were tightly linked and their spatially controlled positioning on a DNA origami nanoantenna structure allowed amplification of the fluorescent output signal via nanophotonics. This enabled the detection of single antibodies using a low-cost and portable smartphone microscope for the first time.

Next, I continued to weaken the link between the input receiving unit and the output operation unit using the conformational change of a dynamic hinge-like DNA origami nanostructure as a communication medium between both units. The structure consisted of two arms joined along the edge with single-stranded DNA connections that formed a flexible hinge and provided rotational motion in the system. In absence of additional interactions, the angle between the arms of the nanostructure was maximized due to Coulomb repulsion caused by the negatively charged DNA building material. Incorporation of additional interactions resulted in the structure being forced into a tensioned state, in which both arms were nearly parallel to each other. By making these interactions responsive to different inputs, I demonstrated the applicability of the dynamic DNA origami structure as a modular biosensing platform for responding to different environmental inputs including DNA, antibodies, antigens, enzymes, and their

activities. In addition to this, the implementation of multiple input receiving units enabled tailoring the responsive window of the biosensor using allostery and cooperativity as regulatory mechanisms. This also allowed to connect outputs with different combinations of inputs using user-programmable Boolean logics, enabling the performance of biocomputation.

Finally, based on the concepts developed for these structures, I used a network of two-state systems to build up a smart DNA origami nanorobot. For this, I reinterpreted reconfigurable DNA origami array structures which were composed of multiple structurally similar so-called anti-junctions as two-dimensional networks of allosterically coupled two-state systems. In the presence of trigger DNA strands, step-by step, all of the anti-junctions in the array underwent a conformational change. To form these arrays into a nanorobot, I introduced different functionalities, e.g. input receiving and output operation units, into individual anti-junctions of the arrays. If multiple functionalities were incorporated into the same array structure, they were connected through conformational change of the whole array structure. Combining them in a rational manner thus necessitated a detailed understanding of the underlying energy landscape. To this end, I developed a double FRET probe to characterize the timing between the conformational changes of individual anti-junctions in the system. Based on these timings, I proposed a model for the energy landscape for the process including energy barriers between intermediates. Using the same assay, I then continued to develop strategies to tune the energy landscape both globally and locally between pre-specified intermediates. This combination of universally designed input receiving and output operation units which, in principle, can be implemented in any of the anti-junctions of the array structure and the detailed understanding and level of control on how these anti-junctions are connected through the energy landscape of their conformational change opened up the door to develop a smart nanorobot overcoming many of the challenges nanodevices typically face. Using this combination enabled receiving multiple different inputs, processing them using multi-level Boolean logic gates and reacting to them by performing multiple output operations under both temporal and allosteric control all on the same structure, ultimately creating a smart nanorobot using allosteric information transfer. I envision further developing allostery as a mechanism for information transfer in DNA origami biosensors and nanorobots will pave the way for their routine application in clinical diagnostics and therapeutics.

Table of contents

1 INTRODUCTION

Throughout history, several technological innovations have exerted transformative influence on society. One of the most significant developments in the 19th century was the advent of the steam engine, which managed to combine unprecedented mechanical power with efficient energy conversion, revolutionizing the way industries functioned and shaping the socioeconomic landscape.[1–4] As demonstrated by the development of nanosheet chips[5,6] containing billions of transistors, each made up of three stacked sheets of silicon of a few nanometer thickness, on a space about the size of a fingernail and mRNA vaccines for COVID-19[7,8] capable of manipulating molecular processes, the focus of research has shifted from the macroscale to the nanoscale. The development of smart devices capable of performing sophisticated task at the nanoscale could lead to a similar quantum leap for humanity in future.

While we are only starting to build such nanodevices in the laboratory in recent years, nature has spent billions of years[9,10] perfecting them. From biomolecular receptors that detect changes in their ligand concentration in order to interact with their environment[11–13] to complex motor proteins that walk on supramolecular tracks with sub-nanometer precision in a stepwise fashion for keeping the tensioned state in a muscle,[14–18] naturally occurring nanomachines perform complex tasks upon their activation by environmental inputs. Imagine being able to artificially build nanodevices capable of mimicking these functionalities, initiating them at will and eventually also surpassing their natural counterparts. DNA nanotechnology offers us a toolbox to achieve just that – it opens the possibility of developing and engineering devices capable of emulating functions and properties of biological systems at the nanoscale.[19–24]

The ideal nanodevice can receive molecular inputs of all sorts (e.g. DNA, RNA, enzymes, small molecules, antibodies, light, or temperature) which are then processed to calculate the optimal plan of action, activating different output operations (e.g. generation of a transduction signal, release of drugs or uptake of small molecules, cleavage reaction) in a spatially and temporally controlled manner (see Figure 1). From receiving the inputs to activating the outputs, each of the steps must be highly efficient, specific, sensitive and controlled to ensure proper functionality of the whole system.

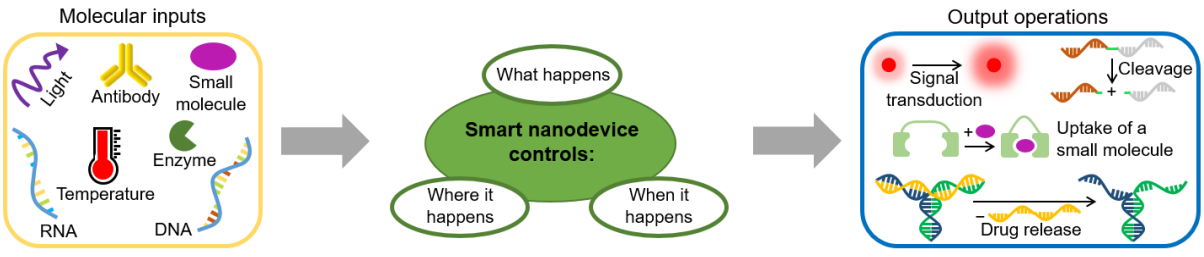

Figure 1: Principle of a smart nanodevice with universal applicability. Nanodevices generally enable performing output operations after sensing molecular inputs. In the ideal case, they allow to achieve arbitrary input – output combinations with spatial and temporal control. As such, they allow to control *what* happens, *where* it happens and *when* it happens.

While these requirements make the development of such versatile nanodevices challenging, they are still highly sought-after. The ability to perform versatile tasks on demand at user-programmed locations is of great benefit for technological applications in the fields of smart drug delivery,[25–27] heterogeneous catalysis[28] and all other fields in which spatiotemporal control of molecular processes is essential. For instance, such nanodevices can find applications in the field of clinical diagnostics.[29,30] The possibility to simultaneously detect different molecular inputs, used for the staging of diseases, on the same nanodevice would facilitate the diagnosis process and thus decrease the time needed to confirm clinical suspicions. An example which illustrates this is the life-threatening coagulation disorder thrombotic thrombocytopenic purpura (TTP). Diagnosis of TTP and differentiation between its two forms requires to detect different inputs. To date, this is achieved by detecting them separately using one complex diagnostic test for each input.[31–33]

DNA origami nanostructures have emerged as excellent platforms for the development of nanodevices.[34–37] DNA origami is a method that enables the pre-programmed self-assembly of complex two-dimensional (2D) and three-dimensional (3D) nanostructures using DNA as a functional material. In a process driven by Watson-Crick base pairing, short single-stranded DNA staple strands guide a long single-stranded DNA scaffold to fold into a pre-programmed structure. In this process, the sequences of the staple strands control the shape of the resulting DNA origami nanostructures. This way, structures of arbitrary shapes can be created.[34] By prescribing functional moieties on staple strands, various types of objects, such as input receiving units or signal transduction units, can be positioned on the DNA origami surface with nanometer precision.[35] This large set of designing possibilities in terms of arbitrary shapes and functionalities, nanometer precise positioning of various chemical modifications in combination with the high stability of DNA itself and a simple one-pot self-assembly makes DNA origami structures ideal candidates for the development of nanodevices.

DNA origami nanodevices are classically separated into the two classes of DNA origami biosensors and DNA origami nanorobots /-machines. While the main purpose of DNA origami biosensors is the detection of molecular inputs, the focus of DNA origami nanorobots lies in the performance of different output operations. For each of these classes, already a number of exciting nanodevices have emerged that utilize the unique advantages offered by DNA origami to address some of the aforementioned requirements for smart nanodevices. The broad variety of molecular inputs receivable by DNA origami nanostructures, for example, has been demonstrated in DNA origami-based biosensors. Here, different binding-based sensors capable of detecting nucleic acids,[38–41] messenger RNAs,[42] specific metal ions,[43] as well as various protein targets including malaria biomarker,[44] platelet-driven growth factor[45] and thrombin[46] at the single-molecule level have been developed.

Besides solely monitoring the presence of specific molecules, DNA origami nanodevices additionally were shown to perform sophisticated computational tasks and output operations. For example, DNA origami nanodevices have been realized capable of releasing or taking up a cargo,[47–49] performing a rotational motion[50] or a chemical reaction[51], and processing logic functions[49,52] – a linkage between input and output operations which becomes increasingly more important with rising complexity of the whole system. Moreover, DNA walker systems have been realized in which DNA

walking strands move steadily and progressively along a track driven by DNA fuel.[53–55] These systems evolved from molecular switches that respond to environmental inputs by transitioning between two or more predefined states and can be combined with cargo transport systems[56] or can be used as signal amplifiers.[57] The concept of molecular switches has also been used to build nanodevices for molecular information coding.[58] Here, structures reconfigure intrinsic patterns while keeping their outline the same which can be used for steganography on the nanoscale: Only when a set of correct keys is added, the cryptographic data is translated into readable patterns.

While these DNA origami nanodevices exemplify the broad range of potential applications, the development of smart nanodevices is so far still hindered by several aspects. Most of the existing DNA origami nanodevices are designed and optimized to perform only one specific operation upon activation by one or more inputs from one specific molecular class. To achieve the highest possible degree of proper functionality, both the unit receiving the inputs and the unit performing the output operation mostly are incorporated into the core DNA origami structure.[35,59–62] This on the one hand creates a tight link between the input and output units, and, on the other hand, makes it difficult to expand the nanodevices further for a broader range of applications. The input and output units are not modularly exchangeable as this would greatly impact the functionality of the core DNA origami structure. As a result, the incorporation of new input/ output units in most cases would necessitate developing and optimizing the DNA origami nanostructure from scratch. Weakening the linkage between input and output units while still maintaining a high degree of functionality, therefore, presents one main challenges when developing a universal DNA nanodevice. Besides being highly specialized, the concentration ranges at which DNA origami nanodevices are responsive for their inputs are fixed by the affinities of the inputs for the input receiving units and span, for single site binding, around two orders of magnitude centered on the dissociation constants of the system-input complexes.[35,63] For technological applications, strategies are required, which allow to tailor this responsive window to input concentrations of interest. Moreover, while DNA origami structures themselves are often complex in nature, when used for nanodevices, they can perform only relatively simple bio-computational tasks and output operations.[35,59,61,64] In combination, this limits wide-spread technological applications of DNA nanodevices. The development of new DNA nanodevices is further hindered by the fact that the detection of the generated outputs often requires low-throughput complex analytical techniques, such as for example atomic force microscopy (AFM), optical tweezers, or fluorescence microscopy (FM).[35,37] Improving the signal output generated by the nanodevice is, therefore, another challenge when developing a universal nanodevice. While all of these challenges have been addressed individually – at least partially, overcoming them all in a single nanodevice was not possible up to now.[35,59–61] However, only when combined, the different aspects of DNA nanodevices can unfold their full power in technological applications.

Nature has developed an effective strategy for tackling many of these challenges with a single approach – transferring information by allostery. Allostery describes the mechanism through which the binding of an input at an active site of a biological macromolecule is changed by the binding of a second input (effector) to another distal site. This can either result in an increase (allosteric activation) or decrease (allosteric inhibition) in input binding. Allostery is intrinsic to the control of many biological processes in living cells including metabolism and signal transduction.[65–67] In these

processes, it enables a defining principle of life – the ability of living organism to adapt biological functions to ever-changing environmental conditions. Allostery achieves this by enabling signal transduction[68,69] and amplification[69,70], logic gating[71,72], and positive and negative cooperative behavior[73,74]. These mechanisms all address problems which – in their combination – are so far unsolved for DNA nanodevices. The ability to precisely control or mimic allosteric information transfer when modularly combining different functionalities in DNA nanodevices, therefore, would be a milestone in the process of developing smart nanodevice.

Allosteric processes generally are defined by two criteria which distinguish them from other regulatory mechanisms. First, the effector – which is chemically distinguishable from the input – binds at a site that is spatially separated from the binding site of the substrate. Second, the effector induces a change in a functional property of the macromolecule.[65,67] Despite its importance for biology, the exact underlying molecular mechanism of allostery so far still is unknown.[67,75] In fact, already Monod referred to it as the second secret of life, second only to the genetic code.[66] Aiming to shine light on this secret, numerous models have been developed.[67,75–80] The current understanding of allostery is based on the so-called ensemble model of allostery[81,82]. The model views an allosteric macromolecule as an ensemble of states which show different binding affinities to the input. The full free energy landscape of the system is modulated in presence of an effector. This shifts the thermodynamic equilibrium between the different states, resulting in a change of input binding to the system. This is exemplarily shown for allosteric activation of a two-state system in Figure 2. The main parameters determining allosteric behavior consequently are the relative free energies of all possible states and the energy barriers of the transitions between the states in the presence versus the absence of an effector.

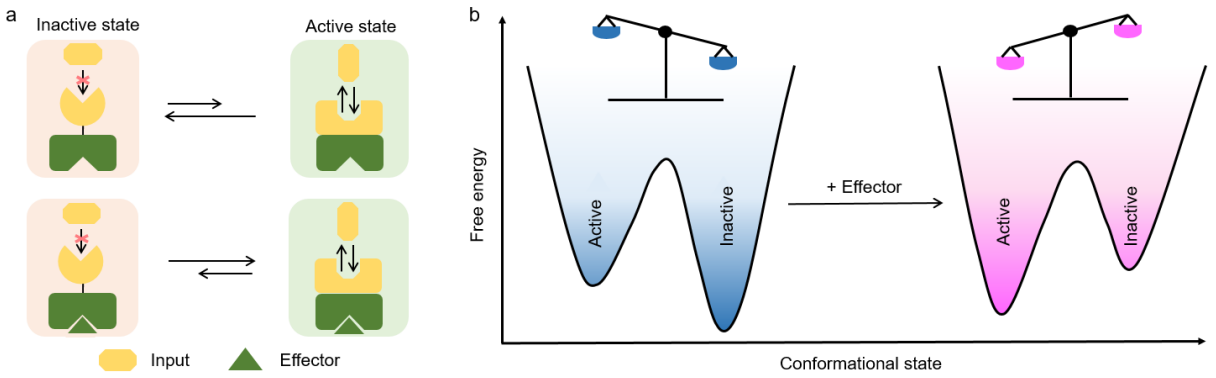

Figure 2: Allosteric activation via a two-state system. (a) Simplified illustration of an allosteric system with one input binding site (yellow) and one effector binding site (green). The system switches between two distinct conformational states (inactive state and active state). The input binding site is designed to bind to an input only in the active state of the system. This links the conformational equilibrium of the system to input binding. Binding of an allosteric effector shifts the thermodynamic equilibrium between the different conformational states towards the active state, resulting in an increase in input binding to the system. (b) Simplified free energy landscape of the system shown in (a) following the binding of an effector which stabilizes the active state of the system.

This work focuses on introducing allosteric information transfer into DNA origami nanostructures to build smart nanodevices. It first focuses on its implementation in existing DNA origami biosensors to address specific of the aforementioned challenges

explicitly for these systems, broadening their applicability (see Chapter 1.1 and Chapter 1.2). Subsequently, the developed concepts are all integrated into a single modular DNA origami structure, resulting in the development of a smart DNA origami nanorobot (see Chapter 1.3). This work guides through the (further) development of three different DNA origami nanodevices. It progresses from a static structure over a dynamic two-state structure to a two dimensional network of two-state systems. Each iteration results in an increased complexity of the underlying DNA origami structure, accompanied by a corresponding enhancement in capabilities and functionalities provided by allostery through information transfer (see Figure 3).

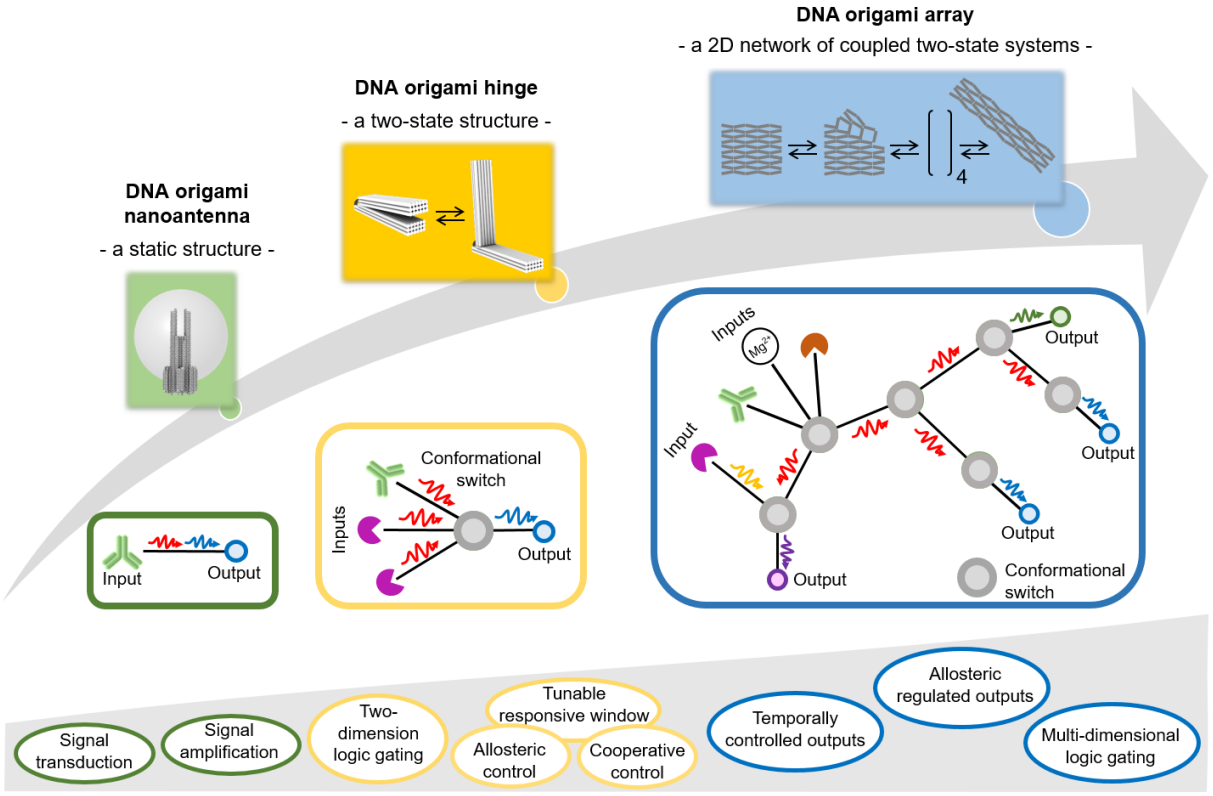

Figure 3: Overview of (further) developed smart DNA origami biosensors and nanorobots. The complexity of the functionalities achievable with the different nanodevices increases from left to right. Left: Schematic representation of a DNA origami nanoantenna – a static DNA origami structure with an attached plasmonic nanoparticle. Incorporation of a sensing assay in this structure enables receiving a single environmental input and transducing it into an amplified optical output signal. Middle: Schematic representation of a DNA origami hinge – a dynamic DNA origami structure which can switch between two conformational states. One of the states is designed with input receiving units for input binding and an output unit to generate an optical signal. This links the conformational equilibrium of the structure with input binding, creating a modular biosensing platform capable of responding to different environmental inputs. Implementing mechanisms of allosteric and cooperative control allows to tune the responsive concentration range of the biosensor. Besides tuning the nanodevices response, the implementation of multiple input receiving units based on the principle of user-programmable Boolean logics, allows to generate quantitative YES/NO answers from different input combinations. Right: Schematic representation of a reconfigurable DNA origami array – a 2D-network of coupled two-state systems. Encoding multiple input receiving units and output operation units into the different two-state systems paves the way for the creation of a smart DNA origami nanorobot capable of receiving different inputs and yielding multi-level logic gated and allosterically regulated output operations under temporal control.

This thesis consists of five chapters. A more detailed description of the research objectives and approaches in this chapter is followed by an overview of the theoretical principles needed for the understanding of the systems developed in this work (Chapter 2). The methods used in this work are described in Chapter 3. Chapter 4 represents a summary of the publications and sets them in the context of the overall framework of this thesis. An outlook can be found in Chapter 5.

1.1 EXPANDING THE INPUT SPECTRUM OF DNA ORIGAMI NANOANTENNAS

Tackling the aforementioned challenge of making DNA nanodevices accessible to low-tech readout devices, generally requires signal amplification strategies. This is achieved by molecular amplification mechanisms[83–86] or physical signal enhancement[87–90] of the output signal itself. Excellent progress towards combining DNA nanodevices with physical signal amplification strategies has been made by the development of DNA origami nanoantennas.[39,91,92] DNA origami nanoantennas rely on the specific arrangement of plasmonic nanoparticles and a single fluorescent molecule positioned in their close proximity in the so-called hotspot region. This tailored positioning enhances the fluorescence of the molecule several fold by plasmonic effects. Recently, we expanded this concept from solely enhancing single fluorescent molecules to enhancing the signal of fluorescence-based diagnostic assays.[38] Here, we demonstrated the detection of single DNA targets specific to antibiotic resistant bacteria in heat deactivated blood serum. The signal amplification provided by plasmonic effects of the DNA origami nanoantenna allowed to increase the fluorescence signal up to a few hundred fold, enabling the detection of single DNA targets on a portable, low-cost and battery driven smartphone device. While this demonstrated the suitability of DNA origami nanoantennas for facilitating the detection of diagnostically relevant molecules, the spectrum of inputs is currently limited to nucleic acids. This limitation does not only apply to DNA origami nanoantennas but represents one of the main challenges when developing DNA origami-based biosensors in general. The construction of DNA origami structures capable of responding to targets not directly interacting with DNA so far scarcely has been explored.[40,41] Hence, general strategies on how to incorporate recognition elements for inputs that go beyond inputs directly interacting with DNA are highly sought after.

A promising strategy potentially capable of providing means to expand the utility of the DNA origami nanoantenna as well as other DNA-origami-based biosensors for a wider range of inputs and possible diagnostic applications has been developed recently.[93,94] Inspired by the principle of naturally occurring signaling molecules – which switch between conformational states as a function of environmental inputs in order to generate output operations – the Ricci group designed nanoswitch systems for allosteric information transfer. DNA containing a fluorophore-quencher pair is used as a scaffold to attach specific recognition elements and transduce target detection through a fluorescence output. In absence of an antibody target, the nanoswitch adopts a stem-loop conformation that opens upon target binding, separating the fluorophore-quencher pair and resulting in a fluorescence signal. With this class of nanoswitch, different antibody targets can be simultaneously detected.[95] A detection limit in the nanomolar range was achieved[95] and the dynamic range of the response possibly can be tuned by varying the sequence of the stem similarly as shown for other two-state systems[96].

In Chapter 4.1, it is demonstrated that the sensing capabilities of DNA origami nanoantennas can be expanded to inputs that go beyond the realm of nucleic acid by incorporating an allosteric nanoswitch systems in their hotspot.

1.2 TWO-STATE DNA ORIGAMI STRUCTURE AS A PLATFORMS TO BUILD A MODULAR AND TUNABLE BIOSENSOR

The challenge of spatially decoupling input receiving units and output operation units while maintaining their functionalities, can be addressed by mimicking the switching principle of naturally occurring signaling molecules[11–13] between an active and an inactive state. Here input receiving units are linked to output operations through a relatively simple conformational change of the signaling molecule itself. This way, even if input receiving units and output operation units are positioned on spatially separated locations on the nanodevice, they can interplay with each other mediated by the conformational change.[35,59]

One of the first designs of a DNA origami biosensor which is based on this principle was reported by Andersen *et al.*[97]. They folded two dimensional DNA origami to a box with a lid which opens in response to DNA binding. Closing of the lid is achieved by introducing complementary single-stranded DNA (ssDNA) overhangs on the lid and on one of the six cube sides. To enable opening of the lid, the ssDNA overhangs on the lid are designed to contain not only the sequence required for closing the cube, but also a single-stranded toehold for strand displacement by the target DNA. The lid and one of the six cube sites is equipped with an acceptor fluorophore and a donor fluorophore, respectively, which comprise a signal transduction element. In the closed state of the DNA origami box, the donor and acceptor fluorophore are in close proximity resulting in efficient *Förster* resonance energy transfer (FRET). Upon opening of the lid via toehold-mediated strand displacement reaction, the donor and acceptor fluorophores are separated, leading to a decrease in FRET efficiency. The spatial seperation of the input receiving units and signal transduction unit enabled to broaden the range of environmental inputs by simply adapting the input receiving units for other inputs.[98] While the DNA origami box can be successfully used to detect different environmental inputs it suffers from long response times in the range of minutes. In attempt to create actuating devices with much faster response time, Marras et al.[99] equipped a hinge-like DNA origami structure[100] with short complementary ssDNA ends on its opposing arms. These ends are designed to rapidly hybridize or de-hybridize in response to changes in cation concentrations. As such, when the cation concentration changes, the structure switches from open to closed, or vice versa. Similar to the DNA origami box, a FRET-probe is used to optically visualized the conformational state of the DNA origami structure. With this design, response times in the millisecond range were achieved.

These two-state DNA origami structures are exceptionally suited for spatially decoupling different units of biosensors. However, they so far focus on the implementation of relatively simple input receiving units detecting only a specific class of molecular inputs and – besides very few exceptions – only detect inputs that directly interact with DNA. They do not explore the great potential of modularly combining

multiple (different) input receiving units as means to perform output operations in response to combinations of inputs of different molecular classes and to tune both their responsive concentration range and selectivity.

A biosensor consisting of multiple input receiving units and one output unit which are decoupled through the DNA origami structure itself is reported in Chapter 4.2. Using DNA origami as a link between the input and output units opens up the possibility of communication between them, enabling the response to a broad range of different environmental stimuli including DNA, antibodies, antigens, and restriction enzymes. Besides solely monitoring one input at a time, this system allows to generate outputs from input combinations by implementing user-programmable Boolean logics. Further, it is shown that by modularly combining multiple input receiving units, mechanisms of cooperative and allosteric control can be implemented. This allows tuning of the responsive window of the biosensor. Moreover, by implementing the same input receiving unit multiple times in the structure, the selectivity of the response can be greatly improved.

1.3 2D NETWORK OF TWO-STATE SYSTEMS TO BUILD A SMART NANOROBOT

As described earlier, the development of smart nanodevices is so far hindered by the absence of universal strategies to couple multiple input receiving units and multiple output operation units together in a rational manner – ideally using hierarchical organization as a communication tool.[101–103] This greatly restricts the possibilities when performing a series of multiple processing operations and output operations in response to different input combinations on nanodevices. If each unit is designed and optimized separately, they must be combined into one programmed modular structure later on. However, when going to the nanoscale, rational organization of the different units in complex systems is difficult to achieve post-assembly.[101] Hence, strategies which allow organizing different units with different functionalities in a pre-programmed and hierarchical manner during assembly of the nanostructure are of great interest. This, on the one hand, would enable creating cascades of different input receiving units and thus allow processing different series of coupled Boolean logic gates with the corresponding inputs, forming the basis for complex computation processes. On the other hand, this would also allow different output processes to be induced both in parallel and in series with a pre-defined order. In combination, this would enable the development of smart nanorobots (see Chapter 4.3).

One possible strategy to achieve this would be to start with a platform consisting of already coupled systems. By implementing functionalities, such as input receiving units or output operation units, to each individual system, these functionalities would automatically be interconnected by the underlying platform. Commonly used systems which are easily encodable with functionalities are two-state systems as described in Chapter 1.2. Thus, a platform in which two-state systems are coupled together in a well-understood manner would be an ideal candidate for this. Ideally, all of the coupled two-state systems additionally were to be identical, such that they could be encoded with functionalities in the same, universal manner.

Reconfigurable DNA origami array systems[104–106] are an exciting new class of DNA origami structures which have great potential in this context. They are composed of

multiple structurally similar building blocks, so-called anti-junctions. Each anti-junction can exist in two stable stacked conformations between which it can switch via an unstable open conformation, thus forming a two-state system. In DNA origami array structures, anti-junctions are coupled together by a scaffold DNA strand. This forces them to initially all adapt the same conformation. A global reconfiguration of these structures can be induced by addition of trigger DNA strands that hybridize to one side of the structure. This triggers the addressed anti-junctions at the edge of the structure to change their conformation. Due to the coupling between all anti-junctions, this conformational change results in the formation of unstable open conformation at neighboring anti-junctions. Driven by the reduction of free energy, the conformational change of the neighboring anti-junctions subsequently occurs, again forming open anti-junctions at their neighboring positions. This process repeats in a diagonal step-wise manner until all anti-junction in the structure are converted. Thus, if different nanodevice units were to be encoded into individual anti-junctions, this would, in principle, allow to use DNA origami array structures as platforms to couple different nanodevice units together in a rational manner and thus to perform multi-level processing and multiple output operations.

Different strategies to implement input receiving units and output operation units in DNA origami array systems have already been developed.[58,107–109] Most of them make use of the overall conformational change of the whole DNA origami array structure as a communicational medium between the different nanodevice units. The great potential of encoding different units into individual anti-junctions as means to couple different nanodevice units together in a rational manner, however, has not yet been explored. Realizing this requires answering three fundamental questions which are addressed in Chapters 4.3.1 – 4.3.3:

1. What is the molecular reconfiguration pathway and what is the exact energy landscape of the multi-step reconfiguration process? A deep understanding of this is necessary as it describes the coupling between the individual anti-junctions.
2. Can we rationally alter the energy landscape both globally and between specific intermediates? This would allow adapting the coupling between specific anti-junctions by rational design and thus set the basis for the third question.
3. Can we couple these alterations in the energy landscape to different nanodevice units? Can we define universal design approaches to incorporate these units in individual anti-junctions of the system? And can we use the multidimensionality of the system to couple a multitude of functionalities together to build up a smart nanorobot?

While especially the first two questions were already explored by initial AFM studies[104,105], AFM as a technique did not allow to resolve reconfiguration kinetics and the exact pathways due to its low temporal resolution and invasiveness. Using FRET probes for signal transduction, the energy landscape of the reconfiguration process was explored at the single-molecule level and the effect of alterations in the design on specific steps of the energy landscape determined (see Chapter 4.3.1 and Chapter 4.3.2). This allowed defining strategies to design input receiving, output operation and timing units which, in principle, can be encoded into any anti-junction in the system. The benefits of this approach based on coupled two-state systems were

then demonstrated by modularly combining different units to enable multi-level Boolean gating, ordered and timed processes, signal amplification and allosteric inhibition (see Chapter 4.3.1 and Chapter 4.3.3). The step from a single two-state system to a network of multiple coupled two-state systems thus represents the evolution of nanodevices from a single dimension to the multidimensional space.

2 THEORETICAL BACKGROUND

2.1 DNA ORIGAMI AS BUILDING BLOCK FOR NANODEVICES

For the development of a smart DNA origami nanodevice which ideally achieves arbitrary input – output combinations, strategies which allow to assemble different input receiving units and output operation units into one modular system are required. To ensure the proper functionality of each unit and also the interplay between different units, they have to be positioned at pre-defined positions with precise distances between each other. This can be achieved using the DNA origami technique[34]. It allows creating nanostructures of any arbitrary shape in a simple self-assembly process. Moreover, its exquisite nanoshape and nanoposition control allows for the precise placement of various modifications. Implementing multiple modifications at specific positions within DNA origami structure provides means to incorporate input receiving units and output operation units into the structure.[34,35] Therefore, it is crucial to understand the self-assembly process of DNA origami structures, what their central construction motif is and how different nanodevice units can be implemented based on different modifications.

2.1.1 THE DNA ORIGAMI TECHNIQUE

DNA origami is the technique of designing and fabricating 2D and 3D nanostructures using DNA as a functional material. In a process driven by Watson-Crick base pairing, short ssDNA “staple” strands (~ 20 – 50 base-pairs) guide a long ssDNA “scaffold” strand (~ 7000 – 9000 base-pairs) to fold into a pre-programmed structure (see Figure 4). In this process, the sequences of the staple strands, each complementary to different parts of the scaffold strand, control the shape of the resulting DNA origami structure. The self-assembly process is carried out in thermodynamic equilibrium by annealing the staple strands and the scaffold over a temperature ramp from 65 °C to 25 °C. This way, billions of identical structures can be synthesized in parallel.[34]

For the introduction of modifications (e.g. fluorescent labels, chemical tags, proteins, ssDNA extension) two different approaches can be used (see Figure 4): the staple strands themselves can be directly labeled with desired modifications in the so-called internal labeling method. In contrast, staple strands can be extended to provide overhangs to which a ssDNA bearing a desired modification can be attached via DNA hybridization.[34,35] Both these methods can be used to incorporate input receiving units and output operation units into DNA origami structures. The internal labeling approach is the method of choice for the incorporation of those nanodevice units whose proper functionality only is given if its individual components are positioned on the nanostructure with single-base pair precision. On the other hand, the external approach is ideally suited when adapting nanodevices for different input – output combinations post-synthetically.

For the communication between input receiving and output operation units, proximity often is used as the decisive criterion: DNA origami structures forming the basis for nanodevices often are designed to switch between different conformational states.

Implementation of input receiving units which bind to inputs only in one of the conformational states allows to couple the conformational equilibrium with input binding and thus to encode input-responsiveness into these systems. The conformational change then changes the proximity between the interacting players of the operation units resulting in the performance of a priory programmed output operation.[97–100]

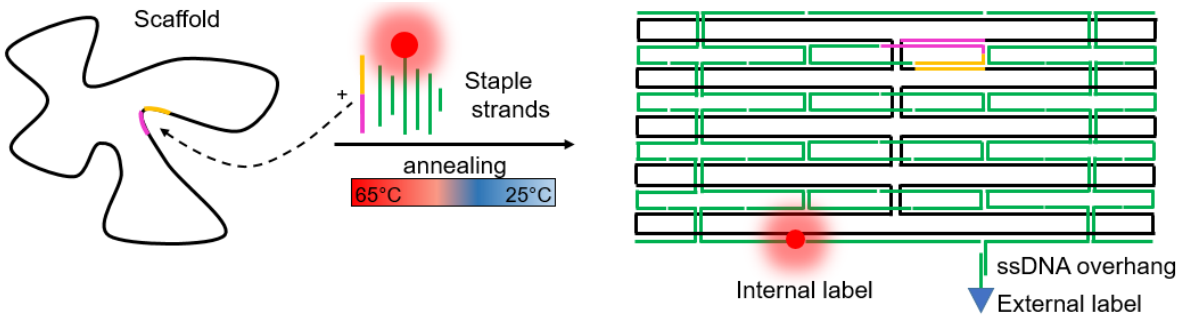

Figure 4: Principle of DNA origami self-assembly. A long ssDNA scaffold strand is folded into a 2D or 3D nanostructure guided by short staple strands. Upon hybridization, the scaffold strand is forced into the desired shape by short staple strands. Different modifications can be incorporated via short ssDNA overhangs (external label) post-synthetically or by including already modified staple strands (internal label).

2.1.2 HOLLIDAY JUNCTIONS AS CENTRAL CONSTRUCTION MOTIF

Holliday junctions are the central construction motives of DNA origami structures. As shown for DNA crystals[110], their properties may influence the shape of DNA nanostructures constructed from them. This makes understanding them both on a structural and energetic level important.

Holliday junctions are four-way junctions formed by the mutual exchange of strand connectivity between two duplex-DNA domains. Depending both on their sequence and solution environment, Holliday junctions adapt different conformations (see Figure 5a and Figure 5b). In the absence of sufficient cations in solution, their four arms are extended into a square-planar geometry (open conformation) to minimize Coulomb repulsion caused by the negatively charged backbones of the DNA building material. These repulsions can be shielded by binding of cations to the backbones, allowing the junction to fold into a more compact and stable conformation with pairs of helical arms coaxially stacked as duplexes. For this so-called stacked conformation, two stable isomers which differ in the choice of their stacking partners exist. They can be transformed into each other via the unstable open conformation through dynamic flipping of their helices.[24,111–117]

The transition kinetic between both stacked isomers is determined by the type of cations and as well as their concentrations. For example, Mg^{2+}-ions are extremely efficient in folding Holliday junctions. Decreasing their concentration in a certain concentration range allows to decrease the activation barrier (ΔE_A) for conformer switching (see Figure 5c), resulting in an increased transition kinetics. While several other multivalent metal ions are also suited for folding junctions, monovalent metal ions are extremely inefficient in doing so. Nevertheless, in combination with multivalent metal ions they can be used to tune the transition kinetics by screening electrostatic

interactions between the multivalent cations and the negatively charged backbone material.[112,116,118–120]

While solution conditions offer the great possibility to tune the transition kinetics between the different isomers of Holliday junctions, the relative population of their isomers is independent of them.[119] It can be derived from the difference in Gibbs free energy of both isomers ($\Delta_R G$) which first and foremost is determined by sequence-dependent stacking interactions.[121–123] Besides that, electrostatic potentials on junction stacking[120] and geometric constrains imposed at the junction[124], which both are also sequence-dependent, have been shown to influence the difference in free energy. As such, the relative population of both isomers is programmable by the junction sequence (see Figure 5d). By varying the junction sequence, Holliday junctions which are heavily biased towards one of the isomers as well as junctions with near-equal populations in each isomer have been fabricated.[114,124–127]

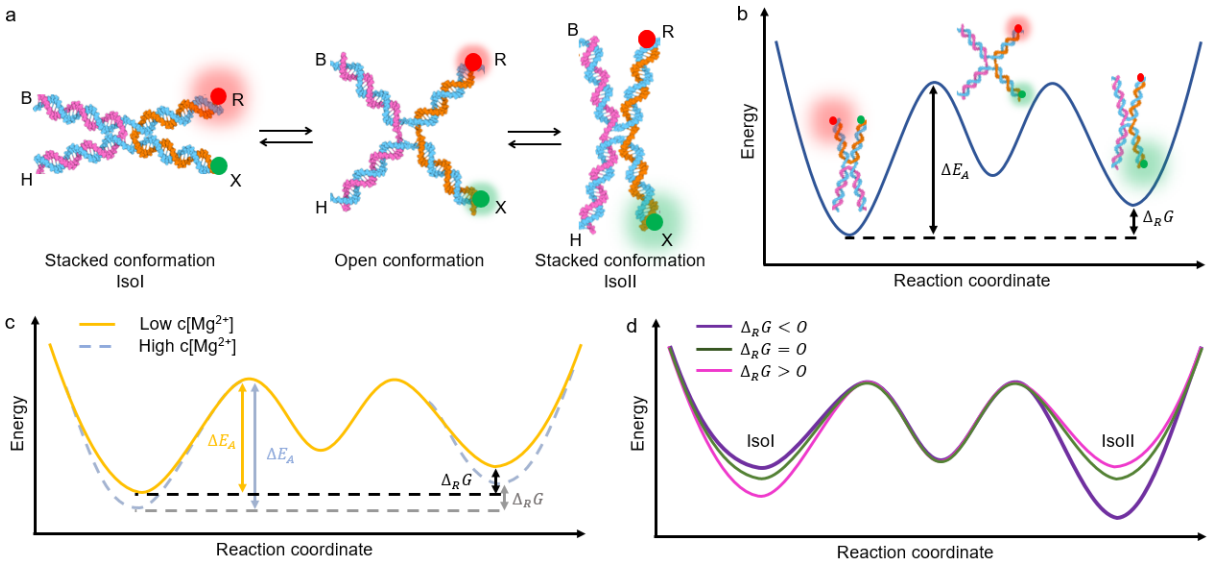

Figure 5: Principle of Holliday junctions. (a) Schematic illustration of a four-way Holliday junction formed by two duplex-DNA domains. The helical arms are depicted B, H, R and X. The Holliday junction switches between two stable stacked conformations (IsoI and IsoII) via an unstable open conformation. The stacked conformations differ in the choice of their stacking partners: in the IsoI conformation B stacks on H and R on X, whereas in the IsoII conformation B stacks on R and H on X. Placing a FRET probe (red and green circle) on different staples around the Holliday junctions offers means to visualize this switching process in single-molecule fluorescence experiments. (b) Simplified energy landscape for the structure shown in (a). (c) Mg^{2+}-ion concentration influences the energy landscape of the switching process of Holliday junctions. In a certain concentration range, the activation barrier for conformer switching can be decreased by lowering the Mg^{2+}-ion concentration. This in turn allows tuning the transition kinetics between the different. (d) Influence of the junction sequence on the energy landscape of the switching process of Holliday junctions. The sequence determines $\Delta_R G$ and thus in turn the relative population of both stacked conformations. By varying the sequence Holliday junction with $\Delta_R G < 0$, $\Delta_R G > 0$ and $\Delta_R G = 0$ can be fabricated.

2.2 FLUORESCENCE OF ORGANIC DYES AS A READOUT FOR NANODEVICES

Especially when optimizing and tuning the properties of nanodevices capable of performing output operations in response to inputs, a detailed understanding of how

their different components behave and interact with each other is necessary. This can be realized best using single-molecule approaches. It takes advantage of its unparalleled sensitivity to obtain a full distribution of values of a specific observable within a sample. Monitoring the behavior of individual molecules, therefore allows obtaining detailed insights into the properties of a systems involving static and dynamic heterogeneities – properties which are not accessible to ensemble measurements.[128,129] Various analytical methods with single molecule detection capability, such as for example AFM,[130,131] transmission electron microscopy (TEM)[132,133] or FM[134,135] have been developed. While all of these methods provide excellent structural information, only the fluorescence approach allows measuring the kinetics and thermodynamics of different processes with high resolution in real-time in a comparably low-invasive fashion.[128,129] Given these advantages, fluorescence of emitters has established as a powerful readout method when developing nanodevices with quick response times, high contrast and good sensitivity.

The intrinsic fluorescence of most biomolecules is, however, weak and not specific in the spectral range generally used in fluorescence-based single-molecule studies. Shining light on these otherwise non-visible biomolecules and their processes, thus requires a transduction unit designed to transduce these processes in form of a change in fluorescence. Organic dyes have been proven to be immensely useful for this.[134,136] They exhibit intrinsic fluorescence properties which can be influenced by their local environment. Attaching organic dyes to biomolecules of interest and monitoring their fluorescence emission, therefore not only allows to localize the biomolecule they are attached to but also to investigate possible biochemical processes they are involved in. Therefore, it is crucial to understand what fluorescence is, which photophysical and photochemical processes influence the fluorescence of organic dyes and how its analytic techniques function.

2.2.1 PRINCIPLES OF FLUORESCENCE AND RELATED PROCESSES

Organic dyes – molecules that exhibit fluorescence usually in the visible range – bear a strongly delocalized π-electron system in which their intrinsic fluorescence properties are programmed. Their energetic states are comprised of different distinct electronic states (S). Each electronic state is separated into different vibrational levels (v) that each is subdivided into different rotational levels.[134] The *Jablonski* diagram shown in Figure 6a gives a comprehensive overview of the basic energetic states of organic dyes and the process of fluorescence that can occur after their illumination with light of suitable energy. Besides that, the basic photophysical processes influencing the fluorescence emission of organic dyes are also illustrated in Figure 6a.

At room temperature, organic dyes usually occupy the lowest vibrational level of the electronic ground state (S_0). They can be promoted to one of the vibrational levels of an electronic excited state S_n ($n \geq 1$) through absorption of a photon (excitation rate, k_{ex}). This process only can occur if the energy of the photon of the excitation light suits the energy difference between the S_0 state and one of the S_n states. As such, the electronic state to which an organic dye is excited depends on the energy of the excitation light. When an organic dye is excited into a higher vibrational level of an electronic state S_n ($n > 1$), subsequently follows (~ 10^{-12} – 10^{-9} s) the non-radiative release of the vibrational energy to the environment through collision with molecules in its local environment (vibrational relaxation rate, k_{vr}). From the lowest vibrational

energy level of an electronic excited state S_n ($n > 1$) follows the rapid (~ 10^{-14} – 10^{-11} s) relaxation of the organic dye into a vibrational level of a lower electronic excited state via internal conversation (internal conversation rate, k_{ic}). The sequence of these non-radiative relaxation pathways – vibrational relaxation and internal conversation – repeats until the lowest vibrational level of the first electronic exited state (S_1) is reached. When a dye has arrived to the lowest vibrational level of the S_1 state, it is metastable, and usually remains there for a few nanoseconds. From this state, organic dyes can return into their electronic ground state via the emission of a photon, the so-called process of fluorescence (fluorescence rate, k_{f}). Fluorescence usually results in an excited vibrational level from which it relaxes to the lowest vibrational level of the S_0 state. This in combination with the fact that organic dyes are preferentially excited into higher vibrational levels leads to an emission spectrum that is red-sifted with respect to the absorption spectrum (see Figure 6b). This phenomena, known as the Stokes shift, enables to filter fluorescence photons from scattered excitation light based on their different wavelength.[134,137,138]

Besides fluorescence, relaxation of an organic dye from the S_1 state to the S_0 state can occur via several other radiative and non-radiative processes. For example, non-radiative relaxation from the S_1 state to the S_0 state can occur via internal conversation. Organic dyes can also relax from the S_1 state over the first triplet state (T_1) to the S_0 state. While relaxation from the S_1 state to the T_1 state is a non-radiative process, called intersystem-crossing (intersystem crossing rate, k_{isc}), relaxation from the T_1 state can occur either non-radiative or radiative (phosphorescence rate, k_{p}). Besides the mentioned processes – dependent on the environment of the organic dye – several other non-radiative energy transfer processes can result in the depopulation of the S_1 state.[134,137,138]

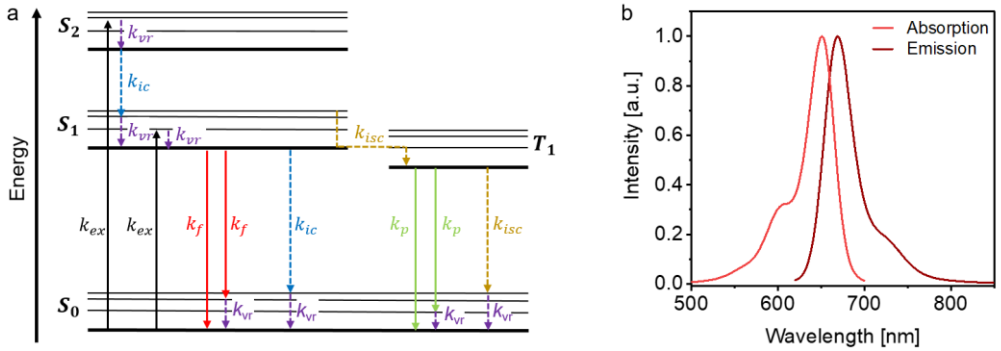

Figure 6: Principles of fluorescence. (a) Simplified representation of a *Jablonski* diagram illustrating the electronic levels of an organic dye and possible transitions between it. The electronic states (bold lines) are depicted by S_0 (electronic ground state), S_1 (first excited state), S_2 (second excited state) and T_1 (first triplet state). Each electronic state is divided into multiple vibrational energy levels (thin lines). Radiative transitions between the states are represented as vertical arrows: excitation (black), fluorescence (red) and phosphorescence (green). Non-radiative pathways are represented as vertical, dashed arrows: vibrational relaxation (purple, dashed), internal conversation (blue, dashed), intersystem crossing (brown, dashed). (b) Absorption (red) and fluorescence (dark red) spectrum of ATTO647N dye attached to DNA.

The main characteristics of organic dyes are the fluorescence quantum yield (Φ) and the fluorescence lifetime (τ). The fluorescence quantum yield of an organic dye is the ratio of the number of emitted photons through fluorescence (n_f) to the total number of absorbed photons during excitation (n_{abs}). The average time a molecule remains in

the excited state S_1 before returning into the ground state S_0 is the so-called fluorescence lifetime. Both these parameters dependent on the rate constant of fluorescence (k_f) an the rate constants of all its competing processes. In the following equations, all rate constants of the competing intrinsic relaxation processes and all rate constants of the competing environmental decay pathways are combined to form only one specific constant k_nf and k_q, respectively.

$$\Phi = \frac{n_f}{n_{abs}} = \frac{k_\mathrm{f}}{k_\mathrm{f} + k_{nf} + k_\mathrm{q}} \tag{1}$$

Assuming first order kinetics for all relaxation processes, the fluorescence lifetime is given by the inverse sum of all decay rate constants.

$$\tau = \frac{1}{k_\mathrm{f} + k_{nf} + k_\mathrm{q}} \tag{2}$$

Measuring the fluorescence quantum yield or the fluorescence lifetime of an organic dye, therefore can be used to investigate the occurrence of environmental decay pathways and thus allows to draw conclusions on its environment.[134,137,138]

2.2.2 FÖRSTER RESONANCE ENERGY TRANSFER

One of the most popular fluorescence readouts when studying biomolecular processes at the single-molecule level is FRET. It is a non-radiative resonance energy transfer generated by intramolecular long-range dipole-dipole coupling between two molecules with one acting as a donor and the other acting as an acceptor. The extent of FRET for a chosen FRET pair depends primarily on their fluorescence quantum yield and the distance between the donor the acceptor. When attached to a biomolecule of interest, a FRET pair thus provides the possibility to measure the distance between the positions the donor and the acceptor is attached to the biomolecule.[134,139,140] Besides FRET between two organic dyes, a similar concept in which the acceptor molecule is non-emissive (dark quencher) can be used.

Whenever a donor is in its S_1 state and an acceptor, whose absorption spectrum overlaps sufficiently with the emission spectrum of the donor is in close proximity, relaxation of the donor from the S_1 state to the S_0 state can occur via FRET (see Figure 7a,b). Besides FRET, relaxation of the donor from the S_1 state to the S_0 state can occur via several other competing processes (see Chapter 2.2.1 and Chapter 2.2.2.1). The ratio of FRET emission among the total amount of processes leading to the relaxation of the donor is the FRET efficiency (E_{FRET}). It depends on the FRET rate constant (k_{FRET}) and the rate constants of all its competing processes.

$$E_{FRET} = \frac{k_{FRET}}{k_\mathrm{f} + k_{nf} + k_\mathrm{q} + k_{FRET}} \tag{3}$$

The FRET rate constant can be expressed as:

$$k_{FRET}(r) = \frac{9000\ln(10)\ \kappa^2\Phi_D}{128\pi^5 N_A r^6 \tau_D} \int_0^\infty \frac{F_D(\nu)\epsilon_A(\nu)}{\nu^4}\, d\nu \tag{4}$$

where r is the distance between the donor and the acceptor, κ is the relative dipole moment orientation of the donor and acceptor, Φ_D the donor quantum yield, N_A is the Avogadro`s constant, τ_D is the fluorescence lifetime of the donor, $F_D(\nu)$ represents the normalized donor emission spectrum, ϵ_A is the molar extinction coefficient of the acceptor at frequency ν. When attached to a biomolecule, free rotation and thus a randomized relative orientation of their dipole moments can be assumed. In this case κ^2 is constant with a value of $\frac{2}{3}$.

Besides r, all of the terms in Equation 4 are physical constants or can be assumed to be constant. Assuming free rotation of the donor and acceptor, a constant overlap integral and donor quantum yield, they can be combined in one constant, the so-called *Förster* radius (R_0).

$$k_{FRET}(r) = \frac{1}{\tau_D}\left(\frac{R_0}{r}\right)^6 \tag{5}$$

where R_0 is the donor-acceptor distance at which the transfer efficiency is 0.5.

If besides FRET no other non-radiative relaxation process occurs, the FRET efficiency is given by:

$$E_{FRET} = \frac{R_0^6}{R_0^6 + r^6} \tag{6}$$

As can be seen from Equation 6 and in Figure 7c, E_{FRET} only can be used to determine distances in the range of $r = 0.5\,R_0$ to $r = 2\,R_0$. With R_0 values of commonly used FRET pairs in the range between 2 – 10 nm, FRET is suitable for measuring distances in the low nanometer range.

After correcting for the cross-talk and background, E_{FRET} can be experimentally determined using the relative fluorescence intensity or lifetime of the donor, in the absence (τ_D and I_D) and presence (τ_{DA} and I_{DA}) of the acceptor.

$$E_{FRET} = 1 - \frac{I_{DA}}{I_D} = 1 - \frac{\tau_{DA}}{\tau_D} \tag{7}$$

When interested in qualitative changes of the distance between the donor and acceptor, it is sufficient to determine relative changes in E_{FRET} based on the

fluoresence intensity of the donor in the presence of the acceptor (I_{AD}) and the fluorescence intensity of the acceptor in presence of the donor (I_{DA}).[134,139,140]

$$E_{FRET_{Rel}} = \frac{I_{AD}}{I_{AD} + I_{DA}} \tag{8}$$

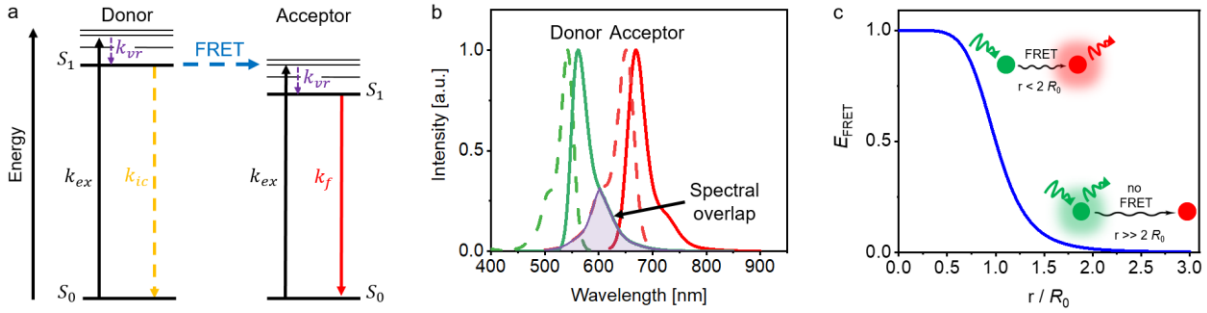

Figure 7: Principles of FRET between two organic dyes. (a) Simplified *Jablonski* diagram illustrating FRET between a donor dye and an acceptor dye. After excitation, relaxation of the donor dye occurs via vibrational relaxation and internal conversation. Through FRET the donor dye passes on its excitation energy to an acceptor dye, resulting in its excitation. The acceptor dye can return into its electronic ground state via fluorescence. (b) Absorption (dashed) and fluorescence (line) spectrum of the donor ATTO542 dye (green) and the acceptor ATTO647N dye (red) and their spectral overlap (blue). For simplicity, only the spectral overlap and not the overlap integral is shown. (c) Distance dependency of FRET efficiency for a FRET pair with a R_0 value of 1. Depending on the distance between both fluorophores, the excited donor fluorophore either relaxes via the process of FRET (r < 2 R_0) or via competing relaxation processes such as fluorescence (r >> 2 R_0). The FRET efficiency is highly sensitive to changes in distance between 0.5 R_0 and 2 R_0.

2.2.2.1 COMPETING PROCESSES OF FRET

The most common photophysical and photochemical processes that need to be considered when analyzing FRET experiments are fluorescence quenching by unwanted quenchers, transitions to dark and dim states, and photobleaching.[136,141,142]

Fluorescence quenching describes all processes in which the fluorescence of a dye is decreased through interaction with an external molecule. Quenching can occur by two different mechanisms. Dynamic quenching occurs when a dye relaxes from the S_1 state to the S_0 state through molecular contact with another molecule, called quencher, in its environment. Besides FRET, the most common non-radiative energy transfer mechanisms resulting in dynamic quenching are photo-induced electron transfer and electron exchange. The extent to which these process occur depends on both, the chosen dye-quencher pair and the distance between the dye and its quencher. Static quenching occurs whenever a non- or only weak fluorescent complex between a dye in the S_0 state and a quencher molecule in its close proximity is formed.[136,137,141]

Dark and dim states occur whenever a dye is promoted into a non-emissive state or a less emissive state. Spontaneous transitions between dark or dim and a fluorescent state result in reversible fluorescence intensity fluctuations, so called blinking.[136] Distinguishing them from dynamic changes within a sample can be challenging.

Besides that, they are the state from which photo-induced irreversible damage of the dyes structures, so-called photobleaching, occurs.

Both, blinking and photobleaching can be minimized by the removal of oxygen and the addition of a reducing/oxidizing system (ROXS) which functions both, as a triplet state and radical state quencher. The principle of a ROXS system is illustrated in Figure 8. A dye in its triplet state is rapidly reduced or oxidized in the presence of a reducing or oxidizing agent yielding a radical anion or radical cation. Radical anions or radical cations are depopulated by the complimentary oxidizing or reducing agent, respectively, resulting in the recovery of the dye in its ground state. In order to prevent photobleaching it is crucial that the reaction sequence of reduction and oxidation is fast.[136,143]

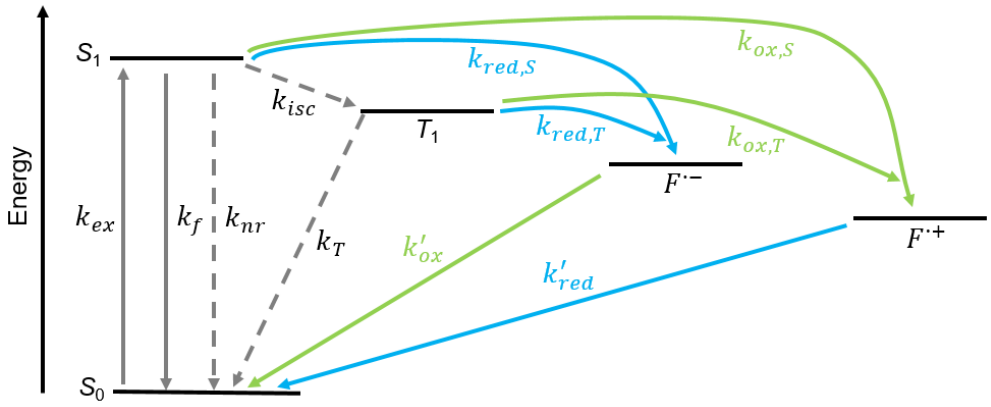

Figure 8: Concept of ROXS. Simplified *Jablonski* diagram of an organic dye with possible excitation and relaxation pathways. The electronic states (bold lines) are depicted by S_0 (electronic ground state), S_1 (first singlet state), T_1 (first triplet state), $F^{\cdot -}$ (radical anion state), and $F^{\cdot +}$ (radical cation state). In the presence of ROXS, triplet states and radical states are rapidly depopulated by oxidation and reduction reactions, resulting in the ground state of the dye.

2.2.3 SINGLE-MOLECULE FLUORESCENCE MICROSCOPY

Confocal fluorescence microscopy and total internal reflection fluorescence (TIRF) microscopy are the two most commonly used analytical techniques in single-molecule FRET experiments. While only confocal fluorescence microscopy provides access to fluorescence lifetime measurements, the great advantage of TIRF microscopy is that many individual molecules can be studied simultaneously.[137,138,144]

In a confocal microscopes (see Figure 9a) a laser beam is focused by a high numerical aperture (NA) microscope objective to a diffraction-limited volume which typically lies in the femto-liter range. Emitted fluorescence and backscattered laser light are then collected by the same microscope objective. A dichroic mirror is used to filter out the backscattered excitation light. This is possible due to the Stokes shift between the excitation light and fluorescence emission. Fluorescence is then focused by a microscope tube lens through a pinhole aperture. The pinhole serves to spatially reject out-of-focal-plane fluorescence and thus creates a diffraction-limited detection-volume. The excitation and emission volume generated by the high NA objective in combination with the pinhole are the main parameters influencing the signal-to-noise ratio that can

be achieved. For the detection of emitted photons, avalanche photo diodes (APDs) can be used. They are generally characterized by a high collection efficiency, fast response time, a high gain at a low dark count and offer the possibility to add a time-correlated single-photon counting (TCSPC) card for fluorescence lifetime measurements. Confocal microscopes generally enable to perform single-molecule measurements from both, molecules diffusing in solution and surface-immobilized molecules. To detect a single-molecule the excitation volume must be occupied with only one molecule. To ensure this, concentration of the fluorescent molecules in the picomolar range are used. When performing surface measurements, the movement of the sample with respect to the laser beam is necessary. This can be achieved by implementing a piezo-electric stage.[137,138,144]

In contrast, in a TIRF microscopes an area of several dozen microns in diameter is illuminated with an evanescent field. The evanescent field is generated at the interface of a glass or quartz coverslip and the sample by total internal reflection (TIR) of the laser beam. To achieve this requires directing a laser beam to the sample above the critical angle. Commonly used techniques for this include prism-type TIRF and objective-type TIRF. In prism-type TIRF microscopes the laser beam is coupled into a prism above the coverslip. In contrast, in objective-type TIRF microscopes (see Figure 9b) the laser beam is coupled through the extreme edge of a high-NA objective. The evanescent field generated by TIR of the laser beam then penetrates into the sample. The evanescent field intensity (E) decreases exponentially with increasing distance from the coverslip-sample interface (z) into the sample:

$$E(z) = E(0)\exp\left(-\frac{z}{d}\right) \tag{9}$$

where $E(0)$ is the intensity of the evanescent field at the coverslip-sample interface, and *d* is the exponential decay distance. The exponential decay of the evanescent field strongly reduces out-of-focus background and thus confines the illuminated volume in TIRF.

The exponential decay distance can be described by:

$$d = \frac{\lambda_0}{2\pi}\sqrt{(n_s^2\sin^2\theta_{in} - n_c^2)} \tag{10}$$

where λ_0 is the wavelength of the excitation light in vacuum, θ_{in} is the angel of the incident light, n_c is the refractive index of the coverslip, and n_s is the refractive index of the refractive index of the sample ($n_s < n_c$).

As shown in Equation 10, the penetration depth scales linearly with the excitation wavelength. Typical penetration depths lie between 100 – 200 nm, thus only molecules close to the surface are excited. A dichroic mirror is used to filter out the backscattered excitation light. The full illuminated area is captured frame by frame using electron multiplying charge-coupled device EMCCD or CMOS cameras.[137,138,144]

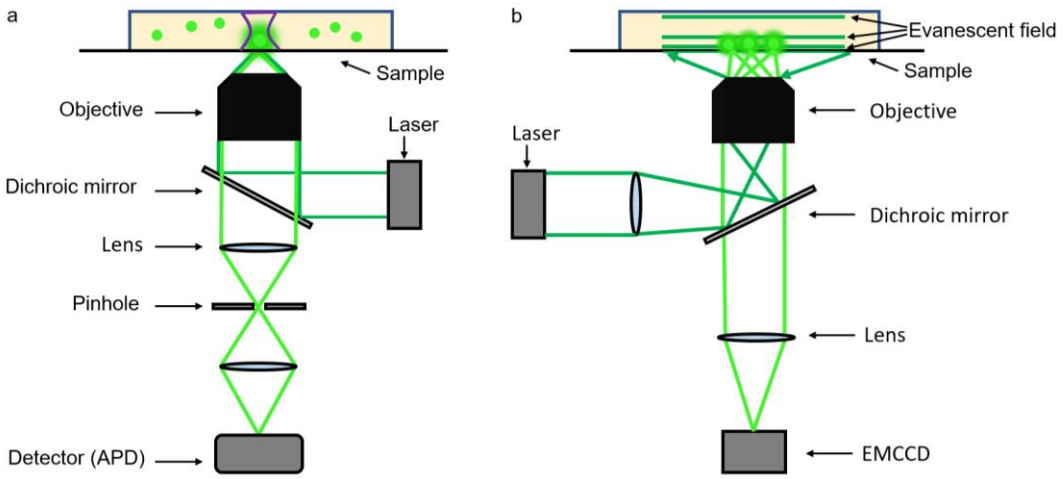

Figure 9: Simplified schematic drawing of two different microscope setups that are used in single-molecule fluorescence measurements. (a) Confocal fluorescence microscope. The objective focuses the light beam on a diffraction limited volume into the sample. Only molecules in this volume are excited. A dichroic mirror is used to filter out the backscattered excitation light. To further reduce the background signal, the out of focus light is rejected by a pinhole. APDs are used to detect the emitted photons. (b) Objective-type TIRF microscope. An area of several dozen microns in diameter is illuminated with an evanescent field. To achieve this, the excitation light of a laser is coupled through the extreme edges of a high-NA objective and directed to the sample at an angle that is above the critical angel. The exponential decay of the evanescent field with increasing distance from the coverslip strongly reduces out-of-focus background and thus confines the illuminated volume in TIRF. The emitted fluorescence is collected by an objective and detected with an EMCCD/CMOS camera.

2.2.4 PRINCIPLES OF FLUORESCENCE ENHANCEMENT BY PLASMONIC EFFECTS

While single-molecule fluorescence microscopy offers many advantages, it also suffers from one major drawback when it comes to possible technological applications: it is a low-throughput, expensive and complex analytical technique. Excellent progress towards simplifying single-molecule detection has been made by the introduction of physical fluorescence signal enhancement methods of fluorescent emitters (e.g. organic dyes, quantum dots).[87–90] By improving the signal-to-noise ratio of single fluorescent molecules using plasmon fields, these methods paved the way for the detection of single-molecules on cost-effective and mobile devices.[38,145] Besides simplifying single-molecule fluorescence detection, physical enhancement methods additionally allow to decrease the measurement time necessary to achieve a sufficient signal-to-noise ratio and simultaneously to push the concentration limit of single-molecule fluorescence detection.[146]

Plasmon fields arise from the interaction between light of a suitable wavelength (λ) and conduction electrons. They can be generated near different metal surfaces including the surfaces of noble metal nanoparticles. When a spherical metal nanoparticle with a diameter $d \ll \lambda$ is excited with light of a suitable wavelength and frequency, respectively, its conduction electrons are collectively displaced from their nuclei generating opposite charges on the nuclei's surface (see Figure 10a). The separation of charges gives rise to a restoring force through Coulomb attractions, ultimately resulting in a collective oscillation of the electrons. This oscillation only can be induced if the frequency of the excitation light corresponds to one of the metal nanoparticles

natural frequencies. The field strength of the plasmon field is determined by the interference of the electrical field from the excitation light and the field generated by the electron oscillation. If these resonance conditions are fulfilled, even small excitation fields can lead to strong plasmon fields. Besides describing the oscillating charges of a nanoparticle as a dipole, they can also be seen as plasmon-polaritons. Plasmon-polaritons that propagate at a metal-dielectric interface as surface bound electromagnetic waves are called surface plasmon-polaritons. If d is smaller than their propagation length, plasmon-polaritons are confined to the nanoparticles geometry. In this case, the surface plasmon resonance is quasi-static. This phenomenon is called localized surface plasmon resonances.[147,148]

When placing an organic dye in close proximity to a spherical metal nanoparticle passing a plasmon field which sufficiently overlaps with the dyes absorption spectra, the possibility of a non-radiative energy transfer to the nanoparticle (nanoparticle absorption rate, k_{abs}^{NP}) opens up an additional relaxation pathway (see Figure 10b). Besides this, it also affects the dyes excitation rate constant and can alter the rate constants of all its relaxation processes – except for k_{isc}. Depending on the level of change of the individual rate constants, this can result in fluorescence enhancement or fluorescence quenching. [147–151] Hence, using plasmon fields to amplify the fluorescence intensity of organic dyes necessitates a detailed understanding of how their different rate constants and the resulting fluorescence properties are influenced.

The excitation rate constant of an organic dye (k_{ex}) is proportional to the electric field it is exposed to (E) and its absorption dipole moment (p)

$$k_{ex} \propto \left|E n_p\right|^2 \tag{11}$$

where n_p is a unit vector pointing in direction of p. When placed in a plasmon field, the excitation rate of a dye thus can be increased. The extent of this increase is described by the excitation rate enhancement factor X.

$$X = \frac{k_{\mathrm{ex}}^{\mathrm{NP}}}{k_{\mathrm{ex}}^{-\mathrm{NP}}} \propto \frac{\left|E(r)^{+\mathrm{NP}} n_p\right|^2}{\left|E(r)^{-\mathrm{NP}} n_p\right|^2} \tag{12}$$

where $E^{-\mathrm{NP}}(r)$ and $E^{+\mathrm{NP}}(r)$ are the electric field strengths in absence and presence of a nanoparticle, respectively. They, in turn, depend on the location of the dye r with respect to the excitation electric field. $k_{\mathrm{ex}}^{-\mathrm{NP}}$ and $k_{\mathrm{ex}}^{\mathrm{NP}}$ are the excitation rate constantes in absence and presence of a nanoparticle. The distance-dependency of X is illustrated in Figure 10c. X is greatest at the surface of the nanoparticle and decreases with distance from the nanoparticles surface.[147–150]

As already described above, plasmon fields change all the rates contributing to the fluorescence quantum yield except for k_{isc}. The factor of the change in the quantum yield *Z* is given by

$$Z = \frac{\Phi^{\mathrm{NP}}}{\Phi^{-\mathrm{NP}}} = \frac{k_{\mathrm{f}}^{\mathrm{NP}}}{k_{\mathrm{f}}^{\mathrm{NP}} + k_{\mathrm{abs}}^{\mathrm{NP}} + k_{\mathrm{nf}}^{\mathrm{NP}}} \frac{k_{\mathrm{f}}^{-\mathrm{NP}} + k_{\mathrm{nf}}^{-\mathrm{NP}}}{k_{\mathrm{f}}^{-\mathrm{NP}}} \tag{13}$$

where Φ^{NP} and $\Phi^{-\mathrm{NP}}$ are the fluorescence quantum yields in presence and absence of the plasmon field and k_{f} and k_{nf} are the fluorescence and non-radiative rate constants, respectively. The superscription $^{\mathrm{NP}}$ and $^{-\mathrm{NP}}$ for rate constants indicate the presence and absence of the plasmon field, respectively. Analogous to the excitation rate enhancement, Z is also highly sensitive on the distance between the dye and the nanoparticle. Typical behaviors of Z and $k_{\mathrm{f}}^{\mathrm{NP}}/k_{\mathrm{f}}^{-\mathrm{NP}}$ as a function of the distance between a fluorophore and a nanoparticle are illustrated in Figure 12c.[147–150]

The overall change of the fluorescence intensity (Γ) of a dye placed near a plasmon field results from the combined effect of the enhancement of the excitation rate and the change in the quantum yield.

$$\Gamma = \mathrm{ZX} = \frac{\Phi^{\mathrm{NP}}}{\Phi^{-\mathrm{NP}}} \frac{k_{\mathrm{ex}}^{\mathrm{NP}}}{k_{\mathrm{ex}}^{-\mathrm{NP}}} \tag{14}$$

When $\Phi^{-\mathrm{NP}}$ is close to unity, then $\Phi^{+\mathrm{NP}}$ will not be higher. In this case, any fluorescence enhancement will be entirely due to an enhanced excitation rate. In contrast, if $\Phi^{-\mathrm{NP}}$ is low, the quantum yield of a fluorophore can be strongly enhanced by nanoparticles that generate a plasmon field. As the excitation and the emission rate constants depend on the distance between the dye and the nanoparticle, the nature and level of Γ, in turn, is also distance-dependent.[147–150]

The plasmons of two individual nanoparticles can be coupled. The electric field between two coupled nanoparticles is stronger and more localized in the gap between two nanoparticles (hotspot) compared to individual nanoparticles (see Figure13d). As a result of this, the fluorescent intensity of a dye molecule can be even more enhanced by placing the dye with nanometer accuracy at the optimal distance between two nanoparticles than by placing it next to a single nanoparticle.[91,148]

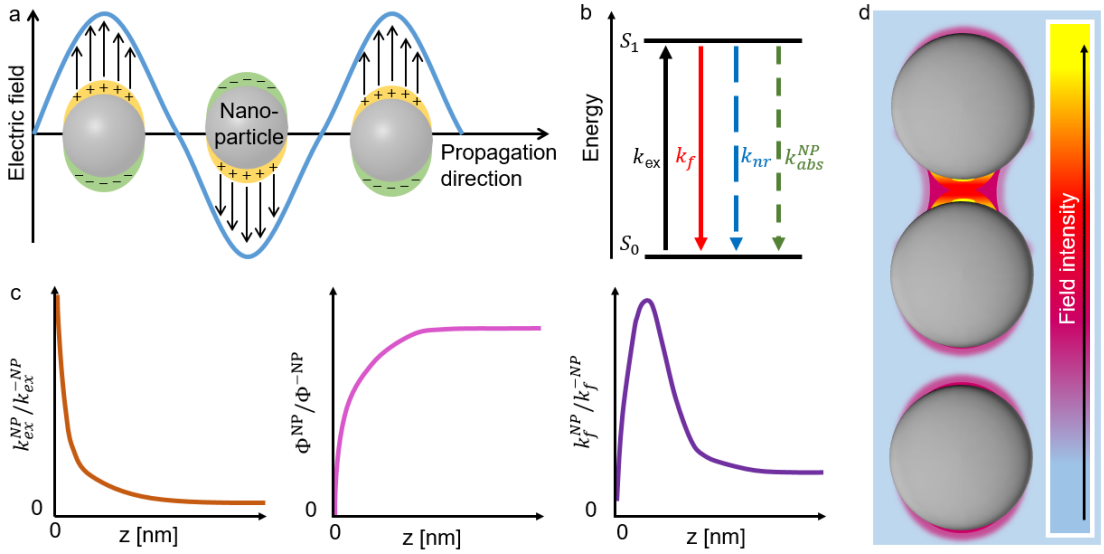

Figure 10: Principles of fluorescence enhancement by plasmonic metal nanoparticles. (a) Schematic representation of an in-phase oscillation of the conduction electrons in metal nanoparticles with the electric field of a propagating electromagnetic wave. (b) Simplified *Jablonski* diagram illustrating an additional non-radiative relaxation pathway (k_{abs}^{NP}) resulting from a non-radiative energy transfer to a nanoparticle in close proximity. (c) Schematic representation of the distance dependency of the ratio of the excitation rates, fluorescence rates and the quantum yields, in presence and absence of a plasmonic nanoparticle. (d) Schematics of the electric field enhancement around a single spherical nanoparticle (top) and around two coupled spherical nanoparticles (bottom). Electromagnetic coupling between two nanoparticles generates stronger and more localized electric fields compared to single nanoparticles.

2.3 USE OF MULTI-INPUT RECEIVING UNIT PROFILES TO IMPLEMENT REGULATORY MECHANISMS IN NANODEVICES

The most popular concept when constructing nanodevices is the use of structures that switch between two distinct conformational states. In one of the states, output operations are activated whereas in the other state they are inactive. Implementation of input receiving units which bind to inputs only in one of both conformational states resulting in its stabilization allows to couple the conformational equilibrium with input binding and thus to encode input-responsiveness into these systems. Conceptually, the simplest system one can create using this design principle is equipped with a single input receiving unit (see Figure 11a and Figure 11b). In this case, input binding follows a hyperbolic relationship between the input concentration ($[\mathrm{input}]$) and the fraction of systems occupied by an input molecule (system occupancy θ) which can be described by a simplified *Hill-Langmuir* function[63,152]

$$\theta = \frac{[\mathrm{input}]}{K_D + [\mathrm{input}]} \tag{15}$$

where K_D is the dissociation constant of the system-input complex. K_D in turn depends on the switching equilibrium constant between the two conformational states of the system (K_S) and the intrinsic input binding affinity of its active conformation (K_D^{A}) as shown in Figure 11a.

$$K_D = K_D^{\mathrm{A}}\left(\frac{1 + K_S}{K_s}\right) \tag{16}$$

The useful concentration range at which the system is responsive, the so-called responsive window, is defined as the range over which θ shifts from 0.1 to 0.9. According to function shown in Equation 16, it is limited to an 81-fold change in the input concentration centered on K_D.[96,153] This is exemplarily depicted for a system with a $K_D$value of 100 nM in Figure 11b.

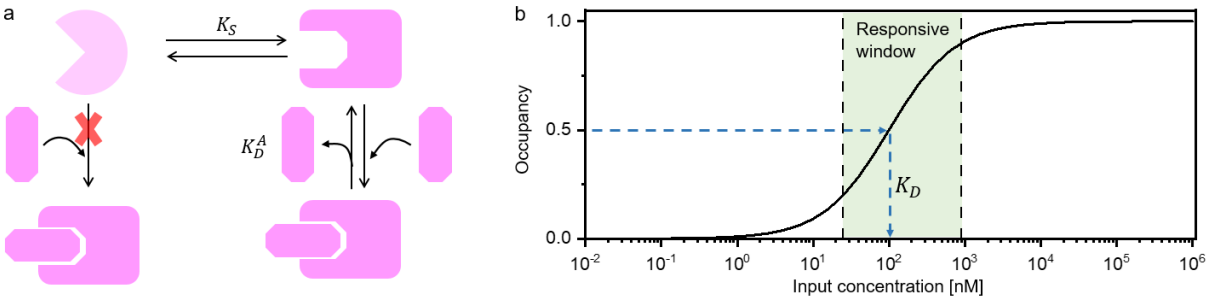

Figure 11: Dynamic two-state system with one input receiving unit. (a) Schematic illustration of a system with one input receiving unit that switches between two conformational states – an active state (box) and an inactive state (circle) as a function of environmental input (octagon). The input receiving unit is designed to bind an input in the active state of the system. This way, the conformational equilibrium of the system is coupled to input binding. While the switching constants (K_S) characterizes the transition between the active and the inactive state of the system, the dissociation constant K_D^{A} is a measure of the intrinsic input binding affinity of the active conformation. (b) Input binding curve of the system shown in (a), assuming $K_D = 100\ nM$. The responsive window is fixed to a 81-fold change in the input concentration centered on the dissociation constant K_D.

The fixed concentration ranges at which these systems are responsive ultimately limits their applicability. While they allow to detect changes in input concentration which vary significantly within this responsive window, tuning this window to detect changes in concentration which are either much larger (e.g. spanning over several orders of magnitude) or much smaller is not possible. This tuning, however, often would be necessary to reach biologically relevant concentration ranges for many biomolecules such as clinically relevant viral loads or various drugs and metabolites.[96,154,155] For the development of a smart DNA origami nanodevice which is responsive to a broad range of inputs within their technologically relevant concentration ranges, it is, therefore, crucial to overcome the limitation of fixed concentration ranges.

Allostery and cooperativity are effective strategies which allow us to do just that.[96,156–161] These regulatory mechanisms both are based on the same design concept: Multiple input receiving units are coupled together in a specific manner which can expand, narrow or shift the responsive concentration window of the corresponding inputs. Besides building the basis for allostery and cooperative behavior,[67,162,163] the

arrangement of multiple interplaying input receiving units also is essential when aiming to connect an output operation with combinations of inputs using Boolean logic gates[164,165]. Multi-input receiving profiles thus form ideal candidates for combining output operations with different regulatory mechanisms in smart nanodevice.

2.3.1 ALLOSTERY AND COOPERATIVITY

Allostery and cooperativity both describe processes by which the binding of an input to an input receiving unit is altered by the binding of molecules, so-called ligands, to distal receiving units. If the distal units are designed to bind ligands which are chemically distinguishable from the input, so-called effector molecules, the process is called allostery.[65,67] In the other case, when the additional units allow to bind chemically identical input molecules, the process is termed cooperativity.[96,163] Both of these regulatory mechanisms can result in either an increase (allosteric activation, positive cooperativity) or a decrease (allosteric inhibition, negative cooperativity) in input binding .

To understand the mechanisms of allostery and cooperativity, it is necessary to take a step back from the proposed two-state system and first focus solely on a system of two coupled input receiving units. In this system, one input receiving unit targets the input of interest whereas the other unit targets a ligand (see Figure 12a). In a simplified model, each of the input receiving units switches independently between two distinct conformational states – a relaxed state and a tensed state (see Figure 12b). Molecules primarily bind to the receiving units in their relaxed state. In the tensed state, binding affinities are low. In the presence of input molecules, a multitude of different complexes occur which are in thermodynamic equilibrium with each other (see Figure 12c and Figure 12d). The position of this equilibrium determines the fraction of systems occupied by an input molecule. In the additional presence of ligands, this equilibrium is disturbed. Due to the coupling between both receiving units, ligand binding can both stabilize/ destabilize the relaxed state of the input receiving unit. This in turn activates/ deactivates input binding to the input receiving unit.

To describe input binding to such a system quantitatively, the hyperbolic function of Equation 16 must be extended further for allosteric and cooperative systems. For allosteric systems, K_D is replaced with an overall dissociation constant $K_{1/2}$ which depends on the concentration of the effector.

$$\theta = \frac{[\text{input}]}{K_{1/2} + [\text{input}]} \tag{17}$$

For allosteric systems, with effectors acting as activators (inhibitors), $K_{1/2}$ is shifted to lower (higher) values in presence of the effector (see Figure 12e). This shifts the responsive window to lower (higher) input concentrations. As such, allosteric systems allow tuning the location of the responsive window. However, the responsiveness such systems still is limited to the same 81-fold change in the input concentration as single site binding.

Introducing cooperativity into systems allows changing this. Here, the bidirectional nature of the coupling between different input receiving units must be accounted for. Similar to allosteric systems, this effects the value of $K_{1/2}$ and additionally necessitates the introduction of a so-called Hill-coefficient n_H. The Hill coefficient reports both on the number of coupled input receiving units and the degree and direction of coupling between them. It thus is a measure of the degree of cooperativity of a system. The fraction of systems occupied by an input molecule then can be described in dependence of both $K_{1/2}$ and n_H by the *Hill-Langmuir* function.

$$\theta = \frac{[\text{input}]^{n_H}}{K_{1/2}^{n_H} + [\text{input}]^{n_H}} \tag{18}$$

For non-cooperative systems, $n_H = 1$. Negatively cooperative systems, in which input binding to one input receiving unit inhibits binding to another, feature a Hill coefficient of $0 < n_H < 1$. This results not only in a shift in the absolute position of $K_{1/2}$ but also in a broadened responsive window spanning over a change in input concentration of more than 81-fold (see Figure 12f). In contrast, in positively cooperative systems input binding to one of the input receiving units activates binding to another. Depending on the number of input receiving units N_{IRU}, Hill coefficients of $1 < n_H \leq N_{IRU}$ can be observed. As a result, the absolute position of $K_{1/2}$ is again shifted but responsive concentration window narrowed (see Figure 12f).[96,163,166]

Obtaining full control over both allosteric and cooperative properties of a system thus would allow rationally tuning responsive concentration windows to arbitrary values. This would necessitate the rational coupling of multiple input receiving units both for the same and for different inputs. The incorporation of such coupled units on a DNA origami two-state system and the parallel coupling of input binding to the conformational state of the system would allow creating nanodevices responding to arbitrarily chosen input concentration windows.

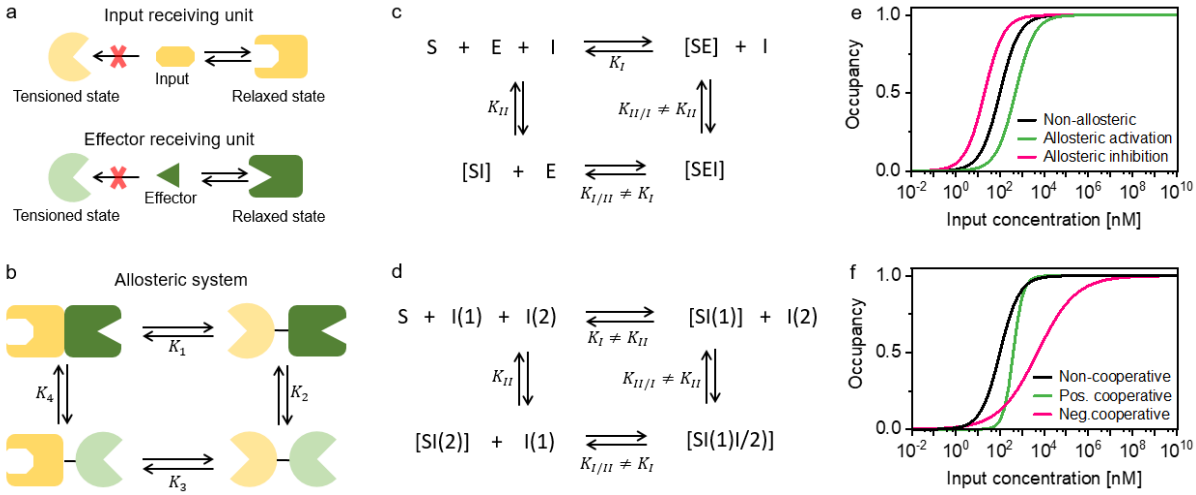

Figure 12: Principles of allostery and cooperativity illustrated for systems with two coupled receiving units. (a) Simplified illustration of an input receiving unit and one effector receiving unit. Each receiving unit can exist in two conformational states – a relaxed state and a tensed state. The units are designed to bind to their input/effector molecules only in their relaxed state. (b) Schematic representation of an allosteric system with one input receiving unit and one effector receiving unit. Each receiving unit of the system switches independently between the different conformational states. The transitions are characterized by the dissociation constants ($K_1 - K_4$). This representation can be adapted to illustrate a cooperative system by simply exchanging the effector receiving unit with an additional input receiving unit. (c) Thermodynamic cycle of the system (S) shown in (b) in the presence of input molecules (I) and effector molecules (E). The system is in thermodynamic equilibrium with three different complexes (system-effector complex [SE], the system-input complex [SI] and the system-effector-input complex [SEI]). Each transition is characterized by a certain dissociation constant ($K_I, K_{II}, K_{I\_II}, K_{II\_I}$). (d) Thermodynamic cycle of a cooperative system (S) with two coupled input receiving units in the presence of input molecules (I). The system is in thermodynamic equilibrium with three different complexes (system-input(1) complex [SI(1)], the system-input(2) complex [SI(2)] and the system-input(1)-input(2) complex [SI(1)I(2)]). Each transition is characterized by a certain dissociation constant ($K_I, K_{II}, K_{I\_II}, K_{II\_I}$). (e) Exemplary input binding curves of an allosteric activated system (green) and an allosteric inhibited system (pink) compared to a non-allosteric system with $K_{1/2} = 100\,nM$ (black). (f) Exemplary input binding curves for positive cooperative behavior (green) and negative cooperative behavior (pink) compared to a non-cooperative system with $K_{1/2} = 100\,nM$ (black).

2.3.2 MOLECULAR LOGIC GATES

In recent years, molecular logic gates have been developed to create molecular devices capable of generating qualitative YES/NO answers upon processing environmental inputs.[164,165] This is achieved by performing logic operations based on Boolean functions upon activation by one or multiple environmental inputs. The logic operations convert the inputs into binary signals and generate a single binary output signal. Boolean functions have been proven to be ideally suited for the realization of molecular logic gates as they can be applied to any type of inputs and outputs expressed as the Boolean FALSE ('0') value and the Boolean TRUE ('1') value. Setting an individual treshold for each input and output enables to distinguish between FALSE and TRUE signals. As such, if an input or output exceeds its treshold, it is regarded as TRUE, and otherwise as FALSE. The basic logic gates include single-input logic gates

(YES gate and NOT gate) , two-input logic gates (OR, XOR, AND, NAND, XOR, XNOR gates) and multi-input logic gates (e.g. MAJ gate and MIN gate) (see Figure 13a-c). In case of single-input logic gates, the value of the output is solely dependent on the value of one input (see Figure 13d). For two-input and multi-input gates, the value of the output signal is determined by the value of all its inputs. This is exemplarly demonstrated for two-input basic logic gates in Figure 13e. Implementing sequencial cascades of these basic logic gates in one system opens up the possibility of taking even more sophisticated decisions – which theoretically can achieve an unlimited level of logic complexity.[19,49,164,165,167–169]

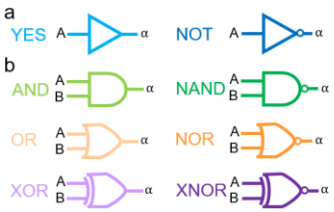

d

Input A	Output α	
	YES	NOT
0	0	1
1	1	0

e

Input		Output α					
A	B	AND	OR	XOR	NAND	NOR	XNOR
0	0	0	0	0	1	1	1
0	1	0	1	1	1	0	0
1	0	0	1	1	1	0	0
1	1	1	1	0	0	0	1

Figure 13: Basic Boolean logic gates. Boolean logic gates enable to generate a single binary output upon processing inputs. (a-c) Sketches of Boolean logic gates for (a) single inputs, (b) two inputs and (c) multiple inputs and (e,f) corresponding output tables of (e) single inputs and (f) two inputs. The MAJ logic gate shown in (c) works analogously to the two-input OR gate: Only if at least one of the input values is 1, the output value is 1. The MIN logic gate functions is the contrary to the MAJ logic gate.

3 MATERIALS AND METHODS

This chapter focuses on briefly describing the methods used for the different experiments. Further details are provided in the materials and methods sections of the corresponding publications.

3.1 GENERATION OF DNA ORIGAMI NANOSTRUCTURES

Three different DNA origami structures were used to build the DNA origami nanodevices presented in this thesis. Their designs are based on a pillar-shaped DNA origami structure[38], a hinge-shaped DNA origami structure[100] and a reconfigurable DNA origami array structure[104,105]. For the incorporation of the different nanostructure components, I used both the internal and the external labeling strategy. The ssDNA coupled peptide used for monitoring protease activity was produced in house via strain promoted the copper-free strain-promoted alkyne-azide [3+2] cycloaddition (SPAAC) from commercial available dibenzylcyclooctyne (DBCO)-modified oligonucleotides and a synthetic peptide with azide groups. Silver nanoparticles were functionalized with a thiol modification at the 3'-end based on previously described procedures.[38] All other unmodified and modified DNA staples used to build the described DNA origami nanodevices were purchased from Eurofins Genomics GmbH (Germany), Integrated DNA Technologies (USA) and Ella Biotech GmbH (Germany). Design of all three DNA origami structures was done with the open-source software caDNAno[170]. The design of both the pillar shaped DNA origami and the hinge shaped DNA origami is based on a p8064 scaffold while the reconfigurable DNA origami structures are based on a p1800G, a p1800R, and a p1800N scaffold respectively. The p8064 scaffold was synthesized in house and all other scaffolds were synthesized by our collaboration partners in Atlanta. The different nanodevice units were implemented by exchanging different staple strands with modified ssDNA strands in the reaction mixture. For DNA origami folding, the scaffold was mixed with modified staples and unmodified staples and the mixture was heated up to 65 °C in a thermocycler. The solution was kept at this temperature before being cooled down to 25 °Cover 16h (pillar-shaped DNA origami structure and hinge-shaped DNA origami structure) and 1 h (reconfigurable DNA origami structure), respectively. The DNA origami structures were purified by size exclusion with Amicon filters or by gel electrophoresis. The structures of assembled DNA origami structures were characterized by atomic force microscopy or transmission electron microscopy. Folded DNA origami structures were either directly measured or stored at – 20°C for further use.

3.2 SINGLE-MOLECULE FLUORESCENCE MEASUREMENTS AND ANALYSIS

To develop and optimize DNA origami nanodevices capable of performing sophisticated tasks, fluorescence scans and fluorescence traces of individual surface-immobilized DNA origami structures were acquired. This was realized using a TIRF microscope or a confocal microscope.

3.2.1 SAMPLE PREPARATION ON MICROSCOPY COVERSLIPS

For single-molecule microscopy measurements, DNA origami samples were immobilized in chambers via biotin-neutravidin interactions. For chamber preparation, adhesive SecureSeal™ Hybridization Chambers (Grace Bio-Labs, USA) were glued on microscope glass slides (Carl Roth GmbH, Germany). To reduce the background generated by fluorescent contaminations, the created chambers were cleaned with KOH. After surface passivation by incubation with bovine serum albumin (BSA)-Biotin, the chambers were incubated with neutravidin. Neutravidin has four binding pockets with which it can bind to both, the surface and biotinylated DNA origami samples. For this we incorporated biotinylated DNA staples in the reaction mixture of the DNA origami structure during folding. The DNA origami solution was diluted to a concentration of ~10 pM and then immobilized on the biotin-neutravidin surface via biotin-neutravidin interactions. This ensured a suitable surface density for single-molecule measurements in every prepared chamber. For some single-molecule fluorescence measurements, an oxidizing and reducing buffer system[171] was used in combination with an oxygen scavenging system to suppress blinking and photobleaching.

3.2.2 CONFOCAL MEASUREMENTS

Confocal microscopy data was acquired on a home-build confocal microscope. The setup was based on an inverted microscope body (IX-83, Olympus Corportation, Japan) and a pulsed white light laser (SuperK Extreme EXW-12, NKT Photonics A/S, Denmark). The wavelengths of 532 nm and 639 nm were used for green excitation and red excitation, respectively. The selection was realized using an acousto-optical tunable filter (AOTF, SuperK Dual AOTF, NKT Photonics A/S, Denmark) which was controlled by a digital controller (AODS 20160 8 R, Crystal Technology, USA) via a computer software (AODS 20160 Control Panel, Crystal Technology, Inc., USA). For alternation of red and green excitation, a second AOTF (AA.AOTF.ns: TN, AA Opto-Electronic, France) controlled via a home-written LabVIEW software (National Instruments, USA) was used. Besides enabling to alter both wavelengths, the second AOTF enabled to further spectrally clean the excitation laser beams. A neutral density filter was used to regulate the laser intensity. Circularly polarized excitation was achieved by combining a linear polarizer and a λ/4 plate. For focusing the excitation laser onto the sample, a dichroic beam splitter (ZT532/640rpc, Chroma Technology, USA) and an immersion oil objective (UPlanSApo 100×, NA = 1.4, WD = 0.12 mm, Olympus Corporation, Japan) were used. Micro-positioning of the sample was performed using a Piezo-Stage (P-517.3CL, E-501.00, Physik Instrumente GmbH&Co. KG, Germany). For recording of fluorescence transients, the laser intensities were set between 100 nW and 500 nW. For confocal scans, 1-2 µW in both colors were used. The emitted light was collected by the same objective. A dichroic beam splitter was used to filter the emitted light from the excitation light. The emitted light was focused on a 50 µm pinhole (Linos AG, Germany) and detected via avalanche photodiodes (SPCM, AQR 14, PerkinElmer, Inc., USA) registered by an TCSPC system (HydraHarp 400, PicoQuant GmbH, Germany). Data processing and analysis was realized using custom-made LabVIEW software (National Instruments, USA) or custom-made Python scrips.

3.2.3 TIRF MEASUREMENTS

TIRF experiments were executed on a commercial TIRF microscope, called Nanomiager, from Oxford Nanoimaging. Red excitation at 638 nm was realized with a 1100 mW laser and green excitation at 532 nm with a 1000 mW laser, respectively. For acquisition of both, single-molecule images and fluorescence intensity traces the relative laser intensities were set to 3.5 mW and 1 mW for green and red excitation, respectively. The emission light was detected with an sCMOS camera. Acquisition of single-molecule fluorescence trances was realized by time-lapsed imaging. Dual colour traces of individual DNA origami structures were recorded by activating the lasers and taking a frame of 100 ms every second separately for both lasers. Measurements were carried out at 37 °C.

Data processing and analysis of fluorescence scans was realized using the commercial software iSMS[172]. For processing and analysis of time-lapse fluorescence intensity traces custom-made Python scrips and the commercial software Fiji[173] were used. Briefly, the acquired movies were first drift corrected using DNA origami structures carrying a fluorophore which is in its fluorescent state throughout the whole measurement period. Fluorescence intensity transients were extracted from each spot appearing in the drift-corrected movie.

3.3 SINGLE-MOLECULE SENSING ASSAYS

Anti-Dig antibody detection assay

For the detection of IgG antibodies, DNA origami structures were folded with antigen functionalities. Antibodies were purchased from Thermo Fisher Scientific (USA). Surface-immobilized structures were incubated with the anti-Dig antibody solution before acquiring single-molecule fluorescence scans on a confocal microscope.

Light detection assay

DNA origami structures used for the detection of light were equipped with a photocleavable linker. Surface-immobilized structures were illuminated with light of a specific wavelength before acquiring single-molecule fluorescence scans on a confocal microscope.

Restriction enzyme activity assay

For monitoring restriction enzyme activity, DNA origami structures were equipped with dsDNA containing a sequence specific for the binding and cleavage of the restriction enzyme. Restriction enzymes were purchased from New England BioLabs (USA). For acquisition of single-molecule fluorescence traces, immediately after addition of the enzymes, the sample chambers were sealed and the DNA origami imaged. For acquisition of single-molecule fluorescence scans, the samples were incubated with the enzyme at 37 °C before imaging.

4 PUBLICATIONS

4.1 SINGLE ANTIBODY DETECTION IN A DNA ORIGAMI NANOANTENNA

Martina Pfeiffer[1], Kateryna Trofymchuk[1], Simona Ranallo, Francesco Ricci, Florian Steiner, Fiona Cole, Viktorija Glembockyte[*] and Philip Tinnefeld[*]

([1] These authors contributed equally, [*] Correspondence)

iScience, volume 24, issue 9, pages 103072 (**2021**)

DOI: 10.1016/j.isci.2021.103072

Signal amplification is a hallmark of cellular function and important in many biological processes. This is commonly achieved by molecular amplification mechanisms.[70,174–177] Besides being of great significance in nature, they are the basis of many diagnostic methods routinely used in clinical laboratories for the diagnosis of diseases.[178–180] Especially in the early onset of diseases, diagnostically relevant input molecules occur at low concentrations. Detecting them necessitates methods capable of generating a signal that is strong enough against background within a reasonable time. To date, this is usually achieved by either amplifying the number of input molecules using polymerase chain reactions[181–183] or amplifying the number of molecules generating the output signal with the help of enzymatic reactions[180,184]. While these molecular amplification strategies can be successfully implemented in diagnostic assays to obtain qualitative and quantitative diagnostic results,[178,179,185] they suffer from major drawbacks. Firstly, they often rely on tedious laboratory-based procedures which – besides being not suitable for the emerging field of point-of-care diagnostics – often result in long time periods passing before clinical suspicions are confirmed by laboratory diagnosis. By then, time is a crucial factor when treating patients. Prolonged diagnosis times can have fatal effects. Secondly, molecular amplification mechanisms can amplify the influence of both contaminations and small deviations from the standard protocol and batch quality. Therefore, there is a crucial need for robust diagnostic technologies which provide reliable and fast diagnostic results. This necessitates using different signal amplification strategies.

DNA origami nanoantennas[38,39,92] are input-responsive biosensors with great potential to fulfil the above-mentioned criteria in future. They are designed and optimized to generate a strong optical output signal after sensing an input. This is achieved by physical signal amplification of the output signal generated in fluorescence-based diagnostic assays by plasmonic effects. A key advantage of this approach is that input molecules can – even if they occur at low concentration – be directly detected without necessitating prior amplification or using a chemical reaction for multiplicating the molecules which generates the output signal. Moreover, the enhanced output signal makes them accessible to simple, low-cost and portable readout devices, offering many exciting applications in the field of point-of-care diagnostics. While this demonstrates the suitability of DNA origami nanoantennas for facilitating the detection of input molecules, when facilitating the detection of

diagnostically relevant targets, their spectrum to date is limited to the detection of nucleic acids. Besides nucleic acids, proteins involving antibodies, are another molecular class which is of great interest for the diagnosis of diseases.[186–188] Expanding the target spectrum of DNA origami nanoantennas from nucleic acids to proteins thus is of clinical interest.

The aim of associated publication P1 (see Chapter 6.5.1) was to address the question of whether the unique properties of DNA origami nanoantennas can be applied to the detection of proteins. To that end, DNA origami nanoantennas were combined with label-free antibody detection by incorporating an allosteric nanoswitch sensor in their plasmonic hotspot, creating a stepping-stone for expanding fluorescence enhanced biosensing beyond the scope of nucleic acids.

For the realization of fluorescence enhanced antibody detection at the single-molecule level, I designed and implemented a nanoswitch sensor, which was inspired by the nanoswitch sensor developed by the Ricci group,[189] into the hotspot of nanoantennas. The nanoswitch sensor is composed of a DNA stem with two ssDNA tails. The stem is modified with a fluorophore-quencher pair. In absence of target molecules, the stem is closed and energy transfer from the fluorophore to the quencher occurs due to their close proximity. The tails are hybridized to ssDNA strands which are functionalized with recognition elements specific for the antibody. Upon bivalent binding of an antibody to the recognition elements, a conformational change occurs. Fluorophore and quencher separate, leading to an increase in fluorescence signal of the fluorophore which can further be enhanced in the hotspot of nanoantennas. To visualize the DNA origami structure, additionally a green dye was incorporated. As a test bed, I designed the nanoswitch to specifically detect anti-Dig antibodies.

To demonstrate the functionality of the nanoswitch sensing unit, I chose the new rectangular DNA origami (NRO)[190,191] as a model structure. In this two-dimensional structure, the nanoswitch sensing unit is expected to be easily accessible for anti-Dig antibody binding. I investigated the opening mechanism of the nanoswitch sensing unit and determined the selectivity, the sensitive concentration range under clinically relevant conditions and the speed of the sensing assay under non-diffusion limited conditions by performing single-molecule measurements on a confocal fluorescence microscope. To evaluate the sensitive concentration range under clinically relevant conditions and to determine the speed under non-diffusion limited conditions, I chose an incubation time of 20 min and an antibody concentration of 100 nM, respectively. The designed nanoswitch sensor appeared to be specific for the target anti-Dig antibody in the low picomolar range and works according to the above-described mechanism. Besides being highly specific, the developed nanoswitch sensor allows for a rapid detection of anti-Dig antibodies – achieving the highest signal gain after just 5 minutes.

I then continued to study the characteristics of the nanoswitch sensing unit in the three-dimensional DNA origami nanoantenna structure containing a 100-nm silver nanoparticle as well as in the same DNA origami nanostructure without nanoparticles serving as a reference. The obtained kinetic values showed that under non-diffusion limited conditions the detection is equally rapid on all three DNA origami structures. To compare the sensitive concentration ranges, I fitted the obtained binding curves and used the antibody concentration at half-maximum signal gain to characterize the

properties of the nanoswitch response ($c_{halfmax}$). The obtained $c_{halfmax}$ values (129 pM, 800 pM and 1.4 nM for the NRO structure, the reference DNA origami structure and the DNA origami nanoantenna structure containing one 100-nm silver nanoparticle) emphasized that the diffusion limited binding of the antibody at low concentrations makes the accessibility of the nanoswitch a crucial factor to be considered when designing nanodevices with low sensitive concentration ranges under diagnostically relevant incubation times. In the two-dimensional NRO nanostructure, the nanoswitch is expected to be easily accessible for the anti-Dig antibody binding, while the accessibility for the target antibody is expected to be lower in the three-dimensional DNA origami nanoantenna structure without nanoparticles. Upon attachment of 100-nm silver nanoparticles, the accessibility of the DNA origami nanoantennas structure should be even further hindered.

To study the fluorescence enhancements achievable in this single-molecule antibody assay, I recorded single-molecule fluorescence transients of the nanoswitch on a confocal microscope. Fluorescence enhancements of up to 60–fold (average of 17±11-fold) were achieved, which allowed the detection of single antibodies on a simple smartphone microscope with low-NA optics.

Overall, the implementation of a nanoswitch sensor in the plasmonic hotspot of DNA origami nanoantennas for the specific detection of antibodies showed that physical signal amplified input detection can be expanded beyond the scope of the nucleic acid realm. This is a crucial step towards potential broad real-world applications in both the field of early detection of diseases and the field of point-of-care diagnostics.

4.2 ENGINEERING MODULAR AND TUNABLE SINGLE MOLECULE SENSORS BY DECOUPLING SENSING FROM SIGNAL OUTPUT

Lennart Grabenhorst[1], **Martina Pfeiffer[1]**, Thea Schinkel, Mirjam Kümmerlin, Jasmin Maglic, Florian Selbach, Gereon Andreas Brüggenthies, Alexander Thomas Murr, Philip Tinnefeld[*] and Viktorija Glembockyte[*]

([1] These authors contributed equally, [*] Correspondence)

Preprint available on BioRxiv

DOI: 10.1101/2023.11.06.56579

From clinical diagnosis, food and drug analysis to environmental sensing, biosensors play a crucial role in our everyday lives. DNA origami nanostructures constitute excellent platforms for the development of new biosensing approaches by templating different sensor components.[34,35,59] Most of the DNA origami biosensors present thus far are designed to answer the question of whether a single input molecule [38,40,99] or a certain combination of two structurally very similar inputs[49,52,97] is present or not. This, similar to other diagnostic assays currently in use, limits them in their application. Especially in clinical diagnosis, the presence of a single biomarker input often can be seen only as an indication for a certain disease. For example, biomarkers currently used to predict different types of cancer often are also present under benign conditions. Here, the parallel detection of a panel of multiple complementary biomarkers convers significant advantages over relying on a single biomarker in clinical diagnosis. It enables a more reliable and comprehensive assessment of the interplay between different factors, thus enhancing the accuracy of disease prediction.[192]

By enabling the coupling of multiple input receiving units to a single output operation, DNA origami theoretically offers us the possibility to achieve this on a single biosensor platform. As demonstrated by several naturally occurring receptors[177,193–195], the extension beyond a single input receiving unit to multiple coupled units offers several key advantages. First and most obviously, it enables the parallel response to the presence or absence of multiple inputs which is of great interest for clinical diagnosis as described above. Besides this, it also provides access to the properties of the responsive concentration window of the inputs. With a single input receiving unit, the responsive concentration window is fixed to a change in input concentration of around two orders of magnitude centered on the dissociation constant of the input-receptor complex and cannot be altered.[96,153] This fixed concentration window however often is far away from biologically relevant concentration changes.[96,154,155] Here, the incorporation of multiple coupled input receiving units towards the same input can provide a solution. It allows shifting, narrowing and widening the responsive window by both allosteric[65,67,163] and cooperative[96,163] mechanisms – always depending on the exact coupling between the different units.

DNA origami could provide access to this coupling. As such, it could form the ideal design platform to create modular and tunable biosensors which respond to different concentrations of multiple inputs in parallel. Up to now, this potential however has been mostly disregarded to generate simple YES/NO answers with regard to the presence of a single input or a combination of two structurally similar inputs.

In associated publication P2 (see Chapter 6.5.2) we suggest a strategy to overcome this self-set limitation. By coupling multiple input receiving units to each other on a modular DNA origami platform, it introduces strategies to rationally combine different classes of input molecules with each other, to create Boolean logic responses from them, to tune the location and width of the responsive windows of these input molecules, and to increase the specificity towards these input molecules. As such, it transfers concepts from naturally occurring receptors to artificially created biosensors and demonstrates the unique features enabled by this.

We designed and characterized a hinge-like DNA origami nanostructure as a basis for the biosensor platform. The design was inspired by a structure developed by Castro group[100] and consists of two stiff arms which are joined along their edges with ssDNA connections. In its equilibrium state (open state), the angle between the arms of the nanostructure is 90° due to Coulomb repulsion caused by the negatively charged DNA building material. By incorporation of linkers in a bridge-like manner between both arms, the structure can be forced into a tensioned state (closed state), in which both arms are nearly parallel to each other. We encoded the input-responsiveness of the system into the linkers such that when a molecular event occurs, the structure switches from closed to open, or vice versa. In order to optically visualize the conformation of the DNA origami structure, we used a FRET pair placed on complementary DNA strands protruding from the two arms of the structure. In the closed state of the structure, these strands are in close proximity such that they can hybridize, giving rise to an efficient FRET. In the open state of the DNA origami nanostructure the strands are separated leading to low FRET.

To study the characteristics of the DNA origami nanostructure, we closed the DNA origami structure using specific DNA closing interactions. We designed the closing interactions such that they can be removed upon addition of opening DNA strands. Performing single-molecule measurements enabled us to determine the efficiency of the closing and opening mechanism and the FRET signal contrast between the closed and the open state. We found that the sensor can be quantitatively switched from its closed state to the open state upon addition of opening DNA strands and vice versa upon subsequent removal of opening DNA strands. The achieved high FRET signal contrast between closed and open states of the sensor allowed clear separation between a sensor appearing in either of the states.

In order to determine the sensitive concentration range of the biosensor, we performed single-molecule titration experiments. Fitting the obtained binding curve with a Hill equation allowed us to characterize the sensitive concentration range in terms of the dissociation constant (K_D) and the Hill coefficient (n_H). While K_D reports on the center of the responsive window, n_H is a measure of cooperativity of a system and defines the width of the responsive window. The biosensor appeared to be responsive to changes in opening DNA strand concentrations of around two orders of magnitude located in the nanomolar range ($n_H \sim 1$, $K_D = 100\,nM$). By stabilizing the closed state with additional DNA-DNA interactions based on principles of allosteric control and by modulating the force that the backbone structure exerts onto the DNA closing interactions with the ion concentration, we identified different strategies which allow to shift the location of the responsive window. Expanding on that, we demonstrated a strategy which allows altering both, the location and the width of the responsive window

simultaneously. To this end, we altered the number of closing DNA-DNA interactions, inspired by the principle of cooperative modulation of the input binding event. By increasing the number from two to six interactions enabled to increase K_D tenfold and n_H two fold.

We then applied the ability of modularly combining multiple DNA-DNA closing interactions to tune the biosensor's specificity. To this end, we included mismatches into the opening interactions and compared the concentration of opening DNA strands required to open the DNA origami structure for no mismatch and with different mismatches. The obtained concentration values showed that with increasing numbers of closing DNA-DNA interactions smaller differences between the perfect opening DNA staple and opening DNA staple can be distinguished.

With the aim to adapt the unique properties of the biosensor to detect a broad range of different biological relevant inputs, we exemplarily chose antibodies, antigens, enzymes and their activities as inputs. The spatial separation of the FRET pair and the linkers in our design hereby enabled us to realize this by simply adapting the closing DNA-DNA interactions or exchanging them with other input receiving units. For monitoring the activity of enzymes, we adapted the DNA-DNA interactions to include the binding and the cleavage sites specific for different nucleases. In the presence of nucleases, the DNA-DNA interactions can be cleaved resulting in the opening of the DNA origami structure. For detecting binding events wherein the input molecule is an antibody or antigen, we incorporated antigens on the opposite arms of the DNA origami structure. Bivalent binding of an antibody to the two antigens can lock the DNA origami structure in its closed state. Subsequent addition and binding of antigens results in the release of the antibody and thus the opening of the structure. By performing single-molecule experiments we demonstrated that each of the designed assays enables a specific detection of its corresponding input.

Finally, we made use of the fact that a single input receiving unit does not suffice to quantitatively close the DNA origami structure to generate logic gated YES/NO outputs in response to the presence of different combinations of inputs. By implementing two different input receiving units, each responsive for one of the input antibodies, we first designed a Boolean OR gate responsive to combinations of two different antibodies. Expanding on that, we also demonstrated that by combining multiple different input receiving units responsive to different inputs on the same construct, logic gated responses in response to inputs of different molecular classes can be realized.

All in all, we designed a modular and tunable DNA origami biosensor. By coupling multiple input receiving units to a single signal output using allosteric and cooperative regulation mechanisms, we introduced strategies to rationally tune the responsive window towards input molecules. We used the same concept to adapt the biosensor towards different targets and to compute Boolean logic responses from different input combinations. This represents an important step towards uncovering the potential of allosteric information transfer in rationally designed nanodevices.

4.3 DNA ORIGAMI ARRAY STRUCTURES AS PLATFORMS FOR SMART NANOROBOTS

In contrast to biosensors, naturally occurring systems not only *detect* the presence of various inputs but also *act* upon the detection event. This action often is not defined by a single output operation but is characterized by a series of different steps which create a cascade of different processes.[196–198] When creating DNA origami nanodevices – which in case of diseases – either hinder or take over the functions of certain biomolecular pathways, it is essential to address and mimic these cascades. While current DNA origami nanorobots can be used to activate single processes, such as drug release[47,199] or uptake[49], they are not suitable for mimicking such a behavior. Their design is often based on that of biosensors and as such is inspired by simple two-state systems in which the states are coupled to each other through a single conformational change. One of the states activates the performance of an output operation whereas the other state hinders it. The population of both states is linked to the presence of inputs which allow shifting it from one state to the other.

By incorporation of multiple input-receiving units, such a design already offers many possibilities regarding the responsiveness to different inputs as described in Chapter 4.2. It, however, lacks a similar level of control over the activation of multiple output operations. By coupling the onset of all output operations to a single conformational change, properties of the response such as the order of events and the timing between them cannot be controlled. This however would be needed when constructing DNA origami nanorobots capable of mimicking naturally occurring cascade processes. In addition to the responsiveness to multiple environmental inputs, here also biocomputing and conducting multi-step responses to these inputs in a controlled manner is necessary. Similar as the coupling of multiple input receiving units to each other extends the capabilities of biosensors, the controlled coupling of all sorts of nanodevice units, including both input and output operation units, would extend the capabilities of DNA origami nanorobots. To date, however, no generalized approach which allows such a coupling exists.

A promising approach in this direction entails starting off with a network of already coupled two-state systems without any functionalities. By encoding different nanodevice units into these systems, they automatically are coupled to each other in an intrinsic manner by the underlying network.

Reconfigurable DNA origami array systems[104–106] pose an interesting candidate in this context. They represent a class of dynamic DNA origami composed of multiple dynamic subunits which are coupled together through allosteric communication. As described in Chapter 1.3, they are composed of structurally similar building blocks, so-called anti-junctions. An anti-junction can occur in two stable conformational states between which it can switch, thus forming an individual two-state system. In DNA origami arrays, the conformations of neighboring anti-junctions are coupled to each other through allosteric communication. Altering the conformation of one anti-junction thus effects the conformation of all anti-junctions. A conformational change of an anti-junction positioned at the edge of the structure, that can be induced by the hybridization of trigger DNA strands, consequently, results in a stepwise conformational change of

all anti-junctions of the structure. This triggerable multistep reconfiguration process could build the basis for the envisioned network of coupled two-state systems represented by the individual anti-junctions. The applicability of DNA origami arrays in smart nanodevices depends on the following two requirements: First, strategies to introduce different functionalities into the individual anti-junctions would need to be developed. Secondly, it is necessary to develop strategies to understand and rationally regulate the allosteric communication in the systems, expressed by the coupling between the addressed anti-junctions. Only if full control on the energetic level of the coupling can be achieved, this control can be transferred to the conducted processes and both bio-computation and order and timing of output operations tuned.

This coupling is directly linked to the energy landscape of the reconfiguration process. The associated publications P3 and P4 (see Chapter 6.5.3 and Chapter 6.5.4) therefore focus on understanding and controlling the energy landscape of the reconfiguration process of a DNA origami array model system. In publication P3 (see Chapter 6.5.3), first, a detailed understanding of the energy landscape including the energy barriers between intermediates in the reconfiguration process is obtained by a novel fluorescence assay. By rational design concepts the energy landscape is then tailored at specific loci in order to alter the coupling between specific anti-junctions and the control this has on the timing of different processes demonstrated. In contrast, publication P4 (see Chapter 6.5.4) does not focus on engineering the energy landscape at specific positions, but on strategies which allow tailoring it globally. In combination, both publications present strategies to control the reconfiguration process and the coupling at all levels. In publication P5 (Chapter 6.5.5), this energetic control is linked to nanodevice functionalities. For this, first universal strategies to encode different input receiving units into individual anti-junctions of the network are introduced. Based on the previously obtained knowledge of the energy landscape of the reconfiguration process, multiple of these units are linked together to provide multi-level Boolean logic responses and combined with output operation units. This enabled the creation of a smart DNA origami nanorobot capable of responding to different input combinations by different series of programmed and allosterically regulated output operations under temporal control.

4.3.1 CONTROLLED MECHANOCHEMICAL COUPLING OF ANTI-JUNCTIONS IN DNA ORIGAMI ARRAYS

Fiona Cole[1], **Martina Pfeiffer**[1], Dongfang Wang[1], Tim Schröder, Yonggang Ke[*] and Philip Tinnefeld[*]

([1] These authors contributed equally, [*] Correspondence)

Submission pending

For studying the reconfiguration process of DNA origami array systems[104–106] at the molecular level, we developed a fluorescence-based single-molecule assay consisting of two FRET-probes which report on the conformational state of anti-junctions at specific locations within the DNA origami array structure. In our assay, we made use of the fact that the distances between the individual arms of the anti-junctions changes upon reconfiguration. Before the reconfiguration process occurs, FRET donors and acceptors are in close proximity, resulting in the quenching of the fluorescence of the FRET donor. In the moment of reconfiguration, the distance between the individual arms of the anti-junctions increases, resulting in the spatial separation of FRET donor and acceptor and consequently the onset of a fluorescence signal. For measurements at the single-molecule level, this dual probe configuration enables a direct measurement of the timing between two different processes occurring in the reconfiguration cascade and as such allows zooming into intermediate steps that remain inaccessible with only one FRET probe. As such, it provides detailed insights into both the possible reaction pathway and the underlying energy landscape.

We applied the assay to record fluorescence intensity transients of the reconfiguration of DNA origami arrays with the two FRET probes placed at four different anti-junctions within the systems. Here, we found that many of the anti-junctions in the system are strongly coupled and their reconfigurations occur simultaneously within our time resolution of 1 s – even when they are distanced over tens of nanometers apart. A time delay was only observed between anti-junctions changing their conformation very early in the reconfiguration process and anti-junctions reconfiguring their conformation later-on.

Based on these findings, we derived an energy landscape of the whole reconfiguration process which features high activation barriers in the beginning of the process and low barriers towards its end. We continued to identify strategies how to alter this energy landscape – both globally and locally only at specific activation barriers by manipulating the coupling between the anti-junctions. While the overall driving force of the reconfiguration can be weakened by reducing the number of added trigger DNA strands, targeting specific activation barriers is possible by modifying anti-junctions which change their conformation in the respective reconfiguration step. This offers a systematic way to control the timing between these steps, thereby enhancing the rational control over the entire process.

We then demonstrated how this temporal control can be applied to DNA nanodevices. For this purpose, we incorporated a cargo release unit into one anti-junction of the

system. Analogue to the principle of allosteric inhibition, the affinity of this cargo release unit towards a cargo DNA strand bound to it weakens upon hybridization of trigger DNA strands to the DNA origami array and the subsequent reconfiguration of the addressed anti-junction. As a result, the cargo DNA strand is released at the corresponding reconfiguration step, potentially offering the possibility of combining it with synchronized temporal coordination.

All together, we developed a double-FRET single-molecule assay which reveals insights into the kinetics and thermodynamics of the multi-step reconfiguration process. Besides greatly improving the understanding of the multi-step reconfiguration process, the assay allowed us to define strategies to tailor the reconfiguration process globally and at pre-defined intermediate steps. Moreover, by targeting the conformation of specific anti-junctions within the reconfiguration process by output operations we showed how the unique properties of DNA origami array systems enable to perform output operations under temporal control.

4.3.2 SEQUENCE EFFECT ON THE THERMODYNAMICS AND TRANSITION KINETICS OF ANTI-JUNCTIONS

Dongfang Wang[1], Fiona Cole[1], **Martina Pfeiffer**[1]**,** Tim Schröder, Philip Tinnefeld[*] and Yonggang Ke[*]

([1] These authors contributed equally, [*] Correspondence)

Submission pending

Achieving full control over a system requires having full control over its individual components. Therefore, a different strategy aiming to obtain full control over the energy landscape of the reconfiguration process of DNA origami array systems[104–106], focuses on understanding and controlling the kinetics and thermodynamics of individual anti-junctions. This includes studying how these characteristics are transferred to DNA origami array systems where multiple anti-junctions are interconnected.

On a structural basis, anti-junctions can be understood as analogs to Holliday junctions. Both anti-junctions and Holliday junctions exist in two stable stacked conformations between which they can transition via an unstable open conformation.[24,112–117] As such, DNA origami arrays can also be interpreted as a network of coupled Holliday junctions. For Holliday junctions, it has been shown that both transition kinetics and thermodynamics can be programmed by their sequence.[114,121,122,124–127] The aim of associated publication P4 was to address the question of whether this programming can be transferred to DNA origami array systems and as such be used to increase the level of control over the energy landscape of their reconfiguration process.

For this purpose, we designed DNA origami array systems consisting of multiple Holliday junctions with identical sequences. We selected three representative junction sequences which are known to energetically (dis)favor the reconfigured conformation of individual Holliday junctions to different degrees and incorporated them into the systems. To characterize the effect the different sequences have on reconfiguration thermodynamics, we determined the reconfiguration yields of DNA origami array systems with the different sequences incorporated via AFM imaging by counting the number of reconfigured and not-reconfigured structures. The stronger a sequence favors the reconfigured conformation of a single Holliday junction, the higher are the obtained reconfiguration yields for the corresponding systems. This indicates that thermodynamic trends for individual Holliday junctions are transferable to DNA origami array systems. We continued to study the effect of the different sequences on the reconfiguration kinetics using a single-color FRET probe for signal transduction. Analogous to the dual-color FRET probe described in Chapter 4.3.1, the fluorescence of the FRET donor of the probe was designed to be strongly quenched prior to reconfiguration and light up upon reconfiguration, allowing the determination of reconfiguration times. In both single-molecule and ensemble fluorescence measurements, we extracted different reconfiguration kinetics for the different systems

which in their trend match the kinetics expected for single Holliday junctions. As such, in addition to thermodynamic trends also kinetic trends are transferable from individual Holliday junctions to DNA origami array systems. In the attempt to use this transferability to further push the regulatory control over the reconfiguration process, we then used this workflow to identify mismatches and free bases in Holliday junctions and the number of added trigger DNA strands as further parameters to tailor the energy landscape of the reconfiguration process.

All in all, we demonstrated several ways to control both the thermodynamics and kinetics of the reconfiguration process. Besides presenting means to control the reconfiguration process, our model represents the first general strategy to study the influence of both structure and environment on anti-junctions. This offers many exciting applications in DNA nanotechnology – where both anti-junctions and Holliday junctions are central construction motifs.

4.3.3 RECONFIGURABLE DNA ORIGAMI ARRAY STRUCTURES AS TWO-DIMENSIONAL NETWORKS OF COUPLED TWO-STATE SYSTEMS

Martina Pfeiffer[1], Fiona Cole[1], Dongfang Wang[1], Yonggang Ke* and Philip Tinnefeld*

([1] These authors contributed equally, * Correspondence)

Submission pending

The creation of smart nanorobots from DNA origami array systems necessitates combining the rational control over the energy landscape of their multistep reconfiguration process gained in Chapters 4.3.1 and 4.3.2 with different nanorobot functionalities. To this end, associated publication P5 (see Chapter 6.5.5) first introduces a universal approach to encode different nanorobot units into individual anti-junctions of DNA origami array systems. The publication then continues to demonstrate the unique features enabled by modularly combining multiple nanorobot units in these systems and connecting them to the energy landscape of the reconfiguration process.

By incorporation of linkers which stabilize one conformation of the targeted anti-junction over the other, anti-junctions can be locked into a pre-defined state. Based on this concept, we introduce a generalized approach for the design of input-receiving units which either activate or inhibit the reconfiguration process. By developing strategies to encode input-responsiveness into these linkers, we exemplarily demonstrated this approach by activating and inhibiting the reconfiguration process by a broad range of inputs including the activities of different restriction enzymes, light, DNA and antibodies. The proper functionalities of the units were confirmed by single-molecule fluorescence measurements using the single-color FRET probe introduced in Chapter 4.3.2 for signal transduction of the reconfiguration.

Depending on which anti-junction in the system an input receiving unit is placed on, we observed differing efficiencies in its inhibition or activation of the reconfiguration process: At some positions, incorporation of a single unit does not suffice to fully activate/ inhibit the process. We rationalized that this is connected to the energy landscape of the reconfiguration process which shows a non-uniform profile. As such, if the same input receiving units targets different steps of the energy landscape, its effect on the overall process differs. By incorporating multiple input receiving units at specified anti-junctions in the system this enabled us to perform biocomputation in form of multi-level Boolean logic gating on-demand. We again used the single-color FRET probe to characterize the performance of the logic gates. We then continued to replace the FRET probe in these systems with a cargo release unit introduced in Chapter 4.3.1. This directly transferred the logic gated activation from a fluorescence onset to the release of a cargo DNA strand, demonstrating the modularity gained by designing nanorobot units based on the anti-junctions.

Finally, we demonstrated how the modularity of our system can be applied to build nanorobots capable of performing a series of output operations both, in a pre-defined order and under temporal control. The order in which output operations are performed

depends on the anti-junction they are placed on. Output operations incorporated in anti-junctions changing their conformation very early in the reconfiguration process are activated earlier then output operations encoded in anti-junctions reconfiguring their conformation later-on. We demonstrated this in an experiment in which we activated two single-color FRET probes by restriction enzyme activity in a pre-defined order and then reversed this order in the second experiment. Besides controlling the timing between output operations by implementing them in anti-junctions reconfiguring in specific steps of the reconfiguration process, another approach to achieve this relies on encoding timing units introduced in Chapter 4.3.1 between them. We demonstrated this by encoding a timing unit between two single-color FRET probes which have shown to light up simultaneously upon activation by restriction enzyme activity. In the presence of the timing unit, we obtained a time lag between both output operations, offering the possibility of combining it with temporal control.

Altogether, we developed a generalized design approach to encode different nanorobot units into individual anti-junctions of DNA origami array systems. By applying this approach to modularly combine multiple nanodevice units in these systems and connecting them to the energy landscape of the reconfiguration process, a smart DNA origami nanorobot capable of processing biocomputational tasks in form of multi-level Boolean logic gating and performing series of different output operations in a programmable order under temporal and allosteric control was developed.

5 CONCLUSION AND FUTURE WORK

5.1 CONCLUSION

The DNA origami technique[34] has matured into powerful method to build biosensors and nanorobots capable of performing output operations in response to environmental inputs. Despite many exciting developments, several key limitations have to be addressed before their unique abilities (i.e. the performance of output operations in response to inputs in complex environments) can be used for broad real-world technological applications.[35,59–61] These challenges, amongst others, include strategies to generate output signals with good signal contrast, simple adaptability to new inputs, to tune the responsive window to relevant input concentration ranges, computing strategies to generate responses to different input combinations and to enable temporal control on the performance of output operations. The work presented in this thesis shows how implementing allosteric information transfer in DNA origami nanostructures allows to overcome the aforementioned challenges.

At first, different strategies which allow to expand the utility of DNA origami nanoantennas beyond the scope of the nucleic acid realm were developed and combined with signal amplification. By incorporation of multiple interacting input-receiving units in a dynamic DNA origami structure, approaches to create Boolean logic responses from both inputs of the same and of different molecular classes, approaches to tune the location and width of the responsive windows of these inputs and approaches to increase the specificity towards these input molecules were introduced. Subsequently, the developed concepts were implemented into a single DNA origami nanostructure, enabling the creation of a smart DNA origami nanorobot capable of overcoming the aforementioned challenges.

The first goal of this thesis was to expand the spectrum of inputs detectable with DNA origami nanodevices beyond the realm of inputs that directly interact with ssDNA. To this end, a novel approach to extend the sensing capability of DNA origami nanoantennas to antibodies that relies on implementing a fluorescence-based nanoswitch in their plasmonic hotspot was provided. It was shown that the nanoswitch can be successfully incorporated in the plasmonic hotspot of DNA origami nanoantennas, providing a mean for the specific detection of antibodies at the single-molecule level. The signal amplification achievable within the plasmonic hotspot enabled the detection of single antibodies using a simple, low-cost and portable optical device. Besides that, relevant characteristics for possible diagnostic applications were investigated. It was proven both that the detection under non-diffusion limited conditions is rapid and that the sensitive concentration window of this sensing platform fits concentration ranges relevant for diagnostic applications. Moreover, the modularity of the developed sensing platform was demonstrated by successfully implementing the nanoswitch in other DNA origami structures – without adapting the nanoswitch itself. Altogether, it was shown that fluorescence-(enhanced) DNA origami sensing biosensors can be expanded beyond the scope of inputs that directly interact with DNA.

Similar to many other DNA origami nanodevices, the nanoswitch was incorporated into the core DNA origami structure to provide the highest possible degree of functionality.

While such a design is effective for the conduction of simple and specific tasks, the resulting tight linkage between the different nanodevice units poses a challenge for the further expansion of the biosensor functionalities.

To address this, the second part of this thesis focused on spatially decoupling input receiving and output operation units. This enabled the development of a smart DNA origami biosensor capable of generating programmed optical output signals in response to diverse input combinations within user-programmable concentration ranges. This was achieved by using the conformational change of a hinge-like DNA origami structure as a communicational medium between multiple input receiving units and an output operation unit. It was demonstrated how – by modularly combining different input receiving units – this structure serves as a generalized platform responsive to different environmental inputs. Furthermore, it was shown that the modularity offered by this structure can be used to tune its sensitive concentration range and tailor its selectivity.

The last goal of this thesis was to create a smart DNA origami nanorobot. To this end, DNA origami array structures consisting of multiple equivalent building blocks, so called anti-junctions, were re-interpreted as two dimensional networks of two-state switches represented by their individual anti-junctions. It was demonstrated that encoding different input receiving and output operation units into individual anti-junctions within the network enables to perform multiple input – output combinations under temporal control. To achieve this, a precise understanding of the underlying reconfiguration process of DNA origami array structures and means for controlling the conformation of individual anti-junctions were crucial. In a first step, a novel double FRET assay was used to reveal insights into the kinetics and thermodynamics of the multi-step reconfiguration process, serving as the foundation for strategies to alter these properties both globally or at intermediate steps. The structural similarity of the anti-junctions then was used to develop generalized strategies for encoding different input receiving units and output operation units into individual anti-junctions. Together with the detailed understanding of the energy landscape and its regulatory mechanisms, this enabled receiving multiple different inputs, processing them using multi-level Boolean logic gates and reacting to them by performing multiple output operations under both temporal and allosteric control all on the same structure, ultimately creating a smart nanorobot using allosteric information transfer.

5.2 SUGGESTIONS FOR FUTURE WORK

5.2.1 TUNING DNA ORIGAMI NANODEVICES FOR DIAGNOSTIC AND THERAPEUTIC APPLICATIONS

This work focused on the development of smart DNA origami biosensors and nanorobots capable of performing output operations in response to a broad range of different biomolecular inputs. Their simple and rational adaptability makes them strong candidates for future diagnostic and therapeutic applications. For the large scale use of these DNA origami nanodevices in commercial clinical technologies, however, several challenges still await innovative solutions and further investigations.

One of these challenges addresses the spectrum of inputs receivable with the developed DNA origami nanodevices. While this thesis greatly expanded this spectrum, it, to date, still is limited to inputs that are – if at all – of only very little interest both for the staging and treatment of diseases. Therefore, one future direction for the projects discussed in Chapter 4 could be focused on expanding the input-responsiveness of the developed nanodevices towards diagnostic relevant input molecules. As proposed in Chapter 4.2 and Chapter 4.3, the spectrum of input molecules receivable by the developed nanodevices could, in principle, be further expanded to arbitrary biomolecular inputs assuming that the biorecognition element to which the input of interest binds is known.

A prime example therefore are proteases. Given their involvement in multiple pathological processes, proteases represent attractive biomarkers for the diagnosis and staging of many diseases. This can exemplarily be illustrated by the metalloprotease ADAMTS-13 which catalyzes the hydrolytic cleavage and thus also the degradation of the blood glycoprotein von Willebrand factor (VWF).[200] Insufficient ADAMTS-13 activity results in the severe coagulation disorder known as TTP. If left untreated, TTP undertakes a rapid course of deterioration and results in death in 72-94% of cases. Plasma therapy (plasma exchange or infusion) starting immediately after the occurrence of the first severe symptoms, however, drastically increases the survival rate of patients. With treatment, the 6-month mortality rate drops to 10-20%.[201,202] Fast and accurate diagnosis of TTP therefore is crucial for an effective treatment, necessitating clinical monitoring of ADAMTS-13 activity. In current diagnostic procedures, malfunctioning ADAMTS-13 protease activity is monitored using the FRETS-VWF73 assay.[203] This assay relies on the fluorescence energy transfer between the donor and acceptor fluorophores positioned on a synthetic VWF73 peptide While this assay (FRETS-VWF73 assay) can be successfully used to monitor the activity of ADAMTS-13 in normal as well as ADAMTS-13 deficient plasma it suffers from poor contrast and requires a large amount of the probe to achieve a detectible response over the course of tens of minutes. Here, the FRET contrast could be potentially improved by positioning the donor and acceptor dyes closer to achieve a high FRET signal in the closed state, this would, however, impair the functionality of ADAMTS-13. This challenge that originated from tight link between the signal recognition and signal transduction elements, is not limited to the FRETS-VWF73 assay, but presents one of the main challenges when developing protease sensors in general. Furthermore, the contrast and sensitivity of the FRETS-VWF73 assay is limited by a low signal-to-noise ratio mainly due to the not optimal detection window in the ultraviolet where most of auto-fluorescence from blood plasma also comes from which can make up more than half of the detected signal. This problem is further exacerbated by a low quantum yield, absorption coefficient and cross section of the chosen fluorophore. A simple substitution of the fluorophore-quencher pair, however, is difficult to realize since only small organic structures can be inserted into the peptide structure without impairing the activity of ADAMTS-13. Spatially separating the peptide from the optical read-out, however, would circumvent these problems. The nanodevices provided in Chapter 4.2 and Chapter 4.3 set the perfect framework to do so.

Employing one of the developed nanodevices to monitor the activity of ADAMTS-13 requires developing an input receiving unit based on the VWF. This could be achieved by adapting the DNA origami biosensor provided in Chapter 4.2. Preliminary

experiments have demonstrated the feasibility of such a protease activity monitoring with the hinge-like DNA origami structure, exemplified with the structurally more simple Tobacco Etch Virus (TEV) protease (see Figure 14). Here, input-responsiveness was achieved by incorporating a peptide serving as a bridging element between both arms of the DNA origami structure. The peptide was not directly incorporated into the DNA origami core structure itself but the structure was designed to provide functionalities enabling the post-synthetic attachment of DNA-coupled peptides (see Figure 14b). The TEV peptide was then modified with two azide functional groups which were covalently bound to DBCO modified ssDNA by strain promoted the copper-free strain-promoted alkyne-azide [3+2] cycloaddition (SPAAC)[204,205] (see Figure 14a) and then incorporated into the DNA origami structure. This project was done in collaboration with Susanne Weber and Professor Luppa, Klinikum rechts der Isar of the Technische Universität München.

I propose that similar to the TEV protease, this structure could be used to monitor ADAMTS-13 activity by exchanging the peptide sequence with a peptide providing the binding and cutting site for ADAMTS-13 protease. The high FRET signal contrast between both conformational states provided by the developed DNA origami nanodevices would open the door for a fast and simple diagnosis of TTP using low-tech fluorescence read-out devices present in routine laboratories. Besides TTP there are many other diseases which would greatly benefit from such detection methods. As such, the developed DNA origami nanodevices should be adaptable for many other clinical relevant inputs.

Similar to the inputs, the spectrum of output operations currently achievable with the developed DNA origami nanodevices is limited. While it is sufficient for the staging of diseases, it is not sufficient for therapeutic treatment where the performance of a specific task (e.g. controlled delivery of drugs to disease tissues or cells or the uptake of pathogens) is desired. As such, another further direction for the projects discussed in Chapter 4.3 could be focused on expanding the controlled release and uptake of molecules from DNA to therapeutic relevant drugs. For example, an exciting direction would be to expand the controlled release of targets towards chemotherapeutics[206–208] – drugs which are used in cancer therapy.

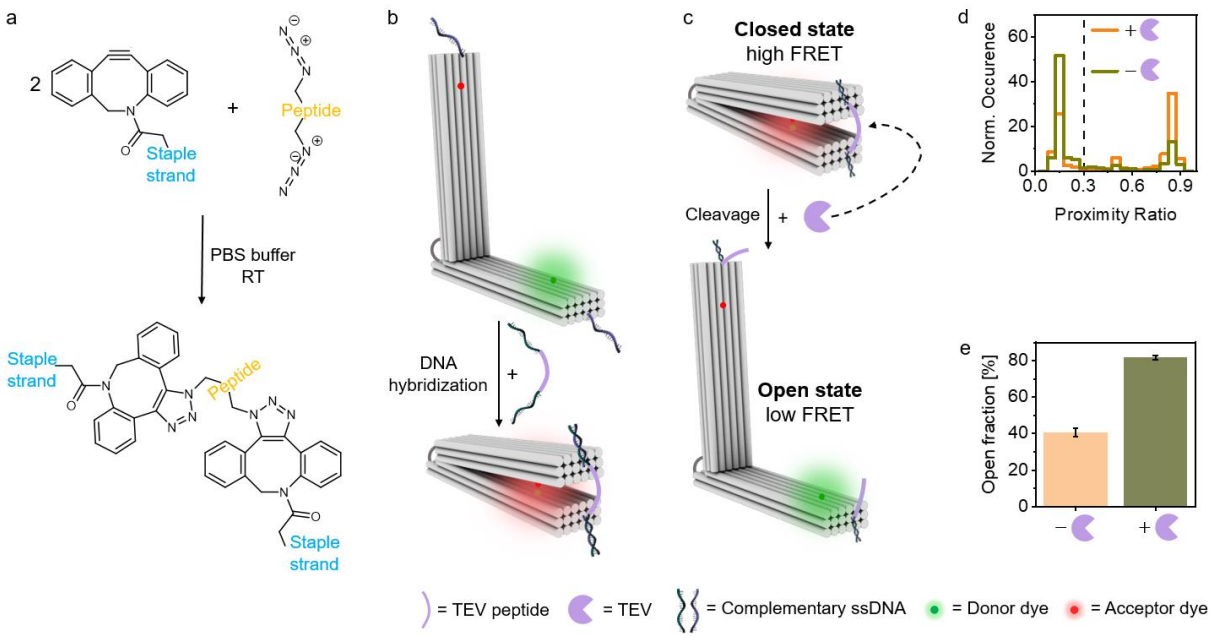

Figure 14: Concept of DNA origami nanodevices as biosensing platform for the detection of protease activity. (a) Coupling of ssDNA and peptide via SPAAC. ssDNA labelled with DBCO is covalently coupled to the biazide-labeled peptide in a SPAAC reaction. The coupling positions correspond to the positions at which DNA and peptide are labelled. (c, d) Design of DNA origami nanodevice for the detection of TEV protease activity. The DNA origami structure is closed with a peptide (substrate of TEV protease) via DNA hybridization. In the absence of proteolytic active TEV the nanodevices is closed leading to a high FRET signal. Cleavage of the peptide bridge by TEV results in the opening of the structure and loss of the FRET signal. (c) Corresponding proximity ratio histograms in the presence and the absence of TEV protease. (d) Corresponding fraction of open DNA origami structures.

Another challenge concerns the stability and functionality of the developed DNA origami nanodevices under physiological conditions. Up until now, their functionality was mainly demonstrated in buffer solution. For possible clinical applications, they, however, have to function reliably under complex physiological conditions, such as in blood, plasma, serum or saliva. Biological fluids contain a large amount of interfering substances and the type and quantity of these contaminants can be highly variable from patient to patient. As such, an exciting future direction could be focused on evaluating and improving the stability and functionality of the developed DNA origami nanodevices. First stability studies have shown that the DNA origami biosensor developed in Chapter 4.2 already shows a certain degree of stability in diluted heparin blood plasma whereas they degrade in diluted citrate plasma within only 10 min (see Figure 15). As such, an important future direction is the improvement of their stability. This could be achieved using recently reported approaches including polymer covers.[209–212] They have shown to improve the chemical stability of DNA nanostructures greatly by providing a protective coat against different degrading conditions. Besides that, self-repair strategies[213] can be used for improving the stability of DNA origami nanodevices by repairing defects caused by interfering substances such as enzyme damage.

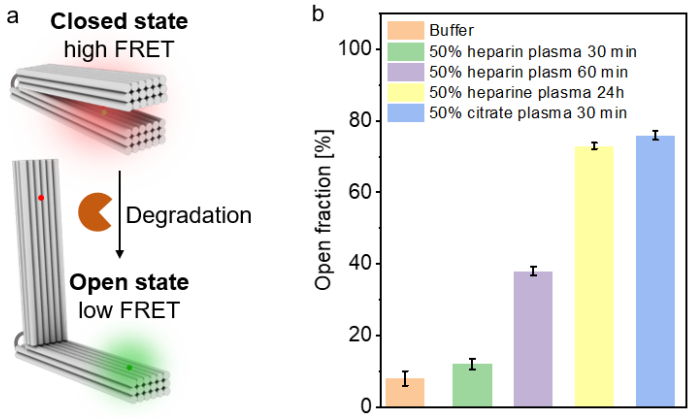

Figure 15: Functionality of DNA origami biosensor provided in Chapter 4 in heparin and citrate blood plasma. (a) Schematic illustration of DNA origami nanodevice with a FRET pair on the two opposing arms of the structure. The structure was folded in its closed state using DNA-DNA closing interactions. In the presence of degrading conditions the structure is expected to open up before complete degradation occurs. (c) Corresponding fraction of open structures under different environmental conditions.

Another major challenge that needs to be addresses before the developed DNA origami nanodevices can be applied in real-world applications are their costs. DNA strands labelled with fluorescent dyes and other markers are currently the most expensive components of DNA origami nanodevices. Thus, minimizing their usage is another important future direction. This could be achieved using graphene surfaces as fluorescence quenchers[214,215] instead of acceptor fluorophores. Moreover, recently developed enzymatic labeling protocols[216–218] to attach the donor fluorophores to the DNA staples by using terminal transferases would allow to minimize the usage of fluorophore modified DNA strands.

For applications in clinical diagnostics, the developed nanodevices would further benefit from an integration with microfluidics[219] to address the mass transport problem and to improve the sensing speed at low target concentrations. Particularly during the initial stages of diseases, diagnostically relevant input molecules occur at low concentrations. As time is a crucial factor when treating patients, this demands methods capable of generating robust signals against the background signal within a reasonable timeframe even at low concentrations. Given that the binding kinetics at low input concentrations are generally limited by diffusion,[220,221] combining the developed DNA origami nanodevices with micro- or nanofluidics could provide means to reduce the time required to achieve a detectable signal.

5.2.2 INVESTIGATION OF BIOLOGICAL PROCESSES WITH IMPROVED RESOLUTION AND WITHOUT THE NEED FOR COMPLEX EXPERIMENTAL SETUPS

Besides their great potential in the field of technological applications, the DNA origami nanodevices and especially their underlying concepts presented in this thesis could become useful tools to investigate chemical and biological processes.

The incorporation of an antibody in a DNA origami nanoantenna (see Chapter 4.1) represents the first study of a protein in their plasmonic hotspot. This opens the door for using the unique advantages offered by DNA origami nanoantennas to study transition paths of biomolecules (see Figure 16). Due to the transient nature of their transition states and intermediates and the resulting short-livety, observing transition paths (e.g. folding/unfolding of proteins or their dimerization reactions) generally is challenging.[222,223] The high count rate achievable within the plasmonic hotspot would provide a strategy to study these processes with greatly improved temporal resolution and thus would offer the possibility to shine light on currently hidden information. To this end, biomolecules or whole biomolecular assays of interest need to be implemented into the plasmonic hotspot. The nanoswitch presented in Chapter 4.3.1 provides the first demonstrated study to position large biomolecules nanometer precisely within the plasmonic hotspot. As such, applying DNA origami nanoantennas to study transitions paths of biomolecules holds great potential to uncover currently not accessible information of biomolecular processes.

In fluorescence microscopy, biomolecular processes are often monitored using a single FRET pair. However, when using only one FRET pair to explore the energy landscape of a biomolecular process, the process can only be monitored by the proximity between two single positions. This restricts the reconstructed energy landscape to a single dimension. Creating a multidimensional representation of the energy landscape currently requires the tedious synchronization of multiple measurements and complex fluorescence microscopy techniques.

Transferring the double FRET assay provided in Chapter 4.3.3 to biomolecules would provide a simple alternative to these complex procedures. By placing two FRET probes at positions which change their conformation in different steps of a reaction, this approach would provide access to the thermodynamics and kinetics of biomolecular reaction cascades on a simple two-color fluorescence microscope and without the need for experimental synchronization. It would allow studying both reaction pathways and their multidimensional energy landscape including sub-steps between intermediates (see Figure 16). The approach additionally would allow to reveal the reaction cascade independent of the often not-measurable induction by input molecules by comparing the reaction times of different sub-steps in single biomolecules. It thus would allow to explore and reconstruct 3D energy landscapes of biomolecular processes. Combining the advantages offered by both the double FRET assay and the DNA origami nanoantenna ultimately would allow the investigation of multidimensional cascade reactions in a simple and direct fashion with high temporal resolution.

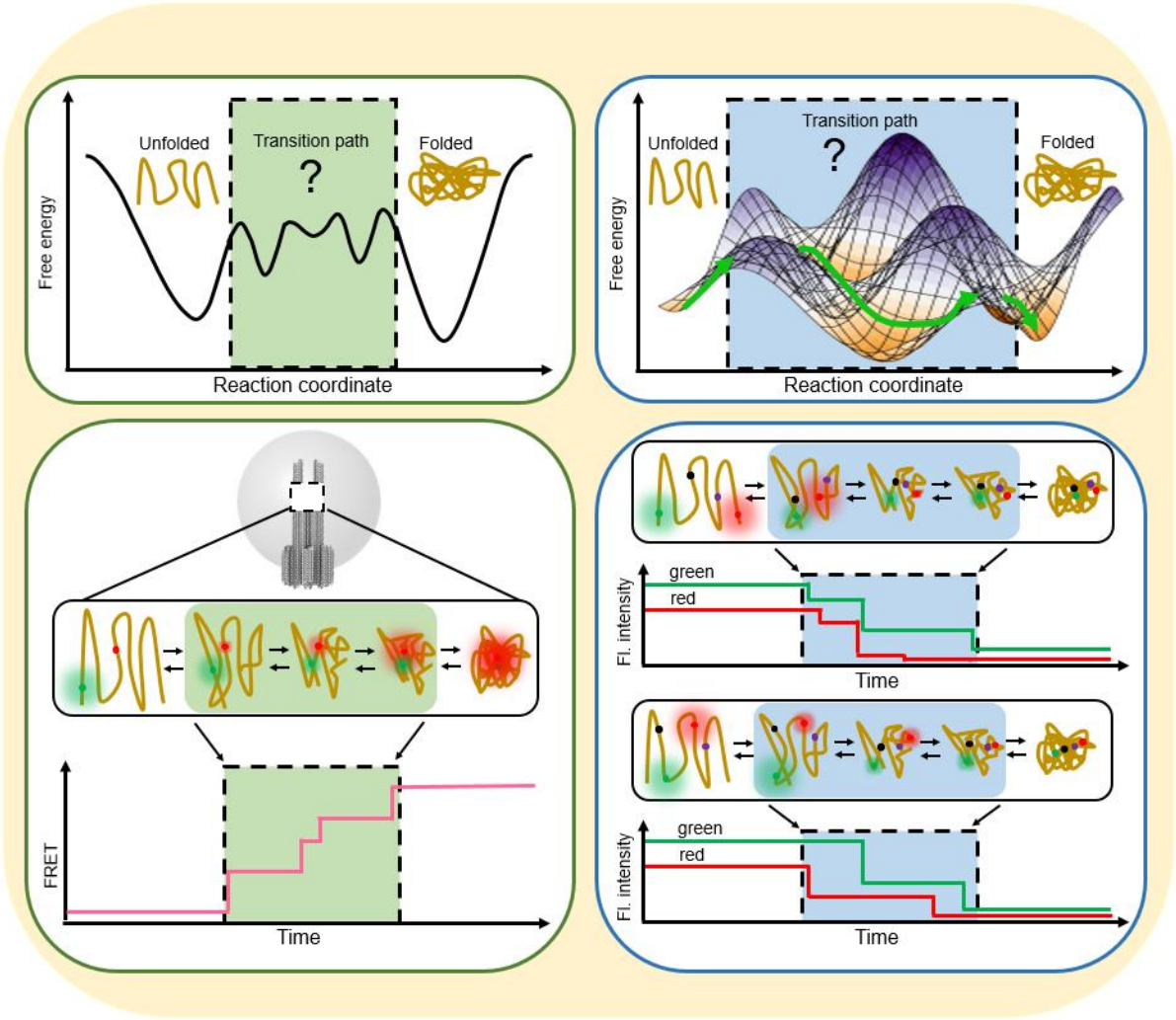

Figure 16: Outlook on the application of DNA origami nanoantennas and double FRET assay to study the energy landscape of protein folding/unfolding process. Schematic illustration of DNA origami nanoantenna with a protein (lower left). The protein can switch between an unfolded and a folded conformation via intermediate states. A FRET pair is used to visualize the conformational state of the protein. Positioning the protein into the plasmonic hotspot could provide a mean to study the underlying transition path of the folding/unfolding process with greatly improved temporal resolution (lower left) and thus would offer the possibility to shine light on currently hidden information (upper left). Schematic illustration of double FRET assay positioned on a protein that switches between an unfolded and a folded state via intermediate states (lower right). Positioning the FRET pairs at different positions could provide access to different sub-steps between intermediates. As such, it would open up the possibility to become a deeper understanding of the underlying energy landscape of the folding/unfolding process in the multi-dimensional space.

Altogether, the work presented in this thesis provides insights into approaches to build smart DNA origami biosensors and nanorobots with allosteric information transfer. By further developing these approaches, many of the current key limitations of DNA origami nanodevices can be overcome, paving the way for their broad real-world applications in different technological fields. My thesis also provides different approaches which could be applied in future to uncover currently not accessible information of biomolecular processes. I envision that the creation of smart DNA origami biosensors and nanorobots will mark the initiation of a revolution in the realm of nanotechnology and have a massive impact on life in the 21st century. Much like the steam engine's role in propelling the industrial revolution during the 19th century, these nanodevices hold the potential to drive significant advancements.

6 APPENDIX

6.1 LIST OF ABBREVIATIONS AND ACRONYMS

AFM	Atomic Force Microscopy
AOTF	Acousto-Optical Tunable Filter
APD	Avalanche Photo Diode
BSA	Bovine Serum Albumin
DBCO	DiBenzylCycloCctyne
DNA	DeoxyriboNucleic Acid
E	Effector
EMCCD	Electron Multiplying Charge-Coupled Device
FM	Fluorescence Microscopy
FRET	Förster Resonance Energy Transfer
I	Input
NA	numerical aperture
NACHOS	NanoAntennas with Cleared HotSpot
NRO	New Rectangular Origami
RNA	RiboNucleic Acid
ROXS	Reducing and Oxidizing System
S	System
[SE]	System-Effector Complex
[SEI]	System-Effector-Input Complex
[SI]	System-Input Complex
ssDNA	single-stranded DeoxyriboNucleic Acid
SPAAC	copper-free Strain-Promoted Alkyne-Azide [3+2] Cycloaddition
TCSPC	Time-Correlated Single-Photon Counting
TEM	Transmission Electron Microscopy
TEV	Tobacco Etch Virus
TIR	Total Internal Reflection
TIRF	total internal reflection fluorescence
TTP	thrombotic thrombocytopenic purpura
VWF	Von Willebrand Factor
2D	Two-Dimensional
3D	Three-Dimensional

6.2 ACKNOWLEDGEMENTS

“Know your energy – this is not only important when designing nanodevices but also on a personal level”

During my PhD journey, I got to learn the value of not only the first statement for research but also of the tremendous importance of the second statement for life in general. I would like to thank the people who kept me from going over my energy maxima and helped me in getting to know my energy and using it efficiently during my PhD journey. It has been a truly exciting time for me.

First of all, I would like to thank my supervisor Prof. Dr. Philip Tinnefeld for serving as my mentor throughout my whole PhD time. Thank you for all your contributions of time and ideas. Furthermore, I am thankful for the freedom you gave to me to follow and develop my own research ideas.

I would like to thank Prof. Dr. Alena Khmelinskaia for being the second evaluator of this thesis and Prof. Dr. Achim Hartschuh, Prof. Dr. med. Peter Luppa, Prof. Dr. Thomas M. Klapötke, Prof. Dr. Silvija Markic to join the thesis committee.

I would like to thank Prof. Dr. Francesco Ricci as well as his student Dr. Simona Ranallo (University of Rome Tor Vergata), Prof. Dr. Yonggang Ke and his former student Prof. Dr. Dongfang Wang (Georgia Tech and Emory University) and Prof. Dr. med. Peter Luppa and Dr. Susanne Weber (Klinikum Rechts der Isar and Technical University of Munich) with whom I had the pleasure of working with throughout collaborations.

A special thanks goes to Viktorija, Katya, Tim, Johann, Kristina, Florian and Fiona for their input and support for scientific questions. For proofreading the manuscript, I am deeply thankful to Kateryna, Viktorija, and Fiona.

I am thankful to all my office mates who created a supportive, joyful working atmosphere. Thanks to: Sarah, Katya, Andres, Patrick, Giovanni, Merve, and Fiona. Especially thanks to Patrick, Giovanni, Merve, and Fiona for not only accepting my ‘babies’ but also taking care of them.

I would also like to extend my gratitude to all the students I have had the privilege to mentor in the laboratory. Thanks to Martin, Stella and Pauline for always pushing every project forward.

I would like to thank Angelika for all the work she is doing for the whole lab. I am also thankful to Ms. Steger, Hilde and Moritz for kindly helping in administrative and organizational matters.

I am especially thankful to Fiona for the time we spent together and the enjoyment it brought.

Of course, I am also thankful to the whole Tinnefeld group and all persons I forgot to mention. Thank you for the enthusiasm your possess for research, as well as the friendship and support you provide to each other. Thanks to my family and friends and all the people I forgot to mention for all their support.

I also would like to thank Studienstiftung des deutschen Volkes for the support by a Promotionsstipendium.

Thanks to Luna, Wastl, Lucky, Xaverl and Charly for your warm support over these years.

6.3 OVERVIEW PUBLICATIONS

[1] These authors contributed equally, * Correspondence

Peer-Reviewed Publication

1. **Martina Pfeiffer**[1], Kateryna Trofymchuk[1], Simona Ranallo, Francesco Ricci, Florian Steiner, Fiona Cole, Viktorija Glembockyte* and Philip Tinnefeld*. Single Antibody Detection in a DNA Origami Nanoantenna, *iScience* **2021**, *24*, 103072.

Manuscripts in preparation

2. Lennart Grabenhorst**[1], Martina Pfeiffer**[1], Thea Schinkel, Mirjam Kümmerlin, Jasmin Maglic, Florian Selbach, Gereon Andreas Brüggenthies, Alexander Thomas Murr, Philip Tinnefeld* and Viktorija Glembockyte*. Engineering modular and tunable single molecule sensors by decoupling sensing from signal output. Preprint available on Biorxiv, DOI: 10.1101/2023.11.06.56579

3. Fiona Cole**[1], Martina Pfeiffer**[1], Dongfang Wang**[1]**, Tim Schröder, Yonggang Ke* and Philip Tinnefeld*. Controlled mechanochemical coupling of anti-junctions in DNA origami arrays. Submission pending.

4. Dongfang Wang**[1]**, Fiona Cole**[1]**, **Martina Pfeiffer**[1]**,** Tim Schröder, Philip Tinnefeld* and Yonggang Ke*. Sequence effect on the thermodynamics and transition kinetics of anti-junctions. Submission pending.

5. **Martina Pfeiffer**[1], Fiona Cole**[1]**, Dongfang Wang**[1]**, Yonggang Ke* and Philip Tinnefeld*. Reconfigurable DNA origami arrays structures as two-dimensional networks of coupled two-state systems. Submission pending.

6.4 REFERENCES

[1] A. Sproule, *James Watt: The story of the development of steam engines and how they created our industrial society*, Exley Pub, Watford, Herts, UK **1994, 1991**.

[2] H. W. Dickinson, *A Short History of the Steam Engine*, Cambridge University Press **2012**.

[3] R. L. Hills, *Transactions of the Newcomen Society* **2006**, *76*, 175.

[4] S. L. Kras, *The steam engine*, Chelsea House Publishers, Philadelphia **2004**.

[5] N. Loubet, T. Hook, P. Montanini, C.-W. Yeung, S. Kanakasabapathy, M. Guillom, T. Yamashita, J. Zhang, X. Miao, J. Wang, A. Young, R. Chao, M. Kang, Z. Liu, S. Fan, B. Hamieh, S. Sieg, Y. Mignot, W. Xu, S.-C. Seo, J. Yoo, S. Mochizuki, M. Sankarapandian, O. Kwon, A. Carr, A. Greene, Y. Park, J. Frougier, R. Galatage, R. Bao, J. Shearer, R. Conti, H. Song, D. Lee, D. Kong, Y. Xu, A. Arceo, Z. Bi, P. Xu, R. Muthinti, J. Li, R. Wong, D. Brown, P. Oldiges, R. Robison, J. Arnold, N. Felix, S. Skordas, J. Gaudiello, T. Standaert, H. Jagannathan, D. Corliss, M.-H. Na, A. Knorr, T. Wu, D. Gupta, S. Lian, R. Divakaruni, T. Gow, C. Labelle, S. Lee, V. Paruchuri, H. Bu, M. Khare, in *2017 Symposium on VLSI Technology*, IEEE **62017**, T230-T231.

[6] R. Pollie, *Engineering* **2021**, *7*, 1655.

[7] Q. Huang, J. Zeng, J. Yan, *Journal of genetics and genomics = Yi chuan xue bao* **2021**, *48*, 107.

[8] M. J. Hogan, N. Pardi, *Annual review of medicine* **2022**, *73*, 17.

[9] E. G. Nisbet, N. H. Sleep, *Nature* **2001**, *409*, 1083.

[10] M. R. Taylor, E. J. Simon, J. L. Dickey, K. Hogan, *Campbell Biology: Concepts & Connections*, Pearson Education Limited, Harlow, United Kingdom **2022**.

[11] N. Mitro, P. A. Mak, L. Vargas, C. Godio, E. Hampton, V. Molteni, A. Kreusch, E. Saez, *Nature* **2007**, *445*, 219.

[12] A. Miyajima, T. Kitamura, N. Harada, T. Yokota, K. Arai, *Annual review of immunology* **1992**, *10*, 295.

[13] J. Wolf, S. Rose-John, C. Garbers, *Cytokine* **2014**, *70*, 11.

[14] A. Yildiz, J. N. Forkey, S. A. McKinney, T. Ha, Y. E. Goldman, P. R. Selvin, *Science* **2003**, *300*, 2061.

[15] Z. Okten, L. S. Churchman, R. S. Rock, J. A. Spudich, *Nature structural & molecular biology* **2004**, *11*, 884.

[16] K. Kitamura, M. Tokunaga, A. H. Iwane, T. Yanagida, *Nature* **1999**, *397*, 129.

[17] A. Ishijima, H. Kojima, H. Higuchi, Y. Harada, T. Funatsu, T. Yanagida, *Biophysical journal* **1996**, *70*, 383.

[18] J. N. Forkey, M. E. Quinlan, M. A. Shaw, J. E. T. Corrie, Y. E. Goldman, *Nature* **2003**, *422*, 399.

[19] Y.-J. Chen, N. Dalchau, N. Srinivas, A. Phillips, L. Cardelli, D. Soloveichik, G. Seelig, *Nature nanotechnology* **2013**, *8*, 755.

[20] A. V. Pinheiro, D. Han, W. M. Shih, H. Yan, *Nature nanotechnology* **2011**, *6*, 763.

[21] Y.-J. Chen, B. Groves, R. A. Muscat, G. Seelig, *Nature nanotechnology* **2015**, *10*, 748.

[22] V. Linko, H. Dietz, *Current opinion in biotechnology* **2013**, *24*, 555.

[23] N. C. Seeman, H. F. Sleiman, *Nat Rev Mater* **2018**, *3*.

[24] N. C. Seeman, *Journal of theoretical biology* **1982**, *99*, 237.

[25] C. Alvarez-Lorenzo, A. Concheiro, *Chemical communications (Cambridge, England)* **2014**, *50*, 7743.

[26] D. Liu, F. Yang, F. Xiong, N. Gu, *Theranostics* **2016**, *6*, 1306.

[27] C. Alvarez-Lorenzo, A. Concheiro (Eds.), *Smart materials for drug delivery*, RSC Publishing, Cambridge, UK **2013**.

[28] R. Prins, A. Wang, X. Li, *Introduction to Heterogeneous Catalysis*, WORLD SCIENTIFIC (EUROPE) **2016**.

[29] J. Pilas, Y. Yazici, T. Selmer, M. Keusgen, M. J. Schöning, *Sensors (Basel, Switzerland)* **2018**, *18*.

[30] E. Katz, J. Wang, M. Privman, J. Halámek, *Analytical chemistry* **2012**, *84*, 5463.

[31] J. E. Sadler, *Blood* **2008**, *112*, 11.

[32] F. Peyvandi, R. Palla, L. A. Lotta, I. Mackie, M. A. Scully, S. J. Machin, *Journal of thrombosis and haemostasis JTH* **2010**, *8*, 631.

[33] M. Furlan, R. Robles, M. Galbusera, G. Remuzzi, P. A. Kyrle, B. Brenner, M. Krause, I. Scharrer, V. Aumann, U. Mittler, M. Solenthaler, B. Lämmle, *The New England journal of medicine* **1998**, *339*, 1578.

[34] P. W. K. Rothemund, *Nature* **2006**, *440*, 297.

[35] P. Wang, T. A. Meyer, V. Pan, P. K. Dutta, Y. Ke, *Chem* **2017**, *2*, 359.

[36] P. Zhan, A. Peil, Q. Jiang, D. Wang, S. Mousavi, Q. Xiong, Q. Shen, Y. Shang, B. Ding, C. Lin, Y. Ke, N. Liu, *Chemical reviews* **2023**, *123*, 3976.

[37] S. Dey, C. Fan, K. V. Gothelf, J. Li, C. Lin, L. Liu, N. Liu, M. A. D. Nijenhuis, B. Saccà, F. C. Simmel, H. Yan, P. Zhan, *Nat Rev Methods Primers* **2021**, *1*.

[38] K. Trofymchuk, V. Glembockyte, L. Grabenhorst, F. Steiner, C. Vietz, C. Close, M. Pfeiffer, L. Richter, M. L. Schütte, F. Selbach, R. Yaadav, J. Zähringer, Q. Wei, A. Ozcan, B. Lalkens, G. P. Acuna, P. Tinnefeld, *Nature communications* **2021**, *12*, 950.

[39] S. E. Ochmann, C. Vietz, K. Trofymchuk, G. P. Acuna, B. Lalkens, P. Tinnefeld, *Analytical chemistry* **2017**, *89*, 13000.

[40] D. Selnihhin, S. M. Sparvath, S. Preus, V. Birkedal, E. S. Andersen, *ACS nano* **2018**, *12*, 5699.

[41] Y. Ke, T. Meyer, W. M. Shih, G. Bellot, *Nature communications* **2016**, *7*, 10935.

[42] Y. Ke, S. Lindsay, Y. Chang, Y. Liu, H. Yan, *Science* **2008**, *319*, 180.

[43] A. Kuzuya, Y. Sakai, T. Yamazaki, Y. Xu, M. Komiyama, *Nature communications* **2011**, *2*, 449.

[44] M. Godonoga, T.-Y. Lin, A. Oshima, K. Sumitomo, M. S. L. Tang, Y.-W. Cheung, A. B. Kinghorn, R. M. Dirkzwager, C. Zhou, A. Kuzuya, J. A. Tanner, J. G. Heddle, *Scientific reports* **2016**, *6*, 21266.

[45] D. Koirala, P. Shrestha, T. Emura, K. Hidaka, S. Mandal, M. Endo, H. Sugiyama, H. Mao, *Angewandte Chemie (International ed. in English)* **2014**, *53*, 8137.

[46] S. Rinker, Y. Ke, Y. Liu, R. Chhabra, H. Yan, *Nature nanotechnology* **2008**, *3*, 418.

[47] S. M. Douglas, I. Bachelet, G. M. Church, *Science* **2012**, *335*, 831.

[48] M. Scherf, F. Scheffler, C. Maffeo, U. Kemper, J. Ye, A. Aksimentiev, R. Seidel, U. Reibetanz, *Nanoscale* **2022**, *14*, 18041.

[49] W. Engelen, C. Sigl, K. Kadletz, E. M. Willner, H. Dietz, *Journal of the American Chemical Society* **2021**, *143*, 21630.

[50] A.-K. Pumm, W. Engelen, E. Kopperger, J. Isensee, M. Vogt, V. Kozina, M. Kube, M. N. Honemann, E. Bertosin, M. Langecker, R. Golestanian, F. C. Simmel, H. Dietz, *Nature* **2022**, *607*, 492.

[51] N. V. Voigt, T. Tørring, A. Rotaru, M. F. Jacobsen, J. B. Ravnsbaek, R. Subramani, W. Mamdouh, J. Kjems, A. Mokhir, F. Besenbacher, K. V. Gothelf, *Nature nanotechnology* **2010**, *5*, 200.

[52] D. Wang, Y. Fu, J. Yan, B. Zhao, B. Dai, J. Chao, H. Liu, D. He, Y. Zhang, C. Fan, S. Song, *Analytical chemistry* **2014**, *86*, 1932.

[53] W. B. Sherman, N. C. Seeman, *Nano Lett.* **2004**, *4*, 1203.

[54] J.-S. Shin, N. A. Pierce, *Journal of the American Chemical Society* **2004**, *126*, 10834.

[55] A. J. Turberfield, J. C. Mitchell, B. Yurke, A. P. Mills, M. I. Blakey, F. C. Simmel, *Physical review letters* **2003**, *90*, 118102.

[56] H. Gu, J. Chao, S.-J. Xiao, N. C. Seeman, *Nature* **2010**, *465*, 202.

[57] D. Wang, C. Vietz, T. Schröder, G. Acuna, B. Lalkens, P. Tinnefeld, *Nano Lett.* **2017**, *17*, 5368.

[58] S. Fan, D. Wang, J. Cheng, Y. Liu, T. Luo, D. Cui, Y. Ke, J. Song, *Angewandte Chemie (International ed. in English)* **2020**, *59*, 12991.

[59] S. Wang, Z. Zhou, N. Ma, S. Yang, K. Li, C. Teng, Y. Ke, Y. Tian, *Sensors (Basel, Switzerland)* **2020**, *20*.

[60] P. Pitikultham, Z. Wang, Y. Wang, Y. Shang, Q. Jiang, B. Ding, *ChemMedChem* **2022**, *17*, e202100635.

[61] J. K. Daljit Singh, M. T. Luu, A. Abbas, S. F. J. Wickham, *Biophysical reviews* **2018**, *10*, 1283.

[62] C. Song, Z.-G. Wang, B. Ding, *Small (Weinheim an der Bergstrasse, Germany)* **2013**, *9*, 2382.

[63] A. V. Hill, *The Journal of physiology* **1909**, *39*, 361.

[64] M. Loretan, I. Domljanovic, M. Lakatos, C. Rüegg, G. P. Acuna, *Materials (Basel, Switzerland)* **2020**, *13*.

[65] J. MONOD, J. P. CHANGEUX, F. JACOB, *Journal of molecular biology* **1963**, *6*, 306.

[66] J. Monod, *Chance and necessity: An essay on the natural philosophy of modern biology*, Penguin, London **1997**.

[67] A. W. Fenton, *Trends in biochemical sciences* **2008**, *33*, 420.

[68] J.-P. Changeux, S. J. Edelstein, *Science* **2005**, *308*, 1424.

[69] B. C. Buddingh', J. Elzinga, J. C. M. van Hest, *Nature communications* **2020**, *11*, 1652.

[70] B. Ma, R. Nussinov, *Proceedings of the National Academy of Sciences of the United States of America* **2009**, *106*, 6887.

[71] V. Galstyan, L. Funk, T. Einav, R. Phillips, *J. Phys. Chem. B* **2019**, *123*, 2792.

[72] W. A. Lim, *Current opinion in structural biology* **2002**, *12*, 61.

[73] R. Gruber, A. Horovitz, *Chemical reviews* **2016**, *116*, 6588.

[74] Y. Yuan, M. F. Tam, V. Simplaceanu, C. Ho, *Chemical reviews* **2015**, *115*, 1702.

[75] S. J. Wodak, E. Paci, N. V. Dokholyan, I. N. Berezovsky, A. Horovitz, J. Li, V. J. Hilser, I. Bahar, J. Karanicolas, G. Stock, P. Hamm, R. H. Stote, J. Eberhardt, Y. Chebaro, A. Dejaegere, M. Cecchini, J.-P. Changeux, P. G. Bolhuis, J. Vreede, P. Faccioli, S. Orioli, R. Ravasio, Le Yan, C. Brito, M. Wyart, P. Gkeka, I. Rivalta, G. Palermo, J. A. McCammon, J. Panecka-Hofman, R. C. Wade, A. Di Pizio, M. Y. Niv, R. Nussinov, C.-J. Tsai, H. Jang, D. Padhorny, D. Kozakov, T. McLeish, *Structure (London, England 1993)* **2019**, *27*, 566.

[76] A. Cooper, *Progress in biophysics and molecular biology* **1984**, *44*, 181.

[77] N. V. Dokholyan, *Chemical reviews* **2016**, *116*, 6463.

[78] H. Frauenfelder, F. Parak, R. D. Young, *Annual review of biophysics and biophysical chemistry* **1988**, *17*, 451.

[79] D. Kern, E. R. P. Zuiderweg, *Current opinion in structural biology* **2003**, *13*, 748.

[80] O. Schueler-Furman, S. J. Wodak, *Current opinion in structural biology* **2016**, *41*, 159.

[81] V. J. Hilser, J. O. Wrabl, H. N. Motlagh, *Annual review of biophysics* **2012**, *41*, 585.

[82] H. N. Motlagh, J. O. Wrabl, J. Li, V. J. Hilser, *Nature* **2014**, *508*, 331.

[83] M. Kühnemund, Q. Wei, E. Darai, Y. Wang, I. Hernández-Neuta, Z. Yang, D. Tseng, A. Ahlford, L. Mathot, T. Sjöblom, A. Ozcan, M. Nilsson, *Nature communications* **2017**, *8*, 13913.

[84] M. Fakruddin, K. S. B. Mannan, A. Chowdhury, R. M. Mazumdar, M. N. Hossain, S. Islam, M. A. Chowdhury, *Journal of pharmacy & bioallied sciences* **2013**, *5*, 245.

[85] L. Gu, W. Yan, Le Liu, S. Wang, X. Zhang, M. Lyu, *Pharmaceuticals (Basel, Switzerland)* **2018**, *11*.

[86] P. Gill, A. Ghaemi, *Nucleosides, nucleotides & nucleic acids* **2008**, *27*, 224.

[87] A. B. Taylor, P. Zijlstra, *ACS sensors* **2017**, *2*, 1103.

[88] D. R. Walt, *Analytical chemistry* **2013**, *85*, 1258.

[89] J.-F. Li, C.-Y. Li, R. F. Aroca, *Chemical Society reviews* **2017**, *46*, 3962.

[90] M. Bauch, K. Toma, M. Toma, Q. Zhang, J. Dostalek, *Plasmonics (Norwell, Mass.)* **2014**, *9*, 781.

[91] G. P. Acuna, F. M. Möller, P. Holzmeister, S. Beater, B. Lalkens, P. Tinnefeld, *Science* **2012**, *338*, 506.

[92] V. Glembockyte, L. Grabenhorst, K. Trofymchuk, P. Tinnefeld, *Accounts of chemical research* **2021**, *54*, 3338.

[93] S. Ranallo, M. Rossetti, K. W. Plaxco, A. Vallée-Bélisle, F. Ricci, *Angewandte Chemie (International ed. in English)* **2015**, *54*, 13214.

[94] S. Ranallo, A. Porchetta, F. Ricci, *Analytical chemistry* **2019**, *91*, 44.

[95] A. Porchetta, R. Ippodrino, B. Marini, A. Caruso, F. Caccuri, F. Ricci, *Journal of the American Chemical Society* **2018**, *140*, 947.

[96] F. Ricci, A. Vallée-Bélisle, A. J. Simon, A. Porchetta, K. W. Plaxco, *Accounts of chemical research* **2016**, *49*, 1884.

[97] E. S. Andersen, M. Dong, M. M. Nielsen, K. Jahn, R. Subramani, W. Mamdouh, M. M. Golas, B. Sander, H. Stark, C. L. P. Oliveira, J. S. Pedersen, V. Birkedal, F. Besenbacher, K. V. Gothelf, J. Kjems, *Nature* **2009**, *459*, 73.

[98] M. S. L. Tang, S. C.-C. Shiu, M. Godonoga, Y.-W. Cheung, S. Liang, R. M. Dirkzwager, A. B. Kinghorn, L. A. Fraser, J. G. Heddle, J. A. Tanner, *Nanomedicine nanotechnology, biology, and medicine* **2018**, *14*, 1161.

[99] A. E. Marras, Z. Shi, M. G. Lindell, R. A. Patton, C.-M. Huang, L. Zhou, H.-J. Su, G. Arya, C. E. Castro, *ACS nano* **2018**, *12*, 9484.

[100] A. E. Marras, L. Zhou, H.-J. Su, C. E. Castro, *Proceedings of the National Academy of Sciences of the United States of America* **2015**, *112*, 713.

[101] D. Wang, L. Yu, C.-M. Huang, G. Arya, S. Chang, Y. Ke, *Journal of the American Chemical Society* **2021**, *143*, 2256.

[102] H. Yan, X. Zhang, Z. Shen, N. C. Seeman, *Nature* **2002**, *415*, 62.

[103] B. Yurke, A. J. Turberfield, A. P. Mills, F. C. Simmel, J. L. Neumann, *Nature* **2000**, *406*, 605.

[104] J. Song, Z. Li, P. Wang, T. Meyer, C. Mao, Y. Ke, *Science* **2017**, *357*.

[105] D. Wang, J. Song, P. Wang, V. Pan, Y. Zhang, D. Cui, Y. Ke, *Nature protocols* **2018**, *13*, 2312.

[106] Y. Cui, R. Chen, M. Kai, Y. Wang, Y. Mi, B. Wei, *ACS nano* **2017**, *11*, 8199.

[107] Y. Liu, H. Ge, Y. Wang, L. Tang, Y. Pei, S. Fan, Y. Song, C. Zhang, J. Song, *Small Structures* **2023**, *4*, 2200167.

[108] S. Fan, B. Ji, Y. Liu, K. Zou, Z. Tian, B. Dai, D. Cui, P. Zhang, Y. Ke, J. Song, *Angewandte Chemie (International ed. in English)* **2022**, *61*, e202116324.

[109] S. Fan, J. Cheng, Y. Liu, D. Wang, T. Luo, B. Dai, C. Zhang, D. Cui, Y. Ke, J. Song, *Journal of the American Chemical Society* **2020**, *142*, 14566.

[110] C. R. Simmons, T. MacCulloch, M. Krepl, M. Matthies, A. Buchberger, I. Crawford, J. Šponer, P. Šulc, N. Stephanopoulos, H. Yan, *Nature communications* **2022**, *13*, 3112.

[111] P. Christen, E. Hofmann (Eds.), *EJB Reviews*, Springer Berlin Heidelberg, Berlin, Heidelberg **1993**.

[112] R. M. Clegg, A. I. Murchie, A. Zechel, C. Carlberg, S. Diekmann, D. M. Lilley, *Biochemistry* **1992**, *31*, 4846.

[113] D. R. Duckett, A. I. H. Murchie, A. Bhattacharyya, R. M. Clegg, S. Diekmann, E. von Kitzing, D. M. J. Lilley, in *EJB Reviews* (Eds.: P. Christen, E. Hofmann), Springer Berlin Heidelberg. Berlin, Heidelberg **1993**, p. 131.

[114] B. F. Eichman, J. M. Vargason, B. H. Mooers, P. S. Ho, *Proceedings of the National Academy of Sciences of the United States of America* **2000**, *97*, 3971.

[115] N. R. Kallenbach, R.-I. Ma, N. C. Seeman, *Nature* **1983**, *305*, 829.

[116] M. Karymov, D. Daniel, O. F. Sankey, Y. L. Lyubchenko, *Proceedings of the National Academy of Sciences of the United States of America* **2005**, *102*, 8186.

[117] R. Holliday, *Genet. Res.* **1964**, *5*, 282.

[118] C. Hyeon, J. Lee, J. Yoon, S. Hohng, D. Thirumalai, *Nature chemistry* **2012**, *4*, 907.

[119] S. A. McKinney, A.-C. Déclais, D. M. J. Lilley, T. Ha, *Nature structural biology* **2003**, *10*, 93.

[120] D. R. Duckett, A. I. Murchie, D. M. Lilley, *The EMBO journal* **1990**, *9*, 583.

[121] P. Yakovchuk, E. Protozanova, M. D. Frank-Kamenetskii, *Nucleic acids research* **2006**, *34*, 564.

[122] D. M. Lilley, in *Mathematics of DNA Structure, Function and Interactions*, Vol. 150 (Eds.: C. J. Benham, S. Harvey, W. K. Olson, D. W. Sumners, D. Swigon), Springer New York. New York, NY **2009**, p. 213.

[123] E. Protozanova, P. Yakovchuk, M. D. Frank-Kamenetskii, *Journal of molecular biology* **2004**, *342*, 775.

[124] D. M. Lilley, R. M. Clegg, *Annual review of biophysics and biomolecular structure* **1993**, *22*, 299.

[125] C. Joo, S. A. McKinney, D. M. J. Lilley, T. Ha, *Journal of molecular biology* **2004**, *341*, 739.

[126] M. R. Adendorff, G. Q. Tang, D. P. Millar, M. Bathe, W. P. Bricker, *Nucleic acids research* **2022**, *50*, 717.

[127] S. M. Miick, R. S. Fee, D. P. Millar, W. J. Chazin, *Proceedings of the National Academy of Sciences of the United States of America* **1997**, *94*, 9080.

[128] C. M. Platnich, F. J. Rizzuto, G. Cosa, H. F. Sleiman, *Chemical Society reviews* **2020**, *49*, 4220.

[129] V. Birkedal, M. Dong, M. M. Golas, B. Sander, E. S. Andersen, K. V. Gothelf, F. Besenbacher, J. Kjems, *Microscopy research and technique* **2011**, *74*, 688.

[130] G. Binnig, H. Rohrer, C. Gerber, E. Weibel, *Physical review letters* **1982**, *49*, 57.

[131] G. Binnig, C. F. Quate, C. Gerber, *Physical review letters* **1986**, *56*, 930.

[132] J. Dubochet, M. Adrian, J. J. Chang, J. C. Homo, J. Lepault, A. W. McDowall, P. Schultz, *Quarterly reviews of biophysics* **1988**, *21*, 129.

[133] M. Stewart, G. Vigers, *Nature* **1986**, *319*, 631.

[134] J. R. Lakowicz, *Principles of fluorescence spectroscopy (3rd ed)*, Springer, New York, Berlin **2006**.

[135] J. W. Lichtman, J.-A. Conchello, *Nature methods* **2005**, *2*, 910.

[136] E. M. S. Stennett, M. A. Ciuba, M. Levitus, *Chemical Society reviews* **2014**, *43*, 1057.

[137] M. Sauer, J. Hofkens, J. Enderlein, *Handbook of fluorescence, spectroscopy and imaging: From single molecules to ensembles*, Wiley-VCH, Weinheim **2011**.

[138] Kubitscheck, F. Bloeck, *Fluorescence Microscopy - From Principles to Biological Applications 2e*, John Wiley & Sons, Inc, [Place of publication not identified] **2017**.

[139] R. Roy, S. Hohng, T. Ha, *Nature methods* **2008**, *5*, 507.

[140] A. Gust, A. Zander, A. Gietl, P. Holzmeister, S. Schulz, B. Lalkens, P. Tinnefeld, D. Grohmann, *Molecules (Basel, Switzerland)* **2014**, *19*, 15824.

[141] J. R. Lakowicz, *Principles of fluorescence spectroscopy*, Springer, New York, NY **2010**.

[142] U. Kubitscheck (Ed.), *Fluorescence microscopy: From principles to biological applications*, Wiley-VCH, Weinheim **2017**.

[143] J. Vogelsang, R. Kasper, C. Steinhauer, B. Person, M. Heilemann, M. Sauer, P. Tinnefeld, *Angewandte Chemie (International ed. in English)* **2008**, *47*, 5465.

[144] A. Gust, A. Zander, A. Gietl, P. Holzmeister, S. Schulz, B. Lalkens, P. Tinnefeld, D. Grohmann, *Molecules* **2014**, *19*, 15824.

[145] C. Vietz, M. L. Schütte, Q. Wei, L. Richter, B. Lalkens, A. Ozcan, P. Tinnefeld, G. P. Acuna, *ACS omega* **2019**, *4*, 637.

[146] P. Holzmeister, G. P. Acuna, D. Grohmann, P. Tinnefeld, *Chemical Society reviews* **2014**, *43*, 1014.

[147] in *Principles of Nano-Optics* (Eds.: L. Novotny, B. Hecht), Cambridge University Press **2012**, p. 378.

[148] E. A. Coronado, E. R. Encina, F. D. Stefani, *Nanoscale* **2011**, *3*, 4042.

[149] K. A. Kang, J. Wang, J. B. Jasinski, S. Achilefu, *Journal of nanobiotechnology* **2011**, *9*, 16.

[150] P. Anger, P. Bharadwaj, L. Novotny, *Physical review letters* **2006**, *96*, 113002.

[151] P. Holzmeister, E. Pibiri, J. J. Schmied, T. Sen, G. P. Acuna, P. Tinnefeld, *Nature communications* **2014**, *5*, 5356.

[152] D. Colquhoun, *Trends in pharmacological sciences* **2006**, *27*, 149.

[153] D. E. Koshland, A. Goldbeter, J. B. Stock, *Science* **1982**, *217*, 220.

[154] C. C. J. Carpenter, *JAMA* **1996**, *276*, 146.

[155] U. Setia, P. A. Gross, *The Journal of infectious diseases* **1976**, *134 Suppl*, S125-9.

[156] M. Rossetti, S. Ranallo, A. Idili, G. Palleschi, A. Porchetta, F. Ricci, *Chemical science* **2017**, *8*, 914.

[157] A. Porchetta, A. Vallée-Bélisle, K. W. Plaxco, F. Ricci, *Journal of the American Chemical Society* **2012**, *134*, 20601.

[158] F. Ricci, A. Vallée-Bélisle, A. Porchetta, K. W. Plaxco, *Journal of the American Chemical Society* **2012**, *134*, 15177.

[159] A. Porchetta, A. Vallée-Bélisle, K. W. Plaxco, F. Ricci, *Journal of the American Chemical Society* **2013**, *135*, 13238.

[160] G. Ortega, D. Mariottini, A. Troina, F. W. Dahlquist, F. Ricci, K. W. Plaxco, *Proceedings of the National Academy of Sciences of the United States of America* **2020**, *117*, 19136.

[161] A. J. Simon, A. Vallée-Bélisle, F. Ricci, H. M. Watkins, K. W. Plaxco, *Angewandte Chemie (International ed. in English)* **2014**, *53*, 9471.

[162] Q. Cui, M. Karplus, *Protein science a publication of the Protein Society* **2008**, *17*, 1295.

[163] G. Ortega, A. Chamorro-Garcia, F. Ricci, K. W. Plaxco, *Annual review of biophysics* **2023**.

[164] S. Erbas-Cakmak, S. Kolemen, A. C. Sedgwick, T. Gunnlaugsson, T. D. James, J. Yoon, E. U. Akkaya, *Chemical Society reviews* **2018**, *47*, 2228.

[165] L. Liu, P. Liu, L. Ga, J. Ai, *ACS omega* **2021**, *6*, 30189.

[166] J. MONOD, J. WYMAN, J. P. CHANGEUX, *Journal of molecular biology* **1965**, *12*, 88.

[167] G. Boole, *The mathematical analysis of logic: Being an essay towards a calculus of deductive reasoning = Die mathematische Analyse der Logik*, Hallescher Verl., Halle/Saale **2001**.

[168] T. Song, A. Eshra, S. Shah, H. Bui, D. Fu, M. Yang, R. Mokhtar, J. Reif, *Nature nanotechnology* **2019**, *14*, 1075.

[169] G. Boole, *An investigation of the laws of thought, on which are founded the mathematical theories of logic and probabilities*, Walton and Maberly, London **1854**.

[170] S. M. Douglas, A. H. Marblestone, S. Teerapittayanon, A. Vazquez, G. M. Church, W. M. Shih, *Nucleic acids research* **2009**, *37*, 5001.

[171] T. Cordes, J. Vogelsang, P. Tinnefeld, *Journal of the American Chemical Society* **2009**, *131*, 5018.

[172] S. Preus, S. L. Noer, L. L. Hildebrandt, D. Gudnason, V. Birkedal, *Nature methods* **2015**, *12*, 593.

[173] *Nature methods* **2012**, *9*, 627.

[174] S.-M. Jeon, *Experimental & molecular medicine* **2016**, *48*, e245.

[175] G. J. Gowans, S. A. Hawley, F. A. Ross, D. G. Hardie, *Cell metabolism* **2013**, *18*, 556.

[176] J. T. B. Crawley, R. de Groot, Y. Xiang, B. M. Luken, D. A. Lane, *Blood* **2011**, *118*, 3212.

[177] Y. Huang, R. Fliegert, A. H. Guse, W. Lü, J. Du, *Cell calcium* **2020**, *85*, 102111.

[178] A. Poschenrieder, M. Thaler, R. Junker, P. B. Luppa, *Analytical and bioanalytical chemistry* **2019**, *411*, 7607.

[179] B. Kaltenboeck, C. Wang, *Advances in clinical chemistry* **2005**, *40*, 219.

[180] S. Aydin, *Peptides* **2015**, *72*, 4.

[181] R. Higuchi, G. Dollinger, P. S. Walsh, R. Griffith, *Bio/technology (Nature Publishing Company)* **1992**, *10*, 413.

[182] R. Higuchi, C. Fockler, G. Dollinger, R. Watson, *Bio/technology (Nature Publishing Company)* **1993**, *11*, 1026.

[183] J. Li, J. Macdonald, F. von Stetten, *The Analyst* **2018**, *144*, 31.

[184] C. K. Dixit, S. K. Vashist, F. T. O'Neill, B. O'Reilly, B. D. MacCraith, R. O'Kennedy, *Analytical chemistry* **2010**, *82*, 7049.

[185] R. M. Lequin, *Clinical chemistry* **2005**, *51*, 2415.

[186] S. B. Nimse, M. D. Sonawane, K.-S. Song, T. Kim, *The Analyst* **2016**, *141*, 740.

[187] T. A. Pollak, J. P. Rogers, R. G. Nagele, M. Peakman, J. M. Stone, A. S. David, P. McGuire, *Schizophrenia bulletin* **2019**, *45*, 233.

[188] C. DeMarshall, E. L. Goldwaser, A. Sarkar, G. A. Godsey, N. K. Acharya, U. Thayasivam, B. A. Belinka, R. G. Nagele, *Journal of neuroimmunology* **2017**, *309*, 51.

[189] S. Ranallo, M. Rossetti, K. W. Plaxco, A. Vallée-Bélisle, F. Ricci, *Angew. Chem.* **2015**, *127*, 13412.

[190] Z. Li, L. Wang, H. Yan, Y. Liu, *Langmuir the ACS journal of surfaces and colloids* **2012**, *28*, 1959.

[191] S. Woo, P. W. K. Rothemund, *Nature chemistry* **2011**, *3*, 620.

[192] R. G. Moore, A. K. Brown, M. C. Miller, S. Skates, W. J. Allard, T. Verch, M. Steinhoff, G. Messerlian, P. DiSilvestro, C. O. Granai, R. C. Bast, *Gynecologic oncology* **2008**, *108*, 402.

[193] R. Sever, C. K. Glass, *Cold Spring Harbor perspectives in biology* **2013**, *5*, a016709.

[194] C. K. Billington, K. C. Kong, R. Bhattacharyya, P. B. Wedegaertner, R. A. Panettieri, T. O. Chan, R. B. Penn, *Biochemistry* **2005**, *44*, 14595.

[195] A. O. Shpakov, *International journal of molecular sciences* **2023**, *24*.

[196] R. Leurs, R. A. Bakker, H. Timmerman, I. J. P. de Esch, *Nature reviews. Drug discovery* **2005**, *4*, 107.

[197] H. L. Sweeney, E. L. F. Holzbaur, *Cold Spring Harbor perspectives in biology* **2018**, *10*.

[198] A. Anders, B. Ghosh, T. Glatter, V. Sourjik, *Nature communications* **2020**, *11*, 3494.

[199] J. R. Burns, B. Lamarre, A. L. B. Pyne, J. E. Noble, M. G. Ryadnov, *ACS synthetic biology* **2018**, *7*, 767.

[200] H. M. Tsai, *Blood* **1996**, *87*, 4235.

[201] M. Bommer, M. Wölfle-Guter, S. Bohl, F. Kuchenbauer, *Deutsches Arzteblatt international* **2018**, *115*, 327.

[202] J. T. B. Crawley, M. A. Scully, *Hematology. American Society of Hematology. Education Program* **2013**, *2013*, 292.

[203] K. Kokame, Y. Nobe, Y. Kokubo, A. Okayama, T. Miyata, *British journal of haematology* **2005**, *129*, 93.

[204] M. F. Debets, C. W. J. van der Doelen, F. P. J. T. Rutjes, F. L. van Delft, *Chembiochem a European journal of chemical biology* **2010**, *11*, 1168.

[205] J. C. Jewett, C. R. Bertozzi, *Chemical Society reviews* **2010**, *39*, 1272.

[206] S. K. Carter, M. Slavik, *Annual review of pharmacology* **1974**, *14*, 157.

[207] B. A. Chabner, T. G. Roberts, *Nature reviews. Cancer* **2005**, *5*, 65.

[208] C. W. Young, J. H. Burchenal, *Annual review of pharmacology* **1971**, *11*, 369.

[209] N. Ponnuswamy, M. M. C. Bastings, B. Nathwani, J. H. Ryu, L. Y. T. Chou, M. Vinther, W. A. Li, F. M. Anastassacos, D. J. Mooney, W. M. Shih, *Nature communications* **2017**, *8*, 15654.

[210] M.-K. Nguyen, V. H. Nguyen, A. K. Natarajan, Y. Huang, J. Ryssy, B. Shen, A. Kuzyk, *Chem. Mater.* **2020**, *32*, 6657.

[211] L. Nguyen, M. Döblinger, T. Liedl, A. Heuer-Jungemann, *Angewandte Chemie (International ed. in English)* **2019**, *58*, 912.

[212] X. Liu, F. Zhang, X. Jing, M. Pan, P. Liu, W. Li, B. Zhu, J. Li, H. Chen, L. Wang, J. Lin, Y. Liu, D. Zhao, H. Yan, C. Fan, *Nature* **2018**, *559*, 593.

[213] M. Scheckenbach, T. Schubert, C. Forthmann, V. Glembockyte, P. Tinnefeld, *Angewandte Chemie (International ed. in English)* **2021**, *60*, 4931.

[214] I. Kaminska, J. Bohlen, S. Rocchetti, F. Selbach, G. P. Acuna, P. Tinnefeld, *Nano Lett.* **2019**, *19*, 4257.

[215] I. Kamińska, J. Bohlen, R. Yaadav, P. Schüler, M. Raab, T. Schröder, J. Zähringer, K. Zielonka, S. Krause, P. Tinnefeld, *Advanced materials (Deerfield Beach, Fla.)* **2021**, *33*, e2101099.

[216] C. Heck, D. Torchinsky, G. Nifker, F. Gularek, Y. Michaeli, E. Weinhold, Y. Ebenstein, *Nanoscale* **2020**, *12*, 20287.

[217] G. Lukinavicius, V. Lapiene, Z. Stasevskij, C. Dalhoff, E. Weinhold, S. Klimasauskas, *Journal of the American Chemical Society* **2007**, *129*, 2758.

[218] A. A. Wilkinson, E. Jagu, K. Ubych, S. Coulthard, A. E. Rushton, J. Kennefick, Q. Su, R. K. Neely, P. Fernandez-Trillo, *ACS central science* **2020**, *6*, 525.

[219] G. Luka, A. Ahmadi, H. Najjaran, E. Alocilja, M. DeRosa, K. Wolthers, A. Malki, H. Aziz, A. Althani, M. Hoorfar, *Sensors (Basel, Switzerland)* **2015**, *15*, 30011.

[220] A. J. Simon, A. Vallée-Bélisle, F. Ricci, K. W. Plaxco, *Proceedings of the National Academy of Sciences of the United States of America* **2014**, *111*, 15048.

[221] Y. Wu, R. D. Tilley, J. J. Gooding, *Journal of the American Chemical Society* **2019**, *141*, 1162.

[222] K. Neupane, D. A. N. Foster, D. R. Dee, H. Yu, F. Wang, M. T. Woodside, *Science* **2016**, *352*, 239.

[223] F. Sturzenegger, F. Zosel, E. D. Holmstrom, K. J. Buholzer, D. E. Makarov, D. Nettels, B. Schuler, *Nature communications* **2018**, *9*, 4708.

6.5 PUBLICATIONS

6.5.1 PUBLICATION P1

Single antibody detection in a DNA origami nanoantenna

by

Martina Pfeiffer[1], Kateryna Trofymchuk[1], Simona Ranallo, Francesco Ricci, Florian Steiner, Fiona Cole, Viktorija Glembockyte* and Philip Tinnefeld*
([1] These authors contributed equally, * Correspondence)

iScience, volume 24, issue 9, pages 103072 (**2021**)
DOI: 10.1016/j.isci.2021.103072

Author contributions:
The initial idea of using nanoswitch systems for the detection of antibodies in DNA origami nanoantennas was proposed by Philip Tinnefeld, Viktorija Glembockyte, Simona Ranallo, and Franccesco Ricci. I designed the sensor, performed the experiments and analyzed the measurements with additional input from Kateryna Trofymchuk and Florian Steiner. I wrote the manuscript with additional input from Viktorija Glembockyte, Kateryna Trofymchuk and Philip Tinnefeld.

iScience

CellPress
OPEN ACCESS

Article

Single antibody detection in a DNA origami nanoantenna

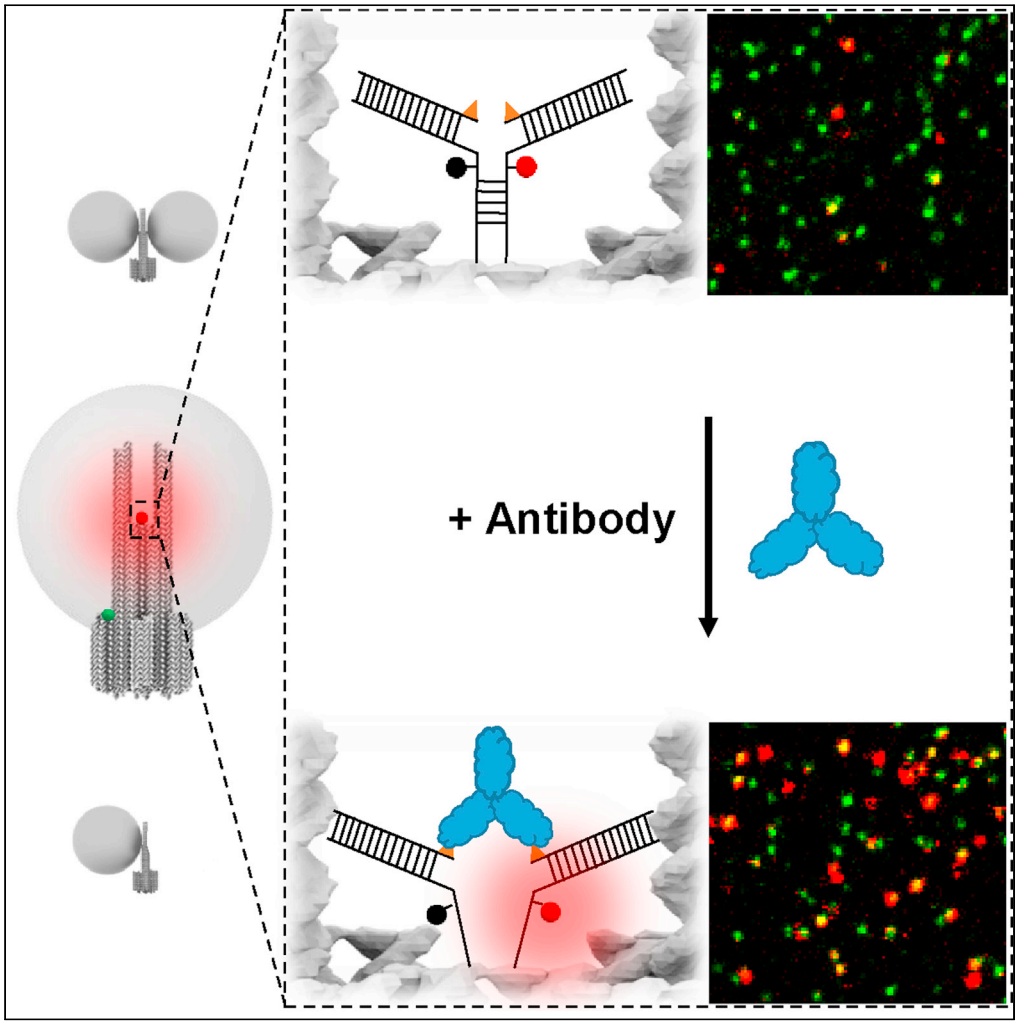

Martina Pfeiffer, Kateryna Trofymchuk, Simona Ranallo, ..., Fiona Cole, Viktorija Glembockyte, Philip Tinnefeld

viktorija.glembockyte@cup.lmu.de (V.G.)
philip.tinnefeld@cup.uni-muenchen.de (P.T.)

Highlights

Single-antibody detection with nanoswitch sensor incorporated in DNA origami structures

Fluorescence-enhanced single antibody detection in DNA origami nanoantennas

Detection of single antibodies on a portable smartphone microscope

Pfeiffer et al., iScience 24, 103072
September 24, 2021
https://doi.org/10.1016/j.isci.2021.103072

iScience

CellPress
OPEN ACCESS

Article

Single antibody detection in a DNA origami nanoantenna

Martina Pfeiffer,[1,4] Kateryna Trofymchuk,[1,4] Simona Ranallo,[2,3] Francesco Ricci,[2] Florian Steiner,[1] Fiona Cole,[1] Viktorija Glembockyte,[1,*] and Philip Tinnefeld[1,5,*]

SUMMARY

DNA nanotechnology offers new biosensing approaches by templating different sensor and transducer components. Here, we combine DNA origami nanoantennas with label-free antibody detection by incorporating a nanoswitch in the plasmonic hotspot of the nanoantenna. The nanoswitch contains two antigens that are displaced by antibody binding, thereby eliciting a fluorescent signal. Single-antibody detection is demonstrated with a DNA origami integrated anti-digoxigenin antibody nanoswitch. In combination with the nanoantenna, the signal generated by the antibody is additionally amplified. This allows the detection of single antibodies on a portable smartphone microscope. Overall, fluorescence-enhanced antibody detection in DNA origami nanoantennas shows that fluorescence-enhanced biosensing can be expanded beyond the scope of the nucleic acids realm.

INTRODUCTION

Over the last decades, DNA nanotechnology (Seeman and Sleiman, 2017) and in particular the DNA origami technique (Rothemund, 2006; Dey et al., 2021) have emerged as an indispensable tool for designing new biosensors on the nanoscale. As introduced by Rothemund (Rothemund, 2006), DNA origami can be used to fabricate various two- or three-dimensional shapes using a long single-stranded (ss) scaffold (about 7000–8000 nucleotides (nt)) and hundreds of short staple strands (about 40 nt). Utilizing the programmable nature of DNA base pairing and functionalized staple strands, a large number of different functionalities can be introduced on the nanoscale. This unprecedented addressability of the DNA origami approach allows arranging different biosensing components, introducing new bio-recognition elements and multiplexing strategies, as well as the implementation of signal transduction and amplification mechanisms. Using DNA origami, a number of biosensors have been developed capable of single-molecule detection of DNA and RNA (Ke et al., 2008; Zhang et al., 2010a; Kuzuya et al., 2011; Ochmann et al., 2017; Selnihhin et al., 2018; Funck et al., 2018; Trofymchuk et al., 2021), single nucleotide polymorphisms (Zhang et al., 2010b; Subramanian et al., 2011), specific metal ions (Ke et al., 2008; Marras et al., 2018), as well as various protein biomarkers (Rinker et al., 2008; Koirala et al., 2014; Godonoga et al., 2016; Raveendran et al., 2020) among many others (Wang et al., 2017a, 2017b, 2020; Chandrasekaran, 2017; Ke et al., 2018; Loretan et al., 2020; Dass et al., 2021).

Nevertheless, the use of these biosensors is often limited to the detection of targets that directly interact with DNA (e.g. nucleic acids or proteins with aptameric probes). The methods that are used to detect the analyte-sensor interactions also often require low-throughput, complex analytical techniques, such as atomic force microscopy, limiting the widespread application of DNA origami biosensors in clinical diagnostics. Recent advances in the development of high-throughput DNA origami-enabled optical (Domljanovic et al., 2017; Funck et al., 2018) or nanopore-based (Keyser, 2016; Raveendran et al., 2020) sensing strategies provide excellent examples of how to bridge this gap. However, general strategies on how to incorporate recognition elements for targets that go beyond nucleic acids (such as antibodies) are still highly sought after (Wang et al., 2020).

Due to its quick response, high contrast, and good sensitivity, fluorescence provides a powerful readout strategy for developing such sensing devices. Using the DNA origami approach, one can also incorporate methods to further amplify the fluorescence response (Wang et al., 2017a). This enables the detection of single target molecules on low-cost optical devices (Trofymchuk et al., 2021). A way to enhance the

[1]Department of Chemistry and Center for NanoScience, Ludwig-Maximilians-Universität München, Butenandtstr. 5-13, 81377 München, Germany

[2]Department of Chemical Science and Technologies, University of Rome, Tor Vergata, Via della Ricerca Scientifica 1, 00133 Rome, Italy

[3]Department of Chemistry and Biochemistry, University of California Santa Barbara, Santa Barbara, CA 93106, USA

[4]These authors contributed equally

[5]Lead contact

*Correspondence: viktorija.glembockyte@cup.lmu.de (V.G.), philip.tinnefeld@cup.uni-muenchen.de (P.T.)

https://doi.org/10.1016/j.isci.2021.103072

fluorescence intensity of a molecule is to put it in a higher electric field environment, which for example is created close to the surface of a plasmonic silver (Ag) or gold (Au) nanoparticle (NP) upon their illumination (plasmonic hotspot) (Novotny and van Hulst, 2011; Purcell, 1946). Even higher electric field enhancement can be achieved in a gap between two plasmonic NPs (Li et al., 2003). Our group has explored this signal amplification strategy to design light antennas on the nanoscale (Acuna et al., 2012; Puchkova et al., 2015; Vietz et al., 2017a) that can be used to amplify the signal of molecular assays (Ochmann et al., 2017; Trofymchuk et al., 2021). In this context, the strength of DNA nanotechnology compared to other approaches of creating plasmonic fluorescence enhancement is the possibility of targeted placement of NPs and fluorescence enhancement with respect to each other. First, we showed that the detection of DNA and RNA specific to Zika virus can be achieved with a fluorescence-quenched hairpin-based assay when positioned next to a plasmonic AgNP, allowing for around 7-fold average fluorescence enhancement (Ochmann et al., 2017). More recently, we also reported a DNA origami NanoAntenna design with a Cleared plasmonic HOt-Spot (NACHOS), which allowed positioning a DNA detection assay in the hotspot of two AgNPs enabling an average fluorescence enhancement of 90-fold and the detection of single target molecules on a low-cost, portable, and battery-driven smartphone device (Trofymchuk et al., 2021).

Here, we address the question of whether DNA origami nanoantennas could be applied to larger targets beyond the realm of nucleic acids, such as antibodies. The use of specific recognition elements capable of eliciting a signal response upon binding of other non-labeled biomolecular targets, including antibodies, could provide means to expand the utility of the DNA nanoantenna, as well as other DNA-origami-based sensors for a wider range of targets and diagnostic applications. A promising strategy to combine the specific recognition of antibody targets with DNA-based biosensors that relies on a DNA nanoswitch has been developed recently (Ranallo et al., 2015, 2019). DNA containing a fluorophore-quencher pair is used as a scaffold to attach specific recognition elements and transduce target detection through fluorescence output. In absence of an antibody target, the nanoswitch adopts a stem-loop conformation that opens upon binding to the antibody target, separating the fluorophore-quencher pair and resulting in a fluorescence signal. With this class of nanoswitch, different antibody targets can be simultaneously detected (Porchetta et al., 2018). A detection limit in the nanomolar range can be achieved (Porchetta et al., 2018) and the dynamic range of the response possibly can also be tuned by varying the sequence of the stem similarly as shown for other nanoswitches (Ricci et al., 2016).

In this work, we report a single-molecule DNA origami-based sensor for antibodies by incorporating nanoswitch recognition elements into DNA origami nanostructures. First, we demonstrate the feasibility of this sensing strategy on a simple new rectangular DNA origami (NRO) structure (Rothemund, 2006; Woo and Rothemund, 2011; Li et al., 2012), showing the specific detection of anti-digoxigenin (Dig) antibodies at sub-nanomolar concentrations within few minutes. We then incorporate the nanoswitch elements in the hotspot of DNA nanoantennas showing that the signal of the nanosensor can be enhanced up to ~60-folds. The single-molecule sensing platform reported here allows us to increase the limit of detection of the nanoswitch and combine it with signal amplification strategies. This allowed us to carry out an exemplary single antibody detection assay on a portable smartphone microscope. Additionally, the modular nature of the DNA origami approach opens exciting possibilities for even further multiplexing in rapid antibody detection.

RESULTS

Detection of anti-dig antibodies with a nanoswitch on the NRO at the single-molecule level

To demonstrate direct detection of antibodies on DNA origami at the single-molecule level, the NRO DNA origami was chosen as a model structure. The simple two-dimensional shape of the NRO provides an ideal platform to incorporate antibody sensing units with high accessibility (Figure 1A, Tables S1 and S2). A sensing unit, which was inspired by the nanoswitch sensor for antibodies developed by the Ricci group (Ranallo et al., 2015), was incorporated into the NRO structure during the DNA origami folding process. The nanoswitch consists of two ssDNA strands protruding from the NRO nanostructure with their 3′- and 5′-ends. Both strands contain a 7-nt long, non-complementary linker sequence followed by a 5-nt long complementary sequence which forms a stem (Figure 1A, Table S2). One of the ssDNA strands is modified with ATTO 647N and the other ssDNA strand is modified with BlackBerry Quencher 650 (BBQ-650), which forms a dye-quencher pair. The stem is followed by DNA anchors on both strands. The DNA anchors allow the hybridization of two Dig-conjugated ssDNA strands which provide binding sites for anti-Dig antibodies (McCreery, 1997). Each NRO nanostructure is equipped with six biotinylated DNA strands for surface immobilization on BSA-biotin-neutravidin coated glass coverslips. Additionally, to aid in identifying each

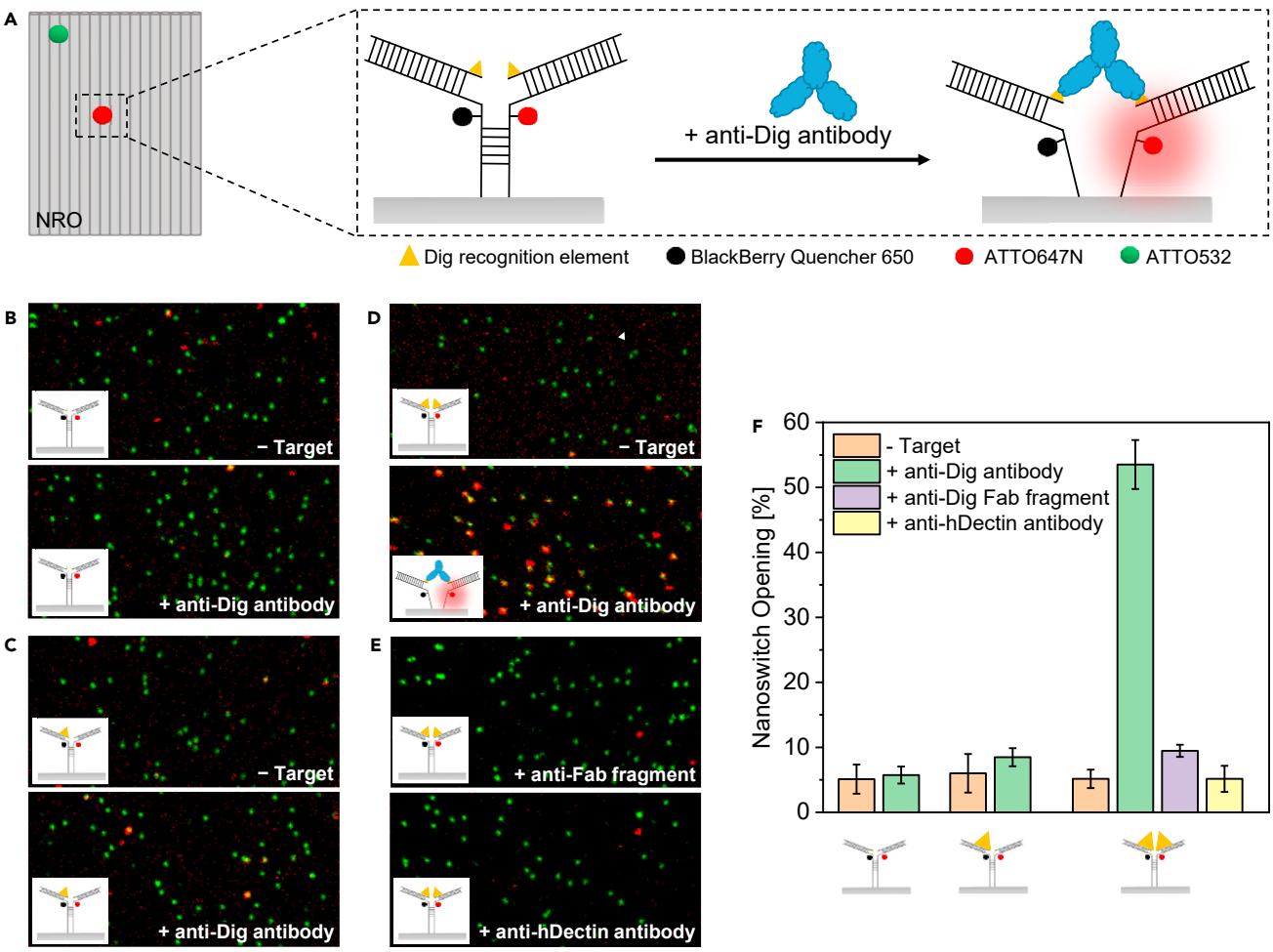

Figure 1. Detection of anti-Dig antibodies with a nanoswitch on the NRO at the single-molecule level

(A) Schematic representation of the NRO nanostructure with an incorporated nanoswitch (dimensions are not to scale). The nanoswitch consists of two DNA strands protruding from the NRO with their 3′ and 5′ ends. Both strands contain a 7-nt long, non-complementary linker sequence followed by a 5-nt long stem. The stem is modified with a dye (ATTO 647N)-quencher (BlackBerry Quencher 650) pair and followed by an ssDNA anchor on both strands. The DNA anchors allow hybridizing two Dig-modified ssDNA strands which form binding sites for Dig binding antibodies to the nanoswitch. In absence of target molecules, the stem is closed and an efficient energy transfer from the fluorophore to the quencher occurs due to their close proximity. Upon bivalent binding of an antibody to the Dig recognition elements, fluorophore and quencher are spatially separated and the fluorescence signal of ATTO 647N is increased. To localize the DNA origami structure, a green-absorbing ATTO 532 dye is incorporated. To test the specificity of the nanoswitch opening and the opening mechanism of the nanoswitch, three different nanoswitch constructs bearing one, two or no Dig recognition elements were investigated.

(B–D) Two-color fluorescence confocal images of surface immobilized NRO-nanoswitch constructs bearing no Dig recognition elements (B), one Dig recognition element (C), and two Dig recognition elements (D) before and after 20 min incubation with 100 nM anti-Dig antibodies.

(E) Two-color fluorescence images of surface immobilized NRO-nanoswitch constructs bearing two Dig recognition elements after incubation with 100 nM anti-Dig Fab fragment (upper) and anti-h-Dectin antibodies (lower), respectively. The images show a field of view of 20 μm × 10 μm. Co-localized green and red spots are attributed to functional NRO structures with an open nanoswitch.

(F) The fraction of open nanoswitches was quantified for every sample by dividing the number of green and red co-localized spots by the total number of green spots from fluorescence confocal scans. Over 300 structures from 5 different areas per sample were analyzed. Error bars represent the standard deviation of the 5 areas.

DNA origami nanosensor position in the single-molecule fluorescence experiments, a green ATTO 532 dye is incorporated in the NRO nanostructure (Figures 1A and S1).

The principle of the nanoswitch is illustrated in Figure 1A. In absence of target molecules, the stem is closed and the dye-quencher pair is in close proximity so that the fluorescence of the ATTO 647N dye is quenched. Bivalent binding of anti-Dig antibodies to the Dig-recognition elements opens the stem and spatially separates fluorophore and quencher. This results in an increase of the fluorescence of ATTO 647N. The binding

of the antibody can be detected in single-molecule confocal fluorescence images (Figures 1B–1E) where red-green colocalized spots are attributed to DNA origami structures with open nanoswitches, whereas only green spots indicate the presence of structures with closed nanoswitches.

Upon antibody binding, the chosen 7-nt long linker and the 5-nt long stem together with the nucleotide where the dye or the quencher are attached to, provide a 26-nt (2 x (7-nt + 5-nt + 1-nt)) long ssDNA spacer between the two Dig-moieties. This spacer length and design is comparable to the 27-nt long ssDNA spacer in the original nanoswitch design (Ranallo et al., 2015) and, based on the approximation of 0.67 nm length per ssDNA base (Chi et al., 2013), is designed to mimic the optimal ~16 nm distance (distance with highest binding affinity) between two Dig binding moieties on DNA origami reported recently (Shaw et al., 2019).

To test the specificity of the nanoswitch opening on the NRO and to investigate the opening mechanism, we studied nanoswitch constructs bearing one, two or no Dig recognition elements. After surface immobilization, fluorescence scans of the three constructs were taken before and after 20 min incubation with 100 nM anti-Dig antibody on a confocal fluorescence microscope (Figures 1B–1D). For all three constructs, surface scans before incubation with the target antibody showed very few co-localized spots indicating only a low fraction of open nanoswitches (Figures 1B–1D). This small number of false positive signals might originate from unspecifically opened nanoswitches, mislabeled nanoswitches (structures in which the quencher was not incorporated), or nanoswitches containing a photobleached BBQ-650 quencher (Holzmeister et al., 2014; Grabenhorst et al., 2020). After incubating the different nanoswitch constructs with anti-Dig antibodies, we noted a significant increase of co-localized spots only for the nanoswitch construct bearing two Dig recognition elements (Figures 1B–1D). This confirms the specific nature of antibody binding to the Dig recognition elements and excludes an opening of the nanoswitch by monovalent binding of one anti-Dig antibody.

We quantified the efficiency of the nanoswitch opening by calculating the fraction of NRO nanostructures with an open nanoswitch (fraction of co-localized green and red spots, Figure 1F). An unpaired T test was used to compare the magnitude of changes in nanoswitch opening (see STAR Methods). For the construct bearing two Dig-recognition elements, the percentage of constructs with open nanoswitches increased from ~5% to ~54% upon addition of anti-Dig antibody while no significant increase was observed for both other constructs, demonstrating specific binding of the anti-Dig antibody to the Dig recognition elements.

To further investigate the opening mechanism and exclude possible cross-reactivity with other bivalent binding antibodies, we incubated the nanoswitch construct with 100 nM anti-Dig Fab fragment and 100 nM anti-hDectin-1 antibody (see Figure 1E). The anti-Dig Fab fragment is a monovalent Dig-binding protein and thus can be used to exclude an opening of the nanoswitch by monovalent binding of two antibodies. We observed only a slight increase (~4%) in the fraction of open nanoswitches upon addition of the anti-Dig Fab fragment compared to the values obtained in presence of anti-Dig antibodies (~49%, see Figure 1F), supporting the assumption that the nanoswitch is primarily open due to the bivalent binding of an anti-Dig antibody which is consistent with the mechanism proposed by Ranallo et al. (Ranallo et al., 2015). Anti-hDectin1 is a bivalent antibody specific for human Dectin-1. The nanoswitch opening measured in presence of anti-hDectin-1 antibodies (~5%) (Figure 1F) was comparable to the unspecific signal gain, further demonstrating that no cross-reactivity occurs. These control experiments confirmed that the nanoswitch is specific for the target anti-Dig antibody and works according to the mechanism depicted in Figure 1A.

Enhancing the output signal of the nanoswitch in the plasmonic hotspot of nanoantennas

To provide physical amplification of the signal upon detection of a single antibody for possible point-of-care diagnostic applications on low-cost setups, we utilized recently developed NACHOS. NACHOS is a three-dimensional DNA origami structure consisting of two pillars each bearing six protruding staple strands (A_{20}) which provide anchor points for 100-nm AgNPs functionalized with ssDNA strands (T_{20}) (Figure 2A, Tables S3–S6). A plasmonic hotspot is created at the bifurcation in the gap between the two pillars and the nanoparticle (see DNA origami sketch and TEM image in Figure 2A (left) and full NACHOS structure in Figure 2A (right)). For immobilization on BSA-biotin-neutravidin coated glass coverslips, the DNA origami structure is equipped with a rigid cross-like shaped base (Figures S2 and S3) that contains six biotin-modified staple strands (Trofymchuk et al., 2021). For identifying NACHOS in single-molecule fluorescence images, a reference green dye ATTO 542 is incorporated at the base of the DNA origami structure.

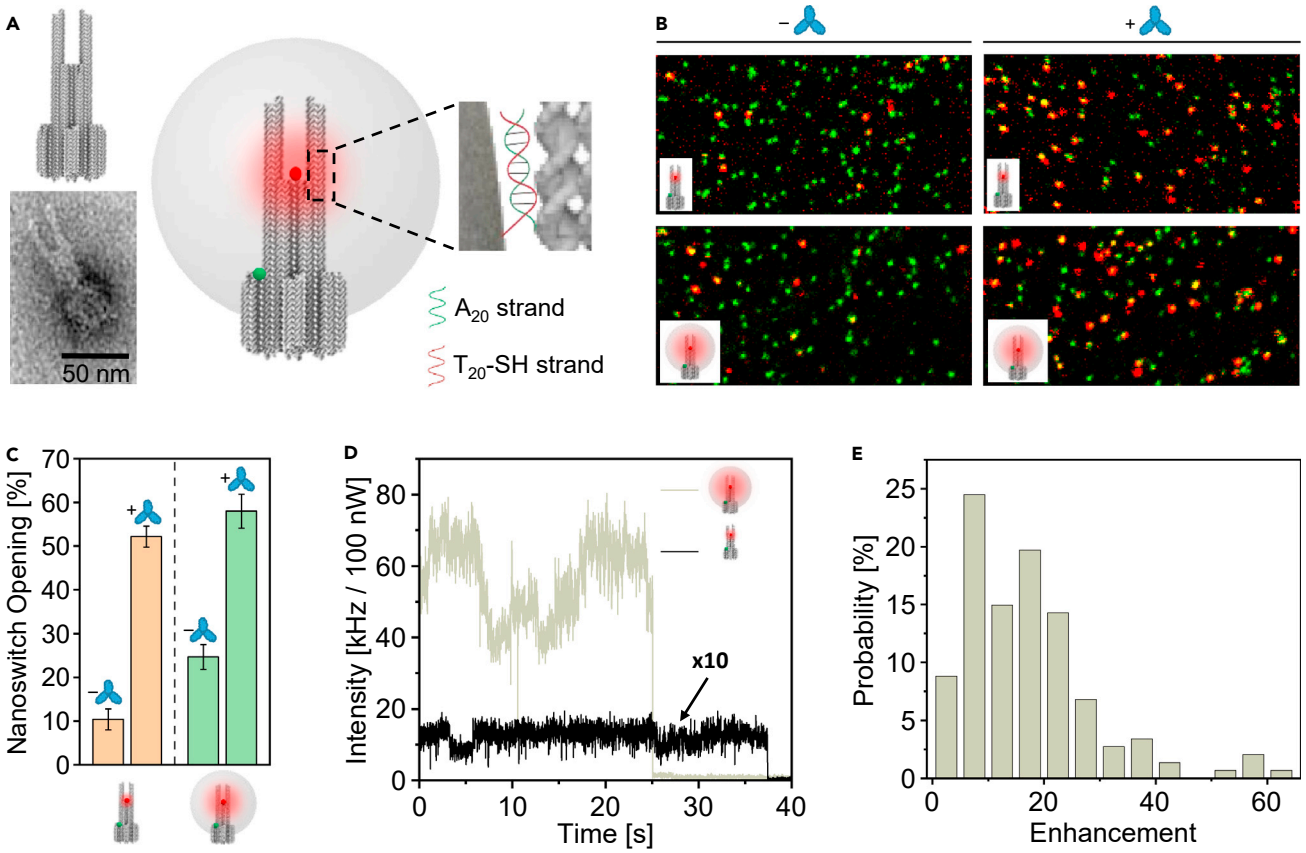

Figure 2. Detection of anti-Dig antibodies with a nanoswitch in the plasmonic hotspot of NACHOS nanostructures with AgNPs

(A) Sketch of the DNA origami structure used for the nanoantenna assembly. A representative class average TEM image of the DNA origami used is shown on the lower left. Schematics of nanoantennas assembly on the right: thiolated DNA-functionalized 100-nm AgNPs are attached to DNA origami nanoantennas via polyadenine (A_{20}) binding strands in zipper-like geometry (Vietz et al., 2016).

(B) Two-color fluorescence confocal images of a reference DNA origami structure without nanoparticles (upper) and with one 100-nm AgNP (lower) before and after 20 min incubation with 100 nM anti-Dig antibodies. The scans show a field of view of 20 μm × 10 μm.

(C) Fraction of open nanoswitches quantified by dividing the number of red-green colocalized spots by the total number of all green spots. Over 400 structures from at least 4 different areas per sample were analyzed. Error bars represent the standard deviation of the 5 areas.

(D) Single-molecule fluorescence intensity transients, measured on a confocal microscope, normalized to the same excitation power of a single ATTO 647N dye incorporated in a DNA origami (black) and in a monomer NACHOS structure containing 100-nm AgNP (olive) excited at 639 nm.

(E) Fluorescence enhancement distribution of the open nanoswitch (ATTO 647N dye) measured in the NACHOS structure. The fluorescence enhancement values were calculated by comparing the intensity of the open nanoswitch (intensity of a single ATTO 647N) in the NACHOS structure to the mean intensity of the open nanoswitch in the reference structure averaged over 113 molecules. A total number of 147 NACHOS structures were analyzed.

In order to study the possible detection of antibodies in the plasmonic hotspot of NACHOS, we incorporated the nanoswitch sensing unit in NACHOS containing a 100-nm AgNP as well as in the same DNA origami nanostructure without NPs serving as a reference. The efficiency of the nanoswitch opening upon the addition of anti-Dig antibodies was then determined analogously to the measurements on the NRO nanosensors (Figure 2B and STAR Methods). In absence of anti-Dig antibodies, nanoswitch openings of ~10% and ~25% were recorded for the reference structure and NACHOS containing 100-nm AgNP, respectively (Figure 2C). The higher level of false-positive signals in the NACHOS structure compared with the reference structure can be related to accelerated photobleaching of BBQ-650 in the hotspot of plasmonic nanoantennas (Grabenhorst et al., 2020). After 20 min incubation with 100 nM anti-Dig antibodies, nanoswitch openings of ~52% and ~57% were measured for the reference structure and NACHOS, respectively. This demonstrates similar accessibility of the nanoswitch for the antibody in the NACHOS structure as in the reference structure and even is comparable to the sterically less complex two-dimensional NRO structure.

Next, we investigated the fluorescence enhancement achievable in this single-molecule antibody diagnostic assay. Single-molecule fluorescence transients of the nanoswitch (Figures 2D and S4) were recorded

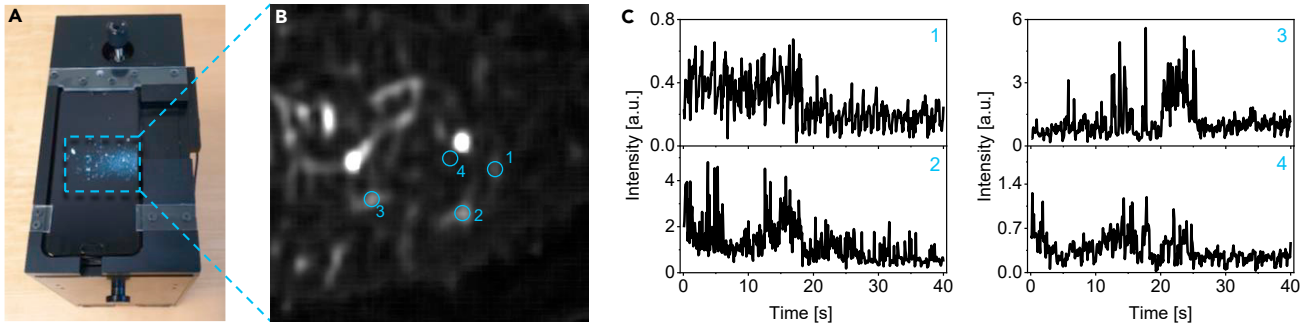

Figure 3. Single antibody detection on a portable smartphone microscope

(A). Photograph of the portable smartphone microscope.

(B) Background corrected fluorescence image of the open nanoswitch (intensity of a single ATTO 647N dye) in NACHOS containing a 100-nm AgNP.

(C) Exemplary fluorescence transients of the nanoswitch (single ATTO 647N dye) in NACHOS containing a 100-nm AgNP measured on a portable microscope setup. Analogous to the single-molecule confocal microscopy, most of the transients demonstrated intensity fluctuations ending with a single bleaching step. The fluorescence transients shown in panel c were extracted from a single movie.

on a confocal microscope for the reference structure and for NACHOS containing AgNPs upon incubation with anti-Dig antibody. Fluorescence enhancement values were calculated by comparing the intensity of the open nanoswitch (intensity of a single ATTO 647N dye) in the NACHOS structure to the mean intensity of the open nanoswitch in the reference structure averaged over 113 molecules. Only transients showing single-step photobleaching (69% and 52% of all recorded transients of the open nanoswitch in the reference structures and the NACHOS structure, respectively, see STAR Methods) were included in the analysis. As shown in Figure 2E, fluorescence enhancement values up to 63-fold were achieved with the NACHOS structure (average fluorescence enhancement 17-fold).

To investigate the possible detection of single antibodies on a simple setup with low-NA optics (Figure 3A) (Vietz et al., 2019; Trofymchuk et al., 2021), we recorded movies of the nanoswitch in the NACHOS nanostructure containing a 100-nm AgNP upon incubation with anti-Dig antibodies. Upon illumination, we were able to observe multiple spots on a smartphone camera (Figure 3B) which bleached upon continuous illumination with a 639-nm laser (Videos S1 and S2). Analogous to the transients recorded on a confocal microscope, most of the transients demonstrated intensity fluctuations ending with single bleaching steps (Figures 3C and S9, STAR Methods), demonstrating the detection of antibodies at the single-molecule level. To the best of our knowledge, these transients represent the first examples of the fluorescence-based detection of single antibodies on a portable smartphone microscope.

Opening kinetics and sensitive concentration range of the nanoswitch on different DNA origami nanostructures

We evaluated the time required to perform the antibody detection assay and the sensitive concentration range of the nanoswitch on the NRO, the reference DNA origami structure without NPs and NACHOS containing a 100-nm AgNP. The kinetics of the nanoswitch opening was quantified under non-diffusion limited conditions by recording confocal fluorescence scans of surface-immobilized DNA origami nanoswitches before and after different incubation times with 100 nM anti-Dig antibodies (Figure S5). To evaluate the sensitive concentration range under clinically relevant conditions, we chose an incubation time of 20 min. We measured the nanoswitch opening before and after 20 min incubation with different anti-Dig antibody concentrations (Figures S6–S8). The efficiency of nanoswitch opening was determined for each incubation time (Figure 4A) and each antibody concentration (Figure 4B), respectively. We found that under non-diffusion limited conditions the detection was equally rapid on the different DNA origami structures (for 100 nM anti-Dig antibodies), achieving the highest signal gain after just 5 min. This is in accordance with the fast nanoswitch opening kinetics in solution reported previously (Ranallo et al., 2015).

The target concentration at which the observed signal change is half the maximum signal change ($C_{HalfMax}$) had values of 129 pM, 800 pM and 1.4 nM for the NRO, the reference DNA origami structure without NPs and the NACHOS structure with one 100-nm AgNP, respectively. We attribute the different $C_{HalfMax}$ values to the different accessibilities of the nanoswitch on the different DNA origami structures. One of the main

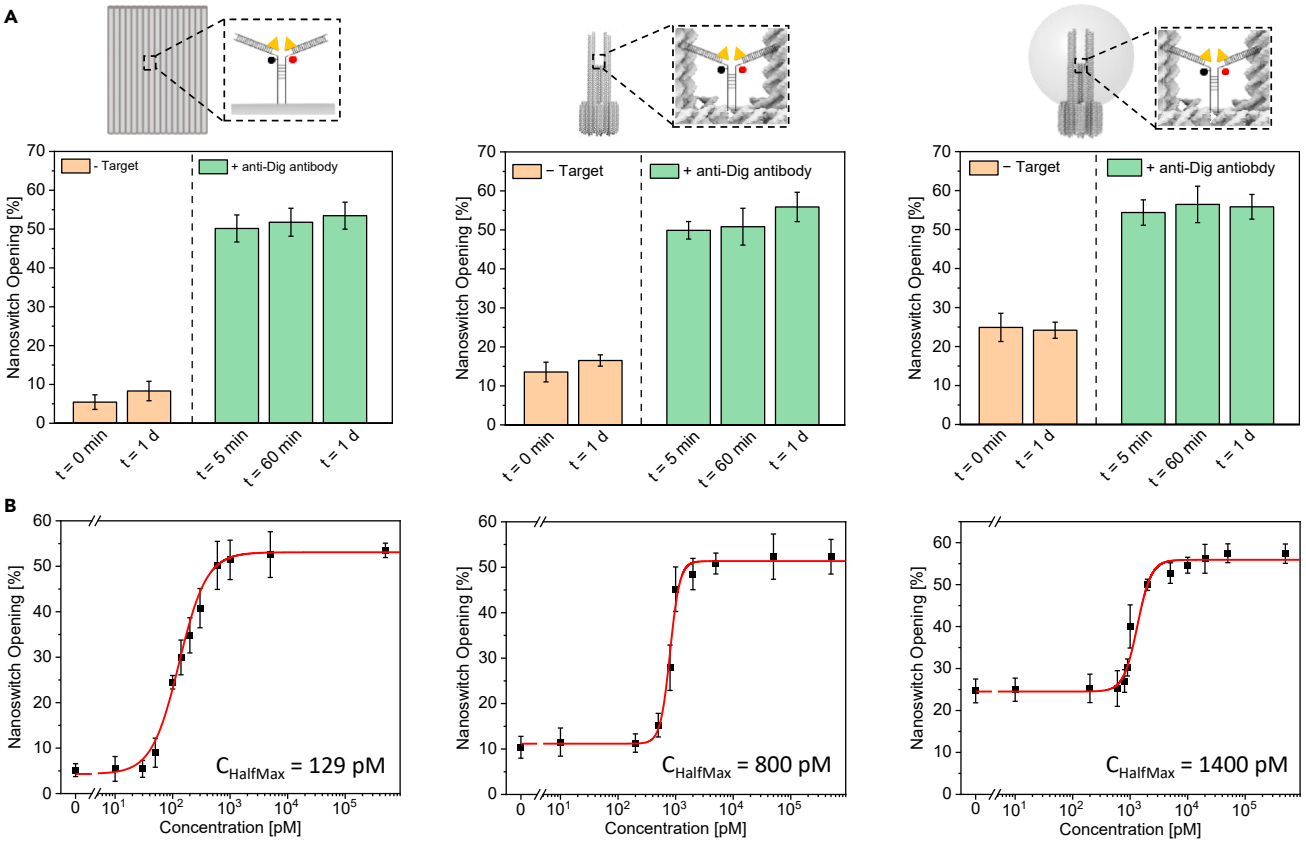

Figure 4. Opening kinetics and sensitive concentration range of the nanoswitch on different DNA origami nanostructures

(A) Nanoswitch opening on the NRO (left), the reference DNA origami structure without NPs (middle) and NACHOS with 100-nm AgNP (right) before and after the incubation with 100 nM anti-Dig antibodies.

(B) Nanoswitch opening versus anti-Dig antibody concentration on the NRO (left), the reference DNA origami structure without NPs (middle) and NACHOS with 100-nm AgNP (right). The fraction of open nanoswitches was quantified from confocal fluorescence scans by dividing the number of red-green colocalized spots by the total number of green spots. Over 300 structures from at least 3 different areas per sample were analyzed. Error bars represent the standard deviation of the areas. For the binding curves the observed nanoswitch opening was fitted using a four-parameter logistic equation (see STAR Methods).

challenges in designing ultrasensitive biosensors are slow binding kinetics at low target concentrations (Simon et al., 2014; Wu et al., 2019). Given that our nanoswitch opening titrations were performed starting at low pM concentrations, very long incubation times would have been required to achieve the equilibrium opening values, and we deemed it more important to report the nanosensor response ($C_{HalfMax}$) under diagnostically relevant conditions (the chosen 20 min incubation time). The diffusion limited binding of the antibody at low concentrations makes the accessibility of the nanoswitch the critical criterion when studying the $C_{HalfMax}$ values (see STAR Methods). In the two-dimensional NRO nanostructure, the nanoswitch is expected to be easily accessible for the anti-Dig antibody binding, while the accessibility for the target antibody is expected to be lower in the three-dimensional NACHOS reference structure. Upon the attachment of 100-nm AgNP, the accessibility of NACHOS structure is even further hindered. These results emphasize that the accessibility of the nanostructure is a crucial factor to be considered when designing biosensors with low sensitive concentration ranges under diagnostically relevant incubation times.

DISCUSSION

Rapidly increasing versatility and complexity of DNA nanostructures together with decrease in production cost of DNA that follows Moore's law (halved every 30 months) (Schmidt et al., 2015) makes them ideal platforms for the development of rapid and low-cost biosensors. While the modular and programmable DNA origami approach has been extensively used for the development of various biosensors, its scope of

different targets is often limited to nucleic acids. In this work, we report a general strategy to incorporate fluorescence-based sensors for antibodies into DNA origami platforms. Building on previous work of nanoswitch sensors for antibodies in solution (Ranallo et al., 2015, 2019; Porchetta et al., 2018), we showed that these nanoswitch sensors can be successfully incorporated in different DNA origami nanostructures to provide rapid and specific detection of antibodies at the single-molecule level.

The clinically relevant concentration for detecting antibodies varies depending on the application. For the detection of antibodies used for the diagnosis of infectious diseases (Fiorentini et al., 2008; Rostenberg and Peñaloza, 1978; Barletta et al., 2004; Raulf et al., 2019), the concentration level expected to have in clinical samples (*i.e.* blood, serum) is – depending on the stage of infection – in the pM to low nM range. Conversely, for the detection of antibodies for other purposes (*e.g.* to monitor immunotherapy), the concentration level of the target antibody can be much higher (high nM low uM range) (Robert et al., 2001; Ji and Lee, 2021; Chames et al., 2009). Thus, the $C_{HalfMax}$ values we achieved here (Figure 4B) show sensitive concentration ranges relevant for diagnostic applications.

The biorecognition elements of the nanoswitch (antigen or small molecule) were not directly incorporated into the DNA origami design but each anchor was designed to carry a cDNA sequence to which different biorecognition elements can be bound post synthetically. This flexible and modular nature of the sensing platform allows one to easily extend it to the detection of other antibodies or biomolecular targets. This sensing approach is also not limited to the detection of bivalent antibodies as it was already demonstrated that monovalent binding of two different antibodies or proteins could also lead to the nanoswitch opening (Ranallo et al., 2015). However, as has been shown before due to the lower affinity of monovalent binding such nanoswitches would require higher antibody (substrate) concentrations to achieve similar signal responses.

On the other hand, the addressability of the DNA origami approach itself opens numbers of exciting directions as well. In this work, we demonstrated how the modular nature of DNA origami can be used to implement a strategy for signal amplification upon antibody detection, leading to an average fluorescence enhancement of 17-fold. This allows the detection on low-cost optical devices which to the best of our knowledge was so far not possible in other single-molecule approaches (Table S7) and thus is a crucial step toward the implementation of point-of-care diagnostics on the single-molecule level. An exciting future direction would be to utilize the unprecedented multiplexing capabilities of DNA origami to extend this platform or apply it for highly multiplexed detection of a large number of clinically relevant targets. It has, for example, been shown that up to 216 distinct fluorescence barcodes can be implemented on a single DNA origami nanostructure opening exciting opportunities in the development of highly multiplexed biosensing strategies (Lin et al., 2012). The nanoswitch sensor platform shown here would allow combining this multiplexing advantage with specific and sensitive (single-molecule level) detection of antibodies on one DNA origami nanostructure.

Limitations of the study

The single-molecule antibody sensing platform, however, also has some limitations, especially in combination with plasmonic signal enhancement by the nanoantenna. One obvious limitation stems from the fact that the relatively small hotspot size of the DNA nanoantennas (such as the NACHOS structure used here), required for high signal enhancement, limits the size of the antibody or the biomolecular target that can be detected. Another challenge is related to the photophysics of fluorophore-quencher pair – we have recently shown that the photobleaching of the quencher molecule (BBQ 650) is accelerated in the hotspot of dimer DNA nanoantennas, leading to an increase of acceptor (ATTO 647N) fluorescence even in absence of target molecules and giving rise to a false-positive signal (Grabenhorst et al., 2020). We also incorporated the nanoswitch in dimer nanoantennas with two NPs to achieve higher fluorescence enhancement. For NACHOS with two 100-nm AgNPs we however observed a large number of red-green colocalized spots even before the addition of target antibodies (Figure S10), which prevented us from using this structure for the detection of antibodies. The higher fraction of active red dyes in the absence the target molecules and giving the rise of false positive signals on the supposedly closed nanoswitch can have different origins. As previously shown (Grabenhorst et al., 2020), higher excitation powers in the dimer hotspot can lead to premature photobleaching of the quencher molecule (BBQ650). Another effect is that quenched dyes are enhanced more than non-quenched dyes as radiative rates are enhanced by nanoantennas so that the efficiency of BBQ650 quenching might not be strong enough (Vietz et al., 2017b). We can therefore not conclusively answer the question whether NACHOS would sterically enable antibody binding in the

hotspot between two NPs. To this end, multiple and more efficient and photostable quencher molecules or replacing the molecular quencher with a small metallic NP (Swierczewska et al., 2011) might improve the assay. Nevertheless, we believe that the single-molecule DNA origami antibody sensor platform introduced here presents a useful starting point to further extending DNA origami sensors beyond the detection of nucleic acids and expanding their scope to antibodies and other sensing applications.

STAR★METHODS

Detailed methods are provided in the online version of this paper and include the following:

- KEY RESOURCES TABLE
- RESOURCE AVAILABILITY
  - Lead contact
  - Materials availability
  - Data and code availability
- METHOD DETAILS
  - Synthesis of DNA origami
  - Functionalization of AgNPs
  - Transmission electron microscopy (TEM) measurements
  - Sample preparation on the coverslip for single-molecule confocal measurements
  - Antibody detection assay
  - Confocal measurements and data analysis
  - Sample preparation for single-molecule measurements on the smartphone microscope
  - Single-molecule measurements and analysis on the smartphone
- QUANTIFICATION AND STATISTICAL ANALYSIS
  - Statistical analysis on nanoswitch opening
  - Impact of photophysics on the antibody assay
  - Sensitive concentration ranges
  - Comparison with other single-antibody assays

SUPPLEMENTAL INFORMATION

Supplemental information can be found online at https://doi.org/10.1016/j.isci.2021.103072.

ACKNOWLEDGMENTS

The authors thank Prof. Tim Liedl/Prof. Joachim Rädler (Ludwig-Maximilians-Universität, Department für Physik, Munich, Germany) for providing access to their facilities especially to the transmission electron microscope. P.T. acknowledges the Deutsche Forschungsgemeinschaft (DFG, German Research Foundation) under Germany's Excellence Strategy — EXC 2089/1–390776260 for funding. P.T. gratefully acknowledges financial support from the DFG (Grant Nos. INST 86/1904-1 FUGG and TI 329/9-2) and BMBF (Grants POCEMON, 13N14336, and SIBOF, 03VP03891). V.G. acknowledges the support by Humboldt Research Fellowships from the Alexander von Humboldt Foundation and European Union's Horizon 2020 research and innovation program under the Marie Skłodowska-Curie. K.T. acknowledges the support by Humboldt Research Fellowships from the Alexander von Humboldt Foundation. S.R. is supported by European Union's Horizon 2020 research and innovation program under the Marie Skłodowska-Curie grant agreement n. 843179 ("DNA-NANO-AB"). The work was also supported by Associazione Italiana per la Ricerca sul Cancro, AIRC (project n. 21965, F.R.) and by the European Research Council, ERC (Consolidator Grant project n. 819160, F.R.). We thank Luna for her support with the smartphone measurements.

AUTHOR CONTRIBUTIONS

M.P., K.T., V.G., and S.R. developed the concept of combining the nanoswitch and DNA origami platforms. M.P., K.T., and V.G. prepared samples, performed, and analyzed the measurements. M.P., K.T., V.G., F.S., and F.C. performed and analyzed the measurements on the smartphone microscope. P.T. and F.R. supervised the project. All authors have written, read, and approved the final manuscript.

DECLARATION OF INTERESTS

P.T. is an inventor on an awarded patent of the described bottom-up method for fluorescence enhancement in molecular assays, EP1260316.1, 2012. The remaining authors declare no competing interests.

Received: June 7, 2021
Revised: July 26, 2021
Accepted: August 27, 2021
Published: September 24, 2021

SUPPORTING CITATIONS

The following references appear in the Supplemental information: Fahie et al., 2015; Li et al., 2002; Rissin et al., 2010.

REFERENCES

Acuna, G.P., Moller, F.M., Holzmeister, P., Beater, S., Lalkens, B., and Tinnefeld, P. (2012). Fluorescence enhancement at docking sites of DNA-directed self-assembled nanoantennas. Science *338*, 506–510. https://doi.org/10.1126/science.1228638.

Barletta, J.M., Edelman, D.C., and Constantine, N.T. (2004). Lowering the detection limits of HIV-1 viral load using real-time immuno-PCR for HIV-1 p24 antigen. Am. J. Clin. Pathol. *122*, 20–27. https://doi.org/10.1309/529T2WDNEB6X8VUN.

Chames, P., Van Regenmortel, M., Weiss, E., and Baty, D. (2009). Therapeutic antibodies: successes, limitations and hopes for the future. Br. J. Pharmacol. *157*, 220–233. https://doi.org/10.1111/j.1476-5381.2009.00190.x.

Chandrasekaran, A.R. (2017). DNA nanobiosensors: an outlook on signal readout strategies. J. Nanomater. *2017*, 2820619. https://doi.org/10.1155/2017/2820619.

Chi, Q., Wang, G., and Jiang, J. (2013). The persistence length and length per base of single-stranded DNA obtained from fluorescence correlation spectroscopy measurements using mean field theory. Phys. A Stat. Mech. Appl. *392*, 1072–1079. https://doi.org/10.1016/j.physa.2012.09.022.

Dass, M., Gür, F.N., Kołątaj, K., Urban, M.J., and Liedl, T. (2021). DNA origami-enabled plasmonic sensing. J. Phys. Chem. C *125*, 5969–5981. https://doi.org/10.1021/acs.jpcc.0c11238.

Dey, S., Fan, C., Gothelf, K.V., Li, J., Lin, C., Liu, L., Liu, N., Nijenhuis, M.A.D., Saccà, B., Simmel, F.C., et al. (2021). DNA origami. Nat. Rev. Methods Primers *1*, 13. https://doi.org/10.1038/s43586-020-00009-8.

Domljanovic, I., Carstens, A., Okholm, A., Kjems, J., Nielsen, C.T., Heegaard, N.H.H., and Astakhova, K. (2017). Complexes of DNA with fluorescent dyes are effective reagents for detection of autoimmune antibodies. Sci.Rep. *7*, 1925. https://doi.org/10.1038/s41598-017-02214-0.

Douglas, S.M., Dietz, H., Liedl, T., Högberg, B., Graf, F., and Shih, W.M. (2009). Self-assembly of DNA into nanoscale three-dimensional shapes. Nature *459*, 414–418. https://doi.org/10.1038/nature08016.

Fahie, M., Chisholm, C., and Chen, M. (2015). Resolved single-molecule detection of individual species within a mixture of anti-biotin antibodies using an engineered monomeric nanopore. ACS Nano *9*, 1089–1098. https://doi.org/10.1021/nn506606e.

Fiorentini, S., Marsico, S., Becker, P.D., Iaria, M.L., Bruno, R., Guzmán, C.A., and Caruso, A. (2008). Synthetic peptide AT20 coupled to KLH elicits antibodies against a conserved conformational epitope from a major functional area of the HIV-1 matrix protein p17. Vaccine *26*, 4758–4765. https://doi.org/10.1016/j.vaccine.2008.06.082.

Funck, T., Nicoli, F., Kuzyk, A., and Liedl, T. (2018). Sensing picomolar concentrations of RNA using switchable plasmonic chirality. Angew. Chem. Int. Ed. Engl. *57*, 13495–13498. https://doi.org/10.1002/anie.201807029.

Glembockyte, V., Lin, J., and Cosa, G. (2016). Improving the photostability of red- and green-emissive single-molecule fluorophores via Ni2+ mediated excited triplet-state quenching. J. Phys. Chem. B *120*, 11923–11929. https://doi.org/10.1021/acs.jpcb.6b10725.

Godonoga, M., Lin, T.-Y., Oshima, A., Sumitomo, K., Tang, M.S.L., Cheung, Y.-W., Kinghorn, A.B., Dirkzwager, R.M., Zhou, C., Kuzuya, A., et al. (2016). A DNA aptamer recognising a malaria protein biomarker can function as part of a DNA origami assembly. Sci. Rep. *6*, 21266. https://doi.org/10.1038/srep21266.

Grabenhorst, L., Trofymchuk, K., Steiner, F., Glembockyte, V., and Tinnefeld, P. (2020). Fluorophore photostability and saturation in the hotspot of DNA origami nanoantennas. Methods Appl. Fluoresc. *8*, 024003.

Holzmeister, P., Wünsch, B., Gietl, A., and Tinnefeld, P. (2014). Single-molecule photophysics of dark quenchers as non-fluorescent FRET acceptors. Photochem. Photobiol. Sci. *13*, 853–858. https://doi.org/10.1039/C3PP50274K.

Ji, E., and Lee, S. (2021). Antibody-based therapeutics for atherosclerosis and cardiovascular diseases. Int. J. Mol. Sci. *22*. https://doi.org/10.3390/ijms22115770.

Ke, Y., Castro, C., and Choi, J.H. (2018). Structural DNA nanotechnology: artificial nanostructures for biomedical research. Annu. Rev. Biomed. Eng. *20*, 375–401. https://doi.org/10.1146/annurev-bioeng-062117-120904.

Ke, Y., Lindsay, S., Chang, Y., Liu, Y., and Yan, H. (2008). Self-assembled water-soluble nucleic acid probe tiles for label-free RNA hybridization assays. Science *319*, 180–183. https://doi.org/10.1126/science.1150082.

Keyser, U.F. (2016). Enhancing nanopore sensing with DNA nanotechnology. Nat. Nanotechnol. *11*, 106–108. https://doi.org/10.1038/nnano.2016.2.

Koirala, D., Shrestha, P., Emura, T., Hidaka, K., Mandal, S., Endo, M., Sugiyama, H., and Mao, H. (2014). Single-molecule mechanochemical sensing using DNA origami nanostructures. Angew. Chem. Int. Ed. *53*, 8137–8141. https://doi.org/10.1002/anie.201404043.

Kuzuya, A., Sakai, Y., Yamazaki, T., Xu, Y., and Komiyama, M. (2011). Nanomechanical DNA origami 'single-molecule beacons' directly imaged by atomic force microscopy. Nat. Commun. *2*, 449. https://doi.org/10.1038/ncomms1452.

Li, K., Stockman, M.I., and Bergman, D.J. (2003). Self-similar chain of metal Nanospheres as an efficient nanolens. Phys. Rev. Lett. *91*, 227402. https://doi.org/10.1103/PhysRevLett.91.227402.

Li, L., Chen, S., Oh, S., and Jiang, S. (2002). In situ single-molecule detection of Antibody−Antigen binding by tapping-mode atomic force microscopy. Anal. Chem. *74*, 6017–6022. https://doi.org/10.1021/ac0258148.

Li, Z., Wang, L., Yan, H., and Liu, Y. (2012). Effect of DNA hairpin loops on the twist of planar DNA origami tiles. Langmuir *28*, 1959–1965. https://doi.org/10.1021/la2037873.

Lin, C., Jungmann, R., Leifer, A.M., Li, C., Levner, D., Church, G.M., Shih, W.M., and Yin, P. (2012). Submicrometre geometrically encoded fluorescent barcodes self-assembled from DNA. Nat. Chem. *4*, 832–839. https://doi.org/10.1038/nchem.1451.

Loretan, M., Domljanovic, I., Lakatos, M., Rüegg, C., and Acuna, G.P. (2020). DNA origami as emerging Technology for the engineering of fluorescent and plasmonic-based biosensors. Materials *13*, 2185.

Marras, A.E., Shi, Z., Lindell, M.G., Patton, R.A., Huang, C.-M., Zhou, L., Su, H.-J., Arya, G., and Castro, C.E. (2018). Cation-activated avidity for rapid reconfiguration of DNA nanodevices. ACS Nano *12*, 9484–9494. https://doi.org/10.1021/acsnano.8b04817.

McCreery, T. (1997). Digoxigenin labeling. Mol. Biotechnol. *7*, 121–124. https://doi.org/10.1007/bf02761747.

Novotny, L., and Van Hulst, N. (2011). Antennas for light. Nat. Photon. *5*, 83–90. https://doi.org/10.1038/nphoton.2010.237.

Ochmann, S.E., Vietz, C., Trofymchuk, K., Acuna, G.P., Lalkens, B., and Tinnefeld, P. (2017). Optical nanoantenna for single molecule-based detection of Zika virus nucleic acids without molecular multiplication. Anal. Chem. *89*, 13000–

13007. https://doi.org/10.1021/acs.analchem.7b04082.

Porchetta, A., Ippodrino, R., Marini, B., Caruso, A., Caccuri, F., and Ricci, F. (2018). Programmable nucleic acid nanoswitches for the rapid, single-step detection of antibodies in bodily fluids. J. Am. Chem. Soc. *140*, 947–953. https://doi.org/10.1021/jacs.7b09347.

Puchkova, A., Vietz, C., Pibiri, E., Wunsch, B., Sanz Paz, M., Acuna, G.P., and Tinnefeld, P. (2015). DNA origami nanoantennas with over 5000-fold fluorescence enhancement and single-molecule detection at 25 muM. Nano Lett. *15*, 8354–8359. https://doi.org/10.1021/acs.nanolett.5b04045.

Purcell, E.M. (1946). Proceedings of the American physical society. Phys. Rev. *69*, 674. https://doi.org/10.1103/PhysRev.69.674.2.

Ranallo, S., Porchetta, A., and Ricci, F. (2019). DNA-based scaffolds for sensing applications. Anal. Chem. *91*, 44–59. https://doi.org/10.1021/acs.analchem.8b05009.

Ranallo, S., Rossetti, M., Plaxco, K.W., Vallée-Bélisle, A., and Ricci, F. (2015). A modular, DNA-based beacon for single-step fluorescence detection of antibodies and other proteins. Angew. Chem. Int. Ed. Engl. *54*, 13214–13218. https://doi.org/10.1002/anie.201505179.

Raulf, M., Joost, M., Sander, I., Hoffmeyer, F., Nowak, D., Ochmann, U., Preisser, A., Schreiber, J., Sennekamp, J., and Koschel, D. (2019). Update of reference values for IgG antibodies against typical antigens of hypersensitivity pneumonitis. Allergo J. Int. *28*, 192–203. https://doi.org/10.1007/s40629-019-0099-x.

Raveendran, M., Lee, A.J., Sharma, R., Wälti, C., and Actis, P. (2020). Rational design of DNA nanostructures for single molecule biosensing. Nat. Commun. *11*, 4384. https://doi.org/10.1038/s41467-020-18132-1.

Ricci, F., Vallée-Bélisle, A., Simon, A.J., Porchetta, A., and Plaxco, K.W. (2016). Using nature's "tricks" to rationally tune the binding properties of biomolecular receptors. Acc. Chem. Res. *49*, 1884–1892. https://doi.org/10.1021/acs.accounts.6b00276.

Rinker, S., Ke, Y., Liu, Y., Chhabra, R., and Yan, H. (2008). Self-assembled DNA nanostructures for distance-dependent multivalent ligand–protein binding. Nat. Nanotechnol. *3*, 418–422. https://doi.org/10.1038/nnano.2008.164.

Rissin, D.M., Kan, C.W., Campbell, T.G., Howes, S.C., Fournier, D.R., Song, L., Piech, T., Patel, P.P., Chang, L., Rivnak, A.J., et al. (2010). Single-molecule enzyme-linked immunosorbent assay detects serum proteins at subfemtomolar concentrations. Nat. Biotechnol. *28*, 595–599. https://doi.org/10.1038/nbt.1641.

Robert, F., Ezekiel, M.P., Spencer, S.A., Meredith, R.F., Bonner, J.A., Khazaeli, M.B., Saleh, M.N., Carey, D., Lobuglio, A.F., Wheeler, R.H., et al. (2001). Phase I study of anti–epidermal growth factor receptor antibody cetuximab in combination with radiation therapy in patients with advanced head and neck cancer. J. Clin. Oncol. *19*, 3234–3243. https://doi.org/10.1200/jco.2001.19.13.3234.

Rostenberg, I., and Peñaloza, R. (1978). Serum IgG and IgD and levels in some infectious and noninfectious diseases. Clin. Chim. Acta *85*, 319–321. https://doi.org/10.1016/0009-8981(78)90310-8.

Rothemund, P.W.K. (2006). Folding DNA to create nanoscale shapes and patterns. Nature *440*, 297–302. https://doi.org/10.1038/nature04586.

Schindelin, J., Arganda-Carreras, I., Frise, E., Kaynig, V., Longair, M., Pietzsch, T., Preibisch, S., Rueden, C., Saalfeld, S., Schmid, B., et al. (2012). Fiji: an open-source platform for biological-image analysis. Nat. Methods *9*, 676–682. https://doi.org/10.1038/nmeth.2019.

Schmidt, T.L., Beliveau, B.J., Uca, Y.O., Theilmann, M., Da Cruz, F., Wu, C.-T., and Shih, W.M. (2015). Scalable amplification of strand subsets from chip-synthesized oligonucleotide libraries. Nat. Commun. *6*, 8634. https://doi.org/10.1038/ncomms9634.

Seeman, N.C., and Sleiman, H.F. (2017). DNA nanotechnology. Nat. Rev. Mater. *3*, 17068. https://doi.org/10.1038/natrevmats.2017.68.

Selnihhin, D., Sparvath, S.M., Preus, S., Birkedal, V., and Andersen, E.S. (2018). Multifluorophore DNA origami beacon as a biosensing platform. ACS Nano *12*, 5699–5708. https://doi.org/10.1021/acsnano.8b01510.

Shaw, A., Hoffecker, I.T., Smyrlaki, I., Rosa, J., Grevys, A., Bratlie, D., Sandlie, I., Michaelsen, T.E., Andersen, J.T., and Högberg, B. (2019). Binding to nanopatterned antigens is dominated by the spatial tolerance of antibodies. Nat. Nanotechnol. *14*, 184–190. https://doi.org/10.1038/s41565-018-0336-3.

Simon, A.J., Vallée-Bélisle, A., Ricci, F., and Plaxco, K.W. (2014). Intrinsic disorder as a generalizable strategy for the rational design of highly responsive, allosterically cooperative receptors. Proc. Natl. Acad. Sci. U S A *111*, 15048. https://doi.org/10.1073/pnas.1410796111.

Subramanian, H.K.K., Chakraborty, B., Sha, R., and Seeman, N.C. (2011). The label-free unambiguous detection and symbolic display of single nucleotide polymorphisms on DNA origami. Nano Lett. *11*, 910–913. https://doi.org/10.1021/nl104555t.

Swierczewska, M., Lee, S., and Chen, X. (2011). The design and application of fluorophore-gold nanoparticle activatable probes. Phys. Chem. Chem. Phys. : PCCP *13*, 9929–9941. https://doi.org/10.1039/c0cp02967j.

Trofymchuk, K., Glembockyte, V., Grabenhorst, L., Steiner, F., Vietz, C., Close, C., Pfeiffer, M., Richter, L., Schütte, M.L., Selbach, F., et al. (2021). Addressable nanoantennas with cleared hotspots for single-molecule detection on a portable smartphone microscope. Nat. Commun. *12*, 950. https://doi.org/10.1038/s41467-021-21238-9.

Vietz, C., Kaminska, I., Sanz Paz, M., Tinnefeld, P., and Acuna, G.P. (2017a). Broadband fluorescence enhancement with self-assembled silver nanoparticle optical antennas. ACS Nano *11*, 4969–4975. https://doi.org/10.1021/acsnano.7b01621.

Vietz, C., Lalkens, B., Acuna, G.P., and Tinnefeld, P. (2016). Functionalizing large nanoparticles for small gaps in dimer nanoantennas. New J. Phys. *18*, 045012.

Vietz, C., Lalkens, B., Acuna, G.P., and Tinnefeld, P. (2017b). Synergistic combination of unquenching and plasmonic fluorescence enhancement in fluorogenic nucleic acid hybridization probes. Nano Lett. *17*, 6496–6500. https://doi.org/10.1021/acs.nanolett.7b03844.

Vietz, C., Schütte, M.L., Wei, Q., Richter, L., Lalkens, B., Ozcan, A., Tinnefeld, P., and Acuna, G.P. (2019). Benchmarking smartphone fluorescence-based microscopy with DNA origami nanobeads: reducing the gap toward single-molecule sensitivity. ACS Omega *4*, 637–642. https://doi.org/10.1021/acsomega.8b03136.

Vogelsang, J., Kasper, R., Steinhauer, C., Person, B., Heilemann, M., Sauer, M., and Tinnefeld, P. (2008). A reducing and oxidizing system minimizes photobleaching and blinking of fluorescent dyes. Angew. Chem. Int. Ed. *47*, 5465–5469. https://doi.org/10.1002/anie.200801518.

Wang, D., Vietz, C., Schröder, T., Acuna, G., Lalkens, B., and Tinnefeld, P. (2017a). A DNA walker as a fluorescence signal amplifier. Nano Lett. *17*, 5368–5374. https://doi.org/10.1021/acs.nanolett.7b01829.

Wagenbauer, K.F., Engelhardt, F.A.S., Stahl, E., Hechtl, V.K., Stömmer, P., Seebacher, F., Meregalli, L., Ketterer, P., Gerling, T., and Dietz, H. (2017). How we make DNA origami. ChemBioChem. https://doi.org/10.1002/cbic.201700377.

Wang, P., Meyer, T.A., Pan, V., Dutta, P.K., and Ke, Y. (2017b). The beauty and utility of DNA origami. Chem *2*, 359–382. https://doi.org/10.1016/j.chempr.2017.02.009.

Wang, S., Zhou, Z., Ma, N., Yang, S., Li, K., Teng, C., Ke, Y., and Tian, Y. (2020). DNA origami-enabled biosensors. Sensors *20*, 6899. https://doi.org/10.3390/s20236899.

Woo, S., and Rothemund, P.W. (2011). Programmable molecular recognition based on the geometry of DNA nanostructures. Nat. Chem. *3*, 620–627. https://doi.org/10.1038/nchem.1070.

Wu, Y., Tilley, R.D., and Gooding, J.J. (2019). Challenges and solutions in developing ultrasensitive biosensors. J. Am. Chem. Soc. *141*, 1162–1170. https://doi.org/10.1021/jacs.8b09397.

Zhang, Z., Wang, Y., Fan, C., Li, C., Li, Y., Qian, L., Fu, Y., Shi, Y., Hu, J., and He, L. (2010a). Asymmetric DNA origami for spatially addressable and index-free solution-phase DNA chips. Adv. Mater. *22*, 2672–2675. https://doi.org/10.1002/adma.201000151.

Zhang, Z., Zeng, D., Ma, H., Feng, G., Hu, J., He, L., Li, C., and Fan, C. (2010b). A DNA-Origami chip platform for label-free SNP genotyping using toehold-mediated strand displacement. Small *6*, 1854–1858. https://doi.org/10.1002/smll.201000908.

STAR★METHODS

KEY RESOURCES TABLE

REAGENT or RESOURCE	SOURCE	IDENTIFIER
Antibodies		
anti-Dig antibodies	Thermo Fisher Scientific, USA	cat#: 700772, PRID: AB_2532342
anti-Dig Fab fragment	Merck, Germany	cat#: 11214667001
Chemicals, peptides, and recombinant proteins		
Magnesium chloride	Sigma-Aldrich, Germany	Cat#: M8266
Tris(hydroxymethyl)aminomethane (Tris)	Sigma-Aldrich, Germany	Cat#: 648314
Sodium chloride	Sigma-Aldrich, Germany	Cat#: S9888
Ethylendiaminetetraacetic acid (EDTA)	Sigma-Aldrich, Germany	Cat#: 03620
100-nm BioPure Silver Nanospheres	nanoComposix, USA	Cat#: HS3822
Tween®20	Thermo Fisher Scientific, USA	Cat#: 85113
Monobasic potassium buffer	Merck, Germany	Cat#: 8709
Dibasic potassium buffer	Merck, Germany	Cat#: 8584
Phosphate buffered saline (PBS)	Sigma-Aldrich	Cat#: P4417-50TAB
Bovine serum albumin (BSA)-Biotin	Sigma-Aldrich, Germany	Cat#: A8549-10MG
Neutravidin	Thermo Fisher Scientific, USA	Cat#: 31050
PEG-8000	Sigma-Aldrich, Germany	87006
Oligonucleotides		
Unmodified ssDNA strands	Eurofins Genomics GmbH, Germany	https://eurofinsgenomics.eu
Modified ssDNA strands (despite BBQ-lalled DNA strands and SH-labeled DNA strands)	Biomers.net GmbH, Germany	https://www.biomers.net
BBQ-lalled DNA strands	Eurofins Genomics GmbH, Germany	https://eurofinsgenomics.eu
T_{20}-SH DNA strands	EllaBiotech, Germany	https://www.ellabiotech.com/
Software and algorithms		
LabView	National Instruments, USA	https://www.ni.com
OriginPro2020	OriginLab, USA	https://www.originlab.com/2020
ImageJ: Fiji	Schindelin et al. 2012	https://imagej.net/software/fiji/
Other		
100 kDa Amicon Ultra filters	Merck	Cat#: MPUFC510024
TEM grids (Formvar/carbon, 400 mesh, Cu)	TedPella, Inc., USA	Cat#: 01702-F
Grace Bio-Labs hybridization chambers	Merck	Cat#: GBL623504-50EA
Microscope coverslips (24 mm × 60mm size and 170 μm thickness)	Carl Roth, Germany	Cat#: H878.2
Transmission electron microscope	JOEL GmbH, Japan	JOEL JEM-1100 microscope
UV-Vis spectrometer NanoDrop 2000	Thermo Fisher Scientific, USA	Cat#: ND-2000
Inverted microscope	Olympus Corporation, Japan	IX83 inverted microscope
78 MHz-pulsed white light laser	NKT Photonics A/S, Denmark	SuperK Extreme EXW-12
acousto-optically tunable filter (AOTF)	NKT Photonics A/S, Denmark	Super Dual AOTF
Digital controller	Crystal Technology, USA	AODS 20160 8 R
AOTF	AA Opto-Electronic, France	AA.AOTF.ns: TN
Dichroic beam splitter	Chroma Technology, USA	ZT532/640rpc
Immersion oil objective	Olympus Corporation, Japan	UPlanSApo 100 x, NA = 1.4, WD = 0.12 mm

(*Continued on next page*)

Continued

REAGENT or RESOURCE	SOURCE	IDENTIFIER
Pinhole	Linos AG, Germany	
Piezo-Stage	Physik Instrumente GmbH&Co. KG, Germany	P-517.3CL, E-501.00
Avalanche Photodiodes	Perkin Elmer Inc., USA	SPCM, AQR 14
TCSPC	PicoQuant GmbH, Germany	HydraHarp 400
Spectral filter (red channel)	Semrock Inc., USA	RazorEdge 647
Spectral filter (green channel)	Semrock Inc., USA	BrightLine HC 582/75
Laser diode	UAB, Lithuania	0638L-11A, Integrated Optics
Objective lens	UCTRONICS, USA	NA = 0.25, LS-40166,
Monochrome camera of the smartphone	P20	Huawei, China
Filter	BrightLine HC 731/137	Semrock Inc., USA

RESOURCE AVAILABILITY

Lead contact

Further information and requests for resources and reagents should be directed to and will be fulfilled by the corresponding author, Philip Tinnefeld (Department of Chemistry and Center for NanoScience, Ludwig-Maximilians-Universität München, Butenandtstr. 5–13, 81,377 München, Germany. Philip.tinnefeld@cup.uni-muenchen.de).

Materials availability

This study did not generate new unique reagents.

Data and code availability

- All raw data reported in this paper will be shared by the lead contact upon request.
- This paper does not report original code.
- Any additional information required to reanalyze the data reported in this paper is available from the lead contact upon request.

METHOD DETAILS

Synthesis of DNA origami

DNA origami structures were designed using the open-source software caDNAno2 (Douglas et al., 2009) and assembled and purified using published protocols (Wagenbauer et al., 2017). For the exact sequences of all unmodified and modified DNA staple strands used to fold the DNA origami structures see Tables S1 and S2 (NRO) and Tables S3 and S4 (DNA origami used to build NACHOS). The BBQ650-labeled staple strands were purchased from Biomers.net GmbH (Germany). All other staples were purchased from Eurofins Genomics GmbH (Germany).

For the DNA origami structure used to build NACHOS, 25 µL of p8064 scaffold (produced in-house) at 100 nM were mixed with 18 µL of unmodified staples pooled from 100 µM original concentration and 2 µL of modified staples pooled from 100 µM original concentration. For DNA origami folding, 5 µL of 10x FoB20 folding buffer (200 mM $MgCl_2$, 50 mM Tris, 50 mM NaCl, 10 mM EDTA) were added and the mixture was subjected to a thermal annealing ramp (Table S5). Folded DNA origamis were purified from excessive staple strands using 100 kDa Amicon Ultra filters (Merk, Germany) with 6 washing steps with a lower ionic strength buffer (5 mM $MgCl_2$, 5 mM Tris, 5 mM NaCl, 1 mM EDTA) at 10 krcf for 5 min and 20°C. To extract the purified DNA origamis, the filter was inverted in a new Eppendorf tube and the sample was recovered by spinning for 2 min at 1 krcf and 20°C.

For the NRO, 10 µL of p7249 scaffold (produced in-house) at 100 nM were mixed with 18 µL of unmodified staples pooled from 100 µM original concentration and 4 µL of modified staples pooled from 100 µM original concentration. Briefly, 10 µL of 10x folding buffer (125 mM $MgCl_2$, 400 mM Tris, 200 mM acetic acid, 10 mM EDTA) were added and the mixture was heated to 65°C in a thermocycler. The solution was kept

at this temperature for 15 min before being cooled down to 25°C with a temperature gradient of – 1°C min^{-1}. Samples were purified from excess staple strands by PEG-precipitation. The reaction mixture was mixed 1:1 (v:v) with precipitation buffer (15% PEG-8000, 10 mM $MgCl_2$, 250 mM NaCl) and spinned at 16,000 g for 45 min at 4°C. The supernatant was discarded and the pellet was re-dissolved in 100 μL storage buffer (12.5 mM $MgCl_2$, 40 mM Tris, 20 mM acetic acid, 10 mM EDTA). The precipitation procedure was carried out 3 times. Finally, the pellet was dissolved in 20 μL storage buffer.

Functionalization of AgNPs

100 nm AgNP (100-nm BioPure Silver Nanospheres (Citrate), nanoComposix, USA) were functionalized with polythymidine (T_{20}) ssDNA strands with a thiol modification at the 3'-end (Ella Biotech GmbH, Germany) based on previously described procedures (Trofymchuk et al., 2021). For the fabrication of T_{20}-functionalized AgNPs, 2 mL of 0.025 mg/mL nanoparticle solution in ultra-pure water (Sigma Aldrich, Germany) was heated to 40°C under permanent stirring at 550 rpm. Briefly, 20 μL of 10% Tween20 (Thermo Fisher Scientific, USA), 20 μL of a 4:5 (v:v) mixture of 1 M monobasic and dibasic potassium phosphate buffers (P8709 and P8584 Sigma Aldrich, Germany) and 20 μL of a 2 nM polythymidine ssDNA strands (T_{20}-SH-3') were added to the nanoparticle solution and stirred at 40°C for 1 h. Then, different amounts of 1x PBS buffer (137 mM NaCl, 2.7 mM KCl, 10 mM Na_2HPO_4, 1.8 mM KH_2PO_4) containing 3.3 M NaCl were added stepwise every three minutes to the mixture, until a final concentration of 750 mM NaCl was reached – for the exact salting procedure see Table S6. Afterward, the solution was centrifuged for 12 min at 2800 g and 20°C. The supernatant was discarded and the pellet, in which the particles were concentrated, was re-suspended in PBS10 buffer (147 mM NaCl, 2.7 mM KCl, 10mM Na_2HPO_4, 3.9 mM KH_2PO_4, 2.9 mM K_2HPO_4, 2.5 mM EDTA, 0.01% Tween20). The washing step was carried out six times. Finally, the NPs were diluted in 1x TE buffer (10 mM Tris, 1 mM EDTA) containing 750 mM NaCl to an absorption of 0.1 (0.1 mm path length) at the excitation maxima on a UV-Vis spectrometer (NanoDrop, 2000; Thermo Fisher Scientific, USA).

Transmission electron microscopy (TEM) measurements

TEM grids (Formvar/carbon, 400 mesh, Cu, TedPella, Inc., USA) were Ar-plasma cleaned and incubated with 5 μL of ~2–10 nM DNA origami sample for 60 s. Grids were washed with 5 μL 2% uranyl formate solution and incubated afterward again with 5 μL 2% uranyl formate solution for staining. TEM imaging was performed on a JOEL JEM-1100 microscope (JEOL GmbH, Japan) with an acceleration voltage of 80 kV.

Sample preparation on the coverslip for single-molecule confocal measurements

Adhesive SecureSeal™ Hybridization Chambers (2.6 mm depth, Grace Bio-Labs, USA) were glued on microscope coverslips of 24 mm × 60 mm size and 170 μm thickness (Carl Roth GmbH, Germany). The created wells were incubated with 1 M KOH for 1 h and washed three times with 1×PBS buffer. After surface passivation by incubation with BSA-Biotin (0.5 mg/mL, Sigma Aldrich, USA) for 15 min, the surface was again washed three times with 1× PBS buffer. 100 μL neutravidin (0.25 mg/mL, Thermo Fisher, USA) was incubated for 10 min and then washed three times with 1× PBS buffer. The DNA origami solution was diluted with 1× TE buffer containing 750 mM NaCl to a concentration of ~10–100 pM and then immobilized on the biotin-neutravidin surface via biotin-neutravidin interactions. For this, 100 μL of the DNA origami sample solution was added and incubated for 3 min. Residual unbound DNA origami was removed by washing the wells three times with 1x TE buffer containing 750 mM NaCl. The density of DNA origami on the surface suitable for single-molecule measurements was checked on a confocal microscope. Nanoantenna samples were then incubated with 150 μL of the T_{20}-functionalized AgNPs in 1x TE buffer containing 750 mM NaCl overnight at room temperature. Unbound NPs were removed by washing the samples three times with 1x TE buffer containing 750 mM NaCl. To prevent the evaporation of the samples, wells were glued with tapes. The samples were then imaged either directly or after performing a sensing procedure in antibody binding buffer (150 mM NaCl, 50 mM Na_2HPO_4, pH 7).

Antibody detection assay

For the detection of anti-Dig antibodies, DNA origami bearing a nanoswitch were immobilized on a surface via biotin-neutravidin interactions and NPs were attached to DNA origami samples in analogous way to the previous section. anti-Dig antibodies (Rb Monoclonal, Thermo Fisher Scientific, USA, cat#: 700,772, PRID: AB_2532342) were diluted to 0.01–500 nM in antibody binding buffer. DNA origami samples were incubated 20 min (unless stated otherwise in the text) with 150 μL of the anti-Dig antibody solution at room temperature before imaging.

Confocal measurements and data analysis

For detection of single-molecule fluorescence, a home-build confocal microscope was used. The setup was based on an inverted microscope (IX-83, Olympus Corportation, Japan) and a 78 MHz-pulsed white light laser (SuperK Extreme EXW-12, NKT Photonics A/S, Denmark) with selected wavelengths of 532 nm and 639 nm. The wavelengths were selected via an acousto-optically tunable filter (AOTF, SuperK Dual AOTF, NKT Photonics A/S, Denmark). This was controlled by a digital controller (AODS, 20160 8 R, Crystal Technology, USA) via a computer software (AODS, 20160 Control Panel, Crystal Technology, Inc., USA). A second AOTF (AA.AOTF.ns: TN, AA Opto-Electronic, France) was used to alternate 532 nm and 639 nm wavelengths if required, as well as to further spectrally clean the laser beam. It was controlled via home-made LabVIEW software (National Instruments, USA). A neutral density filter was used to regulate the laser intensity, followed by a linear polarizer and a λ/4 plate to obtain circularly polarized excitation. A dichroic beam splitter (ZT532/640rpc, Chroma Technology, USA) and an immersion oil objective (UPlanSApo 100×, NA = 1.4, WD = 0.12 mm, Olympus Corporation, Japan) were used to focus the excitation laser onto the sample. Micropositioning was performed using a Piezo-Stage (P-517.3CL, E−501.00, Physik Instrumente GmbH&Co. KG, Germany). The excitation powers at 639 nm were set to 500 nW for the reference samples and to 100 nW for the nanoantennas for the recording of fluorescence transients. For the confocal scans, 1 μW at 532 nm and 1 μW at 639 nm were used for all samples. Emitted light was collected by the same objective and filtered from the excitation light by a dichroic beam splitter. The light was later focused on a 50 μm pinhole (Linos AG, Germany) and detected using avalanche photodiodes (SPCM, AQR 14, PerkinElmer, Inc., USA) registered by an TCSPC system (HydraHarp 400, PicoQuant GmbH, Germany) after additional spectral filtering (RazorEdge 647, Semrock Inc., USA for the red channel and BrightLine HC 582/75, Semrock Inc., USA for the green channel). Custom-made LabVIEW software (National Instruments, USA) was used to process the acquired raw data. Background correction was carried out individually for each transient. The extracted data was analyzed in OriginPro2020.

Sample preparation for single-molecule measurements on the smartphone microscope

Microscope cover slides of 22 mm × 22 mm size and 170 μm thickness (Carl Roth GmbH, Germany) were cleaned with UV-Ozone cleaner (PSD-UV4, Novascan Technologies, USA) for 30 min at 100°C. After this a silicon mask was glued on a coverslip to create a chamber for surface functionalization, DNA origami immobilization (20 pM) and NACHOS assembly. Then the antibody detection assay was performed analogously as described above. The silicon mask was removed, and a double-sided tape was glued on both sides of the cover slide. The cover slides were covered with 76 mm × 26 mm microscope slides (1 mm thickness, Carl Roth GmbH, Germany) which were priory cleaned with UV-Ozone cleaner for 30 min at 100°C. Chambers were sealed before imaging.

Single-molecule measurements and analysis on the smartphone

Single antibody detection measurements on the smartphone were performed using a home-built portable setup (Trofymchuk et al., 2021). The 638 nm laser diode (0638L-11A, Integrated Optics, UAB, Lithuania) with an output power 180 mW that can be driven by various (portable) voltage sources was focused (f = 50 mm) in 45° angle onto the sample. The fluorescence of the molecules was collected using an objective lens (NA = 0.25, LS-40166, UCTRONICS, USA) and detected using a monochrome camera of the smartphone (P20, Huawei, China) after filtering out the excitation light (BrightLine HC 731/137, Semrock Inc., USA). Movies were recorded via FreeDCam application and analyzed with ImageJ (FIJI) equipped with FFMPEG plugin using a home written macro to convert MP4 format of the acquired movies to a TIFF format and find the single-molecule signals and extract the fluorescence intensity as a function of illumination time. The extracted data were analyzed in OriginPro2020.

QUANTIFICATION AND STATISTICAL ANALYSIS

Statistical analysis on nanoswitch opening

An unpaired t test was used to compare the magnitude of changes in nanoswitch opening on the NRO before and after the addition of 100 nM antibodies. The changes in nanoswitch opening before and after incubation with 100 nM anti-Dig antibodies were significant only for the nanoswitch construct bearing two Dig recognition elements ($p < 0.05$). While the changes in nanoswitch opening before and after incubation with anti-hDectin-1 antibody is not significant ($p > 0.05$), we observed a significant increase in nanoswitch opening before and after incubation with anti-Dig Fab fragment ($p < 0.05$). However, the difference before and after incubation with anti-Dig Fab fragment was very small (~4%) even at 100 nM anti-Dig Fab fragment

concentration. Given that the sensitive concentration range of the nanoswitch is way below this (Figure 3B), monovalent binding of two antibodies should not contribute much to the nanoswitch opening in the performed experiments.

Additionally, an unpaired t test was used to compare the changes in nanoswitch opening in NACHOS containing a 100-nm AgNP as well as in the same DNA origami nanostructure without NPs. The changes in nanoswitch opening before and after incubation with 100 nM anti-Dig antibodies was significant for the NACHOS containing a 100-nm AgNP and the DNA origami nanostructure without NPs ($p < 0.05$).

Impact of photophysics on the antibody assay

The single-molecule fluorescence transients of the nanoswitch in both the reference structure and the NACHOS structure upon incubation with anti-Dig antibody show short time blinking and also fluctuations between multiple intensity states. The intensity fluctuations could report on unbinding/rebinding of one of the two binding sites, distance fluctuations between dye and quencher due to the flexibility of ssDNA strands or could also be caused by photophysical processes unrelated to both (e.g. dim and dark states of the ATTO 647N dye, quencher blinking, fluctuations in the interaction between the dye and the Ag nanoparticle (*e.g.* orientation change of the transition dipole moment).

The photophysics of the ATTO 647N dye also were used to confirm the presence of single molecules in the assay. Only transients showing single-step photobleaching – transients with short time blinking and reversible intensity fluctuations between a bright and a dark or dim state – were included in the fluorescence enhancement analysis (69% and 52% of all recorded transients of the open nanoswitch in the reference structures and the NACHOS structure, respectively, Figure 2E). Multi-step photobleaching as observed for some nanostructures can be caused by a spectral shift of the ATTO 647N dye(Vogelsang et al., 2008; Glembockyte et al., 2016) – visible in the transients as an irreversible intensity fluctuation between a bright state and a dim state before photobleaching – or aggregated DNA origami structures. Furthermore, NACHOS transients without any photobleaching step can be related to nanoparticle aggregates on the surface.

Sensitive concentration ranges

For the binding curves in Figure 3B the observed nanoswitch opening (NO) was fitted using the following four parameter logistic equation: $NO = NO_{min} + (NO_{max} - NO_{min})\ [[Ab]^{nH}/([Ab]^{nH} + C_{HalfMax}{}^{nH})]$. Here, NO_{min} and NO_{max} are the minimum and maximum nanoswitch opening values, $C_{HalfMax}$ is the antibody concentration at half-maximum signal after 20 min incubation, nH is the apparent Hill coefficient, and [Ab] is the concentration of the anti-Dig antibody added. This function usually is used for fitting dose-response functions and allows to study cooperativity if all data is collected in equilibrium limit. As we aimed to validate the assay under conditions used for diagnostic applications, we did not perform it in the equilibrium limit but with an incubation time of only 20 min for each target concentration. For this incubation time, binding of the antibody is most probably diffusion limited at low concentrations (Simon et al., 2014; Wu et al., 2019). This becomes apparent when fitting the binding curves as apparent Hill coefficients larger than one are found for all three DNA origami nanostructures. Thus, the performed measurements do not allow determining the K_D value (antibody concentration at half maximum signal gain und equilibrium conditions) but show the sensitive concentration range achievable under clinically relevant conditions, *e.g.* short incubation times. The diffusion limitation shifts the $C_{HalfMax}$ to higher values than the K_D value. They thus represent the upper K_D limit.

Comparison with other single-antibody assays

The nanoswitch-based single-antibody detection assay was compared with three previously reported single-molecule antibody detection assays (Table S7). Criteria with possible relevance for point-of-care clinical applications were selected.

iScience, Volume *24*

Supplemental information

Single antibody detection

in a DNA origami nanoantenna

Martina Pfeiffer, Kateryna Trofymchuk, Simona Ranallo, Francesco Ricci, Florian Steiner, Fiona Cole, Viktorija Glembockyte, and Philip Tinnefeld

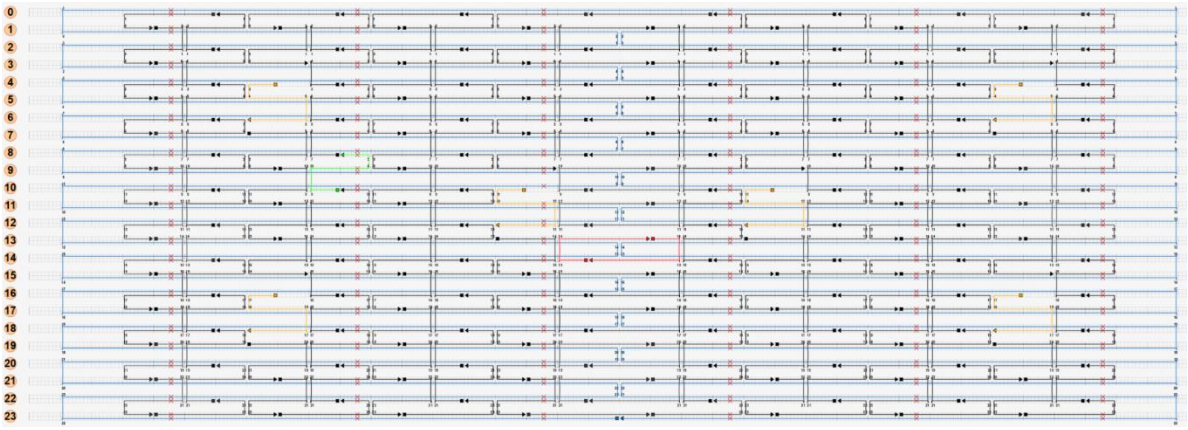

Figure S1. Staple layout of the NRO DNA origami nanostructure (yellow = biotin staples, red = nanoswitch staples, green = base dye staple), Related to STAR Methods.

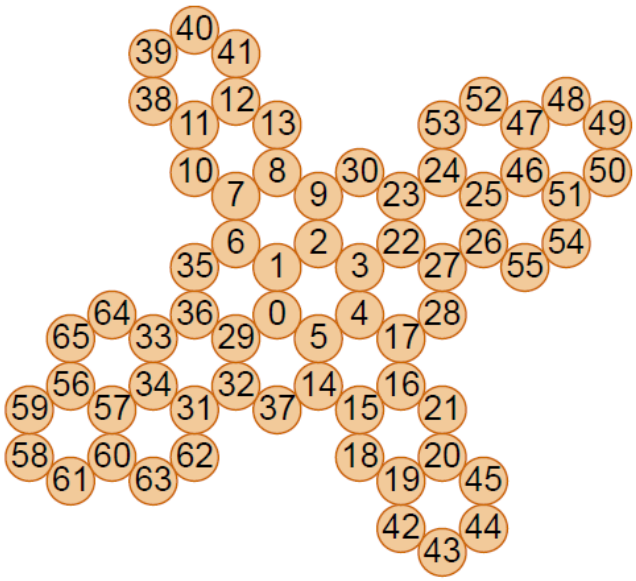

Figure S2. Base layout of the DNA origami nanostructure used to build NACHOS, Related to STAR Methods.

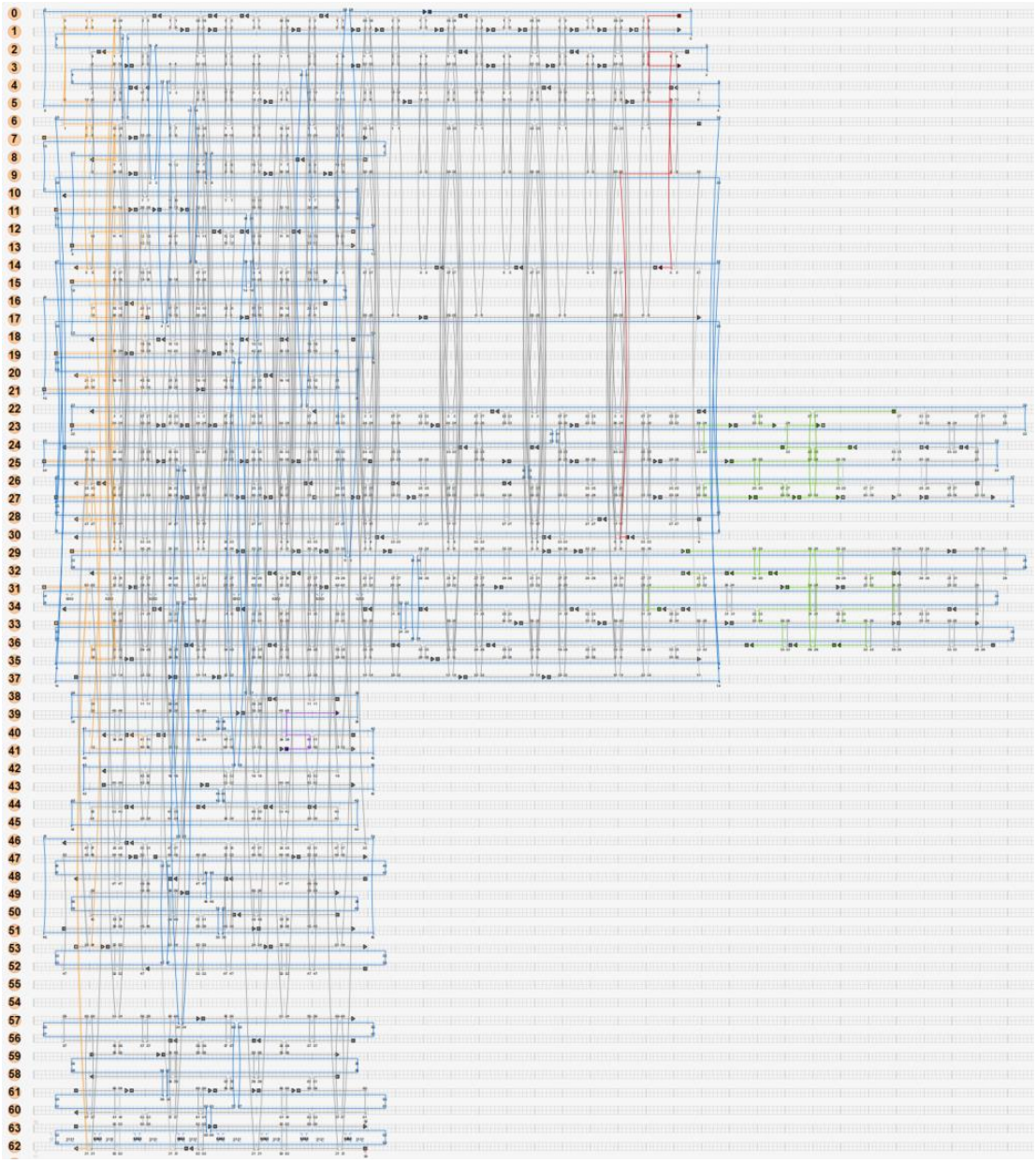

Figure S3. Staple layout of the NACHOS DNA origami nanostructure (yellow = biotin staples, red = nanoswitch staples, green = nanoparticle binding staples, purple = base dye staple), Related to STAR Methods.

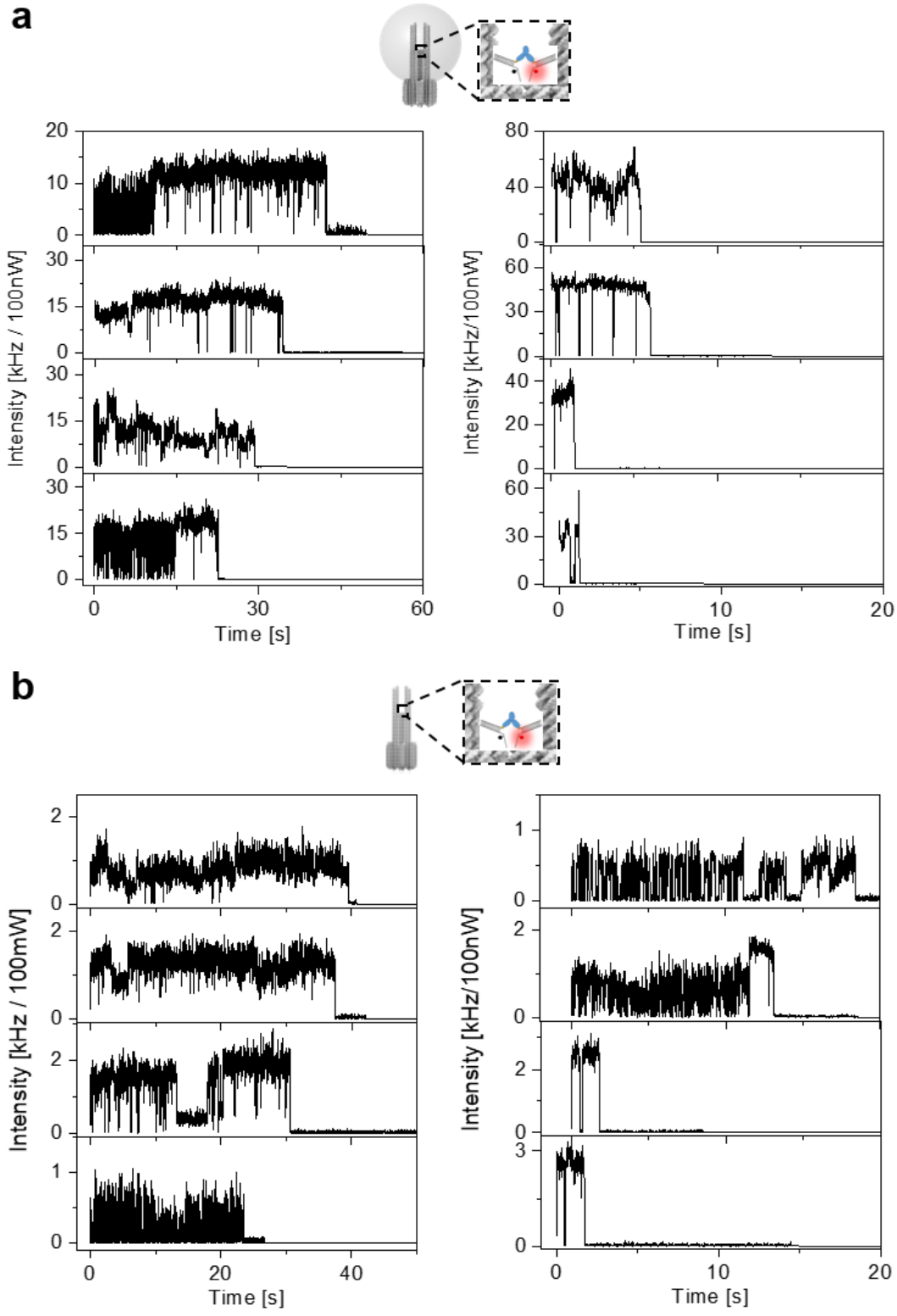

Figure S4. Exemplary single-molecule transients of open nanoswitch (ATTO 647N dye) in NACHOS containing one AgNP (a) and in DNA origami reference structures without AgNPs (b). The samples are measured at 639 nm with 100 nW and 500 nW excitation power for panel (a) and (b), respectively, and the transients are normalized to the same excitation power. Related to Figure 2.

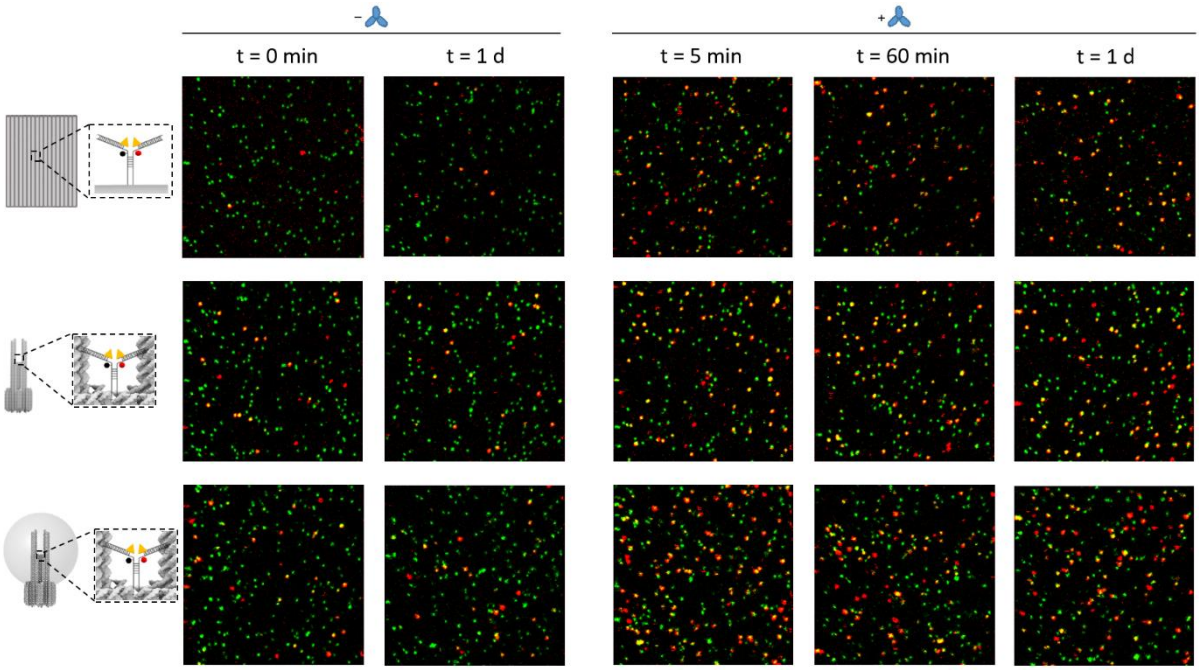

Figure S5. Opening kinetics of the nanoswitch on different DNA origami structures. Two-color fluorescence confocal images of nanoswitch on the NRO (upper row), the reference DNA origami structure without NPs (middle row) and with one 100-nm AgNP attached (lower row) before and after different incubation times with 100 nM anti-Dig antibodies. The scans show a field of view of 20 µm x 20 µm. Excitation was carried out at 532 nm and 639 nm with 1 µW. Related to Figure 4.

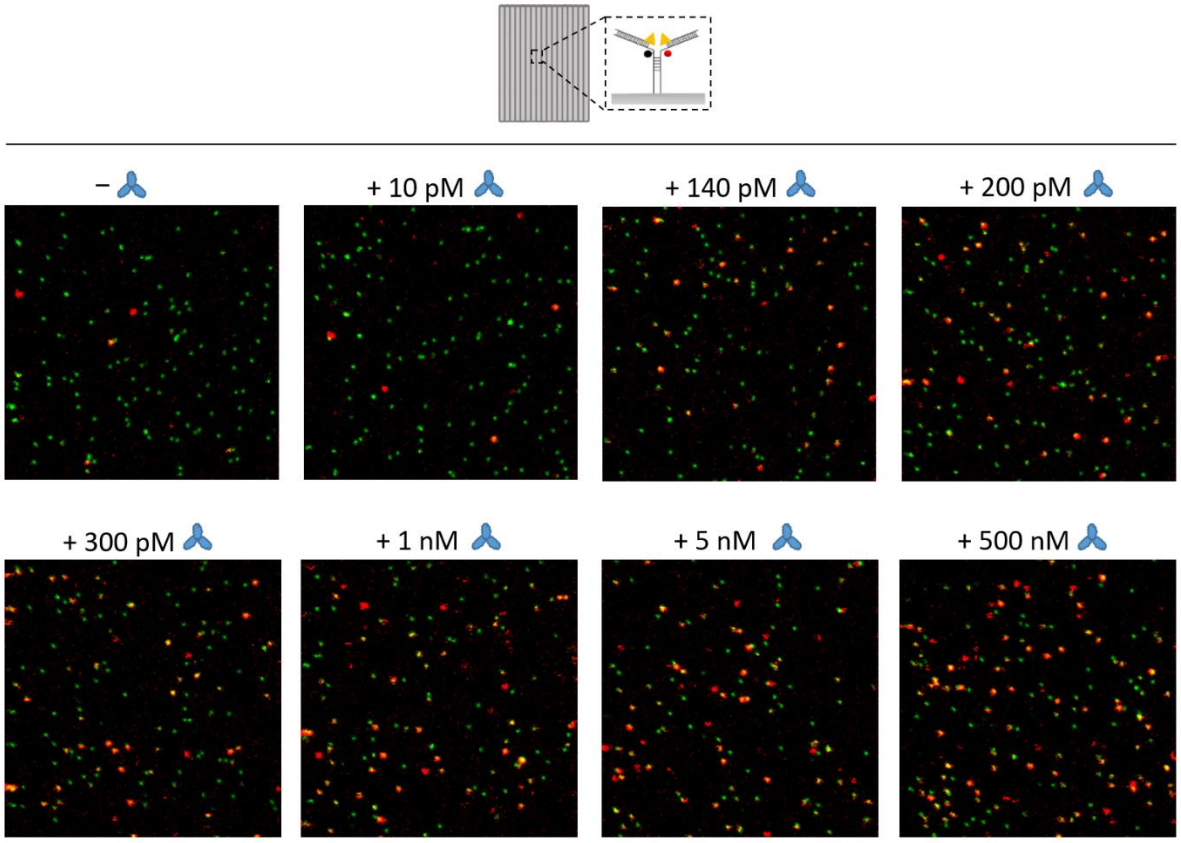

Figure S6. Two-color fluorescence confocal images of nanoswitch on the NRO before and after 20 min incubation with different amounts of anti-Dig antibodies. The scans show a field of view of 20 µm x 20 µm. Excitation was carried out at 532 nm and 639 nm with 1 µW. Related to Figure 4.

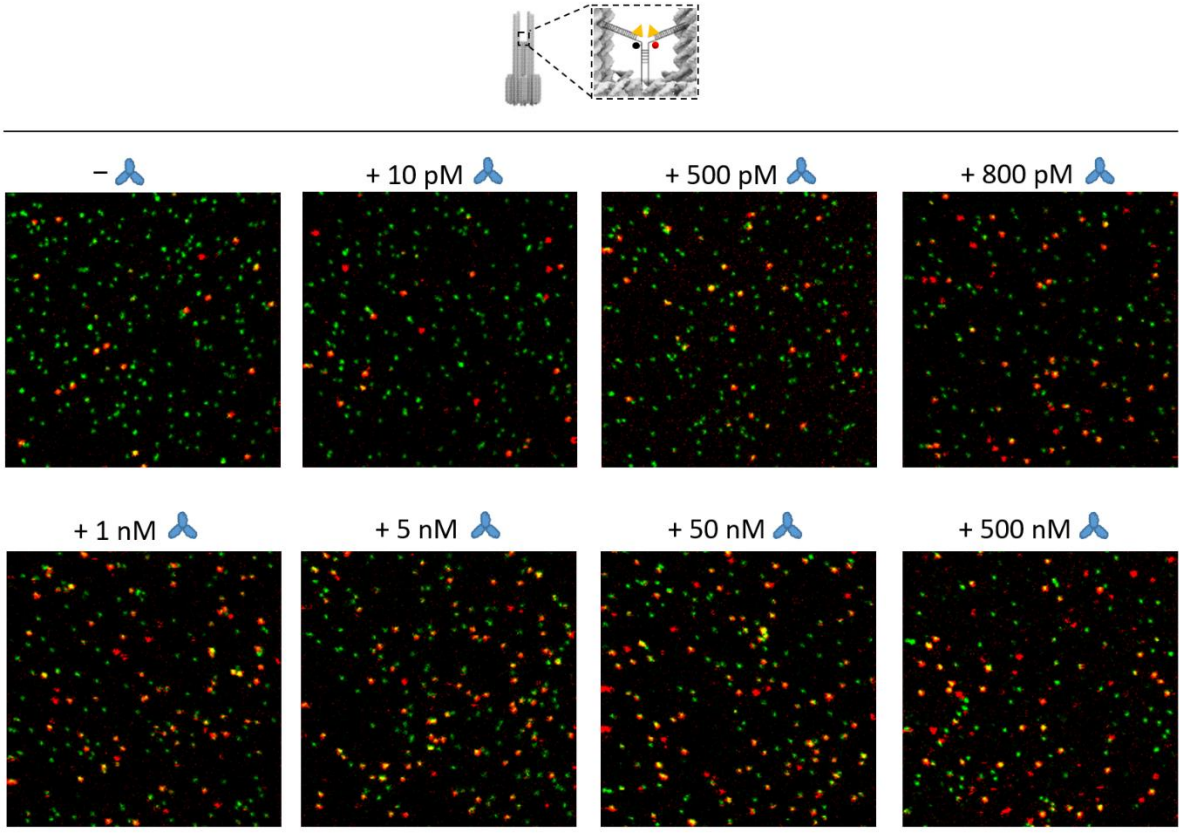

Figure S7. Two-color fluorescence confocal images of nanoswitch on a reference DNA origami structure without NPs before and upon 20 min incubation with different amounts of anti-Dig antibodies. The scans show a field of view of 20 µm x 20 µm. Excitation was carried out at 532 nm and 639 nm with 1 µW. Related to Figure 4.

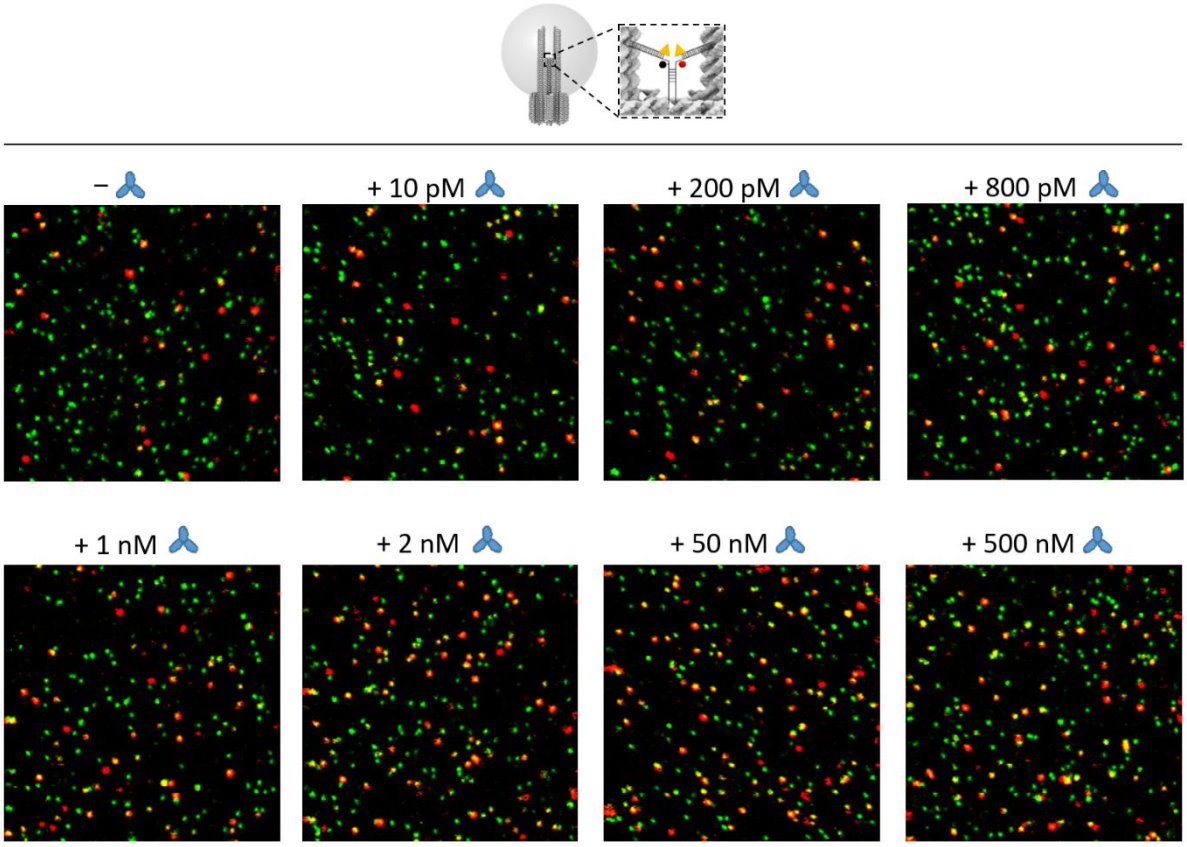

Figure S8. Two-color fluorescence confocal images of nanoswitch in the NACHOS structure containing one 100-nm Ag NP before and after 20 min incubation with different amounts of anti-Dig antibodies. The scans show a field of view of 20 µm x 20 µm. Excitation was carried out at 532 nm and 639 nm with 1 µW. Related to Figure 4.

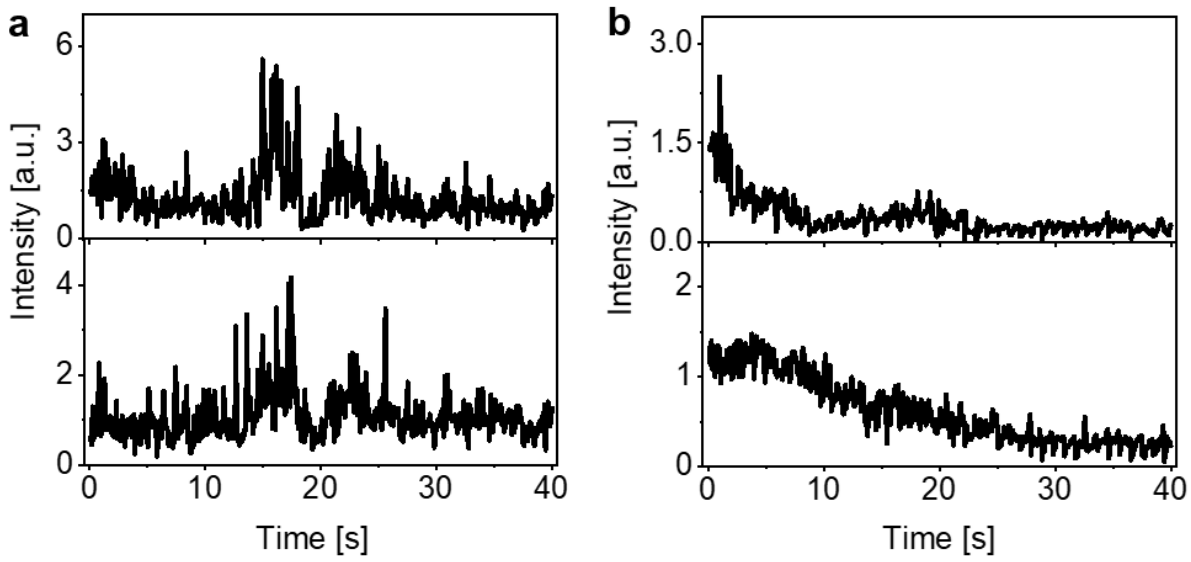

Figure S9. Exemplary fluorescence transients of the nanoswitch (single ATTO 647N dye) in NACHOS containing a 100-nm AgNP measured on a portable smartphone microscope setup. (a) Fluorescence transients with intensity fluctuations ending with single bleaching steps. (b) Fluorescence transients with multiple bleaching steps. Related to Figure 3.

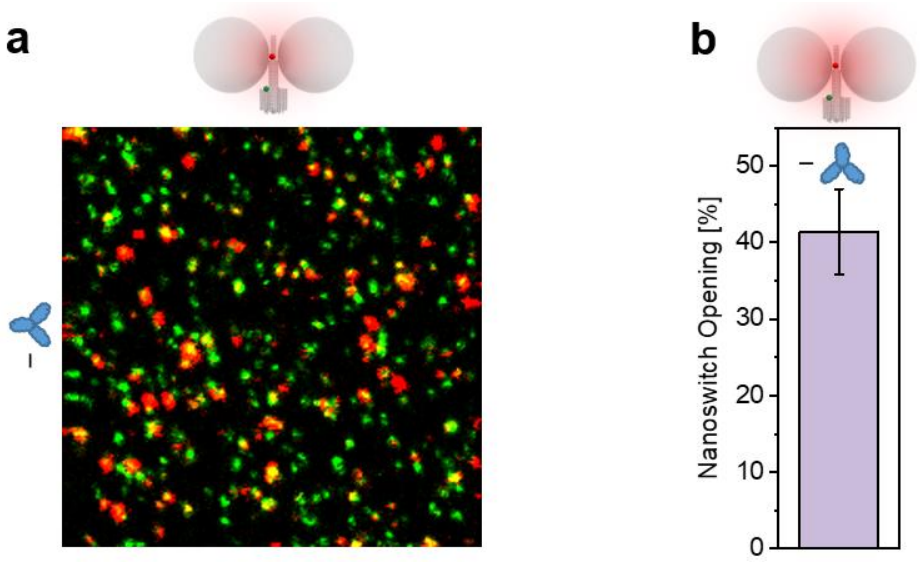

Figure S10. Non-specific signal of nanoswitch in the hotspot of NACHOS containing two 100-nm Ag NPs. (a) Two-color fluorescence confocal image of NACHOS with two 100-nm Ag NPs in the absence of anti-Dig antibodies. The scan shows a field of view of 20 µm x 20 µm. Excitation was carried out at 532 nm and 639 nm with 1 µW. (b) Fraction of open nanoswitches quantified by dividing the number of red-green colocalized spots by the total number of green spots. Over 400 structures from 4 different areas per sample were analyzed. Error bars represent the standard deviation of the 5 areas. Related to STAR Methods.

Table S1. Staple strands used to fold the NRO DNA origami nanostructures, Related to STAR Methods.

Name	Sequence (5'→3')
1	CATAAATCTTTGAATACCAAGTGTTAGAAC
2	GATGTGCTTCAGGAAGATCGCACAATGTGA
3	GCAATTCACATATTCCTGATTATCAAAGTGTA
4	GATTTAGTCAATAAAGCCTCAGAGAACCCTCA
5	TCACCAGTACAAACTACAACGCCTAGTACCAG
6	CCAATAGCTCATCGTAGGAATCATGGCATCAA
7	GCTTTCCGATTACGCCAGCTGGCGGCTGTTTC
8	AAAGGCCGGAGACAGCTAGCTGATAAATTAATTTTTGT
9	AAATTAAGTTGACCATTAGATACTTTTGCG
10	AAGCCTGGTACGAGCCGGAAGCATAGATGATG
11	TCATTCAGATGCGATTTTAAGAACAGGCATAG
12	GCCATCAAGCTCATTTTTTAACCACAAATCCA
13	TATAACTAACAAAGAACGCGAGAACGCCAA
14	TTGCTCCTTTCAAATATCGCGTTTGAGGGGGT
15	GTATAGCAAACAGTTAATGCCCAATCCTCA
16	AAAGTCACAAAATAAACAGCCAGCGTTTTA
17	GGCCTTGAAGAGCCACCACCCTCAGAAACCAT
18	TTAACGTCTAACATAAAAACAGGTAACGGA
19	AGTATAAAGTTCAGCTAATGCAGATGTCTTTC
20	TCAAATATAACCTCCGGCTTAGGTAACAATTT
21	TTTCGGAAGTGCCGTCGAGAGGGTGAGTTTCG
22	GAGGGTAGGATTCAAAAGGGTGAGACATCCAA
23	TATTAAGAAGCGGGGTTTTGCTCGTAGCAT
24	GCCCTTCAGAGTCCACTATTAAAGGGTGCCGT
25	ATGCAGATACATAACGGGAATCGTCATAAATAAAGCAAAG
26	AGCCAGCAATTGAGGAAGGTTATCATCATTTT
27	TAAATGAATTTTCTGTATGGGATTAATTTCTT
28	AAACAGCTTTTTGCGGGATCGTCAACACTAAA
29	GCGCAGACAAGAGGCAAAAGAATCCCTCAG
30	AGAGAGAAAAAAATGAAAATAGCAAGCAAACT
31	GACAAAAGGTAAAGTAATCGCCATATTTAACAAAACTTTT
32	ACACTCATCCATGTTACTTAGCCGAAAGCTGC
33	CTACCATAGTTTGAGTAACATTTAAAATAT
34	TATATTTTGTCATTGCCTGAGAGTGGAAGATTGTATAAGC
35	CGGATTGCAGAGCTTAATTGCTGAAACGAGTA
36	GTACCGCAATTCTAAGAACGCGAGTATTATTT
37	TCTTCGCTGCACCGCTTCTGGTGCGGCCTTCC
38	GCAAGGCCTCACCAGTAGCACCATGGGCTTGA
39	ATTACCTTTGAATAAGGCTTGCCCAAATCCGC
40	CTTATCATTCCCGACTTGCGGGAGCCTAATTT
41	TTATACCACCAAATCAACGTAACGAACGAG
42	GATGGTTTGAACGAGTAGTAAATTTACCATTA
43	GCACAGACAATATTTTTGAATGGGGTCAGTA
44	AGCAAGCGTAGGGTTGAGTGTTGTAGGGAGCC
45	TCCACAGACAGCCCTCATAGTTAGCGTAACGA
46	ATTATACTAAGAAACCACCAGAAGTCAACAGT
47	TAAGAGCAAATGTTTAGACTGGATAGGAAGCC
48	ATACATACCGAGGAAACGCAATAAGAAGCGCATTAGACGG
49	CAACTGTTGCGCCATTCGCCATTCAAACATCA
50	GATGGCTTATCAAAAAGATTAAGAGCGTCC
51	TAGGTAAACTATTTTTGAGAGATCAAACGTTA
52	AGGCAAAGGGAAGGGCGATCGGCAATTCCA
53	ATTATCATTCAATATAATCCTGACAATTAC
54	GAAATTATTGCCTTTAGCGTCAGACCGGAACC
55	AATGGTCAACAGGCAAGGCAAAGAGTAATGTG
56	ATACCCAACAGTATGTTAGCAAATTAGAGC
57	CACCAGAAAGGTTGAGGCAGGTCATGAAAG
58	ATCCCAATGAGAATTAACTGAACAGTTACCAG
59	CATGTAATAGAATATAAAGTACCAAGCCGT
60	CCAACAGGAGCGAACCAGACCGGAGCCTTTAC
61	GCTATCAGAAATGCAATGCCTGAATTAGCA

62	GACCTGCTCTTTGACCCCCAGCGAGGGAGTTA
63	AGGAACCCATGTACCGTAACACTTGATATAA
64	CAGCGAAACTTGCTTTCGAGGTGTTGCTAA
65	ACAACTTTCAACAGTTTCAGCGGATGTATCGG
66	CAGCAAAAGGAAACGTCACCAATGAGCCGC
67	ACCTTTTTATTTTAGTTAATTTCATAGGGCTT
68	CGATAGCATTGAGCCATTTGGGAACGTAGAAA
69	GCCCGAGAGTCCACGCTGGTTTGCAGCTAACT
70	ATTTTAAAATCAAAATTATTTGCACGGATTCG
71	ACCTTGCTTGGTCAGTTGGCAAAGAGCGGA
72	CTGAGCAAAAATTAATTACATTTTGGGTTA
73	CCTGATTGCAATATATGTGAGTGATCAATAGT
74	TCAATATCGAACCTCAAATATCAATTCCGAAA
75	CTTTAGGGCCTGCAACAGTGCCAATACGTG
76	AATAGTAAACACTATCATAACCCTCATTGTGA
77	TCACCGACGCACCGTAATCAGTAGCAGAACCG
78	GCCCGTATCCGGAATAGGTGTATCAGCCCAAT
79	TGTAGCCATTAAAATTCGCATTAAATGCCGGA
80	TCGGCAAATCCTGTTTGATGGTGGACCCTCAA
81	TGACAACTCGCTGAGGCTTGCATTATACCA
82	CCACCCTCTATTCACAAACAAATACCTGCCTA
83	CCCGATTTAGAGCTTGACGGGGAAAAAGAATA
84	AAGTAAGCAGACACCACGGAATAATATTGACG
85	CACATTAAAATTGTTATCCGCTCATGCGGGCC
86	TTAAAGCCAGAGCCGCCACCCTCGACAGAA
87	ATATTCGGAACCATCGCCCACGCAGAGAAGGA
88	TTCTACTACGCGAGCTGAAAAGGTTACCGCGC
89	AACGTGGCGAGAAAGGAAGGGAAACCAGTAA
90	GAATTTATTTAATGGTTTGAAATATTCTTACC
91	AGCGCGATGATAAATTGTGTCGTGACGAGA
92	AACGCAAAGATAGCCGAACAAACCCTGAAC
93	GCCTCCCTCAGAATGGAAAGCGCAGTAACAGT
94	AAAGCACTAAATCGGAACCCTAATCCAGTT
95	GCCAGTTAGAGGGTAATTGAGCGCTTTAAGAA
96	AAGGCCGCTGATACCGATAGTTGCGACGTTAG
97	TTTTATTTAAGCAAATCAGATATTTTTTGT
98	CTTTTGCAGATAAAAACCAAAATAAAGACTCC
99	CCTAAATCAAAATCATAGGTCTAAACAGTA
100	AGACGACAAAGAAGTTTTGCCATAATTCGAGCTTCAA
101	AGAAAACAAAGAAGATGATGAAACAGGCTGCG
102	CGCGCAGATTACCTTTTTTAATGGGAGAGACT
103	CACAACAGGTGCCTAATGAGTGCCCAGCAG
104	GCGGAACATCTGAATAATGGAAGGTACAAAAT
105	TAAAAGGGACATTCTGGCCAACAAAGCATC
106	AATTGAGAATTCTGTCCAGACGACTAAACCAA
107	GCGAAAAATCCCTTATAAATCAAGCCGGCG
108	AACACCAAATTTCAACTTTAATCGTTTACC
109	TAAATCAAAATAATTCGCGTCTCGGAAACC
110	GCGAACCTCCAAGAACGGGTATGACAATAA
111	TTAGGATTGGCTGAGACTCCTCAATAACCGAT
112	ATCGCAAGTATGTAAATGCTGATGATAGGAAC
113	GCGGATAACCTATTATTCTGAAACAGACGATT
114	AAGGAAACATAAAGGTGGCAACATTATCACCG
115	ACCCTTCTGACCTGAAAGCGTAAGACGCTGAG
116	ATATTTTGGCTTTCATCAACATTATCCAGCCA
117	TCAAGTTTCATTAAAGGTGAATATAAAAGA
116	TCTAAAGTTTTGTCGTCTTTCCAGCCGACAA
119	TTCCAGTCGTAATCATGGTCATAAAAGGGG
120	AATACTGCCCAAAAGGAATTACGTGGCTCA
121	TTTATCAGGACAGCATCGGAACGACACCAACCTAAAACGA
122	TTGACAGGCCACCACCAGAGCCGCGATTTGTA
123	CTGTGTGATTGCGTTGCGCTCACTAGAGTTGC
124	GCGAGTAAAAATATTTAAATTGTTACAAAG
125	CGAAAGACTTTGATAAGAGGTCATATTTCGCA

126	TCATCGCCAACAAAGTACAACGGACGCCAGCA
127	TTAACACCAGCACTAACAACTAATCGTTATTA
128	TTATTACGAAGAACTGGCATGATTGCGAGAGG
129	ACAACATGCCAACGCTCAACAGTCTTCTGA
130	CATTTGAAGGCGAATTATTCATTTTTGTTTGG
131	TGAAAGGAGCAAATGAAAAATCTAGAGATAGA
132	TGGAACAACCGCCTGGCCCTGAGGCCCGCT
133	TACCGAGCTCGAATTCGGGAAACCTGTCGTGCAGCTGATT
134	GTTTATTTTGTCACAATCTTACCGAAGCCCTTTAATATCA
135	ACAAACGGAAAAGCCCCAAAAACACTGGAGCA
136	GTTTATCAATATGCGTTATACAAACCGACCGTGTGATAAA
137	ACGGCTACAAAAGGAGCCTTTAATGTGAGAAT
138	GACCAACTAATGCCACTACGAAGGGGGTAGCA
139	CTCCAACGCAGTGAGACGGGCAACCAGCTGCA
140	ACCGATTGTCGGCATTTTCGGTCATAATCA
141	CAGAAGATTAGATAATACATTTGTCGACAA
142	TGCATCTTTCCCAGTCACGACGGCCTGCAG
143	TTAGTATCACAATAGATAAGTCCACGAGCA
144	GTTTTAACTTAGTACCGCCACCCAGAGCCA
145	TTAATGAACTAGAGGATCCCCGGGGGGGTAACG
146	CTTTTACAAAATCGTCGCTATTAGCGATAG
147	ATCCCCCTATACCACATTCAACTAGAAAAATC
148	AGAAAGGAACAACTAAAGGAATTCAAAAAAA
149	AACAAGAGGGATAAAAATTTTTAGCATAAAGC
150	GCCGTCAAAAAACAGAGGTGAGGCCTATTAGT
151	TGTAGAAATCAAGATTAGTTGCTCTTACCA
152	GAGAGATAGAGCGTCTTTCCAGAGGTTTTGAA
153	CCACCCTCATTTTCAGGGATAGCAACCGTACT
154	CTTTAATGCGCGAACTGATAGCCCCACCAG
155	CCAGGGTTGCCAGTTTGAGGGGACCCGTGGGA
156	CAAATCAAGTTTTTTGGGGTCGAAACGTGGA
157	ACGCTAACACCCACAAGAATTGAAAATAGC
158	TACGTTAAAGTAATCTTGACAAGAACCGAACT
159	TAATCAGCGGATTGACCGTAATCGTAACCG
160	TTTTCACTCAAAGGGCGAAAAACCATCACC
161	GCCTTAAACCAATCAATAATCGGCACGCGCCT
162	AATAGCTATCAATAGAAAATTCAACATTCA
163	CATCAAGTAAAACGAACTAACGAGTTGAGA
164	CAGGAGGTGGGGTCAGTGCCTTGAGTCTCTGAATTTACCG
165	AAATCACCTTCCAGTAAGCGTCAGTAATAA
166	CTCGTATTAGAAATTGCGTAGATACAGTAC
167	TTTACCCCAACATGTTTTAAATTTCCATAT
168	GTCGACTTCGGCCAACGCGCGGGGTTTTTC
169	CGTAAAACAGAAATAAAAATCCTTTGCCCGAAAGATTAGA
170	AGGCTCCAGAGGCTTTGAGGACACGGGTAA
171	TTTAGGACAAATGCTTTAAACAATCAGGTC
172	AATACGTTTGAAAGAGGACAGACTGACCTT
173	CTTAGATTTAAGGCGTTAAATAAAGCCTGT
174	TAAATCGGGATTCCCAATTCTGCGATATAATG
175	AACAGTTTTGTACCAAAAACATTTTATTTC
176	CTGTAGCTTGACTATTATAGTCAGTTCATTGA
177	AACGCAAAATCGATGAACGGTACCGGTTGA

Table S2. Modified staple strands used to fold the NRO. Staple strands used for immobilization of the NRO (biotinX), the nanoswitch (nanoswitchX, DigX) and fluorescence labelling (loc_dyeATTO 542), Related to STAR Methods.

Name	Sequence (5'→3')
biotin1	biotin-CGGATTCTGACGACAGTATCGGCCGCAAGGCGATTAAGTT
biotin2	biotin-AGCCACCACTGTAGCGCGTTTTCAAGGGAGGGAAGGTAAA
biotin3	biotin-ATAAGGGAACCGGATATTCATTACGTCAGGACGTTGGGAA
biotin4	biotin-GAGAAGAGATAACCTTGCTTCTGTTCGGGAGAAACAATAA
biotin5	biotin-TAGAGAGTTATTTTCATTTGGGGATAGTAGTAGCATTA
biotin6	biotin-GAAACGATAGAAGGCTTATCCGGTCTCATCGAGAACAAGC
loc_dye ATTO 532	TAAATCATATAACCTGTTTAGCTAACCTTTAA-ATTO 532
nanoswitch1	CAAGAATAAAACGCCACTG T-ATTO 647N-TTCCCTCTTCTT GTAATAAGTTAGGCAGAGGCATTTATGATATT
nanoswitch2	CAACCGTTTCAAATCACCATCAATTCGAGCCATTCTTCTGGGAAT-BBQ650-GTCACCGCAAAATAAGAACA
Dig1	Dig-CAGTGGCGTTTTATTCTTGT
Dig2	TGTTCTTATTTTGCGGTGAC-Dig

Table S3. Unmodified staple strands used to fold the NACHOS DNA origami structure, Related to STAR Methods.

Name	Sequence (5'→3')
1	TTTAAATGTTTGCTGAGATTTAGGACCCACGCGAA
2	TTAGAACGCAATTAAGACAAATACATACATAAA
3	TTTAAGCAAATTCACAAAGTATTAAGAGGCTCGGA
4	TAAATACCCGGATATCATCAACGGTCAATCATAAGACCATCGATAC
5	GAAGGGATAGCGAGATAGTTCCGGCCAGGAAGAAGAATGAGGT
6	GCAACTGGCGAAAGGGGAGTAAAGTTGCCGGAGTGAGACCGGTCCAAAC
7	ACGAGGAGAGGCGGTTTGATGGTGGGGCCCACCCT
8	CGGTGTACAGACCAACAAAGCTAACGGAAAAAATCTACG
9	AATATCGGCACGCGCGGGCCGGAAGCATAAAAGCT
10	CAGAACAATATATCGGCCATCAAACACAGTTGAAAGGAA
11	TGAGGAAAACAGCCTGATTGCTTTGTTGC
12	GAACGCCTCCATATTATTTTA
13	AGTTCTGTCCCCCCCGAGGCGCTGGCAAGTGTTTG
14	CTTAAATCCCGGCGGTTGTG
15	AGCAATACTTCATCACGCAAATATCGCCAGTA
16	TTCATTTACCATATTGCGGAACAAAGAA
17	CTACAATTTTTTTGAAGAAAAAGCTTTAAAACAGAAATAAAGAAAAAT
18	CCTACATATCTAAAGCATCACCTCAAATTTGC
19	GGTGGCTCCAACGGCATTTCGCACTCAATCCACGCCATCCA
20	CGGAATTACCGTGTCGCAAGACAAAGAAAACAGTAAACAAAC
21	TTTCAATGATAAATTAATGC
22	GTCGAGGACCCGCCGCACCTTTTACATCCGCTGAGCAT
23	GTAATCAGAAACGAGCCTTTAGTGCCTTCTCAGAACGA
24	GCGACCCACCAAGTAGAATCATTAAAGGTGAAAATA
25	GTCTGAGCAAAAGAAGATAATGGGAAGGAG
26	TCACGCGTGGGAACAAATGTCACTGCGCGCCGCGG
27	ATTAGAGCATTTTTGCGAGCTGAAAAGGTCTA
28	TGTGATAAATTTAGCCGGAACGAGATATATTCTCA
29	TCCCGGGCGAAAGCCACCGTCTTTCCAGAGCCGAA
30	AATAAACCAGAATCTTTTCATAATCAGGA
31	CAGACCAGTTACAAAATAAAGGCTTCAGTAGGAGTATTATTAATGC
32	CGTAGGCGCATAACTGACCAACTTTGTTGCGCGATACATTGCAAAAG
33	AATAATAACCGGCGCAGAGAGTAATCTCGCCT
34	CATTATATTTTATCTTCTGACCTAAAGATGATCAATATA
35	AGGACGTTAAGAACGGTTTAATTTCAACGAGAAACCAA
36	AGGAGGCTTTAACGCCAAACGAACTGCTCAT
37	ACCACCCTTAGATGAGTGACCTGTCGTGCCAGAAT
38	GGTGATAAGAACTGGCATGATAATAACAGCCCTTTAATATC
39	CCCCTTTTCTTGTGTGAAATTGTTAAAGCACTTGT
40	CATTTAAACTCCATATAGATTCATCAGTGAACAAGAAACTCATC
41	AACAGACAATAGTTTATCCGCTGGTAAATGTGCAG
42	CGGATCGGATGTGCTGCAAGGCGATCAGTGCCAGGTGGAGCC
43	CCGAGCTCGAACTTGACGAAAGGTAAGAGGCATTTATTT
44	TGGGCACTAAAAAAGAGTCTGTCCTTTGATTTCAAACTTAC
45	GAGTCAACTAATTTAGGCAAGTAATCCTGAACAGA
46	AGAGTTCGTAAAGCTGATCTCATAAGGATTGACTGCCAGTTTGAGGCAG
47	TACGCGGGATACGAGGGCAACGGAATTATACCAAG
48	ATCCTTTGCAACAGGAAAAACGCT
49	GAAGGTATTATCACCCAGCAAAATCACCTTACCATTAGC
50	TTGCAAAGACAAAAGGGAATGAAATAGCAAGCAGCACC
51	GCAAGACTGGATAGCGTGAATCCCCTGTATGCGC
52	AGCACCCTCAAATCCTCCAGGAAGGGTCATTCCTTTAATTGTACAGGTG
53	TTTGCGTATTGACAATTCCACACAAAATTGGG
54	AAACGGACGACGTCGGTGACGCAACAGCGAGTATAGTTATTTTGATGGGG
55	ATATAATACACGTACTACACCAGCTAACACCATTCACCAGTCACA
56	TATTTTAACCTCAAAAGCTGCATTGCCTGGGGTGCCTAAATCCTTAGAC
57	AAAGGAAGCTTGATGTTGAAACCTG
58	GTCAGACCTCAAGAGAAGGAT
59	TTATCAGCTTGCTTACACTAT
60	AAAAATTAAAGCCTATTATTCTGAAGTTGATAGATTGCAAACCCTC

61	TTTGCGGGCCTCTGTGGTGCT
62	CACCGGAATCATTTCAAAATTATTT
63	TAAAGGAAGCTCTGGAACTGCGAACGAGTAGGCATAAACTGTAATGTCA
64	GAGCGTCCACTACCTCCGTAATTTTAGTTACAAAATCGCCGT
65	TACCAGAATCAAGTTTGCCTTATTTAAAAACTAATAAGACCGCCATGC
66	GCAGCAGAGGTCGTCGCAATTGCG
67	TGAGATCGGCTATAATATACCGACAGGGAAAGAGCGAAAGGAGCGGCAGT
68	CTTGGTAACGCCAGGGTACGACGTGGAT
69	CGCGCAGTATATTCGACAATGAATATACAGTA
70	AAGAGGTAGTACCTTGAGAAAGGCCGGACAATGCCATAGTAG
71	TGCACGACAATTGCGAATGCCCCCTCGGCTGGCCA
72	GCTTTGAGGACTAATACGAAGAAAACGAAAGAGGCCCCAGCGGATT
73	ATATAAAATTCATATGGTTTATTACCGAGGAA
74	GCAGTTGGTAAAAAGGCGGCCGCGTGGTGGGTGGTAGCAGGCTGCA
75	GTCCTTTCATGCATGTCCCAGTAAAGTGCCCGTATAAAAGGAGGTAATC
76	ACATTACAAAGGATTAAGGTGCCGTCGAGAGGACATGAAACAA
77	TAGTACTAAAGTACGGTGCCGAAAGATTTTTGATTGTAATTTTGTTGGGT
78	AGTGAATTTTCCTCAAACCCTCAGAGCCACCGAACCCACAC
79	TTATTCGGTCGGGTATTAGCCGTTTTTTCGATTTA
80	TCATCGTAACATTCCAAGAACATAGCCCCCT
81	GCCGCTACCACCACTGCCGTATCCGCTCGGCGCCAGCTGGTC
82	ACAGTGCTTTACCGAACGAACTGGTTGCTAGCGGTAAC
83	TGCCCGCTTTCCAGGTGTTGTTC
84	ATAGAGCCGCACTCCAAGTC
85	GCGGTCAGTATAGAAGATTAGCCCTTAAAGGGATTTTAG
86	GGGGTTTATATCGCATATGCATTGACCATTAGATA
87	ATTCTAGCGATGTGTAAAAATGAATCGGCCAAAAA
88	AAGTTTTGACGCTCAAATCCGGTATTCTAATAA
89	TACTGTGTCGAAATCCGCAAAGTATAGCAAC
90	TATTAAATCATACAAAATCATAGCGTCAAATTAT
91	CACGGGGGTAATAGTAAAACAGTTAGACGTTAGCCCTCAACAACCCAG
92	GACACGTAGATCCTTATTACG
93	ACCAACATGGCGCGTAACGATCTTACAACATTTTG
94	TTAAAGAGATCTATGACCGCTAAATCGGTTGTCCC
95	AAAAGAATTTCTTAAACATTACGAGACCAAAA
96	CCTAGTTTCCTTTCACCACTTGTAGCAGCACCGACAGTATCGGCCTACCG
97	CTGTCATACCGGCCCTGGCCCTGAGAAGA
98	AACTGTAAAACGACGGCTAAGTTGCGC
99	AAAGTCTTTCCTTATAAGAGTGTACACAGACAGTAAATGAG
100	GCAAACCACGGTTTTGTCACAATCAAAAGTAACCG
101	CATTGAAGACAGTTCATGAGGAAGTTGGGTAAATAC
102	AATTGTTTCATTCCATATTCAAAAAGCTATCAATTG
103	AGAGAGAAATAACAAGCGTTTGCCATAAGTA
104	TCAATGCTCAGTACCAGGGAGACTCGATTGGCCCA
105	ACCTTATGCGATTTTGGGAAGACAACATTAA
106	TAGTATCAAATTCTTACAGGCGTTTTAGCGAAACG
107	AGCGGGAGCTAAACAGGAGTTTTTACAATAGATTT
108	ACGGAGCCGTTAATCAGTGAGGCCTTG
109	TTTGACCGCCAGGAAAGCTAATCAGAGCAAACAAA
110	AGGAAGCGCAGCGATCCCGTGCCGCCGGAACGTAAACGATGCTGATACG
111	AGGACGTCAGACTGTAGC
112	ACTGTATCACCGTACTCCAGTTAACTGAATTCCGCCACTACGTGAAAATC
113	GAAAATTCGCAGGCGCTCAGATGCCGGGTTAATCTCCAAAGAGAACCTG
114	TCGCCGGCTGGAGGTTTCTTTGCTCACTTTTGGGTAGCTACT
115	CGACACGCCAAATTACCGCGCCCAAAATCCAAGCC
116	CAGAGCGGGGTCATTGCGTCTGGCCGGTTGAGCAGTCTTGCCCCC
117	TCCCATGCGTTCTTTGCCGATTTTCAGGTTTACGG
118	TAAAAGGAATGGCTATTAGTCGAACTGAAAAA
119	TCAGTGAGAATCAAATCAGATATAGAACAGCCCTCAGAGTACCGTTAATC
120	CTATGAGTAATGTGTAGAAAAGGGTTAA
121	AGACCGGCAAACGCGGTCCGTTTT
122	GGACAAATCACCTCAATATGAAAATTTGACGCTCA
123	TTTGACCAAAAGAAATACGTAATGCCACAGACTTTCATC
124	AAAAATAGGAGCCGGGCTCAGCAAATCGTTAAAAGGAGGCC

125	AATCAAGAATTGAGTTAAATAGCATTTTTTGTTATCCCTAGCAAGCGCC
126	GAATTGCCAGAATTCAACTATTACACCCAAATACCAGAACGAGTAG
127	GTTGCGTCGGATTCTCGTAGCATTCCTCGTAA
128	AGCCAACGTGGCACCAGAATCTTACCAACGCTACC
129	GCCACGAAACGTTCGCCACGTGCATCCGTAATGGGATAGGGCC
130	ATCCTGAAAACAAACCTTTTTTAATGGACGCGAGAGGTTTGA
131	TGCCTATAATAGGTATTATAGGATAAAAGCATAGTAAGAGCATCGA
132	ATCAAGATTGTTTGTATTCCTGATTATCATTTAATAAACTTT
133	CAAGGGGCAACTCATGGTCATAGCTAAGGGAGAGA
134	ACCGAGGCTGGCTGACCTTTCATTAGGTAGAAACCAGTC
135	GAGAACAAGCAAAACCAAATCAATATTTCGTCACTACAAGGATTTT
136	TTTGGACATTCTGGCCAATTGGCAGGCCTGCA
137	TGTACGGAGGGAAGTGAGCGCTTTAAGAATAGAAAAGAAACGCAAA
138	TACGTATCATGACTTGCGGGAGGTATCCTGAACCACCACTTGATATAT
139	ACGGAACGTCATTTAGTGATGAAGGCATAAAACTGGTGCCCCGGAA
140	GCAGCAACAATATCGAAGAACAGTAATAACATCACACC
141	GAGGGAATCCTGAGAAGTGGCCGATAAAACATATT
142	AAAACCGCCACCCTCAGATTTTAACGATACAGTCACCGGGATA
143	GTTTACCAGACGACTCAGAAGAGTCTGGAAAAGCCCAAA
144	AGACAATCGCCATTAAAAAAGAATCAGCAGA
145	TAGCGAGTCTTTACTCGATGATGTACCCCTTCCTGCTG
146	ATAACGGTAATTTTCACACCGATAGAAAGAG
147	TTCAAATTGAATTAATTAATT
148	GTACGAACGTTATTAATCTGTTTACTTTTTAATTAAAGCGA
149	TGTGCGGTTGCGGTATGCTCA
150	AGGCTTGCCCTGACTTTAATC
151	TGCTTCTGTAAACGAATTA
152	ATCTAGCCAGCAGCATCCCAGCGGTGCCGGTAATAATTTCGTAAA
153	AAGTTTGACCATAACAAAGTTTTGTCGAAGGAATGACAACAGGA
154	GGACGTCACCCGGTCGCAGTTTCATGTGCACGTTT
155	AATCAAATTAGTACCGCCACCGAGTAACGCGTCATCCGGAACCGCGCCTAAC
156	CGGAGAGCGGGAGAAATAAAGCCTCAGAATT
157	ACAGTGCGACTTTACAAACAAAAGCCAAGTCAATACTATCATTTCC
158	TACATCAAACTGAAAAAGAGACGCATACCAGTCGG
159	CGTGTGAATTATTAAGAGGGAGAAACAATAAACGTCAGACTCG
160	ACTAAATGGGCTTGAGATTGGCT
161	TGAGCAAAGCGTAAGTATAGCCCGGTTCGGAACCAGAATCCCTCAGAAAC
162	TCACAGAGAGTAACCCAAGCTATCCCAGCGCACGGAAATTGCAAC
163	ATACAGAACCCTTCTGACGTCTGAAAGAGCCA
164	GATAAAATCAGAGCCGGGACATCCCTTACACTAAA
165	CGCCAGCCAGAAAGCGTACTGAGTATGGTGCT
166	ATCCATGTAATAGATTAAGCACGTATAACGTGCGCTAGTTT
167	CATAACAGTTGATTACTCGGT
168	AACAAAATCGGCACGCTGCGCGTAACAGGGCGTTT
169	TGAAAGCCCAAAAGAAACCGACATTAGGGAGG
170	CCAGAGCGCCATACAGCGCCATGTTGATTCAGAAGCTAACAG
171	TTCCTCGCACGCTGATGGATTATTTACACAGAGATGTGGCAC
172	CTTAGCATCAGACGATCCACAACTATCTTTCCCAG
173	TACGCCAATTTAGAGCTTAATCTCACCCACCATAAGAAA
174	TATTTGCCGTTGCACATCTGCCCTTCACCGGTGTA
175	ACCATCGATAGGCCGGAAATTAGAGCGTCACCGACT
176	TTTAGAACCCTCATATATTTTAAATGGACAGTCGGTCAGG
177	TAGCATTTTGGGGCGCGGATGGCTTAGATCCAACA
178	AGCAAACGCTTAATAGCTATATTTTCATAACATCCAATA
179	TAATTACTAGCCTTAAATCAAGATTTTGCACAGCATTGGAGGCAG
180	TGATCGGGAAAGCTAACTCACATTTATTAATGCTTAGGTTG
181	GAAAGGAAGGGAAGAACCGGCGATCCCCGGCCGTGAGAGCCTCCGTCACGT
182	GAAGGTTATCTAAAAT
183	AAGGCCGCTTTTTGCG
184	CACCCTGAACAAGCCG
185	CTCGTCGCTGGCCCTCCTCCGTGCCTTAATTTAGAAACCAGTAC

Table S4. Modified staple strands used to fold NACHOS DNA nanostructure. For immobilization on a surface via biotin-neutravidin interaction staple strands biotinX were used. The nanoswitch strands (nanoswitch X) and Dig strands (DigX) were used to build the nanoswitch. For NP binding Np1-Np6 and Np1-Np12 were used for the NACHOS structure containing one or two AgNPs, respectively. Related to STAR Methods.

Name	Sequence (5'→3')
biotin1	biotin-AGAATATAAAGTCCCATCCGTTCTTCGGGG
biotin2	biotin-AGTTACCAGAAGGAAAGCAGATAAGTCAGAGGGTAA TCGCA
biotin3	biotin-ACAACTTTCAACTGAGGCTATGT
biotin4	biotin-AGGGCGATCGGTGCGGTGCGCAACCGGAAACAATC GGCGGG
biotin5	biotin-TTCATCGGCATTGACGGGACCAATAGACCCTCAATT CATTCCAA
biotin6	biotin-TAGATGGGCGCATCGTAACTTCAGGCGCCT
loc_dye ATTO 542	TTTGTGATCTCACGTAAATTTCTGCTCA-ATTO 542
nanoswitch1	CAAGAATAAAACGCCACTGT-ATTO 647N-TTCCCTCTTCTT GGAACAAGACGCCGCCCCAG
nanoswitch2	TAATCACTGTTGCCCTGATTAAATACGTTAATATTCTTCTGGGAAT -BBQ650- GTCACCGCAAAATAAGAACA
Dig1	Dig-CAGTGGCGTTTTATTCTTGT
Dig2	TGTTCTTATTTTGCGGTGAC-Dig
Np1	CATTTCGTCAACATGTTTTAAGTTTTAATTCGAGAAAAAAAAAAAAAAAAAAA
Np2	GGTTATATAACTATATGTGAATAAAAAAAAAAAAAAAAAAAAAA
Np3	AATCATACAGCCTGTTTTGCTGAATATAATGCGAAAAAAAAAAAAAAAAAAAA
Np4	AATATAATCCAATGATAAATAAGGCGTTAAAAAAAAAAAAAAAAAAAAAA
Np5	AAATCACCATCAATATGATATGACCGGAAAAAAAAAAAAAAAAAAAAA
Np6	AAAAGTTTGAGTAACATTATCAAAAAAAAAAAAAAAAAAAA
Np7	ACCATCAACCGTTCTAGCCGCAAAAAAAAAAAAAAAAAAAAAA
Np8	ATAAAAATGCTGATGCAATGTGAAAAAAAAAAAAAAAAAAAA
Np9	AAAGAATTAGCAAAATTAAGCAGCCTTTAAAAAAAAAAAAAAAAAAAA
Np10	ACCACCAAAGGGTTAGAACCTCAATTACGAATAACCTAAAAAAAAAAAAAAAAAA AA
Np11	CTTCAAAGCTGTAGCCAAATGGTCAATAAGCAAGGCATAAAAATTAAAAAAAAAA AAAAAAAAAA
Np12	AATACCGATCATCAGATTATACTTCTGAATGATGACATAAATCAAAAAAAAAAAA AAAAAAA

Table S5. Temperature ramp used for folding the NACHOS DNA origami nanostructure, Related to STAR Methods.

Temperature [°C]	Time [s]
65	120
64	180
63	180
62	180
61	180
60	900
59	900
58	1800
57	2700
56	3600
55	4500
54	5400
53	5400
52	5400
51	5400
50	5400
49	5400
48	5400
47	5400
46	5400
45	5400
44	3600
43	3600
42	2700
41	1800
39	1800
38	900
37	480
36	480
35	480
34	480
33	480
32	480
31	480
30	480
29	120
28	120
27	120
26	120
25	120
20	120

Table S6. Protocol for NP salting procedure. PBS3300 was added every 3 minutes until a final concentration of 750 mM was reached. Related to STAR Methods.

Step	PBS3300 [µL]
1	10
2	10
3	20
4	20
5	20
6	20
7	50
8	50
9	50
10	50
11	100
12	100
13	100

Table S7. Comparison of the nanoswitch-based single-antibody detection assay with three previously reported single-molecule antibody detection assays, Related to STAR Methods.

Characteristics	**Single-antibody detection assay**			
	DNA origami nanoantenna approach	**Atomic force microscopy approach (Li et al., 2002)**	**Enzyme-linked immunosorbent assay(Rissin et al., 2010)**	**Monomeric nanopore approach(Fahie et al., 2015)**
Sensitivity	Low pM – low nM range	Tested only in μM range	< 10 fM	nM range
Complexity and cost of setup used to detect the antibody	Can be combined with low-cost point-of-care devices	Low-throughput and expensive analytical technique	High-throughput but rather complex analytical technique	Could potentially be combined with low-cost point-of-care devices
Multiplexing capability	High due to separation of signal recognition and signal transduction unit	Low due to low-throughput of analytical technique	High	High
Assay time	20 min	30 min	Total 6 h	> 10 min
Complexity of the assay	Single-step detection	Single-step binding and single-washing step	Multiple-steps (wash- and reagent addition steps)	Single-step detection
Challenges for possible clinical applications	Scaling up the synthesis of NACHOS	Low-throughput	Assay time Complexity of setup	Signal-to-noise ratio

6.5.2 PUBLICATION P2

Engineering modular and tunable single molecule sensors by decoupling sensing from signal output

by

Lennart Grabenhorst[1], **Martina Pfeiffer[1]**, Thea Schinkel, Mirjam Kümmerlin, Jasmin Maglic, Florian Selbach, Gereon Andreas Brüggenthies, Alexander Thomas Murr, Philip Tinnefeld[*] and Viktorija Glembockyte[*]
([1] These authors contributed equally, [*] Correspondence)

Preprint available on BioRxiv

DOI: 10.1101/2023.11.06.56579

Author contributions:
The initial idea of the modular and tunable biosensor was proposed by Viktorija Glembockyte and Philip Tinnefeld. I, Viktorija Glembockyte and Lennart Grabenhorst further conceptualized it. Viktorija Glembockyte and Lennart Grabenhorst designed the biosensor platform, optimized the FRET contrast and developed the methods to tune the selectivity and sensitivity with the help of Thea Schinkel, Alexander Thomas Murr and Thea Schinkel. Florian Selbach and Gereon Andreas Brüggenthies performed TEM measurements. I designed, measured and analyzed antibody, nuclease detection, multiplexed detection assays. I wrote parts of the manuscript.

Engineering Modular and Tunable Single Molecule Sensors by Decoupling Sensing from Signal Output

Lennart Grabenhorst [1†], Martina Pfeiffer[1†], Thea Schinkel [1], Mirjam Kümmerlin [1], Jasmin B. Maglic [1], Gereon A. Brüggenthies [1], Florian Selbach [1], Alexander T. Murr[1], Philip Tinnefeld [1*], and Viktorija Glembockyte [1*]

[1]Department of Chemistry and Center for NanoScience, Ludwig-Maximilians-Universtität München, Butenandtstr. 5-13, 81377 München, Germany
[†]These authors contributed equally.
[*]Correspondence should be addressed to P.T. (philip.tinnefeld@cup.uni-muenchen.de) and V.G. (viktorija.glembockyte@cup.uni-muenchen.de)

Abstract: Biosensors play key roles in medical research and diagnostics, but there currently is a lack of sensing platforms that combine easy adaptation to new targets, strategies to tune the response window to relevant analyte concentration ranges and allow for the incorporation of multiple sensing elements to benefit from multivalency. Utilizing a DNA origami nanostructure as a scaffold for arranging the different sensor components, we here propose an approach for the development of modular and tunable single-molecule sensors capable of detecting a variety of biomolecular targets such as nucleic acids, antibodies and restriction enzymes while offering mechanisms to tune the dynamic window, the specificity and the cooperativity of the sensor.

Fluorescent sensors are our gateway to a deeper understanding of cellular processes [1–4] and diseases [5–7]. A typical biosensor consists of two functional units: a biorecognition element capable of sensing an analyte or biological activity and a signal transduction element translating it into measurable readout. For virtually every biomolecular target of interest to medical research or diagnostics, it is possible to find a molecule (e.g., antibody, receptor, or aptamer) that binds to it with high specificity and sensitivity. Given that the conformational change upon target binding is often very small, one of the key challenges in transforming these binders into useful fluorescence sensors lies in achieving a measurable fluorescence signal (e.g., change in fluorescence intensity or Fluorescence Resonance Energy Transfer (FRET) between donor and acceptor labels) upon binding. This challenge has been addressed by a number of elegant modular strategies which generalize and simplify the development of new biosensors, for example, by engineering superstructures that elicit large conformational changes upon target binding with the help of semi-synthetic protein chimeras [8–13], chemically induced dimerization [14, 15], de novo protein design [15, 16] or by using conditionally stable ligand-binding domains [17, 18].

A second fundamental challenge in developing new sensors lies in tailoring their response window to the analyte concentration of interest. Binding of a ligand to a single-site recognition element produces a hyperbolic dose-response curve with a fixed response window spanning roughly two orders of magnitude. This limits the utility of the sensor in applications that require either great sensitivity (sharp signal response) or quantification of target molecules in a concentration window that varies or spans several orders of magnitude [19]. Mimicking nature's tricks to overcome this challenge, mechanisms of allosteric control [20–23], sequestration [24], and cooperativity [25–29] have been implemented in synthetic sensor and signaling systems. While these approaches have demonstrated impressive tuning capabilities in aptamer-based sensors enabling measurement of target concentrations across orders of magnitude [22] or narrowing of the response window to as little as 3-fold, they lack the modularity required for straightforward extension to arbitrary analytes. Possible ways to shift the response window of the sensor (e.g., by introducing a mutation in the binding site [11, 14, 15, 17] or changes to the scaffolding structure [8, 9, 16]) have also been outlined in modular sensing platforms, yet, most of these approaches rely on single-site binding and cannot harness additional tuning and design advantages available to multivalent sensors (e.g., cooperativity or multiplexing).

Strategies to simultaneously decouple sensing from signal transduction, tune the response window of the sensor and combine multiple sensing elements are of great interest, as they would allow independent tuning of sensor

properties and thus greatly increase the speed at which new sensors can be developed. However, a global sensor approach that addresses all these challenges in one platform has yet to be realized. To lay out fundamental strategies that could combine all these requirements, in this work we harnessed the nanoscale arranging capabilities and modularity of DNA origami nanostructures. Using a dynamic nanostructure to assemble different sensor elements, we obtained almost digital FRET signal readout with single-molecule sensitivity, outlined strategies to tune the response and specificity of a sensor as well as developed multiplexed sensors capable of more complex sensing operations.

Engineering of a spatially decoupled signal transduction element

To decouple sensing from signal output and build a sensor platform with a high optical contrast, we utilized a well-studied dynamic hinge-like DNA origami nanostructure capable of undergoing large conformational changes [30–32]. It consists of two ca. 65-nm long arms connected by a single-stranded scaffold DNA region (Fig. 1A). In absence of additional interactions, the two arms of the structure fluctuate around an equilibrium angle of ca. 90° (Fig. 1B, upper panel). However, by introducing complementary DNA-DNA interactions between the two arms of the structure it can be folded and purified in a closed conformation, in which both arms are almost parallel to each other (Fig. 1B, lower panel). In the model sensing platform, closing interactions are designed with a single-stranded toehold overhang allowing for toehold-mediated opening of the structure by addition of complementary single-stranded (ss) DNA "opening" strands. At the same time, a short toehold overhang is left upon binding the opening strand, allowing for the displaced closing strand to in turn displace the opening strand and reclose the structure, thereby mimicking a reversible receptor-ligand interaction (Figs. 1A, S1, S2, and S16).

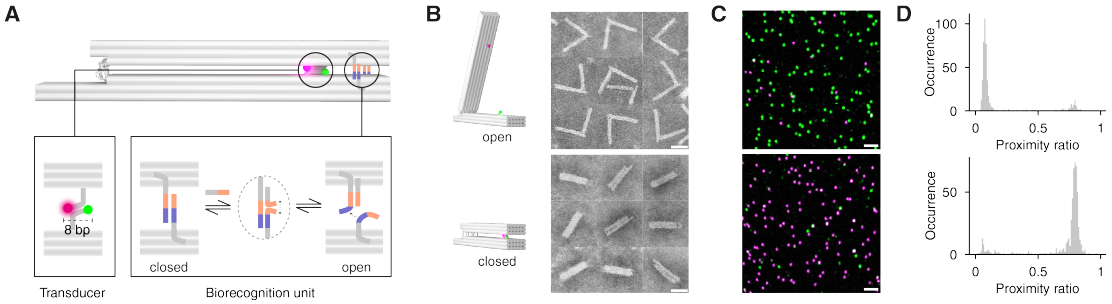

Figure 1: Design of the modular biosensor platform. **(A)** DNA origami nanostructure used to arrange and decouple sensing from signal output. The signal transduction element consists of a donor (ATTO542) and an acceptor (ATTO647N) dye forming a FRET pair (bottom left) brought together in the orientation required for high FRET in the closed state by weak 8 base pair (bp) DNA hybridization. In the model sensor platform, the biorecognition element is mimicked by a reversible closing interaction based on toehold-mediated DNA strand displacement reaction(s) (bottom right). **(B)** Snapshots from transmission electron micrographs of the sensors in each of the conformations (scale bar: 40 nm, for full micrographs see Fig. S3). **(C)** Confocal microscopy scans of surface immobilized biosensors in the open (top) and closed (bottom) conformation (scale bar: 2 µm). **(D)** Corresponding spot wise PR histograms illustrating the high FRET contrast between closed and open states of the sensor.

The signal transduction element consists of bright and photostable donor (ATTO542) and acceptor (ATTO647N) fluorophores positioned on the opposing arms of the hinge forming a FRET pair (Fig. 1A, lower left). We studied different sensor designs at the single-molecule level by incorporating biotinylated ssDNA strands protruding at the bottom of one of the arms, immobilizing the structures on BSA-biotin/Neutravidin coated coverslips and performing single-molecule confocal scans. The extent of FRET in different sensor designs was characterized by calculating the proximity ratio (PR, defined as $I_{Red}/(I_{Red} + I_{Green})$) for each nanosensor. The signal transduction element was engineered to minimize the effect of the flexibility of the nanostructure and the impact of changes in ionic strength on the PR distributions (Fig. S4, oxDNA [33] simulations in Videos S1-S2). To this end, two complementary ssDNAs protruding from each of the arms were used to define the orientation of the two dyes, leading to a narrow distribution of high FRET values ($\langle PR_{closed} \rangle$ ca. 0.77, Fig. 1D, top). Upon addition of sufficient ssDNA target, the sensor can be opened and the large conformational change results in negligible FRET ($\langle PR_{open} \rangle$ ca. 0.08, Fig. 1D, bottom). This high FRET contrast allowed for the unambiguous assignment of the two conformational states and enabled the detailed characterization of the sensor response.

Tuning the response window of the biosensor

A universal sensor platform would allow to readily assemble new sensors from a large pool of already existing receptor-ligand interactions. This calls for strategies to tune both, onset, and sharpness, of the sensor response to enable monitoring relevant concentration changes of target molecules without the need to re-engineer these interactions. In natural receptor-ligand systems, this is commonly achieved by hierarchical assembly of multiple binding units or allosteric modulation of the binding interaction [34]. We laid out and tested several strategies inspired by naturally occurring mechanisms to tune the signal response of our sensor platform without altering the biorecognition interaction itself. The high signal contrast between open and closed conformations enabled us to read out the equilibrium distributions with high precision and thus conduct single-molecule titration experiments with the ligand in our model sensor platform being the opening ssDNA target (Fig. 2A). By quantifying the fraction of open sensors (PR<0.3, Fig. 2B) at each target concentration and fitting the resulting binding curve with the Hill equation, we could characterize the biosensor properties in terms of overall affinity $K_{1/2}$ which represents the target concentration where half of the structures are opened, and the Hill coefficient n_H, which is a measure of the cooperativity of a system (Fig. 2B).

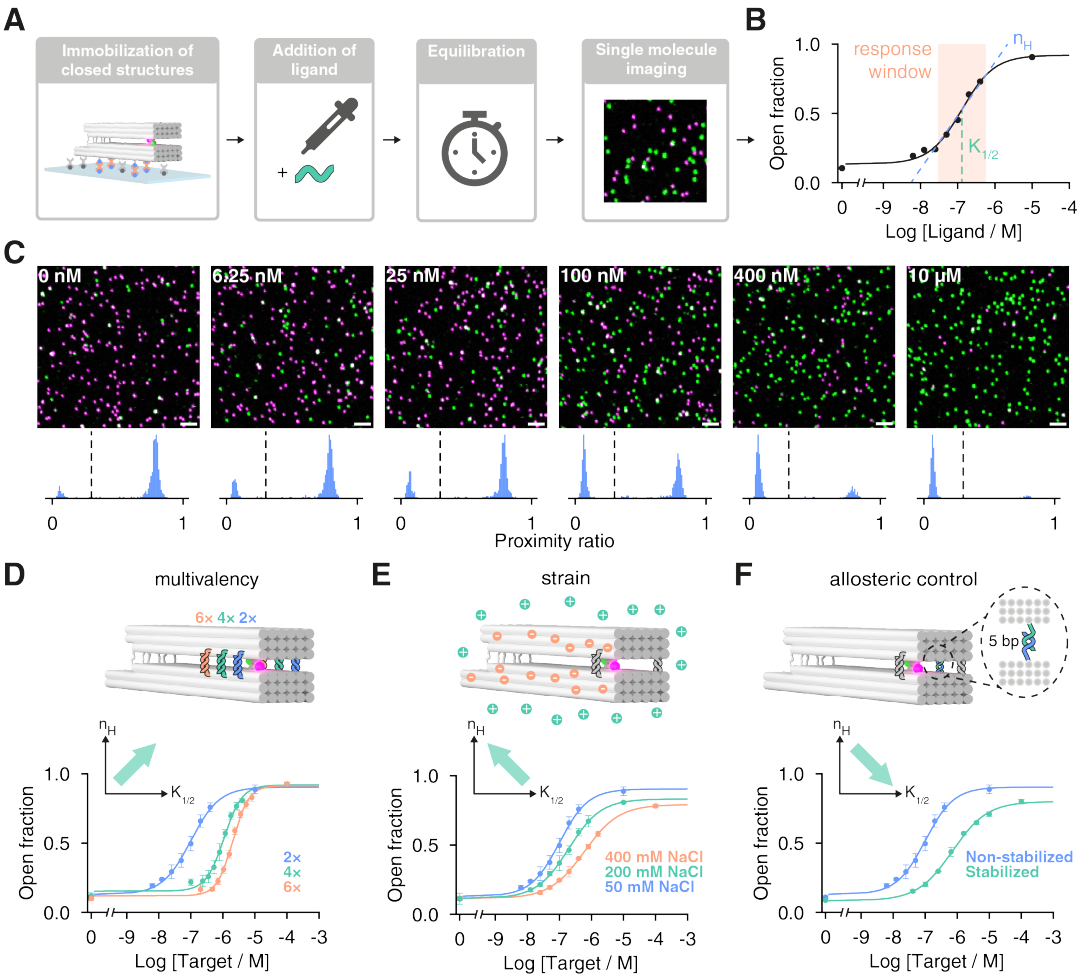

Figure 2: Studying and tuning the response window of the sensors on the single molecule level. **(A)** Workflow to investigate the response window of different sensor designs: sensors are immobilized via Biotin-NeutrAvidin interactions. For each target concentration, one surface is prepared, and a defined concentration of target is added. After equilibration, confocal scans are acquired, and the fraction of closed structures is determined by analyzing on average 681 single nanosensors for each concentration. **(B)** The response window, i.e. the overall affinity of the sensor ($K_{1/2}$) and the extent of cooperativity (n_H) are determined by fitting the titration curve with the Hill equation. **(C)** Example confocal fluorescence scans for different target concentrations with respective PR histograms shown below (scale bar: 2 µm, dashed line represents the PR threshold used to assign sensors as open). **(D)** Increasing the number of sensing elements shifts the $K_{1/2}$ of the sensor to higher values and increases the cooperativity. **(E)** Decreasing the ionic strength increases the coulombic repulsion and destabilizes the closed state of the sensor, leading to lower $K_{1/2}$ and higher n_H. **(F)** Introducing additional DNA-DNA stabilization interactions stabilizes the closed state of the sensor and leads to an increase of $K_{1/2}$ and a decrease of n_H. Titration curves show mean values of three independent measurements with the error bars corresponding to the standard deviation

Inspired by naturally occurring multivalent systems, we rationalized that increasing the number of closing interactions will stabilize the closed state and shift the response window range of the sensor to higher concentrations. Thus, we investigated the effect of the number of biorecognition elements on the overall signal response. As expected, going from two to four sensing elements led to an almost 10-fold increase in $K_{1/2}$ (from 100±10 nM to 1.09±0.09 μM, respectively) and adding two more closing interactions further doubled $K_{1/2}$ to 2.03±0.10 μM (Fig. 2D). Additionally, multivalency also induced cooperative behavior to our system: going from two to four interactions, n_H increased from 0.98±0.08 to 1.55±0.15, respectively, while in the sensor with six interactions, we achieved a cooperativity of 1.73±0.13. We propose that this cooperativity is a result of strain in the closed state of the sensor acting on all interactions induced by coulombic repulsion (i.e., opening of one interaction increases the force acting on the remaining ones). Altogether, increasing the number of sensing elements in these multivalent sensors provided a strategy to sharpen the signal response (narrowing the response window from ≈80-fold to ≈12-fold) due to arising cooperativity.

To introduce an orthogonal tuning strategy, we set out to alter the force that the backbone structure exerts on the closing interactions. We reasoned that, as shown in earlier studies [31, 32], this can be achieved by decreasing the ionic strength which leads to increased coulombic repulsion. We characterized the properties of the sensor containing two closing interactions while varying the ionic strength (i.e., decreasing NaCl concentration, Fig. 2E). As expected, decreasing ionic strength from 400 mM NaCl to 50 mM NaCl led to an earlier response, shifting $K_{1/2}$ by 6-fold from 601±20 nM to 100±10 nM, which we attributed to destabilization of the closed state of the sensor. Interestingly, the cooperativity was also sensitive to the ionic strength: we obtained n_H values of 0.81±0.02, 0.87±0.04, 0.98±0.08 in the presence of 400 mM, 200 mM, and 50 mM NaCl, respectively (Fig. 2D). This result is in line with our earlier assumption that cooperativity increases with coulombic repulsion. The negative cooperativity obtained at higher ionic strengths, however, highlights the existence of a competing cooperative process. Here, multiple closing interactions facilitate the reclosing (consistent with a slightly lower fraction of completely open sensors), in turn, providing means to extend the response window of the sensor. Overall, the destabilization of the closed sensor provided a mechanism to increase the cooperativity and shift the sensor opening window to lower concentrations providing an orthogonal direction in the n_H vs. $K_{1/2}$ space (insets in Fig. 2D and 2E).

Finally, by including additional ssDNA strands that hybridize to each other in the closed conformation we demonstrated the possibility to achieve allosteric modulation in our sensor platform. Introduction of two transient (5 bp) DNA-DNA interactions on the inside of the two arms of the structure led to a 7-fold increase of $K_{1/2}$ from 100±10 nM to 705±65 nM (Fig. 2F) illustrating the sensitivity of this platform to small alterations. Varying the strength of these stabilizing interactions would allow to fine-tune the overall affinity of the sensor. Analogous to what was observed at increasing ionic strengths (Fig. 2E), the stabilization of the closed state via this strategy has led to a decrease in n_H from 0.98±0.08 to 0.8±0.05 consistent with facilitated reclosing. Altogether, the three illustrated approaches present strategies to tune the onset ($K_{1/2}$) and sharpness (n_H) of the sensor without altering the sensing interaction itself with strategies that are orthogonal to each other (insets in Figs. 2D-F) and can be combined to cover an extended $K_{1/2}$ and n_H parameter space.

Harnessing multivalency for increased target specificity

One of the key properties sought after when developing biosensors is the ability to detect the target analyte specifically in a large pool of other similar biomolecules. As such, we investigated whether we could utilize multiple sensing elements to improve the specificity of the nanosensor platform. We rationalized that increasing the number of sensing elements would amplify the overall energetic difference of opening the sensor by two energetically similar targets. To confirm this, we first studied the opening of a nanosensor containing four DNA-DNA closing interactions in the presence of 17-nt perfectly matching DNA target as well as targets containing one (C-C mismatch, ΔΔG from the perfectly matched target of 5.4 kcal/mol as estimated by NUPACK [35], Fig. S5) and two (C-C + T-T mismatch, ΔΔG ≈6.2 kcal/mol) nucleotide mismatches (green and orange in Fig. 3A). When exposed to perfectly matched target the nanosensor opened at nanomolar concentrations, whereas in the presence of targets containing one and two nucleotide mismatches no opening was observed even at 10 μM (Fig. 3B) illustrating the ability of our sensor to specifically detect the perfectly matched target even in ≈1000-fold excess of similar off-targets.

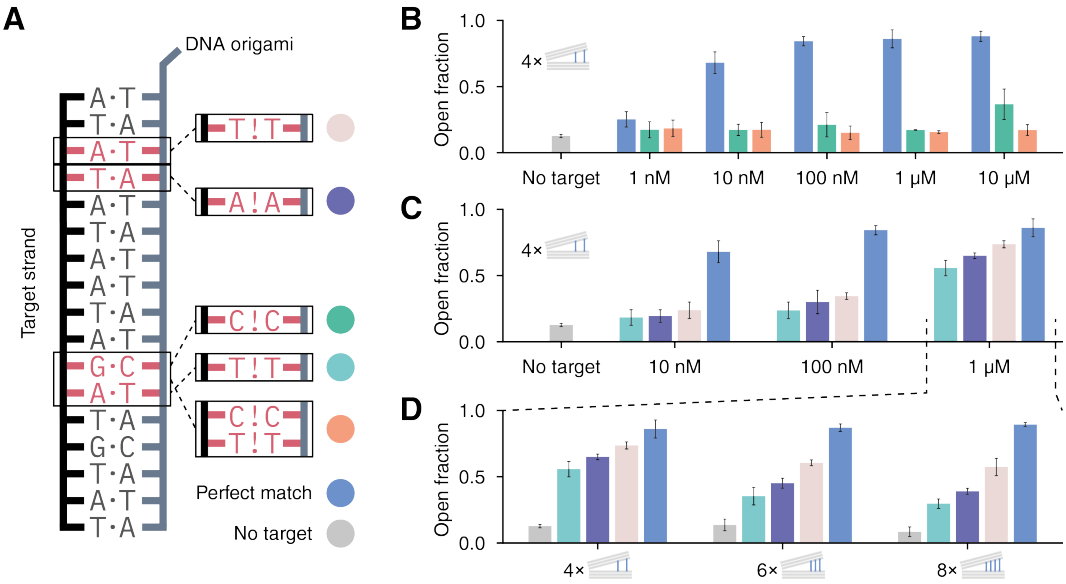

Figure 3: Harnessing sensor multivalency for increased target specificity. **(A)** Schematic of the model receptor-ligand opening interaction (left). For testing specificity of different sensor designs, we included mismatches into the opening interaction (right), mimicking a ligand (off-target) with similar binding strength. **(B)** Comparing the perfectly matched opening interaction (blue) to an interaction with one (green) and two (orange) single nucleotide mismatches shows drastic differences in sensor response: while perfectly matched target (blue) opens the sensor at nanomolar concentrations, both mismatched targets exhibit almost no response up to 10 μM concentration. **(C)** Increasing the number of closing interactions from 4 to 8 increases the capabilities of the sensor to differentiate these targets from the perfect match as illustrated with the sensor opening measured in the presence of 1 μM target concentrations. Plots show the mean values of three independent measurements with the error bars corresponding to the standard deviation. Examples for all confocal fluorescence scans can be found in Fig. S6.

Exploring this potential further, we investigated whether we could differentiate off-targets with even smaller ΔΔGs (2.3 — 3.6 kcal/mol (Fig. S5), A-A and T-T mismatches) when compared to the perfect match (beige, purple, and cyan in Fig. 3A). By incubating the nanosensor containing four closing interactions with different targets, we could show that at up to 100 nM target concentration it is possible to clearly differentiate the energetically similar off-targets by both comparing the equilibrium fraction of open nanosensors (Fig. 3C) or by monitoring the nanosensor opening kinetics (Fig. S7). Nonetheless, as the concentration of the target strands is further increased to 1 μM (Fig. 3C) this differentiation becomes more difficult. While the specificity of the nanosensor at micromolar concentrations of targets may be less relevant for detection of nucleic acids, we deemed that it is still crucial for the utility of the modular sensing platform, where the desired response of the sensor lies at higher concentrations (e.g., continuous sensing of metabolites). Therefore, we conducted additional studies with nanosensors containing 6 and 8 closing interactions to demonstrate that one could harness the multivalency to further improve the specificity when desired. As shown in Fig. 3D, increasing the multivalency of the sensor increased the differences in opening fraction when compared to the perfect match. With the nanosensor containing 8 closing interactions, we were able to differentiate between two off-targets with single T-T and A-A nucleotide mismatches (beige and purple in Fig. 3A, respectively) that have an estimated difference in binding energy as little as 0.51 kcal/mol (less than 1 k_BT, Fig. S5).

Extension to other biomolecular targets and incorporation of logic sensing operations

We next demonstrated that the large optical signal contrast developed in our model sensing platform (Figs. 1-2) can indeed be swiftly and modularly adapted to build sensors for other biomolecular targets without the need to re-engineer and optimize the signal transduction element. A single molecule nanosensor for anti-Digoxigenin (anti-Dig) antibodies was engineered by incorporating two specific Dig antigen biorecognition elements on each sensor arm (Fig. 4A). To facilitate the binding of the antibodies and to meet the required geometry for bivalent binding [36] the nanosensor was initially kept in the closed (high FRET) state via DNA-DNA interactions. After surface immobilization and excess antibody incubation (100 nM), DNA opening staples were added which resulted in ≈85% sensors still in the closed state (Fig. 4A, upper panel and Fig. 4B) suggesting that the sensor

is held in the closed state by the bivalent binding of the antibody. In absence of the antibody, on the other hand, the nanosensors opened almost quantitatively (Fig. 4A, lower panel and Fig. 4B). As illustrated in corresponding single-molecule fluorescence scans (Fig. 4A) and PR histograms (Fig. 4B) the near digital signal contrast optimized for the model sensor is still preserved for this antibody nanosensor. Additionally, we also evaluated the specificity (Figs. S8 and S9) as well as the potential of this antibody sensor to be useful in more complex biological fluids by performing the antibody assay described above in 50% blood plasma (Fig. 4C and Fig. S10). The obtained percentages of open sensors measured in blood plasma were within experimental error when compared to those measured in buffer, confirming that neither stability of the DNA origami nanosensor nor the performance of the antibody binding assay were compromised. Additionally, we also evaluated the sensitive concentration range of the anti-Dig antibody assay under clinically relevant conditions (20 min incubation) to show that the antibody concentration at which the signal change is half the maximum signal change ($C_{half-max}$) lies at 104 pM, which is in accordance to previously reported values [37] and in a concentration range relevant for diagnostic applications [38] (Fig. S11).

Next, we studied whether the sensor platform can also be utilized for the detection of enzymatic activities. Usually, optical enzyme cleavage sensors (e.g., for protease or nuclease activity assays) are designed by placing two labels (donor and acceptor or donor and quencher) close to the substrate binding site in a manner that leads to loss of FRET or turn-on of fluorescence signal upon substrate cleavage. In designing such sensors, one is faced with the inherent conflict between placing the labels close enough to the cleavage site to achieve high optical contrast but far enough not to influence the enzyme-substrate binding which results in many rounds of optimization and often suboptimal signal contrast. This challenge can be globally addressed by the sensor scheme proposed here where target recognition is decoupled and spatially separated from the transduction element. To illustrate this, we designed a single molecule activity sensor for the nuclease XhoI: without the need to re-engineer the transduction element, we simply incorporated the 6 bp restriction sites for XhoI in the DNA-DNA closing interactions (Fig. 4D). In the presence of enzymatically active XhoI, the closing interactions are cleaved leading to an opening of the DNA origami sensor and a loss of FRET (Figs. 4E and S12). In contrast, no opening is observed if the nanosensors are closed with DNA-DNA interactions containing no XhoI cleavage sites, confirming the desired specificity (Figs. 4E, 4F, and S13). One of the main advantages using DNA origami as a building platform is the ability to modularly exchange and combine different recognition elements on one sensor platform to achieve multiplexed detection of more than one analyte as well as to engineer logic sensing operations. To illustrate this, we designed a sensor capable of detecting two different (anti-Dig and anti-DNP) antibodies (Fig. 4G) that acts as a molecular OR gate. Two different antigens (Dig and DNP) were incorporated on the opposing arms of the nanosensor closed via DNA-DNA interactions. Upon addition of DNA opening strands the nanosensor opens when neither of the antibodies are present and stays closed if either or both antibodies are present (Fig. 4I). Fig. 4H and Fig. S14 illustrate that the high FRET contrast is still preserved despite a more complex sensing scheme. In fact, as illustrated in Fig. 4J, the multiplexed sensing is not restricted to the same type of biorecognition elements: by incorporating the XhoI restriction site and another DNA-DNA closing interaction we could build a logic AND gate for two different biomolecular targets: one based on a binding event, and one based on a cleavage reaction. Here we could show that the sensor only opens when both, XhoI and DNA targets, are present (Figs. 4K, L, and Fig. S15). Altogether, the modularity the DNA origami offers to incorporate different biorecognition elements, combined with the preserved robust FRET readout opens many possibilities to engineer new biosensors as well as logical sensing schemes for answering more complex diagnostic questions.

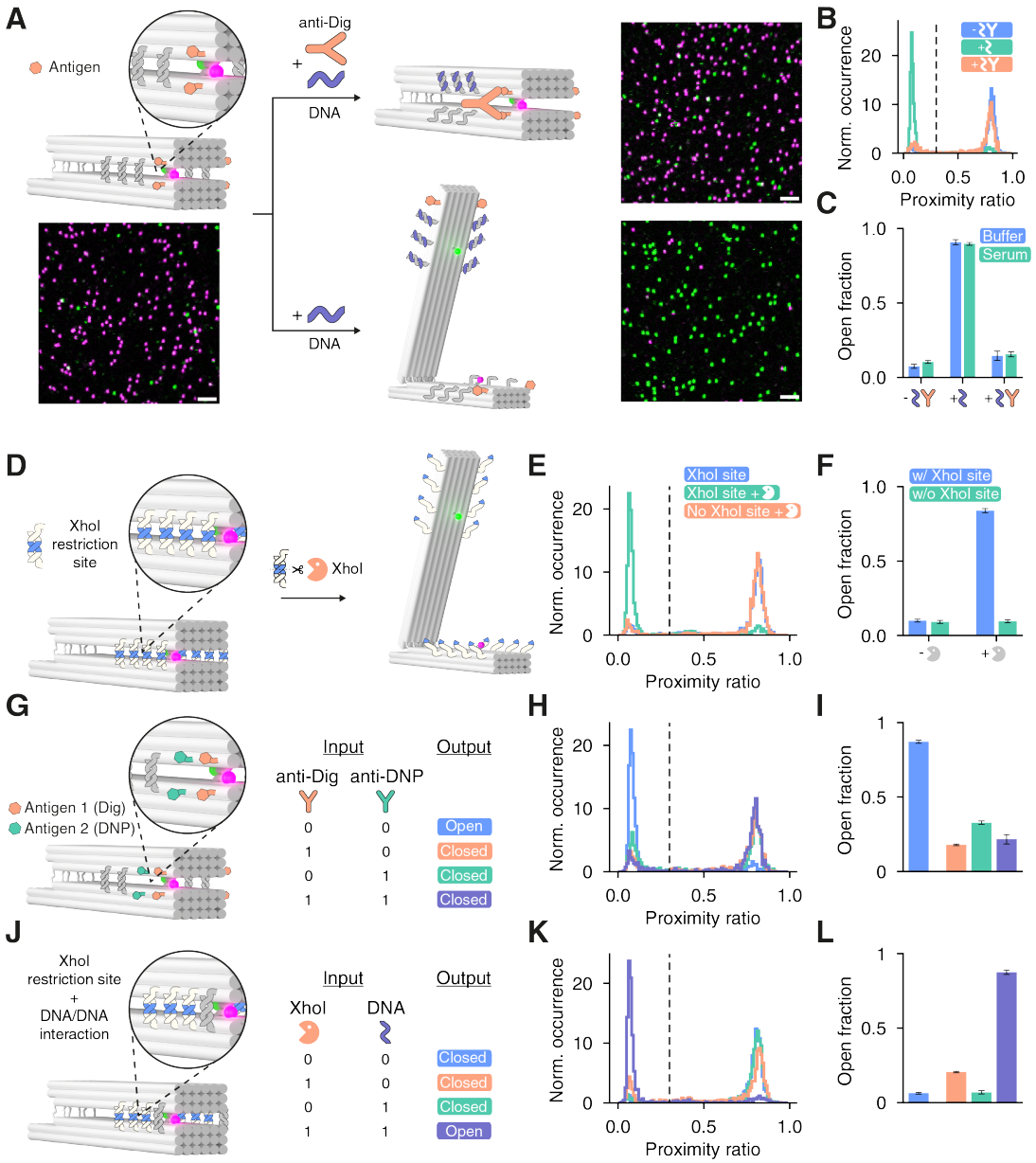

Figure 4: Extension of the sensor platform to different molecular targets and introduction of logic sensing operations. **(A)** Detection of antibodies by incorporation of antigen recognition elements (Dig) on the opposing arms of nanosensor kept in the closed state via DNA-DNA interactions. Upon addition of DNA opening strands the nanosensor stays closed in the presence and opens in the absence of anti-Dig antibodies. The high signal contrast is illustrated by confocal microscopy scans (scale bar: 2 µm). **(B)** Spot-wise PR histograms obtained for the antibody sensor in the absence (blue) and in the presence of DNA opening strands (cyan) as well as in the presence of DNA opening strands and 100 nM anti-Dig antibody (orange). **(C)** Corresponding fraction of open antibody nanosensors obtained in buffer as well as blood plasma. **(D)** Detection of enzymatic activity by incorporation of nuclease-specific restriction site in the DNA-DNA closing interaction. **(E)** Spot wise PR histograms obtained for nanosensors containing the XhoI restriction site in the absence (green) and presence (blue) of XhoI. No opening was observed for nanosensors without the specific restriction site in the presence of XhoI (orange). **(F)** Corresponding fraction of open nuclease nanosensors with and without restriction site. **(G)** Multiplexed detection of two different antibodies (anti-Dig and anti-DNP) via a molecular OR gate is achieved via the incorporation of two different antigens (Dig and DNP) on the opposing arms of the closed nanosensor. Upon addition of DNA opening strands the nanosensor stays closed if either or both antibodies are present. **(H)** Spot wise PR histograms for antibody nanosensor inputs shown in (G). **(I)** Corresponding fraction of open nanosensors for different antibody nanosensor inputs. **(J)** Multiplexed detection of two different biomolecular targets (nucleic acid and restriction enzyme) via a logic AND gate can be achieved by incorporation of the restriction site and another DNA-DNA closing interaction. The nanosensor opens only in the presence of both, nucleic acid, and restriction enzyme targets. **(K)** Corresponding spot wise PR histograms obtained for different molecular inputs of shown in (J). **(L)** Corresponding fraction of open nanosensors for different nanosensor inputs. Bar plots show the mean values of three independent measurements (each include at least 423 single nanosensors) with the error bars corresponding to the standard deviation.

One of the main advantages using DNA origami as a building platform is the ability to modularly exchange and combine different recognition elements on one sensor platform to achieve multiplexed detection of more than one analyte as well as to engineer logic sensing operations. To illustrate this, we designed a sensor capable of detecting two different (anti-Dig and anti-DNP) antibodies (Figure 4G) that acts as molecular OR gate. Two different antigens (Dig and DNP) were incorporated on the opposing arms of the nanosensor closed via DNA-DNA interactions. Upon addition of DNA opening strands the nanosensor opens when neither of the antibodies are present and stays closed if either or both antibodies are present (Figure 4I). Figure 4H and Figure S14 illustrate that the high FRET contrast is still preserved despite a more complex recognition scheme. In fact, as illustrated in Figure 4J, the multiplexed sensing is not restricted to the same type of biorecognition elements: by incorporating the XhoI restriction site and another DNA-DNA closing interaction we could build a logic AND gate for two different biomolecular targets. Here we could show that the sensor only opens when both, XhoI and DNA targets, are present (Figure 4K, L, and Figure S15). Altogether, the modularity the DNA origami offers to incorporate different biorecognition elements, combined with the preserved robust FRET readout opens many possibilities to engineer new biosensors as well as logical sensing schemes for answering more complex diagnostic questions.

Discussion

General and modular strategies to assemble sensors have the potential to vastly speed up the development of new diagnostic tools for health and disease research. Here, we have developed a generalizable approach to create DNA origami-based synthetic sensing systems with high optical signal contrast and single-molecule sensitivity. We harnessed the modularity of DNA origami nanostructures to: 1) modularly assemble all the elements of the sensor, 2) spatially decouple the biorecognition and signal transduction domains, 3) provide a large conformational change required for large FRET contrast, 4) tune the sensor response by (de)stabilization of the scaffolding structure, 5) engineer multivalent sensors which enabled improved specificity, multiplexing, logic sensing, and additional tuning capabilities via cooperativity.

Optical single molecule sensors allow to detect and monitor target analytes with ultimate sensitivity and unprecedented spatial resolution. However, achieving a large FRET contrast in single-molecule DNA origami sensors so far has been challenging: low FRET contrast and broad FRET distributions often require averaging over few hundreds of single molecules to differentiate between the two states of the sensor [39–42]. Here, we combined two different tricks to tackle this: a large conformational change and an additional transient guiding interaction to control the placement of the dyes in the FRET pair – which led to narrow FRET distributions and allowed the clear differentiation of the two sensor states on the single molecule level. In practice, the modularity and the ability to immobilize the sensors on the surface in a specific orientation [43] would make this approach readily extendable to other readout mechanisms, such as electrochemical readout [44], fluorescence quenching (e.g., by a graphene surface [45, 46]), or bioluminescence energy transfer [9, 11, 17] as well pave the way towards highly multiplexed sensor chips.

Tuning of the response window of new sensors without altering the sensing element itself, in turn, allows to modularly exploit the existing and, thanks to protein design, rapidly growing space of small molecule binders. Here, we presented orthogonal strategies to offer generalizable ways to cover a broad range of n_H as well as $K_{1/2}$ values for sensors based on reversible target-ligand binding, either through cooperativity, allosteric control or altered stability of the DNA nanostructure. The ability to achieve cooperativity in synthetic sensor systems thus far has been a challenging task and is limited to a handful examples [28]. Additionally, it often comes at the price of reduced affinity [27]. Therefore, orthogonal tuning mechanisms, such as the ones outlined here are of particular interest and provide a promising strategy to modularly engineer cooperativity in synthetic sensors. Given the vast number of parameters one can possibly alter in the platform reported here, there are several additional parameters one could explore to shift the sensor response (e.g., positioning of sensor elements, equilibrium opening angle, or even the DNA origami structure itself). Further investigation of all these factors that influence and maximize the degree of cooperativity would not only be of interest for the development of new biosensors but also for building cooperative nanoscale actuators. Moreover, as shown in this work, the ability to incorporate multiple sensing elements in one platform provides the added benefit of increased target specificity.

The DNA origami approach allowed us to swap out biorecognition elements without affecting the high FRET contrast, illustrating the truly modular nature of this platform. We could not only create biosensors for different

biological targets, but also combine them to achieve logical and multiplexed sensing schemes, something that so far has not been possible in modular protein-based sensor platforms. One exciting avenue to explore going forward would be the utilization of de novo designed binding proteins [15, 16] as sensing elements, combining the many possibilities of protein design with a high-contrast single molecule readout. One of the challenges that would have to be addressed, however, is the stability of DNA origami-based sensors. Here we showed that the sensor is still functional in 50% blood plasma, but further studies will be needed to fully assess the stability of the sensors in complex chemical environments or live cells. Recent progress on stabilization strategies for DNA origami structures [47–49] offers many options that can be tested to achieve maximal performance. Altogether, the modularity, tunability, and sensitivity of the platform should enable the rapid development of tailored and complex sensors for a wide range of analytes, and highlights many of the advantages the DNA origami approach offers to tackle these problems.

References

1. Abdelfattah, A. S. *et al.* Bright and photostable chemigenetic indicators for extended in vivo voltage imaging. *Science* **365,** 699–704. doi:10.1126/science.aav6416 (2019).
2. Chen, Y.-N., Cartwright, H. N. & Ho, C.-H. In vivo visualization of nitrate dynamics using a genetically encoded fluorescent biosensor. *Sci. Adv.* **8,** eabq4915. doi:10.1126/sciadv.abq4915 (2022).
3. Cambronne, X. A. *et al.* Biosensor reveals multiple sources for mitochondrial NAD(+). *Science* **352,** 1474–7. doi:10.1126/science.aad5168 (2016).
4. Xue, L. *et al.* Probing coenzyme A homeostasis with semisynthetic biosensors. *Nat. Chem. Biol.* **19,** 346–355. doi:10.1038/s41589-022-01172-7 (2023).
5. Olsen, R. H. J. *et al.* TRUPATH, an open-source biosensor platform for interrogating the GPCR transducerome. *Nat. Chem. Biol.* **16,** 841–849. doi:10.1038/s41589-020-0535-8 (2020).
6. Marvin, J. S. *et al.* A genetically encoded fluorescent sensor for in vivo imaging of GABA. *Nat. Methods* **16,** 763–770. doi:10.1038/s41592-019-0471-2 (2019).
7. Ino, D., Tanaka, Y., Hibino, H. & Nishiyama, M. A fluorescent sensor for real-time measurement of extracellular oxytocin dynamics in the brain. *Nat. Methods* **19,** 1286–1294. doi:10.1038/s41592-022-01597-x (2022).
8. Brun, M. A., Tan, K.-T., Nakata, E., Hinner, M. J. & Johnsson, K. Semisynthetic Fluorescent Sensor Proteins Based on Self-Labeling Protein Tags. *J. Am. Chem. Soc.* **131,** 5873–5884. doi:10.1021/ja900149e (2009).
9. Griss, R. *et al.* Bioluminescent sensor proteins for point-of-care therapeutic drug monitoring. *Nat. Chem. Biol.* **10,** 598–603. doi:10.1038/nchembio.1554 (2014).
10. Xue, L., Prifti, E. & Johnsson, K. A General Strategy for the Semisynthesis of Ratiometric Fluorescent Sensor Proteins with Increased Dynamic Range. *J. Am. Chem. Soc.* **138,** 5258–5261. doi:10.1021/jacs.6b03034 (2016).
11. Yu, Q. *et al.* Semisynthetic sensor proteins enable metabolic assays at the point of care. *Science* **361,** 1122–1126. doi:10.1126/science.aat7992 (2018).
12. Vecchia, M. D. *et al.* Spectrally Tunable Forster Resonance Energy Transfer-Based Biosensors Using Organic Dye Grafting. *ACS Sens.* **7,** 2920–2927. doi:10.1021/acssensors.2c00066 (2022).
13. Hellweg, L. *et al.* A general method for the development of multicolor biosensors with large dynamic ranges. *Nat. Chem. Biol.* **19,** 1147–1157. doi:10.1038/s41589-023-01350-1 (2023).
14. Beltran, J. *et al.* Rapid biosensor development using plant hormone receptors as reprogrammable scaffolds. *Nat. Biotechnol.* **40,** 1855–1861. doi:10.1038/s41587-022-01364-5 (2022).
15. Glasgow, A. A. *et al.* Computational design of a modular protein sense-response system. *Science* **366,** 1024–1028. doi:10.1126/science.aax8780 (2019).
16. Quijano-Rubio, A. *et al.* De novo design of modular and tunable protein biosensors. *Nature* **591,** 482–487. doi:10.1038/s41586-021-03258-z (2021).
17. Feng, J. *et al.* A general strategy to construct small molecule biosensors in eukaryotes. *eLife* **4,** e10606. doi:10.7554/eLife.10606 (2015).
18. Tucker, C. L. & Fields, S. A yeast sensor of ligand binding. *Nat. Biotechnol.* **19,** 1042–1046. doi:10.1038/nbt1101-1042 (2001).
19. Ricci, F., Vallée-Bélisle, A., Simon, A. J., Porchetta, A. & Plaxco, K. W. Using Nature's "Tricks" To Rationally Tune the Binding Properties of Biomolecular Receptors. *Acc. Chem. Res.* **49,** 1884–1892. doi:10.1021/acs.accounts.6b00276 (2016).

20. Choi, B. *et al.* Artificial allosteric control of maltose binding protein. *Phys. Rev. Lett.* **94,** 038103. doi:10.1103/PhysRevLett.94.038103 (2005).

21. Vallée-Bélisle, A., Ricci, F. & Plaxco, K. W. Engineering Biosensors with Extended, Narrowed, or Arbitrarily Edited Dynamic Range. *J. Am. Chem. Soc.* **134,** 2876–2879. doi:10.1021/ja209850j (2012).

22. Porchetta, A., Vallee-Belisle, A., Plaxco, K. W. & Ricci, F. Using distal-site mutations and allosteric inhibition to tune, extend, and narrow the useful dynamic range of aptamer-based sensors. *J. Am. Chem. Soc.* **134,** 20601–4. doi:10.1021/ja310585e (2012).

23. Hariri, A. A. *et al.* Continuous optical detection of small-molecule analytes in complex biomatrices. *bioRxiv.* doi:10.1101/2023.03.03.531030 (2023).

24. Chamorro-Garcia, A. *et al.* The sequestration mechanism as a generalizable approach to improve the sensitivity of biosensors and bioassays. *Chem. Sci.* **13,** 12219–12228. doi:10.1039/D2SC03901J (2022).

25. Dueber, J. E., Mirsky, E. A. & Lim, W. A. Engineering synthetic signaling proteins with ultrasensitive input/output control. *Nat. Biotechnol.* **25,** 660–2. doi:10.1038/nbt1308 (2007).

26. Simon, A. J., Vallee-Belisle, A., Ricci, F. & Plaxco, K. W. Intrinsic disorder as a generalizable strategy for the rational design of highly responsive, allosterically cooperative receptors. *Proc. Natl. Acad. Sci. U.S.A.* **111,** 15048–53. doi:10.1073/pnas.1410796111 (2014).

27. Ortega, G. *et al.* Rational design to control the trade-off between receptor affinity and cooperativity. *Proc. Natl. Acad. Sci. U.S.A.* **117,** 19136–19140. doi:10.1073/pnas.2006254117 (2020).

28. Ortega, G., Chamorro-Garcia, A., Ricci, F. & Plaxco, K. W. On the Rational Design of Cooperative Receptors. *Annu. Rev. Biophys.* **52,** 319–337. doi:10.1146/annurev-biophys-091222-082247 (2023).

29. Simon, A. J., Vallée-Bélisle, A., Ricci, F., Watkins, H. M. & Plaxco, K. W. Using the Population-Shift Mechanism to Rationally Introduce "Hill-type" Cooperativity into a Normally Non-Cooperative Receptor. *Angew. Chem. Int. Ed.* **53,** 9471–9475. doi:10.1002/anie.201403777 (2014).

30. Marras, A. E., Zhou, L., Su, H. J. & Castro, C. E. Programmable motion of DNA origami mechanisms. *Proc. Natl. Acad. Sci. U.S.A.* **112,** 713–8. doi:10.1073/pnas.1408869112 (2015).

31. Marras, A. E. *et al.* Cation-Activated Avidity for Rapid Reconfiguration of DNA Nanodevices. *ACS Nano* **12,** 9484–9494. doi:10.1021/acsnano.8b04817 (2018).

32. Shi, Z. & Arya, G. Free energy landscape of salt-actuated reconfigurable DNA nanodevices. *Nucleic Acids Res.* **48,** 548–560. doi:10.1093/nar/gkz1137 (2020).

33. Sulc, P. *et al.* Sequence-dependent thermodynamics of a coarse-grained DNA model. *J. Chem. Phys.* **137,** 135101. doi:10.1063/1.4754132 (2012).

34. Smock, R. G. & Gierasch, L. M. Sending signals dynamically. *Science* **324,** 198–203. doi:10.1126/science.1169377 (2009).

35. Zadeh, J. N. *et al.* NUPACK: Analysis and design of nucleic acid systems. *J. Comput. Chem.* **32,** 170–3. doi:10.1002/jcc.21596 (2011).

36. Shaw, A. *et al.* Binding to nanopatterned antigens is dominated by the spatial tolerance of antibodies. *Nat. Nanotechnol.* **14,** 184–190. doi:10.1038/s41565-018-0336-3 (2019).

37. Pfeiffer, M. *et al.* Single antibody detection in a DNA origami nanoantenna. *iScience* **24,** 103072. doi:10.1016/j.isci.2021.103072 (2021).

38. Iyer, A. S. *et al.* Persistence and decay of human antibody responses to the receptor binding domain of SARS-CoV-2 spike protein in COVID-19 patients. *Sci. Immunol.* **5,** eabe0367. doi:10.1126/sciimmunol.abe0367 (2020).

39. Selnihhin, D., Sparvath, S. M., Preus, S., Birkedal, V. & Andersen, E. S. Multifluorophore DNA Origami Beacon as a Biosensing Platform. *ACS Nano* **12,** 5699–5708. doi:10.1021/acsnano.8b01510 (2018).

40. Ochmann, S. E. *et al.* DNA Origami Voltage Sensors for Transmembrane Potentials with Single-Molecule Sensitivity. *Nano Lett.* **21,** 8634–8641. doi:10.1021/acs.nanolett.1c02584 (2021).

41. Büber, E. *et al.* DNA Origami Curvature Sensors for Nanoparticle and Vesicle Size Determination with Single-Molecule FRET Readout. *ACS Nano* **17,** 3088–3097. doi:10.1021/acsnano.2c11981 (2023).

42. Domljanovic, I. *et al.* DNA origami book biosensor for multiplex detection of cancer-associated nucleic acids. *Nanoscale* **14,** 15432–15441. doi:10.1039/d2nr03985k (2022).

43. Gopinath, A. *et al.* Absolute and arbitrary orientation of single-molecule shapes. *Science* **371,** eabd6179. doi:10.1126/science.abd6179 (2021).

44. Williamson, P., Ijas, H., Shen, B., Corrigan, D. K. & Linko, V. Probing the Conformational States of a pH-Sensitive DNA Origami Zipper via Label-Free Electrochemical Methods. *Langmuir* **37,** 7801–7809. doi:10.1021/acs.langmuir.1c01110 (2021).

45. Ghosh, A. *et al.* Graphene-based metal-induced energy transfer for sub-nanometre optical localization. *Nat. Photonics* **13,** 860–865. doi:10.1038/s41566-019-0510-7 (2019).

46. Kaminska, I. *et al.* Graphene Energy Transfer for Single-Molecule Biophysics, Biosensing, and Super-Resolution Microscopy. *Adv. Mater.* **33,** e2101099. doi:10.1002/adma.202101099 (2021).

47. Chandrasekaran, A. R. Nuclease resistance of DNA nanostructures. *Nat. Rev. Chem.* **5,** 225–239. doi:10.1038/s41570-021-00251-y (2021).

48. Scheckenbach, M., Schubert, T., Forthmann, C., Glembockyte, V. & Tinnefeld, P. Self-Regeneration and Self-Healing in DNA Origami Nanostructures. *Angew. Chem. Int. Ed.* **60,** 4931–4938. doi:10.1002/anie.202012986 (2021).

49. Wassermann, L. M., Scheckenbach, M., Baptist, A. V., Glembockyte, V. & Heuer-Jungemann, A. Full Site-Specific Addressability in DNA Origami-Templated Silica Nanostructures. *Adv. Mater.* **35,** e2212024. doi:10.1002/adma.202212024 (2023).

Acknowledgements

We thank Prof. T. Liedl and Prof. J. Rädler for providing access to transmission electron microscopy facilities and the members of the Tinnefeld lab for discussion and feedback, especially Dr. F. Steiner. We also thank Michael Scheckenbach for initial AFM measurements.

Funding

This work was supported by the European Union's Horizon 2020 research and innovation program under the Marie Skłodowska-Curie actions (grant agreement no. 840741, GLUCORIGAMI), the German Research Foundation (DFG, grant number GL 1079/1-1, project number 503042693 to V.G. as well as project number 201269156, SFB 1032 Project A13 and INST 86/1904-1 FUGG to P.T.) as well as the Bavarian Ministry of Science and the Arts through the ONE MUNICH Project "Munich Multiscale Biofabrication". V.G. is also grateful for the support by a Humboldt Research Fellowship from the Alexander von Humboldt Foundation. M.P. acknowledges support by Studienstiftung des deutschen Volkes.

Author contributions

V.G. and P.T. conceived the idea and directed the project. V.G., P.T., L.G. and M.P. further conceptualized the research. L.G. designed the DNA origami sensor and performed oxDNA simulations. L.G., V.G., M.K., and J.M. tested and optimized the design of the sensor and the signal transduction element. F.S. and G.A.B. performed TEM measurements. L.G. and V.G. implemented the sensor tuning strategies and carried out and analyzed single molecule titration experiments with the help of G.A.B. and A.T.M.; T.S. and V.G. designed and carried out the sensor specificity studies. M.P. carried out and analyzed antibody, nuclease detection, multiplexed detection assays. L.G. wrote the code for single-molecule data analysis. L.G. and V.G. prepared figures. V.G., L.G. and P.T. wrote the manuscript with additional input from M.P.; all authors reviewed and accepted the manuscript.

Competing interests

The authors declare no competing interests.

Data and materials availability

All experimental data supporting the findings of this work will be made available from a public repository. The custom code for the analysis of single molecule confocal scans is available online (https://gitlab.lrz.de/tinnefeldlab/cospota).

Methods

DNA origami design and synthesis

DNA origami nanostructures were designed in caDNAno [1] according to a design published by Marras et al. [2]. All staple strands were ordered at Integrated DNA Technologies, Inc., Belgium except for the fluorescently labeled strands, which were ordered at biomers.net GmbH, Germany. For detailed folding recipes and sequences, see Supplementary Text and Tables S1-S8. The folding was executed in a thermocycler using the temperature ramp as described earlier [3]. After folding, samples were subjected to agarose gel electrophoresis; we employed 1.5% w/v gels in 1×TAE buffer supplemented with 10 mM $MgCl_2$. Gels were run for at least 3 hours at 70 V. Then, gels were inspected using a gel documentation system (Fusion FX, Vilber Deutschland GmbH, Germany) where we used the red fluorescence channel to identify the bands containing closed DNA origami sensors (an example scan is shown in Fig. S16). These bands were cut using a scalpel and placed on Parafilm. Then, the gel fragments were squeezed with a small glass slide wrapped in Parafilm to extract the DNA origami nanostructures. For storage, we aliquoted the origami solution to 200 µL PCR tubes: we mixed 40 µL of origami solution with 8 µL of 5 M NaCl solution to minimize degradation. Two slightly different versions of the nanosensors were used for different applications - for details on the differences, see Tables S1-S7 and supporting text.

Coarse-grained simulations of DNA origami nanostructures

caDNAno design files were converted to oxDNA [4–6] input files using the tacoxDNA web server [7], the closing interactions were manually added in oxView [8] and the resulting structure was simulated at 20 °C, 400 mM NaCl on the oxDNA.org server [9] with the standard settings as well as the recommended relaxation procedure.

Transmision electron microscopy (TEM) measurements

TEM grids (Formvar/carbon, 400 mesh, Cu, TedPella, Inc., USA) were Ar-plasma cleaned and incubated for 2 min with DNA origami sample (5 µL, 1-5 nM). Grids were washed with 2% uranyl formate solution (5 µL) and incubated for another 4 s with 2% uranyl formate solution (5 µL) for staining. TEM imaging was performed on a JEM-1100 microscope (JEOL GmbH, Japan) with an acceleration voltage of 80 kV.

Preparation of microscopy samples

Microscope slides (24 mm × 60 mm size and 170 µm thickness (Carl Roth GmbH, Germany)) were cleaned in a UV/ozone cleaner (PSD-UV4, Novascan Technologies, USA) for 30 mins at 100 °C. Then, CoverWell perfusion chambers (Grace Bio-Labs, 0.5 mm deep) were glued on top of the slides and the glue was strengthened by heating on a hot plate for ca. 20 s at 100 °C. Then, the chambers were cleaned with 1 M KOH by incubating for 10 mins and then washing with 1× PBS four times. Surfaces were passivated by incubating with BSA-Biotin (1 mg/mL in 1× TE with 50 mM NaCl, Thermo Fisher Scientific, USA) and subsequent washing with 1× PBS buffer three times. Then, chambers were incubated with 0.25 mg/mL NeutrAvidin (Thermo Fisher Scientific, USA) in 1× PBS for 10 mins followed by final washing with 1× PBS three times. DNA origami solutions were diluted in immobilization buffer (10 mM TRIS, 10 mM $MgCl_2$, 750 mM NaCl) as required to reach the desired surface density of DNA origami sensors (50–100 pM), which was checked on the confocal microscope. When the desired density was reached, the surfaces were washed in the respective buffer that was used for the experiment.

Single-molecule confocal microscopy measurements

Home-built confocal microscope based on an Olympus IX-83 body (Japan) was used to acquire single molecule fluorescence scans. A supercontinuum white light laser pulsed at 78 MHz (SuperK Extreme, NKT Photonics, Denmark) was used to excite the samples. The excitation wavelength was selected using an acousto-optically tunable filter (SuperK Dual AOTF, NKT Photonics, Denmark) controlled by a digital controller (AODS 20160 8R, Crystal Technology, USA). If needed, a second acousto-optically tunable filter (AA.AOTF.ns:TN, AA Opto-Electronic, France) controlled with a home-written LabVIEW (National Instruments, USA) program was used to alternate between two wavelengths (532- and 639-nm). We used a neutral density filter, a linear polarizer and a $\lambda/4$ plate to achieve circularly polarized excitation light of the desired intensity. For the single-molecule confocal scans 532-nm (2 µW) excitation was used. The excitation light was sent to the sample through an oil

immersion objective (UPlanSApo 100×, NA=1.4, WD=0.12 mm, Olympus, Japan) via a dichroic beam splitter (zt532/640rpc, Chroma, USA). A piezo stage (P-517.3CL, E-501.00, Physik Instrumente GmbH&Co. KG, Germany) was used to move the sample in X-Y. The sample was kept in focus over extended periods with the help of a z-drift compensation system (IX3-zdc2-83, Olympus, Japan). The emitted light was collected with the same objective and separated from the excitation light with the same dichroic beam splitter. Then, the emission light was sent through a 50-µm pinhole, the two emission channels were split using beam splitter (640DCXR, AHF Analysetechnik AG, Germany), additionally filtered with two emission filters (RazorEdge 647, Semrock Inc., USA for the red channel and BrightLine HC 582/75, Semrock Inc., USA for the green channel) and focused onto the single photon detectors (SPCM, AQR 14, PerkinElmer, USA). A custom LabVIEW program was used for data acquisition.

Single-molecule wide-field microscopy measurements

For detection of single-molecule fluorescence transients, a commercial wide-field/TIRF microscope Nanoimager from Oxford Nanoimaging Ltd. was used. Red excitation at 638 nm was realized with a 1100 mW laser, green excitation at 532 nm with a 1000 mW laser, respectively. The relative laser intensities were set to ca. 3.5 mW for green and to ca. 1 mW for red excitation. The microscope was set to TIRF illumination. Data acquisition was initialized by time-lapsed imaging. A frame of 100 ms was recorded every second separately for both excitation lasers. Measurements were carried out at 37 °C.

Single-molecule titrations

For each DNA target concentration a separate chamber with closed nanosensors (Version 2) was prepared. Single-molecule titrations were conducted in the buffer containing 10 mM Tris and 10 mM $MgCl_2$ with varying amounts of NaCl (see Table S9 for details). Serial dilutions of the 15 bp opening strand (see Table S8) were prepared in the same buffer and each chamber was filled with the opening staple solution and closed using adhesive seal tabs (Grace Bio-Labs, USA). The samples were incubated overnight at room temperature to ensure that the thermal equilibrium has been reached even for very low (nM) target concentrations. The opening of the sensors was quantified by acquiring single-molecule fluorescence scans on the confocal microscope.

Single-molecule pulsed interleaved excitation FRET measurements in solution

For single-molecule FRET measurements of freely diffusing nanostructures (Fig. S7) we used a home-built setup based on an Olympus IX-71 inverted microscope (for a detailed description of the setup, see Ref. [10]). The slides were prepared analogously to single-molecule measurements for surface immobilized samples except the slides were not incubated with NeutrAvidin to measure freely diffusing nanosensors in solution at 500 pM–1 nM concentrations. We used pulsed interleaved excitation with a 532-nm laser at 4 µW intensity and a 640-nm laser at 5 µW excitation intensity at 40 MHz repetition rate, respectively. The data was analyzed with the PAM [11] software. All channel burst search was performed to select the single bursts and ALEX 2CDE and |TDX-TAA| filters were used the filter the selected burst data.

Single-molecule studies of target specificity

Nanosensors used for studying target specificity (Version 1) contained a shorter 11 bp closing interactions (for a full list of sequences see Table S8). For each (off) target concentration a separate chamber with closed nanosensors was prepared, filled with the solution containing the target DNA in 10 mM Tris, 1 mM EDTA, 5 mM $MgCl_2$ and 750 mM NaCl and closed using adhesive seal tabs (Grace Bio-Labs, USA). Samples were incubated overnight to ensure that thermal equilibrium was reached, and the open fraction was determined by performing single-molecule fluorescence scans on the confocal microscope.

Antibody detection assay

Nanosensors used for the detection of IgG antibodies (Version 1) were equipped with two digoxigenin (Dig) functionalities and/or two dinitrophenol (DNP) functionalities per sensor arm (see Table S7 for modified sequences). Additionally, four and six 11 bp DNA-DNA closing interactions, respectively, were incorporated to facilitate bivalent binding of the target antibody in a bridge-like manner to the opposite arms of the nanosensor

(Table S3). For each sample a separate chamber with closed nanosensors was prepared. anti-Dig antibodies (Rb monoclonal, Thermo Fisher Scientific, USA, Catalog # 700772, AB_2532342) and/or anti-DNP antibodies (Rat monoclonal, Thermo Fisher Scientific, USA Catalog # 04-8300, AB_2532964) were diluted to 100 nM in the buffer or diluted heparin blood plasma containing 10 mM Tris, 1 mM EDTA, and 750 mM NaCl. Chambers were filled with the antibody solution and incubated for 30 min. Following antibody binding, the DNA-DNA closing interactions were removed by a strand displacement mechanism upon 10 min incubation with 100 µM 17 bp DNA opening DNA strands (Table S8). The closing of the nanosensor by bivalent binding of antibodies was quantified by acquiring single-molecule fluorescence scans on the confocal microscope.

Restriction enzyme activity assay

For monitoring restriction enzyme activity, nanosensors (Version 1) were equipped with six or eight 11 bp DNA-DNA closing interactions containing a 6 bp sequence (Table S6) specific for the binding and cleavage of the restriction enzyme XhoI. For each sample a separate chamber with closed nanosensors was prepared and filled with 1×CutSmart™ buffer (New England BioLabs, USA) containing 50 mM potassium, 20 mM Tris-acetate, 10 mM magnesium acetate, and 100 µg/ml recombinant albumin. 0.5 µL of XhoI (20.000 units/mL, New England BioLabs, USA) were added and incubated for 10 min. The opening of the nanosensor by the cleavage of the DNA-DNA interactions was quantified by acquiring single-molecule fluorescence scans on the confocal microscope. For monitoring the cutting kinetics of the XhoI restriction enzyme cleavage reaction of the closing interactions, single-molecule fluorescence transients were recorded on a wide-field microscope after the addition of 0.5 µL of XhoI (20.000 units/mL, New England BioLabs, USA).

Data analysis

A python script was used to process the acquired single photon counting data which is available on GitLab `https://gitlab.lrz.de/tinnefeldlab/cospota`). Briefly, the software finds single spots using a wavelet decomposition-based approach and then calculates the spotwise PR as $PR = I_{Red}/(I_{Red} + I_{Green})$. We used the spotwise PR to distinguish between open (PR<0.3) and closed (PR>0.3) conformations. Data was plotted and fitted using Matplotlib, Scipy and Numpy. For the estimation of $K_{1/2}$ and n_H, we used the modified Hill equation:

$$\theta([T]) = \theta_{start} + (\theta_{end} - \theta_{start}) \frac{[T]^{n_H}}{K_{1/2}^{n_H} + [T]^{n_H}} \quad (1)$$

which also allowed fitting the start (θ_{start}) and end (θ_{end}) points of the titration curve given by the target concentration $[T]$ and the occupancy at each concentration $\theta([T])$. The reported errors are standard errors of the fit.

Supplemental References

1. Douglas, S. M. *et al.* Rapid prototyping of 3D DNA-origami shapes with caDNAno. *Nucleic Acids Res.* **37,** 5001–6. doi:10.1093/nar/gkp436 (2009).
2. Marras, A. E., Zhou, L., Su, H. J. & Castro, C. E. Programmable motion of DNA origami mechanisms. *Proc. Natl. Acad. Sci. U.S.A.* **112,** 713–8. doi:10.1073/pnas.1408869112 (2015).
3. Trofymchuk, K. *et al.* Addressable nanoantennas with cleared hotspots for single-molecule detection on a portable smartphone microscope. *Nat. Commun.* **12,** 950. doi:10.1038/s41467-021-21238-9 (2021).
4. Ouldridge, T. E., Louis, A. A. & Doye, J. P. Structural, mechanical, and thermodynamic properties of a coarse-grained DNA model. *J. Chem. Phys.* **134,** 085101. doi:10.1063/1.3552946 (2011).
5. Snodin, B. E. *et al.* Introducing improved structural properties and salt dependence into a coarse-grained model of DNA. *J. Chem. Phys.* **142,** 234901. doi:10.1063/1.4921957 (2015).
6. Rovigatti, L., Sulc, P., Reguly, I. Z. & Romano, F. A comparison between parallelization approaches in molecular dynamics simulations on GPUs. *J. Comput. Chem.* **36,** 1–8. doi:10.1002/jcc.23763 (2015).
7. Suma, A. *et al.* TacoxDNA: A user-friendly web server for simulations of complex DNA structures, from single strands to origami. *J. Comput. Chem.* **40,** 2586–2595. doi:10.1002/jcc.26029 (2019).

8. Poppleton, E. *et al.* Design, optimization and analysis of large DNA and RNA nanostructures through interactive visualization, editing and molecular simulation. *Nucleic Acids Research* **48,** e72–e72. doi:10.1093/nar/gkaa417 (May 2020).

9. Poppleton, E., Romero, R., Mallya, A., Rovigatti, L. & Sulc, P. OxDNA.org: a public webserver for coarse-grained simulations of DNA and RNA nanostructures. *Nucleic Acids Res.* **49,** W491–W498. doi:10.1093/nar/gkab324 (2021).

10. Schroder, T. *et al.* Shrinking gate fluorescence correlation spectroscopy yields equilibrium constants and separates photophysics from structural dynamics. *Proc. Natl. Acad. Sci. U.S.A.* **120,** e2211896120. doi:10.1073/pnas.2211896120 (2023).

11. Schrimpf, W., Barth, A., Hendrix, J. & Lamb, D. C. PAM: A Framework for Integrated Analysis of Imaging, Single-Molecule, and Ensemble Fluorescence Data. *Biophys. J.* **114,** 1518–1528. doi:10.1016/j.bpj.2018.02.035 (2018).

Supplementary Information for

Engineering Modular and Tunable Single Molecule Sensors by Decoupling Sensing from Signal Output

Lennart Grabenhorst[1]†, Martina Pfeiffer[1]†, Thea Schinkel[1], Mirjam Kümmerlin[1], Jasmin B. Maglic[1], Gereon A. Brüggenthies[1], Florian Selbach[1], Alexander T. Murr[1], Philip Tinnefeld[1]*, and Viktorija Glembockyte[1]*

[1]Department of Chemistry and Center for NanoScience, Ludwig-Maximilians-Universtität München, Butenandtstr. 5-13, 81377 München, Germany

†These authors contributed equally.

*Correspondence should be addressed to P.T. (philip.tinnefeld@cup.uni-muenchen.de) and V.G. (viktorija.glembockyte@cup.uni-muenchen.de)

Supplementary Text

Detailed DNA origami folding procedure

16 µL of unmodified staples were mixed with 4 µL of modified staples, 5 µL of FoB20 and 25 µL of p8064 scaffold (produced in-house). Modified staples consisted of the desired modified staples and the respective unmodified staples to replace the modified staples that were not desired in the respective experiment. An exemplary recipe for the modified master mix for the 2×13 sample from Fig. 2 is given below:

Red and green dye strands (2×1 µL)
Row 4 closing staples (4×1 µL)
Row 1-3 staples without closing interactions (12×1 µL)
Biotin 1-4 (4×1 µL)
Stabilization staples without stabilizing interactions (4×1 µL)

We used two slightly different versions of the DNA origami design. Version 1 was used in the experiments described in Fig. 3 and 4 in the main text, while Version 2 was used in the experiments described in Fig. 2. The staples needed for Version 1 of the sensor are described in Tables S1, S3, S5-S7 and the staples needed for Version 2 of the sensor are described in Tables S2, S4 and S5.

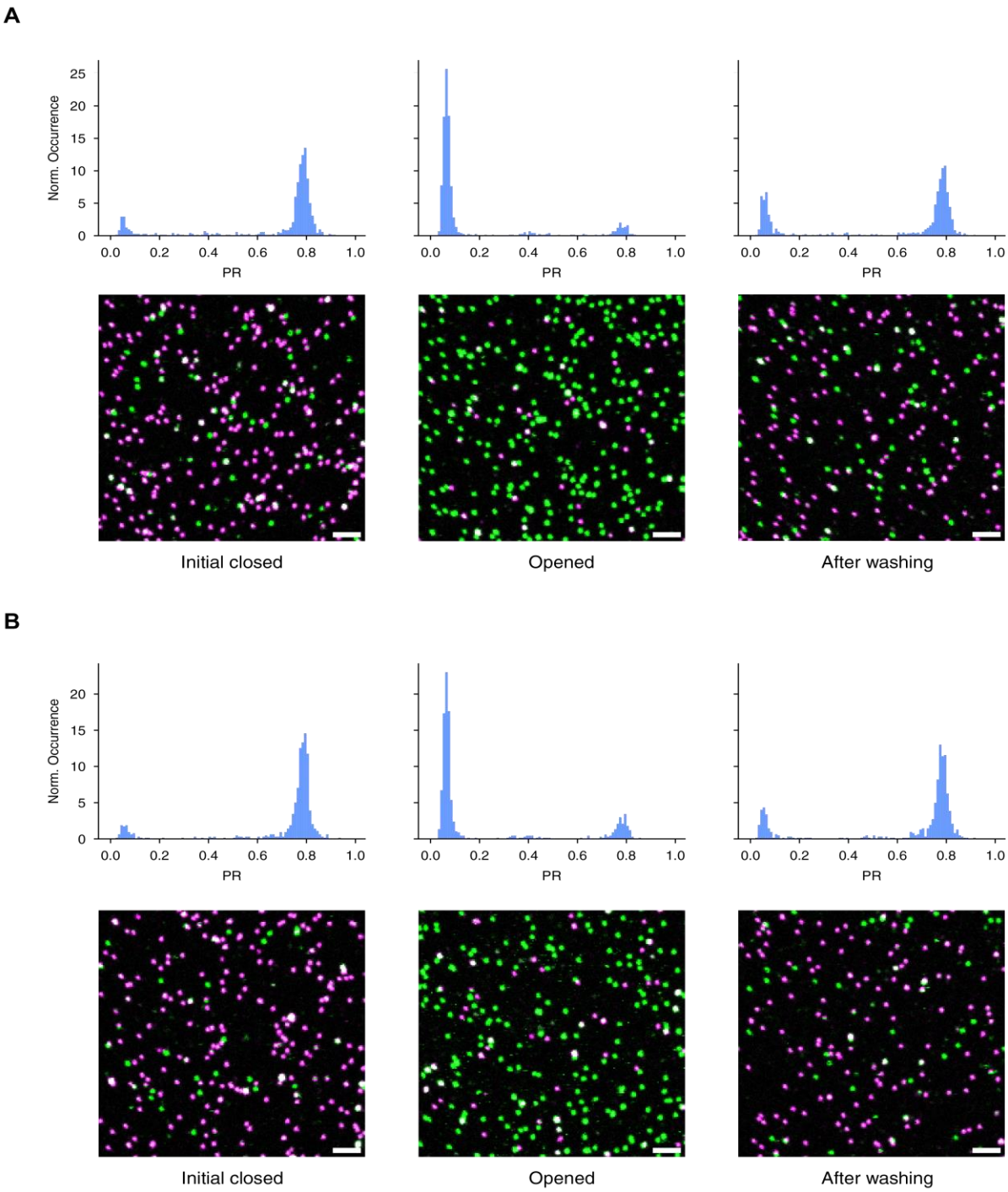

Fig. S1. Reclosing of the hinge nanostructure with two closing interactions measured in the presence of 50 mM (**A**) and 400 mM (**B**) NaCl. Samples were opened by incubating them with 100 µM opening strands for 1h. Afterwards, they were washed at least 10 times with the respective buffer and scans were taken after approximately 190 hours to allow for complete equilibration.

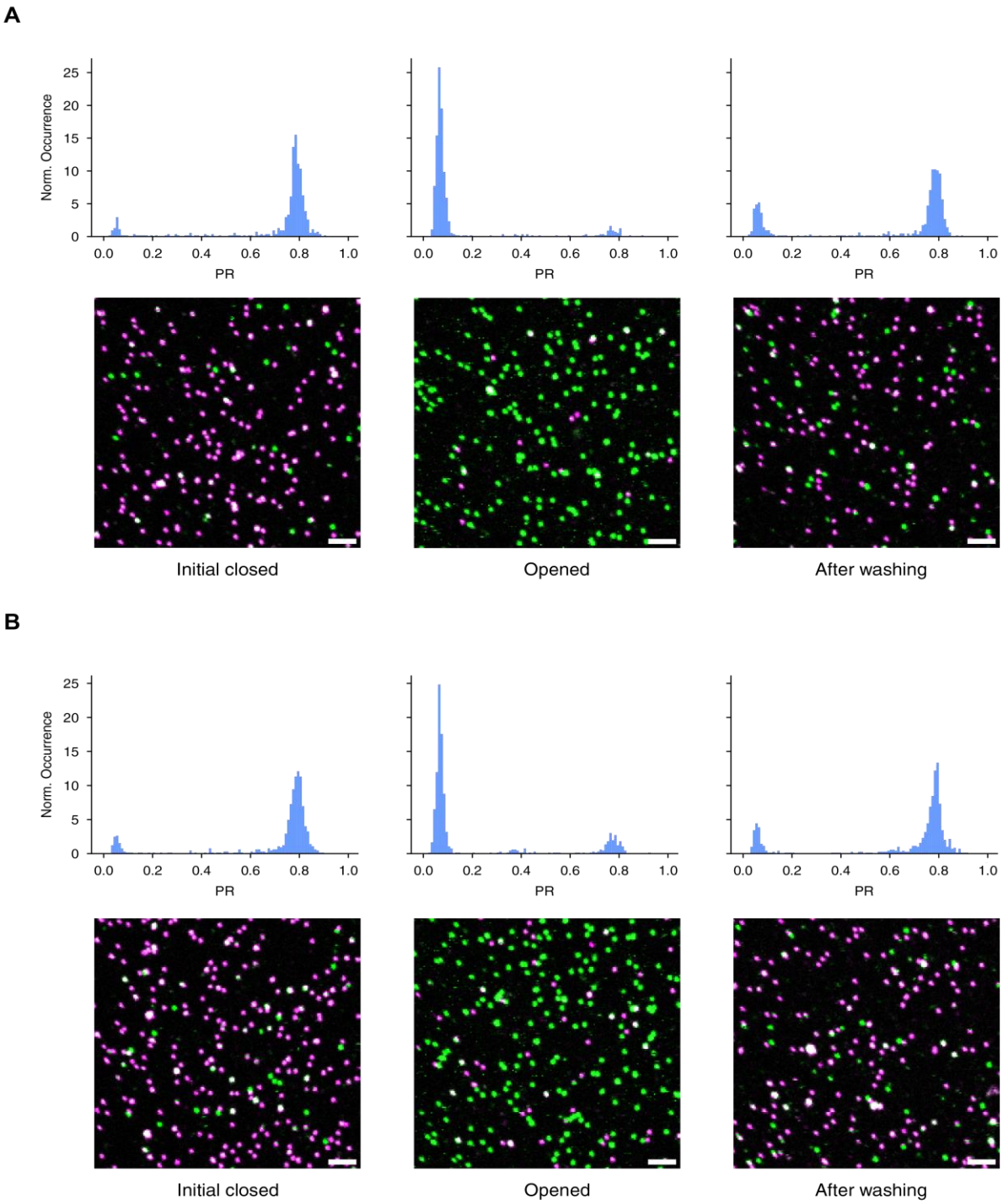

Fig. S2. Reclosing of the hinge nanostructure with four closing interactions measured in the presence of 50 mM (**A**) and 400 mM (**B**) NaCl. Samples were opened by incubating them with 100 µM opening strands for 1h. Afterwards, they were washed at least 10 times with the respective buffer and scans were taken after approximately 190 hours to allow for complete equilibration.

Closed structures

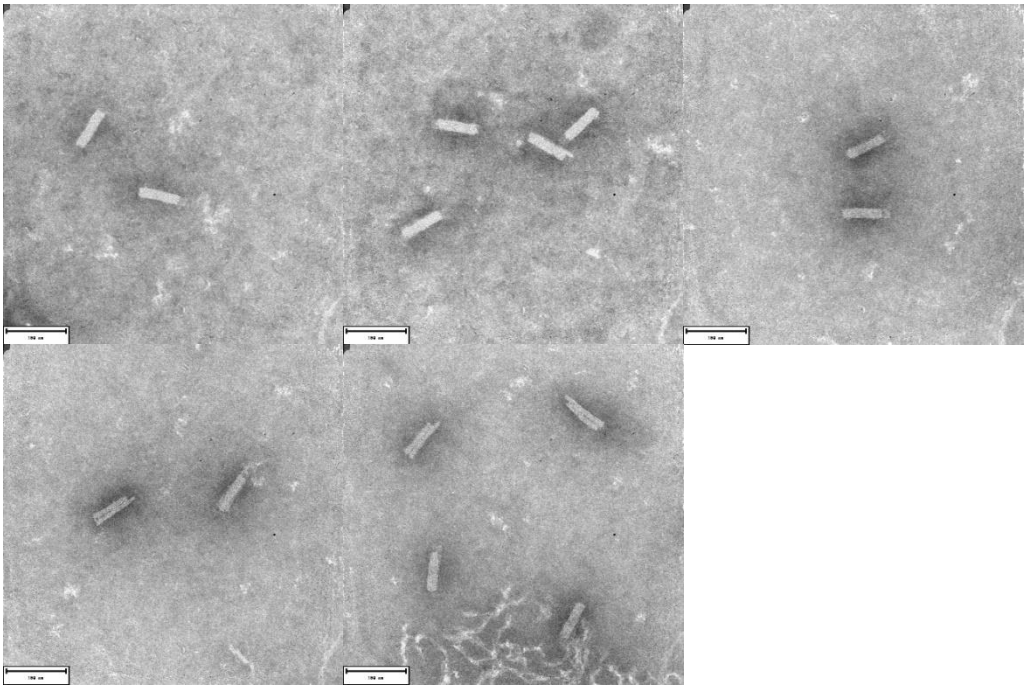

Open structures

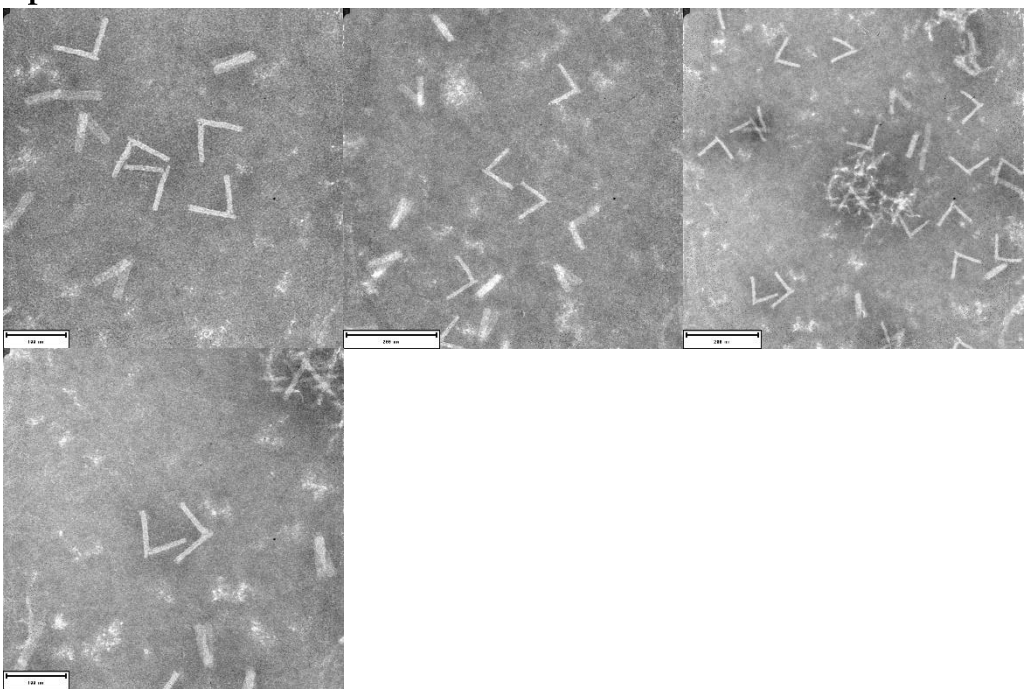

Fig. S3. Full field of view of the TEM micrographs used for the collage shown in Fig. 1B.

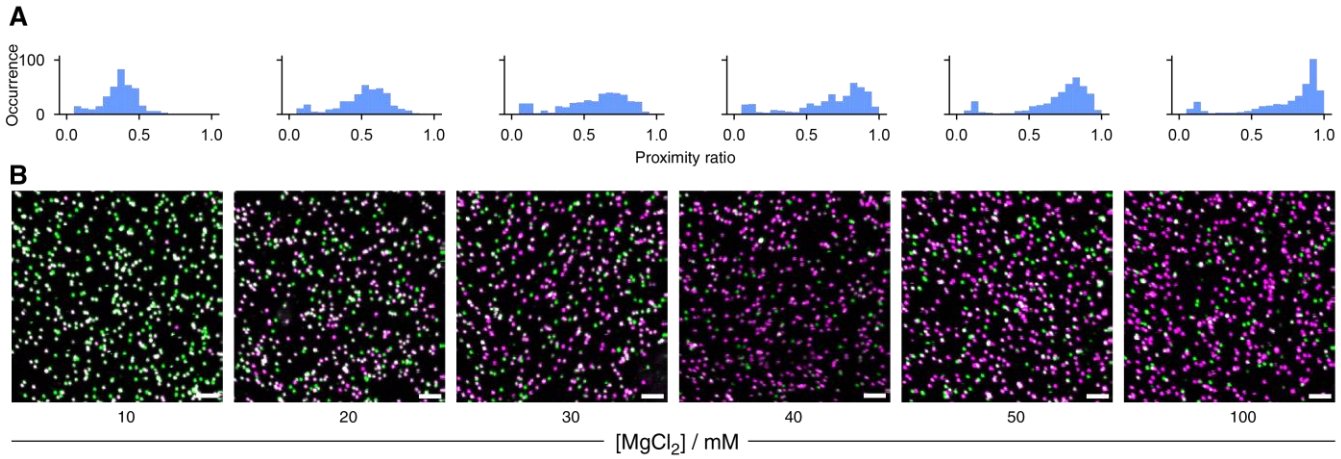

Fig. S4. FRET proximity ratios (**A**) and single molecule confocal scans (**B**) obtained for Version 1 of the nanosensor with a FRET pair consisting of ATTO532 and ATTO647N incorporated directly onto the hinge arms (Table S5) at different ionic strengths (increasing concentrations of $MgCl_2$). Scale bar: 2 μm.

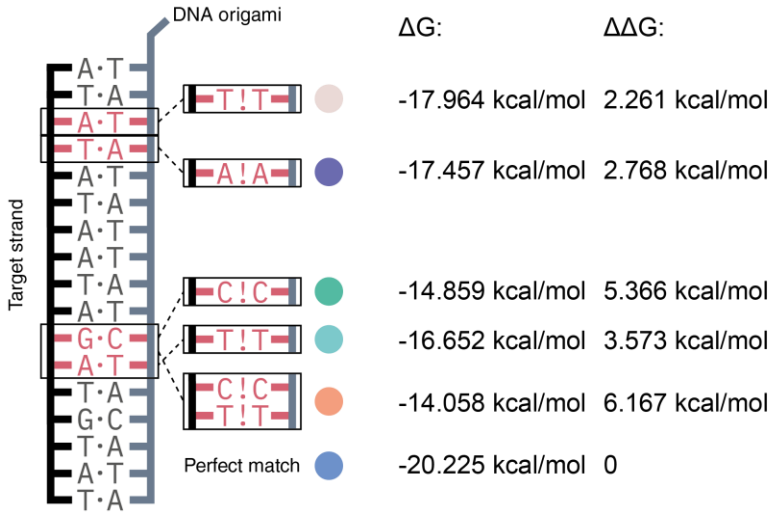

Fig. S5. Binding free energies (ΔG) for the different off-targets as well as for the perfect match as shown in Fig. 3 in the main text, as calculated by NUPACK at 25°C in a buffer containing 750 mM NaCl and 5 mM $MgCl_2$. ΔΔG is the difference in binding free energy when compared to the perfectly matched target.

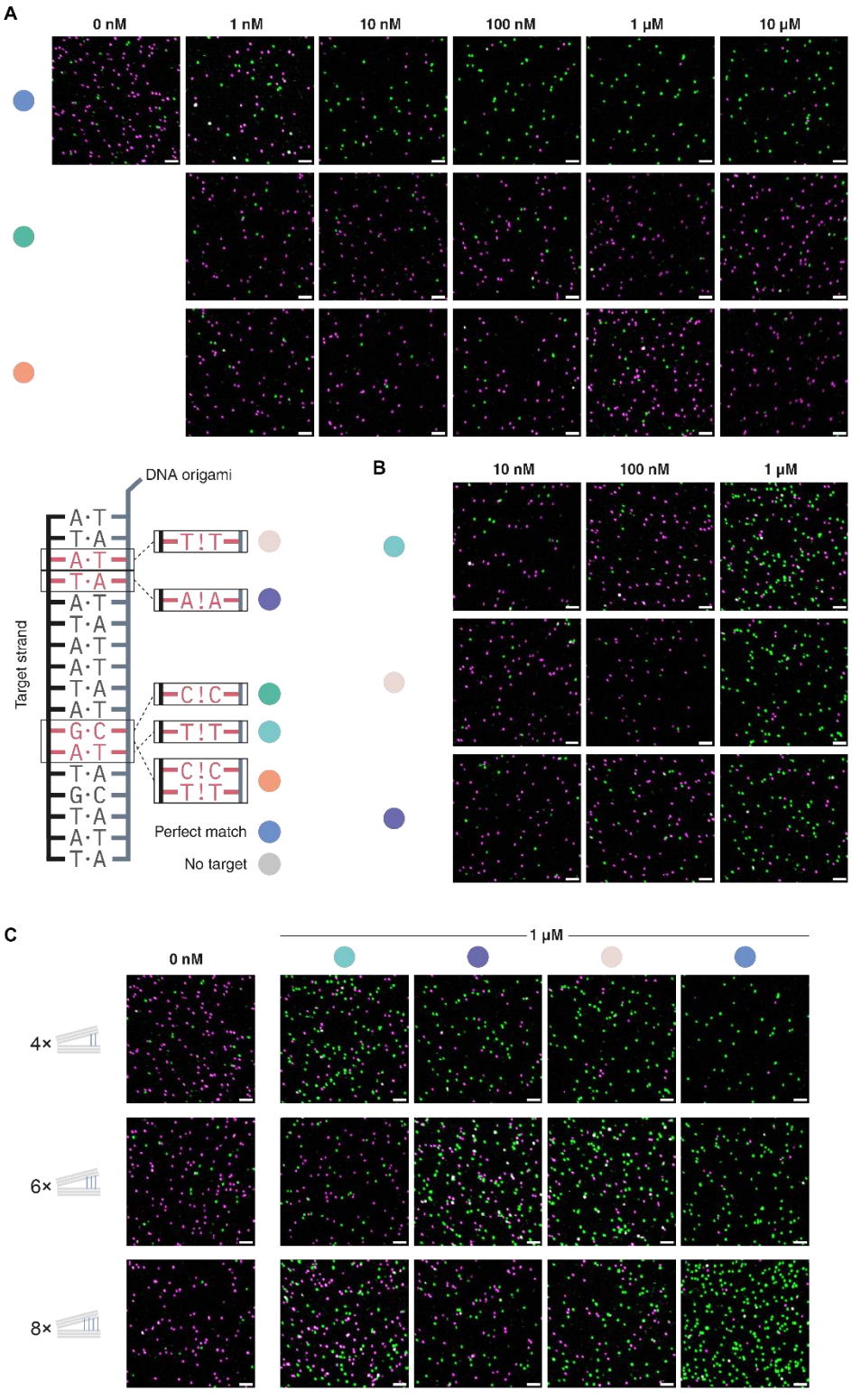

Fig. S6. Exemplary confocal microscopy scan images of the experiments shown in Fig. 3B (**A**), Fig. 3C (**B**) and Fig. 3D (**C**). Scale bar: 2 µm.

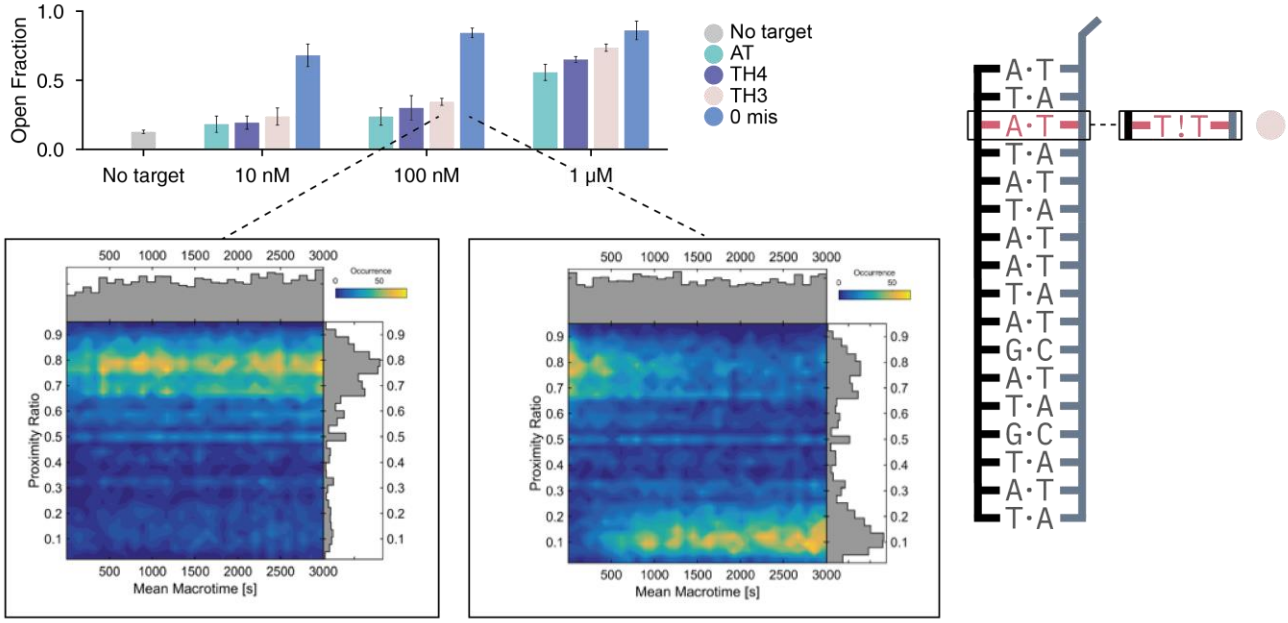

Fig. S7. Nanosesnor opening kinetics (proximity ratio vs. time) obtained for 100 nM of the target containing a single nucleotide mismatch (left) and 100 nM of perfectly matched target (right) measured at 1 nM concentration of DNA origami nanosensor containing 4 closing interactions.

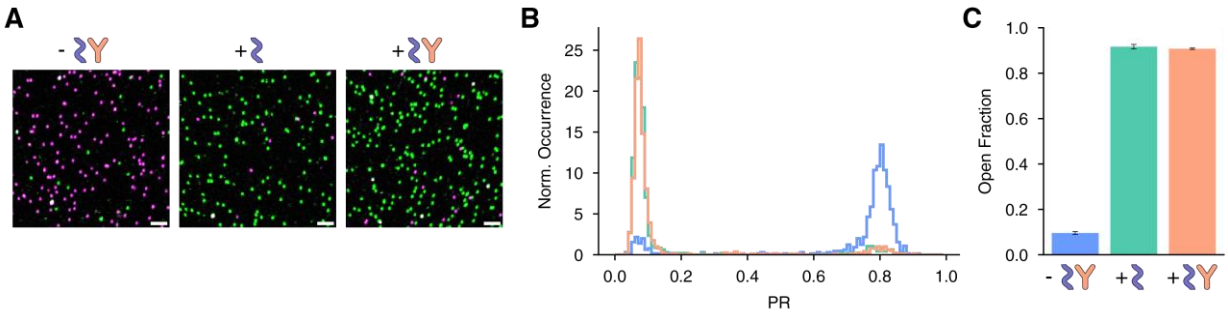

Fig. S8. Control experiment for nanosensor containing no Dig recognition elements. In this case, opening of the sensor is observed even after incubation (100 nM, 30 min) with anti-Dig antibodies. (**A**) Exemplary confocal microscopy scans. Scale bar: 2 μm. (**B**) Proximity ratio histograms for one experiment. (**C**) Fraction of open sensors. Error bar represents the standard deviation obtained from three independent measurements.

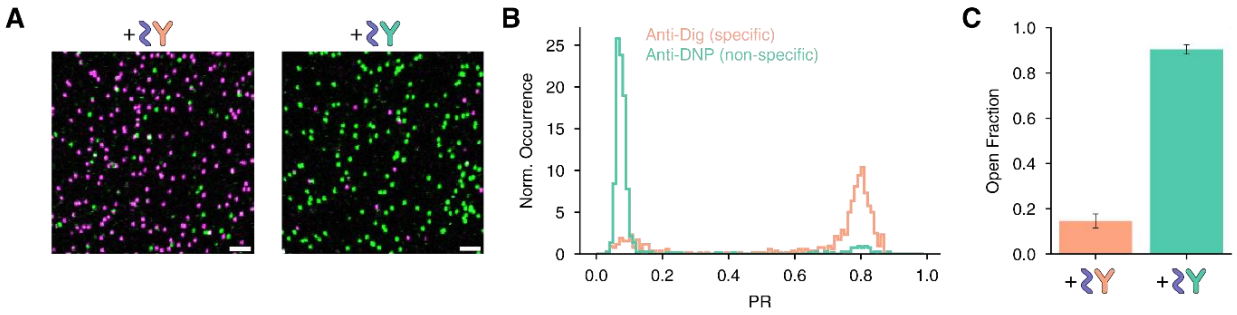

Fig. S9. Comparison of the extent of opening for sensor with Dig antigens when incubated with 100 nM of the corresponding specific antibody (Anti-Dig, orange) to 100 nM of a non-specific antibody (Anti-DNP, green). (**A**) Exemplary confocal microscopy scan images. Scale bar: 2 µm. (**B**) Proximity ratio histograms for one experiment. (**C**) Fraction of open sensors. Error bar represents the standard deviation obtained from three independent measurements.

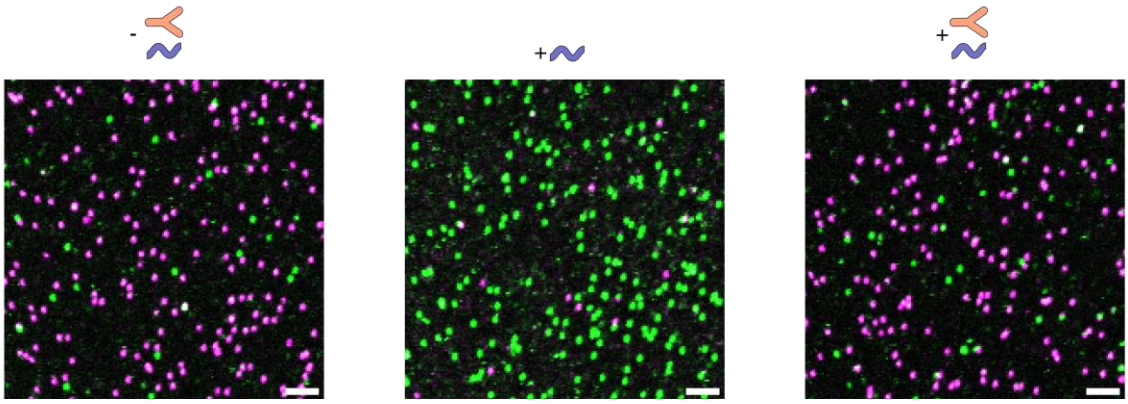

Fig. S10. Exemplary confocal microscopy scans for the data acquired for the antibody sensor (data shown in Fig. 4C before addition of the target (left), upon the addition of DNA opening strand alone (middle) and upon incubation of 100 nM antiDig antibody and addition of DNA opening strands (right) in heparin plasma. Scale bar: 2 μm.

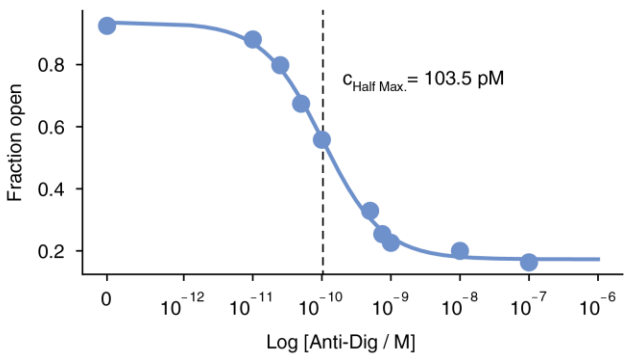

Fig S11. Estimation of the response window of the Anti-Dig antibody nanosensor. We achieve a $c_{Half\text{-}Max.}$ value of 103.5 pM.

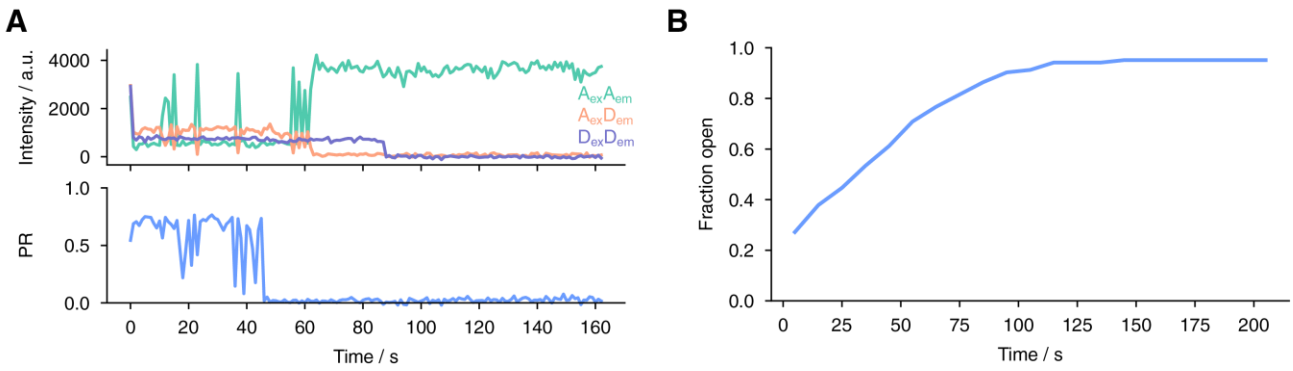

Fig. S12. Kinetics of the XhoI restriction enzyme reaction. **(A)** Exemplary single-molecule FRET trace and **(B)** Average of 103 single-molecule transients of the cleavage reaction of the closing interactions (66 units/mL XhoI, 10 min incubation) monitored by the DNA origami sensor. The FRET transients of the single DNA origami sensors were recorded on a wide-field microscope.

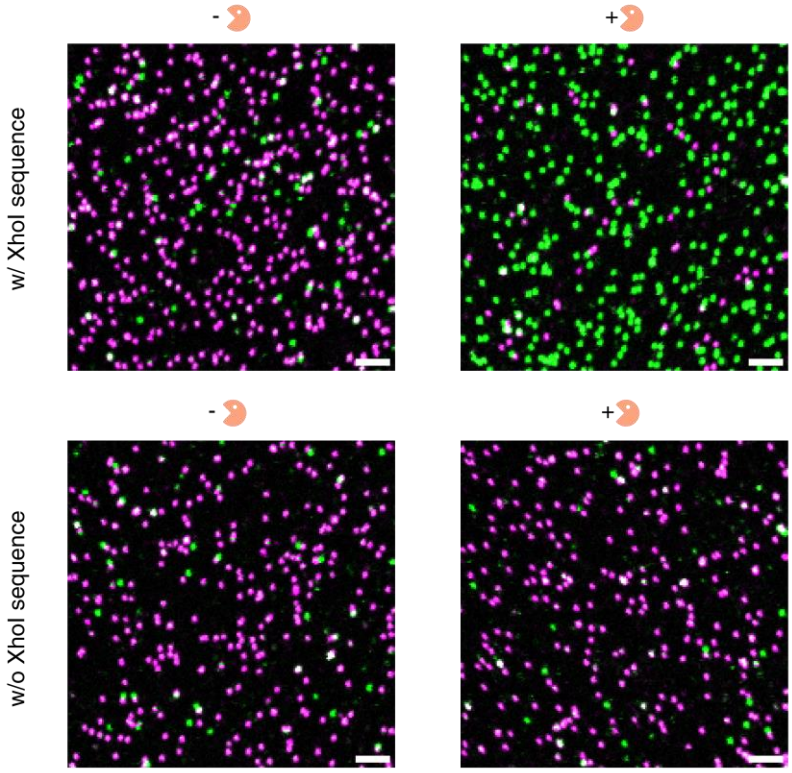

Fig. S13. Exemplary confocal microscopy scan images obtained for the nuclease nanosensor (shown in Fig. 4D-F). Scale bar: 2 μm.

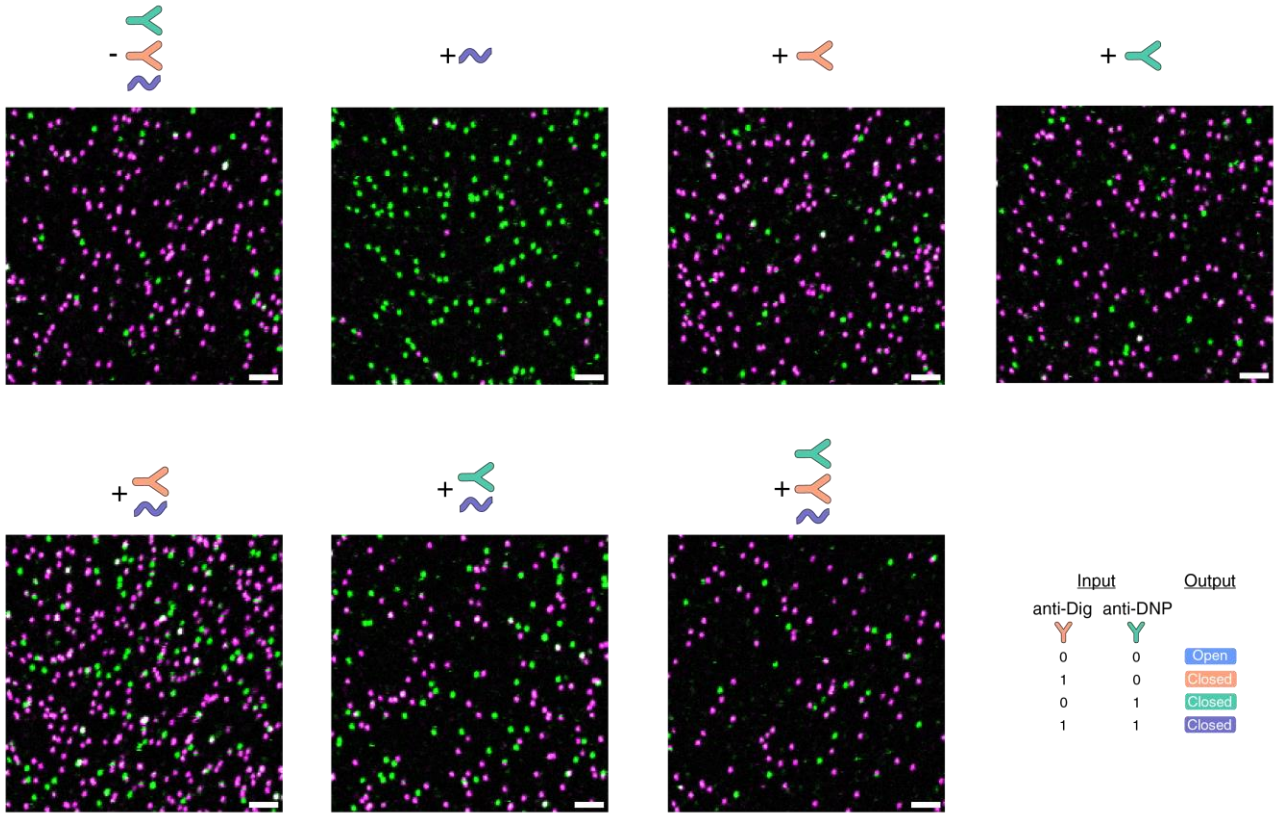

Fig. S14. Exemplary confocal microscopy scan images obtained for the multiplexed sensor for antiDig (orange) and anti-DNP (cyan) antibodies (OR gate) as shown in Fig. 4G-I. Scale bar: 2 μm.

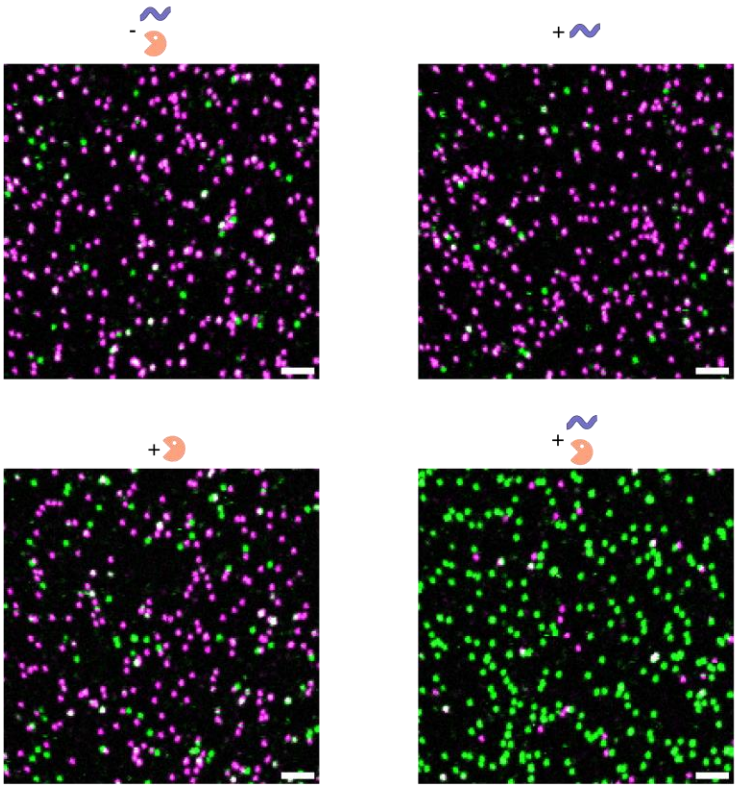

Fig. S15. Exemplary confocal microscopy scan images for the multiplexed nuclease and nucleic acid sensor (AND gate) shown in Fig. 4J-L. Scale bar: 2 μm.

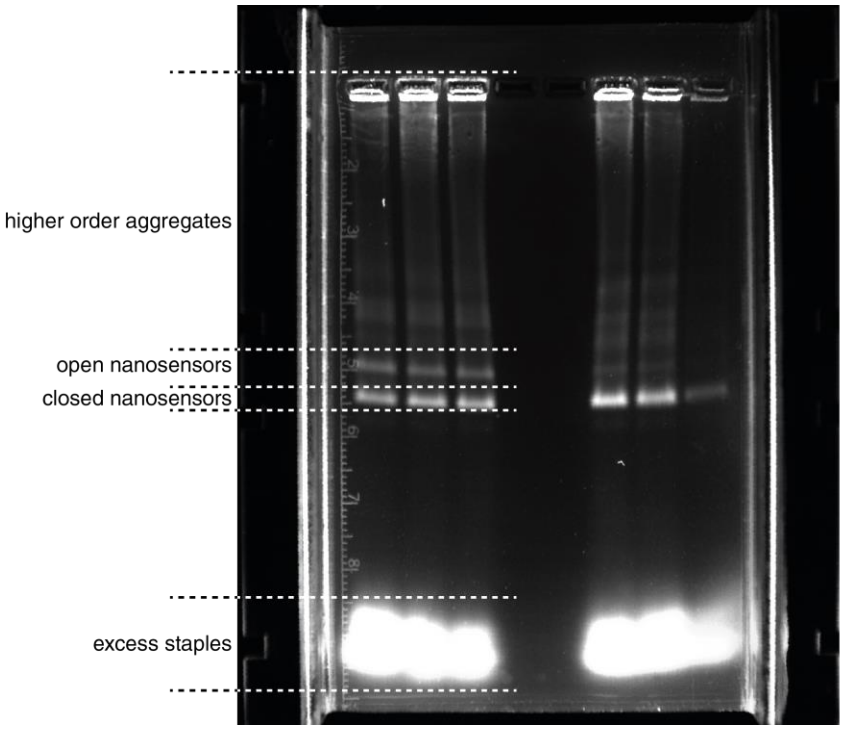

Fig. S16. Exemplary fluorescence scan of an agarose gel used for purification of the nanosensors. The respective band was then cut using a scalpel.

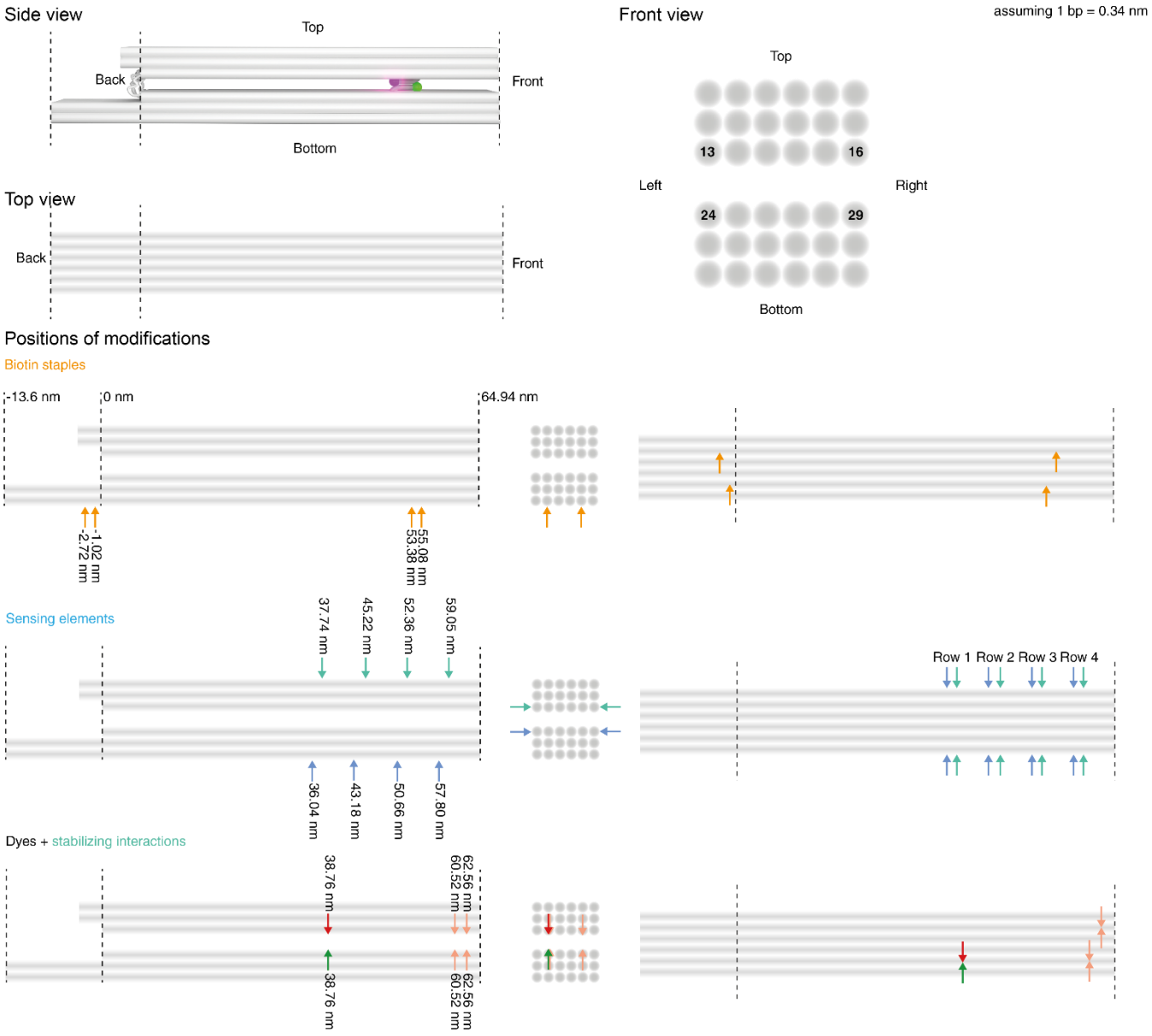

Fig. S17. Depiction of the placement of the modifications (FRET pair, sensing elements, biotin staples used for immobilization as well as stabilizing interactions) in the nanostructure. The numbering in the front view represents the helix numbering in caDNAno and are also used to indicate the positions of the sensing elements in Tables S3, S4, S6, and S7.

Table S1. Unmodified DNA origami staple sequences used for Version 1 of the nanosensor.

ID	Sequence (5'->3')
1	AAATATCCCATATGTTCAGGCAAATCCAGTGATGACAGTTGGGCGGTTGTAAATC
2	ATATTACCAAATACCTGTAATTCTAAAACTTT
3	GCTGGGAATCAAAGAAACGTAGACGGGAGAATTAACTGAACACCCA
4	GTCCACTAAATCCCTTTAAACCAAGGCGGGCCTGT
5	ACGTGGACTCCAACGT
6	CAAAGGGCTCAAAAATCAAGCCGTGTATGTTAGCAAAGGTGCTGCGGC
7	GAGCACGTATCCAAATTTACCGCGAACTGGCAAAGAAACGCAAAGACATTAC
8	CGTGGAACTCAAACTATCGGAAATGGATAAGAG
9	AAATTAGTAATAACATCATCACACGAATTTAGGCACCG
10	TTTACGAGCGTGGCGTTTTATAGCCGATTTACCAGCGCCAAAGTATC
11	AGGGCAAATTAACCGTTGGCCAACAGAGAATCGCAGAA
12	CAGCCGAAATCGGCAATTAAAGA
13	CACCCAGCAGTGTTTTGAGGCCACCGAGTAAAGCGTAAGAAAGCCAAAAGCCTG
14	TATATAAATCAAAAGAAT
15	CGCTAAACAACCCTAATTGGAAAAACGCTCATGGGCCAGCCAAGAACAAGGAAAATAG
16	TATAAACAGCCAAAGTCA
17	CTAACTTCTTTGCAGGAGGCCGATTAAAGGGA
18	ACTCCTTAAAGCGCATATTTTTTGTTTAACGGAAAAACCCAGAACA
19	AAAGCCCAATAGCCAGTAATTATTTACAACAGAGGTGAGGCGGTGCTG
20	GCTTTTGTCACAATCAATATTAG
21	CCAGCAGGCGAAAATCCTGTTTGATGGTGGTCAGAATGCGTAC
22	TCCTTTACAGAGAGAATAACATAAAAACAGGGTTACGCATTTTATTTAGGT
23	AACATATTATTTATCCCAATAA
24	CGCACAGGGTGCACTCTGTCGTAGAAAATACATACATAAAGAAA
25	CCATCGCCGTAAAAAAAGC
26	CATTGACCTAAAAATTACCTTCAAATATAATTTTAAAAGTTTGAGTAACA
27	AGCTGTGATAACAAAATTAAGTTGGCACTCGTATT
28	ACCCACCGGAAAAAGAAGGGAAGGTTGAAGTATTAGACTTTACAAACAAAACA
29	AGACGATCCAGCGCAGGTTTTCACGGTCATAC
30	CACTGCGCGCCTCGGCCTTTAATCGCAGTAAA
31	GCAACCGACAAATCATCGTAGTAATATCGTCTATCACTTTGAC
32	GAATTTCGAGCAAGCAAAAGTAGAACTTTCCTC
33	CATTCCCTTTTTAAGAAAAGTTAAGCCCATCTTACCAACGCTATAGAC
34	CTCTCTGAATAATGGAAGGGAGCGGAGAATTT
35	ATATTCACAAACAAATGTACATCGTTGCTTCTAGACAAAGCATAG
36	GCTCATTTGCCGCCAGAGGGTAAAGTTAAACG

37	CACCAGACGATATCAAAATTATTTGCAATCATTTTCTAAAGCA
38	GTCTCATTTGTTTAATGGAGATAAATTGGCAGATTCACCAGCTTGCCTGTCAGA
39	TATCACCAGTAGCACCACCACG
40	TAATTTCATTAAAGGTGAATACAAAAGGAGTAGGGCTCCCGACTTCCATCAC
41	CCGGAACACCGGAACGCTTTGAA
42	TAGTGAACAAGAAAAATAACCAATCAAACGGG
43	GTCTGAGAGACTACCTTTTAGA
44	AGATTTGAAATAGAGGCATTAAGTTTAAATAATAACGGAATACCCTG
45	ATCGGTTAAATACATATTTATCATATGGACAAAGTTACC
46	CCTAGGAATTGAATGATGAACTTTTACAGCCACCCTCAGAGCCACC
47	CGCCCCTTCTGACCTGAAAAGAGTCTGTGCGGGAGTATCCTGAAATAATA
48	CGCCTGGCCCTGAGACGCGTGCCATAGCGTCTGCTGTAGTCGAGCTTGATAAATT
49	GGGTGGAATTCGTAGCGAGAGATAACAGTCAGCAGCGTAAAGGAATTGCGAATTTTT
50	GGGGTTTCTGCCAGCAGAGTTGCAGAGTAGTA
51	TTCCAGATGCCGGGTTACGCAAACGCAACGCAAGAAAACAGGGAGAGATCTTAGGATT
52	CCGAGCTCGTTTTTCGATTTTAAGAACTGGCAGGGAACCCATGAGGA
53	TGAAACTCGTTTATAGATTTAGTTAA
54	CGGATCCGCCGGGCGCGGTATGCCAACAAATCATACGTC
55	TGGGGAATGCAGCATTTGGGACAA
56	GCATGCGTCCGTGAGCCTCCGCTGATTGTCAACTT
57	AAACCATTCCATGCTTTTGGACTTTTTGAACTGACCAACTTTGAA
58	GGTACGAACGAGCCAGACGAGGTAAAATACGAGGCGCAGACGGT
59	GCTGATTGCCGTTCCGCTGCAGCCGAATATAACAATA
60	TCGTCGCTAAATCGTTTATGCAACTAATAGTAGCCCGAAACTACAGAGGC
61	GCCTGTAATACTATTGTAAATATGGGATCGGATAAGTGCCGTC
62	ACGTAAATCGGTCATTAAATTCTTTCCAGTATAGCCCGGAATAG
63	GGAAAAAATTCGTGTACCAGGAACAACAAAGACAGCATCGGAGGAC
64	TTACCAGTATTCGCCAGACGACGACAGTATCTGATATAAGACGTTA
65	GCGAATCATTTTTAATAAAGCTTTTCACGCCGCTTTT
66	AAAACGAGCGATTAATCTCCGTGGGAACAAAGAGCCACTGA
67	CTCTGAATTTACCGTTACGCAGAAAAGCCCCAGATAAAAATTCTA
68	GTAAGGTACTGGTAATAAGTTGAGAAGGATACAAAGG
69	ATGGCTTTCCGGCACCTGGTGAAGATATTTAATTTGCGGGTTCAA
70	CTGGCACTCCAGCCAGCTTTTGATGATAATAAGCAAGGATAGCTTTTTCGTC
71	TCTGTAGCAATAGAACGCGACTTTCCAGGAGAGATAACCCACAAGA
72	GTGTATTTTTGAATGGCTAGGAGCACTTATTCATCCTGATTCGCCTCCC
73	CCGTGCAACCGTACTGCGTAACGATCTAAAGAAT
74	CGTCGGATGTTGGGTAACGCCA
75	CCCTGAGAGTATTAAGAG
76	TTAATGAAGATCGTGCCGGAAACCAGGCAAAGCGCCCCC
77	CAATCATAGTTACAGGAGGTTTAGTACCGCCACCCTTTGGTGTCATC

78	AAAAACGGATAAGCAGCAACCGCAAGATGCGGTATCATTTCGCGTAA
79	TGGCACAACGCCCCACCCTCAGAACCGCCACCCTCACGGCGGATAGC
80	CAGCGCCAAGCTCCGTCGGTGGTGCCATGGCGCTTTTATATTTTATACATAATAAA
81	TAGCATGTCAATCATAAAATGCAAGTCAAATCCAGGTC
82	AGAATTAGATAGAGCCGGCGCTCACAATTCCACAAGCTGCATACGAACTA
83	TCTACTAACATTAAAGTAACACCACCCTCATTTTCAGGGATAG
84	AACATTTATTTCGGTCCGTTCTCACGGAAAAAGAGCCA
85	CCCATCCAATGGCAGCATTCAGAGGTGGAGCCGGCCAG
86	AGCCGCACTCAAAGCATAAAGTGTAAAGCCCG
87	AAGAGGTCATTTTTGCGAATCCCCGGTCTTTA
88	CTGAAAGCGGAGACCTTCATCAAGAGTAATCTTGAGAG
89	GGGTAAAGTACAGCAACGGGACTTCAA
90	AACCTTGTTATCGTCACTGTTGCCCTGCTGGTGCTGAATTAAGCTAAC
91	GAGCAACCTAAATCCGCGACCTGCTCCATGTTACTAATCTACGTCAT
92	ATTCAACTTGCCTAATAGCGGGGT
93	AAACATCATAAATATTCATTGGATGGCTACTC
94	AATTGGGCGGCTGGCTTTGCATCAAAAAGATTTTTTAATCTC
95	TAATCATTGACAGATGAACGGTGTA
96	ACGGAACATGTCGAAAACGAAAGAGGCAAAACGCATAACAATAA
97	AAGGCTTGCCCTGACCAAGAACCCCTGACT
98	CAGACCAGGCGCATATTGAGATGAGACTGGTGTTC
99	AGAGGTGAATTAGTTTTGCCGAGGATCCACTGGTGTGTTCAGCGGCA
100	CAATCATATCATTATAACCAAAATAATCATGGAGGTTTCTTTGCTCGTCGGA
101	GAAACAAAGTACAGAGATTTA
102	CGGATATTCATTACCCAAATCAACTGCTCATCTTTAAAC
103	TTTGAACGAGGGTGGTGTCTATGACCCTCCGGCCAAGATAGACTTTCTCCGGCTT
104	TAAACAAAAGAACCTTATGCTTTTCACCAGTGAGACGGGCAACATCACAGTTAGAGG
105	AGTTTCCAGTCACCCTTGATTCCCATAAAGCTGCCGGACTCGCCATGT
106	CCACTACGTGCAGGGAGTTTGACCATTAGCAAGTCTG
107	ACACTTTGTATCATCGCCTGATAAATTGACATTATGGAATTACGAGC
108	GACCCCCATTGCGCCGGCGCGAGCGCATCAAT
109	ATAAATCAGTACCTTTTTTGATTAATGTGT
110	ATATCGCGAAGAGGAAAAATGTTTGTTTAATTCCCTTCAC
111	GCGGGATCTTAAACGCGATAAAACCAGTCAGTTTGCGTATTGGGCGCCA
112	AGGTTGAAAATCTCCAAAAACAGCCCTAGGAACGCAGATGGGCCGGTGCG
113	TGATTTCGAGGTGAATTTCCATGTACCTGTGAGCG
114	AGGATTAGAGAAAAATCACTCAAATGTCAGTGAAT
115	CAAACCATCAATATGATATTC
116	GCTCAAAGCGAACCAGACCCAGAAGCCGGAATCGCCAGAACGCAAGCGG
117	AATGCCGGAGAGGACTAGAAGCCTGTTTTAAAAACG
118	CAGTTTCAGCGGAGTGAGATTTTCTGCG

119	AAGGTCGGTCGCTGAGGCTAAGGCACCAACACTATTAATAAATAATGAA
120	GAAAGGCAATCGATGGTAAAACACAGTTAA
121	TTCGTAAAAGGAAACAGTAGCGACCGGAAACGTCACCAATGGTG
122	TTAATCTAAAATATCTTTATTAGTCTTACTAGAAACGCTCAACGCGA
123	CTATCAGGTCAACCGTTTTTAGAAATTGCTAGCGGTGC
124	GTAAATGAAATAGAAAAAAACATTGGAAGTTTATCCCTTACCCGGGTA
125	GTCGTTTTGTTATTTGAGGGTTCAGGCTGCGCAACTG
126	GCATTCCACAGAAAAGGCTGCAA
127	GTTTCGTCACCAGCGGTTTATAGCATTAATGTTT
128	GCTGAGACTCCTCAATTAACGGGATCAGAAACAGCGGA
129	AGCGGGGTTTTGCTCAGTAC
130	CAGGTTTGCTAAACAGTAGCTATTTTTAAGATTGTCAGGAGTCGTCATAC
131	GAGAGGGTGGCCTCAGATTTTGTTTTTGTGAGGAGCACATCCTCATAACAT
132	GTGTATCTCTGCCAGAATCAGCACGTACAGTGTAGAACGTCAGCGGGCT
133	CTATTATTCTGAAACCCGTATAA
134	AGTCTGGAGCAAACAAGAGCGGAGACATGCCTGAG
135	CGCTGTAACCTCCATGCTGATCTAATGCAGAAC
136	AGAGTTCGCTATTATTATACTATTAAAGCCAGAATGGAAAGCGCA
137	ATCAAAGCCAGCAGCAAAATGTGAGTCCTACCATTGGCCTTG
138	TCACCTTCAGTATTATTAATTTATAAAGTACATATAATGATTAAG
139	AACCTTTTTAATCAGAAATAATTGACAGGAGGTTGAGGCAGGTCGTAATCAGTAC
140	TCATTACATTTTAACGTCCACCAGAA
141	TCGCAATAGTATTATCATCATATTCCTGATTATCTTG
142	ATAAATATTTTAGACACCGCCACGCTCAATCGTCTGCCTT
143	AATCCTGAAGATGATTTAGATTAAGA
144	TTTGGAATTAATTTTCCCTTATATGTAAGGCT
145	AGAAGAATAACCACATAAAAAAATCATAGCAG
146	GCGTAGATCGTTATTCAAACCCTCAATCAATCCAGC
147	ATACAGTTTCGACAAAATCAACAGTTGAAAAAAC
148	GTACACAAACATGTCATAGCCTTGAGCCATTTGGGAAGAAAATACAACGCCATT
149	CGGATTCGTTCAATTATTCA
150	GCGTTCCAAGATAATCGGCCAGTTTGGAACAAGA
151	GACGACAAACTCATCGTTGCAACATACGAGCATGTAG
152	AAAACATTTTGTGCAACAGTGCCACGCTGAGAATAACGCGAGGTCCAGAC
153	AATCATCTTCTAGCAAGGCAGAATCAAGTTTGCCTCCGCCAGCAAGAAATT
154	TGTACCAGTAATAATACCGAACGAACCAATCTGG
155	TTCAAATATCAATATTGAAAAATGCGGAACAAAGAAACCACCAGAAGGTT
156	ACCGCAGCAAAAGCGCGTTTTCATCGGCAGAGCCGCAGATGAAT
157	TAAAGTCACCGACCCCTTATTAGCGTTTCAGA
158	TTTAGTATGAGGCGAATAACAACTAGCCGTCAATAGATAATACATTTG

Table S2. Unmodified DNA origami staple sequences used for Version 2 of the nanosensor.

ID	Sequence (5'->3')
1	GCTGGGAATCAAAGAAACGTAGACGGGAGAATTAACTGAACACCCA
2	TCATTACATTTTAACGTCCACCAGAA
3	CAGCCGAAATCGGCAATTAAAGA
4	CAGGTTTGCTAAACAGTAGCTATTTTTAAGATTGTCAGGAGTCGTCATAC
5	CTCTGAATTTACCGTTACGCAGAAAAGCCCCAGATAAAAATTCTA
6	GTACACAAACATGTCATAGCCTTGAGCCATTTGGGAAGAAAATACAACGCCATT
7	CAACATACGAGGCATAAAATGGTCCGATATATAGCCTTTAATTGTATTA
8	AAGGCTTGCCCTGACCAAGAACCCCTGACT
9	AACATTTATTTCGGTCCGTTCTCACGGAAAAAGAGCCA
10	TTTAGTATGAGGCGAATAACAACTAGCCGTCAATAGATAATACATTTG
11	CATTCCCTTTTTAAGAAAAGTAAGCAGAGCGAACCTTAATTGAGATAGAAGAACTGATAGC
12	CGCACAGGGTGCACTCTGTCGTAGAAAATACATACATAAAGAAA
13	AATGGGATAGGTCACGCAGAACCGTGTA
14	GCGTAGATCGTTATTCAAACCCTCAATCAATCCAGC
15	GCGGGATCTTAAACGCGATAAAACCAGTCA
16	TTACCAGTATTCGCCAGACGACGACAGTATCTGATATAAGACGTTA
17	GAATTTCGAGCAAGCAAAAGTAGAACTTTCCTC
18	GGTACGAACGAGCCAGACGAGGTAAAATACGAGGCGCAGACGGT
19	ATAAATCAGTACCTTTTTTGATTAATGTGT
20	CACTGCGCGCCTCGGCCTTTAATCGCAGTAAA
21	AGTTTCCAGTCACCCTTGATTCCCATAAAGCTGCCGGACTCGCCATGT
22	GCATGCGTCCGTGAGCCTCCGCTGATTGTCAACTT
23	GCATTCCACAGAAAAGGCTGCAA
24	GAGAGGGTGGCCTCAGATTTTGTTTTTGTGAGGAGCACATCCTCATAACAT
25	CGTGGAACTCAAACTATCGGAAATGGATAAGAG
26	CCACTACGTGCAGGGAGTTTGACCATTAGCAAGTCTG
27	AAACATCATAAATATTCATTGGATGGCTACTC
28	AACATATTATTTATCCCAATAA
29	ATCGGTTAAATACATATTTATCATATGGACAAAGTTACC
30	GTCTGAGAGACTACCTTTTAGA
31	CCGTGCAACCGTACTGCGTAACGATCTAAAGAAT
32	CCCATCCAATGGCAGCATTCAGAGGTGGAGCCGGCCAG
33	TGGCACAACGCCCCACCCTCAGAACCGCCACCCTCACGGCGGATAGC
34	GTCGTTTTGTTATTTGAGGGTTCAGGCTGCGCAACTG
35	GCTTTTGTCACAATCAATATTAG
36	AACCTTGTTATCGTCACTGTTGCCCTGCTGGTGCTGAATTAAGCTAAC
37	AACCTTTTTAATCAGAAATAATTGACAGGAGGTTGAGGCAGGTCGTAATCAGTAC

38	AATGCCGGAGAGGACTAGAAGCCTGTTTTAAAAACG
39	AGGGCAAATTAACCGTTGGCCAACAGAGAATCGCAGAA
40	AGCCTAATTTGCCAGTGAGCTA
41	AAACCATTCCATGCTTTTGGACTTTTTGAACTGACCAACTTTGAA
42	CGGATATTCATTACCCAAATCAACTGCTCATCTTTAAAC
43	ATCAAAGCCAGCAGCAAAATGTGAGTCCTACCATTGGCCTTG
44	TCGTCGCTAAATCGTTTATGCAACTAATAGTAGCCCGAAACTACAGAGGC
45	GAAAGATTCATCAGTTACGGAGATCATCTTT
46	ACACTTTGTATCATCGCCTGATAAATTGACATTATGGAATTACGAGC
47	GCCTGTAATACTATTGTAAATATGGGATCGGATAAGTGCCGTC
48	CAATCATAGTTACAGGAGGTTTAGTACCGCCACCCTTTGGTGTCATC
49	CTCTCTGAATAATGGAAGGGAGCGGAGAATTT
50	GGGTAAAGTACAGCAACGGGACTTCAA
51	AAGAGGTCATTTTTGCGAATCCCCGGTCTTTA
52	TAGCATGTCAATCATAAAATGCAAGTCAAATCCAGGTC
53	TTTGAACGAGGGTGGTGTCTATGACCCTCCGGCCAAGATAGACTTTCTCCGGCTT
54	ACGGAACATGTCGAAAACGAAAGAGGCAAAACGCATAACAATAA
55	AGCCGCACTCAAAGCATAAAGTGTAAAGCCCG
56	CCAGCAGGCGAAAATCCTGTTTGATGGTGGTCAGAATGCGTAC
57	CAATCATATCATTATAACCAAAATAATCATGGAGGTTTCTTTGCTCGTCGGA
58	CTATCAGGTCAACCGTTTTTAGAAATTGCTAGCGGTGC
59	AGTCTGGAGCAAACAAGAGCGGAGACATGCCTGAG
60	ATTTTCGCAAGAAAAATAAGGCCCATTAAAAAAAGGGACAT
61	TGGGGAATGCAGCATTTGGGACAA
62	GCTGATTGCCGTTCCGCTGCAGCCGAATATAACAATA
63	ATGGCTTTCCGGCACCTGGTGAAGATATTTAATTTGCGGGTTCAA
64	GTCCACTAAATCCCTTTAAACCAAGGCGGGCCTGT
65	CACCAGACGATATCAAAATTATTTGCAATCATTTTCTAAAGCA
66	TGAAACTCGTTTATAGATTTAGTTAA
67	ATTCAACTTGCCTAATAGCGGGGT
68	AGACGATCCAGCGCAGGTTTTCACGGTCATAC
69	TTAATGAAGATCGTGCCGGAAACCAGGCAAAGCGCCCCC
70	GGGGTTTCTGCCAGCAGAGTTGCAGAGTAGTA
71	GTGTATTTTTGAATGGCTAGGAGCACTTATTCATCCTGATTCGCCTCCC
72	TCGGGAGAAACAATAAAGGAT
73	AAGGTCGGTCGCTGAGGCTAAGGCACCAACACTATTAATAAATAATGAA
74	ATATTACCAAATACCTGTAATTCTAAAACTTT
75	CGCTAAACAACCCTAATTGGAAAAACGCTCATGGGCCAGCCAAGAACAAGGAAAATAG
76	CTAACTTCTTTGCAGGAGGCCGATTAAAGGGA
77	TAAACAAAAGAACCTTATGCTTTTCACCAGTGAGACGGGCAACATCACAGTTAGAGG
78	AGAATTAGATAGAGCCGGCGCTCACAATTCCACA

79	TTCAAATATCAATATTGAAAAATGCGGAACAAAGAAACCACCAGAAGGTT
80	CCGGAACACCGGAACGCTTTGAA
81	CGGATTCGTTCAATTATTCA
82	TGTACCAGTAATAATACCGAACGAACCAATCTGG
83	GTCTCATTTGTTTAATGGAGATAAATTGGCAGATTCACCAGCTTGCCTGTCAGA
84	CAGTTTCAGCGGAGTGAGATTTTCTGCG
85	TAGTGAACAAGAAAAATAACCAATCAAACGGG
86	GTTTCGTCACCAGCGGTTTATAGCATTAATGTTT
87	AGGTTGAAAATCTCCAAAAACAGCCCTAGGAACGCAGATGGGCCGGTGCG
88	CAGACCAGGCGCATATTGAGATGAGACTGGTGTTC
89	AAAGCCCAATAGCCAGTAATTATTTACAACAGAGGTGAGGCGGTGCTG
90	GAGCACGTATCCAAATTTACCGCGAACTGGCAAAGAAACGCAAAGACATTAC
91	CCATCGCCGTAAAAAAAGC
92	AAAACATTTTGTGCAACAGTGCCACGCTGAGAATAACGCGAGGTCCAGAC
93	CGGATCCGCCGGGCGCGGTATGCCAACAAATCATACGTC
94	GCGAATCATTTTTAATAAAGCTTTTCACGCCGCTTTT
95	AGGATTAGAGAAAAATCACTCAAATGTCAGTGAAT
96	AGCGGGGTTTTGCTCAGTAC
97	AATCATCTTCTAGCAAGGCAGAATCAAGTTTGCCTCCGCCAGCAAGAAATT
98	CAAACCATCAATATGATATTC
99	GCGTTCCAAGATAATCGGCCAGTTTGGAACAAGA
100	GAAACAAAGTACAGAGATTTA
101	CCTAGGAATTGAATGATGAACTTTTACA
102	CATTGACCTAAAAATTACCTTCAAATATAATTTTAAAAGTTTGAGTAACA
103	GCTCAAAGCGAACCAGACCCAGAAGCCGGAATCGCCAGAACGCAAGCGG
104	AAATTAGTAATAACATCATCACACGAATTTAGGCACCG
105	ACCCACCGGAAAAAGAAGGGAAGGTTGAAGTATTAGACTTTACAAACAAAACA
106	TGATTTCGAGGTGAATTTCCATGTACCTGTGAGCG
107	GTGTATCTCTGCCAGAATCAGCACGTACAGTGTAGAACGTCAGCGGGCT
108	GCTGAGACTCCTCAATTAACGGGATCAGAAACAGCGGA
109	GTAAGGTACTGGTAATAAGTTGAGAAGGATACAAAGG
110	GCTCATTTGCCGCCAGAGGGTAAAGTTAAACG
111	CTGGCACTCCAGCCAGCTTTTGATGATAATAAGCAAGGATAGCTTTTTCGTC
112	CAGCGCCAAGCTCCGTCGGTGGTGCCATGGCGCTTTTATATTTTATACATAATAAA
113	GGGTGGAATTCGTAGCGAGAGATAACAGTCAGCAGCGTAAAGGAATTGCGAATTTTT
114	TATAAACAGCCAAAGTCA
115	GGACGTTGGGAAGAAATAGCCGGAACGTAATG
116	AGAGTTCGCTATTATTATACTATTAAAGCCAGAATGGAAAGCGCA
117	TTCGTAAAAGGAAACAGTAGCGACCGGAAACGTCACCAATGGTG
118	AGCTGTGATAACAAAATTAAGTTGGCACTCGTATT
119	CCCTGAGAGTATTAAGAG

120	AAAACGACGGCCAGTTTTCATCAATAGTAGTCAGCTTGCCAACAACCATCGCCCAGA
121	GGAAAAAATTCGTGTACCAGGAACAACAAAGACAGCATCGGAGGAC
122	TCACCTTCAGTATTATTAATTTATAAAGTACATATAATGATTAAG
123	AGAAGAATAACCACATAAAAAAATCATAGCAG
124	ACCGCAGCAAAAGCGCGTTTTCATCGGC
125	TCGCAATAGTATTATCATCATATTCCTGATTATCTTG
126	CTGAAAGCGGAGACCTTCATCAAGAGTAATCTTGAGAG
127	ACGTGGACTCCAACGT
128	ATACAGTTTCGACAAAATCAACAGTTGAAAAAAC
129	CACCCAGCAGTGTTTTGAGGCCACCGAGTAAAGCGTAAGAAAGCCAAAAGCCTG
130	AGAGGTGAATTAGTTTTGCCGAGGATCCACTGGTGTGTTCAGCGGCA
131	AATCCTGAAGATGATTTAGATTAAGA
132	TCCTTTACAGAGAGAATAACATAAAAACAGGGTTACGCATTTTATTTAGGT
133	AGATTTGAAATAGAGGCATTAAGTTTAAATAATAACGGAATACCCTG
134	TTAATCTAAAATATCTTTATTAGTCTTACTAGAAACGCTCAACGCGA
135	GACCCCCATTGCGCCGGCGCGAGCGCATCAAT
136	CGCCTGGCCCTGAGACGCGTGCCATAGCGTCTGCTGTAGTCGAGCTTGATAAATT
137	GAGCAACCTAAATCCGCGACCTGCTCCATGTTACTAATCTACGTCAT
138	ATATTCACAAACAAATGTACATCGTTGCTTCTAGACAAAGCATAG
139	ACGTAAATCGGTCATTAAATTCTTTCCAGTATAGCCCGGAATAG
140	CAAAGGGCTCAAAAATCAAGCCGTGTATGTTAGCAAAGGTGCTGCGGC
141	CGCCCCTTCTGACCTGAAAAGAGTCTGTGCGGGAGTATCCTGAAATAATA
142	AAATATCCCATATGTTCAGGCAAATCCAGTGATGACAGTTGGGCGGTTGTAAATC
143	ATATCGCGAAGAGGAAAAATGTTTGTTTAATTCCCTTCAC
144	CTATTATTCTGAAACCCGTATAA
145	TAAAGTCACCGACCCCTTATTAGCGTTTCAGA
146	TATATAAATCAAAAGAAT
147	TTTACGAGCGTGGCGTTTTATAGCCGATTTACCAGCGCCAAAGTATC
148	TTCCAGATGCCGGGTTACGCAAACGCAACGCAAGAAAACAGGGAGAGATCTTAGGATT
149	CGCTGTAACCTCCATGCTGATCTAATGCAGAAC
150	AAAAACGGATAAGCAGCAACCGCAAGATGCGGTATCATTTCGCGTAA
151	GTAAATGAAATAGAAAAAAACATTGGAAGTTTATCCCTTACCCGGGTA
152	TCTGTAGCAATAGAACGCGACTTTCCAG
153	AATTGGGCGGCTGGCTTTGCATCAAAAAGATTTTTTAATCTC
154	TAATCATTGACAGATGAACGGTGTA
155	ATAAATATTTTAGACACCGCCACGCTCAATCGTCTGCCTT
156	GCAACCGACAAATCATCGTAGTAATATCGTCTATCACTTTGAC
157	TCTACTAACATTAAAGTAACACCACCCTCATTTTCAGGGATAG
158	ACTCCTTAAAGCGCATATTTTTTGTTTAACGGAAAAACCCAGAACA
159	CCGAGCTCGTTTTTCGATTTTAAGAACTGGCAGGGAACCCATGAGGA
160	TTTGGAATTAATTTTCCCTTATATGTAAGGCT

161	TAATTTCATTAAAGGTGAATACAAAAGGAGTAGGGCTCCCGACTTCCATCAC
162	GACGACAAACTCATCGTTGCAACATACGAGCATGTAG
163	GAAAGGCAATCGATGGTAAAACACAGTTAA
164	TATCACCAGTAGCACCACCACG
165	CGTCGGATGTTGGGTAACGCCA
166	AAATCCTTTGCCCGAATTTCAGGTTAACAATTAGACTG
167	GTCACCTCACCGGAAACAATCG

Table S3. Closing staples and fluorescently labelled staples used in Version 1 of the nanosensor. For the closing interactions, the number of the caDNAno helix is indicated (see Fig. S17). Yellow and Red indicate complementary sequences. Green indicates the toehold used for opening. Blue indicates additional spacer elements.

Name-HelixID	**Sequence (5'->3')**
Row1-top16	ATACATCTATTATATATTGAGGGTAATTGAGCGCTGAAACCGATATCCGGTAACA
Row1-top13	ATACATCTATTATATATTCCACCACCAGAGCCGTTAGC
Row1-bot24	AATAGATGTATTTATATATTGCGGGACGTTGGGAAGAAATAGCCGGAACGTAATG
Row1-bot29	AATAGATGTATTTATATATTTTGGGAAGGGCGATGCATCGTAA
Row2-top13	ATACATCTATTATATATTTTCAAGCCTAATTTGCCAGTGAGCTA
Row2-top16	ATACATCTATTATATATTTTACCCTCATTTTCGCAAGAAAAATAAGGCCCATTAAAAAAAGGGACAT
Row2-bot24	AATAGATGTATTTATATATTTTCGGCCAACGCGCGGGGAGAG
Row2-bot29	AATAGATGTATTTATATATTTTGGCCTCTTCGCTATTACCCACGGGAATAATTCGCAGGCAAGCCAA
Row3-top13	ATACATCTATTATATATTTTTATTGAGTAAGCAGAGCGAACCTTAATTGAGATAGAAGAACTGATAGC
Row3-top16	ATACATCTATTATATATTTTTACCTCGGGAGAAACAATAAAGGAT
Row3-bot24	AATAGATGTATTTATATATTTTTCGTGCCCAACATACGAGGCATAAAATGGTCCGATATATAGCCTTTAATTGTATTA
Row3-bot29	AATAGATGTATTTATATATTTTTCTGAATGGGATAGGTCACGCAGAACCGTGTA
Row4-top13	ATACATCTATTATATATTTTTTAGAGCAAGAAACAATGAGCTATCTAGCCTTAAACCAGTATAATAC
Row4-top16	ATACATCTATTATATATTTTTTTCAGAGCCGCCACCCTGCCATCTTCCTGAGCATCATAATTTAATG
Row4-bot24	AATAGATGTATTTATATATTTTTTCTTGAAAGATTCATCAGTTACGGAGATCATCTTT
Row4-bot29	AATAGATGTATTTATATATTTTTTTGCAAGCGGCCAGTTTTCATCAATAGTAGTCAGCTTGCCAACAACCATCGCCCAGA
Green_dye_non_hybridizing	AATTCTCAGAGCAATTCTGATGGGTAATCATAGCTGTTTCCTGTG-[ATTO542]
Red_dye_non_hybridizing	GTTAGAATCAGAGCGGTACAAAATAGAAGGCTGGAAAC-[ATTO647N]

Red_dye_1nt_spacer	GTTAGAATCAGAGCGGTACAAAATAGAAGGCTGGAAACTCTGACGGC-[ATTO647N]
Green_dye_1nt_spacer	AATTCTCAGAGCAATTCTGATGGGTAATCATAGCTGTTTCCTGTGTGCCGTCAG-[ATTO542]

Table S4. Modified (closing, stabilization and fluorescently labelled) staples used in Version 2 of the sensor. For the closing interactions, the number of the caDNAno helix is indicated (see Fig. S17). Yellow and Red indicate complementary sequences. Green indicates the toehold used for opening. Blue indicates additional spacer elements.

Name-HelixID	**Sequence (5'->3')**
Row1-top13	ATATCACGAGCACATCAGTACGAGGGTAATTGAGCGCTGAAACCGATATCCG GTAACA
Row1-top16	GTGCTCGTGATATTTTTCCACCACCAGAGCCGTTAGC
Row1-bot24	GTGCTCGTGATATTTTTGCGGTTTGCGTATTGGGCGCCA
Row1-bot29	ATATCACGAGCACATCAGTACTTGGGAAGGGCGATGCATCGTAA
Row2-top13	ATATCACGAGCACATCAGTACTCAGAGAGATAACCCACAAGA
Row2-top16	GTGCTCGTGATATTTTTTTTTACCCTCAGAGCCGCAGATGAAT
Row2-bot24	GTGCTCGTGATATTTTTTTTTCGGCCAACGCGCGGGGAGAG
Row2-bot29	ATATCACGAGCACATCAGTACGGCCTCTTCGCTATTACCCACGGGAATAATT CGCAGGCAAGCCAA
Row3-top13	ATATCACGAGCACATCAGTACTTATTGAGTTAAGCCCATCTTACCAACGCTA TAGAC
Row3-top16	GTGCTCGTGATATTTTTTTTTTTACCGCCACCCTCAGAGCCACC
Row3-bot24	GTGCTCGTGATATTTTTTTTTTTCGTGCCAGCTGCATACGAACTA
Row3-bot29	ATATCACGAGCACATCAGTACTTCTGGCGAAAGGGGGATGTGC
Row4-top13	ATATCACGAGCACATCAGTACTTTAGAGCAAGAAACAATGAGCTATCTAGCC TTAAACCAGTATAATAC
Row4-top16	GTGCTCGTGATATTTTTTTTTTTTTCAGAGCCGCCACCCTGCCATCTTCCTG AGCATCATAATTTAATG
Row4-bot24	GTGCTCGTGATATTTTTTTTTTTTTCTTTCCAGTCGGGAAACCTGT
Row4-bot29	ATATCACGAGCACATCAGTACTTTTGCAAGGCGATTAATCTCCGTGGGAACA AAGAGCCACTGA
5bp_stabilisation_1	CATTGCACCCACGCAACCAGCTTGACGTTGTTTTTTAGACC
5bp_stabilisation_2	TTAATTGCGTTGCGCTCACTGCCTTTTTTCACAC
5bp_stabilisation_3	AACGGTACGCCAGAATCCTGAGATACAATTTGTTTTGATACCGATTTTTTGTG TG
5bp_stabilisation_4	TTGAGGGAATATTGACGGAAATTACAAAATCATTTTTTGGTCT

Red_dye_3nt_spacer	GTTAGAATCAGAGCGGTACAAAATAGAAGGCTGGAAACTTTCTGACGGC-[ATTO647N]
Green_dye_3nt_spacer	AATTCTCAGAGCAATTCTGATGGGTAATCATAGCTGTTTCCTGTGTTTGCCGTCAG-[ATTO542]

Table S5. Biotinylated staples for immobilization of DNA origami nanostructures used in both versions of the sensor. Blue indicates additional spacer elements.

Name	**Sequence (5'->3')**
Biotin1	5'Biotin-TTTATTGCCGGTTGATAGTCAGTGCCTTGAGTAACAGTGCATGAA
Biotin2	5'Biotin-TTTATTATAGTGGAAGCAATAGAGCTTACCCTCATATATTTTTGTAC
Biotin3	5'Biotin-TTTCAAACTCTTCCTGTTGACCGT
Biotin4	5'Biotin-TTTATACACCGCCAAAATACAGGTA

Table S6. DNA-DNA closing interactions used for XhoI nanosensors. Shown in purple is restriction site of XhoI. The number of the caDNAno helix is indicated (see Fig. S17).

Name-HelixID	**Sequence (5'->3')**
Row1-top 13	ATACTCGAGTTATATATTGAGGGTAATTGAGCGCTGAAACCGATATCCGGTAACA
Row1-top16	ATACTCGAGTTATATATT CCACCACCAGAGCCGTTAGC
Row1-bot24	AACTCGAGTATTTATATATTGCGGGACGTTGGGAAGAAATAGCCGGAACGTAATG
Row1-bot29	AACTCGAGTATTTATATATT TTGGGAAGGGCGATGCATCGTAA
Row2-top 13	ATACTCGAGTTATATATTTTCAAGCCTAATTTGCCAGTGAGCTA
Row2-top16	ATACTCGAGTTATATATTTACCCTCATTTTCGCAAGAAAAATAAGGCCCATTAAAAAAAGGGACAT
Row2-bot24	AACTCGAGTATTTATATATTTTCGGCCAACGCGCGGGGAGAG
Row2-bot29	AACTCGAGTATTTATATATTTGGCCTCTTCGCTATTACCCACGGGAATAATTCGCAGGCAAGCCAA
Row3-top 13	ATACTCGAGTTATATATTTTATTGAGTAAGCAGAGCGAACCTTAATTGAGATAGAAGAACTGATAGC
Row3-top16	ATACTCGAGTTATATATTTTACCTCGGGAGAAACAATAAAGGAT
Row3-bot24	AACTCGAGTATTTATATATTTTCGTGCCCAACATACGAGGCATAAAATGGTCCGATATATAGCCTTTAATTGTATTA
Row3-bot29	AACTCGAGTATTTATATATTTTCTGAATGGGATAGGTCACGCAGAACCGTGTA
Row4-top 13	ATACTCGAGTTATATATTTTTCAGAGCCGCCACCCTGCCATCTTCCTGAGCATCATAATTTAATG
Row4-top16	ATACTCGAGTTATATATTTTTTCAGAGCCGCCACCCTGCCATCTTCCTGAGCATCATAATTTAATG
Row4-bot24	AACTCGAGTATTTATATATTTTTCTTGAAAGATTCATCAGTTACGGAGATCATCTTT
Row4-bot29	AACTCGAGTATTTATATATTTTTTGCAAGCGGCCAGTTTTCATCAATAGTAGTCAGCTTGCCAACAACCATCGCCCAGA

Table S7. Antigen modified staples that were used in a sensor for anti-Dig and anti-DNP antibodies. The number of the caDNAno helix is indicated (see Fig. S17). Blue indicates additional spacer element.

Name-HelixID	**Sequence (5'->3')**
Row1-top16	[DNP]TGAGGGTAATTGAGCGCTGAAACCGATATCCGGTAACA
Row1-top13	[DNP]TCCACCACCAGAGCCGTTAGC
Row1-bot24	[DNP]TGCGGGACGTTGGGAAGAAATAGCCGGAACGTAATG
Row1-bot29	[DNP]TTTGGGAAGGGCGATGCATCGTAA
Row4-top13	[DIG]TTTAGAGCAAGAAACAATGAGCTATCTAGCCTTAAACCAGTATAATAC
Row4-top16	[DIG]TTTTCAGAGCCGCCACCCTGCCATCTTCCTGAGCATCATAATTTAATG
Row4-bot24	[DIG]TTTCTTGAAAGATTCATCAGTTACGGAGATCATCTTT
Row4-bot29	[DIG]TTTTGCAAGCGGCCAGTTTTCATCAATAGTAGTCAGCTTGCCAACAACCA TCGCCCAGA

Table S8. Sequences of opening strands used in different sensor constructs. Red indicates the mismatch.

Name	**Sequence (5'->3')**
15 bp interaction	ACTGATGTGCTCGTG
17 bp interaction	ATATATAATAGATGTAT
17 bp mismatch GC	ATATATAATA**C**ATGTAT
17 bp mismatch AT	ATATATAATAG**T**TGTAT
17 bp mismatch GC+AT	ATATATAATA**CT**TGTAT
17 bp mismatch Toehold AT	AT**T**TATAATAGATGTAT
17 bp mismatch Toehold TA	ATA**A**ATAATAGATGTAT

Table S9. Fit results as well as buffer compositions for the titration data shown in Fig. 2.

Sample	Buffer	$K_{1/2}$	n_H
2x13	10 mM Tris, 10 mM $MgCl_2$, 50 mM NaCl	100.08 ± 10.43 nM	0.9782 ± 0.084
2x13	10 mM Tris, 10 mM $MgCl_2$, 200 mM NaCl	195.05 ± 12.36 nM	0.8709 ± 0.041
2x13	10 mM Tris, 10 mM $MgCl_2$, 400 mM NaCl	601.19 ± 19.57 nM	0.8075 ± 0.019
2x13 stabilized	10 mM Tris, 10 mM $MgCl_2$, 50 mM NaCl	704.97 ± 64.84 nM	0.7997 ± 0.049
4x13	10 mM Tris, 10 mM $MgCl_2$, 50 mM NaCl	1087.31 ± 85.60 nM	1.5459 ± 0.1524
6x13	10 mM Tris, 10 mM $MgCl_2$, 50 mM NaCl	2025.14 ± 102.35 nM	1.7335 ± 0.1255

6.5.3 PUBLICATION P3

Controlled mechanochemical coupling of anti-junctions in DNA origami arrays

by

Fiona Cole[1], **Martina Pfeiffer**[1], Dongfang Wang[1], Tim Schröder, Yonggang Ke[*] and Philip Tinnefeld[*]
([1] These authors contributed equally, [*] Correspondence)

Submission pending

Author contributions:
The initial idea of the project was proposed by Philip Tinnefeld and my collaboration partner Yonggang Ke. Dongfang Wang designed the DNA origami structure. Fiona Cole designed the FRET probe, performed the corresponding measurements and wrote the analysis software. I designed the cargo release unit and the artificial energy barriers, performed the corresponding measurements and analyzed all data. Tim Schröder performed preliminary measurements on another DNA origami structure and discussed data. I wrote the manuscript together with Fiona Cole and Philip Tinnefeld.

Controlled mechanochemical coupling of anti-junctions in DNA origami arrays

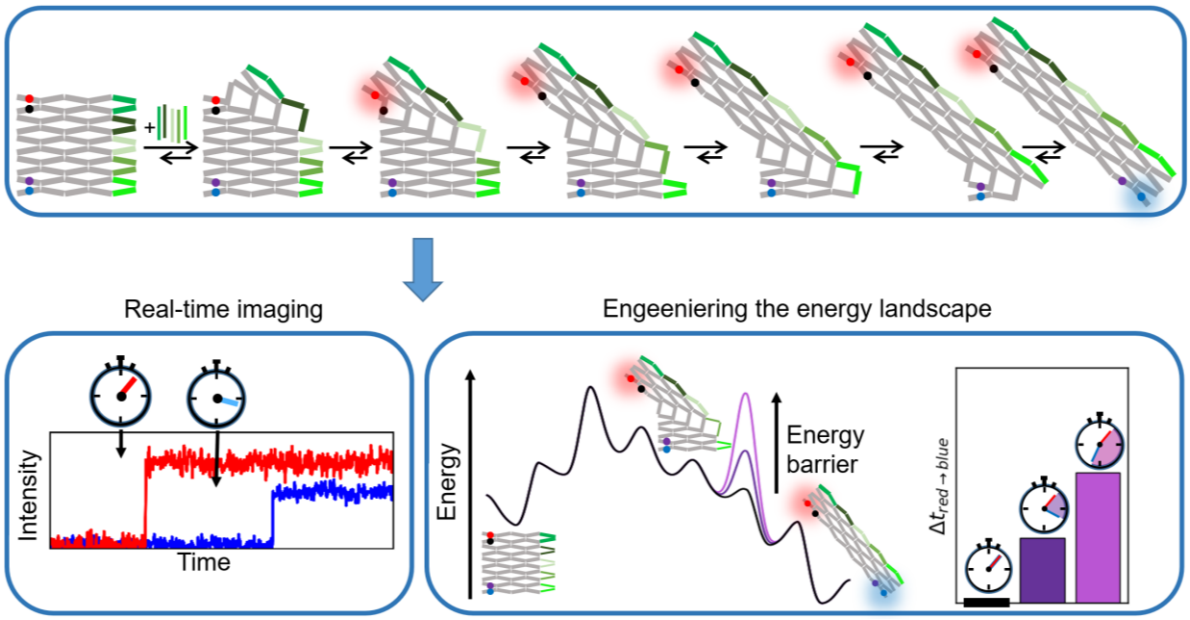

Controlled mechanochemical coupling of anti-junctions in DNA origami arrays

Fiona Cole [1,4], Martina Pfeiffer [1,4], Dongfang Wang [2,3,4], Tim Schröder [1], Yonggang Ke [2*] and Philip Tinnefeld [1*]

[1] Department of Chemistry and Center for NanoScience, Ludwig-Maximilians-Universität München, Butenandtstr. 5-13, 81377 München, Germany

[2] Wallace H. Coulter Department of Biomedical Engineering, Emory University and Georgia Institute of Technology, Atlanta, GA 30322, USA

[3] School of Biomedical Engineering and Suzhou Institute for Advanced Research, University of Science and Technology of China, Suzhou 215123, China

[4] These authors contributed equally

[*] Correspondence: philip.tinnefeld@cup.uni-muenchen.de, yonggang.ke@emory.edu

Summary

Allostery is a hallmark of cellular function and important in every biological system. Still, we are only starting to mimic it in the laboratory. Here, we introduce an approach to study aspects of allostery in artificial systems. We use a DNA origami domino array structure which – upon binding of trigger DNA strands – undergoes a stepwise allosteric conformational change. Using two FRET probes placed at specific positions in the DNA origami, we zoom in into single steps of this reaction cascade. Most of the steps are strongly coupled temporally and occur simultaneously. Introduction of activation energy barriers between different intermediate states alters this coupling and induce a time delay. We then apply these approaches to release a cargo DNA strand at a predefined step in the reaction cascade to demonstrate the applicability of this concept in tuneable cascades of mechanochemical coupling with both spatial and temporal control.

Introduction

Allostery is defined as the thermodynamic and mechanochemical coupling of binding reactions to remote conformational changes in molecular systems.[1–4] Nature provides us with a large variety of allosteric systems capable of regulating and modulating biological activity. Allosteric networks enable signal transduction[5,6] and amplification[6–8], logical gating[9,10] and cooperative and anti-cooperative behavior[11,12]. Attaining a similar level of control over these processes in laboratory would allow rationally designing and developing biomolecular networks.[13,14] Building artificial systems capable of mimicking allostery therefore represents a major bioengineering goal.[15–19]

Reconfigurable DNA origami array systems have great potential to become a platform to accommodate controlled allosteric cascade reactions over several tens of nanometers (see Fig. 1a).[15,17,18] They consist of multiple equivalent DNA anti-junctions

that each exist in two stable conformations between which they can switch through an unstable open conformation (Fig. 1b). Reconfiguration of the whole system is induced by addition of trigger DNA strands that – by hybridization to certain anti-junctions at the edge – stabilize one conformation of the addressed anti-junctions over the other. In a continuous transformation reaction, these anti-junctions relay their conformational information to neighboring anti-junctions causing them to change their conformation. This reaction repeats until all anti-junction in the array are converted in a diagonal, stepwise, highly coordinated manner. As such, the chemical energy of the trigger DNA strands binding to the structure is first converted to mechanical energy which then propagates through the structure inducing the conformational change.

Our understanding of the cascading transformation in DNA origami arrays has already been greatly improved in previous work where the transformation of DNA structures to different shapes[17,18,20–23], the initiation of proximity induced operations by the transformation process[24,25] and the realization of cascaded reactions[26] were demonstrated. However, the precise nature of the underlying energy landscape and of the transformation kinetics has remained elusive. The lack of knowledge on the mechanism of the transformation at the molecular level prevents us from controlling allosteric behavior in these systems. Therefore, there is a crucial need for new methods to acquire a deeper understanding of the energy landscape and coupling between individual anti-junctions in the transformation process. Can the coupling be altered and how does it influence the timing of the transformation as well as the possibility to create functional devices from reconfigurable DNA origami array systems?

So far, the transformation process was verified by atomic force microscopy (AFM), gel chromatography and gel chromatography combined with ensemble fluorescence measurements.[18,27] Gel chromatography analyzes only the start and the end point of the transformation process,[18,20–22,27] while AFM imaging throughout the transformation process can reveal intermediate states. These states indicate a diagonal transformation pathway which minimizes the number of simultaneously open, unstable conformations of anti-junctions. However, AFM cannot reveal the actual transformation kinetics and pathways, due to the low temporal resolution of AFM and the interference from DNA-mica and DNA-cantilever interactions.[18,22]

Here, we establish a fluorescence-based single-molecule assay to measure the time it takes for the transformation to propagate from one specific anti-junction to another non-invasively. To this end, two pairs of FRET probes were placed on two selected anti-junctions in the reconfigurable DNA origami array system. The FRET probes report on the conformation of the anti-junctions they are placed on which allows measuring their transformation times. Comparing the transformation times at different anti-junctions in single structures revealed the propagation process independent of induction (binding), diffusion or experimental synchronization commonly required by classical chemical kinetics measurements. What's more, the free selection of FRET-probe anti-junction combination allowed zooming in into every substep of the transformation process and characterizing it at the single-molecule level additionally providing access to subpopulations and kinetic heterogeneity.

Our double-FRET-probe assay provides access to important aspects of allostery in artificial systems and adds timing as an additional dimension. For a small reconfigurable DNA origami model system, we showed that most steps in the transformation cascade are coupled and how their coupling can be influenced by introducing modifications in the structure. Our understanding of the underlying energy landscape was finally used to release a cargo DNA strand at a predefined step in the transformation cascade to demonstrate the applicability of this concept in tuneable allosteric reactions.

Results

DNA origami array structure as a programmable platform for reaction cascades

We designed a small reconfigurable DNA origami array structure as a model system to establish our assay and to study allostery and mechanochemical coupling in the transformation reaction (Fig. 1a, Supplementary Tables S1-S3). The model structure is composed of 5 × 2.5 anti-junctions that can be transformed by hybridization of five trigger DNA strands to the right side of the structure. For the trigger DNA strands, an asymmetric design is chosen that energetically favors the initiation of the transformation reaction at the top right corner rather than at the bottom right corner (see Supplementary Fig. S1). This ensures that the transformation reaction always starts from the same corner, facilitating the direct comparison of transformation times of individual anti-junctions

AFM imaging confirmed the successful formation of the untransformed DNA origami model structure in a square-like shape when assembled without addition of trigger DNA strands (Fig. 1c). Overnight incubation with 50 nM of the five trigger DNA strands resulted in the quantitative transformation of the structure into its transformed oblong conformation (Fig. 1d).

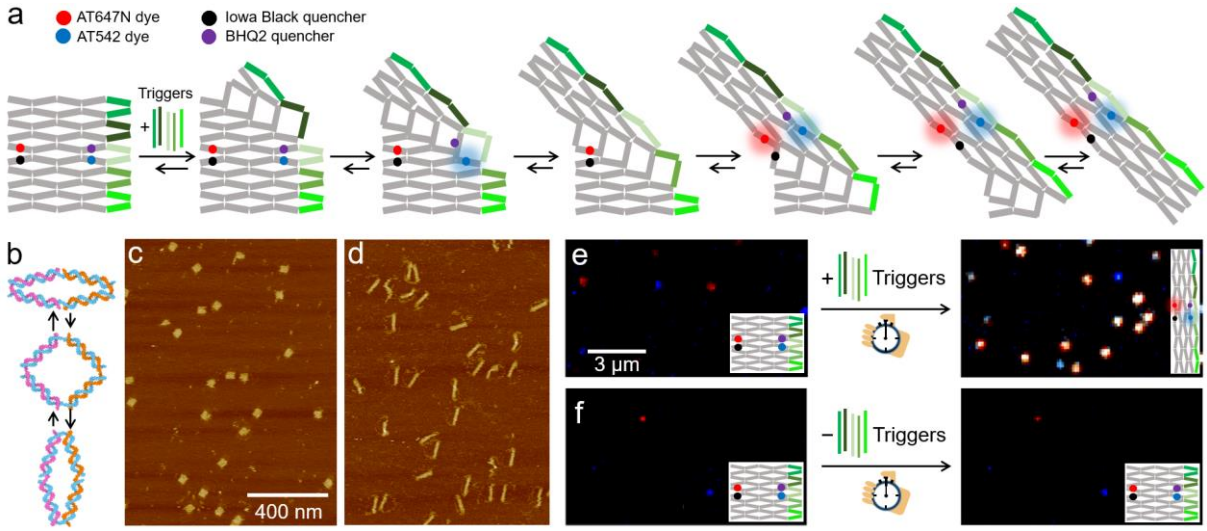

Figure 1. Concept for following the transformation reaction of reconfigurable DNA origami array structures on the single-molecule level in real time. (a) Scheme of the DNA origami array model structure transforming upon addition of DNA trigger strands. Red and green FRET probes (ATTO647N-IowaBlack RQ and ATTO542-BHQ2, red/ black and blue/ purple circles) are placed at the positions at which the transformation reaction is studied. The transformation process occurs diagonally starting either from the top right corner as shown in the sketch or from the bottom right corner. (b) Sketch of conformational flipping of a single anti-junction. Blue DNA strands represent sections of the scaffold strand, whereas pink and orange strands represent different staple strands. (c, d) AFM images of the DNA origami array (c) before and (d) after overnight incubation with trigger strands indicate a successful transformation of the structure. (e, f) Exemplary TIRF images of the DNA origami array structure before and after incubation with and without trigger strands. Fluorescence of ATTO647N is shown in red, fluorescence of ATTO542 in blue and co-localized fluorescence of both in white.

As the distances between the individual arms of the anti-junctions change during the transformation reaction, we placed two FRET-pairs as signal transduction elements that report on the transformation at specific locations within the DNA origami. In the FRET-pairs, we used photostable, single-molecule optimized fluorophores as donor dyes in the green and red spectral region (ATTO542 and ATTO647N), respectively. Appropriate dark-quenchers (IowaBlack RQ and BHQ2) as FRET acceptors were placed such that the donor was strongly quenched before the transformation reaction and lighted up in the moment of transformation. This “turn-on” configuration as exemplarily shown in the sketch of Fig. 1a ensured discrimination of transformation events from photobleaching events. Surface-immobilized structures were imaged via total internal reflection fluorescence (TIRF) microscopy using green and red, alternating excitation (see Supplementary Fig. S1, Materials and Methods for experimental details). In the resulting images, blue, red and white spots represent fluorescence of ATTO542, ATTO647N and co-localized fluorescence of both dyes, respectively.

We recorded TIRF images of DNA origami arrays bearing FRET probes (positions of FRET probes as in Fig.1a) before and after 25 min incubation with and without five trigger DNA strands. The corresponding TIRF images are shown in Fig. 1e and 1f. Before incubation, the fluorescence of both dyes is quenched. Only a small number of spots is visible which could be attributed to either mislabeled or partially transformed

structures (Fig. 1e and 1f, left images). After incubation with trigger DNA strands, we noted a significant increase of spots of co-localized fluorescence of ATTO542 and ATTO647N which did not occur after incubation without trigger DNA strands (Fig. 1e and 1f, right images). This demonstrates that the trigger induced transformation reaction of the DNA origami array structure occurred and that it could be visualized by fluorescence imaging. With a DNA reference dye for localizing DNA origami structures, we determined the transformation yield as studied with the FRET probes to have values of 79% and 95% depending on the position of the FRET probe (Supplementary Fig. S2).

Real time single-molecule observation of the transformation reaction pathway of DNA origami arrays

Next, we explored the dynamics of the transformation reaction upon addition of the five trigger DNA strands. To extract dynamic information of the transformation of individual anti-junctions in the structures, we used time-lapse imaging (alternating 640 nm and 532 nm excitation, 100 ms every 1 s per color) on the same area and extracted dual-color fluorescence transients of single structures.

Fig. 2a shows an exemplary transient recorded during the transformation reaction (for additional transients see Supplementary Fig. S3). The transient exhibits a single-step increase in fluorescence intensity occurring simultaneously for both FRET probes within the time resolution of 1 s of our measurement followed by single-step photobleaching. We interpreted the single-step increase in fluorescence as the transformation reaction progressing through the corresponding anti-junction and defined the time between the addition of the trigger DNA staples and this increase as the transformation time of the corresponding anti-junction. The transformation times at the positions of the FRET probes were extracted separately for each structure from the transients (Fig. 2b).

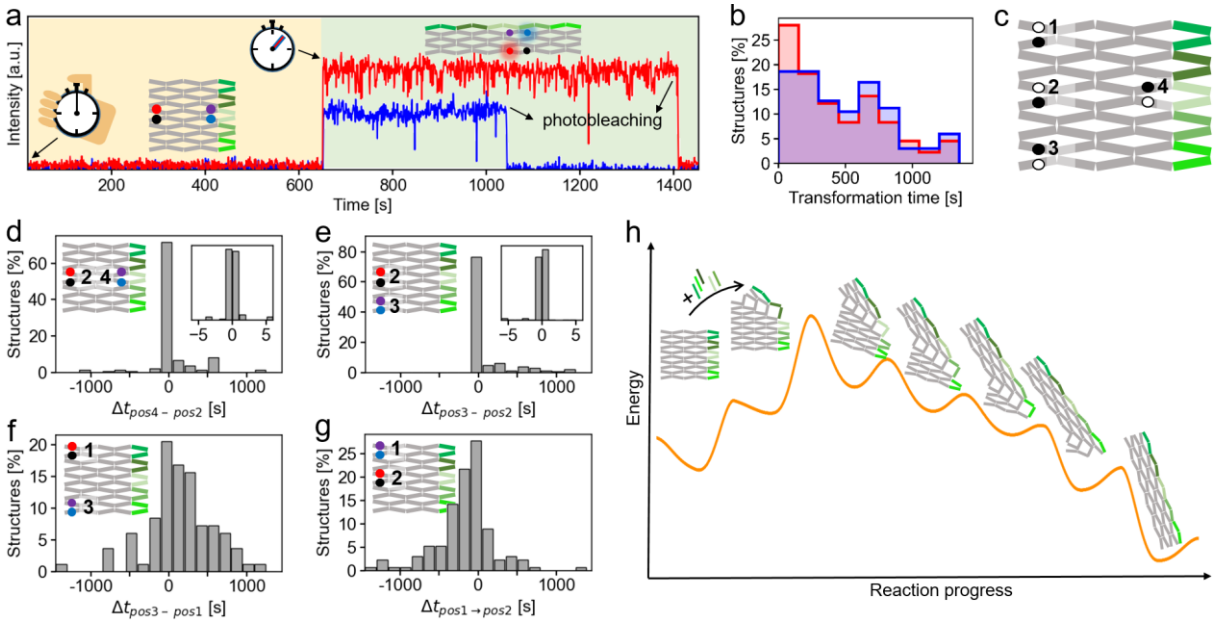

Figure 2. Real-time imaging of the transformation reaction of DNA origami arrays. (a) Representative single-molecule fluorescence intensity transients of DNA origami array with a green and a red FRET probe incorporated after addition of five trigger DNA strands at 0 s. The time the transformation occurs at the red and the green FRET probe positions is marked with an arrow. Fluorescence of ATTO647N and ATTO542 is shown in red and blue, respectively. (b) Transformation time after addition of five trigger DNA strands at the position of the red FRET probe and the green FRET probe. (c) Scheme of the different positions used for the placement of the FRET probes on DNA origami arrays for tracking the transformation reaction. (d-g) Time difference between the transformation occurring at the positions of the green and red FRET probes for different FRET probe positions. (h) Proposed, simplified energy landscape of the transformation reaction.

To visualize the transformation behavior of different anti-junction combinations, we assembled four different DNA origami array structures bearing red and green FRET probes at different anti-junctions (Position 1-4, Fig. 2c). We extracted the time differences *Δt* between the transformation occurring at the position of the green and of the red FRET probe for each single construct (Fig. 2d-2g). For the FRET probes used for the transient in Fig. 2a, this *Δt* is, for example, 0 s which is the dominating value for the anti-junction combination surveilled by the FRET probes at position 2 and 4 (Fig. 2c and 2d). Transients and transformation times for the other FRET probe combinations are provided in Supplementary Fig. S3-S7.

Time difference distributions of the transformation reactions of DNA origami array structures bearing FRET probes at Position 2 and 4 and at Position 2 and 3 showed a narrow unimodal distribution (Fig. 2d and 2e). With the exception of a few outlier values, the transformation at the studied positions occurred simultaneously within our temporal resolution of 1 s. In contrast, a time delay between the transformation at Positions 1 and Position 3 was noticed (Fig. 2f). The transformation occurred first at Position 1 and reached Position 3 after an average time of 198 s (see Supplementary Fig. S8 for controls). When the FRET probes were placed at Positions 1 and 2 (Fig. 2g), the transformation again first occurred at Position 1 before progressing to

Position 2. In combination, this implies the transformation first occurring at Position 1 before progressing to Positions 2-4 which is in accordance with the intended asymmetric trigger DNA strand design (see Supplementary Fig. S1).

Based on our single-molecule fluorescence measurements and previously reported AFM data,[18] we propose a model for the energy landscape of the transformation reaction in our DNA origami array (Fig. 2h). Start and end points of the transformation reaction are the thermodynamically stable transformed and untransformed conformations in which all anti-junctions adapt the same conformation. In all transformation intermediates, some anti-junctions adapt an unstable open conformation. We estimate the energy of those intermediates based on their number of open anti-junctions. The more open anti-junctions a conformation has, the less stable it is. Hybridization of all five trigger DNA strands tilts the energy landscape of the transformation reaction towards the transformed conformation. During the first and second step of the diagonal transformation reaction, the number of anti-junctions which are forced into their thermodynamically unfavored open conformation increases. Thus, the corresponding steps are accompanied by high activation energies, resulting in the measured time delay between the transformation occurring at Position 1 and all other positions. In consecutive steps, the number of instable open anti-junctions remains the same and eventually decreases which explains the observed quasi-simultaneous transformation at these positions.

Mechanochemical coupled and uncoupled transformation of anti-junctions in DNA origami array structures

To study the coupling between the transformation steps and how it can be influenced, we first reduced the driving force of the transformation reaction by reducing the number of added trigger DNA strands from all five to only the upper four. Fig. 3a-3f shows exemplary single-molecule fluorescence transients of structures with FRET probes placed at different positions. Upon addition of all five trigger DNA strands, over 90% of all transients showed only one irreversible transformation step – independent of the positions of the FRET probes (Fig. 3a, 3b and 3g, Supplementary Figs. S3-S6).

When adding only the upper four trigger DNA strands, a significant fraction of transients showed intensity fluctuations between two well-defined levels for Positions 2-4 (Fig. 3c-3f, Supplementary Fig. S9). In contrast, at Position 1, the fraction of transients exhibiting fluctuations remained at a similarly low level as when adding all five trigger DNA strands (Fig. 3d, 3f and 3g, Supplementary Fig. S9). We ascribe the emerging fluctuations to reversible transformations of the respective anti-junctions.

A comparison of the transformation times between the studied positions (Fig. 3h, Supplementary Fig. S10) shows the same trends as the transformation upon addition of all five trigger DNA strands. As such, the transformation reaction first irreversibly progresses through Position 1 followed by simultaneous time-delayed reversible transformations at Positions 2-4. However, the time between the transformation occurring at Position 1 and Positions 2-4 increased compared to the time upon addition of all five trigger DNA strands (Fig. 3h). While this indicates that the kinetics of the overall transformation reaction was slowed down by reducing the number of trigger

DNA strands added, it did not affect the coupling between anti-junctions to an extent that we could visualize their separate transformations. Further reduction of the number of trigger DNA strands to three or less led to the transformation reaction being either incomplete or not initiated at all.

To further investigate the fluctuating behaviour of the anti-junctions upon addition of the upper four trigger DNA strands, we quantified the amount of fluctuating structures 24 h after addition of the trigger DNA strands. While in many cases, the reversible fluctuations ceased and the fully transformed conformation was adapted in the first 25 min after addition of the trigger DNA strands (Fig. 3c, 3d and 3f), 24 h after addition of the upper four trigger DNA strands, still a substantial fraction of 30% of fluctuating structures was observed. This shows that structures can return from the fully transformed to a fluctuating state (Supplementary Fig. S11).

Interestingly, for Positions 2-4, the reversible transformations seemed to occur quasi-simultaneously at the different anti-junctions (Fig. 3c and 3e, Supplementary Fig. S9). To quantify the extent of this correlated behavior, we introduced the coupling parameter *C* (Supplementary Fig. S12) that reports on the time two anti-junctions spend in the same conformation (untransformed or transformed) compared to the time they spend in differing conformations. A maximum value of $C = 1$ corresponds to a DNA origami array with maximally coupled junctions in which only fully correlated fluctuations occur. The closer the value is to $C = 0$, the larger is the time the studied junctions spend in differing conformations and the smaller is the extent of coupling. Systems with $C > 0.95$ are considered fully coupled.

Fig. 3i-3l show the coupling distributions for the transformation of DNA origami arrays with FRET probes at the strongly coupled Positions 2 and 4, and at the less coupled Positions 1 and 3 upon addition of all five and only the upper four trigger DNA strands. In the coupled system, 67% and 56% of all structures exhibited perfect coupling for the transformation upon addition of five and four trigger DNA strands, respectively, indicating that in many structures also all fluctuations are fully correlated. The coupling distribution of the less coupled systems also feature a small distinct peak at $C > 0.95$ (highlighted by the orange bar, 8% and 23% for the addition of five and four trigger DNA strands, respectively) and an additional larger right-skewed distribution close to $C = 0$. Thus, the majority of all systems exhibit largely uncoupled behavior. The coupling distributions of all other studied systems are shown in Supplementary Fig. S13 and are in good agreement with the proposed transformation reaction cascade starting at Position 1 and progressing to Positions 2-4 at which strongly coupled behavior was observed.

By reducing the number of added trigger DNA strands from five to the upper four, the untransformed conformation was destabilized less, resulting in a slower transformation reaction (Fig. 3h). The destabilization of the transformed conformations yielded reversible transformations at 37°C (Fig. 3m and 3n) as described by the energy landscape in Fig. 3o.

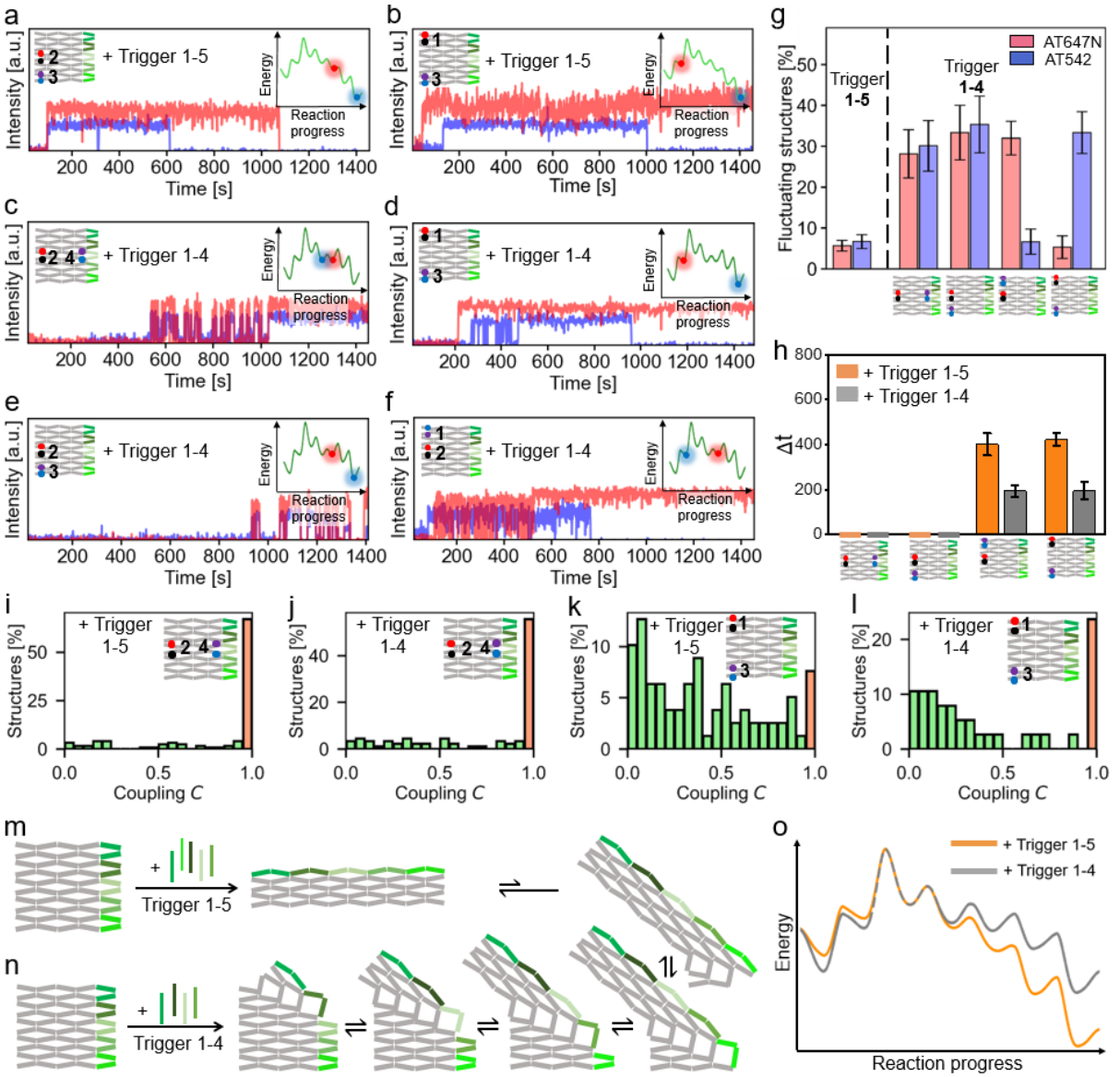

Figure 3. Reversibility and coupling in the transformation reaction upon addition of different numbers of trigger DNA strands. (a-f) Representative single-molecule fluorescence intensity transients of DNA origami arrays with FRET probes placed at different positions upon the addition of (a, b) all five trigger DNA strands and (c-f) only the upper four trigger strands at 0 s. (g) Fraction of structures exhibiting fluctuations between the untransformed and transformed conformation at the different positions of the FRET probes upon addition of all five or the upper four trigger strands. Error bars represent the standard error of at least 80 structures. (h) Mean absolute time differences for the transformation occurring at the different positions upon addition of five trigger strands and upon the addition of the upper four trigger DNA strands. For designs in which the majority of structures exhibited a time delay between the transformation at the different positions, only non-perfectly coupled structures with $\Delta t \neq 0$ s were considered. All plots show the mean values and standard errors of Gaussian fits to the corresponding time difference distributions. (i-l) Coupling histograms for DNA origami array structures with the FRET probes at different positions. The fraction of structures exhibiting full coupling is indicated by an orange bar. (m, n) Scheme of the transformation reaction upon addition of five and the upper four trigger strands. (o) Proposed, simplified energy landscape of the transformation reaction with four and five trigger strands.

Decoupling of anti-junctions in DNA origami array structures by introduction of artificial activation energy barriers

With a deeper understanding on the transformation mechanism, we then aimed for modulating the transformation reaction via selective decoupling of anti-junctions. First, we weakened the coupling between individual positions, i.e., between Positions 2 and 3, by engineering the energy landscape at the corresponding step to introduce a heightened activation energy barrier (Fig. 4a). In addition to an unmodified reference (Design 1), three DNA origami arrays bearing FRET probes at Positions 2 and 3 were assembled (Fig. 4b, Supplementary Table S4). In the second array, a locking mechanism was introduced. The mechanism consists of two complementary DNA strands protruding from the origami surface which are in close proximity in the untransformed and further apart in the transformed conformation. Hybridization of the two strands thus stabilizes the untransformed conformation and increases the energy necessary to induce the transformation at the corresponding position (Design 2). For the third and fourth array (Designs 3 and 4), staple strands around positions of central anti-junctions in the structure were left out during assembly of the structures (Supplementary Table S4).

The time lags between the transformation occurring at Position 2 and 3 upon addition of all five trigger DNA strands are shown in Fig. 4c for all four designs (Supplementary Fig. S14 for time difference histograms). The corresponding coupling distributions are shown in Fig. 4d-4f. In Design 1, the transformation at Positions 2 and 3 was strongly coupled (Fig. 4d) with $C > 0.95$ for 73% of all structures. In Design 2, the extent of coupling was reduced and only 40% of all structures exhibited a coupling of $C > 0.95$ (Fig. 4e). This tendency became even more pronounced for Design 3, for which only 12% of structures exhibited a coupling of $C > 0.95$. In the uncoupled structures of Design 2, the transformation preferentially occurred first at Position 2 before progressing to Position 3. In Design 3, the order of events was reversed and the transformation occurred at Position 3 before progressing to Position 2. For Design 4, the transformation stopped after Position 2 such that it did not progress to Position 3 at all, rendering the global transformation incomplete.

The data shows that the energy landscape of the transformation reaction could be specifically tailored to selectively weaken the coupling between Position 2 and 3 to different extents in Designs 2-4. We concluded that the incorporation of locking units (Design 2) and leaving out staple strands (Design 3, 4) at positions transforming at different steps in the transformation reaction cascade form efficient tools to engineer different extents of coupling and time delays within cascade systems.

Using Design 2, we additionally studied the energy transport efficiency of the transformation reaction at the position of the locking unit. By stepwise increasing the number of hybridizing base pairs of the locking unit (Supplementary Table S4), we systematically varied the hybridization energy of the unit. Quantification of the number of structures transforming at Position 3 within 25 min revealed a 50% transport efficiency for a hybridization energy of 16.0 ± 0.5 kcal/ mol (Supplementary Fig. S15).

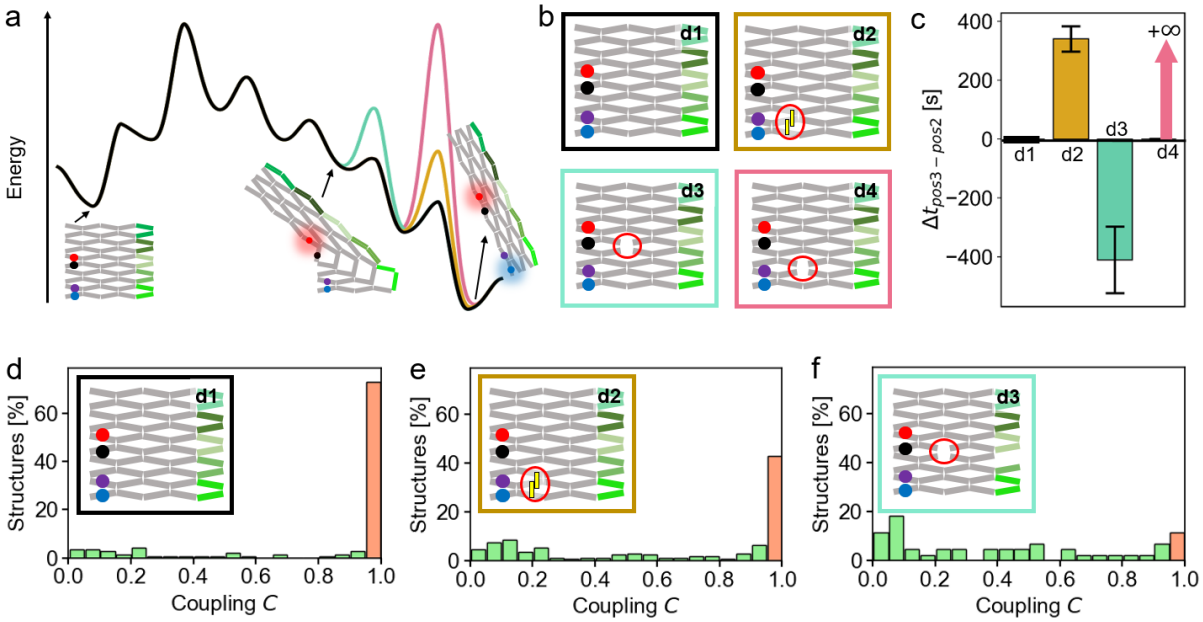

Figure 4. Temporal decoupling of different steps in the transformation reaction by artificially introducing energy barriers. (a, b) Mechanisms used to engineer the energy landscape. d1 corresponds to the unmodified reference, d2 to a system with a locking unit incorporated and d3 and d4 to systems with missing central anti-junctions. (c) Lag times for the transformation to progress from Position 2 to Position 3 upon addition of all five trigger DNA strands in the systems shown in (b). Error bars represent the standard deviation of the Gaussian fit of the corresponding time difference histograms. For designs in which the majority of structures exhibited a time delay between the transformation at the different positions, only non-perfectly coupled structures with $\Delta t \neq 0$ s were considered. All plots show the mean values and standard errors of Gaussian fits to the corresponding time difference distributions. (d-f) Corresponding coupling histograms. The fraction of structures exhibiting full coupling ($C > 0.95$) is indicated by an orange bar.

Besides quantifying how much energy is transferable at a specific step in the transformation reaction, we also demonstrated the transfer of a cargo DNA strand to the environment. Based on the principle of allosteric inhibition, we designed a cargo release unit to which a cargo DNA strand binds in the untransformed conformation. Upon binding of the trigger DNA strands to the transformation origami and the subsequent transformation of the cargo release unit, the binding of the cargo DNA strand to the unit is weakened, resulting in its release. In this process, the mechanical energy of the conformational change is reconverted to chemical energy to dehybridize the cargo DNA strand from the structure – tens of nanometers away from the initial activation site. (Supplementary Fig. S16 and S17, Supplementary Note S1).

Conclusion

In conclusion, we established a double-FRET single molecule assay to reveal insights into the allosteric transformation reaction cascade of reconfigurable DNA origami

arrays. The assay allowed zooming in into single steps of the cascade process, making it possible to characterize the transformation reaction cascade including intermediates. For our DNA origami array model structure, the energy landscape pre-dominantly depends on the number of open anti-junctions of the intermediates. As such, the first few steps are accompanied by comparably high activation energies whereas all following steps occur quasi-simultaneously. Our assay allowed us to define strategies to tailor the transformation reaction cascade both globally and at pre-defined steps. Incorporation of different locking elements into the structure introduces artificial energy barriers, resulting in weakened coupling between selected intermediates which, in the extreme, leads to altered transformation pathways or incomplete transformations.

The principal findings should be applicable to more complex DNA origami array systems. Such systems could feature different proximity-induced operations. Exemplarily, we demonstrated a cargo DNA strand released at a predefined step in the transformation reaction cascade (see Supplementary Figure S15). The combination of the transformation reaction cascade with its intrinsic allosteric control, the addressability of the DNA origami approach and the findings our double-FRET single molecule assay revealed, DNA origami arrays reveals its potential for a universal platform to engineer spatially controlled reactions of information and energy transfer. In addition to the prototypical allosteric transfer of spatial information, we added the dimension of temporal control as timing between certain elements could be engineered. Overall, we envision that further developing these approaches will pave the way for DNA origami array systems being used as a platform for programmable, artificial reaction networks containing elements such as cooperativity and anti-cooperativity,[28] rows of logical gating[29,30] as well as signal amplification[31] and transduction over several tens of nanometers.

Resource availability

Lead contact

Philip Tinnefeld: Department of Chemistry and Center for NanoScience, Ludwig-Maximilians-Universität München, Butenandtstr. 5-13, 81377 München, Germany. Philip.tinnefeld@cup.uni-muenchen.de

Materials and Methods

Synthesis of DNA origami arrays

DNA origami structures were designed using the open-source software caDNAno2 (Douglas et al., 2009) and assembled and purified using published protocols (Wagenbauer et al., 2017). For the exact sequences of all unmodified and modified DNA staple strands used to fold the DNA origami structures see Tables S1 and S2. DNA staple strands were purchased from Eurofins Genomics GmbH (Germany) and Integrated DNA Technologies (USA).

For DNA origami folding, 25.0 µL of in house produced p1800 scaffold at 100 nM were mixed with 3.4 µL of unmodified staples, 2.3 µL of loop staples and 8.6 µL of modified staples pooled from 100 µM original concentration. Briefly, 5.0 µL of 10x TAE buffer (400 mM Tris, 400 mM acetic acid, 10 mM EDTA, pH 8), 6.0 µL of 100 mM $MgCl_2$ and 7.1 µL water were added and the mixture was heated to 65 °C in a thermocycler. The solution was kept at this temperature for 15 min before being cooled down to 25 °C with a temperature gradient of – 1 °C min^{-1}. Folded DNA origamis were purified from excessive staple strands by gel electrophoresis. All gels were ran using a 1.5% agarose gel, 1xTAE (40 mM Tris, 40 mM acetic acid, 1 mM EDTA, pH 8) containing 12.5 mM $MgCl_2$ for 2 hours at 6 V/cm. The target band containing DNA origami was cut from the gel and DNA origami solution extracted from the band via squeezing.

Atomic force microscopy (AFM) measurements

The AFM imaging was carried out on the Multimode VIII system (Bruker). 2 µL of the sample was deposited onto freshly cleaved mica surface. Take 80 µL 1×TE buffer with 10 mM $MgCl_2$ to fill the sample area. The sample was imaged in liquid mode using commerical tips (SNL-10, Bruker). The imaging results were analyzed with Nanoscope analysis (Bruker).

Sample preparation on the coverslip for single-molecule widefield measurements

For chamber preparation, adhesive SecureSeal™ Hybridization Chambers (2.6 mm depth, Grace Bio-Labs, USA) were glued on microscope coverslips of 24 mm × 60 mm size and 170 µm thickness (Carl Roth GmbH, Germany). The created wells were incubated with 1 M KOH for 1 h and washed three times with 1×PBS buffer. After surface passivation by incubation with BSA-Biotin (0.5 mg/mL, Sigma Aldrich, USA) for 10 min, the surface was washed with 200 µL 1× PBS buffer. 150 µL neutravidin (0.25 mg/mL, Thermo Fisher, USA) was incubated for 10 min and then washed three times with 150 µL 1× PBS buffer. Surface immobilization was achieved via biotin-neutravidin interactions. For this, we incorporated one biotinylated DNA staple strand in the loop of the DNA origami structure during folding. The DNA origami solution was diluted with 1× TE buffer containing 750 mM NaCl to a concentration of ~10 pM and then immobilized on the biotin-neutravidin surface via biotin-neutravidin interactions. For this, 150 µL of the DNA origami sample solution was added and incubated for 5 min. Residual unbound DNA origami was removed by washing the chambers with 150 µL 1x TE buffer containing 750 mM NaCl. The density of DNA origami on the surface suitable for single-molecule measurements was checked on a TIRF microscope. For single-molecule fluorescence measurements, an oxidizing and reducing buffer system (1x TAE, 12.5 mM $MgCl_2$, 2 mM Trolox/Troloxquinone)[32] was used in combination with an oxygen scavenging system (12 mM protocatechuic acid, 56 µM protocatechuate 3,4-dioxygenase from pseudomonas sp., 1% glycerol, 1 mM KCl, 2 mM Tris HCl, 20 µM EDTA-Na_2*$2H_2O$) to suppress blinking and photobleaching.

Loading of the cargo release unit

The cargo release unit was loaded with an ATTO542 labelled cargo DNA strand by incubating surface immobilized origami structures with 100 nM cargo strand in 1x TAE containing 12.5 mM $MgCl_2$ for 10 min. To remove excess cargo DNA strands, samples were washed three times with 150 µL 1x TE buffer containing 750 mM NaCl and then prepared for imaging.

DNA origami transformation procedure

For the transformation of DNA origami structures, an excess of trigger DNA strands (50 nM) were added to photostabilized DNA origami sample chambers at 37 °C. Immediately after addition of the trigger strands, the sample chambers were sealed and the DNA origami imaged.

Wide-field measurements

For detection of single-molecule fluorescence, a commercial wide-field/TIRF microscope Nanoimager from Oxford Nanoimaging Ltd. was used. Red excitation at 638 nm was realized with a 1100 mW laser, green excitation at 532 nm with a 1000 mW laser, respectively. The relative laser intensities were set to 9% for green and to 18% for red excitation. The microscope was set to TIRF illumination. Data acquisition was initialized by activating the lasers and taking a frame of 100 ms every second separately for both excitation lasers (with a time lag of 0.5 s between them) over a measurement period of 25 min. Measurements were carried out at 37 °C.

Data analysis

Data processing and analysis of time-lapse movies was realized using custom-written Python scripts. Briefly, the acquired movies were first drift corrected using DNA origami structures carrying fluorophores which were in their fluorescent state throughout the whole measurement as fiducial markers. Spots appearing during the measurement were detected from the drift-corrected movies and dual-color background-subtracted fluorescence intensity transients of those spots extracted. To determine transformation times and coupling of single structures, the corresponding transients were fitted using a Hidden Markov model (HMM). In this model, two levels corresponding to the untransformed (level 0) and transformed state (level 1) of the structure were defined. Transformation times were defined as the time a structure switches from its untransformed state to its transformed state and subsequently remains in its transformed state for at least 10 s for the first time. They were extracted from the fitted HMM transients. For the calculation of the Coupling between different positions in a structure, transformations state occupancy density plots were created from the dual-color HMM transients. As the ATTO647N and the ATTO542 fluorescence transients were recorded with a time lag of 0.5 sec between them, data points measured in the frame directly before and directly after intensity jumps as determined by the HMM fits

were excluded to not artificially weaken the Coupling. The further workflow for calculating the Coupling is given in Supplementary Figure S11.

For determining the fraction of fluorophores experiencing photobleaching over the 25 min measurement period, all transients were considered. For all further transient analysis, only transients in which both fluorophores turned into their fluorescent state were considered.

All Python scripts used for data analysis are available from the authors upon reasonable request.

Acknowledgments

P.T. gratefully acknowledges financial support from the Federal Ministry of Education and Research (BMBF) and the Free State of Bavaria under the Excellence Strategy of the Federal Government and the Länder through the ONE MUNICH Project Munich Multiscale Biofabrication. Y.K. acknowledges the support of a DOE grant DE-SC0020996. M.P. acknowledges the support by Studienstiftung des Deutschen Volkes. The authors thank Luna, Charly and Xaverl for their support with the measurements and Angelika, Hildegard, Frau Steger and Herr Ehrl for lab upkeep.

Author contributions

All authors conceived and developed the concept. M.P., D.W. and F.C. prepared samples, performed and analyzed the measurements. Y.K. and P.T. supervised the project. All authors have written, read and approved the final manuscript.

Declaration of interests

The authors declare no conflict of interest.

Data availability

All data are available upon reasonable request from the corresponding author.

References

(1) MONOD, J.; JACOB, F. Teleonomic mechanisms in cellular metabolism, growth, and differentiation. *Cold Spring Harbor symposia on quantitative biology* **1961**, *26*, 389–401. DOI: 10.1101/sqb.1961.026.01.048.
(2) Monod, J.; Changeux, J.-P.; Jacob, F. Allosteric proteins and cellular control systems. *Journal of Molecular Biology* **1963**, *6* (4), 306–329. DOI: 10.1016/S0022-2836(63)80091-1.
(3) Monod, J.; Wyman, J.; Changeux, J.-P. On the nature of allosteric transitions: A plausible model. *Journal of Molecular Biology* **1965**, *12* (1), 88–118. DOI: 10.1016/s0022-2836(65)80285-6.
(4) Koshland, D. E.; Némethy, G.; Filmer, D. Comparison of experimental binding data and theoretical models in proteins containing subunits. *Biochemistry* **1966**, *5* (1), 365–385. DOI: 10.1021/bi00865a047.
(5) Changeux, J.-P.; Edelstein, S. J. Allosteric mechanisms of signal transduction. *Science (New York, N.Y.)* **2005**, *308* (5727), 1424–1428. DOI: 10.1126/science.1108595.
(6) Buddingh', B. C.; Elzinga, J.; van Hest, J. C. M. Intercellular communication between artificial cells by allosteric amplification of a molecular signal. *Nature communications* **2020**, *11* (1), 1652. DOI: 10.1038/s41467-020-15482-8. Published Online: Apr. 3, 2020.
(7) Ma, B.; Nussinov, R. Amplification of signaling via cellular allosteric relay and protein disorder. *Proceedings of the National Academy of Sciences of the United States of America* **2009**, *106* (17), 6887–6888. DOI: 10.1073/pnas.0903024106. Published Online: Apr. 22, 2009.
(8) Zhu, L.; Anslyn, E. V. Signal amplification by allosteric catalysis. *Angewandte Chemie (International ed. in English)* **2006**, *45* (8), 1190–1196. DOI: 10.1002/anie.200501476.
(9) Galstyan, V.; Funk, L.; Einav, T.; Phillips, R. Combinatorial Control through Allostery. *The journal of physical chemistry. B* **2019**, *123* (13), 2792–2800. DOI: 10.1021/acs.jpcb.8b12517. Published Online: Mar. 4, 2019.
(10) Lim, W. A. The modular logic of signaling proteins: building allosteric switches from simple binding domains. *Current Opinion in Structural Biology* **2002**, *12* (1), 61–68. DOI: 10.1016/S0959-440X(02)00290-7.
(11) Gruber, R.; Horovitz, A. Allosteric Mechanisms in Chaperonin Machines. *Chemical Reviews* **2016**, *116* (11), 6588–6606. DOI: 10.1021/acs.chemrev.5b00556. Published Online: Jan. 4, 2016.
(12) Yuan, Y.; Tam, M. F.; Simplaceanu, V.; Ho, C. New look at hemoglobin allostery. *Chemical Reviews* **2015**, *115* (4), 1702–1724. DOI: 10.1021/cr500495x. Published Online: Jan. 21, 2015.
(13) Zhang, C.; Ma, X.; Zheng, X.; Ke, Y.; Chen, K.; Liu, D.; Lu, Z.; Yang, J.; Yan, H. Programmable allosteric DNA regulations for molecular networks and nanomachines. *Science advances* **2022**, *8* (5), eabl4589. DOI: 10.1126/sciadv.abl4589. Published Online: Feb. 2, 2022.
(14) Kholodenko, B.; Yaffe, M. B.; Kolch, W. Computational approaches for analyzing information flow in biological networks. *Science signaling* **2012**, *5* (220), re1. DOI: 10.1126/scisignal.2002961. Published Online: Apr. 17, 2012.

(15) Yan, Q.; Wang, Y.; Shi, J.; Wei, B. Allostery of DNA nanostructures controlled by enzymatic modifications. *Nucleic Acids Res* **2020**, *48* (13), 7595–7600. DOI: 10.1093/nar/gkaa488.
(16) Pfeiffer, M.; Trofymchuk, K.; Ranallo, S.; Ricci, F.; Steiner, F.; Cole, F.; Glembockyte, V.; Tinnefeld, P. Single antibody detection in a DNA origami nanoantenna. *iScience* **2021**, *24* (9), 103072. DOI: 10.1016/j.isci.2021.103072. Published Online: Sep. 1, 2021.
(17) Cui, Y.; Chen, R.; Kai, M.; Wang, Y.; Mi, Y.; Wei, B. Versatile DNA Origami Nanostructures in Simplified and Modular Designing Framework. *ACS nano* **2017**, *11* (8), 8199–8206. DOI: 10.1021/acsnano.7b03187. Published Online: Jul. 6, 2017.
(18) Song, J.; Li, Z.; Wang, P.; Meyer, T.; Mao, C.; Ke, Y. Reconfiguration of DNA molecular arrays driven by information relay. *Science (New York, N.Y.)* **2017**, *357* (6349). DOI: 10.1126/science.aan3377. Published Online: Jun. 22, 2017.
(19) Gerling, T.; Wagenbauer, K. F.; Neuner, A. M.; Dietz, H. Dynamic DNA devices and assemblies formed by shape-complementary, non-base pairing 3D components. *Science (New York, N.Y.)* **2015**, *347* (6229), 1446–1452. DOI: 10.1126/science.aaa5372.
(20) Wang, D.; Song, J.; Wang, P.; Pan, V.; Zhang, Y.; Cui, D.; Ke, Y. Design and operation of reconfigurable two-dimensional DNA molecular arrays. *Nature protocols* **2018**, *13* (10), 2312–2329. DOI: 10.1038/s41596-018-0039-0.
(21) Wang, D.; Yu, L.; Huang, C.-M.; Arya, G.; Chang, S.; Ke, Y. Programmable Transformations of DNA Origami Made of Small Modular Dynamic Units. *Journal of the American Chemical Society* **2021**, *143* (5), 2256–2263. DOI: 10.1021/jacs.0c10576. Published Online: Feb. 2, 2021.
(22) Wang, D.; Yu, L.; Ji, B.; Chang, S.; Song, J.; Ke, Y. Programming the Curvatures in Reconfigurable DNA Domino Origami by Using Asymmetric Units. *Nano letters* **2020**, *20* (11), 8236–8241. DOI: 10.1021/acs.nanolett.0c03348. Published Online: Oct. 23, 2020.
(23) Liu, Y.; Cheng, J.; Fan, S.; Ge, H.; Luo, T.; Tang, L.; Ji, B.; Zhang, C.; Cui, D.; Ke, Y.; Song, J. Modular Reconfigurable DNA Origami: From Two-Dimensional to Three-Dimensional Structures. *Angewandte Chemie (International ed. in English)* **2020**, *59* (51), 23277–23282. DOI: 10.1002/anie.202010433. Published Online: Oct. 13, 2020.
(24) Fan, S.; Wang, D.; Cheng, J.; Liu, Y.; Luo, T.; Cui, D.; Ke, Y.; Song, J. Information Coding in a Reconfigurable DNA Origami Domino Array. *Angewandte Chemie (International ed. in English)* **2020**, *59* (31), 12991–12997. DOI: 10.1002/anie.202003823. Published Online: May. 20, 2020.
(25) Fan, S.; Cheng, J.; Liu, Y.; Wang, D.; Luo, T.; Dai, B.; Zhang, C.; Cui, D.; Ke, Y.; Song, J. Proximity-Induced Pattern Operations in Reconfigurable DNA Origami Domino Array. *Journal of the American Chemical Society* **2020**, *142* (34), 14566–14573. DOI: 10.1021/jacs.0c06061. Published Online: Aug. 12, 2020.
(26) Fan, S.; Ji, B.; Liu, Y.; Zou, K.; Tian, Z.; Dai, B.; Cui, D.; Zhang, P.; Ke, Y.; Song, J. Spatiotemporal Control of Molecular Cascade Reactions by a Reconfigurable DNA Origami Domino Array. *Angewandte Chemie (International ed. in English)* **2022**, *61* (9), e202116324. DOI: 10.1002/anie.202116324. Published Online: Jan. 11, 2022.

(27) Liu, Y.; Ge, H.; Wang, Y.; Tang, L.; Pei, Y.; Fan, S.; Song, Y.; Zhang, C.; Song, J. Multistep Transformations of DNA Origami Domino Array via Mechanical Forces. *Small Structures* **2022**, 2200167. DOI: 10.1002/sstr.202200167.
(28) Simon, A. J.; Vallée-Bélisle, A.; Ricci, F.; Plaxco, K. W. Intrinsic disorder as a generalizable strategy for the rational design of highly responsive, allosterically cooperative receptors. *Proceedings of the National Academy of Sciences of the United States of America* **2014**, *111* (42), 15048–15053. DOI: 10.1073/pnas.1410796111. Published Online: Oct. 6, 2014.
(29) Chatterjee, G.; Dalchau, N.; Muscat, R. A.; Phillips, A.; Seelig, G. A spatially localized architecture for fast and modular DNA computing. *Nature Nanotech* **2017**, *12* (9), 920–927. DOI: 10.1038/nnano.2017.127. Published Online: Jul. 24, 2017.
(30) Shah, S.; Wee, J.; Song, T.; Ceze, L.; Strauss, K.; Chen, Y.-J.; Reif, J. Using Strand Displacing Polymerase To Program Chemical Reaction Networks. *Journal of the American Chemical Society* **2020**, *142* (21), 9587–9593. DOI: 10.1021/jacs.0c02240. Published Online: May. 12, 2020.
(31) Wang, B.; Barahona, M.; Buck, M. Engineering modular and tunable genetic amplifiers for scaling transcriptional signals in cascaded gene networks. *Nucleic Acids Res* **2014**, *42* (14), 9484–9492. DOI: 10.1093/nar/gku593. Published Online: Jul. 16, 2014.
(32) Cordes, T.; Vogelsang, J.; Tinnefeld, P. On the mechanism of Trolox as antiblinking and antibleaching reagent. *Journal of the American Chemical Society* **2009**, *131* (14), 5018–5019. DOI: 10.1021/ja809117z.

Supporting Information

Controlled mechanochemical coupling of anti-junctions in DNA origami arrays

Fiona Cole [1,4], Martina Pfeiffer [1,4], Dongfang Wang [2,3,4], Tim Schröder [1], Yonggang Ke [2*] and Philip Tinnefeld [1*]

[1] Department of Chemistry and Center for NanoScience, Ludwig-Maximilians-Universität München, Butenandtstr. 5-13, 81377 München, Germany

[2] Wallace H. Coulter Department of Biomedical Engineering, Emory University and Georgia Institute of Technology, Atlanta, GA 30322, USA

[3] School of Biomedical Engineering and Suzhou Institute for Advanced Research, University of Science and Technology of China, Suzhou 215123, China

[4] These authors contributed equally

[*] Correspondence: philip.tinnefeld@cup.uni-muenchen.de, yonggang.ke@emory.edu

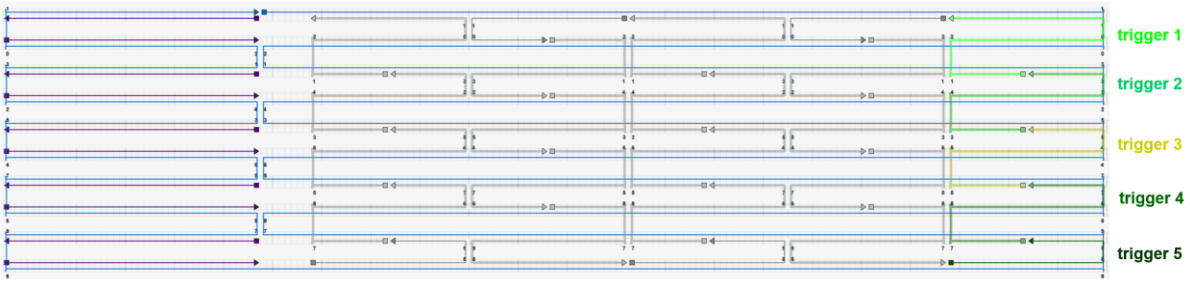

Figure S1. Design of the 5 × 2.5 reconfigurable DNA origami array model structure in its untransformed conformation. Blue, gray, purple and green lines represent the scaffold strand, core DNA staple strands of the structure, loop staple strands and trigger DNA strands, respectively. The DNA loop spans the structure from one end to the other, but does not participate in the transformation process. By labeling one of the staple strands with biotin, we use it as anker point for surface immobilization via biotin-neutravidin interactions. This allows us to avoid directly tethering the core structure (gray staples) to the surface which could possibly affect the transformation process. Trigger DNA strands 1-4 all have the same length of 65 base pairs. Trigger DNA strand 5 is shorter, consisting of only 39 base pairs. As the transformation process is starts either at the upper right (trigger 1) or lower right corner (trigger 5), this asymmetry induces a preferential transformation starting point. The longer length of trigger 1 compared to trigger 5 results in the transformation preferentially starting from the upper right corner.

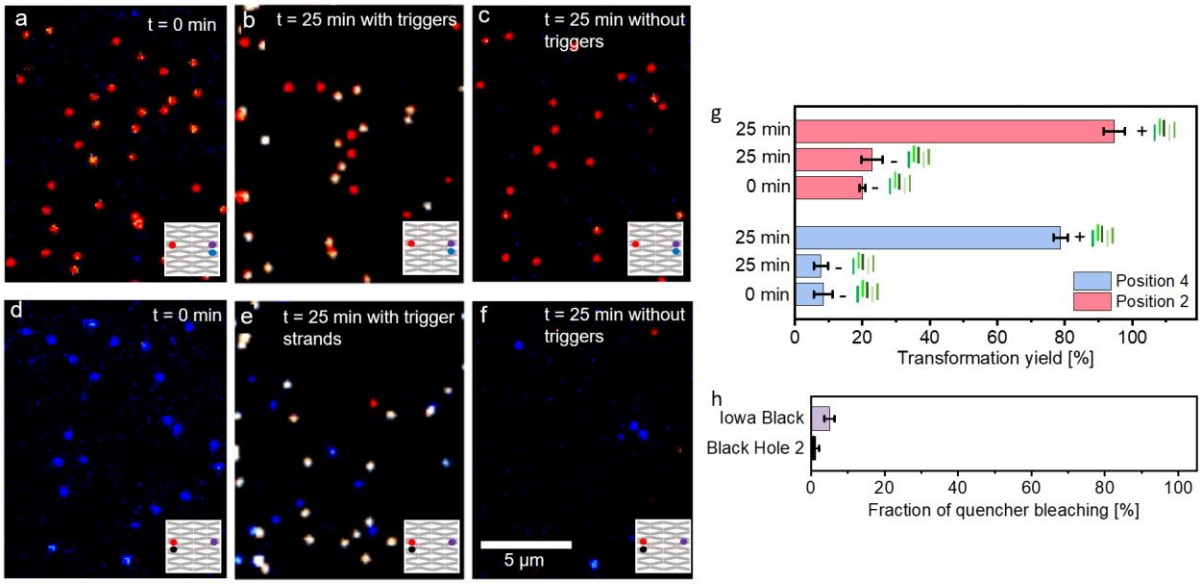

Figure S2. Transformation of reconfigurable DNA origami array structures on the single-molecule level. (a-f) Exemplary TIRF images of DNA origami array with (a) the green dye-quencher pair and a red co-localization dye and (b) the red dye-quencher pair and a green co-localization pair incorporated after 25 min incubation (b,e) with all five trigger DNA strands and (c,f) without trigger DNA strands. (g) Transformation yield obtained at the red and the green dye-quencher pair position after 0 min and 25 min of incubation with and without of all five trigger DNA strands. (h) Fraction of quencher molecules photobleached during the measurement period of 25 min. The fractions were extracted from the intensity transients recorded from the images shown in (a) and (d). Error bars in (g,h) represent the standard error of at least 200 structures.

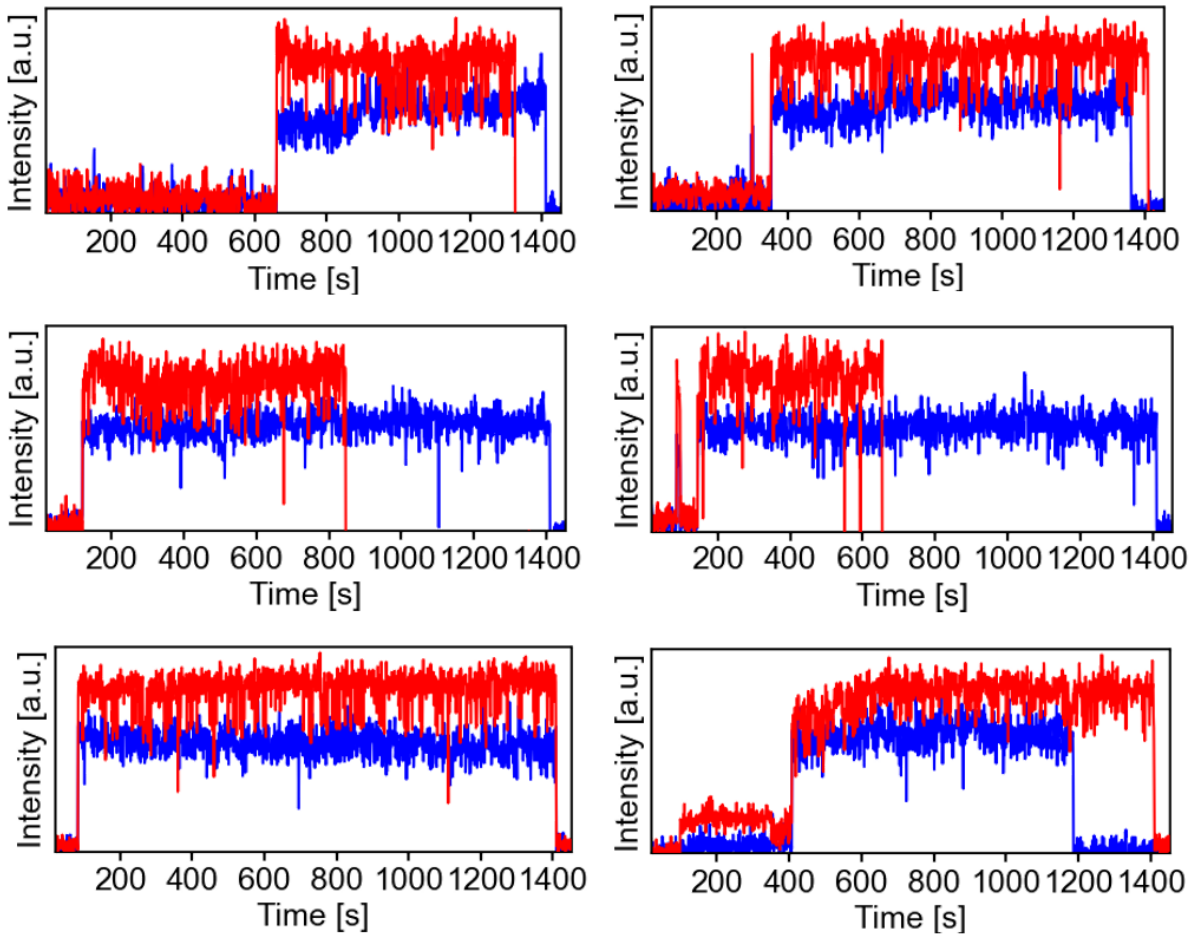

Figure S3. Representative single-molecule fluorescence intensity transients of DNA origami array structures with the red and the green FRET probe at Position 4 and Position 2, respectively, recorded after addition of all five trigger DNA strands at 0 s. Fluorescence of ATTO647N is shown in red, fluorescence of ATTO542 in blue.

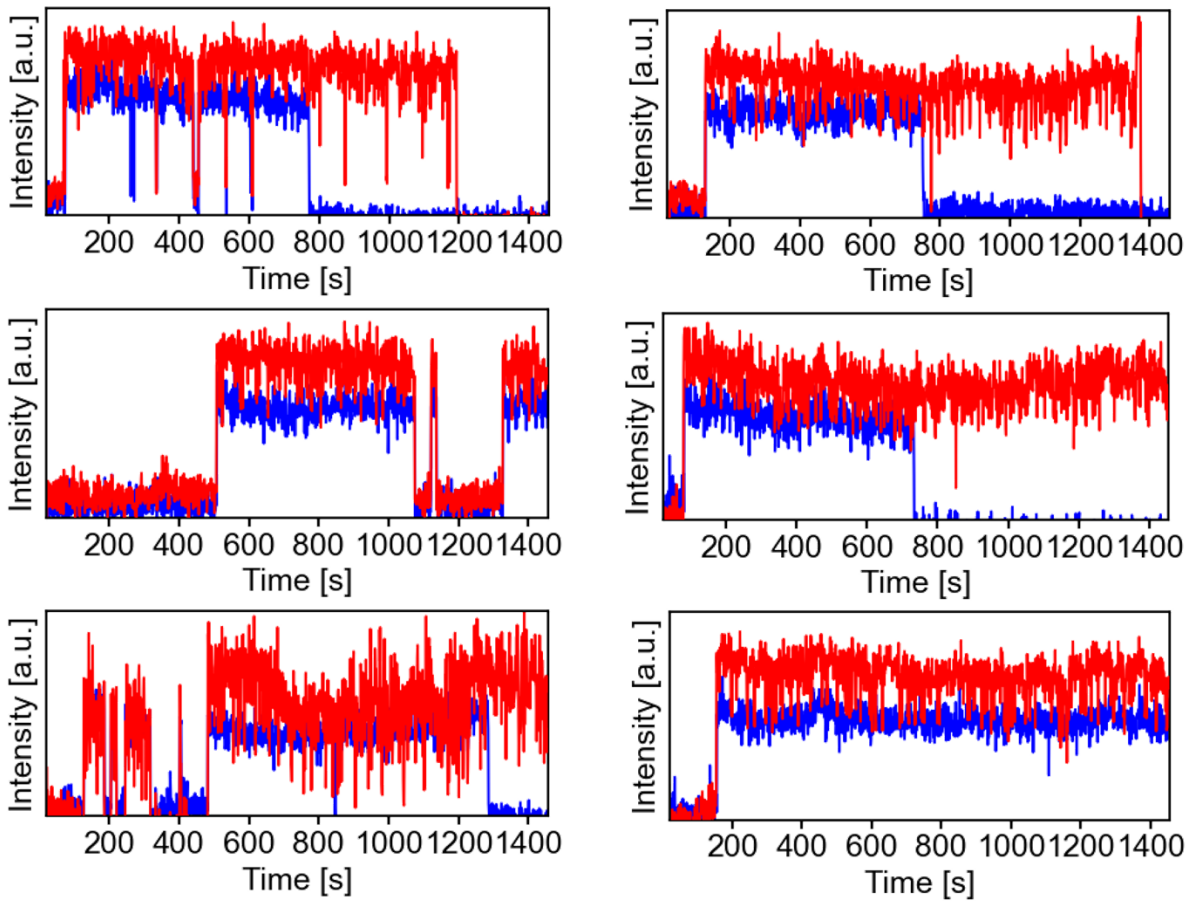

Figure S4. Representative single-molecule fluorescence intensity transients of DNA origami array structures with the red and the green FRET probe at Position 2 and Position 3, respectively, recorded after addition of all five trigger DNA strands at 0 s. Fluorescence of ATTO647N is shown in red, fluorescence of ATTO542 in blue.

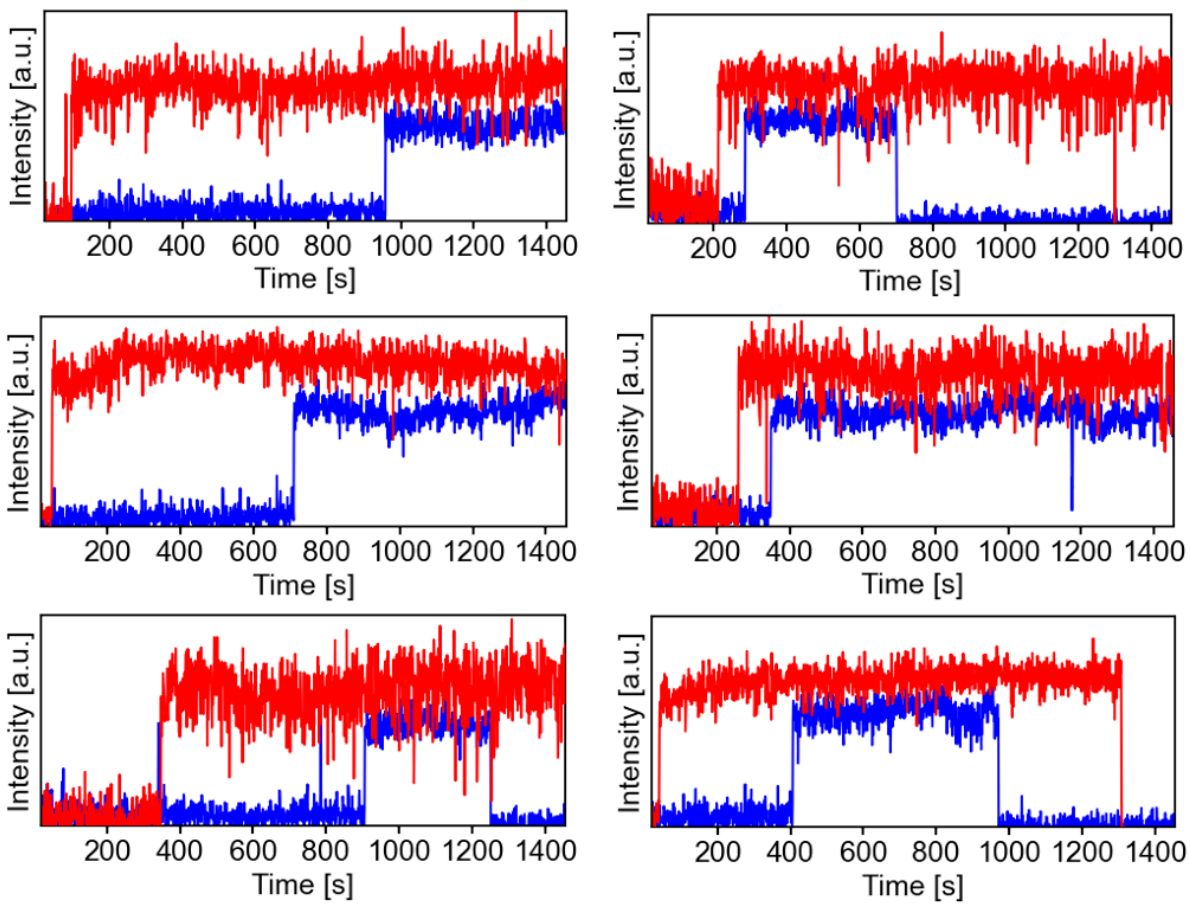

Figure S5. Representative single-molecule fluorescence intensity transients of DNA origami array structures with the red and the green FRET probe at Position 1 and Position 3, respectively, recorded after addition of all five trigger DNA strands at 0 s. Fluorescence of ATTO647N is shown in red, fluorescence of ATTO542 in blue.

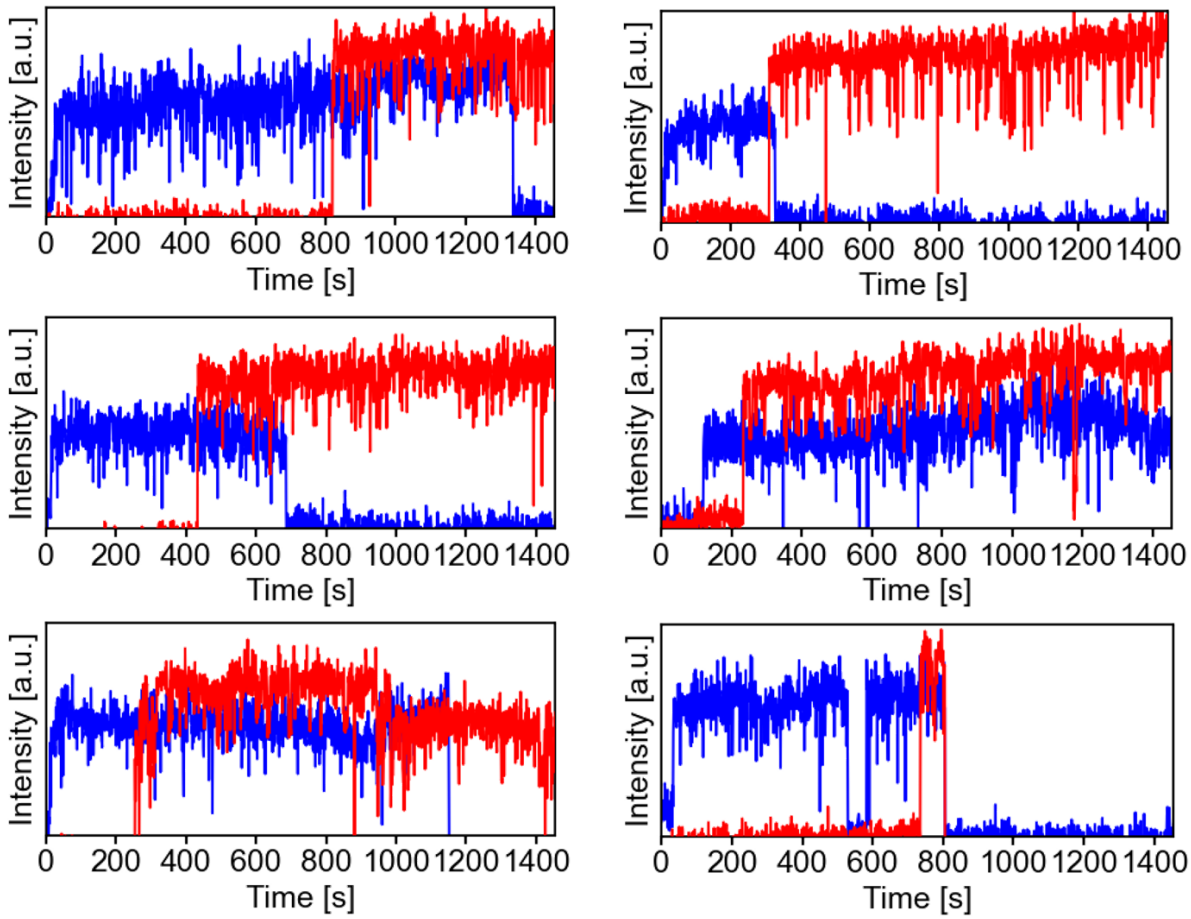

Figure S6. Representative single-molecule fluorescence intensity transients of DNA origami array structures with the red and the green FRET probe at Position 2 and Position 1, respectively, recorded after addition of all five trigger DNA strands at 0 s. Fluorescence of ATTO647N is shown in red, fluorescence of ATTO542 in blue.

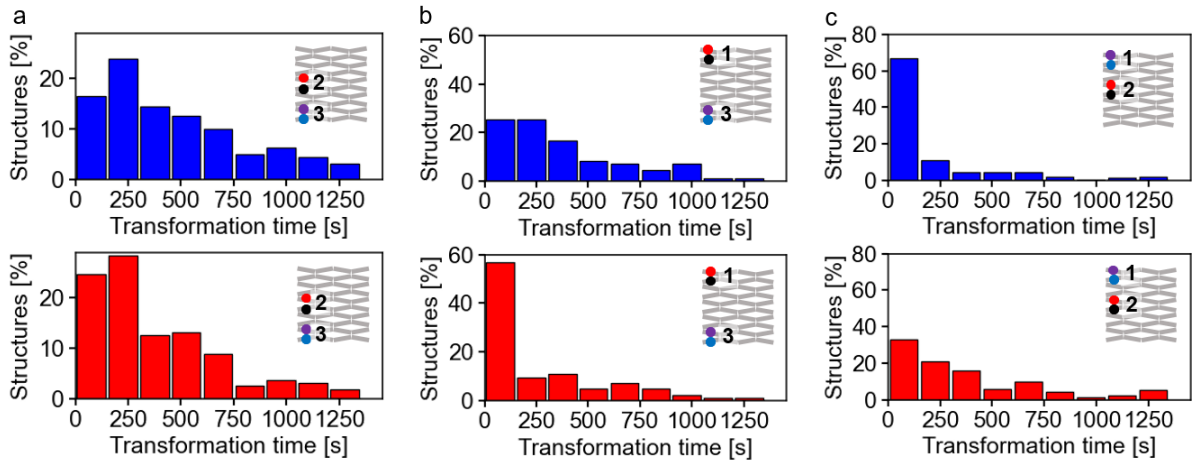

Figure S7. Transformation times at the position of the green dye-quencher pair (upper row) and at the position of the red dye-quencher pair (lower row) after addition of all five trigger DNA strands for DNA origami array structures with the dye-quencher incorporated at different positions. (a) Position 2 and 3, (b) Position 1 and 3 and (c) Position 1 and 2.

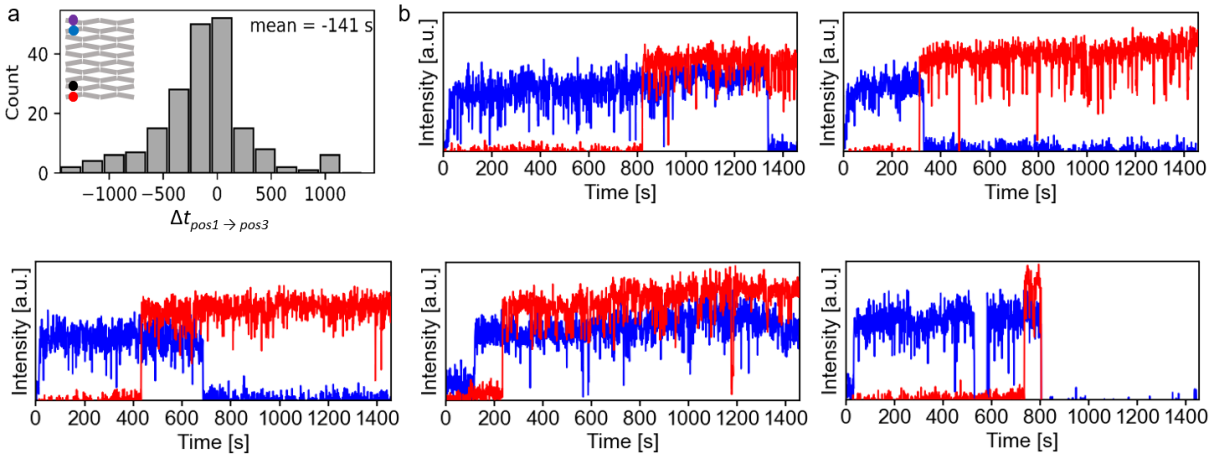

Figure S8. Transformation process of DNA origami array with the green and red FRET probes at switched positions in comparison to Figure 2f. The green dye-quencher pair was placed at Position 1 and the red dye-quencher pair at Position 3. (a) Time difference between the transformation occurring at the positions of the green and red dye-quencher pairs positioned at Position 1 and Position 3, respectively. As for the design with the FRET probes placed at the switched positions in Figure 2f, the transformation preferentially first occurs at Position 1, confirming that this tendency was caused by the structure itself and not by differing interactions of the red and green FRET probes with DNA (e.g. stickiness).[1] (b) Representative single-molecule fluorescence intensity transients of a surface-immobilized DNA origami array structures recorded after addition of all five trigger DNA strands at 0 s. Fluorescence of ATTO647N is shown in red, fluorescence of ATTO542 in blue.

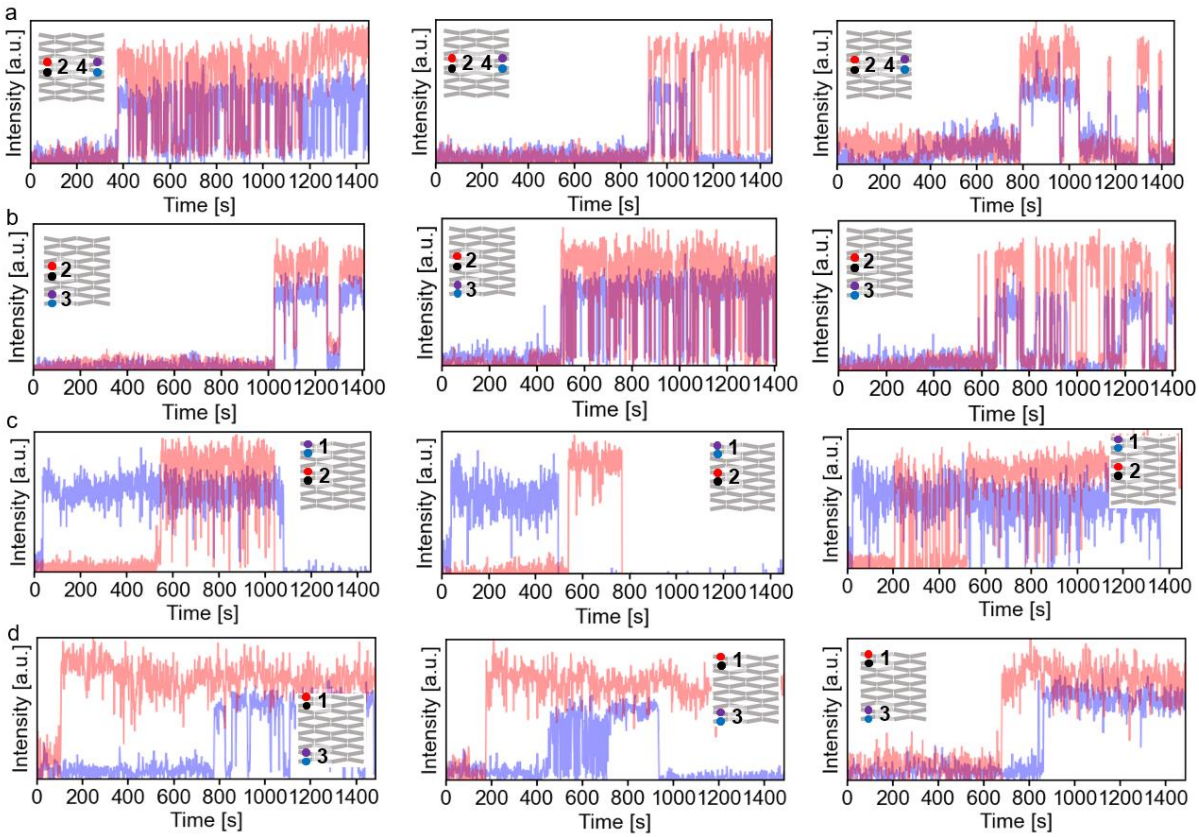

Figure S9. Representative single-molecule fluorescence intensity transients of surface-immobilized DNA origami arrays with the red and the green dye-quencher pair incorporated at different positions. (a) Position 4 and Position 2, (b) Position 3 and Position 2, (c) Position 1 and Position 2, (d) Position 1 and Position 3 recorded after addition of the upper four trigger DNA strands at 0 s. Fluorescence of ATTO647N is shown in red, fluorescence of ATTO542 in blue.

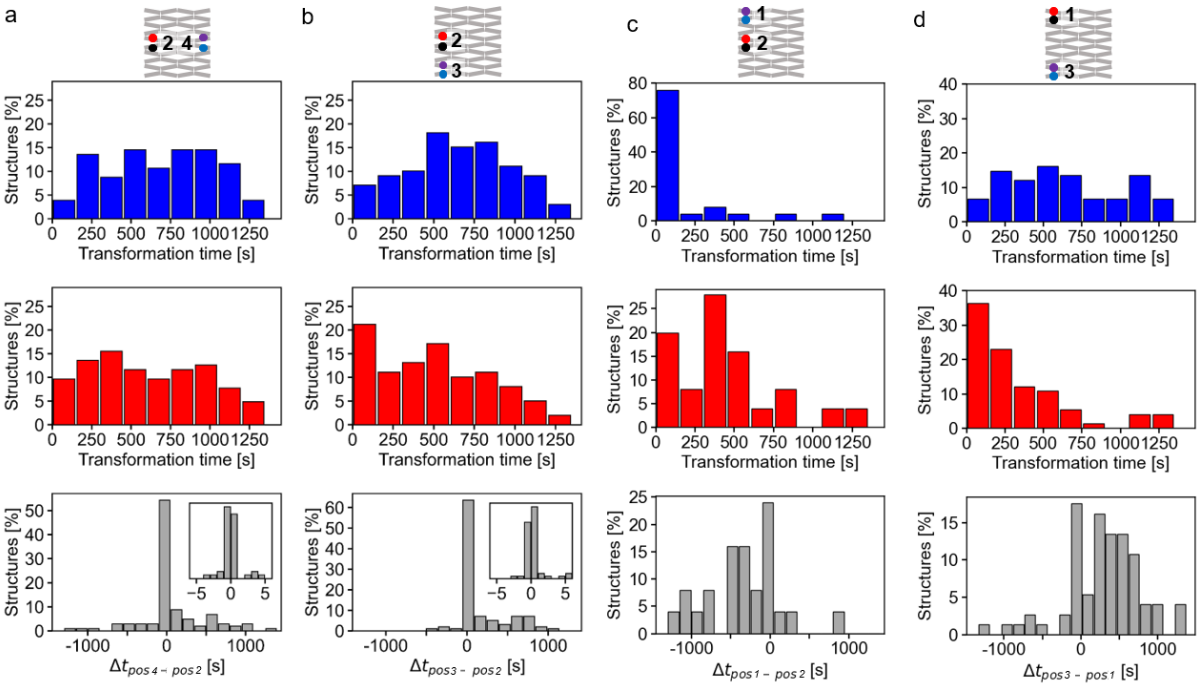

Figure S10. Transformation times at the position of the green dye-quencher pair (upper row) and at the position of the red dye-quencher pair (middle row) and time differences between the transformation at the position of the green dye-quencher pair and the position of the red-dye quencher pair after addition of the upper four trigger DNA strands with the dye-quencher incorporated at different positions. (a) Position 4 and 2, (b) Position 3 and 2 and (c) Position 3 and 1.

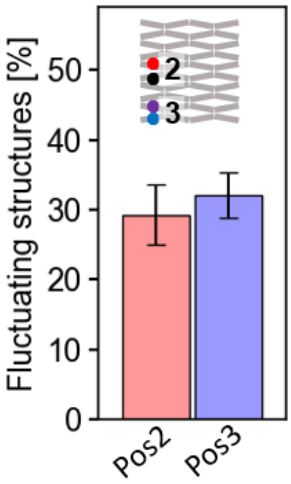

Figure S11. Fraction of structures showing intensity fluctuations after 24 h incubation with four trigger DNA strands. Error bars represent the standard error of 82 structures.

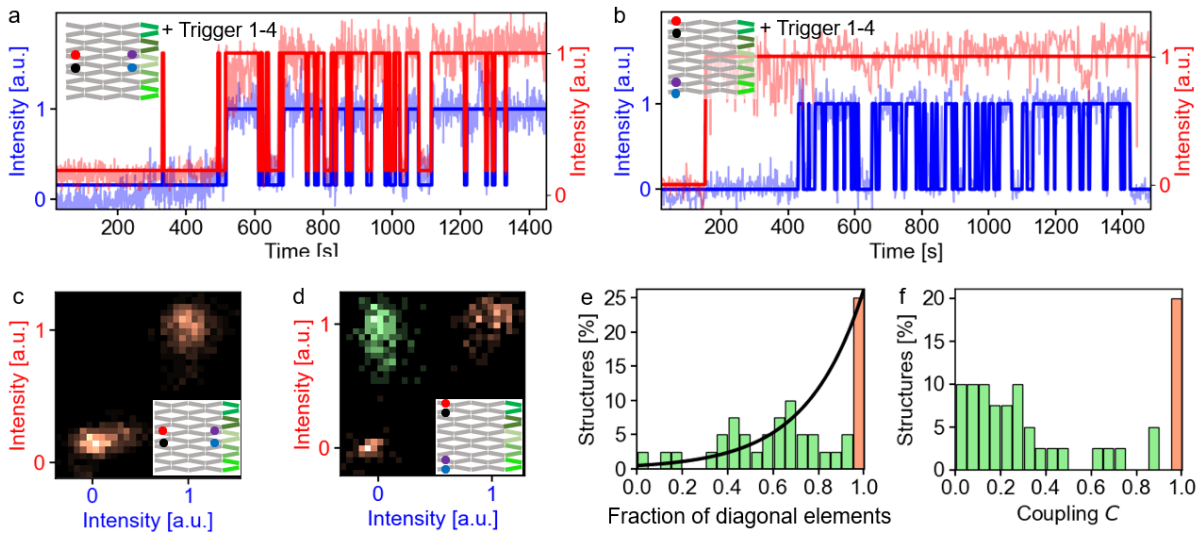

Figure S12. Determination of the Coupling C. (a, b) Representative single-molecule fluorescence intensity transients of DNA origami arrays with the red and the green FRET probe incorporated at (a) Position 2 and 4 and (b) Position 1 and 3, of ATTO542 fluorescence (blue transients) and ATTO647N fluorescence (red transient) after addition of the upper four trigger DNA strands. The Coupling of the transformation between two positions in a DNA origami structure is calculated using the transformation state occupancy density plots of the corresponding positions in the structure. (c,d) transformation state occupancy density plots for a system exhibiting (c) $C = 1$ and (d) with $C < 0.95$. In these density plots, the fraction of diagonal elements with respect to the total number of both diagonal and off-diagonal elements is determined. (e) Exemplary distribution of the fractions of diagonal elements calculated for the structures shown in (b). The Coupling between two positions in a system is calculated by weighing the fraction of diagonal elements with the exponential distribution $C = \exp\left(-4\ (1 - \text{fraction})\right)$ shown by the black line. This separates perfectly coupled systems (C = 1) from slightly uncoupled systems. (f) Resulting Coupling distribution for the data shown in (e). The fraction of structures exhibiting full coupling is indicated by an orange bar.

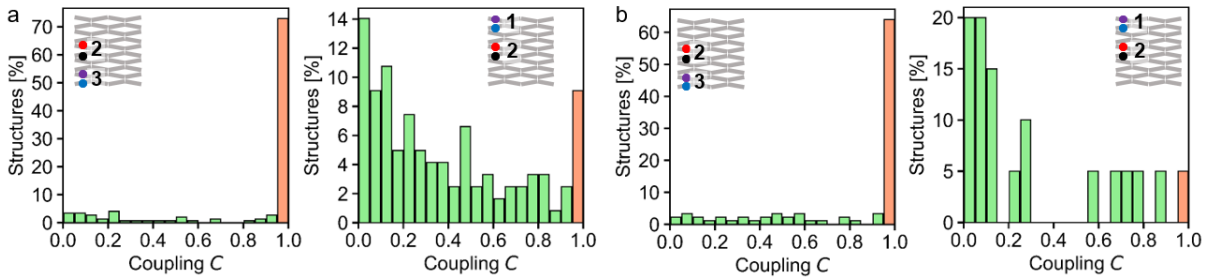

Figure S13. Coupling histograms for the dye quencher pairs at different positions upon the addition of different numbers of trigger DNA strands. (a) all five trigger DNA strands and (b) only the upper four trigger DNA strands.

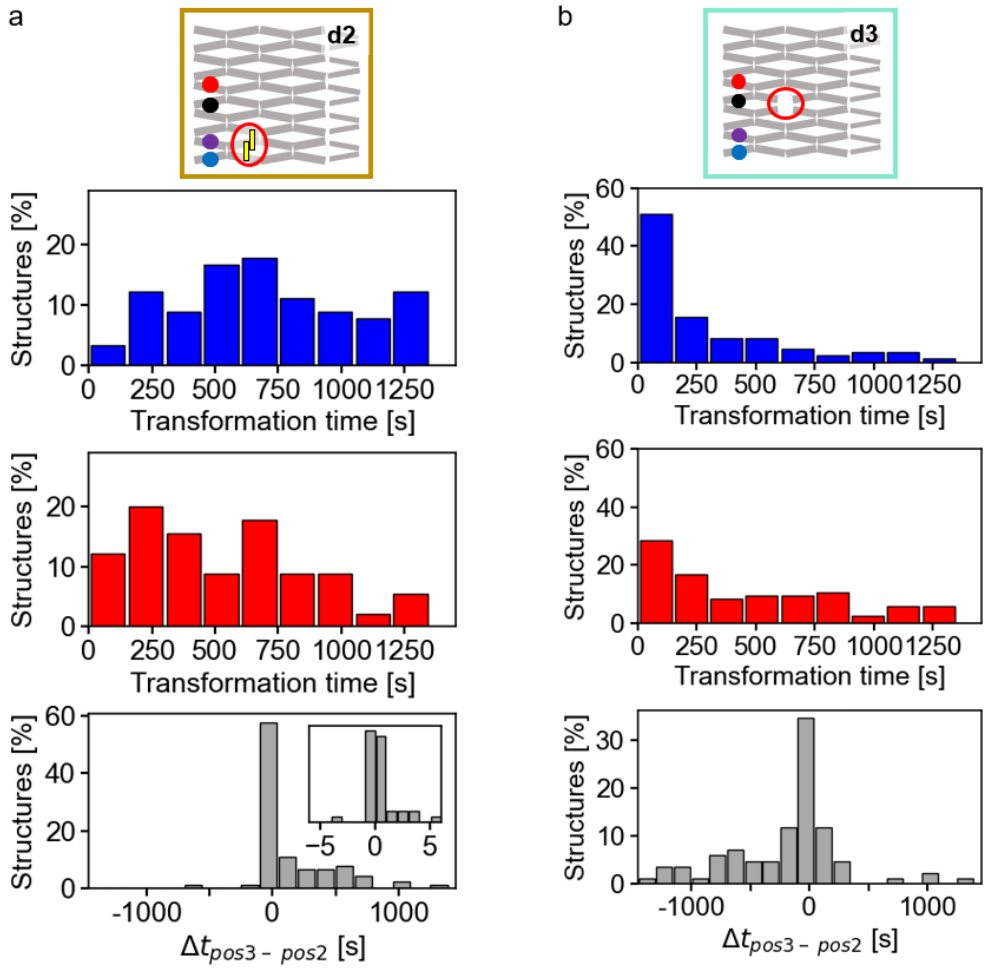

Figure S14. Transformation times at the position of the green dye-quencher pair (upper row) and at the position of the red dye-quencher pair (middle row) and time differences between the transformation at the position of the green dye-quencher pair and the position of the red-dye quencher pair after addition of all five trigger DNA strands with the dye-quencher pairs incorporated Position 3 and Position 2 to different DNA origami array constructs. (a) DNA origami arrays with a looking unit incorporated and (b) DNA origami arrays with missing staples at an anti-junction (red circle). For determination of the mean time differences shown in Figure 4c only non-perfectly coupled structures with $\Delta t \neq 0$ s were considered.

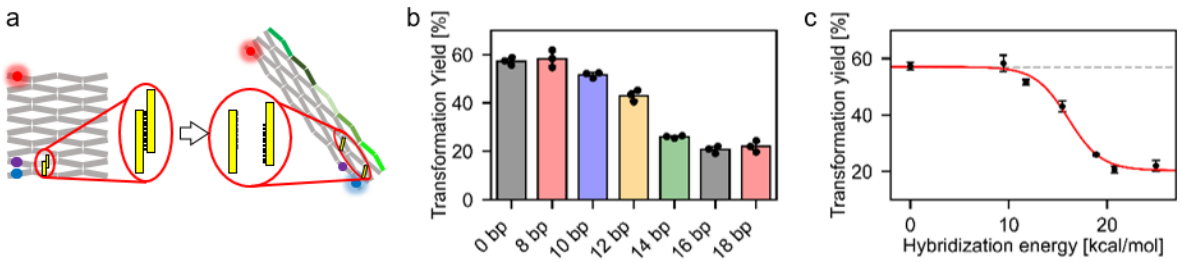

Figure S15. Energy transport efficiency at the position of the locking unit. (a) Origami design for determining the energy transport efficiency. We systematically varied the number of hybridizing base pairs of the locking unit and thus its hybridization energy and then determined the transformation yield at the lower left position (Position 3). For colocalization, we additionally placed an AT647N dye at Position 1. (b) Transformation yields after 25 min incubation with five trigger DNA strands at the lower left position (Position 3) for different numbers of hybridizing base pairs in the locking unit. Transformation yields were determined from TIRF images by dividing the number of colocalized red-green spots by the total number of red spots. (c) Transformation yield as a function of the hybridization energy of the locking unit. The data points were fitted by a logistic function (red curve) to determine the hybridization energy at which 50% energy transfer occurs within 25 min as 16.0±0.5 kcal/mol. The grey dashed line represents the fraction of co-localized spots in a origami with a 0 bp locking unit folded in its transformed state. Hybridization energies were estimated using NUPACK.[2] Error bars in (b,c) represent the standard deviation in transformation yield of three TIFR images (at least 300 single nanostructures per image).

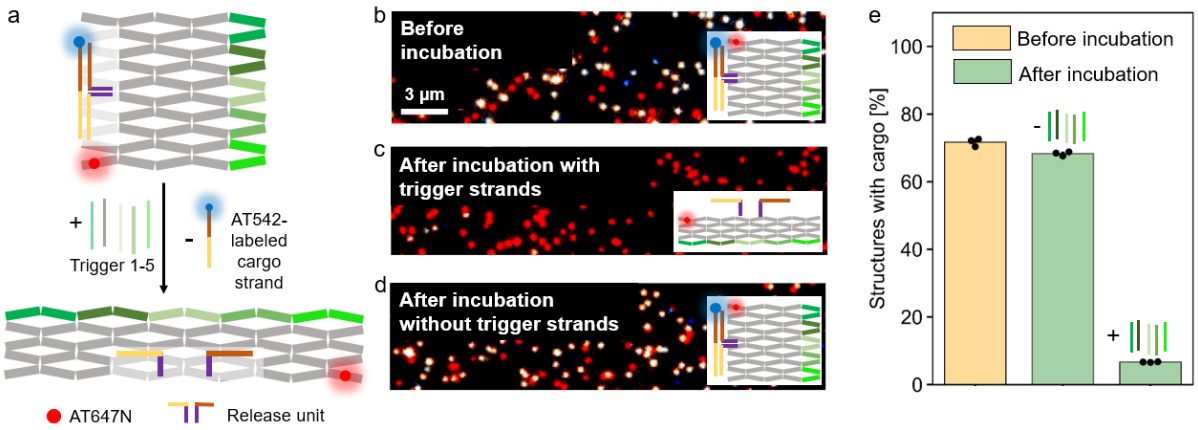

Figure S16. Cargo release. (a) Scheme of the procedure of cargo release. (b) TIRF image of the DNA origami array bearing a catching unit after incubation with an ATTO542 labeled cargo strand. (c, d) TIRF images of DNA origami arrays carrying ATTO542 labeled cargo strand after 25 min incubation (c) without and (d) with all five trigger DNA strands. (e) Corresponding fractions of DNA origami array structures carrying a cargo DNA strand. Error bars represent the standard deviation in the fractions calculated from three TIFR images (at least 300 single nanostructures per image).

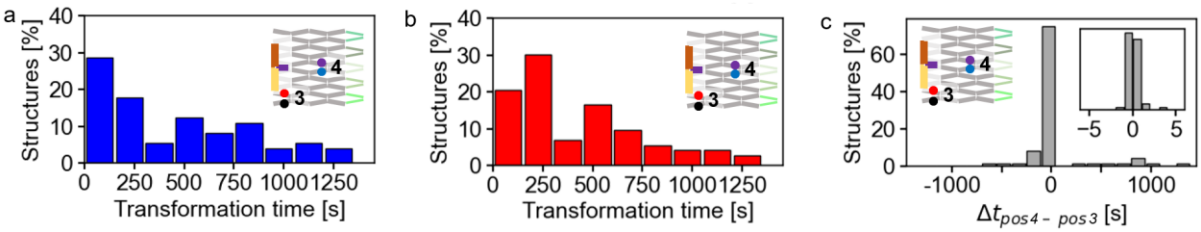

Figure S17. Transformation of DNA origami arrays with an incorporated cargo release unit and the green dye-quencher pair incorporated at Position 4 and the red dye-quencher pair at position 3. (a, b) Transformation time at the position of (a) the green dye quencher pair and (b) the red dye-quencher pair. Time difference between the transformation occurring at the positions of the green and red dye-quencher pairs.

Table 1. Core staples from the 5‘ to the 3’ end for the DNA origami array structure.

ID	Sequence (5‘ to 3‘)	Function
C1	GGAGTCCTCATAGATGGTTCGAGGTAAACCCACTTTCTGATGTCATGATGCT	core
C2	GCGGAAATCTTCGAATTGGTTGACTGGCCCAAGATCTCGAGTGCTTAGACTT	core
C3	GTTGAGGCTGCGCGGTCCAGGATGGTCAGCAGTGAGTTTCCCAGATGCTGAC	core
C4	CTTGTCTTCAAAGAGTCCTTCAAGGACTGCAGGAGGCATCAACTCTCAGCAG	core
C5	AATCTTATATTTGATTCGCGGATGGTCACTTCACCCTGGAGGTGCGGCTCTG	core
C6	GAGAGCTGCGTCTCCCCTCCAAGGACTTCATTGCAGTATCGCAGGTCATCGT	core
C7	AGTGATCGGGTGGAGCAGCCTTGGCCACGATGGTATCGGATATTGTCGCCCA	core
C8	CCTGGTTGACGAGATCGTCCAGTTCGGCGAGTTTCCTTGAGAATGCCTGCGT	core
C9	CTCATCGAAACAGAGATCTGTGATGGGAACAGAGAAGGGACTCAATCTGGTGCAGGGAGTGATCTTTTTT	core
C10	TTTTTGCGAAAGGTGATCCAATCTTCATTGGAACAGATCCAGCC	core
C11	ATGGCACAACTTGAGTTGTCACGCACTCCTTCAGCAGCGACGGAAGATGTGTCGATGTTAGTATATTTTT	core
C12	CTTCATCTCCAGGAGGTTTCGACGTTATTGGACAAGGGTCCTCCAGGAACTC	core
C13	GTCACCGAACAGCTGCCGCGAGGCAGACCCAGCAAGCGTCCATTTCTTGGAATCCCTGCTGGAAC	core
C14	GGTTCTGCAAATTCTCCTTCCAATCCTTGATCAGCTTCTCCGCGTGAGTTCA	core
C15	GATCTTTCAGGTTCAGGTGTTCTCCGCGGACGTACTTCTCACTCCTCAAACAAGTAGGTCTTAGTTTTTT	core
C16	TTTTTTGAGGCGGTCGTGCCAATTCATCAGGAGATAGGGATAAC	core
C17	TACCGGACTCTGTGTTACCTGGGTCTCCTCCAGGGTCTT	core
C18	TTTTTCTGCTCCAATTTGTTCACCAGCTGTTCCCACAGCTCCCT	core
C19	CTCCGATGAAGTTCGTGACGCGATTGTCCTTCTTGATATCGAATATGGTTGA	core
C20	GGGTAGTCAAGGGAAAGCGAGGGAAGGCGCTGCGCTTCGACGTTATTCTTGA	core
X1	CCAAATCAAGTTTTTTGGGGTCGAGGTGCCGTAAAGCACTAA	loop
X2	AAACCGTCTATCAGGGCGATGGCCCACTACGTGAACCATCAC	loop
X3	GTCCACTATTAAAGAACGTGGACTCCAACGTCAAAGGGCGAA	loop
X4	GGTACCCCGAAATCGGCAAAATCCCTTATAAATCAAAAGAAT	loop
X5	AAGGAGCGGGCGCTAGGGCGCTGGCAAGTGTAGCGGTCACGC	loop
X6	AGCCCGAGATAGGGTTGAGTGTTGTTCCAGTTTGGAACAAGA	loop
X7	ATCGGAACCCTAAAGGGAGCCCCCGATTTAGAGCTTGACGGG	loop

X8	TGCGCGTAACCACCACACCCGCCGCGCTTAATGCGCCGCTAC	loop
X9	AGGGCGCGTGGATCCGTCGAGAATCAGTGCTTTCAGTTTCAG	loop
X10	GAAAGCCGGCGAACGTGGCGAGAAAGGAAGGGAAGAAAGCGA	loop

Table 2. Trigger staples from the 5‘ to the 3’ end used to transform the DNA origami array structure. Trigger staples are labelled according to the position they can bind to the DNA origami array structure, starting from the upper right corner to the lower right corner.

ID	Sequence (5‘ to 3‘)	Function
T1	AGTTCCCTGAGTTCCCACCTCAGATTGGAGCTTGACAGTCATCACAGAAGCTCCTCCACTTTCCTTTTT	trigger 1
T2	CCGCGACCAAAGTCCGATCAGTGTGAACACAGCACCCACGCCCCACAAACC	trigger 2
T3	TGAATCACGGATTCCCACCCTGTTGAATCTGGTCTGCTCTTTGGGCAGGGT	trigger 3
T4	TCGGCCAAGCACTCCAGAGTTGATACCAGCAAACAGCTTCTTGAGGTGAGAC	trigger 4
T5	TTTTTTTAATTGCGTTCTCCACATCTTCGGTAAACTTGATCTGT	trigger 5

Table 3. Staples for labelling the DNA origami array structure with fluorescent dye – quencher pairs at different positions (Position 1-4).

ID	Sequence (5‘ to 3‘)	Function
B1	**Biotin**-GAAAGCCGGCGAACGTGGCGAGAAAGGAAGGGAAGAAAGCGA	biotin
L1	CTGCAGGAGGCATCAACTCTCAGCAG	Position 2 replacement
L2	CAGTGAGTTTCCCAGATGCT	Position 2 replacement
L3	GTTGAGGCTGCGCGGTCCAGGATGGTCAG-**ATTO647N**	Position 2 AT647N
L4	**IowaBlack**-GACCTTGTCTTCAAAGAGTCCTTCAAGGA	Position 2 Iowa Black
R1	GCCCAAGATCTCGAGTGCTTAGACTT	Position 4 replacement
R2	CCACTTTCTGATGTCATGAT	Position 4 replacement
R3	**ATTO542**-GCTGCGGAAATCTTCGAATTGGTTGACTG	Position 4 AT542
R4	GGAGTCCTCATAGATGGTTCGAGGTAAAC-**BHQ2**	Position 4 BHQ2
U1	CAGCAAGCGTCCATTTCTTG	Position 1 replacement
U2	**ATTO647N**-GAATCCCTGCTGGAAC	Position 1 AT647N
U3	GTCACCGAACAGCTGCCGCGAGGCAGACC-**IowaBlack**	Position 1 Iowa Black
U4	**ATTO542**-GAATCCCTGCTGGAAC	Position 1 AT542
U5	GTCACCGAACAGCTGCCGCGAGGCAGACC-**BHQ2**	Position 1 BHQ2
D1	ATTGGACAAGGGTCCTCCAGGAACTC	Position 3 replacement
D2	ACCTGGGTCTCCTCCAGGGT	Position 3 replacement
D3	**ATTO647N**-CTTCTTCATCTCCAGGAGGTTTCGACGTT	lower position AT647N
D4	TACCGGACTCTGTGTT-**IowaBlack**	Position 3 Iowa Black
D5	**ATTO542**-CTTCTTCATCTCCAGGAGGTTTCGACGTT	Position 3 AT542
D6	TACCGGACTCTGTGTT-**BHQ2**	Position 3 BHQ2

Table 4. Staples for temporally decoupling the transformation process at the left and lower position in the DNA origami array structure and for determining the energy transport efficiency at the position of the locking unit. For the temporal decoupling in design 2, a locking unit with 12 hybridizing base pairs (Dec1_12bp) was used.

ID	Sequence (5‘ to 3‘)	Function
Dec1_ 8bp	GGGTAGTCAAGGGAAAGCGAGGGAAGGCGCTGCGC TTCGACGTTATTCTTGAATG TTTTT TACGATAC	Decoupling Design 2, 8 bp
Dec1_ 10bp	GGGTAGTCAAGGGAAAGCGAGGGAAGGCGCTGCGC TTCGACGTTATTCTTGAATG TTTT ACTACGATAC	Decoupling Design 2, 10 bp
Dec1_ 12bp	GGGTAGTCAAGGGAAAGCGAGGGAAGGCGCTGCGC TTCGACGTTATTCTTGAATG TTT CGACTACGATAC	Decoupling Design 2, 12 bp
Dec1_ 14bp	GGGTAGTCAAGGGAAAGCGAGGGAAGGCGCTGCGC TTCGACGTTATTCTTGAATG TT CACGACTACGATAC	Decoupling Design 2, 14 bp
Dec1_ 16bp	GGGTAGTCAAGGGAAAGCGAGGGAAGGCGCTGCGC TTCGACGTTATTCTTGAATG T GTCACGACTACGATAC	Decoupling Design 2, 16 bp
Dec1_ 18bp	GGGTAGTCAAGGGAAAGCGAGGGAAGGCGCTGCGC TTCGACGTTATTCTTGAATG T CCGTCACGACTACGATAC	Decoupling Design 2, 18 bp
Dec2	GCACAACTTGAGTTGTCACGCACTCCTTCAGCAGCG ACGGAAGATGTGTCGA T GTATCGTAGTCGTGACGGCC	Decoupling Design 2
Dec3	ACGCGATTGTCCTTCTTGATATCGAATATGGTTGA	Decoupling Design 3
Dec4	AGGGAAGGCGCTGCGCTTCGACGTTATTCTTGA	Decoupling Design 3
Dec5	GAGAGCTGCGTCTCCCCTCCAAGGACTTCATTGCAG TATCGCAGGTCATCGTCTCCGATGA	Decoupling Design 3
Dec6	CCTGGTTGACGAGATCGTCCAGTTCGGCGAGTTTCC TTGAGAATGCCTGCGTGGGTAGT	Decoupling Design 3
Dec7	TTTTTCTGCTCCAATTTGTTCACCAGCTGTTCCCACA GCTCCCTGAGAGCTGC	Decoupling Design 4
Dec8	GTCACGCACTCCTTCAGCAGCGACGGAAGATGTGTC GATGTTAGTATATTTTT	Decoupling Design 4
Dec9	GGGTAGTCAAGGGAAAGCGAGGGAAGGCGCTGCGC TTCGACGTTATTCTTGAATGGCACAA	Decoupling Design 4
Dec10	TCCAAGGACTTCATTGCAGTATCGCAGGTCATCGT	Decoupling Design 4

Note S1. Temporal and spatial controlled proximity-induced reactions in DNA origami array structures. Temporally and spatially controlled proximity-induced reaction cascades could find exciting applications e.g. in a cargo release process. For this, a cargo release unit was positioned on the DNA origami array structure at Position 2.

The cargo release unit is formed by two DNA strands protruding from the DNA origami array on neighboring helices. They contain a 6-nt complementary sequence which forms a stem followed by a 10-nt non-complementary sequence on each strand to which an ATTO542-labelled single-stranded DNA strand containing a 20-nt complementary sequence can permanently hybridize. Due to the opening of the stem, the distance between the arms of the catching unit becomes too large to enable a permanent binding of the cargo strand to both arms and the cargo is released. Thus, the release of the cargo strand could be initiated by addition of trigger DNA strands and performed at the pre-programmed position in the transformation cascade. The unbinding of the cargo strand was detected in single-molecule TIRF images (Supplementary Figure 14b-d) where white spots of co-localized fluorescence of ATTO647N and ATTO542 are attributed to DNA origami structures with a bound cargo release strand while red spots of ATTO647N fluorescence indicate the presence of DNA origami array structures bearing no cargo strand. Blue spots of ATTO542 fluorescence were attributed to non-specific bound cargo strands or DNA origami array structures with a bound cargo and an unlabeled ATTO647N DNA strand. After 25 min incubation with trigger DNA strands the number of co-localized spots decreased drastically (see Supplementary Figure 14c) while only a slight drop in the number of co-localized spots was observed upon incubation without trigger strands (Supplementary Figure 14d). Quantification (Supplementary Figure 14e) confirmed the specific nature of cargo release strand unbinding initiated by the transformation process. Interestingly, the introduction of the cargo release process did not induce a time delay between the FRET probes framing the cargo release unit (see Supplementary Figure 15).

Sequence of the p1800 scaffold used to fold the DNA origami array structure from 5' to 3' end:

TACGAAGAGTTCCAGCAGGGATTCCAAGAAATGGCCAATGAAGATTGGATCAC
CTTTCGCACTAAGACCTACTTGTTTGAGGAGTGCCTGATGAATTGGCACGACCG
CCTCAGGAAAGTGGAGGAGCATTCTGTGATGACTGTCAAGCTCCAATCTGAGG
TGGGCAAATATAAGATTGTTATCCCTATCTAGAAGTACGTCCGCGGAGAACACC
TGCCACCCGATCACTGGCTGGATCTGTTACGCTTGCTGGGTCTGCCTCGCGGC
ACATCTCTGGAGAAACTGCTGTTCGGTGACCTGCTGAGAGTTGCCGATACCATC
GTGGCCAAGGCTGCTAACCTGAAAGATCTGAACTCACGCGGCCAGGGTGAAGT
GACCATCCGCGAATAACTCAGGGAACTGGATTTGTGGGGCGTGGGTGCTGTGT
TCACACTGATCGGCTATGAGGACTCCCAGAGCCGCACCTAGAAGCTGATCAAG
GATTGGAAGGAGCTCGTCAACCAGGTGGGCGACAATATATGCCTCCTGCAGTC
CTTGAAGGACTCACCATACTATAAAGGCTTTGAAGACAAGGTCAGCATCTGGGC
AAGGAAACTCGCCGAACTGGACGATAATTTGCAGAACCTCAACCATATTCGCAG
AAAGTGGGTTTACCTCGAACCATACTTTGGTCGCGGAGCCCTGCCCAAAGAGC
AGACCAGATTCAACAGGGTGGGCGAAGATTTCCGCAGCATCATGACATATATCA
AGAAGGACAATCGCGTCACGCCCTTGACTACCCACGCAGGCATTCTAAACTCA
CTGCTGACCATCCTGGACCAATTGCAGAGATGCCAGCGCAGCCTCAACGAGTT
CCTGGAGGCGAAGCGCAGCGCCTTCCCTCGCTTTAACTTCATCGGAGACGATG
ACCTGCGCGAGATCTTGGGCCAGTCAACCAATTAATCCGTGATTCAGTCTCACC
TCAAGAAGCTGTTTGCTGGTATCAACTCTGGCTGTTTCGATGAGAAGTCTAAGC
ACTATACTGCAATGAAGTCCTTGGAGGGGCAAGTTGTGCCATTCAAGAATAACG
TACCCTTGTCCAATAACGTCGAAACCTGGCTGAACGATCTGGCCCTGGAGATG
AAGAAGACCCTGGAGGCGCTGCTGAAGGAGTGCGTGACAACTAGACGCAGCT
CTCAGGGAGCTGTGGGCCCTTCTCTGTTCCCATCACAGATCTAGTGCTTGGCC
GAACAGATCAAGTTTACCGAAGATGTGGAGAACGCAATTAAAGATCACTCCCTG
CACCAGATTGAGTAACAGCTGGTGAACAAATTGGAGCAGTATACTAACATCGAC
ACATCTTCCGTAGACCCAGGTAACACAGAGTCCGGTATTCTGGAGCTGAAACTG
AAAGCACTGATTCTCGACGGATCCACGCGCCCTGTAGCGGCGCATTAAGCGCG
GCGGGTGTGGTGGTTACGCGCAGCGTGACCGCTACACTTGCCAGCGCCCTAG
CGCCCGCTCCTTTCGCTTTCTTCCCTTCCTTTCTCGCCACGTTCGCCGGCTTTC
CCCGTCAAGCTCTAAATCGGGGGCTCCCTTTAGGGTTCCGATTTAGTGCTTTAC
GGCACCTCGACCCCAAAAAACTTGATTTGGGTGATGGTTCACGTAGTGGGCCA
TCGCCCTGATAGACGGTTTTTCGCCCTTTGACGTTGGAGTCCACGTTCTTTAAT
AGTGGACTCTTGTTCCAAACTGGAACAACACTCAACCCTATCTCGGGCTATTCT
TTTGATTTATAAGGGATTTTGCCGATTTCGGGGTACC

References

(1) Jahnke, K.; Grubmüller, H.; Igaev, M.; Göpfrich, K. Choice of fluorophore affects dynamic DNA nanostructures. *Nucleic Acids Res* **2021**, *49* (7), 4186–4195. DOI: 10.1093/nar/gkab201.

(2) Zadeh, J. N.; Steenberg, C. D.; Bois, J. S.; Wolfe, B. R.; Pierce, M. B.; Khan, A. R.; Dirks, R. M.; Pierce, N. A. NUPACK: Analysis and design of nucleic acid systems. *Journal of computational chemistry* **2011**, *32* (1), 170–173. DOI: 10.1002/jcc.21596.

6.5.4 PUBLICATION P4

Sequence effect on the thermodynamics and transition kinetics of anti-junctions

by

Dongfang Wang[1], Fiona Cole[1], **Martina Pfeiffer**[1], Tim Schröder, Philip Tinnefeld[*] and Yonggang Ke[*]
([1] These authors contributed equally, [*] Correspondence)

Submission pending

Author contributions:
The initial idea of the project was proposed by my collaboration partners Yonggang Ke and Dongfang Wang. Dongfang Wang designed the DNA origami array structures and synthesized the corresponding scaffolds. He performed and analyzed the AFM measurements of this work. Tim Schröder performed preliminary fluorescence measurements. I designed, performed and analyzed the single-molecule fluorescence measurements and helped with the ensemble fluorescence measurements and their analysis. Fiona Cole performed and analyzed the ensemble fluorescence measurements and helped with the single-molecule fluorescence measurements and their analysis. I wrote parts of the manuscript. Philip Tinnefeld and Yonggang Ke supervised the project.

Sequence effect on the thermodynamics and transition kinetics of DNA origami arrays

Dongfang Wang [2,3,4], Fiona Cole [1,4], Martina Pfeiffer [1,4], Philip Tinnefeld [1*] and Yonggang Ke [2*]

[1] Department of Chemistry and Center for NanoScience, Ludwig-Maximilians-Universität München, Butenandtstr. 5-13, 81377 München, Germany

[2] Wallace H. Coulter Department of Biomedical Engineering, Emory University and Georgia Institute of Technology, Atlanta, GA 30322, USA

[3] School of Biomedical Engineering and Suzhou Institute for Advanced Research, University of Science and Technology of China, Suzhou 215123, China

[4] These authors contributed equally

[*] Correspondence: yonggang.ke@emory.edu, philip.tinnefeld@cup.uni-muenchen.de

Abstract

Holliday junctions have become the central construction motif in DNA nanotechnology. Depending both on their sequence and environment, these DNA four-way junctions can adapt different conformations between which they can switch. Despite their importance in DNA nanotechnology, it however has scarcely been studied how the sequence affects the thermodynamics and kinetics of the constructed nanostructures. Here, we constructed dynamic DNA origami arrays consisting of multiple Holliday junctions of the same sequence which can switch between two conformations. We find the sequence of the junction affects both kinetics and thermodynamics of the DNA origami transition in accordance with the energy model proposed for single junctions. Furthermore, the repetitive incorporation of the same junction in the DNA origami amplifies kinetic and thermodynamic differences occurring in single Holliday junctions of different sequences and allows resolving them in ensemble FRET measurements for the first time. We then continue to study the effect of mismatches and free bases in Holliday junctions on DNA origami transitions, demonstrating the universal applicability of this approach. The good correlation between the collective properties of DNA origami array and the energy model for composed single Holliday junction also makes the DNA origami array as the model to study individual Holliday junction.

Introduction

DNA self-assembly utilizes information stored in the DNA sequences to fabricate prescribed objects. The self-assembly of nucleic acids has demonstrated their powerful capabilities in constructing various nanoobjects in the last four decades. DNA origami[1] and the modular assembly of DNA-brick[2, 3] are demonstrated to be two successful strategies for designing arbitrary nanostructures with full addressability. Meanwhile, dynamic DNA nanotechnology has led to the development of various nanomachines, capable of performing sophisticated tasks under external instructions, such as biosensing[4] and nanorobots[5-7]. Recently, the success of DNA self-assembly was extended into the microscope range[8-11]. Among these DNA nanostructures, the DNA

four-way junction, which is adapted from natural Holliday junction, as well as its variations (e.g. 3,5, or 6-way junctions), have become the central construction elements in many self-assembly methodologies. Efforts in the past mainly focus on the four-way junction as the construction element and neglect the fact that its own preferences may strongly affect the assembled structures. Thus, a thorough understanding of how junction sequence affects the thermodynamics and kinetics of assembled structures can help the design and prediction of user-specified DNA shapes and nanomachines.

The Holliday junction is a branched nucleic acid structure with four double-stranded arms. It presents several conformations in different buffers or with different sequences on the junction. Previous studies from theoretical and experimental methods have characterized the structure of Holliday junction and its dynamics[12-25]. People have identified the isolated Holliday junction isomers in different salt environments[26, 27]. It has been shown that magnesium concentration[28] and sequence near the junction position[29-31] could affect the ratio of two stacked conformational isomers. Other factors were reported to the contribution of the observed isomer ratios, such as the geometric constraints imposed at the junction core[26], and the sequence-dependent electrostatic potential[24] on junction stacking preferences. MD simulations of J1 and J24 junction sequence demonstrated that stacking and geometric factors contributed to their structural changes[32]. Besides, the dynamics of individual Holliday junction has been studied using NMR and single-molecule fluorescence methodology[28, 33, 34]. Natural Holliday junction participates in the gene recombination process and can slide through the junction while maintaining the base pairing due to the symmetrical sequences near the junction. Immobile Holliday junctions[35, 36], also known as the immobile four-way junctions, were artificially created as a model of natural Holliday junctions and have been proposed as the structural building blocks in DNA nanotechnology. In the last decades, the strand sequences of DNA nanostructures were usually generated randomly. It was recently showed that the sequences of Holliday junctions had major impacts on the DNA crystal formation[37]. Other study indicated different sequences influenced the folding thermodynamics of DNA structures[38]. However, it remains to explore in detail how the Holliday junction sequences affect the thermodynamics and kinetics of the assembled DNA structures.

We previously established a DNA Domino origami array which comprised of many Holliday junctions.[39] The assembly of the DNA Domino origami array results in the defaulted conformation I if no triggers are present (Figure 1A and 1B). Upon hybridization of triggers to the edge of the structure, a conformational change is induced resulting in conformation II. In previous work, the junction sequences in the DNA origami array were randomly assigned. Here, we designed same junction sequences in the DNA origami arrays to evaluate the sequence effect on the thermodynamics and transition kinetics of the DNA origami array (see Figure 1C). Individual Holliday junction with proposed energy model can translate their sequence effects into the DNA origami arrays. The DNA origami array adopts two distinct conformations corresponding to the isomers of single Holliday junction, which enables the characterization of thermodynamics by AFM imaging. Besides, the dynamics of DNA origami transformation represents the transition process of many small Holliday junctions and allows the kinetic measurement of Holliday junction using both single-molecule and ensemble fluorescence assays. Moreover, the repeat arrangement of same Holliday junctions in the array amplifies the junction‘s thermodynamic and kinetic differences and thus allows to resolve the influence of the junctions sequence. We further studied how DNA mismatch, free bases effects as well as the magnesium

concentration influences the junction‘s thermodynamic and kinetic, demonstrating the universal applicability of our approach to characterize the thermodynamics and kinetics of DNA structures.

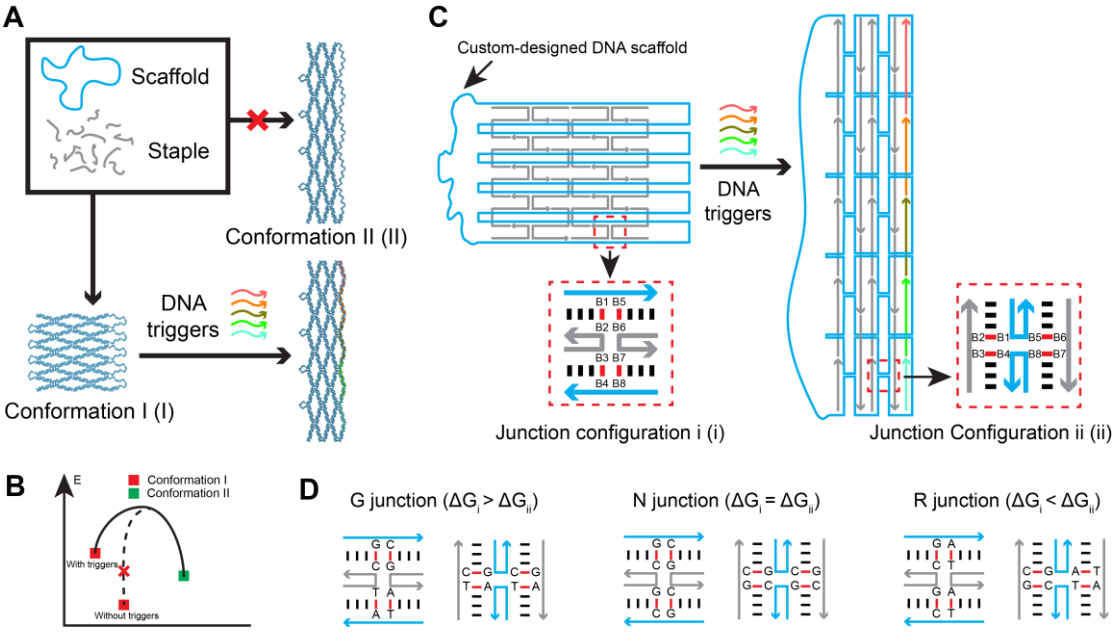

Figure 1. Schematics for sequence effect study of Holliday junctions on reconfigurable DNA origami arrays. A. The assembly of DNA scaffold and core staples results in conformation I of the array, which can further switch into conformation II with the addition of five DNA triggers. However, the mixtures can’t assembly into conformation II directly without trigger strands. B. Simplified free energy model for the conformation I and II of DNA origami arrays. C. The design of two conformations of the DNA origami arrays. Each array conformation is designed by connecting multiple the same antiparallel stacked conformation of Holliday junction. The blue strands of the Holliday junction represent the DNA scaffold when integrating on the DNA origami array. D. Three representative Holliday junctions used in this study with different sequence combinations at the junction position. Based on the energy analysis of both stacked configuration, G junction favored configuration ii and R favored i, while N had no favor over two configurations.

Results

Thermodynamics

In a first step, we characterized how the sequence of the four base-stacking pairs at the Holliday junction affect both the thermodynamics and transition kinetics in DNA origami structures. For single Holliday junctions among the 36 junction sequence combinations (see Figure S1), the energy of both stacked conformations I and II can be estimated by comparing the free energies (ΔG) of the four base-stacking pairs at the junction separately for each conformation (see Figure S2).

To study how energetic differences of Holliday junction conformations with different sequences translate their thermodynamic and kinetic properties to dynamic DNA origami systems composed of these Holliday junctions, we selected three representative junction sequence combinations, named G, N and R junction (see Figure 1D). The G and R junction correspond to the two junction sequence combinations which exhibit the largest difference in free energy between both stacked

Holliday junction conformations and favor the stacked conformation ii, i, respectively. The N junction represents a Holliday junction in which both conformations have the same free energy such that no conformation is favored over the other. We designed three reconfigurable DNA origami array structures (G, N and R structure, see Figure S3) composed of 18 Holliday junctions which correspond to the G, N and R junction, respectively. The self-assembly of DNA origami arrays presented different conformations in the presence or absence of triggers. In the absence of five trigger DNA strands, the structure resulted in the initial square-like shaped conformation (I). In presence of triggers, the resulting structures adopts an oblong shape (II), making both conformations easily distinguishable with AFM imaging (see Figure 2A and 2B).

To study the thermodynamics of the DNA origami arrays, we assembled all three structures with and without the five trigger DNA strands with one-pot annealing. We then recorded AFM images of the structures and determined the conformation II ratio as the fraction of structures in their transformed conformation from these images (see Figure 2C, Figure S8-S13). In absence and presence of all five trigger DNA strands, all structures quantitatively adapted the conformation I and conformation II, indicating the successful transformation specifically induced by the trigger DNA staples. As the for all structures quantitative transformation upon addition of all five trigger DNA strands did not allow resolving possible differences in thermodynamics between the different structures, we stepwise reduced the number of trigger DNA strands during the annealing process. As the trigger DNA strands are the driving force for stabilizing the conformation II, we hypothesized that this would stabilize the conformation I and thus push the equilibrium of the assembled structures further towards it, possibly making differences resolvable.

While one-pot assembly with only the upper four trigger DNA strands still resulted in a near quantitative transformation of all structures, a further reduction in the number of trigger DNA strands to only the upper three revealed differences in the conformation II yield for the G, N and R structure. With a value of 97.9±1.2% the G structure had the highest conformation II yield, followed by the N structure with a yield of 84.2±5.7% and the R structure with the lowest conformation II yield of 74.5±12.4%. With values of 52.8±6.6%, 37.8±5.0% and 7.8±4.8% for the G, N and R structure, respectively, these differences became even more pronounced when assembling the structures with only the upper two trigger DNA strands. Assembling with only one trigger DNA strand did not initiate the transformation process for any of the structures.

The lower conformation II ratio observed for all structures when reducing the number of trigger DNA strands is in good agreement with the assumption of a destabilizing effect of the trigger DNA strands on the conformation I on the DNA origami structures. Based on the measurement series we thus proposed a simplified energy model for the transformation described in Figure 2D. In absence of trigger DNA strands, the free energy of conformation I is significantly lower than the free energy of conformation II. The addition of each trigger DNA strand increases the free energy of conformation I until it eventually is significantly higher than that of the conformation II, explaining the quantitative conformation II upon addition of all five trigger DNA strands during the assembly.

The differences in conformation II ratio for the G, R and N structures when adding only the upper three or the upper two trigger DNA strands indicate that thermodynamic properties of the stacked conformations of single Holliday junctions are transferred to DNA origami structures composed of these Holliday junctions. G junctions have a lower free energy in conformation II as opposed to their conformation I while R junctions have

a lower free energy in their conformation I compared with the conformation II and N junctions show no favors towards either conformation. Therefore, the G structure shows the highest yields of conformation II followed by both the N structure and the R structure with the lowest yields. As such, sequence-dependent trends in the thermodynamics of the switching of Holliday junctions can be directly transferred to trends in thermodynamics of DNA origami transformations – which correspond to the global transition of many Holliday junctions. This finding is important not only for improving the design of dynamic DNA structures in future, but also gives access to thermodynamic properties of single Holliday junctions through DNA origami systems, facilitating their characterization. The arrangement of multiple Holliday junctions with the same sequence in a single DNA origami structure amplifies thermodynamic differences between different sequences: The DNA origami transformation represents the collective behavior of all incorporated Holliday junctions and as such enables resolving thermodynamic trends for different Holliday junctions by a broad variety of means by which they were previously not accessible, such as AFM imaging. The use of DNA origami additionally allows tuning the sensitive range of measurements: the addition of different numbers of trigger DNA strands allow varying the differences in free energy of the untransformed and transformed structures in a controlled manner independent to the possible effect of different DNA sequences.

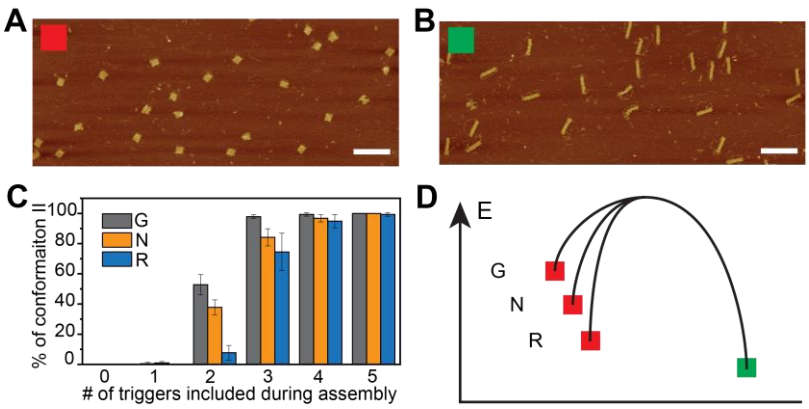

Figure 2. Thermodynamic study of DNA origami arrays. A and B. AFM images of conformation I and II of DNA origami array (G array). Scale bar: 200nm. C. Conformation II ratio in the assembled structures of three DNA origami arrays with different number of triggers during assembly. D. Simplified free energy model of two conformations for three DNA origami arrays (G, N, and R).

In a next step, we extended our studies from thermodynamics to the kinetic regime. For this, we designed a FRET assay which allowed us to track the conformation of the DNA origami structure over time. We placed a FRET probe composed of a red ATTO647N donor dye and an IowaBlack@RQ quencher as a signal transduction element on the arms of a representative Holliday junction in the structure. The principle of the FRET probe is illustrated in Figure 3A and S14a. In the untransformed DNA origami conformation, ATTO647N and IowaBlack@RQ are in proximity and the fluorescence of ATTO647N is quenched. In the transformed structure, the distance between ATTO647N and IowaBlack@RQ increases, resulting in an increased ATTO647N fluorescence which allows differentiation of both conformations via fluorescence.

To validate the performance of the FRET assay, we performed the thermodynamic characterization in single-molecule fluorescence measurements. For this, we equipped the structures with one biotinylated DNA strand for surface immobilization on BSA-biotin-neutravidin coated glass coverslips and additionally incorporated a green ATTO542 dye to identify each DNA origami position on the glass coverslips. We recorded fluorescence images of the DNA origami array structures before and after overnight incubation with and without different numbers of DNA staples at 37 °C on a total internal reflection (TIRF) microscope and quantified the transformation yield of the DNA origami array structures by calculating the fraction of DNA origami array structures in their transformed state (fraction of spots of co-localized ATTO542 and ATTO647N fluorescence of the total number of spots of ATTO542 fluorescence). Analogous to the AFM data, we observed the highest transformation yields for the G structure followed by both the N and the R structure (see Figure S14b), validating the performance of the FRET assay.

Kinetics

To extract kinetic information of the transformation process at the single-molecule level, we used time-lapsed imaging (excitation at 640 nm, 100 ms every 1 s) on the same area and extracted one-color fluorescence transients of single G, N and R DNA origami array structures bearing the FRET probe upon the addition of two trigger DNA strands. The transients exhibit single-step increase in fluorescence intensity (see Figure S15a). We interpreted the single-step increase in fluorescence as the transformation of the structure and defined the time between the addition of the DNA staples and this increase as the transformation time. The transformation times were extracted separately for each single structures from the transients (see Figure S15b). The corresponding transformation kinetics of all three structures are shown in Figure 3C. For the G structure, we obtained the fastest apparent rate constant with 0.126 /min ±0.023. For the N structure, the apparent rate constant was 0.080 /min ± 0.006. This tendency became even more pronounced for the R structure, which showed the apparent rate constant of 0.018 /min ± 0.005. The data shows that the sequence of single Holliday junctions translate their kinetic properties to the DNA origami array structures.

We additionally studied the influence of monovalent and bivalent cations on the transformation kinetics. Base-stacking has been shown to be sensitive to magnesium concentration and higher magnesium would enhance the base-stacking.[39] Reducing the magnesium concentration from 12.5 mM to 2 mM and additionally increasing the sodium concentration to 500 mM slowed down the mean transformation time of all three DNA origami array structures (see Figure S16 and Figure S17), indicating that the free energy of the conformation I and II is increased.

We then continued to study the possibility of resolving the kinetic differences occurring in the G, N and R structure in ensemble FRET measurements using a real-time PCR. We recorded kinetic scans of the three different DNA origami structures for 60 min at 30°C upon addition of all five trigger DNA strands and without trigger DNA strands (see Figure 3D-3H). We noted a significant increase in fluorescence intensity for all three structures upon incubation with five trigger DNA staples while the transformation process was not initiated at all upon incubation without trigger DNA strands. This finding implies that the FRET probe allows studying the kinetics of the DNA origami array. Notably, for the G and N structure, the transformation occurred quasi-

simultaneously upon incubation with all five trigger strands (0.21±0.03 and 0.20±0.02). In contrast, a time delay between the transformation in the R and the G and N structure was noticed upon incubation with all five trigger DNA strands (0.14±0.01). In combination, this implies that only the difference in the activation energy of the R structure and the G and N structure, respectively, is high enough to be resolvable within the measurement.

To further study the kinetics of the transformation process, we increased the activation energy of the transformation process by reducing the number of added trigger DNA strands from all five to only the upper one. The transition kinetics was slowed down gradually when the trigger DNA strands was reduced. Notably, when adding only the upper four trigger DNA strands, we notified a difference in the transformation kinetics of the G and the N structure (0.15±0.02 and 0.12±0.02) (see Figure 3I). Further reduction of the number of trigger DNA strands to three or two slowed down the ensemble kinetics but could still differentiate their kinetics (see Figure 3F and 3G). Addition of only one trigger strand did not initiate the transformation process at all (see Figure 3H). In combination, this shows that the repetitive incorporation of the same junction in the DNA origami amplifies the kinetic differences occurring in single Holliday junctions of different sequences and thus can be resolved in ensemble FRET measurements.

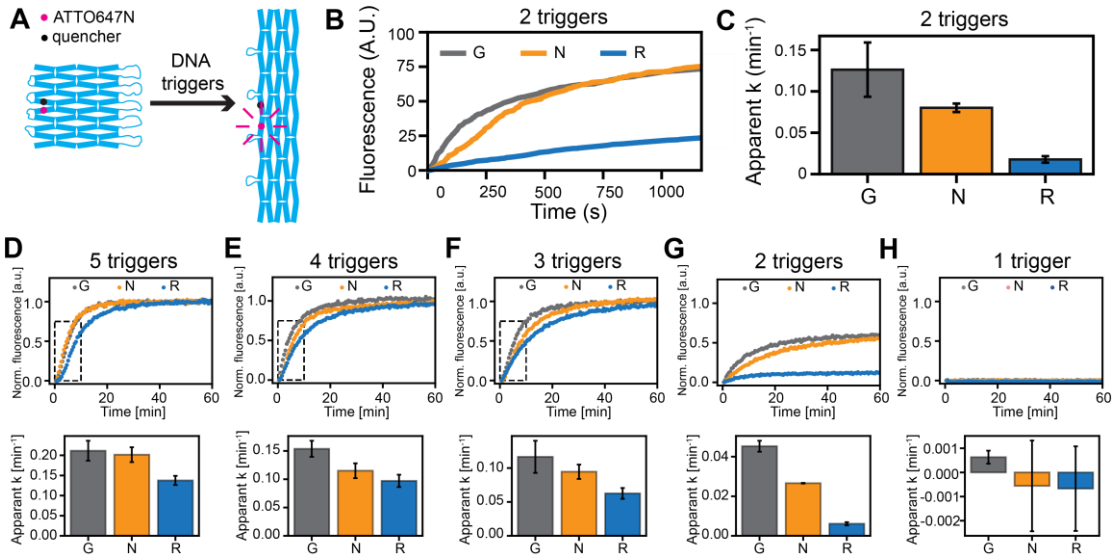

Figure 3. Kinetic study of DNA origami arrays. A. Fluorescent labeling of DNA origami arrays for the kinetic study. The ATTO647N and the quencher were labeled on the DNA strands in close proximity on the left side of DNA origami arrays. Before transformation, the fluorescence was quenched due to the close proximity with the quencher. After transformation, the fluorescence was enhanced due to the increased distance between ATTO647N and quencher. B. Single-molecule fluorescence kinetics of three DNA origami arrays with 2 triggers input. The experiment was performed for three times in 37℃ in TE buffer with 6 mM $MgCl_2$. C. The apparent rate constant k for three DNA origami arrays with 2 trigger input during the transformation. D to H. Top: ensemble fluorescence kinetics for the transformation of three DNA origami arrays with different number of triggers. The experiments were performed for three times in 30℃ in TE buffer with 6 mM $MgCl_2$. Below: The apparent rate constant k for three DNA origami arrays with different number of trigger input during the transformation.

The observed kinetic differences for the three DNA origami arrays indicated that three Holliday junctions had different kinetics and transferred such property to the origami structures. The transition between the two stacked conformations of junction involves two steps: the breaking of four base-stacking pairs and the forming new base-stacking pairs (see Figure S18a). The first step needs external energy input to bypass the energy barrier which is called activation energy (E_a) (see Figure S18b), while the second step does not consume energy. The E_a of three junctions can be calculated by the sum of the free energy of four base-pair stacking. Figure S18c to S18e listed the E_a of three junctions. G junction has the lowest E_a and R junction has the highest E_a. As the transition kinetics of conformation i to ii is E_a-dependent, lower E_a indicates faster kinetics, explaining the observed kinetic differences in both single-molecule and ensemble assays.

DNA mismatch effect

With a deeper understanding on how the canonical Watson-Crick (WC) base pairing sequence of single Holliday junctions effects the kinetic and thermodynamic properties of DNA origami arrays, we then aimed for investigating the effect of noncanonical sequence defects on the thermodynamics and kinetics of the transformation process. Representative for noncanonical sequence defects, we studied DNA mismatches and free bases. DNA mismatches are defects in the WC base-pairing occurring when two non-complementary bases are aligned on the same base-pair position in a DNA duplex. Compared with the canonical WC base-pairing where strong base-stacking occurs between two neighboring base pairs, the base-stacking near the DNA mismatch position is expected to be weakened. To explore this, we incorporated two mismatches for each Holliday junction (see Figure 4A). The two mismatches were assigned on different junction positions, resulting different thermodynamic preferences. For example, for mismatches on the position B5/B6 and B3/B4 in the configuration i, each DNA helix had one mismatch in configuration i and ii, thus named symmetric mismatch (M1). For the mismatches on B3/B4 and B7/B8 in configuration i, the two mismatches were on one DNA helix in configuration i but on two DNA helices in configuration ii, here named type M2. The reversed case was M3, where the mismatches on two DNA helices in configuration i and one DNA helices in configuration ii. The three types of mismatches had different energy models. As shown in figure 4B, in comparing the energy of configuration i for three types of mismatches, M1 and M3 had two mismatches on two DNA helices, thus has similar energy level and both should be higher than M2, where two mismatches on one DNA helix. For configuration ii, M1 and M2 had similar energy level and both were higher than M3.

To examine the mismatch effect on the thermodynamics of DNA origami arrays, we designed M1 and M2 for G structure, M1 and M3 for R structure (see Figure S21), and assembled the origami structures with and without mismatches. The conformation II ratio was extracted using AFM imaging (see Figure 4C-4D, Figure S22-S33). The fraction of conformation II structures increased with the number of added trigger DNA strands, being in good agreement with previous results. Interestingly, the mismatches showed different thermodynamic effect for the G and R structure. For the G structure, a higher fraction of transformed structures was obtained in the presence of the mismatch G_M1 while the implementation of the mismatch G_M2 resulted in a lower yield. In the presence of either R_M1 or R_M3, an increased yield of transformed structures was obtained for the R structure. Although introducing mismatches results in an increase of the energy of the conformation I and II, the extent of increase for both

conformations is different for the two structures. This leads to the uncertainness of the free energy differences between I and II and this difference may vary depending on each specific mismatch. Although quantitative calculation of mismatch effect on the thermodynamics of Holliday junction is lacking, our method presents an experimental strategy to verify the mismatch effect on the thermodynamics of DNA origami arrays.

The mismatch effect on the transition kinetics of DNA origami arrays was also investigated. The R origami array as well as its mismatched structures R_M1 and R_M3 were measured with transformation kinetics using single-molecule fluorescence assay and ensemble fluorescence method. In the ensemble fluorescence assay with five triggers (see Figure 4E and 4F), both mismatched structures R_M1 and R_M2 showed increased kinetics compared with R structure and had similar apparent rate constants. We further reduced the trigger number from five to two to differentiate the kinetics of R_M1 and R_M3 (see Figure 4G and 4H). The reduced trigger number slowed down the overall kinetics of three structures. Interestingly, R_M1 and R_M2 presented significant kinetic differences. This phenomenon was further verified using the single-molecule fluorescence assay (see Figure 4H to 4J). We additionally studied the kinetics of G structure and its mismatched structures G_M1 and G_M2 and found the two mismatched structures also had higher apparent rate constant than G structure (see Figure S34 and S35). We reason that the increased transition kinetics in mismatched structures is due to the increased free energy of conformation I, which reduces the activated energy for the transformation.

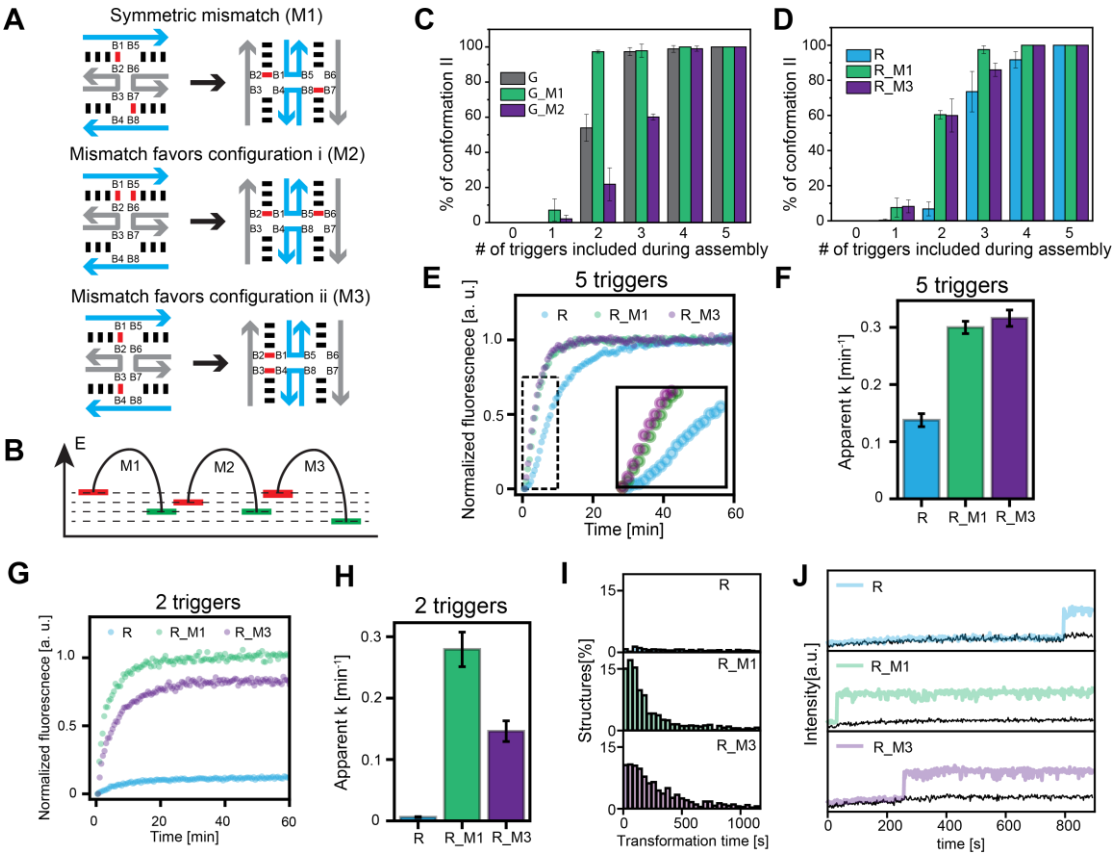

Figure 4. Mismatch effect on the thermodynamics and kinetics of the DNA origami arrays. A. Three types of mismatches on the Holliday junction used for the mismatch effect study. B. Free energy model for the DNA origami arrays with three types of mismatches. C and D. Conformation II ratio in the DNA origami array G and R and their mismatched variations. E. Ensemble fluorescent kinetics of R array with perfect match and M1 and M3 mismatches with 5 trigger input. F. The apparent rate constant k obtained in E. The experiments were performed for three times in 30℃ in TE buffer with 6 mM $MgCl_2$. G. Single-molecule fluorescent kinetics for R array and the M1 and M3 mismatches with 2 trigger input. H. The apparent rate constant k obtained in G. The experiments were performed for three times in 37℃ in TE buffer with 6 mM $MgCl_2$. I. The single structure transformation time distribution for the R array and M1 and M3 mismatches. J. Representative transformation fluorescence traces for the R array and M1 and M3 mismatches. The black line represented the background signal.

Free bases effect

Apart from the mismatch, we also engineered the free bases at the junction and studied the influence on DNA origami arrays. The position, number or the base type of the inserted bases can be programmed at the junction. As a representative example, we inserted a base “A” on the top strand of the junction and a base “T” on the bottom strand, as illustrated in Figure S36a. Both strands with insertions are on the DNA scaffold in the DNA origami array. To experimentally investigate the free bases effect, we produced a new DNA scaffold 1880RF based on the R structure to evaluate the assembled structure. We assembled two samples using the new scaffold with 5 triggers or without triggers. As shown in Figure S36b, both samples showed the same mobility in the agarose gel electrophoresis. The excised samples were further investigated with AFM imaging. Both samples exhibited in conformation II (Figure S36c and S36d). The assembled sample without triggers turned out in conformation II

demonstrated the increased free energy of conformation I after insertion of two bases at the junction. A base insertion in the blue strand at the junction (in configuration i) causes a small loop in the DNA duplex, which produces the weakened base-stacking at the junction. Whereas in the configuration ii, the inserted bases are between two DNA helices and base-stacking at the junction is scarcely affected. This explains the increased free energy of configuration i after the DNA base insertion.

Conclusion

We developed a DNA origami array model to study the junction sequence effect on the thermodynamics and transition kinetics. This model translated the thermodynamics and transition kinetics of individual Holliday junction into the collective behaviors of DNA origami array composing of the same junction sequence. The origami array amplifies the thermodynamic and kinetics differences of Holliday junctions with different sequences and enables the ensemble kinetic characterization of their differences for the first time. The experimental results demonstrated the agreement of collective behaviors of DNA origami arrays with the corresponding Holliday junction based on the energy model for single Holliday junction.

This approach not only help the understanding of how junction sequence influences the assembled DNA nanostructures, it also provides new methods to tune the transformation kinetics of the DNA origami array, as a complementary way to previously reported methods such as changing the external factors (temperatures or formamide) or structural design. We demonstrated two strategies to tune the global transformation kinetics of the origami array, namely, by changing the junction sequences in every Holliday junction in the array and the environmental magnesium concentration. Moreover, it is also possible to program the local transformation kinetics by engineering heterogeneous junction sequences in the selected regions of the array.

This approach also serves as a model to investigate the thermodynamics and transition kinetics of Holliday junctions with different factors. The origami array reflects the properties of the individual Holliday junction and provides an easy way to reveal the small changes in thermodynamics and kinetics by sequence effects. Although we focus the junction core sequence effect in this work, this model is applicable to study other effects on the Holliday junction. Structurally, the sequences near the junction core or even the distant junction arm sequences can be investigated using this model. Mechanical constrains or sequence-dependent electrostatic potentials, nicks, or other structural effects can be studied as well. Environmentally, beside the magnesium concentration studied in this work, other buffer conditions, or chemical reagents may influence the Holliday junction's preferences. In general, this model can be used to study many structural and environmental effects on Holliday junction. A thorough understanding of Holliday junction's preferences and its influence on the assembled structures can eventually promote the advance of DNA nanotechnology.

References:

(1) Rothemund, P. W. K. Folding DNA to create nanoscale shapes and patterns. *Nature* **2006**, *440* (7082), 297-302.

(2) Wei, B.; Dai, M.; Yin, P. Complex shapes self-assembled from single-stranded DNA tiles. *Nature* **2012**, *485* (7400), 623-626.

(3) Ke, Y.; Ong Luvena, L.; Shih William, M.; Yin, P. Three-Dimensional Structures Self-Assembled from DNA Bricks. *Science* **2012**, *338* (6111), 1177-1183.
(4) Ke, Y.; Meyer, T.; Shih, W. M.; Bellot, G. Regulation at a distance of biomolecular interactions using a DNA origami nanoactuator. *Nat. Commun.* **2016**, *7* (1), 10935.
(5) Thubagere Anupama, J.; Li, W.; Johnson Robert, F.; Chen, Z.; Doroudi, S.; Lee Yae, L.; Izatt, G.; Wittman, S.; Srinivas, N.; Woods, D.; Winfree, E.; Qian, L. A cargo-sorting DNA robot. *Science* **2017**, *357* (6356), eaan6558.
(6) Douglas Shawn, M.; Bachelet, I.; Church George, M. A Logic-Gated Nanorobot for Targeted Transport of Molecular Payloads. *Science* **2012**, *335* (6070), 831-834.
(7) Gerling, T.; Wagenbauer, K. F.; Neuner, A. M.; Dietz, H. Dynamic DNA devices and assemblies formed by shape-complementary, non–base pairing 3D components. *Science* **2015**, *347* (6229), 1446-1452.
(8) Yao, G.; Zhang, F.; Wang, F.; Peng, T.; Liu, H.; Poppleton, E.; Šulc, P.; Jiang, S.; Liu, L.; Gong, C.; Jing, X.; Liu, X.; Wang, L.; Liu, Y.; Fan, C.; Yan, H. Meta-DNA structures. *Nat. Chem.* **2020**, *12* (11), 1067-1075.
(9) Ong, L. L.; Hanikel, N.; Yaghi, O. K.; Grun, C.; Strauss, M. T.; Bron, P.; Lai-Kee-Him, J.; Schueder, F.; Wang, B.; Wang, P.; Kishi, J. Y.; Myhrvold, C.; Zhu, A.; Jungmann, R.; Bellot, G.; Ke, Y.; Yin, P. Programmable self-assembly of three-dimensional nanostructures from 10,000 unique components. *Nature* **2017**, *552* (7683), 72-77.
(10) Tikhomirov, G.; Petersen, P.; Qian, L. Fractal assembly of micrometre-scale DNA origami arrays with arbitrary patterns. *Nature* **2017**, *552* (7683), 67-71.
(11) Wagenbauer, K. F.; Sigl, C.; Dietz, H. Gigadalton-scale shape-programmable DNA assemblies. *Nature* **2017**, *552* (7683), 78-83.
(12) Duckett, D. R.; Murchie, A. I. H.; Diekmann, S.; von Kitzing, E.; Kemper, B.; Lilley, D. M. J. The structure of the holliday junction, and its resolution. *Cell* **1988**, *55* (1), 79-89.
(13) Murchie, A. I. H.; Clegg, R. M.; Krtzing, E. v.; Duckett, D. R.; Diekmann, S.; Lilley, D. M. J. Fluorescence energy transfer shows that the four-way DNA junction is a right-handed cross of antiparallel molecules. *Nature* **1989**, *341* (6244), 763-766.
(14) Clegg, R. M.; Murchie, A. I. H.; Zechel, A.; Carlberg, C.; Diekmann, S.; Lilley, D. M. J. Fluorescence resonance energy transfer analysis of the structure of the four-way DNA junction. *Biochemistry* **1992**, *31* (20), 4846-4856.
(15) Eichman, B. F.; Vargason, J. M.; Mooers, B. H. M.; Ho, P. S. The Holliday junction in an inverted repeat DNA sequence: Sequence effects on the structure of four-way junctions. *Proc. Natl. Acad. Sci. U. S. A.* **2000**, *97* (8), 3971-3976.
(16) Ho, P. S. Structure of the Holliday junction: applications beyond recombination. *Biochem. Soc. Trans.* **2017**, *45* (5), 1149-1158.
(17) Shida, T.; Iwasaki, H.; Shinagawa, H.; Kyogoku, Y. Characterization and Comparison of Synthetic Immobile and Mobile Holliday Junctions1. *J. Biochem.* **1996**, *119* (4), 653-658.
(18) Yadav, R. K.; Yadava, U. Molecular dynamics simulation of hydrated d(CGGGTACCCG)4 as a four-way DNA Holliday junction and comparison with the crystallographic structure. *Molecular Simulation* **2016**, *42* (1), 25-30.
(19) Starr, F. W.; Wang, W.; Nocka, L. M.; Wiemann, B. Z.; Hinckley, D. M.; Mukerji, I. Holliday Junction Thermodynamics and Structure: Comparisons of Coarse-Grained Simulations and Experiments. *Biophys. J.* **2016**, *110* (3), 178a.
(20) Yu, J.; Ha, T.; Schulten, K. Conformational model of the Holliday junction transition deduced from molecular dynamics simulations. *Nucleic Acids Res.* **2004**, *32* (22), 6683-6695.
(21) Eis, P. S.; Millar, D. P. Conformational distributions of a four-way DNA junction revealed by time-resolved fluorescence resonance energy transfer. *Biochemistry* **1993**, *32* (50), 13852-13860.
(22) Litke, J. L.; Li, Y.; Nocka, L. M.; Mukerji, I. Probing the Ion Binding Site in a DNA Holliday Junction Using Förster Resonance Energy Transfer (FRET). *Int. J. Mol. Sci.* **2016**, *17* (3), 366.
(23) Várnai, P.; Timsit, Y. Differential stability of DNA crossovers in solution mediated by divalent cations. *Nucleic Acids Res.* **2010**, *38* (12), 4163-4172.

(24) Duckett, D. R.; Murchie, A. I.; Lilley, D. M. The role of metal ions in the conformation of the four-way DNA junction. *EMBO J.* **1990**, *9* (2), 583-590.
(25) Møllegaard, N. E.; Murchie, A. I.; Lilley, D. M.; Nielsen, P. E. Uranyl photoprobing of a four-way DNA junction: evidence for specific metal ion binding. *EMBO J.* **1994**, *13* (7), 1508-1513.
(26) Lilley, D. M. J.; Clegg, R. M. The Structure of the Four-Way Junction in DNA. *Annu. Rev. Biophys. Biomol. Struct.* **1993**, *22* (1), 299-328.
(27) Lilley, D. M. J. Structures of helical junctions in nucleic acids. *Q. Rev. Biophys.* **2000**, *33* (2), 109-159.
(28) Hyeon, C.; Lee, J.; Yoon, J.; Hohng, S.; Thirumalai, D. Hidden complexity in the isomerization dynamics of Holliday junctions. *Nat. Chem.* **2012**, *4* (11), 907-914.
(29) Miick, S. M.; Fee, R. S.; Millar, D. P.; Chazin, W. J. Crossover isomer bias is the primary sequence-dependent property of immobilized Holliday junctions. *Proc. Natl. Acad. Sci. U. S. A.* **1997**, *94* (17), 9080-9084.
(30) Carlström, G.; Chazin, W. J. Sequence Dependence and Direct Measurement of Crossover Isomer Distribution in Model Holliday Junctions using NMR spectroscopy. *Biochemistry* **1996**, *35* (11), 3534-3544.
(31) Overmars, F. J. J.; Altona, C. NMR study of the exchange rate between two stacked conformers of a model holliday junction11Edited by I. Tinoco. *J. Mol. Biol.* **1997**, *273* (3), 519-524.
(32) Adendorff, M. R.; Tang, G. Q.; Millar, David P.; Bathe, M.; Bricker, William P. Computational investigation of the impact of core sequence on immobile DNA four-way junction structure and dynamics. *Nucleic Acids Res.* **2022**, *50* (2), 717-730.
(33) McKinney, S. A.; Déclais, A.-C.; Lilley, D. M. J.; Ha, T. Structural dynamics of individual Holliday junctions. *Nat. Struct. Biol.* **2003**, *10* (2), 93-97.
(34) Karymov, M.; Daniel, D.; Sankey, O. F.; Lyubchenko, Y. L. Holliday junction dynamics and branch migration: Single-molecule analysis. *Proc. Natl. Acad. Sci. U. S. A.* **2005**, *102* (23), 8186-8191.
(35) Kallenbach, N. R.; Ma, R.-I.; Seeman, N. C. An immobile nucleic acid junction constructed from oligonucleotides. *Nature* **1983**, *305* (5937), 829-831.
(36) Seeman, N. C. Nucleic acid junctions and lattices. *J. Theor. Biol.* **1982**, *99* (2), 237-247.
(37) Simmons, C. R.; MacCulloch, T.; Krepl, M.; Matthies, M.; Buchberger, A.; Crawford, I.; Šponer, J.; Šulc, P.; Stephanopoulos, N.; Yan, H. The influence of Holliday junction sequence and dynamics on DNA crystal self-assembly. *Nat. Commun.* **2022**, *13* (1), 3112.
(38) Gambietz, S.; Stenke, L. J.; Saccà, B. Sequence-dependent folding of monolayered DNA origami domains. *Nanoscale* **2023**, *15* (31), 13120-13132.
(39) Song, J.; Li, Z.; Wang, P.; Meyer, T.; Mao, C.; Ke, Y. Reconfiguration of DNA molecular arrays driven by information relay. *Science* **2017**, *357* (6349), eaan3377.
(40) Wang, D.; Song, J.; Wang, P.; Pan, V.; Zhang, Y.; Cui, D.; Ke, Y. Design and operation of reconfigurable two-dimensional DNA molecular arrays. *Nat. Protoc.* **2018**, *13* (10), 2312-2329.

Supporting Information

Sequence effect on the thermodynamics and transition kinetics of DNA origami arrays

Dongfang Wang [2,3,4], Fiona Cole [1,4], Martina Pfeiffer [1,4], Philip Tinnefeld [1*] and Yonggang Ke [2*]

[1] Department of Chemistry and Center for NanoScience, Ludwig-Maximilians-Universität München, Butenandtstr. 5-13, 81377 München, Germany

[2] Wallace H. Coulter Department of Biomedical Engineering, Emory University and Georgia Institute of Technology, Atlanta, GA 30322, USA

[3] School of Biomedical Engineering and Suzhou Institute for Advanced Research, University of Science and Technology of China, Suzhou 215123, China

[4] These authors contributed equally

[*] Correspondence: yonggang.ke@emory.edu, philip.tinnefeld@cup.uni-muenchen.de

Materials. Chemically synthesized DNA short strands were purchased from IDT (www.idtdna.com) and were used without further purification. All other reagents were purchased from Sigma-Aldrich or New England Biolabs.

DNA origami design and folding. The DNA origami was designed with the software CaDNAno (http://cadnano.org/)[1]. For DNA Origami folding, 10 nM scaffold together with a tenfold excess of each staple strand was mixed in 1×TE (10 mM Tris, 1 mM EDTA; pH 8.0) buffer with 6 mM $MgCl_2$. In the annealing process, the folding mixture was heated at 80°C and slowly cooled down to 25°C at the rate of -1°C/3 min. Afterwards, the folded DNA origami was purified from excess staple strands by agarose gel electrophoresis.

Agarose gel electrophoresis. DNA origami samples were subjected to agarose gel electrophoresis at 70 V for 2-3 hours in an ice water bath. Gels were prepared with 0.5 ×TBE buffer containing 10 mM $MgCl_2$ and 0.005% (v/v) Ethidium Bromide. To purify the sample, the gel was illuminated under UV light. The target band was cut and the sample was extracted by squeezing.

AFM imaging. Take 2 µL samples and deposit onto freshly cleaved mica. Fill the sample area with 80 µL 1×TE buffer with 10 mM $MgCl_2$. The samples were imaged on a Multimode VIII system (Bruker) in liquid mode using commercial tips (SNL-10, Bruker).

Production of custom DNA scaffold

The method follows a published paper[2] to produce custom DNA scaffold. The method uses a pScaf vector, which is commercially available on http://www.addgene.org/111401/. To produce custom DNA scaffold, a gene with prescribed sequence should be designed first. The gene contains the sequence with prescribed sequence and two restriction enzyme-recognition overhangs on both ends. The pScaf vector and gene were first digested by KpnI and BamHI enzymes and purified by agarose gel electrophoresis. Then pScaf vector and gene were mixed with 1:5 ratio and linked by T4 DNA ligase with overnight reaction. The mixtures were transformed into competent DH5α cells. The cells grow in a LB plate containing 100 µg/ml carbenicillin in 37˚C overnight. Select three colonies and do a miniprep to collect the plasmids. The plasmids were then digested by KpnI and BamHI and verified on the agarose gel electrophoresis. Correct insertion of gene into pScaf would show correct bands in the gel. Select the plasmid showing correct bands in the gel. The recombinant pScaf plasmid and helper plasmid pSB4423 were co-transformed into competent XL1-blue cells and incubated on a LB plate containing 50 µg/ml carbenicillin and 10 µg/ml chloramphenicol in 30˚C for two days. Select one colony to continue the growth in 2×YT medium and collect the custom DNA scaffold following the standard protocol for extracting ssDNA from M13 cells.

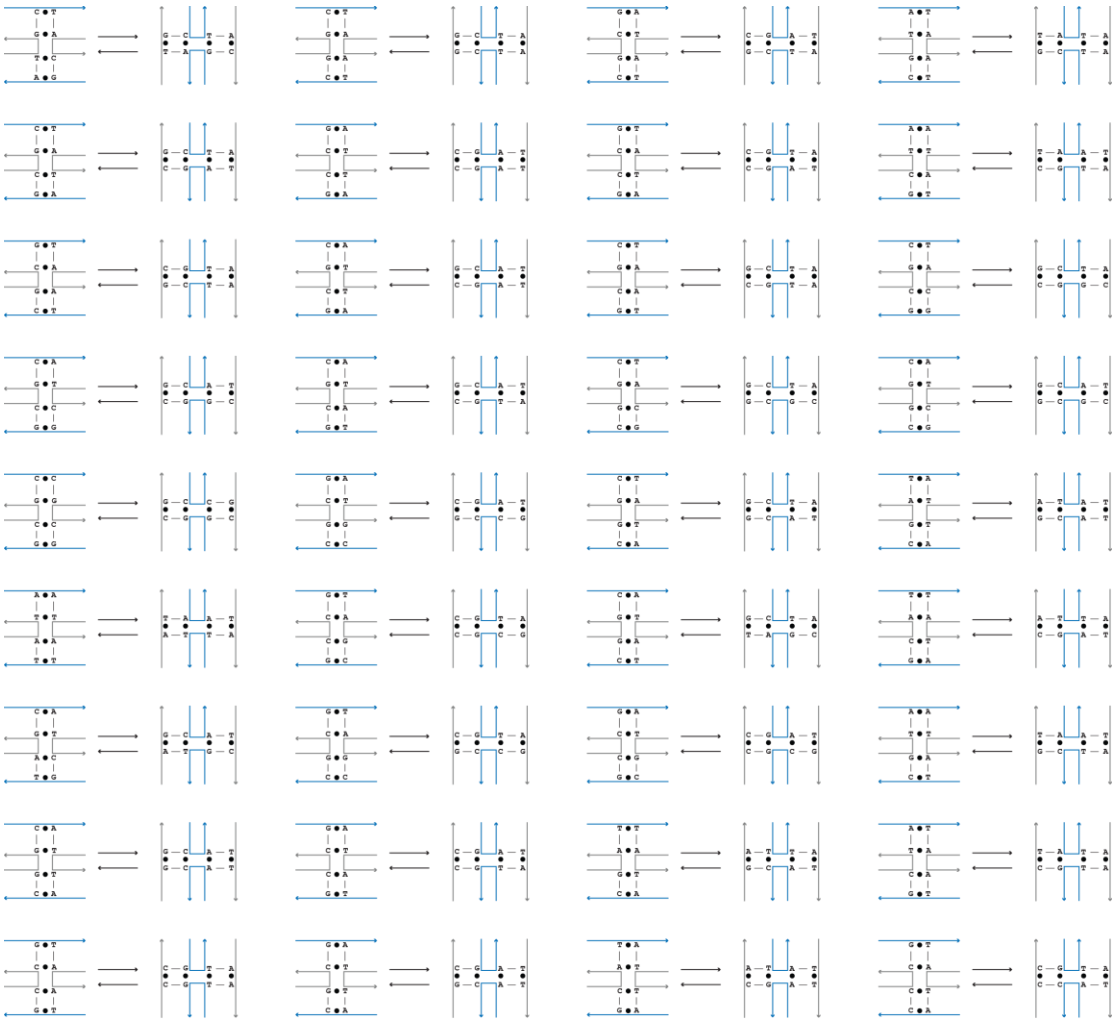

Figure S1. 36 sequence combinations of four-way junctions with two stacked antiparallel conformations.

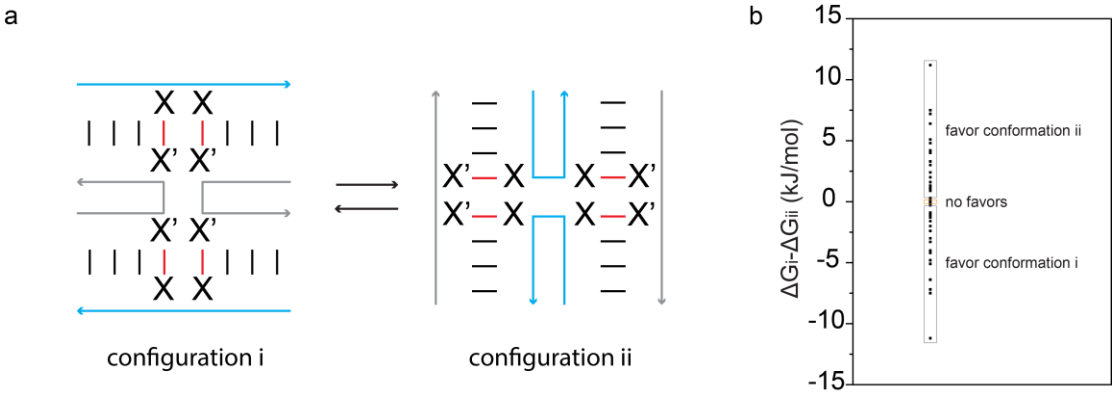

Figure S2. Sequence combinations at the DNA junction with switchable conformations (a) and plot of free energy differences ($\Delta\Delta G=\Delta G_i-\Delta G_{ii}$) between two stacked conformations under different sequence combinations (b). The thermodynamic data for base stacking was referenced from the literature[3].

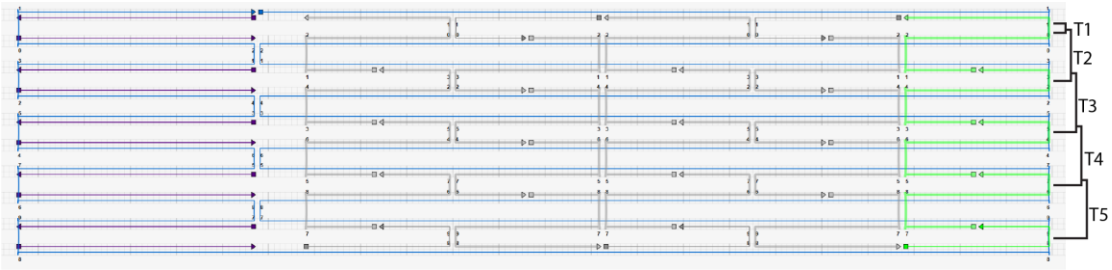

Figure S3. Design of DNA origami array with Cadnano software. Holliday junctions are connected into 9 × 2 arrays with a junction distance of 26-nt. The blue strand represents the DNA scaffold. Grey strands are used for core strands for assembling the DNA origami. Purple strands are forming the loop with the extra DNA scaffold. Green strands are triggers used for the transformation of DNA origami array. T1 to T5 represents the number of triggers from top to bottom.

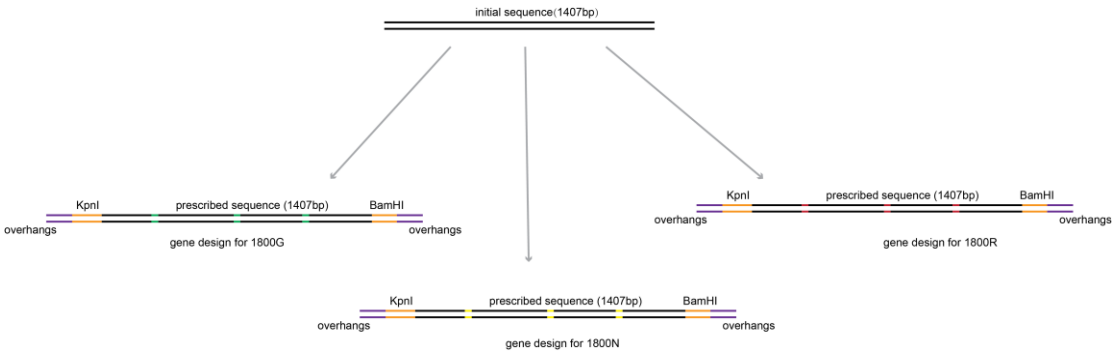

Figure S4. Gene design for producing three DNA scaffolds. First, an initial random sequence (1407 bp) was generated. Then prescribed sequence at the specific positions were assigned at the initial sequence to generate custom genes. Two restriction enzyme recognition sequences by KpnI and BamHI and 12 bp overhangs were assigned on both ends of the gene.

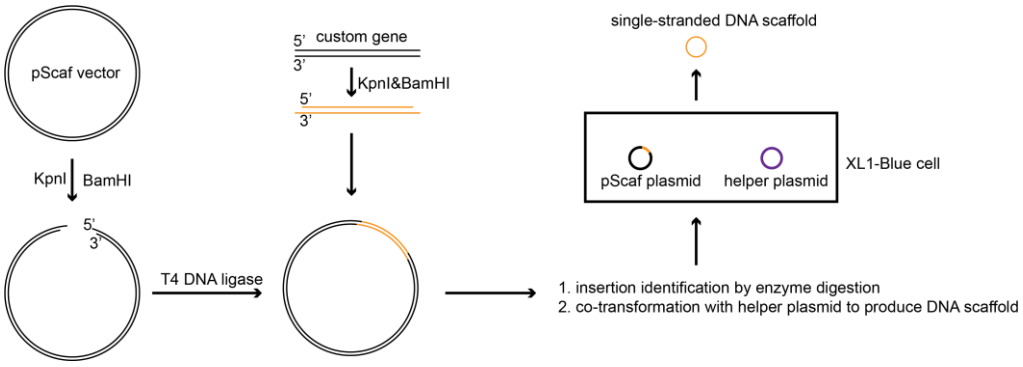

Figure S5. Procedures for producing custom DNA scaffold using pScaf vector. The pScaf vector and custom gene were digested by enzyme KpnI and BamHI. Then the vector and gene were ligated together by the T4 DNA ligase. The recombined plasmid was transformed into competent DH5α cells and successful ligation were verified by enzyme digestion of the new plasmid followed by agarose gel electrophoresis. The recombined plasmid and helper plasmid were co-transformed into competent XL1-Blue cells to produce custom ssDNA.

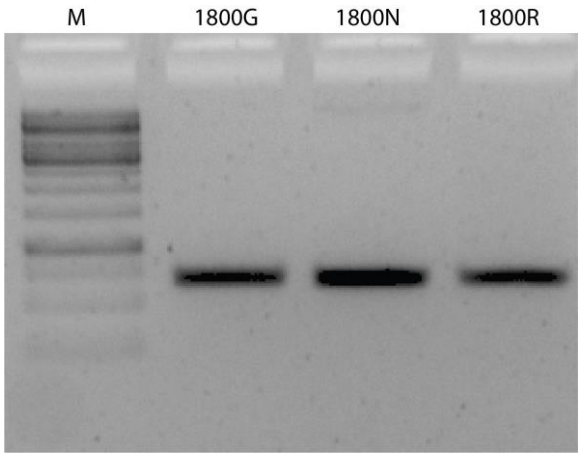

Figure S6. Agarose gel electrophoresis of custom DNA scaffold 1800G, 1800N and 1800R. M: 1kb DNA ladder.

Table S1. DNA scaffold sequences for the DNA origami.

1800G

tacgaagagttccagcagggattccaagaaatgGCcaatgaagattggatcacctttcgca
ctaagacctacttgtttgaggagtGCctgatgaattggcacgaccgcctcaggaaagtgga
ggagcattctgtgatgactgtcaagctccaatctgaggtggGCaaatataagattgttatc
cctatcTAgaagtacgtccgcggagaacacctGCcacccgatcactggctggatctgtTAc
gcttgctgggtctgcctcgcggcacatctctggagaaactgctgttcggtgacctgctgag
agttGCcgataccatcgtggccaaggctgcTAacctgaaagatctgaactcacgcgGCcag
ggtgaagtgaccatccgcgaaTAactcagggaactggatttgtggggcgtgggtgctgtgt
tcacactgatcgGCtatgaggactcccagagccgcaccTAgaagctgatcaaggattggaa
ggaGCtcgtcaaccaggtgggcgacaataTAtgcctcctgcagtccttgaaggactcacca
tactataaaggctttgaagacaaggtcagcatctggGCaaggaaactcgccgaactggacg
aTAatttgcagaacctcaaccatattcGCagaaagtgggtttacctcgaaccaTActttgg
tcgcggagccctgcccaaagagcagaccagattcaacagggtggGCgaagatttccgcagc
atcatgacaTAtatcaagaaggacaatcgcgtcacGCccttgactacccacgcaggcattc
TAaactcactgctgaccatcctggaccaattgcagagatgccagcgcagcctcaacgagtt
cctggagGCgaagcgcagcgccttccctcgcttTAacttcatcggagacgatgacctgcGC
gagatcttgggccagtcaaccaatTAatccgtgattcagtctcacctcaagaagctgtttg
ctggtatcaactctgGCtgtttcgatgagaagtctaagcacTAtactgcaatgaagtcctt
ggagggGCaagttgtgccattcaagaataacgTAcccttgtccaataacgtcgaaacctgg
ctgaacgatctggccctggagatgaagaagaccctggagGCgctgctgaaggagtgcgtga
caacTAgacgcagctctcagggagctgtggGCccttctctgttcccatcacagatcTAgtg
cttggccgaacagatcaagtttaccgaagatgtggagaacgcaattaaagatcactccctg
caccagattgagTAacagctggtgaacaaattggagcagtatactaacatcgacacatctt
ccgTAgacccaggtaacacagagtccggtattctggagctgaaactgaaagcactgattct
cgacggatccacgcgccctgtagcggcgcattaagcgcggcgggtgtggtggttacgcgca
gcgtgaccgctacacttgccagcgccctagcgcccgctcctttcgctttcttcccttcctt
tctcgccacgttcgccggctttccccgtcaagctctaaatcgggggctccctttagggttc
cgatttagtgctttacggcacctcgaccccaaaaaacttgatttgggtgatggttcacgta
gtgggccatcgccctgatagacggtttttcgccctttgacgttggagtccacgttctttAa
tagtggactcttgttccaaactggaacaacactcaaccctatctcgggctattcttttgat
ttataagggattttgccgatttcggggtacc

1800N

tacgaagagttccagcagggattccaagaaatgGCcaatgaagattggatcacctttcgca
ctaagacctacttgtttgaggagtGCctgatgaattggcacgaccgcctcaggaaagtgga
ggagcattctgtgatgactgtcaagctccaatctgaggtggGCaaatataagattgttatc
cctatcGCgaagtacgtccgcggagaacacctGCcacccgatcactggctggatctgtGCc
gcttgctgggtctgcctcgcggcacatctctggagaaactgctgttcggtgacctgctgag
agttGCcgataccatcgtggccaaggctgcGCacctgaaagatctgaactcacgcgGCcag
ggtgaagtgaccatccgcgaaGCactcagggaactggatttgtggggcgtgggtgctgtgt
tcacactgatcgGCtatgaggactcccagagccgcaccGCgaagctgatcaaggattggaa
ggaGCtcgtcaaccaggtgggcgacaataGCtgcctcctgcagtccttgaaggactcacca
tactataaaggctttgaagacaaggtcagcatctggGCaaggaaactcgccgaactggacg
aGCatttgcagaacctcaaccatattcGCagaaagtgggtttacctcgaaccaGCctttgg
tcgcggagccctgcccaaagagcagaccagattcaacagggtggGCgaagatttccgcagc
atcatgacaGCtatcaagaaggacaatcgcgtcacGCccttgactacccacgcaggcattc
GCaactcactgctgaccatcctggaccaattgcagagatgccagcgcagcctcaacgagtt
cctggagGCgaagcgcagcgccttccctcgcttGCacttcatcggagacgatgacctgcGC
gagatcttgggccagtcaaccaatGCatccgtgattcagtctcacctcaagaagctgtttg
ctggtatcaactctgGCtgtttcgatgagaagtctaagcacGCtactgcaatgaagtcctt
ggagggGCaagttgtgccattcaagaataacgGCcccttgtccaataacgtcgaaacctgg
ctgaacgatctggccctggagatgaagaagaccctggagGCgctgctgaaggagtgcgtga
caacGCgacgcagctctcagggagctgtggGCccttctctgttcccatcacagatcGCgtg
cttggccgaacagatcaagtttaccgaagatgtggagaacgcaattaaagatcactccctg
caccagattgagGCacagctggtgaacaaattggagcagtatactaacatcgacacatctt
ccgGCgacccaggtaacacagagtccggtattctggagctgaaactgaaagcactgattct
cgacggatccacgcgccctgtagcggcgcattaagcgcggcgggtgtggtggttacgcgca
gcgtgaccgctacacttgccagcgccctagcgcccgctcctttcgctttcttcccttcctt
tctcgccacgttcgccggctttccccgtcaagctctaaatcgggggctccctttagggttc
cgatttagtgctttacggcacctcgaccccaaaaaacttgatttgggtgatggttcacgta
gtgggccatcgccctgatagacggtttttcgccctttgacgttggagtccacgttctttAa
tagtggactcttgttccaaactggaacaacactcaaccctatctcgggctattcttttgat
ttataagggattttgccgatttcggggtacc

1800R

tacgaagagttccagcagggattccaagaaatgGAcaatgaagattggatcacctttcgca
ctaagacctacttgtttgaggagtGActgatgaattggcacgaccgcctcaggaaagtgga
ggagcattctgtgatgactgtcaagctccaatctgaggtggGAaaatataagattgttatc
cctatcTCgaagtacgtccgcggagaacacctGAcacccgatcactggctggatctgtTCc
gcttgctgggtctgcctcgcggcacatctctggagaaactgctgttcggtgacctgctgag
agttGAcgataccatcgtggccaaggctgcTCacctgaaagatctgaactcacgcgGAcag
ggtgaagtgaccatccgcgaaTCactcagggaactggatttgtggggcgtgggtgctgtgt
tcacactgatcgGAtatgaggactcccagagccgcaccTCgaagctgatcaaggattggaa
ggaGAtcgtcaaccaggtgggcgacaataTCtgcctcctgcagtccttgaaggactcacca
tactataaaggctttgaagacaaggtcagcatctggGAaaggaaactcgccgaactggacg
aTCatttgcagaacctcaaccatattcGAagaaagtgggtttacctcgaaccaTCctttgg
tcgcggagccctgcccaaagagcagaccagattcaacagggtggGAgaagatttccgcagc
atcatgacaTCtatcaagaaggacaatcgcgtcacGAccttgactacccacgcaggcattc
TCaactcactgctgaccatcctggaccaattgcagagatgccagcgcagcctcaacgagtt
cctggagGAgaagcgcagcgccttccctcgcttTCacttcatcggagacgatgacctgcGA
gagatcttgggccagtcaaccaatTCatccgtgattcagtctcacctcaagaagctgtttg
ctggtatcaactctgGAtgtttcgatgagaagtctaagcacTCtactgcaatgaagtcctt
ggagggGAaagttgtgccattcaagaataacgTCcccttgtccaataacgtcgaaacctgg
ctgaacgatctggccctggagatgaagaagaccctggagGAgctgctgaaggagtgcgtga
caacTCgacgcagctctcagggagctgtggGAccttctctgttcccatcacagatcTCgtg
cttggccgaacagatcaagtttaccgaagatgtggagaacgcaattaaagatcactccctg
caccagattgagTCacagctggtgaacaaattggagcagtatactaacatcgacacatctt
ccgTCgacccaggtaacacagagtccggtattctggagctgaaactgaaagcactgattct

cgacggatccacgcgccctgtagcggcgcattaagcgcggcgggtgtggtggttacgcgca
gcgtgaccgctacacttgccagcgccctagcgcccgctcctttcgctttcttcccttcctt
tctcgccacgttcgccggctttccccgtcaagctctaaatcgggggctccctttagggttc
cgatttagtgctttacggcacctcgaccccaaaaaacttgatttgggtgatggttcacgta
gtgggccatcgccctgatagacggtttttcgccctttgacgttggagtccacgttctttAa
tagtggactcttgttccaaactggaacaacactcaaccctatctcgggctattcttttgat
ttataagggattttgccgatttcggggtacc

1800RF

tacgaagagttccagcagggattccaagaaatgGCAcaatgaagattggatcacctttcgc
TactaagacctacttgtttgaggagtGCActgatgaattggcacgaccgcctcaTggaaag
tggaggagcattctgtgatgactgtcaagctccaatctgaggtggGCAaaatataagattg
ttatccctatcTACgaagtacgtccgcggagaacacctGCAcacccgatcactggctggat
ctgtTACcgcttgctgggtctgcctcgcggcacatctctggagaaactgctgttcggtgac
ctgctgagagttGCAcgataccatcgtggccaaggctgcTACacctgaaagatctgaactc
acgcgGCAcagggtgaagtgaccatccgcgaaTACactcagggaactggatttgtggggcg
tgggtgctgtgttcacactgatcgGCAtatgaggactcccagagccgcaccTACgaagctg
atcaaggattggaaggaGCAtcgtcaaccaggtgggcgacaataTACtgcctcctgcagtc
cttgaaggactcaccatactataaaggctttgaagacaaggtcagcatctggGCAaaggaa
actcgccgaactggacgaTACatttgcagaacctcaaccatattcGCAagaaagtgggttt
acctcgaaccaTACctttggtcgcggagccctgcccaaagagcagaccagattcaacaggg
tggGCAgaagatttccgcagcatcatgacaTACtatcaagaaggacaatcgcgtcacGCAc
cttgactacccacgcaggcattcTACaactcactgctgaccatcctggaccaattgcagag
atgccagcgcagcctcaacgagttcctggagGCAgaagcgcagcgccttccctcgcttTAC
acttcatcggagacgatgacctgcGCAgagatcttgggccagtcaaccaatTACatccgtg
attcagtctcacctcaagaagctgtttgctggtatcaactctgGCAtgtttcgatgagaag
tctaagcacTACtactgcaatgaagtccttggagggGCAaagttgtgccattcaagaataa
cgTACcccttgtccaataacgtcgaaacctggctgaacgatctggccctggagatgaagaa
gaccctggagGCAgctgctgaaggagtgcgtgacaacTACgacgcagctctcagggagctg
tggGCAccttctctgttcccatcacagatcTACgtgcttggccgaacagatcaagtttacc
gaagatgtggagaacgcaattaaTagatcactccctgcaccagattgagTACacagctggt
gaacaaattggagcagTtatactaacatcgacacatcttccgTACgacccaggtaacacag
agtccggtattctggagctgaaactgaaagcactgattctcgacggatccacgcgccctgt
agcggcgcattaagcgcggcgggtgtggtggttacgcgcagcgtgaccgctacacttgcca
gcgccctagcgcccgctcctttcgctttcttcccttcctttctcgccacgttcgccggctt
tccccgtcaagctctaaatcgggggctcccttttagggttccgatttagtgctttacggcac
ctcgaccccaaaaaacttgatttgggtgatggttcacgtagtgggccatcgccctgataga
cggtttttcgccctttgacgttggagtccacgttctttAatagtggactcttgttccaaac
tggaacaacactcaaccctatctcgggctattcttttgatttataagggattttgccgatt
tcggggtacc

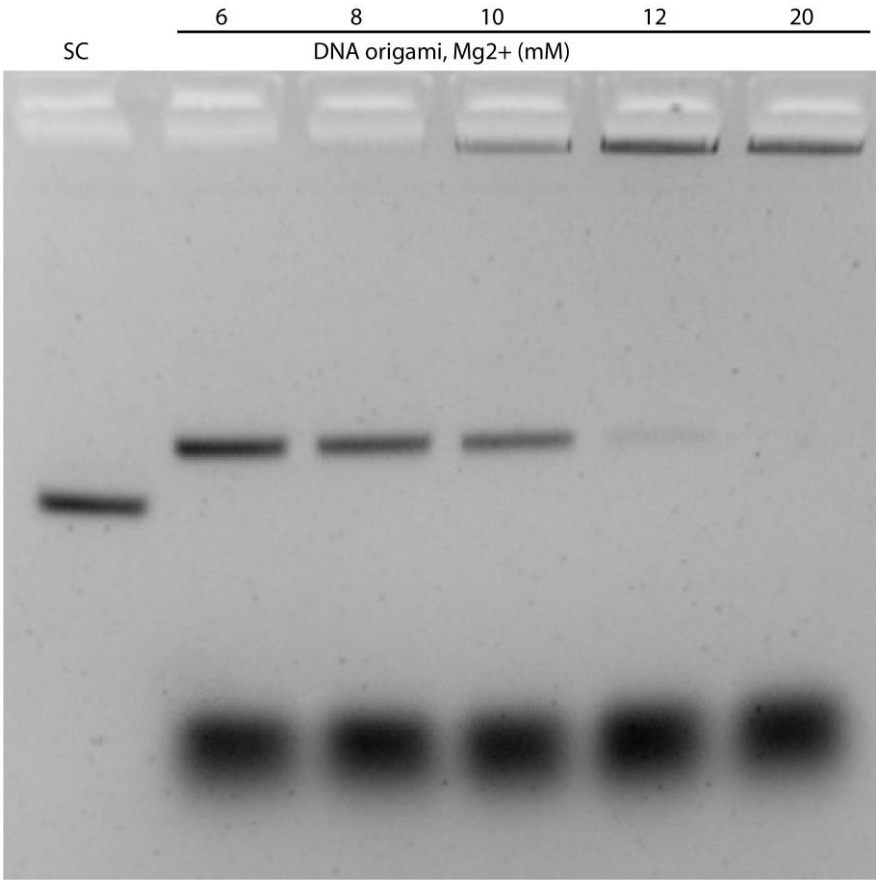

Figure S7. Screening of Mg^{2+} concentration for one-pot assembly of 9×2 G array. SC: DNA scaffold 1800G.

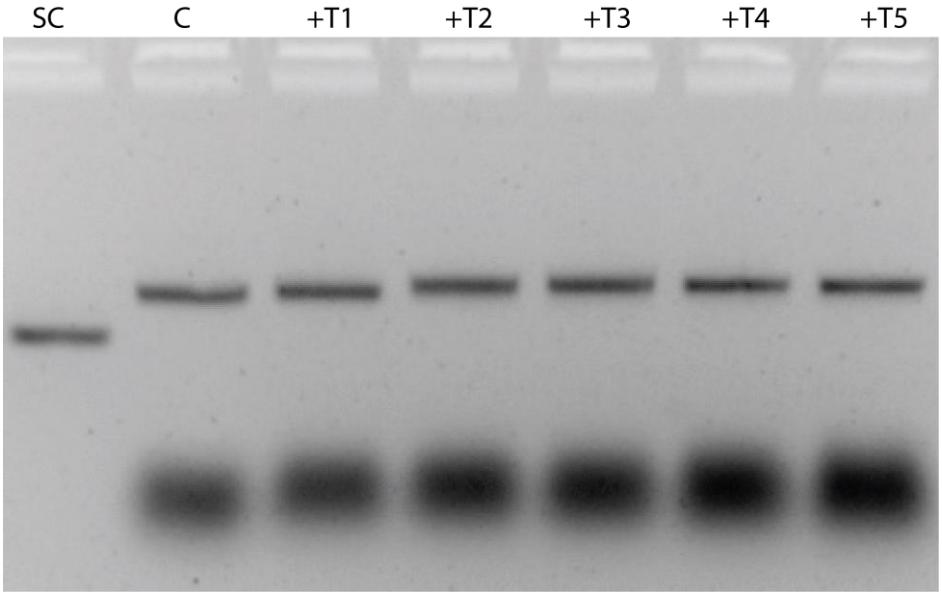

Figure S8. Agarose gel electrophoresis of G arrays from one-pot assembly with different number of triggers. SC: DNA scaffold 1800G. C: core structure without triggers. T1-T5: 1-5 trigger strands.

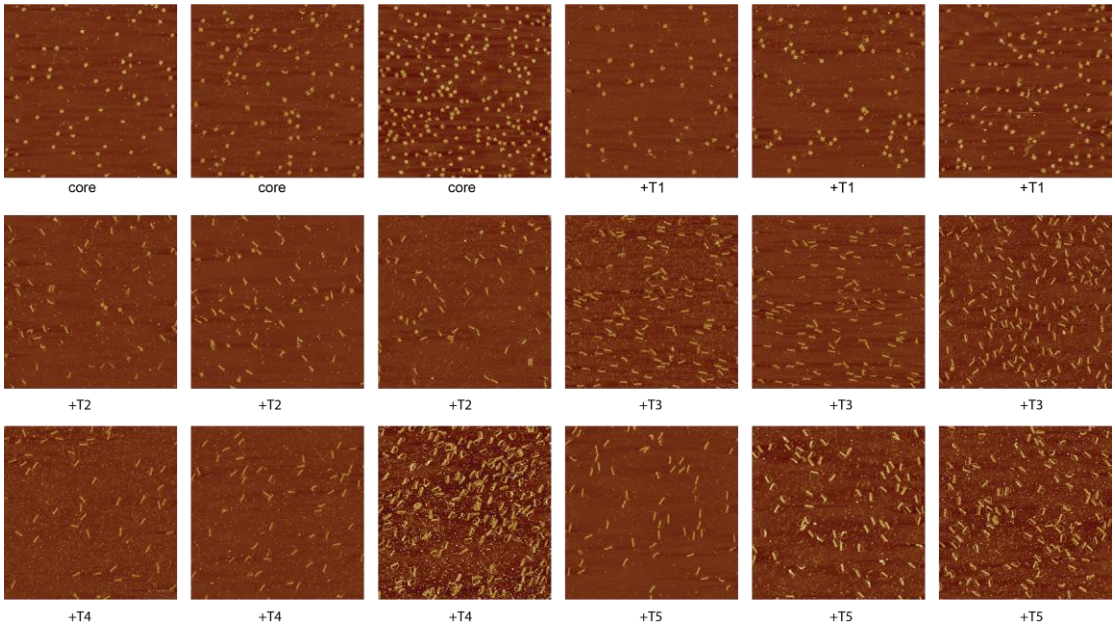

Figure S9. AFM images for G arrays from one-pot assembly with different number of triggers. Core: DNA origami array without triggers.

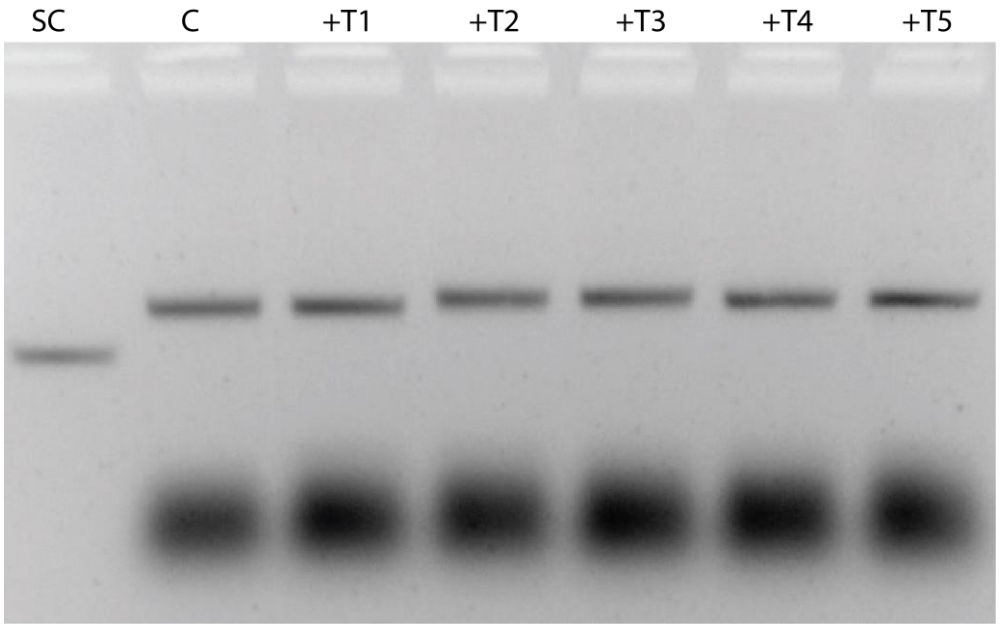

Figure S10. Agarose gel electrophoresis of N arrays from one-pot assembly with different number of triggers. SC: DNA scaffold 1800N. C: core structure without triggers. T1-T5: 1-5 trigger strands.

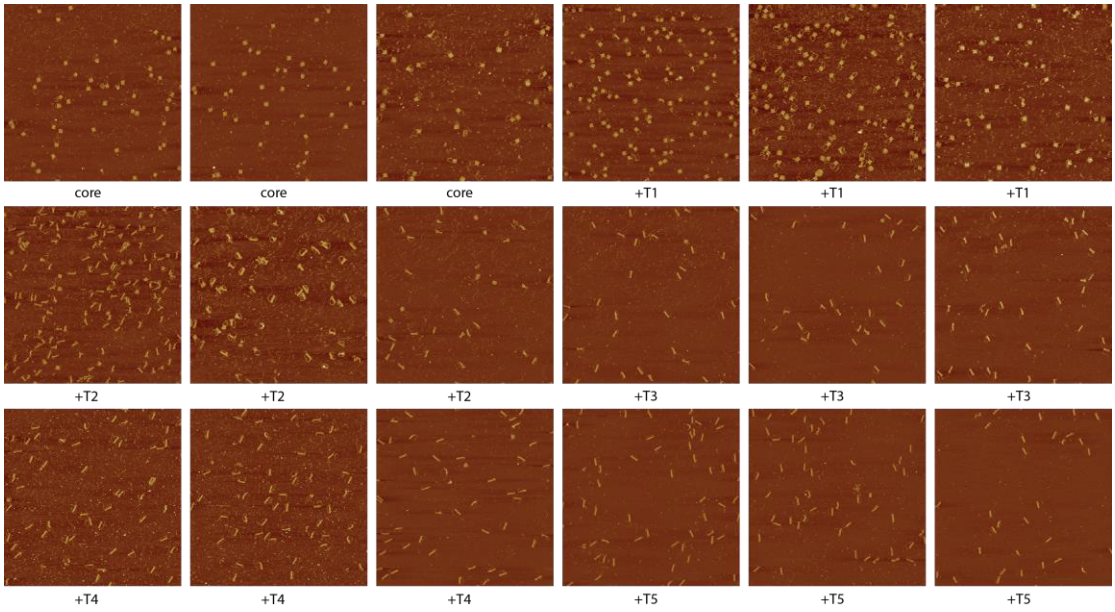

Figure S11. AFM images for N arrays from one-pot assembly with different number of triggers.

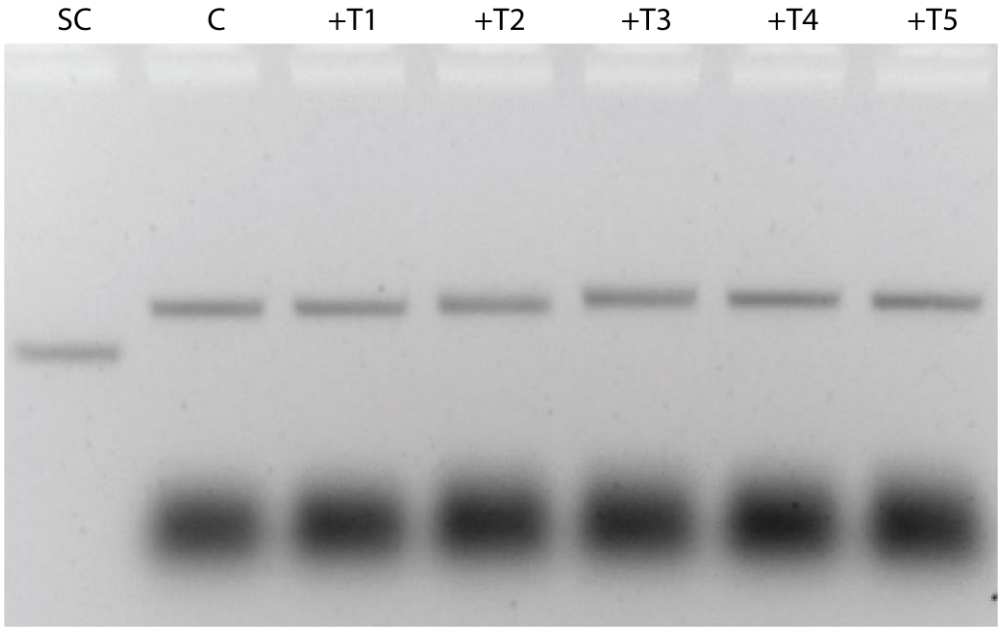

Figure S12. Agarose gel electrophoresis of R arrays from one-pot assembly with different number of triggers. SC: DNA scaffold 1800R. C: core structure without triggers. T1-T5: 1-5 trigger strands.

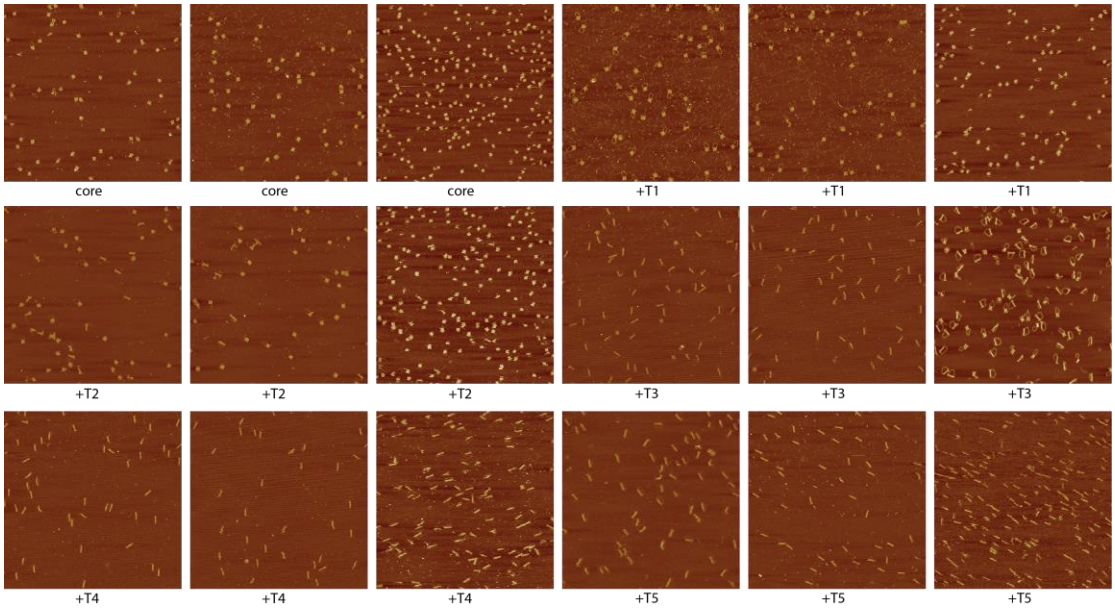

Figure S13. AFM images for R arrays from one-pot assembly with different number of triggers.

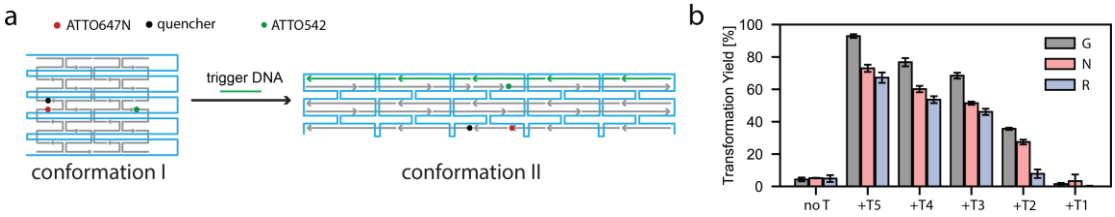

Figure S14. Transformation yields of DNA origami arrays using single-molecule fluorescence method. a) fluorescent labelling for the DNA origami arrays. ATTO647N and the quencher Iowa Black® RQ were labelled at the left side of the structures. ATTO542 was labelled on the right side of structures for the identification of origami structures. Before transformation, ATTO647N was quenched and only green fluorescence signal was observed. After transformation, with the increased distance of ATTO647N and Lowa black® RQ, both ATTO647N and ATTO542 were detected. The detection of ATTO647N represented the successful transformation of the array. b) transformation yield of three origami arrays under different number of trigger strands.

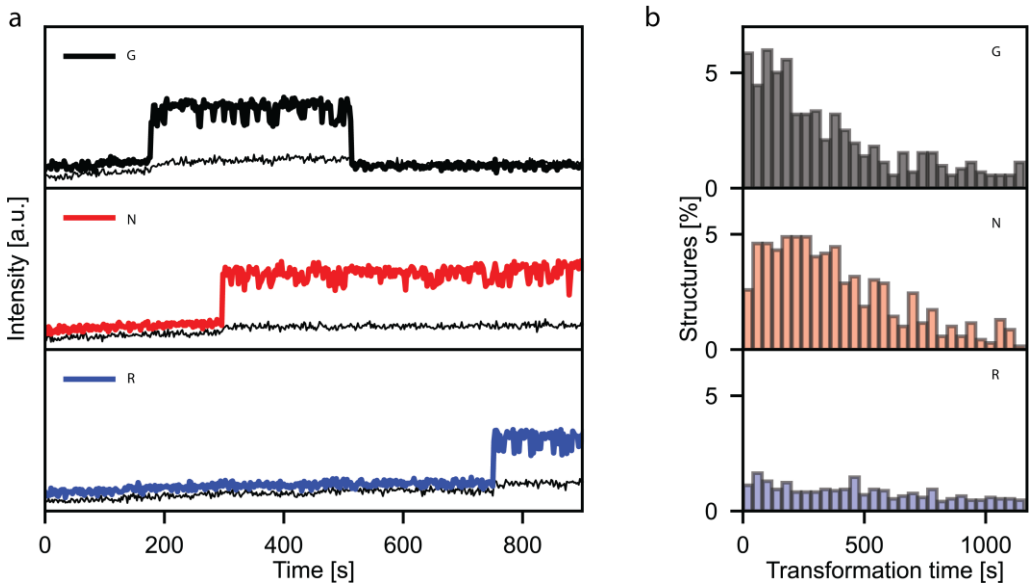

Figure S15. Single-molecule kinetics of DNA origami arrays with two triggers. a) Example fluorescence traces for the origami transformation. b) Transformation time distributions for three origami arrays with two triggers under 6 mM $MgCl_2$ and 37°C.

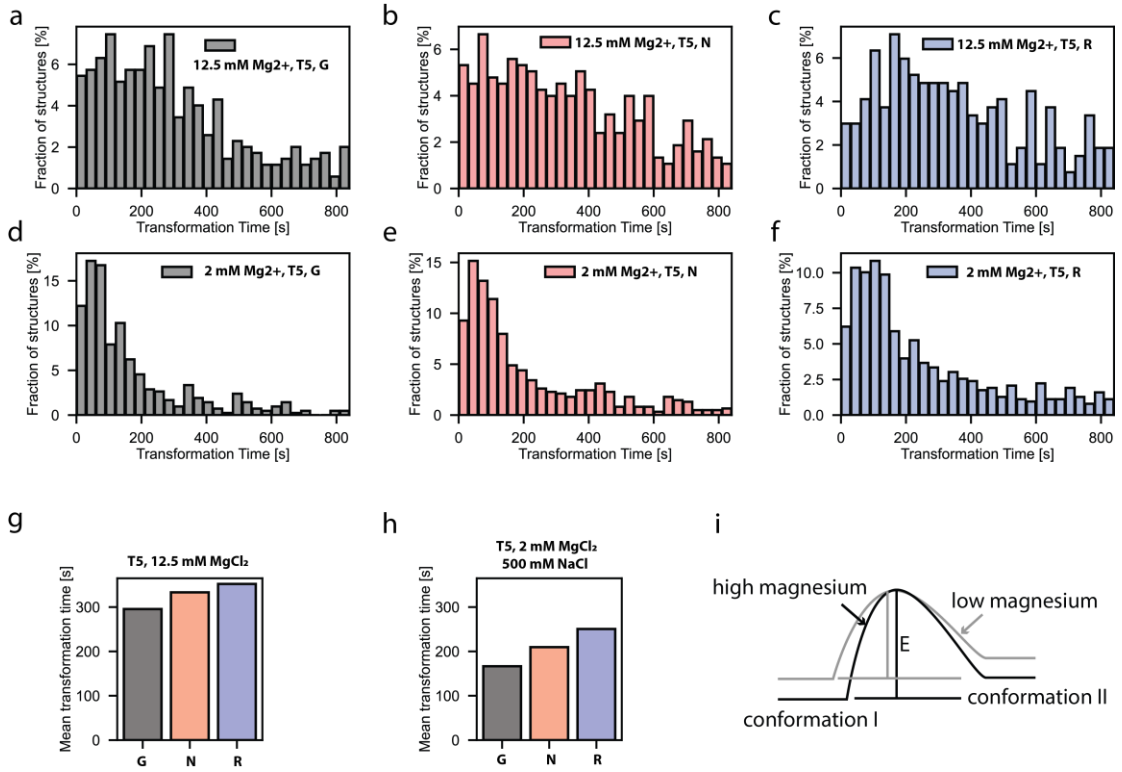

Figure S16. Magnesium concentration effect on the transformation kinetics of DNA origami arrays. a)-f) transformation time distributions for three DNA origami arrays under 12.5 mM $MgCl_2$ and 2 mM $MgCl_2$ and 500 mM NaCl. g) Mean transformation time of three DNA origami arrays using 5 triggers in 12.5 mM $MgCl_2$. The measurements were performed at 37°C. h) Mean transformation time of three DNA origami arrays using 5 triggers 2 mM $MgCl_2$ and 500 mM NaCl. The measurements were performed at 37°C. i) Simplified energy model of DNA origami array in low and high magnesium concentration.

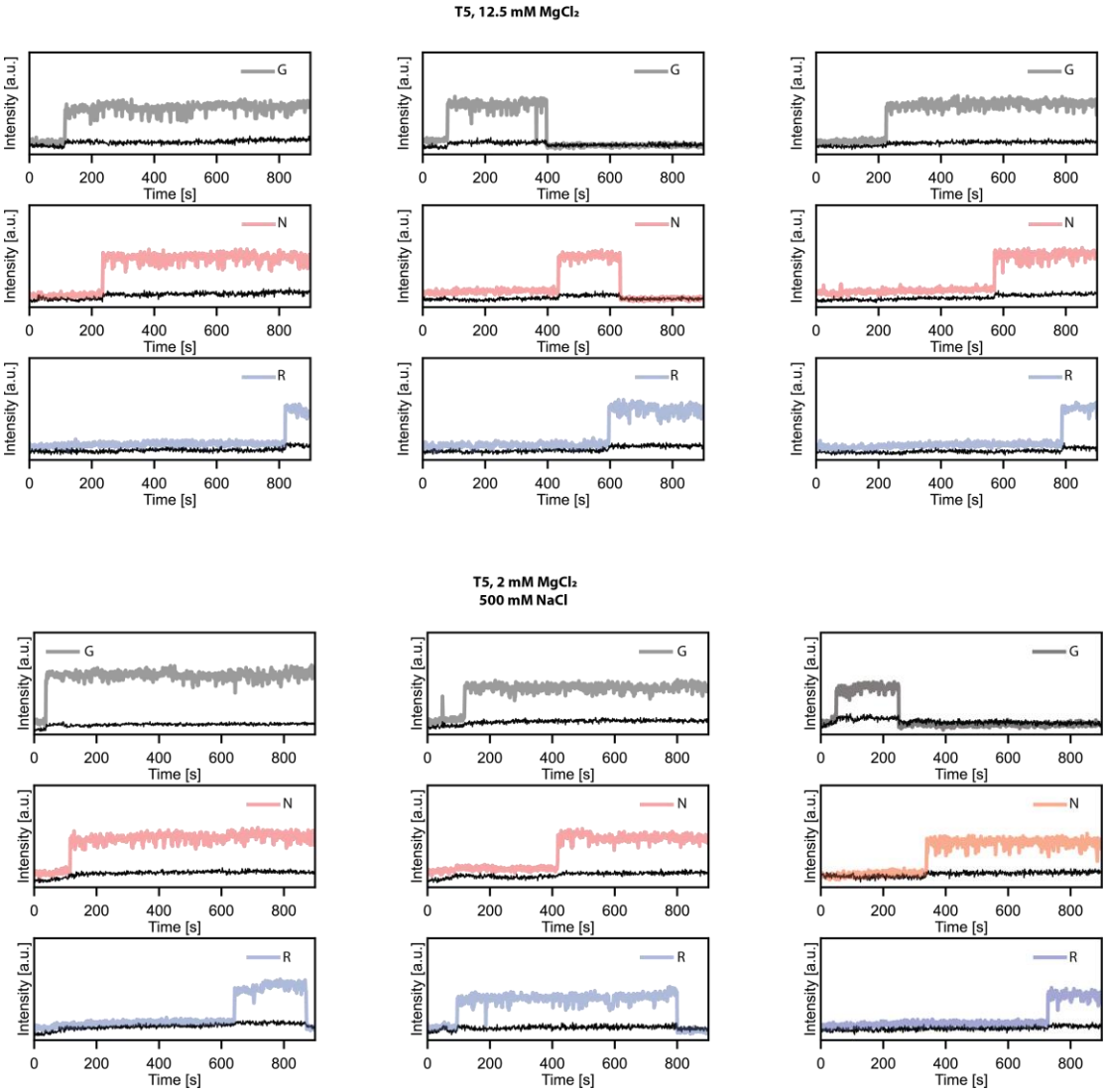

Figure S17. Example fluorescence traces for the DNA origami array transformation in 12.5 mM $MgCl_2$ and 2 mM $MgCl_2$ with 500 mM NaCl using five triggers. The measurements were performed at 37°C.

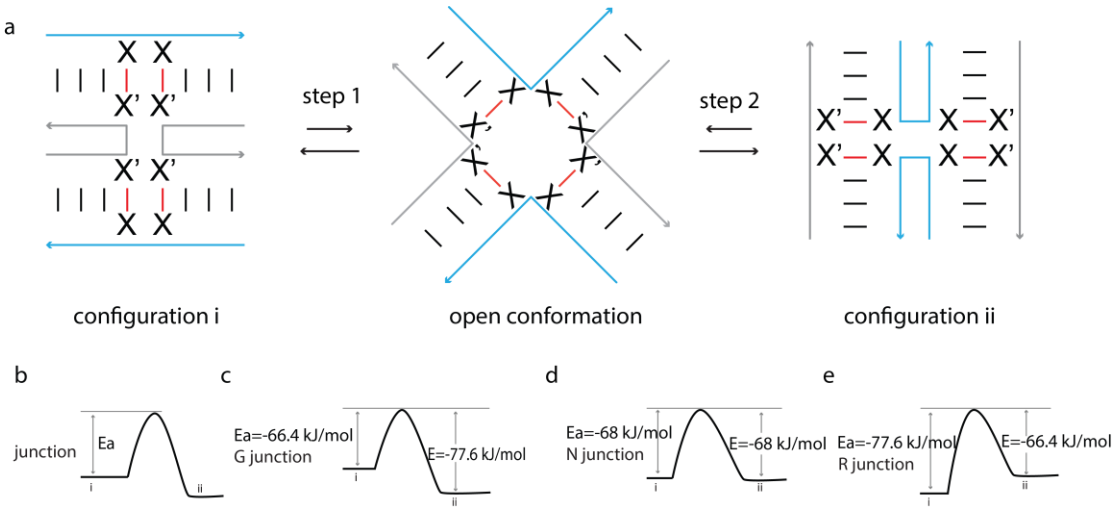

Figure S18. a. The switch between two configurations of Holliday junction through an open conformation. X represents any base of the four DNA bases and X' represents the complementary base. b. Energy model for the transformation of an individual DNA junction. The junction needs certain activation energy (Ea) to bypass the energy barrier for the transformation. c, d and e. Energy barrier for three Holliday junctions.

Ensemble fluorescence measurements. For ensemble transformation kinetics measurements, DNA origami samples were assembled by mixing 20 nM DNA scaffold, 200 nM DNA staples, 10 nM ATTO647N modified staple and 20 nM quencher modified staple in 1xTE buffer and 6 mM Mg^{2+}. The mixtures were annealed from 80°C to 25°C with the rate of -1°C/3 min. 200 nM triggers were added to the core structures and their fluorescence measured in a real-time PCR machine (Rotor-Gene Q, Qiagen, USA). Fluorescence measurements were carried out at 30 °C over a time of 60 min and a data point was taken every 30 s. All measurements were repeated three times. To normalize the fluorescence measurements to the completely transformed sample, the fluorescence after 60 min of samples to which all five triggers were added and the fluorescence of the untransformed samples were used as reference points for the untransformed and transformed sample, respectively (see Figure S20a-c). An additional experiment in which the samples to which all five triggers were added were heated to 50 °C for 1.5 h directly after the measurement showed no additional increase in fluorescence intensity, indicating that their fluorescence after 60 min measurement time represents the completely transformed sample and can be used for normalization (see Figure S19d-f)

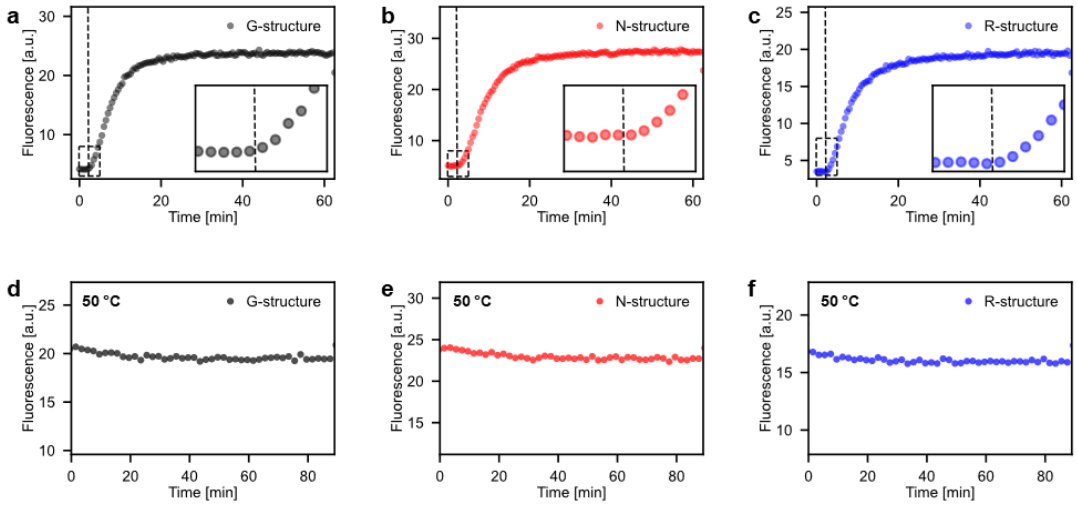

Figure S19 Non-normalized fluorescence intensity transients upon addition of five triggers. (a-c) Combined fluorescence transients of the measurements of the untransformed samples before and after addition of the five triggers for the G, N and R structure. The addition of the triggers is indicated by a dashed line. The insets show a zoom-in of the area highlighted by the dashed box. (d-f) Fluorescence transients recorded directly after the transformation measurement for the samples shown in a-c at 50 °C.

Overall transformation kinetics as convolution of the kinetics of multiple steps. Unlike the single-exponential decay observed in dwell time histograms for the switching kinetics of single Holliday junctions,[1] for the DNA origami arrays, we obtained nonexponential transformation time distributions that displayed a rising phase followed by a decay in the single-molecule experiments. Analogously, the ensemble measurements showed an initial phase of increasing transformation rates. Such a behavior cannot be described by kinetic laws of single step processes but is characteristic for the convolution of the kinetics of multiple steps. As such, the array transformation most probably consists of multiple consecutive steps, an assumption which is in good agreement with previous studies. They describe the DNA origami transformation as a multi-step process. In each of these steps, different Holliday junctions in the arrays switch their conformation, ultimately resulting in the transformation of the whole structure.

Extracting 'apparent' transformation rate constants from the ensemble measurements. To compare the kinetics of the transformation of the different structures, we defined an apparent transformation rate constant k. The calculation of k is exemplarily described for the transformation of the G, N and R structure upon addition of five triggers in Supplementary Fig. 20. First, the normalized fluorescence transients were calculated as described above (Supplementary Fig. 20a). These transients describe the change in concentration of the transformed structures over time. By subtracting the normalized fluorescence values from one, the change in concentration of the untransformed structures was depicted (Supplementary Fig. 20b). Similar to single-step first order kinetics, the apparent transformation rate constant k was then extracted as the negative slope of linear fits to the logarithmic representation of the plots shown in Supplementary Fig. 20b (Supplementary Fig. 20c). For the linear fit, only data points recorded between 2 min and 15 min were considered to exclude both the initial phase of increasing transformation rates and the end point of the transformation reaction.

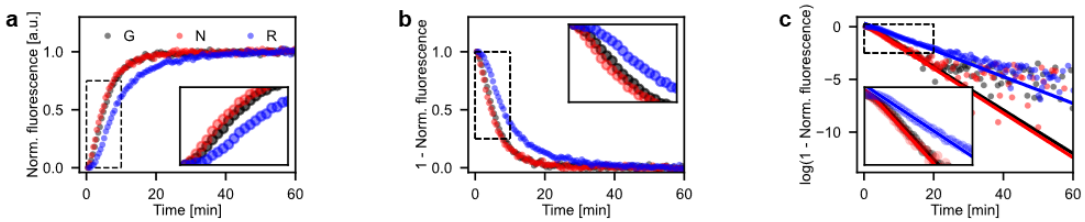

Figure S10 Extracting apparent transformation rate constants from the ensemble measurements. (a) Normalized fluorescence transients for the transformation of the G, N and R-structure upon addition of all five triggers. The transients describe the gradual increase in concentration of the transformed structure. (b) By subtracting the normalized fluorescence from one, the resulting transients describe the change in concentration of the untransformed structure over time. (c) The apparent transformation rate constants k was extracted as the negative slope of the linear fits to the logarithmic transients of the data shown in b. For the linear fit, only data points between 2 min and 15 min were considered to exclude both the initial phase of increasing transformation rates and the end point of the transformation reaction. The insets show a zoom-in of the areas highlighted by the dashed boxes.

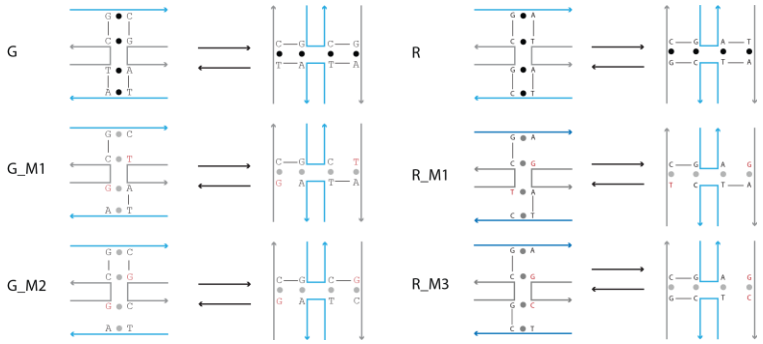

Figure S21 Junction sequences for mismatches of G and R DNA origami arrays.

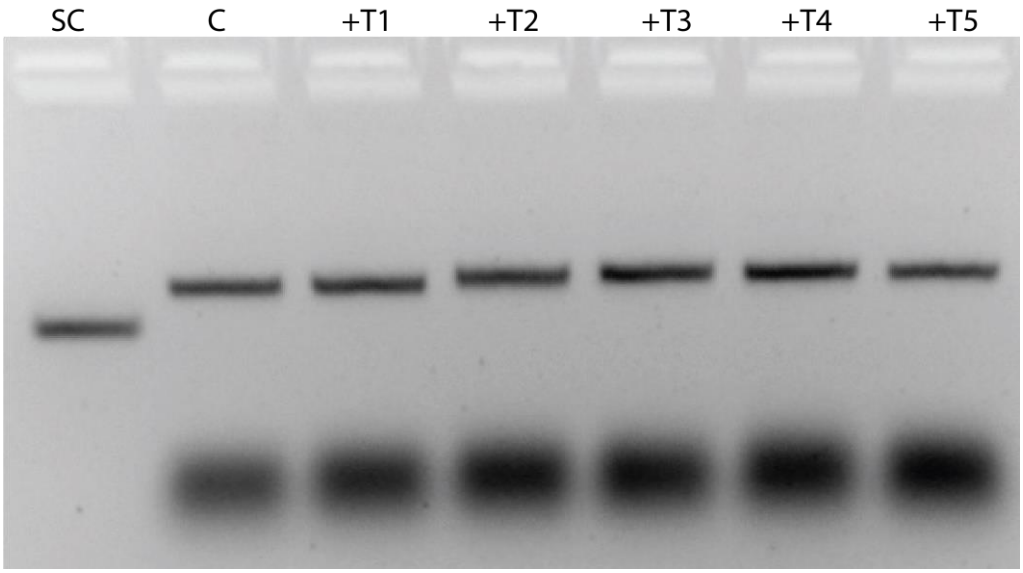

Figure S22. Agarose gel electrophoresis of G arrays from one-pot assembly with different number of triggers.

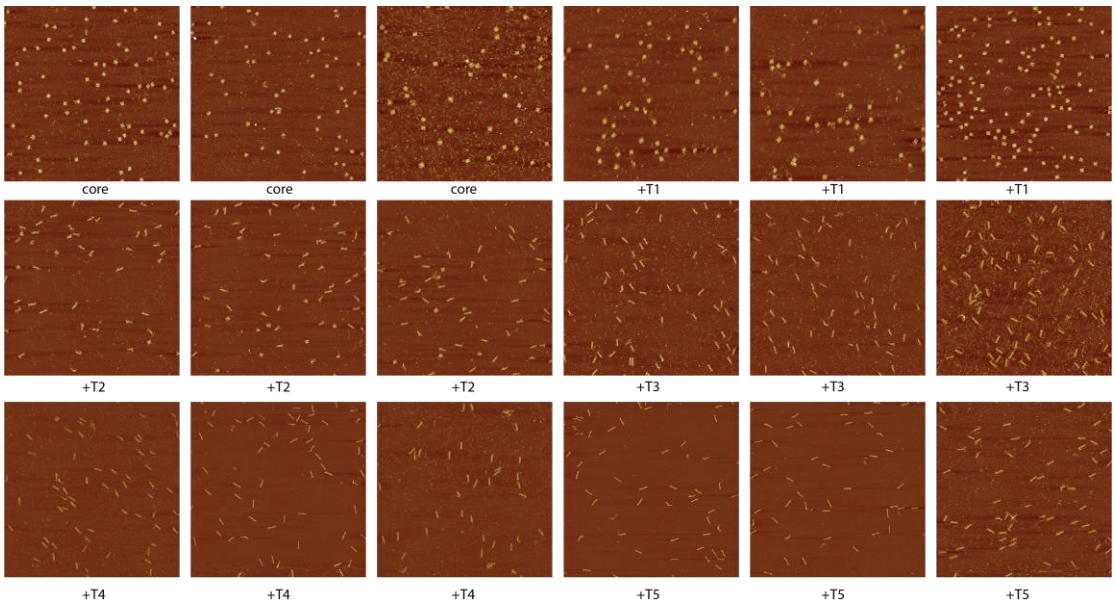

Figure S23. AFM images of G arrays from one-pot assembly with different number of triggers.

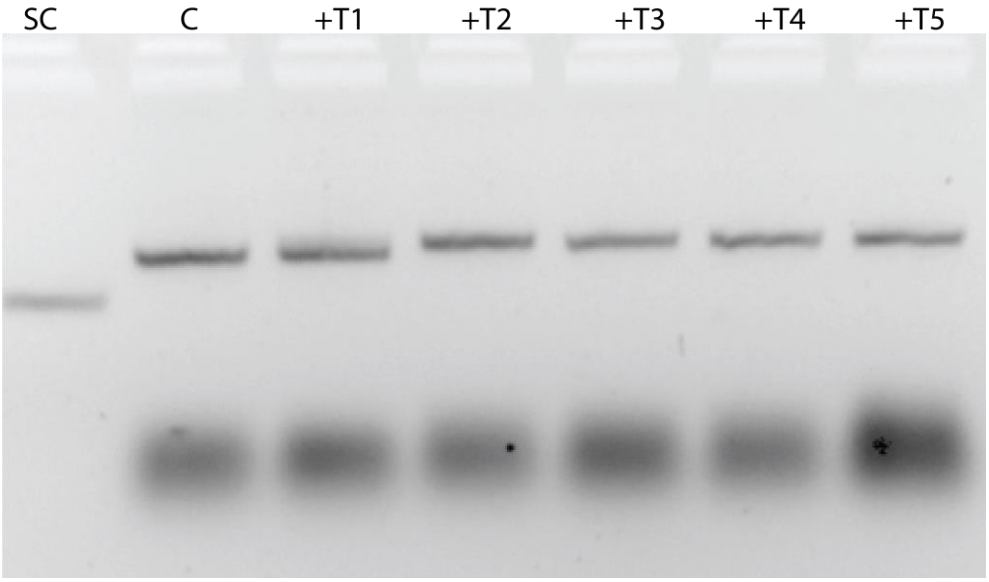

Figure S24. Agarose gel electrophoresis of G_M1 arrays from one-pot assembly with different number of triggers.

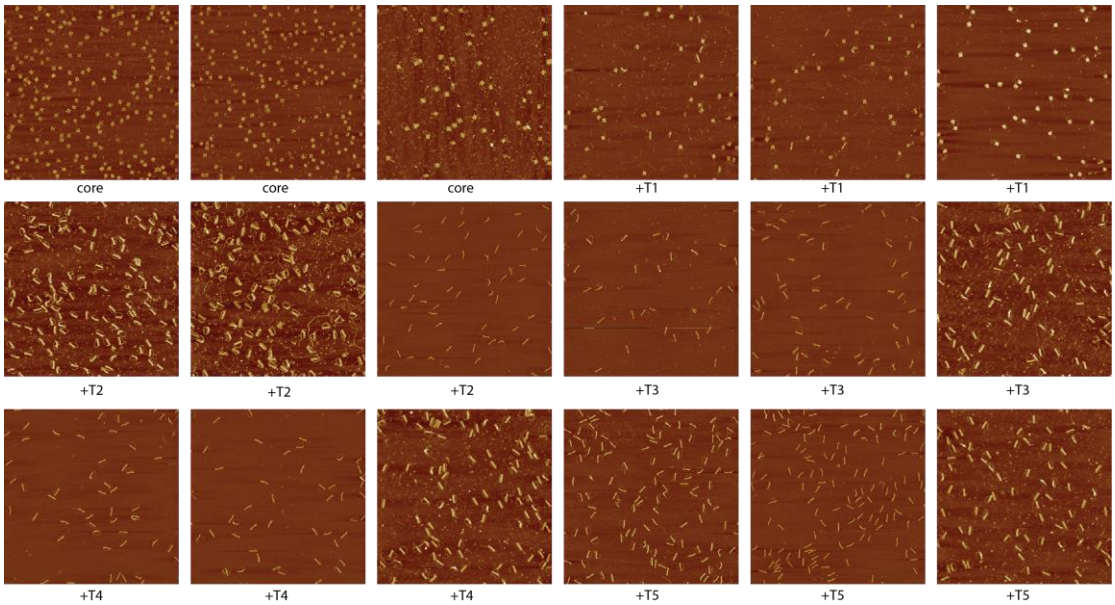

Figure S25. AFM images of G_M1 arrays from one-pot assembly with different number of triggers.

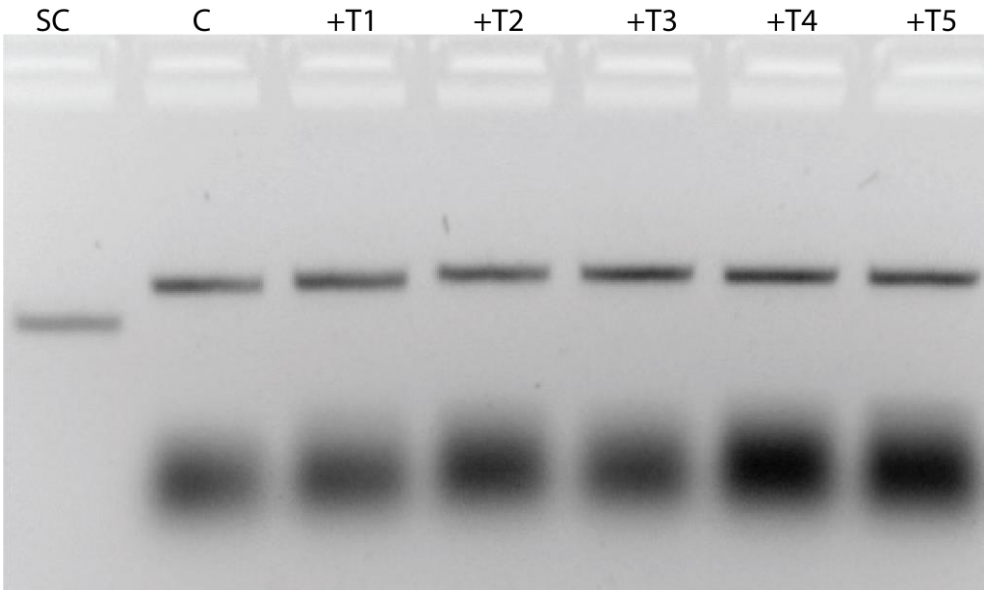

Figure S26. Agarose gel electrophoresis of G_M2 arrays from one-pot assembly with different number of triggers.

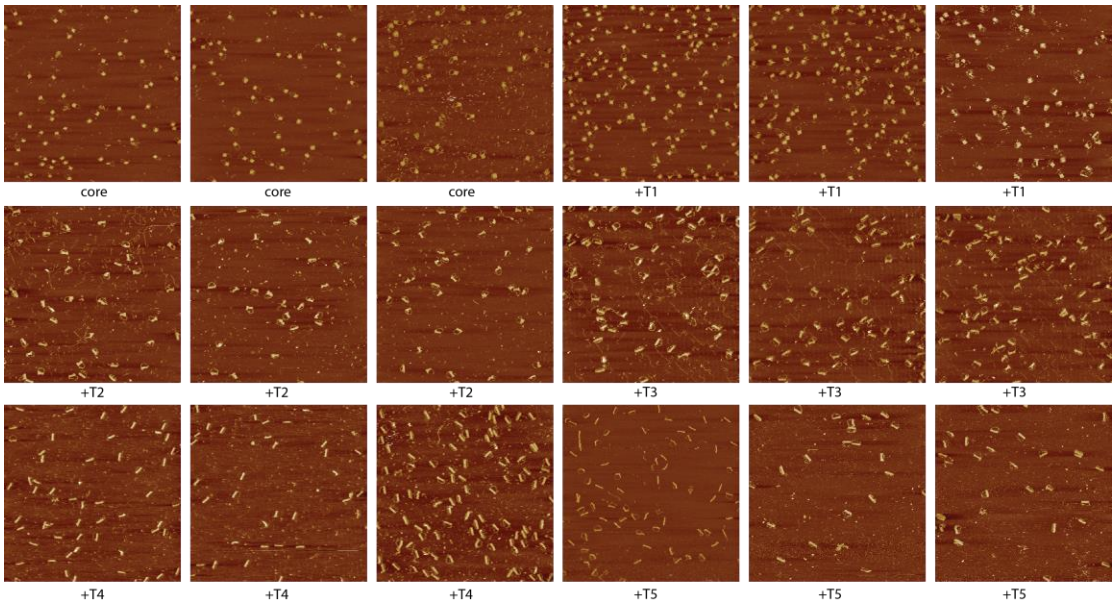

Figure S27. AFM images of G_M2 arrays from one-pot assembly with different number of triggers.

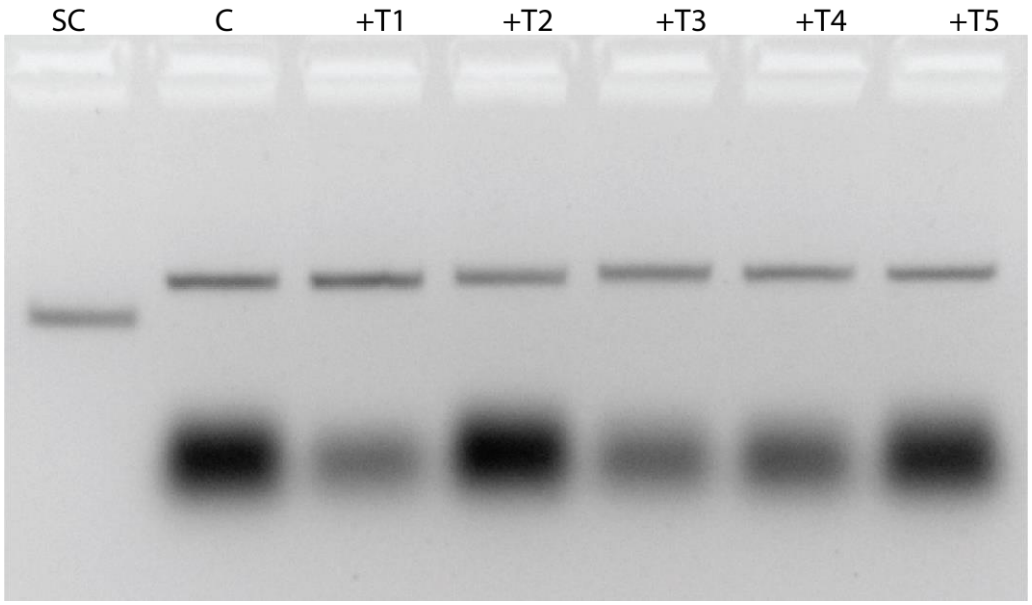

Figure S28. Agarose gel electrophoresis of R arrays from one-pot assembly with different number of triggers.

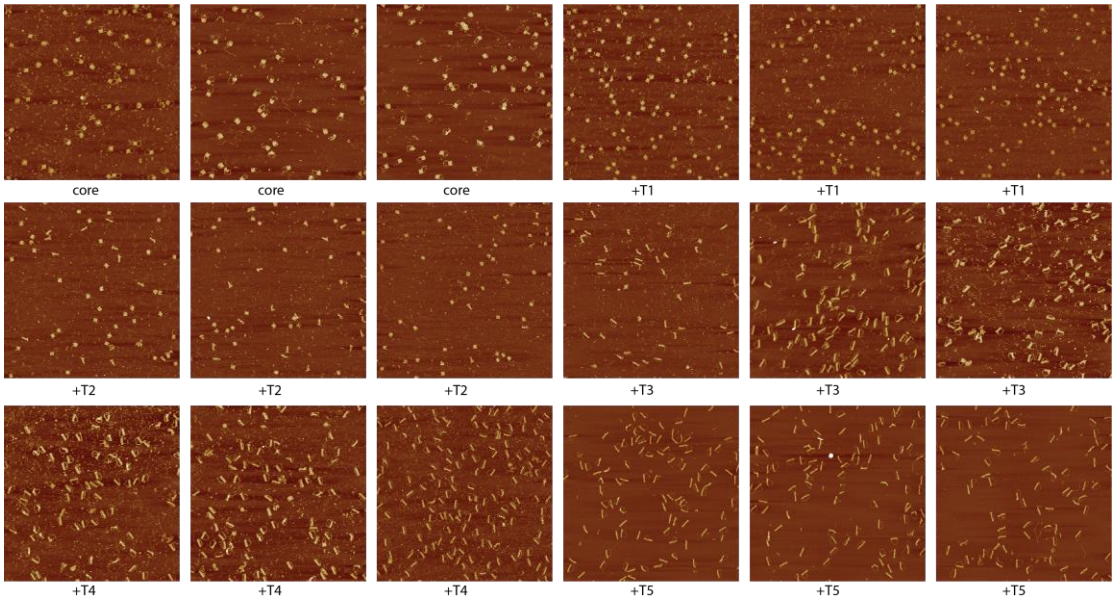

Figure S29. AFM images of R arrays from one-pot assembly with different number of triggers.

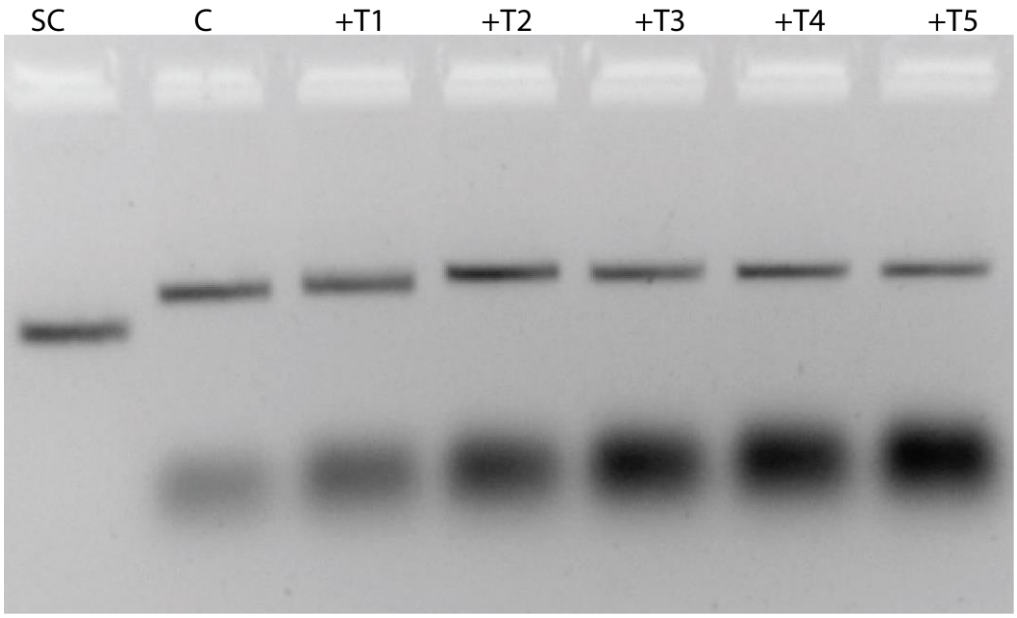

Figure S30. Agarose gel electrophoresis of R_M1 arrays from one-pot assembly with different number of triggers.

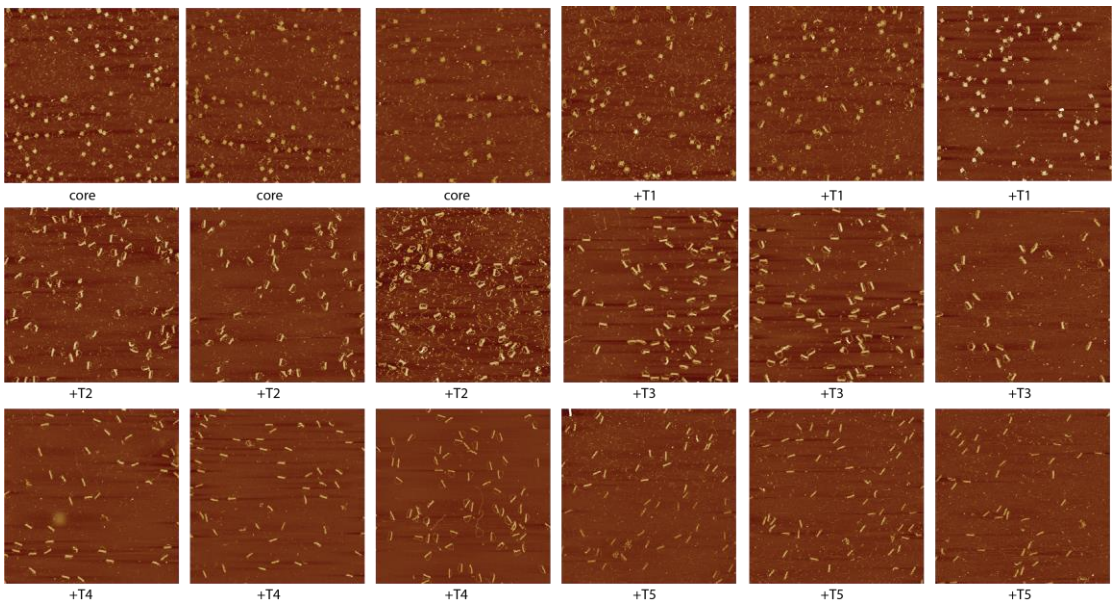

Figure S31. AFM images of R_M1 arrays from one-pot assembly with different number of triggers.

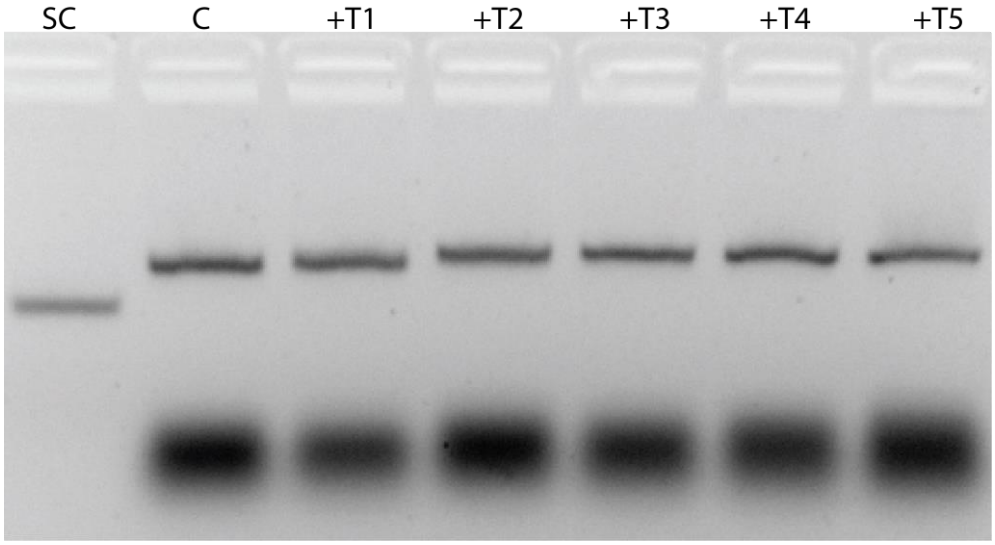

Figure S32. Agarose gel electrophoresis of R_M3 structure from one-pot assembly with different number of triggers.

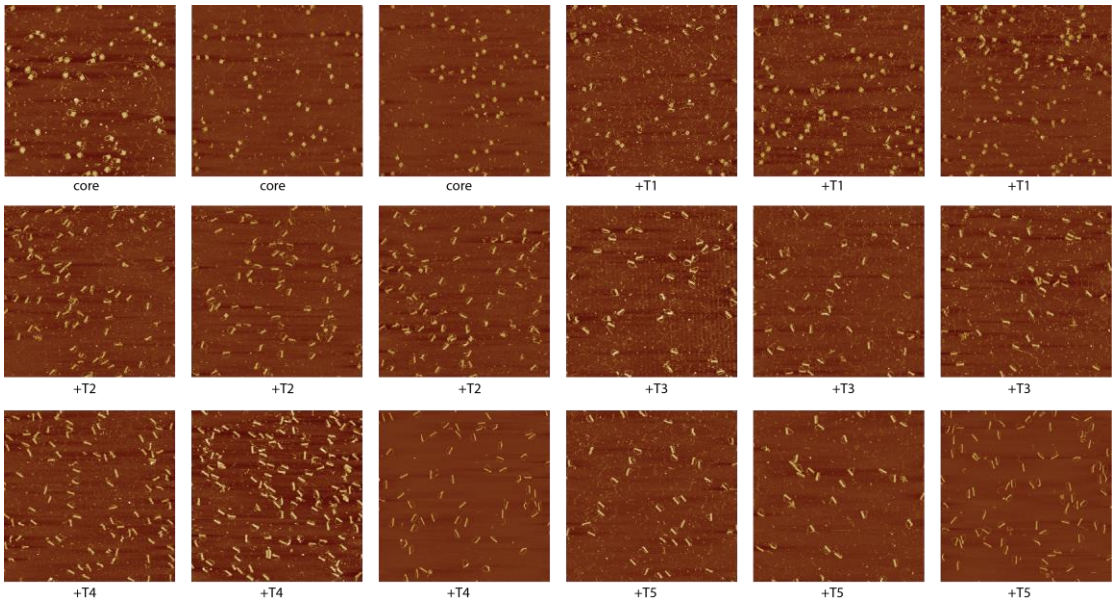

Figure S33. AFM images of R_M3 structure from one-pot assembly with different number of triggers.

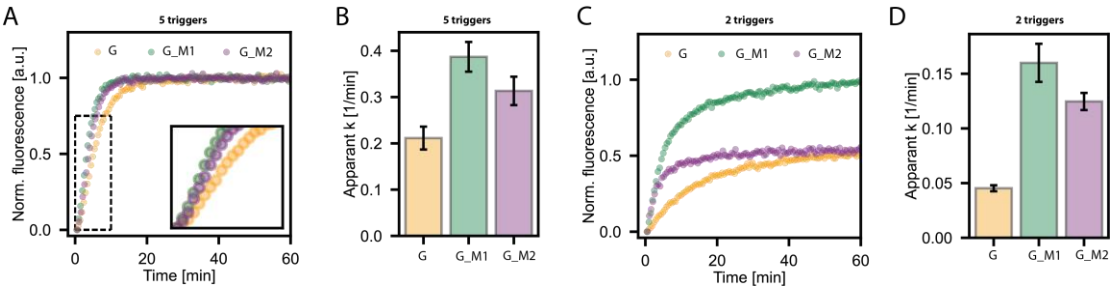

Figure S34. Ensemble kinetics for G array and its mismatched structures.

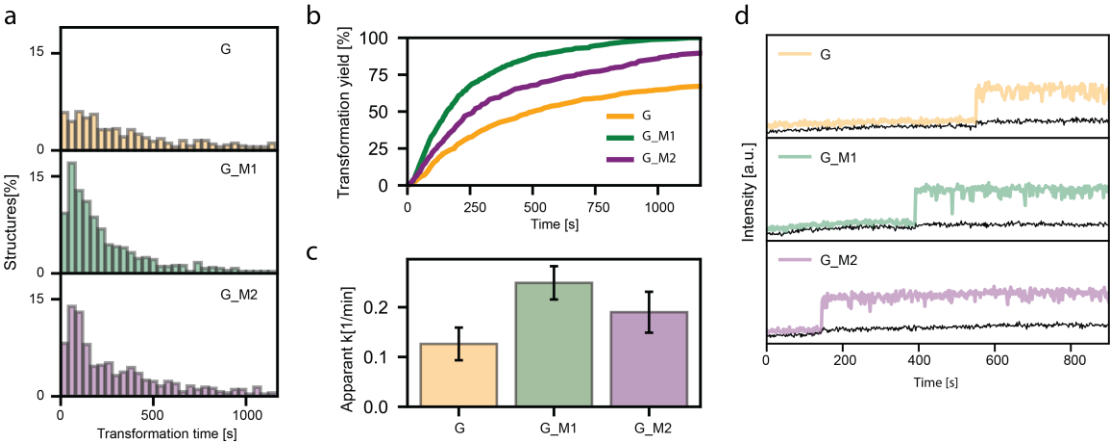

Figure S35. Single-molecule kinetics for G array and its mismatched structures. a) Single-molecule transformation time distribution of G array and its mismatched structures. b) Single-molecule kinetics of G array and the mismatched structures. c) Apparent rate constant for the G array and the mismatched structures in b. d) Representative single-molecule transformation traces for G array and the mismatched structures.

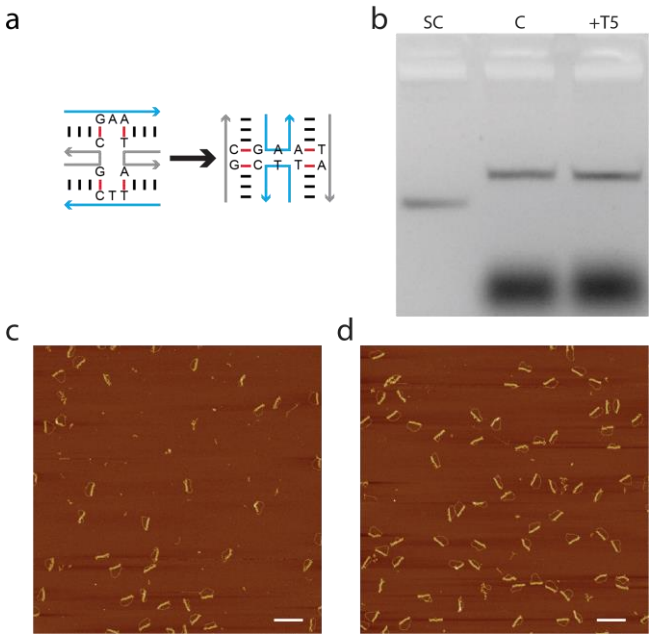

Figure S36. DNA base insertion effect. a) Two bases “A” and “T” were inserted into top and bottom strands of the Holliday junction. The strand with blue color represented the scaffold strand when integrated in the DNA origami array. b) Electrophoresis of agarose gel for the DNA origami structures containing free bases at the junction without and with five trigger strands. Lane SC: DNA scaffold 1800RF. Lane C: core structures without triggers. c) and d) showed the AFM imaging of samples without and with five triggers, respectively. Scale bars: 200 nm.

Table S2. DNA sequences for G origami structures.

Start	End	Sequence	Comment
2[194]	0[182]	AGTTCCCTGAGTTCCCACCTCAGATTGGAGCTTGACAGTCATCACAGAATGCTCCTCCACTTTCCTTTTT	trigger strand
4[194]	2[195]	CCGCGACCAAAGTCCGATCAGTGTGAACACAGCACCCACGCCCCACAAATCC	trigger strand
6[194]	4[195]	TGAATCACGGATTCCCACCCTGTTGAATCTGGTCTGCTCTTTGGGCAGGGCT	trigger strand
8[194]	6[195]	TCGGCCAAGCACTCCAGAGTTGATACCAGCAAACAGCTTCTTGAGGTGAGAC	trigger strand
9[182]	8[195]	TTTTTTTAATTGCGTTCTCCACATCTTCGGTAAACTTGATCTGT	trigger strand
0[69]	0[28]	GGTACCCCGAAATCGGCAAAATCCCTTATAAATCAAAAGAAT	loop strand
1[28]	1[69]	AGCCCGAGATAGGGTTGAGTGTTGTTCCAGTTTGGAACAAGA	loop strand
2[69]	2[28]	GTCCACTATTAAAGAACGTGGACTCCAACGTCAAAGGGCGAA	loop strand
3[28]	3[69]	AAACCGTCTATCAGGGCGATGGCCCACTACGTGAACCATCAC	loop strand
4[69]	4[28]	CCAAATCAAGTTTTTTGGGGTCGAGGTGCCGTAAAGCACTAA	loop strand
5[28]	5[69]	ATCGGAACCCTAAAGGGAGCCCCCGATTTAGAGCTTGACGGG	loop strand
6[69]	6[28]	GAAAGCCGGCGAACGTGGCGAGAAAGGAAGGGAAGAAAGCGA	loop strand
7[28]	7[69]	AAGGAGCGGGCGCTAGGGCGCTGGCAAGTGTAGCGGTCACGC	loop strand
8[69]	8[28]	TGCGCGTAACCACCACACCCGCCGCGCTTAATGCGCCGCTAC	loop strand

9[28]	9[69]	AGGGCGCGTGGATCCGTCGAGAATCAGTGCTTTCAGTTTCAG	loop strand
0[129]	1[116]	TTTTTGCGAAAGGTGATCCAATCTTCATTGGAACAGATCCAGCC	core strand
0[181]	1[168]	TTTTTTGAGGCGGTCGTGCCAATTCATCAGGAGATAGGGATAAC	core strand
1[117]	3[116]	AGTGATCGGGTGGAGCAGCCTTGGCCACGATGGTATCGGATATTGTCGCCCA	core strand
1[169]	3[168]	AATCTTATATTTGATTCGCGGATGGTCACTTCACCCTGGAGGTGCGGCTCTG	core strand
2[90]	0[78]	GTCACCGAACAGCTGCCGCGAGGCAGACCCAGCAAGCGTCCATTTCTTGGAATCCCTGCTGGAAC	core strand
2[142]	0[130]	GATCTTTCAGGTTCAGGTGTTCTCCGCGGACGTACTTCTCACTCCTCAAACAAGTAGGTCTTAGTTTTTT	core strand
3[117]	5[116]	CCTGGTTGACGAGATCGTCCAGTTCGGCGAGTTTCCTTGAGAATGCCTGCGT	core strand
3[169]	5[168]	GGAGTCCTCATAGATGGTTCGAGGTAAACCCACTTTCTGATGTCATGATGCT	core strand
4[90]	2[91]	CTTGTCTTCAAAGAGTCCTTCAAGGACTGCAGGAGGCATCAACTCTCAGCAG	core strand
4[142]	2[143]	GGTTCTGCAAATTCTCCTTCCAATCCTTGATCAGCTTCTCCGCGTGAGTTCA	core strand
5[117]	7[116]	GGGTAGTCAAGGGAAAGCGAGGGAAGGCGCTGCGCTTCGACGTTATTCTTGA	core strand
5[169]	7[168]	GCGGAAATCTTCGAATTGGTTGACTGGCCCAAGATCTCGAGTGCTTAGACTT	core strand
6[90]	4[91]	GTTGAGGCTGCGCGGTCCAGGATGGTCAGCAGTGAGTTTCCCAGATGCTGAC	core strand
6[142]	4[143]	CTCCGATGAAGTTCGTGACGCGATTGTCCTTCTTGATATCGAATATGGTTGA	core strand
7[117]	9[129]	ATGGCACAACTTGAGTTGTCACGCACTCCTTCAGCAGCGACGGAAGATGTGTCGATGTTAGTATATTTTT	core strand
7[169]	9[181]	CTCATCGAAACAGAGATCTGTGATGGGAACAGAGAAGGGACTCAATCTGGTGCAGGGAGTGATCTTTTTT	core strand
8[90]	6[91]	CTTCATCTCCAGGAGGTTTCGACGTTATTGGACAAGGGTCCTCCAGGAACTC	core strand
8[142]	6[143]	GAGAGCTGCGTCTCCCCTCCAAGGACTTCATTGCAGTATCGCAGGTCATCGT	core strand
9[78]	8[91]	TACCGGACTCTGTGTTACCTGGGTCTCCTCCAGGGTCTT	core strand
9[130]	8[143]	TTTTTCTGCTCCAATTTGTTCACCAGCTGTTCCCACAGCTCCCT	core strand

Table S3. DNA sequences for N origami structure.

Start	End	Sequence	Comment
2[194]	0[182]	AGTTCCCTGAGTGCCCACCTCAGATTGGAGCTTGACAGTCATCACAGAATGCTCCTCCACTTTCC	trigger strand
4[194]	2[195]	CCGCGACCAAAGGCCGATCAGTGTGAACACAGCACCCACGCCCCACAAATCC	trigger strand
6[194]	4[195]	TGAATCACGGATGCCCACCCTGTTGAATCTGGTCTGCTCTTTGGGCAGGGCT	trigger strand
8[194]	6[195]	TCGGCCAAGCACGCCAGAGTTGATACCAGCAAACAGCTTCTTGAGGTGAGAC	trigger strand
9[182]	8[195]	TTAATTGCGTTCTCCACATCTTCGGTAAACTTGATCTGT	trigger strand
0[69]	0[28]	GGTACCCCGAAATCGGCAAAATCCCTTATAAATCAAAAGAAT	loop strand
1[28]	1[69]	AGCCCGAGATAGGGTTGAGTGTTGTTCCAGTTTGGAACAAGA	loop strand
2[69]	2[28]	GTCCACTATTAAAGAACGTGGACTCCAACGTCAAAGGGCGAA	loop strand
3[28]	3[69]	AAACCGTCTATCAGGGCGATGGCCCACTACGTGAACCATCAC	loop strand
4[69]	4[28]	CCAAATCAAGTTTTTTGGGGTCGAGGTGCCGTAAAGCACTAA	loop strand
5[28]	5[69]	ATCGGAACCCTAAAGGGAGCCCCCGATTTAGAGCTTGACGGG	loop strand
6[69]	6[28]	GAAAGCCGGCGAACGTGGCGAGAAAGGAAGGGAAGAAAGCGA	loop strand
7[28]	7[69]	AAGGAGCGGGCGCTAGGGCGCTGGCAAGTGTAGCGGTCACGC	loop strand
8[69]	8[28]	TGCGCGTAACCACCACACCCGCCGCGCTTAATGCGCCGCTAC	loop strand
9[28]	9[69]	AGGGCGCGTGGATCCGTCGAGAATCAGTGCTTTCAGTTTCAG	loop strand
0[129]	1[116]	GCGAAAGGTGATCCAATCTTCATTGGCACAGATCCAGCC	core strand
0[181]	1[168]	TGAGGCGGTCGTGCCAATTCATCAGGCGATAGGGATAAC	core strand
1[117]	3[116]	AGTGATCGGGTGGCGCAGCCTTGGCCACGATGGTATCGGCTATTGTCGCCCA	core strand
1[169]	3[168]	AATCTTATATTTGCTTCGCGGATGGTCACTTCACCCTGGCGGTGCGGCTCTG	core strand
2[90]	0[78]	GTCACCGAACAGCTGCCGCGAGGCAGACCCAGCAAGCGGCCATTTCTTGGAATCCCTGCTGGAAC	core strand
2[142]	0[130]	GATCTTTCAGGTGCAGGTGTTCTCCGCGGACGTACTTCGCACTCCTCAAACAAGTAGGTCTTAGT	core strand

3[117]	5[116]	CCTGGTTGACGAGCTCGTCCAGTTCGGCGAGTTTCCTTGCGAATGCCTGCGT	core strand
3[169]	5[168]	GGAGTCCTCATAGCTGGTTCGAGGTAAACCCACTTTCTGCTGTCATGATGCT	core strand
4[90]	2[91]	CTTGTCTTCAAAGAGTCCTTCAAGGACTGCAGGAGGCAGCAACTCTCAGCAG	core strand
4[142]	2[143]	GGTTCTGCAAATGCTCCTTCCAATCCTTGATCAGCTTCGCCGCGTGAGTTCA	core strand
5[117]	7[116]	GGGTAGTCAAGGGCAAGCGAGGGAAGGCGCTGCGCTTCGCCGTTATTCTTGA	core strand
5[169]	7[168]	GCGGAAATCTTCGCATTGGTTGACTGGCCCAAGATCTCGCGTGCTTAGACTT	core strand
6[90]	4[91]	GTTGAGGCTGCGCGGTCCAGGATGGTCAGCAGTGAGTTGCCCAGATGCTGAC	core strand
6[142]	4[143]	CTCCGATGAAGTGCGTGACGCGATTGTCCTTCTTGATAGCGAATATGGTTGA	core strand
7[117]	9[129]	ATGGCACAACTTGCGTTGTCACGCACTCCTTCAGCAGCGCCGGAAGATGTGTCGATGTTAGTATA	core strand
7[169]	9[181]	CTCATCGAAACAGCGATCTGTGATGGGAACAGAGAAGGGCCTCAATCTGGTGCAGGGAGTGATCT	core strand
8[90]	6[91]	CTTCATCTCCAGGAGGTTTCGACGTTATTGGACAAGGGGCCTCCAGGAACTC	core strand
8[142]	6[143]	GAGAGCTGCGTCGCCCCTCCAAGGACTTCATTGCAGTAGCGCAGGTCATCGT	core strand
9[78]	8[91]	TACCGGACTCTGTGTTACCTGGGTCGCCTCCAGGGTCTT	core strand
9[130]	8[143]	CTGCTCCAATTTGTTCACCAGCTGTGCCCACAGCTCCCT	core strand

Table S4. DNA sequences for R origami structure.

Start	End	Sequence	
2[194]	0[182]	AGTTCCCTGAGTGCCCACCTCAGATTGGAGCTTGACAGTCATCACAGAATGCTCCTCCACTTTCC	trigger strand
4[194]	2[195]	CCGCGACCAAAGGCCGATCAGTGTGAACACAGCACCCACGCCCCACAAATCC	trigger strand
6[194]	4[195]	TGAATCACGGATGCCCACCCTGTTGAATCTGGTCTGCTCTTTGGGCAGGGCT	trigger strand
8[194]	6[195]	TCGGCCAAGCACGCCAGAGTTGATACCAGCAAACAGCTTCTTGAGGTGAGAC	trigger strand
9[182]	8[195]	TTAATTGCGTTCTCCACATCTTCGGTAAACTTGATCTGT	trigger strand
0[69]	0[28]	GGTACCCCGAAATCGGCAAAATCCCTTATAAATCAAAAGAAT	loop strand
1[28]	1[69]	AGCCCGAGATAGGGTTGAGTGTTGTTCCAGTTTGGAACAAGA	loop strand
2[69]	2[28]	GTCCACTATTAAAGAACGTGGACTCCAACGTCAAAGGGCGAA	loop strand
3[28]	3[69]	AAACCGTCTATCAGGGCGATGGCCCACTACGTGAACCATCAC	loop strand
4[69]	4[28]	CCAAATCAAGTTTTTTGGGGTCGAGGTGCCGTAAAGCACTAA	loop strand
5[28]	5[69]	ATCGGAACCCTAAAGGGAGCCCCCGATTTAGAGCTTGACGGG	loop strand
6[69]	6[28]	GAAAGCCGGCGAACGTGGCGAGAAAGGAAGGGAAGAAAGCGA	loop strand
7[28]	7[69]	AAGGAGCGGGCGCTAGGGCGCTGGCAAGTGTAGCGGTCACGC	loop strand
8[69]	8[28]	TGCGCGTAACCACCACACCCGCCGCGCTTAATGCGCCGCTAC	loop strand
9[28]	9[69]	AGGGCGCGTGGATCCGTCGAGAATCAGTGCTTTCAGTTTCAG	loop strand
0[129]	1[116]	GCGAAAGGTGATCCAATCTTCATTGTAACAGATCCAGCC	core strand
0[181]	1[168]	TGAGGCGGTCGTGCCAATTCATCAGTAGATAGGGATAAC	core strand
1[117]	3[116]	AGTGATCGGGTGTAGCAGCCTTGGCCACGATGGTATCGTATATTGTCGCCCA	core strand
1[169]	3[168]	AATCTTATATTTTATTCGCGGATGGTCACTTCACCCTGTAGGTGCGGCTCTG	core strand
2[90]	0[78]	GTCACCGAACAGCTGCCGCGAGGCAGACCCAGCAAGCGGCCATTTCTTGGAATCCCTGCTGGAAC	core strand
2[142]	0[130]	GATCTTTCAGGTGCAGGTGTTCTCCGCGGACGTACTTCGCACTCCTCAAACAAGTAGGTCTTAGT	core strand
3[117]	5[116]	CCTGGTTGACGATATCGTCCAGTTCGGCGAGTTTCCTTTAGAATGCCTGCGT	core strand
3[169]	5[168]	GGAGTCCTCATATATGGTTCGAGGTAAACCCACTTTCTTATGTCATGATGCT	core strand
4[90]	2[91]	CTTGTCTTCAAAGAGTCCTTCAAGGACTGCAGGAGGCAGCAACTCTCAGCAG	core strand
4[142]	2[143]	GGTTCTGCAAATGCTCCTTCCAATCCTTGATCAGCTTCGCCGCGTGAGTTCA	core strand
5[117]	7[116]	GGGTAGTCAAGGTAAAGCGAGGGAAGGCGCTGCGCTTCTACGTTATTCTTGA	core strand
5[169]	7[168]	GCGGAAATCTTCTAATTGGTTGACTGGCCCAAGATCTCTAGTGCTTAGACTT	core strand
6[90]	4[91]	GTTGAGGCTGCGCGGTCCAGGATGGTCAGCAGTGAGTTGCCCAGATGCTGAC	core strand
6[142]	4[143]	CTCCGATGAAGTGCGTGACGCGATTGTCCTTCTTGATAGCGAATATGGTTGA	core strand
7[117]	9[129]	ATGGCACAACTTTAGTTGTCACGCACTCCTTCAGCAGCTACGGAAGATGTGTCGATGTTAGTATA	core strand

7[169]	9[181]	CTCATCGAAACATAGATCTGTGATGGGAACAGAGAAGGTACTCAATCTGGTGCAGGGAGTGATCT	core strand
8[90]	6[91]	CTTCATCTCCAGGAGGTTTCGACGTTATTGGACAAGGGGCCTCCAGGAACTC	core strand
8[142]	6[143]	GAGAGCTGCGTCGCCCCTCCAAGGACTTCATTGCAGTAGCGCAGGTCATCGT	core strand
9[78]	8[91]	TACCGGACTCTGTGTTACCTGGGTCGCCTCCAGGGTCTT	core strand
9[130]	8[143]	CTGCTCCAATTTGTTCACCAGCTGTGCCCACAGCTCCCT	core strand

References:

(1) Douglas, S. M.; Marblestone, A. H.; Teerapittayanon, S.; Vazquez, A.; Church, G. M.; Shih, W. M. Rapid prototyping of 3D DNA-origami shapes with caDNAno. *Nucleic Acids Res.* **2009**, *37* (15), 5001-5006.
(2) Nafisi, P. M.; Aksel, T.; Douglas, S. M. Construction of a novel phagemid to produce custom DNA origami scaffolds. *Synth. Biol.* **2018**, *3* (1), ysy015.
(3) Friedman, R. A.; Honig, B. A free energy analysis of nucleic acid base stacking in aqueous solution. *Biophys. J.* **1995**, *69* (4), 1528-1535.

6.5.5 PUBLICATION P5

Reconfigurable DNA origami array structures as two-dimensional networks of coupled two-state systems

by

Martina Pfeiffer[1], Fiona Cole[1], Dongfang Wang[1], Yonggang Ke[*] and Philip Tinnefeld[*]
([1] These authors contributed equally, [*] Correspondence)

Submission pending

Author contributions:
I proposed the initial idea of the project together with Fiona Cole. The initial origami design and scaffold were provided by Dongfang Wang. I designed the input responsive units and the output units, performed the corresponding measurements and analyzed the data. Fiona Cole designed the Boolean logic gates, performed the corresponding measurements and analyzed the data. I designed, measured and analyzed the combination of multiple inputs with logic gating and multiple temporally controlled outputs together with Fiona Cole. I wrote the manuscript together with Fiona Cole and Philiip Tinnefeld. The project was supervised by Philip Tinnefeld and Yonggang Ke.

Reconfigurable DNA origami arrays as networks of coupled two-state systems to build modular nanodrobots

Martina Pfeiffer[1,4], Fiona Cole [1,4], Dongfang Wang [2,3,4], Yonggang Ke [2*] and Philip Tinnefeld [1*]

[1] Department of Chemistry and Center for NanoScience, Ludwig-Maximilians-Universität München, Butenandtstr. 5-13, 81377 München, Germany

[2] Wallace H. Coulter Department of Biomedical Engineering, Emory University and Georgia Institute of Technology, Atlanta, GA 30322, USA

[3] School of Biomedical Engineering and Suzhou Institute for Advanced Research, University of Science and Technology of China, Suzhou 215123, China

[4] These authors contributed equally

* Correspondence: philip.tinnefeld@cup.uni-muenchen.de, yonggang.ke@emory.edu

Summary

DNA origami nanodevices allow us to mimic cellular functions in a rationally controlled manner. They describe machineries which respond to environmental stimuli by conducting different tasks. To date, this mostly is achieved by constructing conformational two-state switches which upon activation by stimuli change their conformation resulting in the performance of a priorly programmed task. Their applicability however is often limited to a single, specific stimuli – output combination due to their intrinsic properties as two-state systems only. This makes expanding them further to include multiple stimuli/ outputs challenging. Here, we address this problem by introducing reconfigurable DNA origami arrays as a coupled network of two-state systems. We use this network to create a universal design strategy for DNA origami nanorobots by normalizing multiple different input receiving and operational units such that they can be incorporated into any two-state system of our network. This allows the simple design of nanorobots capable of receiving different environmental stimuli as inputs, computing the response to the received inputs using multi-level Boolean logic gating and yielding multiple programmed output operations with a controlled order, timing and spatial position. We expect that this strategy will be a crucial step towards further developing DNA origami nanorobots for applications in many technological fields.

Introduction

From biomolecular receptors that respond to changes in their target concentrations [1–3] to complex motor proteins that walk on supramolecular tracks for keeping the tensioned state in a muscle [4–6], naturally occurring machines perform sophisticated tasks upon their activation by environmental stimuli. Over the last decades, the DNA origami technique [7,8] has emerged as an indispensable tool for designing devices capable of emulating functions and properties of these naturally occurring machines on the nanoscale.

Most current DNA origami nanodevices are designed and optimized to perform a specific operation such as cargo release [9–11], a rotational motion [12–14] or a chemical reaction [15,16] after sensing chemical or physical stimuli. This mostly is achieved by inducing a single, relatively simple conformational change in the nanodevice by the environmental stimuli, causing it to act as a two-state switch. The conformational change then changes the proximity between interacting players of the operational block of the nanodevice in a controlled manner, resulting in the performance of a priorly programmed operation. However, the fact that this concept is based on a single conformational change makes expanding it further challenging. For the realization of more sophisticated nanodevices capable of autonomously performing a series of multiple operations in response to different combinations of environmental stimuli, so far no general concept exists.

Reconfigurable DNA origami array systems [17–19] form obvious and promising candidates in this context (see Fig. 1a,b). They represent a class of dynamic DNA origami systems that are composed of multiple, structurally similar blocks – so-called antijunctions (see Fig. 1a). Antijunctions are small symmetric constructs containing four DNA duplex domains of equal length which are pairwise stacked as well as four dynamic nicking points. They exist in two stable conformations with reversed stacking order between which they can switch via an instable open conformation. As such, they can be interpreted as simple two-state switches similar to most DNA origami nanodevices currently in use. When arranged in reconfigurable DNA origami array systems, multiple antijunctions are coupled to each other by a long scaffold DNA strand. The scaffold DNA strand threads through the whole system, interconnecting the individual antijunctions and forcing them to all adapt the same conformation. Induced by the hybridization of fuel DNA strands to certain antijunctions at the edge of the structure, the conformation of the whole system then can be reconfigured in a diagonal stepwise manner (see Fig. 1b). In each of the steps, a row of antijunctions in the system undergoes a conformational change, ultimately resulting in the reconfiguration of the whole structure. A reconfigurable DNA origami array system as a whole consequently can be interpreted as a two-dimensional network of coupled two-state switches represented by its individual antijunctions. Thus, if functionalities could be encoded into individual antijunctions, these systems would have potential to become generalized platforms for the development of sophisticated nanodevices capable of performing multiple operations both in series and/ or in parallel.

The coupling between individual antijunctions in these systems is described by their multistep reconfiguration process. Previous studies already uncovered the underlying

energy landscape of this process (see Fig. 1c) [17,18] and demonstrated how – by incorporation of energy barriers – the coupling between different antijunctions can be rationally altered to retard or even fully stop the reconfiguration at a priorly specified intermediate step. Additionally, it was shown that the full reconfiguration of DNA origami arrays generally can be used to activate different proximity-induced operations such as the onset of catalytic activity [20], the performance of different pattern operations involving writing, erasing and shifting [21], the generation of an optical output signal [22], or the release of cargo DNA strands. Besides this, the spectrum of environmental stimuli which can induce the reconfiguration was expanded beyond the realm of nucleic acids to also include heightened potassium ion concentrations [22] and DNA polymerase activity [23]. However, similar to most of the output operations, these stimuli did not target the conformation of a specific antijunction in the system. They rather targeted the overall conformation of the whole system itself disregarding the potential of its intermediates and reducing it to a simple two-state switch.

Here, we regard the network of antijunctions in reconfigurable DNA origami array systems as the "hardware" of a programmable DNA nanorobot which can be programmed with a software framework described in this work (see Fig. 1d). With its individual antijunctions, this hardware provides a set of nodes with known connectivity given by the network's energy landscape as well as a well-defined starting point. In our software framework, each antijunction within the system is considered as a potential input, output or timing node. By subscribing them with a functionality, the energy landscape of the transformation process is altered at the position where the corresponding node changes its conformation. While input nodes introduce an additional environmental-responsive activation barrier, timing nodes introduce only a small activation barrier, thus resulting in the temporal delay of the transformation (see Fig. 1c). For output nodes, the effect on the energy landscape depends on the exact functionality. Computation of the hardware is then allosterically driven by fuel DNA strands.

In a rational design driven approach, we exploited the structural similarity of all nodes and developed a software package to address them all in the same, universal manner. As a consequence, we demonstrate how different inputs, such as enzyme activities, proteins, DNA and light, are modularly combined with a range of operations, including cargo release, fluorescence on- and offset, signal amplification, and more to achieve arbitrary input – output combinations on demand (see Fig. 1d). Additionally, we highlight how our comprehensive understanding of both the pathway and energy landscape of the array system's reconfiguration process enables us to implement order dependencies, timing control and multi-level logic gating as well as simplicity of designing orthogonal operations

by exploiting the antijunction's symmetric nature (see Fig. 1a). As such, this innovative merge of hardware and software promises a new era of versatile nanoscale devices.

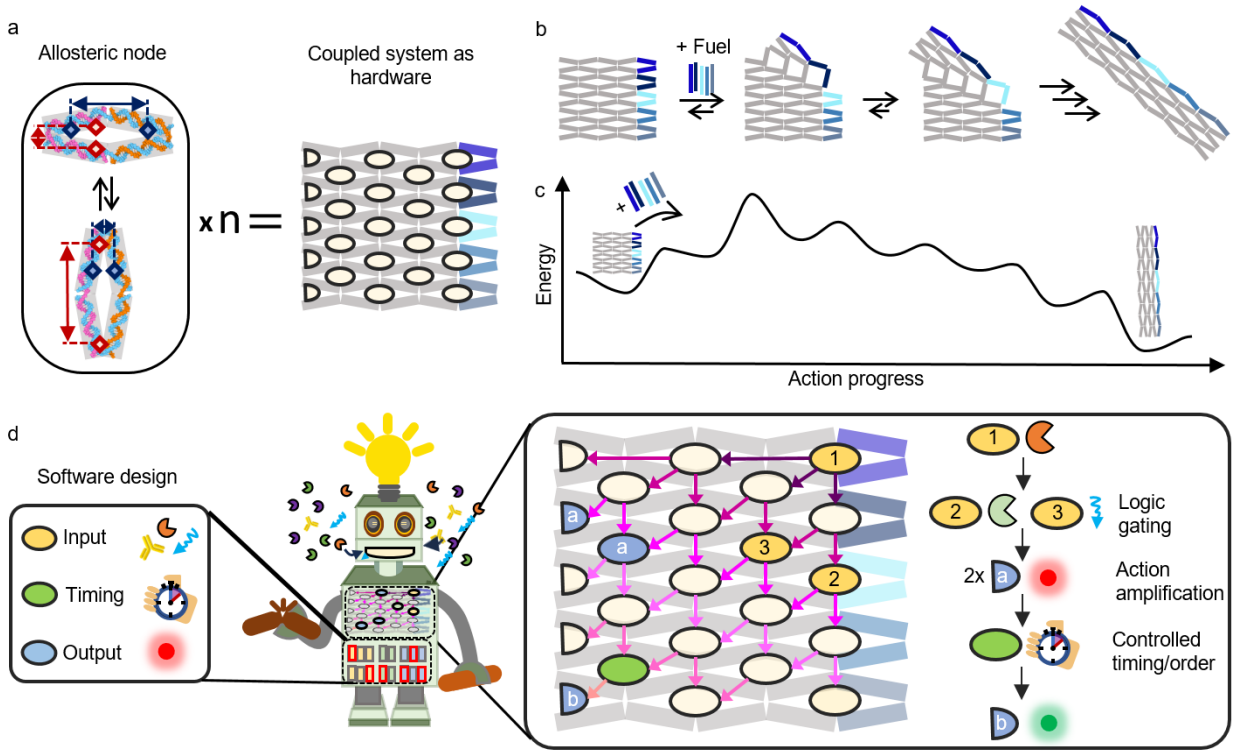

Figure 1: Concept of a modular reconfigurable DNA origami nanorobot. (a) Sketch of multiple allosteric nodes coupled together in a reconfigurable DNA origami array forming the hardware basis of the design of the nanorobot. The nodes are indicated by ellipses at the corresponding positions at the DNA origami array. The basis of an allosteric node is a so-called anti-junction which switches between two conformational states. Due to the symmetric nature of the antijunction, the switching can be used to both increase (red) and decrease (dark blue) the distance between markers placed on the antijunction depending on which domains they are placed on. (b) Sketch of the reconfiguration process of the unmodified DNA origami array structure upon hybridization of fuel DNA strands (blue lines) to the right side of the structure. The array changes its conformation in a diagonal stepwise manner starting either from the top right corner as shown here or from the bottom right corner. (c) Simplified sketch of the energy landscape of the multistep reconfiguration process. (d) The software of the designed nanorobot is formed by developing generalized strategies to encode environmental responsiveness to different target, timing and output operations are into single allosteric nodes (left panel). The nanorobot is then formed by programming different nodes of the DNA origami array hardware with the software (middle panel). The arrows hereby represent the connectivity between the different units. This enables the robot to respond autonomously to targets in its environment in a pre-programmed, multistep manner (right panel).

Results

SEPP (Synchronized Execution of Programmable Processes) is based on a small reconfigurable DNA origami array structure composed of 5 x 2.5 antijunctions that can be transformed by hybridization five fuel DNA strands to the right side of the structure (see Fig. 1a, b). The transformation process is characterized by five intermediates the energy of which increases during the first two steps of the transformation process before decreasing again (see Fig. 1c). Our software framework, especially the input and timing nodes, targets the energy barriers between these intermediate and the start and the end point of the transformation. To characterize SEPP at the single-molecule level with fluorescence microscopy, we additionally incorporated a biotinylated ssDNA strand in the DNA origami array structure for surface-immobilization on BSA-biotin/Neutravidin coated glass slides (see Supplementary Fig. S1).

Design of environmental-responsive input nodes

Environmental responsiveness is encoded into the antijunction nodes by the introduction of environmental-responsive locking units which stabilize one conformation of the targeted node over the other. This results in an energetic bias either hindering or favoring the transformation of the whole array (see Fig. 2a). By varying the number of added fuel DNA strands, we adjust the energy levels of the untransformed and transformed state of the array to lie close together such that presence of multiple locking units becomes the decisive factor for the transformation to occur. In presence of the corresponding environmental input, the units are unlocked, and the energetic bias is removed, resulting in an activation or inhibition of the transformation process, respectively. Based on this principle, we designed locking units responsive to ssDNA, restriction enzyme activity, light and antibodies (see Fig. 2, Supplementary Fig. S2-S4).

For single-stranded DNA (ssDNA) as an input, locking units are formed by two ssDNA strands protruding from two domains of the targeted antijunction nodes. The ssDNA strands contain a complementary section which hybridizes when both domains are in close proximity. Depending on which domains they are placed on, hybridization of the strands occurs either in the untransformed or transformed conformation of the nodes (see Fig. 2b, upper and lower panel), resulting in their energetic stabilization. To enable unlocking, one of the protruding ssDNA strands is designed with a single-stranded toehold overhang. This allows for unlocking by toehold-mediated strand displacement with a complementary ssDNA input.

The successful implementation of the ssDNA locking units was verified using a fluorescence onset unit placed on an antijunction node transforming further downstream in the transformation process. The fluorescence onset unit reports on the conformational state of the node it is placed on (see Fig. 2b). It is based on a red dye-quencher probe (ATTO647N – IowaBlackRQ) positioned on two different domains of an antijunction node which are in close proximity in the untransformed state of the antijunction node. The

proximity increase between these domains caused by the transformation of the corresponding node results in an increased fluorescence signal of the dye molecule. This allowed to distinguish the untransformed from the transformed state of the node. We additionally incorporated an ATTO542 dye into the arrays and quantified the fraction of arrays in their transformed state (transformation yield) from dual-color single-molecule TIRF images of surface-immobilized array structures collected in absence and presence of the ssDNA input (see Fig. 2c, Materials and Methods).

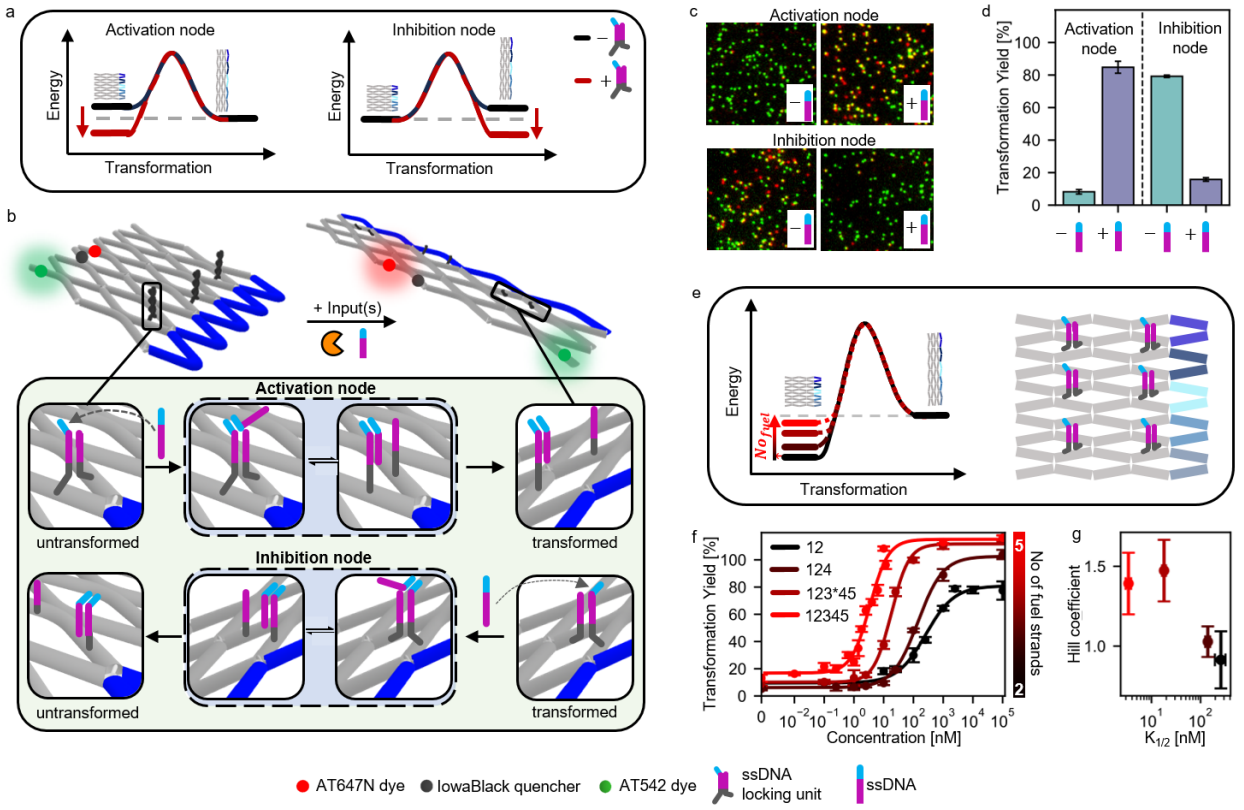

Figure 2. Environmentally responsive activation and inhibition nodes. (a) Energy schemes showing the influence of a locking unit in activation and inhibition nodes on the transformation process. In presence of their inputs, this effect is nullified. The energy schemes in absence of the locking units are programmed priorly by adding different combinations of fuel DNA strands. (b) Sketch of the DNA origami nanorobot bearing environmentally responsive nodes, a red dye-quencher FRET pair (ATTO647N-IowaBlackRQ) reporting on the state of the nanorobot and a green dye (ATTO542) for co-localization (upper panel). Nodes responsive to ssDNA activating and inhibiting the transformation are based on a reversible dsDNA lock which is unlocked via a toehold-mediated strand displacement reaction with a ssDNA input (lower panel). (c) Exemplary TIRF images of DNA origami nanorobots bearing ssDNA-responsive activation and inhibition nodes after incubation with fuel DNA strands 1,2 and 1,3* respectively and without and with the ssDNA input. (d) Corresponding transformation yields. (e) Strategy for tuning the responsive concentration window of the ssDNA input. When incorporating multiple ssDNA locking units, increasing the number of added fuel DNA strands results in a destabilization of the untransformed state of the array. (f) Increasing the number of added fuel DNA strands from strands 1,2 over 1,2,4 and 1,2,3*,4,5 to 1,2,3,4,5, shifted the responsive window. (g) Impact of the number of added fuel DNA strands on $K_{1/2}$ and the Hill coefficient.

With transformation yields of xx% and xx%, arrays with three ssDNA activation and inhibition nodes incorporated were predominantly in their untransformed and transformed state in absence of ssDNA input, respectively. Upon addition of ssDNA input, the transformation yield increased to xx% for the array with activation nodes and decreased to xx% for the array with inhibition nodes, demonstrating the orthogonal usability of the same DNA locking unit with near quantitative responses (see Fig. 2d). As this process was reversible (see Supplementary Fig. S5), our control over the energy landscape of the system provides additional access to tune the location ($K_{1/2}$) and width of the responsive concentration window towards the ssDNA input without modifying the ssDNA locking unit itself. When incorporating six ssDNA activation units into the array, increasing the number of added fuel DNA strands from two to five led to an increased mechanical strain exerted on the untransformed conformation of the array (see Fig. 2e). This resulted in an over 75-fold decrease in $K_{1/2}$ (from 260±60 nM to 3.4±0.4 nM) while simultaneously increasing the Hill coefficient from 0.9±0.2 to 1.4±0.2 and thus narrowing the responsive concentration window (see Fig. 2f-g). Replacing one of the ssDNA activation units with a unit destabilizing the untransformed state of the array, introduced an additional tuning strategy for the responsive window and shifted $K_{1/2}$ down to 1.1±0.1 nM (Supplementary Fig. S6). In combination, both strategies allowed shifting $K_{1/2}$ over 225-fold without modifying the ssDNA locking unit itself. This promises a good adaptability of these tuning strategies towards other inputs without the need for re-engineering the input-responsive locking units to create different affinities towards the inputs.

We then demonstrated the simple adaptability of our universal design approach towards other inputs. The designs of input nodes responsive to restriction enzyme activity and light are based on ssDNA locking units containing a restriction enzyme-specific restriction site and a light-cleavable linker, respectively. The locks were cleaved in presence of active restriction enzyme or light of a specified wavelength, effectively unlocking it (see Fig. 2e, Supplementary Fig. S2 and Supplementary Fig. S3). When implemented as activation nodes in DNA array systems, they responded specifically to their respective inputs (XhoI, StuI and BamHI restriction enzyme and light of 365 nm) by transforming quantitatively only in their presence (see Fig. 2f, Supplementary Fig. S2 and Supplementary Fig. S3) after addition of fuel DNA strands which can be pre-loaded onto the structure (see Supplementary Fig. S7). We further extended SEPP's spectrum of inputs to proteins which do not directly interact with DNA by designing an input unit responsive to IgG antibodies and demonstrating its application in inhibition nodes (see Supplementary Fig. S4).

Computation of different inputs based on Boolean logics

In the design of our locking units, the presence of a single unit alone does not suffice to quantitatively initiate or inhibit the transformation process (Supplementary Note 2, Fig. S8). This design anticipates the rational creation of computation schemes, thus providing the ability to respond to diverse input combinations in a pre-programmed manner. We

systematically characterized the impact of restriction enzyme locking units positioned at different nodes, both individually and in combinations (see Figure 3a and Supplementary Fig. S8). Notably, when comparing the effects of the same locking unit positioned at two different nodes in an otherwise identical design, we observed significant differences in the obtained transformation yields (see Fig. 3a). When the locking unit was positioned at a node transforming during the first step of the transformation process, the transformation was inhibited. In contrast, placing the unit at a node transforming during the fourth step resulted in a heightened transformation yield of 70%. This finding aligns with the profile of the energy landscape of the transformation process and is also consistent with all other studied locking unit combinations (Supplementary Note S1, Supplementary Fig. S8). The tilted profile of the energy landscape indicates a weakened effect of an incorporated locking unit, the further downstream the corresponding antijunction node is in the transformation cascade. Using this dependence and placing multiple locking units specific to various inputs at predefined antijunction nodes on the same structure, we established a computation framework to program responses to diverse input combinations based on Boolean logic gates.

We first implemented basic Boolean AND and OR gates responsive to combinations of the restriction enzymes XhoI and StuI. We again used a fluorescence onset unit to confirm the designed responsiveness of the system. For the AND gate, only upon addition of both restriction enzymes a near quantitative transformation of all structures occurred (see Fig. 3b, Supplementary Figure S9) whereas for the OR gate already the addition of one restriction enzyme resulted in transformation yields of above 70% (see Fig. 3c, Supplementary Figure S9). The applicability of these gates is not limited to inputs of the same molecular class. Our modular design strategy of locking units for example allows the simple exchange of the XhoI locking unit with a light locking unit in the OR gate design while maintaining the functionality of the gate (see Fig. 3d, Supplementary Figure S9). This demonstrates how inputs of different molecular classes can be processed on the same structure in DNA origami arrays.

Both the AND and the OR gate designs demonstrate low leakages in all logical FALSE conditions, with the TRUE state providing at least fourfold higher transformation yields in all cases. The low leakages of these basic gates allow expanding the concept further to also include multi-level logic gates. We used the multistep nature of the transformation cascade to – figuratively speaking – create cascades of multiple logic gates and connect them in series. Using the prior characterization of the effect of restriction enzyme locking units at different position as a basis, we designed two multi-level logic gates of different complexity: A 3xAND gate which is comprised of two logic AND gates connected in series (see Fig. 3e, Supplementary Figure S10) as well a gate which only gives a positive response if at least two of its three inputs are present (see Supplementary Figure S11). We found that both systems provided leakages in all logical FALSE conditions that were statistically distinguishable from the transformation yields obtained for the TRUE states, demonstrating the successful implementation of the designed gates. Besides logic gating,

the modularity offered by SEPP enables multiplexing as an additional pathways to process multiple inputs in parallel (see Supplementary Fig. S12).

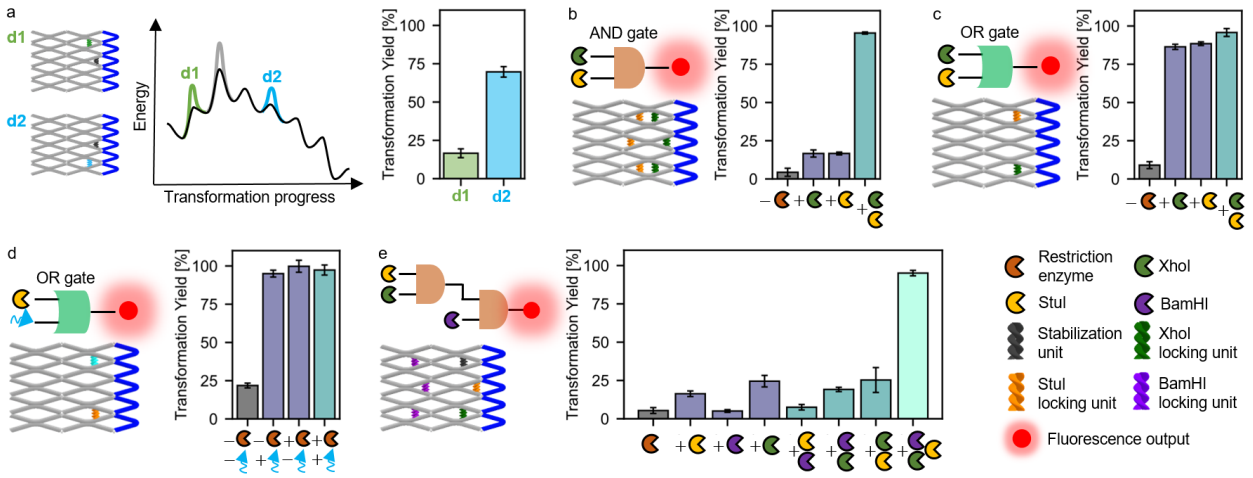

Figure 3. DNA origami array nanorobot processing one- and multi-level Boolean logic gates. One- level and multi-level Boolean logic gates responsive to combinations of restriction enzymes and light were implemented by combining different restriction enzyme/ light locking units and stabilization units. The molecular logic is programmed by the number and position of the incorporated units. Additionally, a red fluorescence onset unit was incorporated to confirm the designed responsiveness of the studied systems. (a) Comparison of the transformation yields of two array designs. The designs differ only in the position of one locking unit marked in green (d1) and blue (d2) that target different positions in the energy landscape of the transformation process. (b) Schematic design of a basic logic AND gate responsive to combinations of XhoI and StuI and obtained transformation yields. (c) Schematic design of a basic logic OR gate responsive to combinations of XhoI and StuI and obtained transformation yields. (d) Schematic design of a basic logic OR gate responsive to combinations of StuI and light and obtained transformation yields.(e) Schematic design of a 3xAND gate and obtained transformation yields. Error bars show the standard deviation from the mean. In addition to possible inputs, all DNA origami arrays were incubated with fuel DNA strands 1-5.

Combining logical gated input operations with output operations

The aim of smart nanorobots not only includes programming responses to different input combinations but also the conduction of these responses if the required conditions are met. Up to now, we used a simple fluorescence onset unit to generate output signals. To demonstrate the modular adaptability of our system to different output operations, we continued to combine our input-responsive locking units with a more complex output operation unit. As an example, we chose a cargo release unit, which upon activation releases a fluorescently labelled (ATTO542 dye) cargo DNA strand from the system the design of which is based on previous work (see Fig. 4a, Supplementary Note S2).

First, we combined the cargo release unit with restriction enzyme locking units specific to the activity of BamHI. Here, we additionally incorporated an ATTO647N dye in the DNA

origami array structures to visualize their locations and quantify the percentage of structures carrying a cargo DNA strand from dual-color TIRF microscopy images.

After assembly, DNA origami arrays near quantitatively carried the cargo DNA strand (see Supplementary Fig. S13). Upon incubation with and without enzyme, the percentage of structures carrying the cargo dropped from 98% to 75% and 20%, respectively (see Fig. 4b-d). While this indicated some unspecific cargo release, the majority of all cargo was only released in presence of the restriction enzyme. We attribute the unspecific loss of the cargo strand in absence of the restriction enzyme to the increased instability of the cargo release unit at 37 °C (see Supplementary Note S2, Supplementary Fig. S13). As we achieved both the implementation of logic gates and variable input-output combinations, we then continued to use the modularity of our system to combine all of the above. We designed structures which compute the controlled release of cargo in response to combinations of XhoI and BamHI activity. Both when connecting the restriction enzyme activities in an AND and OR logic gate, only if the gate gave a positive response, a high fraction of cargo was released (see Fig. 4e,f, Supplementary Fig. S14, S15).

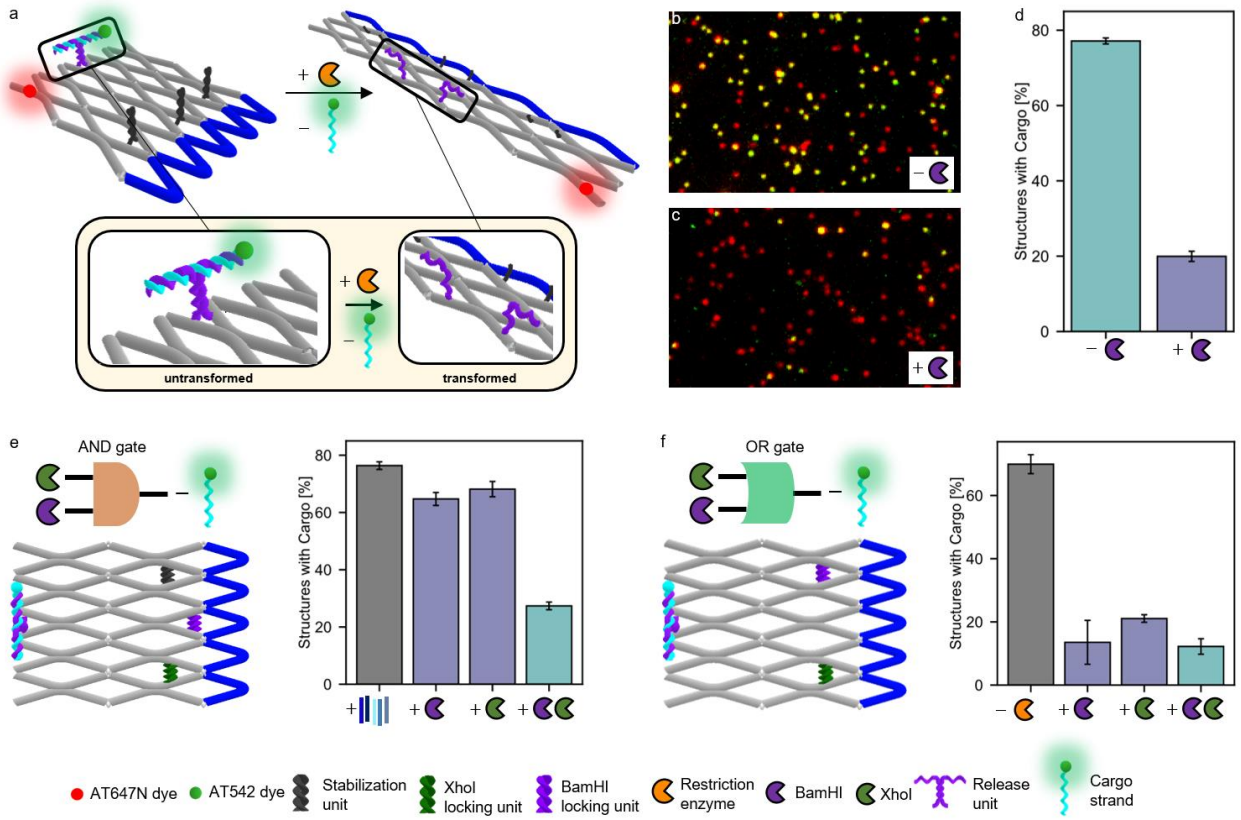

Figure 4. Proximity-induced output operation generated upon molecular inputs by DNA origami array nanorobot. (a) Schematic representation of DNA origami array structures which release a cargo DNA strand in response to the activity of BamHI. (b,c) TIRF images of the DNA origami array nanodevice after incubation (b) without and (c) with BamHI. (d) Corresponding fractions of DNA origami array nanodevices with a bound cargo DNA strand. (e,f) Schematic representation of DNA origami array nanodevices computing the controlled release of a cargo in response to the presence of combinations of XhoI and BamHI and corresponding fractions of DNA origami array nanodevices with a bound cargo DNA strand for an AND (e) and an OR (f) logic gate. In addition to possible inputs, all DNA origami arrays were incubated with fuel DNA strands 1-5.

To control order and timing between different events, we used designs introduced in earlier works as timing units. Timing units slightly heighten the activation barrier at a certain intermediate step in the transformation cascade and thus introduce an increased time lag between operations placed on antijunctions transforming before and after them. We demonstrated this exemplarily by positioning a timing unit between two fluorescence onset units. In absence of the timing unit, the fluorescence onset units lit up simultaneously upon activation by restriction enzyme activity. If a timing unit was incorporated, a time lag between both fluorescence onsets was achieved for the majority of all structures. The order in which the fluorescence onset units light up can be reversed by switching the antijunction nodes they are incorporated in (see Supplementary Fig. S16).

We then set out to make full use of our designed software framework and combined all developed unit types in a single system, using ssDNA and restriction enzyme input units, fluorescence on- and offset output units (see Supplementary Fig. S17) as well as a timing unit (see Fig. 5a). In the absence of inputs, SEPP showed only a red fluorescence signal (see Fig. 5b,c). Upon activation by a ssDNA input and XhoI restriction enzyme activity combined to a logic AND gate, SEPP switched off the red fluorescent signal (see Fig. 5b,c). Depending on whether an additional timing unit was incorporated or not, SEPP lit up an additional green fluorescent signal either after the red fluorescence offset occurred or simultaneous to it (see Fig. 5b-g). This good agreement between programmed function and execution exemplifies the control achievable in programmed systems using SEPP.

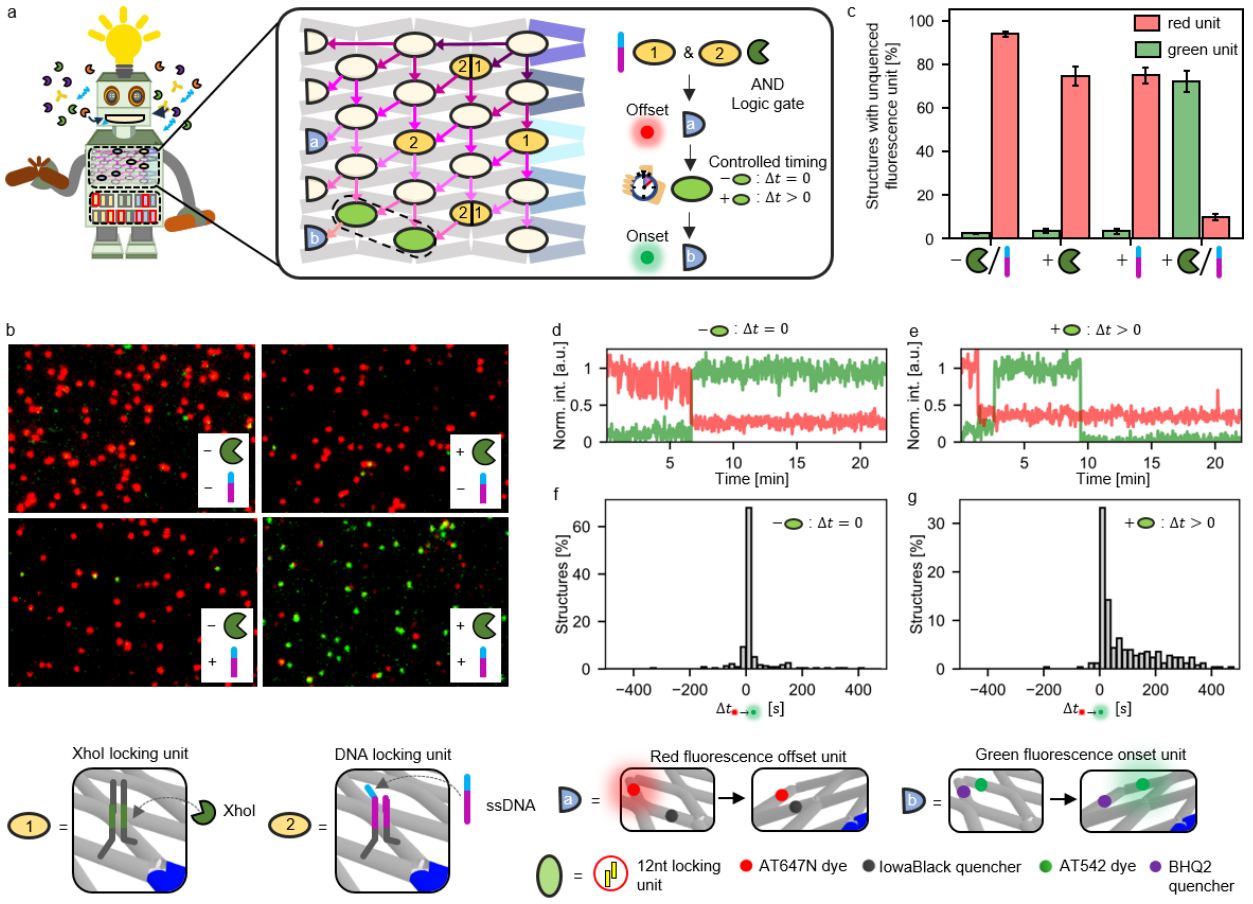

Figure 5. DNA origami array nanorobot performing output operations under temporal control after processing a Boolean logic AND gate based on restriction enzyme activity and ssDNA binding. (a) Schematic design of a DNA origami arrray nanorobot programmed to perform a series of operations with the corresponding plan of action . (b) TIRF images of the DNA origami array nanorobot after incubation with different combinations of restriction enzyme and/or ssDNA (c) Corresponding fraction of structures with unquenched green and red fluorescence units. (d,e) Exemplary single-molecule transients for structures without (d) and with (e) a timing unit incorporated. (f,g) Time between the occurrence of the red fluorescence-offset and the green fluorescence onset for structures without (f) and with (g) a timing unit incorporated. In addition to possible inputs, all DNA origami arrays were incubated with fuel DNA strands 1-5.

Discussion

We demonstrated the rational development of DNA origami nanorobots using the network of coupled two-state systems offered by DNA origami arrays as a programmable hardware. By designing a software package which defines different units, we showed how a wide range of functionalities can be encoded into any of the network's two-state systems and coupled together through the network's energy landscape. We designed input units responsive to ssDNA, light, restriction enzyme activity and antibodies. When incorporated into the DNA origami arrays, these units activate and/ or inhibit the nanorobot. By combining multiple units on a single DNA array structure, we developed strategies to tune the responsive input concentration window, shifting $K_{1/2}$ overto 200-fold. We used the same strategy to incorporate Boolean logic gating, creating specific responses for different input combinations, both with inputs of the same and different molecular classes. Subsequently, we demonstrated the potential of the modularity of this software-hardware combination. We programmed a nanorobot that combines activation by different inputs with Boolean logic gating and a sequence of output operations conducted in a predefined order and under temporal control and demonstrated its proper functionality.

Overall, we expect that expanding our software package to include further proximity-based operations will be straight-forward. Including further input and output software units that – besides the demonstrated cargo release and fluorescence on-/offset – enable e.g. the on-demand onset of catalysis or cargo uptake, will pave the way for a broad range of applications in the fields of clinical diagnosis and therapeutics.

Resource availability

Lead contact

Philip Tinnefeld: Department of Chemistry and Center for NanoScience, Ludwig-Maximilians-Universität München, Butenandtstr. 5-13, 81377 München, Germany. Philip.tinnefeld@cup.uni-muenchen.de

Materials and Methods

Synthesis of DNA origami arrays

DNA origami structures were designed using the open-source software caDNAno2 [24] and assembled and purified using published protocols [25] For the exact sequences of all unmodified and modified DNA staple strands used to fold the DNA origami structures see Tables SX and SX. DNA staple strands were purchased from Eurofins Genomics GmbH (Germany) and Integrated DNA Technologies (USA).

For DNA origami folding, 10 nM of in house produced p1800 scaffold (see Supplementary Note S3) in 1xTAE (400 mM Tris, 400 mM acetic acid, 10 mM EDTA, pH 8) containing 12.5 mM was mixed with a 10-fold excess of all unmodified and a 30-fold excess of all modified oligonucleotides, respectively. The mixture was heated to 65 °C in a thermocycler and kept at this temperature for 15 min before being cooled down to 25 °C with a temperature gradient of – 1 °C min^{-1}. Folded DNA origamis were purified from excessive staple strands by gel electrophoresis. All gels were ran using a 1.5% agarose gel, 1xTAE containing 12.5 mM $MgCl_2$ for 2 hours at 6 V/cm. The target band containing DNA origami was cut from the gel and DNA origami solution extracted from the band via squeezing.

Sample preparation on the coverslip for single-molecule widefield measurements

For chamber preparation, adhesive SecureSeal™ Hybridization Chambers (2.6 mm depth, Grace Bio-Labs, USA) were glued on microscope coverslips of 24 mm × 60 mm size and 170 µm thickness (Carl Roth GmbH, Germany). The created wells were incubated with 1 M KOH for 1 h and washed three times with 1×PBS buffer. After surface passivation by incubation with BSA-Biotin (0.5 mg/mL, Sigma Aldrich, USA) for 10 min, the surface was washed with 200 µL 1× PBS buffer. 150 µL neutravidin (0.25 mg/mL, Thermo Fisher, USA) was incubated for 10 min and then washed three times with 150 µL 1× PBS buffer. Surface immobilization was achieved via biotin-neutravidin interactions. For this, we incorporated one biotinylated DNA staple strand in the loop of the DNA origami structure during folding. The DNA origami solution was diluted with 1× TE buffer containing 750 mM NaCl to a concentration of ~10 pM and then immobilized on the biotin-neutravidin surface via biotin-neutravidin interactions. For this, 150 µL of the DNA origami sample solution was added and incubated for 5 min. Residual unbound DNA origami was removed by washing the chambers with 150 µL 1x TE buffer containing 750 mM NaCl. The density of DNA origami on the surface suitable for single-molecule measurements was checked on a TIRF microscope. For acquisition of single-molecule fluorescence movies, an oxidizing and reducing buffer system (1x TAE, 12.5 mM $MgCl_2$, 2 mM Trolox/Troloxquinone)[26] was used in combination with an oxygen scavenging system (12 mM protocatechuic acid, 56 µM protocatechuate 3,4-dioxygenase from pseudomonas sp., 1% glycerol, 1 mM KCl, 2 mM Tris HCl, 20 µM EDTA-Na_2*$2H_2O$) to suppress blinking and photobleaching. If not stated otherwise, for acquisition of single TIRF images, no oxidizing and reducing buffer system was added.

Reconfiguration of DNA origami array structures in response to different molecular inputs

ssDNA detection assay

For the detection of ssDNA, DNA origami array structures were folded with ssDNA locking units. After surface-immobilization, 50 nM fuel DNA strands in 1xTE buffer containing 750 mM NaCl and if not stated otherwise 2 uM ssDNA input were added. The samples

were incubated at 37 °C for 15 min and dual-color TIRF images recorded. For titration curve measurements, samples were incubated overnight to ensure equilibrium conditions.

Restriction enzyme activity assay

For the detection of restriction enzyme activity, DNA origami array structures were folded with restriction enzyme locking units. 50 nM of all five fuel DNA strands in 1xTAE buffer containing 12.5 mM $MgCl_2$ and 2 µL of XhoI (20,000 units/ml, New England BioLabs, USA), StuI (10,000 units/ml, New England BioLabs, USA) or BamHI (100,000 units/ml, New England BioLabs, USA) were added to surface-immobilized DNA origami samples. To determine transformation yields, the structures were incubated for 15 min at 37 °C and dual-color TIRF images recorded. To measure transformation time distributions (e.g. for the incorporation of timing units), sample chambers were sealed immediately after addition of the enzymes and the photostabilization system and dual-color movies of the DNA origami arrays acquired for 20 min at 37 °C.

Light detection assay

For the detection of light of 365 nm, DNA origami structures were folded with alight-responsive locking unit. 50 nM of all five fuel DNA strands in 1xTAE buffer containing 12.5 mM $MgCl_2$ were added to surface-immobilized DNA origami samples and the samples illuminated with light of 365 nm for 5 min. After subsequent incubation at 37 °C for 15 min, dual-color TIRF images were recorded.

Anti-Dig antibody detection assay

For the detection of anti-Dig antibodies, DNA origami array structures were folded with two Dig recognition elements. 50 nM of fuel DNA strands 1 and 2 in 1xTE buffer containing 750 mM NaCl and 100 nM anti-Dig antibodies (Rb Monoclonal, Thermo Fisher Scientific, cat#: 700772, PRID: AB_2532342) were added to surface-immobilized DNA origami samples. Samples were incubated at 37 °C for 15 min and dual-color TIRF images recorded.

Boolean logic gating and cargo release assays

For the measurement of Boolean logic gates and cargo release, surface-immobilized DNA origami structures were incubated with 50 nM fuel DNA strands 1-5 in 1xTAE buffer containing 12.5 mM $MgCl_2$ and the different restriction enzyme/ light inputs at 37 °C as described above and dual-color TIRF images recorded.

Nanorobot measurement combining multiple inputs with multiple outputs

For the nanorobot measurement which combines multiple inputs with multiple outputs (see Fig. 5), surface-immobilized DNA origami array structures were incubated with 50 nM fuel DNA strands 1-5 in 1xTAE buffer containing 12.5 mM $MgCl_2$ and different combinations of 2 uL BamHI/ 2 uM ssDNA at 37 °C as described above. For determining the fraction of structures with unquenched fluorescent units, dual-color TIRF images were recorded after 15 min incubation time. For determining the time delay between the red fluorescence offset and the green fluorescence onset, sample chambers were sealed immediately after addition of both inputs and the photostabilization system and dual-color movies of the DNA origami arrays acquired for 20 min at 37 °C.

Wide-field measurements

For detection of single-molecule fluorescence, a commercial wide-field/TIRF microscope Nanoimager from Oxford Nanoimaging Ltd. was used. Red excitation at 638 nm was realized with a 1100 mW laser, green excitation at 532 nm with a 1000 mW laser, respectively. The relative laser intensities were set to 9% for green and to 18% for red excitation. The microscope was set to TIRF illumination. Measurements were carried out at 37 °C. For quantifying transformation yields and the percentage of structures carrying cargo, dual-color fluorescence images were acquired. For recording fluorescence movies, the lasers were activated and a frame of 100 ms was taken every second separately for both excitation lasers (with a time lag of 0.5 s between them) over a measurement period of 20 min.

Data analysis

We quantified the percentage of transformed structures by dividing the number of green (ATTO 542) and red (ATTO647N) co-localized spots by the total number of green spots from dual-color TIRF fluorescence scans. To account for a labelling efficiency < 100%, the percentage of co-localized spots was normalized by the percentage of co-localized spots of a DNA origami array folded with all five fuel DNA strands to calculate transformation yields. In the normalization sample, AFM imaging confirmed the full transformation of all structures in previous work. For structures with a cargo release unit incorporated, the percentage of structures carrying cargo was determined analogously.

Data processing and analysis of time-lapse movies was realized using custom-written Python scripts. Briefly, the acquired movies were first drift corrected using DNA origami structures carrying fluorophores which were in their fluorescent state throughout the whole measurement as fiducial markers. Spots appearing during the measurement were detected from the drift-corrected movies and dual-color background-subtracted

fluorescence intensity transients of those spots extracted. To determine transformation times of single structures, the corresponding transients were fitted using a Hidden Markov model (HMM). In this model, two levels corresponding to the quenched (level 0) and unquenched state (level 1) of the corresponding fluorescence unit were defined. For fluorescence onset (offset) units, transformation times were defined as the time a structure switches from its quenched (unquenched) state to its unquenched (quenched) state and subsequently remains in it for at least 10 s for the first time. They were extracted from the fitted HMM transients. To determine transformation time distributions, only structures showing an intensity change in both colors were considered.

For titration curve measurements, the transformation yields obtained upon incubation with different concentrations of ssDNA input [*DNA*] were calculated from dual-color TIRF images as described above. $K_{1/2}$ and the Hill coefficient n_H were subsequently determined by fitting the calculated transformation yields Y to the modified Hill equation.

$$Y([DNA]) = Y(0) + \big(Y(\infty) - Y(0)\big) \cdot \frac{[DNA]^{n_H}}{K_{1/2}^{n_H} + [DNA]^{n_H}}$$

where $Y(0)$ and $Y(\infty)$ give the start and the end points of the titration.

For determining the fraction of structures with unquenched fluorescence unit in Fig. 5, we quantified the total number of structures in a TIRF image by counting the number of both weak (quenched) and bright (unquenched) red fluorescent spots. The fraction of red unquenched fluorescence units was then calculated as the fraction of the bright red spots of the total number of red spots. As green quenched fluorescence units were not visible in TIRF images, the fraction of green unquenched fluorescence units was calculated by dividing the number of green spots by the total number of red spots and subsequently normalizing them by the fraction of colocalized red and green spots in fully transformed DNA origami arrays.

Acknowledgments

P.T. gratefully acknowledges financial support from the Federal Ministry of Education and Research (BMBF) and the Free State of Bavaria under the Excellence Strategy of the Federal Government and the Länder through the ONE MUNICH Project Munich Multiscale Biofabrication. Y.K. acknowledges the support of a DOE grant DE-SC0020996. M.P. acknowledges the support by Studienstiftung des Deutschen Volkes. The authors thank Luna, Charly and Xaverl for their support with the measurements and Angelika, Frau Steger and Herr Ehrl for lab upkeep.

Author contributions

All authors conceived and developed the concept. M.P., F.C. and D.W. prepared samples, performed and analyzed the measurements. Y.K. and P.T. supervised the project. All authors have written, read and approved the final manuscript.

Declaration of interests

The authors declare no conflict of interest.

Data and code availability

All data and codes used in this study are available upon reasonable request from the corresponding authors.

References

(1) Mitro, N.; Mak, P. A.; Vargas, L.; Godio, C.; Hampton, E.; Molteni, V.; Kreusch, A.; Saez, E. The nuclear receptor LXR is a glucose sensor. *Nature* **2007**, *445* (7124), 219–223. DOI: 10.1038/nature05449. Published Online: Dec. 24, 2006.

(2) Miyajima, A.; Kitamura, T.; Harada, N.; Yokota, T.; Arai, K. Cytokine receptors and signal transduction. *Annual review of immunology* **1992**, *10*, 295–331. DOI: 10.1146/annurev.iy.10.040192.001455.

(3) Wolf, J.; Rose-John, S.; Garbers, C. Interleukin-6 and its receptors: a highly regulated and dynamic system. *Cytokine* **2014**, *70* (1), 11–20. DOI: 10.1016/j.cyto.2014.05.024. Published Online: Jun. 28, 2014.

(4) Kitamura, K.; Tokunaga, M.; Iwane, A. H.; Yanagida, T. A single myosin head moves along an actin filament with regular steps of 5.3 nanometres. *Nature* **1999**, *397* (6715), 129–134. DOI: 10.1038/16403.

(5) Yildiz, A.; Forkey, J. N.; McKinney, S. A.; Ha, T.; Goldman, Y. E.; Selvin, P. R. Myosin V walks hand-over-hand: single fluorophore imaging with 1.5-nm localization. *Science (New York, N.Y.)* **2003**, *300* (5628), 2061–2065. DOI: 10.1126/science.1084398. Published Online: Jun. 5, 2003.

(6) Okten, Z.; Churchman, L. S.; Rock, R. S.; Spudich, J. A. Myosin VI walks hand-over-hand along actin. *Nature structural & molecular biology* **2004**, *11* (9), 884–887. DOI: 10.1038/nsmb815. Published Online: Aug. 1, 2004.

(7) Rothemund, P. W. K. Folding DNA to create nanoscale shapes and patterns. *Nature* **2006**, *440* (7082), 297–302. DOI: 10.1038/nature04586.

(8) Dey, S.; Fan, C.; Gothelf, K. V.; Li, J.; Lin, C.; Liu, L.; Liu, N.; Nijenhuis, M. A. D.; Saccà, B.; Simmel, F. C.; Yan, H.; Zhan, P. DNA origami. *Nat Rev Methods Primers* **2021**, *1* (1). DOI: 10.1038/s43586-020-00009-8.

(9) Douglas, S. M.; Bachelet, I.; Church, G. M. A logic-gated nanorobot for targeted transport of molecular payloads. *Science (New York, N.Y.)* **2012**, *335* (6070), 831–834. DOI: 10.1126/science.1214081.

(10) Burns, J. R.; Lamarre, B.; Pyne, A. L. B.; Noble, J. E.; Ryadnov, M. G. DNA Origami Inside-Out Viruses. *ACS synthetic biology* **2018**, *7* (3), 767–773. DOI: 10.1021/acssynbio.7b00278. Published Online: Feb. 9, 2018.

(11) Engelen, W.; Sigl, C.; Kadletz, K.; Willner, E. M.; Dietz, H. Antigen-Triggered Logic-Gating of DNA Nanodevices. *Journal of the American Chemical Society* **2021**, *143* (51), 21630–21636. DOI: 10.1021/jacs.1c09967. Published Online: Dec. 20, 2021.
(12) Pumm, A.-K.; Engelen, W.; Kopperger, E.; Isensee, J.; Vogt, M.; Kozina, V.; Kube, M.; Honemann, M. N.; Bertosin, E.; Langecker, M.; Golestanian, R.; Simmel, F. C.; Dietz, H. A DNA origami rotary ratchet motor. *Nature* **2022**, *607* (7919), 492–498. DOI: 10.1038/s41586-022-04910-y. Published Online: Jul. 20, 2022.
(13) Marras, A. E.; Shi, Z.; Lindell, M. G.; Patton, R. A.; Huang, C.-M.; Zhou, L.; Su, H.-J.; Arya, G.; Castro, C. E. Cation-Activated Avidity for Rapid Reconfiguration of DNA Nanodevices. *ACS nano* **2018**, *12* (9), 9484–9494. DOI: 10.1021/acsnano.8b04817. Published Online: Sep. 4, 2018.
(14) Andersen, E. S.; Dong, M.; Nielsen, M. M.; Jahn, K.; Subramani, R.; Mamdouh, W.; Golas, M. M.; Sander, B.; Stark, H.; Oliveira, C. L. P.; Pedersen, J. S.; Birkedal, V.; Besenbacher, F.; Gothelf, K. V.; Kjems, J. Self-assembly of a nanoscale DNA box with a controllable lid. *Nature* **2009**, *459* (7243), 73–76. DOI: 10.1038/nature07971.
(15) Voigt, N. V.; Tørring, T.; Rotaru, A.; Jacobsen, M. F.; Ravnsbaek, J. B.; Subramani, R.; Mamdouh, W.; Kjems, J.; Mokhir, A.; Besenbacher, F.; Gothelf, K. V. Single-molecule chemical reactions on DNA origami. *Nature nanotechnology* **2010**, *5* (3), 200–203. DOI: 10.1038/nnano.2010.5. Published Online: Feb. 28, 2010.
(16) Fu, J.; Yang, Y. R.; Johnson-Buck, A.; Liu, M.; Liu, Y.; Walter, N. G.; Woodbury, N. W.; Yan, H. Multi-enzyme complexes on DNA scaffolds capable of substrate channelling with an artificial swinging arm. *Nature nanotechnology* **2014**, *9* (7), 531–536. DOI: 10.1038/nnano.2014.100. Published Online: May. 25, 2014.
(17) Song, J.; Li, Z.; Wang, P.; Meyer, T.; Mao, C.; Ke, Y. Reconfiguration of DNA molecular arrays driven by information relay. *Science (New York, N.Y.)* **2017**, *357* (6349). DOI: 10.1126/science.aan3377. Published Online: Jun. 22, 2017.
(18) Wang, D.; Song, J.; Wang, P.; Pan, V.; Zhang, Y.; Cui, D.; Ke, Y. Design and operation of reconfigurable two-dimensional DNA molecular arrays. *Nature protocols* **2018**, *13* (10), 2312–2329. DOI: 10.1038/s41596-018-0039-0.
(19) Cui, Y.; Chen, R.; Kai, M.; Wang, Y.; Mi, Y.; Wei, B. Versatile DNA Origami Nanostructures in Simplified and Modular Designing Framework. *ACS nano* **2017**, *11* (8), 8199–8206. DOI: 10.1021/acsnano.7b03187. Published Online: Jul. 6, 2017.
(20) Fan, S.; Ji, B.; Liu, Y.; Zou, K.; Tian, Z.; Dai, B.; Cui, D.; Zhang, P.; Ke, Y.; Song, J. Spatiotemporal Control of Molecular Cascade Reactions by a Reconfigurable DNA Origami Domino Array. *Angewandte Chemie (International ed. in English)* **2022**, *61* (9), e202116324. DOI: 10.1002/anie.202116324. Published Online: Jan. 11, 2022.
(21) Fan, S.; Cheng, J.; Liu, Y.; Wang, D.; Luo, T.; Dai, B.; Zhang, C.; Cui, D.; Ke, Y.; Song, J. Proximity-Induced Pattern Operations in Reconfigurable DNA Origami Domino Array. *Journal of the American Chemical Society* **2020**, *142* (34), 14566–14573. DOI: 10.1021/jacs.0c06061. Published Online: Aug. 12, 2020.
(22) Liu, Y.; Ge, H.; Wang, Y.; Tang, L.; Pei, Y.; Fan, S.; Song, Y.; Zhang, C.; Song, J. Multistep Transformations of DNA Origami Domino Array via Mechanical Forces. *Small Structures* **2023**, *4* (2), 2200167. DOI: 10.1002/sstr.202200167.
(23) Yan, Q.; Wang, Y.; Shi, J.; Wei, B. Allostery of DNA nanostructures controlled by enzymatic modifications. *Nucleic acids research* **2020**, *48* (13), 7595–7600. DOI: 10.1093/nar/gkaa488.

(24) Douglas, S. M.; Dietz, H.; Liedl, T.; Högberg, B.; Graf, F.; Shih, W. M. Self-assembly of DNA into nanoscale three-dimensional shapes. *Nature* **2009**, *459* (7245), 414–418. DOI: 10.1038/nature08016.
(25) Wagenbauer, K. F.; Engelhardt, F. A. S.; Stahl, E.; Hechtl, V. K.; Stömmer, P.; Seebacher, F.; Meregalli, L.; Ketterer, P.; Gerling, T.; Dietz, H. How We Make DNA Origami. *Chembiochem : a European journal of chemical biology* **2017**, *18* (19), 1873–1885. DOI: 10.1002/cbic.201700377. Published Online: Aug. 10, 2017.
(26) Cordes, T.; Vogelsang, J.; Tinnefeld, P. On the mechanism of Trolox as antiblinking and antibleaching reagent. *Journal of the American Chemical Society* **2009**, *131* (14), 5018–5019. DOI: 10.1021/ja809117z.

Supporting Information

Reconfigurable DNA origami arrays as networks of coupled two-state systems to build modular nanodevices

Martina Pfeiffer[1,4], Fiona Cole [1,4], Dongfang Wang [2,3,4], Yonggang Ke [2*] and Philip Tinnefeld [1*]

[1] Department of Chemistry and Center for NanoScience, Ludwig-Maximilians-Universität München, Butenandtstr. 5-13, 81377 München, Germany

[2] Wallace H. Coulter Department of Biomedical Engineering, Emory University and Georgia Institute of Technology, Atlanta, GA 30322, USA

[3] School of Biomedical Engineering and Suzhou Institute for Advanced Research, University of Science and Technology of China, Suzhou 215123, China

[4] These authors contributed equally

* Correspondence: philip.tinnefeld@cup.uni-muenchen.de, yonggang.ke@emory.edu

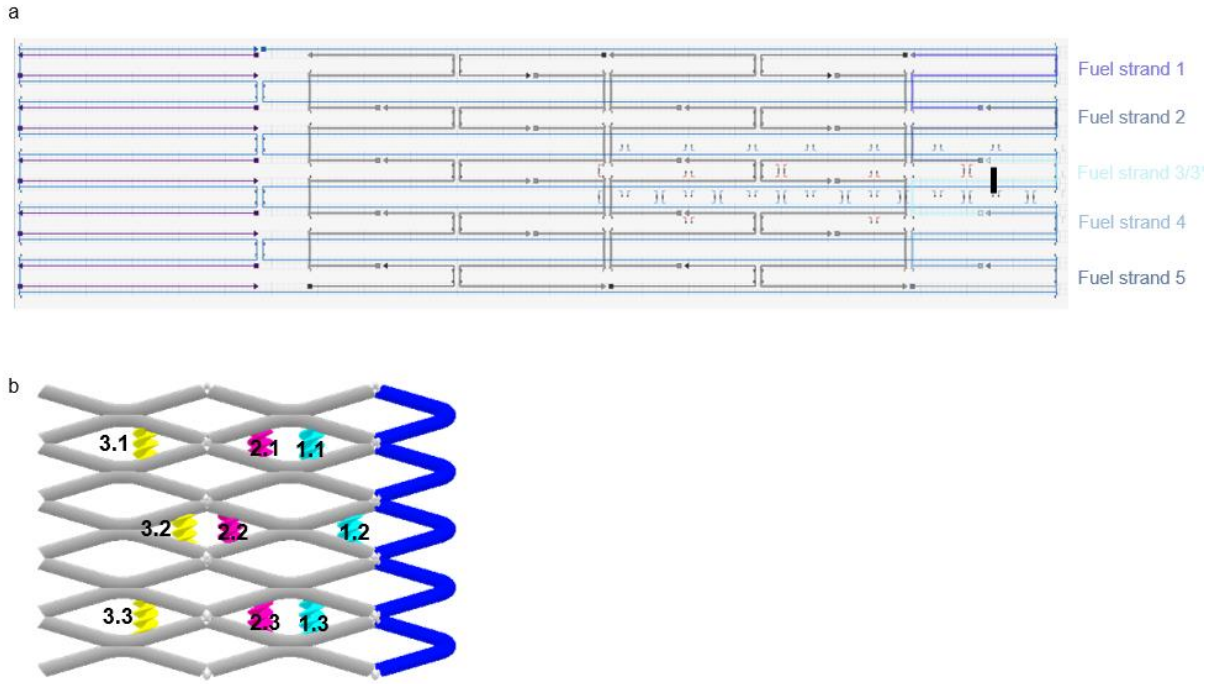

Figure S1. Design of the 5 × 2.5 reconfigurable DNA origami array structure in its untransformed conformation. (a) Blue, gray, purple and blue lines represent the scaffold strand, core DNA staple strands of the structure, loop staple strands and fuel DNA strands, respectively. The DNA loop spans the structure from one end to the other, but does not participate in the transformation process. By labeling one of the staple strands with biotin, we use it as an anchor point for surface immobilization via biotin-neutravidin interactions. Fuel DNA strands 1-4 all have the same length of 65 base pairs. Fuel DNA strand 5 is shorter, consisting of only 39 base pairs. Fuel strand 3* is shortened version of fuel strand 3 consisting of only 25 base pairs. The position of its 5-prime end is marked with a black line. As the transformation process is starts either at the upper right or lower right corner, this asymmetry induces a preferential transformation starting point. The longer length of fuel DNA strand 1 compared to fuel DNA strand 5 results in the transformation preferentially starting from the upper right corner. (b) Sketch illustrating the positions of the activation locking units specific to ssDNA, restriction enzyme activity and light at different anti-junctions of the DNA origami array structure.

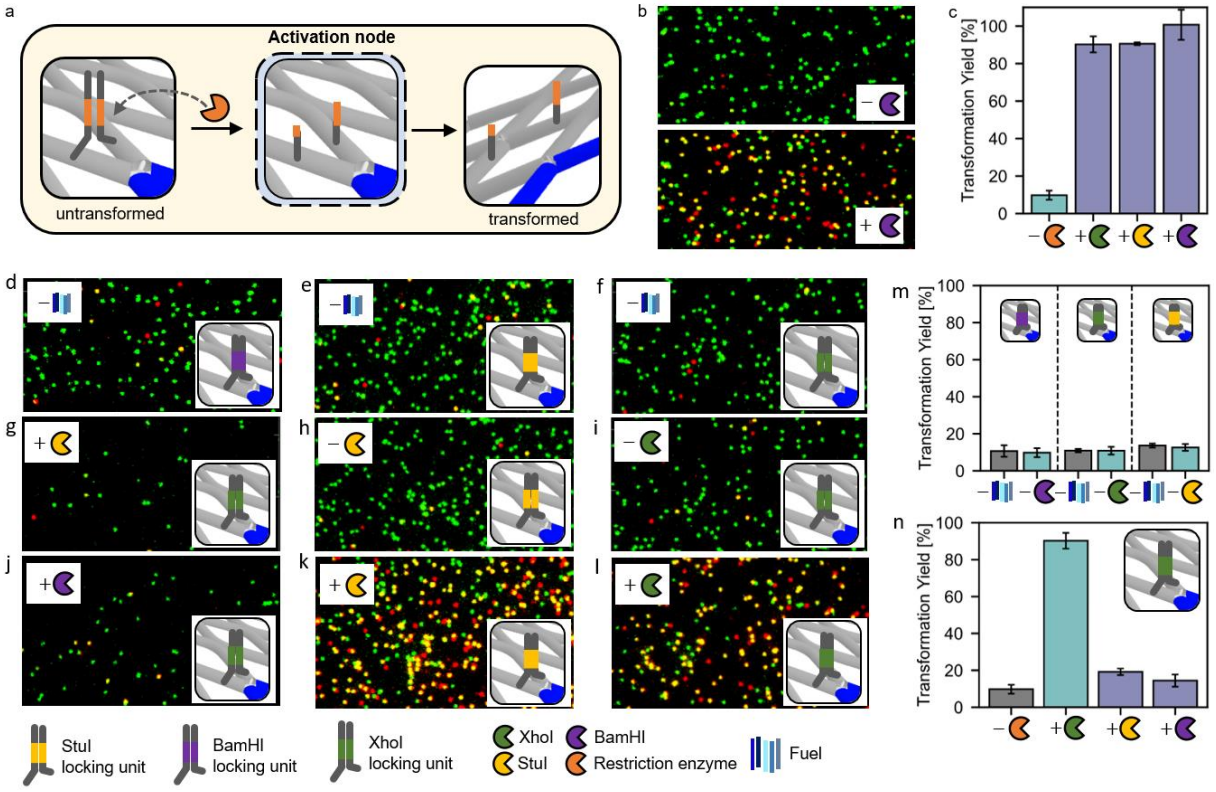

Figure S2. Restriction enzyme activity as input. (a) Sketch of nodes responsive to restriction enzyme activity. Their design is based on a dsDNA lock containing the restriction enzyme-specific cleavage and binding site. The lock is cleaved in presence of active restriction enzyme. (b) Exemplary TIRF images of DNA origami array structures with three restriction enzyme locking units (positions 1.1, 1.2 and 1.3) containing the binding and cleavage site for BamHI before and after incubation with DNA fuel strands and after incubation with fuel strands and BamHI. (c). Transformation yields of DNA origami array structures with three restriction enzyme locking units containing the binding and cleavage site for BamHI, StuI and XhoI, respectively, before and after incubation with DNA fuel strands and BamHI, StuI and XhoI, respectively. (d-l) Exemplary TIRF images of DNA origami array structures with three restriction enzyme locking units before and after incubation with DNA fuel strands and after incubation with fuel strands and restriction enzymes. (m,n) Corresponding transformation yields. (m) when adding the fuel DNA strands (-Enzyme) no significant increase in transformation yield was observed, indicating that by introduction of the restriction enzyme locking units, the transformation process could not induced by the fuel DNA strands alone. (n) Only in presence of XhoI, DNA origami array structures with three XhoI locking units showed a high transformation yield, indicating good specificity. In addition to possible inputs, all DNA origami arrays were incubated with fuel DNA strands 1-5.

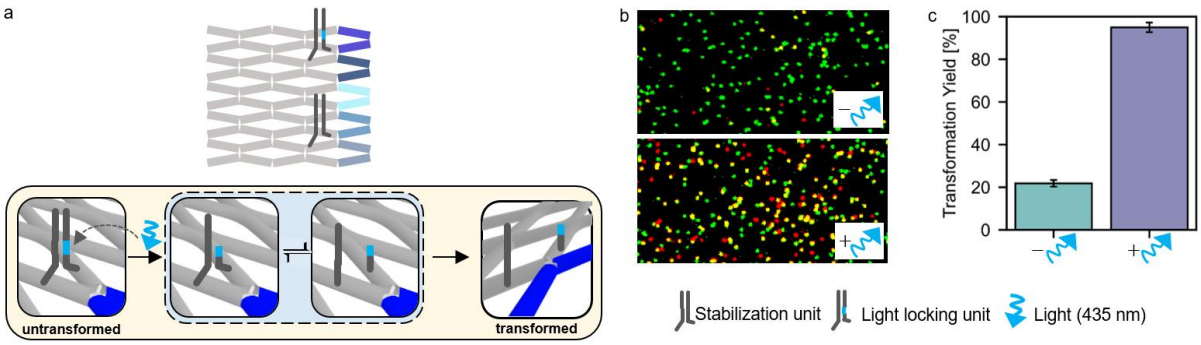

Figure S3. Light as input. (a) Sketch of nodes responsive to light. The design is based on a dsDNA lock containing a light-cleavable linker which is cleaved in presence of light). (b) Exemplary TIRF images of DNA origami array structures with a light-cleavable locking unit (position 1.1) and an additional stabilization unit which stabilizes the untransformed state of the array and does not interact with any inputs (position 1.3) incubated with fuel DNA strands 1-5 in the presence and absence of light. (c) Corresponding transformation yields.

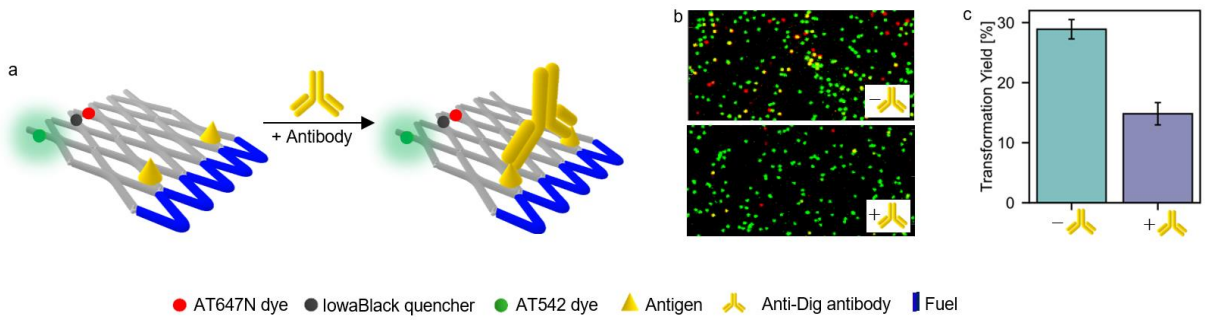

Figure S4. Antibody as input. (a) Sketch of DNA origami array structure bearing two antigens as binding elements for an antibody. Bivalent binding of an antibody inhibits the transformation process. (b) Exemplary TIRF images of DNA origami array structures with Dig antigen input units before (upper) and after (middle) incubation with fuel DNA strands 1,2 and after incubation with anti-Dig antibodies and fuel DNA strands 1,2 (lower). (b) Corresponding transformation yields.

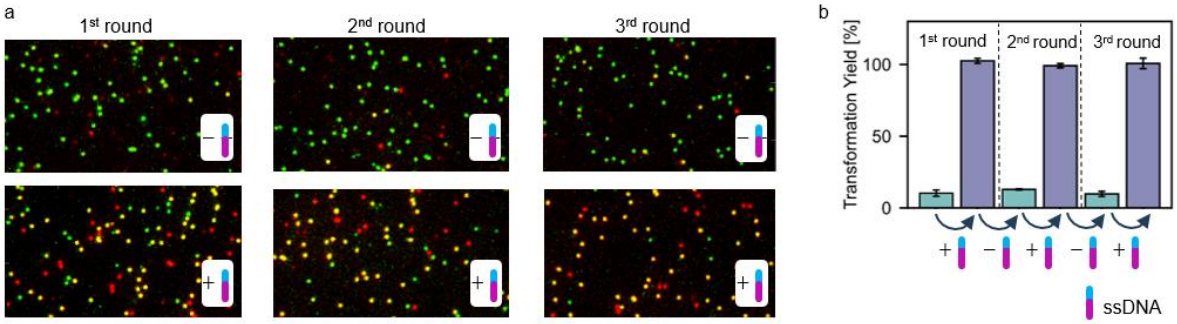

Figure S5. Reversibility of the transformation process activated by ssDNA input. (a) Exemplary TIRF images of DNA origami array structures with six ssDNA activation units (positions 1.1-1.3, 3.1-3.3) incorporated throughout three rounds of incubation with ssDNA input, washing and incubation without ssDNA inputs. The measurements were carried out in the presence of fuel DNA strands 1,2,4. (b) Corresponding transformation yields. In addition to ssDNA as a possible input, the DNA origami arrays were incubated with fuel DNA strands 1-5 throughout all steps.

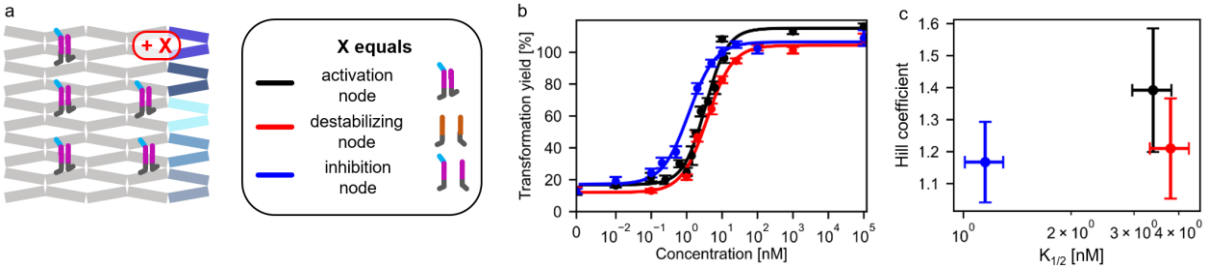

Figure S6. Effect of the additional incorporation of different units to a DNA array carrying five ssDNA activation units on the responsive concentration window of the ssDNA input. (a) Design of the DNA origami array carrying five ssDNA activation units and additionally a variable unit X. Activation and inhibition units stabilize the untransformed and the transformed conformation of the antijunction node they are placed on, respectively. Their stabilizing effect is removed by binding of the ssDNA input to the unit. In contrast, destabilizing units stabilize the transformed conformation of the antijunction node they are placed on but do not interact with the ssDNA input. (b) Varying the unit X shifted the responsive window. (g) As expected, the addition of a destabilizing and an inhibition unit resulted in lower Hill coefficients than the addition of another activation unit. Also, the introduction of these units shifted $K_{1/2}$ to different extents. In addition to ssDNA as a possible input, all DNA origami arrays were incubated with fuel DNA strands 1-5.

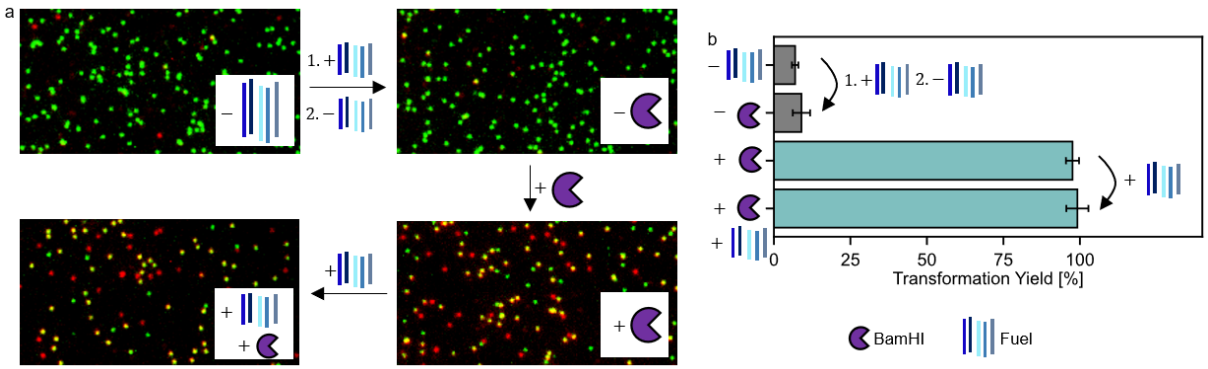

Figure S7. Pre-loading DNA origami array structures with fuel DNA strands. We first incubated a DNA origami array structures with three BamHI locking units (positions 1.1, 1.2 and 1.3) with the fuel DNA strands before removing unbound fuels in solution by five washing steps. Subsequent addition of BamHI resulted in a near quantitative transformation of all structures, demonstrating the successful pre-loading with fuel strands and creation of the pre-tensioned state. The near quantitative transformation was confirmed by again adding the fuel DNA strands at the end of the assay which did not result in a significant increase in transformation yield. Thus, we conclude that pre-loading the fuel DNA strands and their attached energy in a quantitative manner is possible (a) Exemplary TIRF images of the DNA origami arrays before incubation with fuel DNA strands (upper left), after incubation with fuel DNA strands 1-5 which then were removed from solution (upper right), after incubation with BamHI (lower right) and again adding the fuel DNA strands 1-5 (lower left). (b) Corresponding transformation yields.

Supplementary Note 1. Effect of restriction enzyme input units specific for XhoI placed at different positions as well as combinations of these units.

For studying the inhibition effect of locking units on the overall transformation process, we placed different numbers of locking units specific for XhoI at different antijunctions nodes in the system (see Fig. S8a, S8b). Depending on which antijunction the locking units are placed on, we observed different efficiencies in its inhibition of the reconfiguration process. We found that the position-dependency is directly linked to the energy landscape of the reconfiguration process: the further right the antijunction of the input unit is positioned in the DNA array, the earlier it reconfigures its conformation in the transformation process and the larger is the effect of the corresponding locking unit on the overall transformation yield. This is in good agreement with the proposed energy landscape which is tilted upwards in the first steps before exhibiting a downhill profile. In an upwards tilt, the additional energy barrier of the same size has a larger effect than in a downhill tilt. Due to the identical design of the developed restriction enzyme locking units specific for XhoI, StuI, BamHI we expect that the obtained position-dependencies to be transferable to StuI and BamHI. We used the position-dependency to define design strategies for Boolean logic AND and OR gates (see Fig. S8c-f).

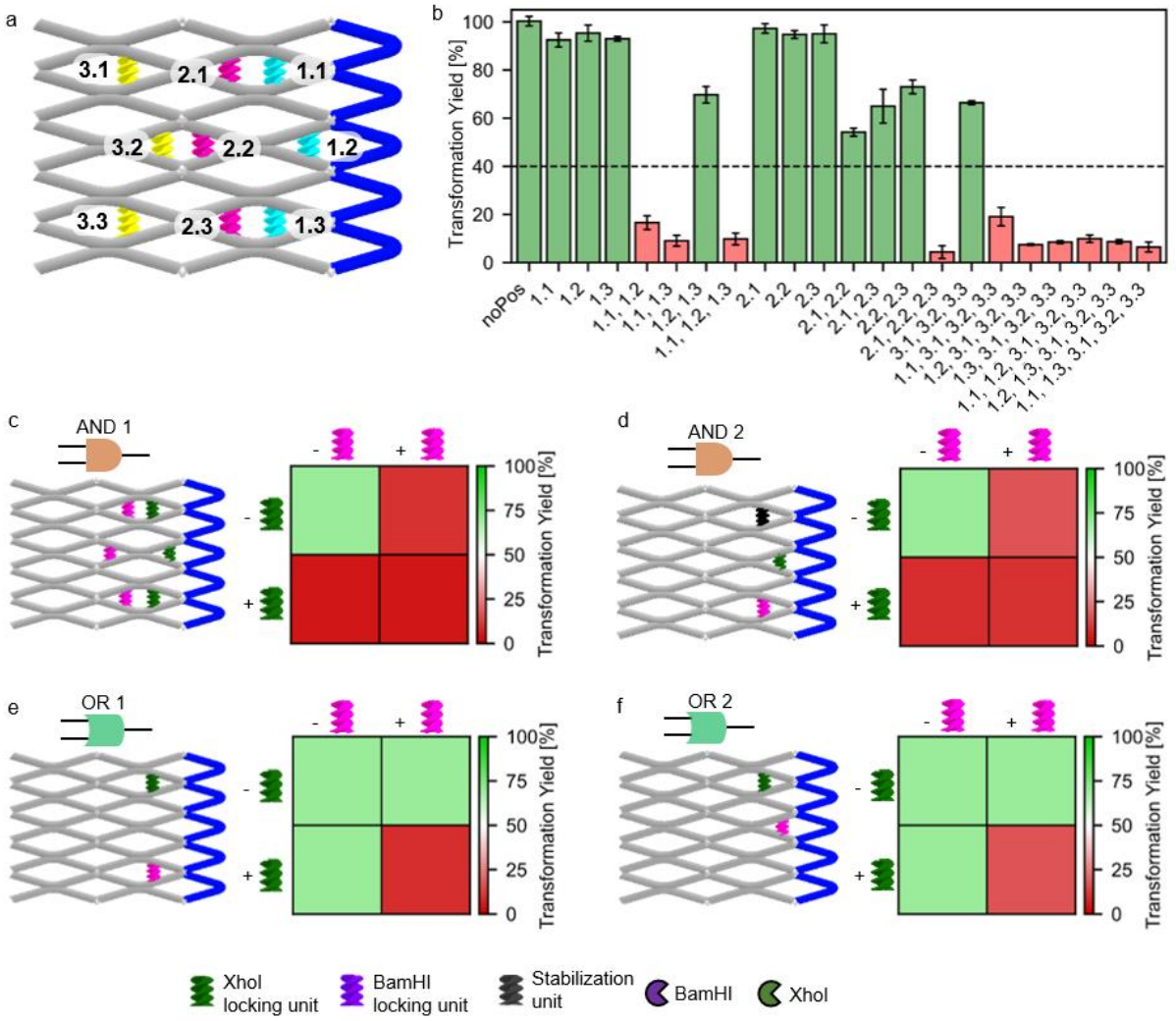

Figure S8. Effect of locking units specific for XhoI placed at different positions as well as combinations of these units. (a) Sketch illustrating the nomenclature of the XhoI locking units positioned at different anti-junctions of the DNA origami array structure. (b) Transformation yields of DNA origami array structures with different combinations of XhoI locking units incorporated. The yields were obtained after incubation with the fuel DNA strands but in absence of restriction enzyme. DNA origami arrays with transformation yields above 40% (dashed line) are considered successfully transformed and marked in green. DNA origami arrays exhibiting lower transformation yields are marked in red. (c-f) Two possible DNA origami array configurations for Boolean logic AND (c,d) and OR (e,f) gates using two types of restriction enzyme as inputs. The corresponding restriction enzyme locking units are marked in the designs in pink and forest green (left sketches). Stabilization units which stabilize the untransformed state of the antijunction node they are placed on and are inactive towards either of the restriction enzymes are marked in black. The transformation yields obtained for DNA origami arrays with (+) and without (-) the locking units incorporated indicate the possibility of implementing Boolean logic gates based on restriction enzyme activity (right plots). Transformation yields are the same as in (b). When applying the designs to restriction enzyme activities, the absence (presence) of a locking unit corresponds to the presence (absence) of a restriction enzyme which cleaves the unit. As such, the configurations are expected to correspond to AND (c,d) gates and OR (e,f) gates with respect to the activity of restriction enzymes. The designs of (c) and (e) are used in Figure 3 of the main paper. Multi-level Boolean logic gates were designed analogously. All DNA origami arrays were incubated with fuel DNA strands 1-5.

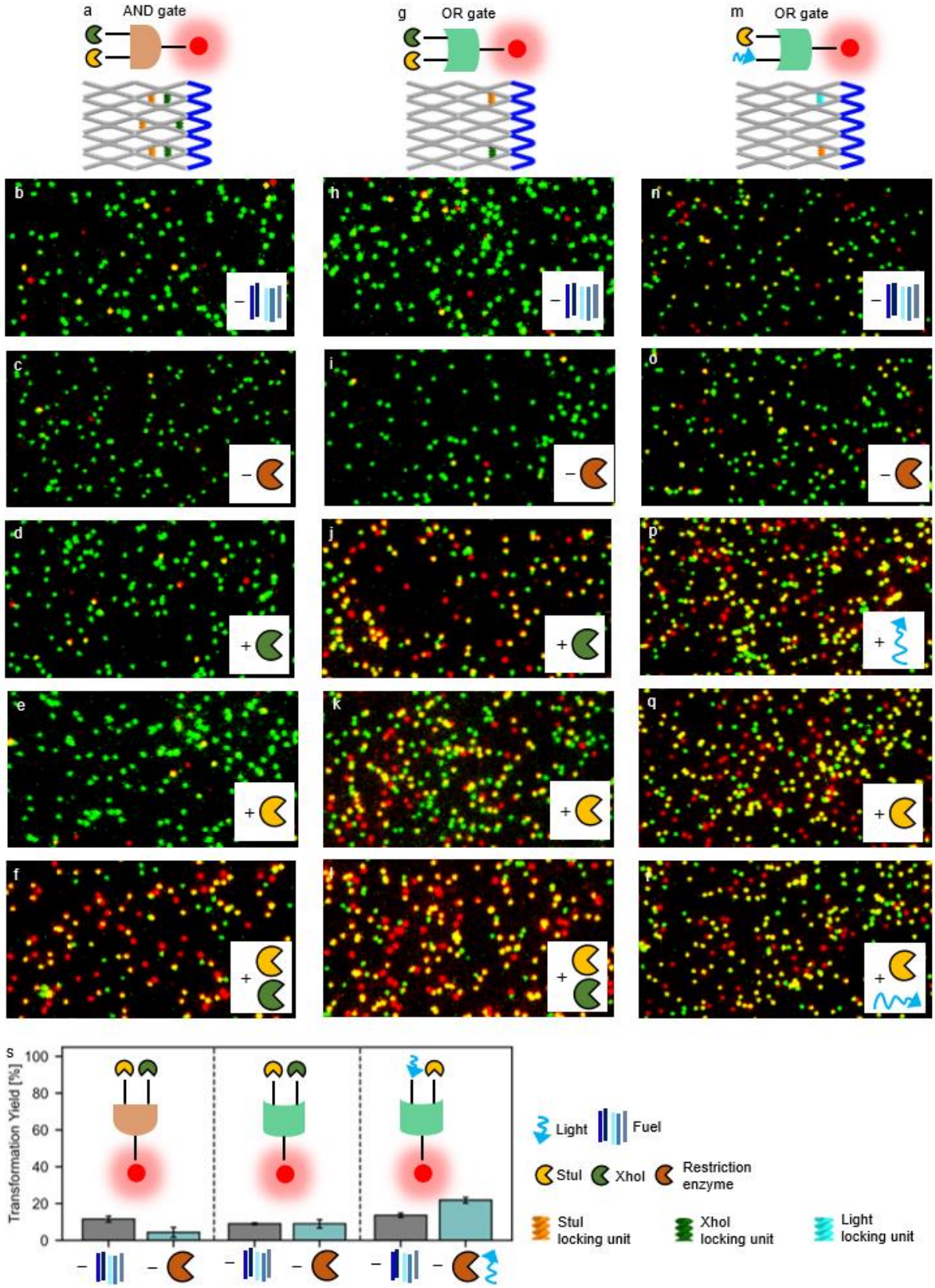

Figure S9. DNA origami array nanodevices processing one-level Boolean logic gates. (a-f) Schematic representation of DNA origami array structures with (a) an AND logic gate responsive to combinations of StuI and XhoI and (b-f) exemplary TIRF images before and upon addition of different inputs. (g-l) Schematic representation of DNA origami array structures with (g) an OR logic gate responsive to combinations of StuI and XhoI and (h-l) exemplary TIRF images before and upon addition

of different inputs. (m-q) Schematic representation of DNA origami array structures with (m) an AND logic gate responsive to combinations of StuI and light and (m-q) exemplary TIRF images before and upon addition of different inputs. (s) Corresponding transformation yields. In addition to possible inputs, all DNA origami arrays were incubated with fuel DNA strands 1-5.

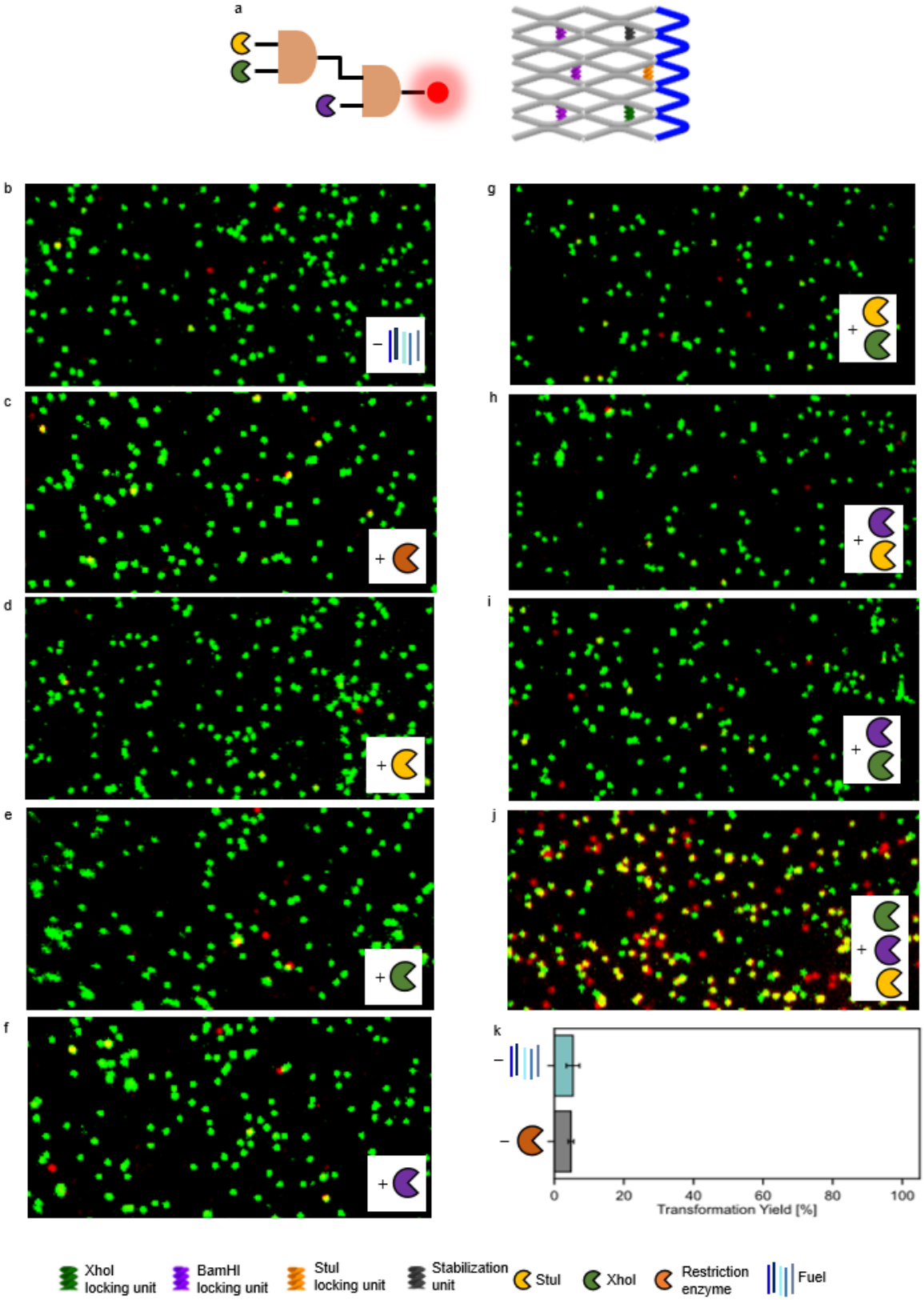

Figure S10. DNA origami array nanodevices processing a 3xAND gate. (a-j) Schematic representation of DNA origami array structures with a 3xAND logic gate responsive to combinations of StuI, XhoI and BamHI and (b-j) exemplary TIRF images before and upon addition of different inputs. (k) Transformation yields obtained before and after incubation with fuel DNA strands but without restriction enzymes. In addition to possible inputs, all DNA origami arrays were incubated with fuel DNA strands 1-5.

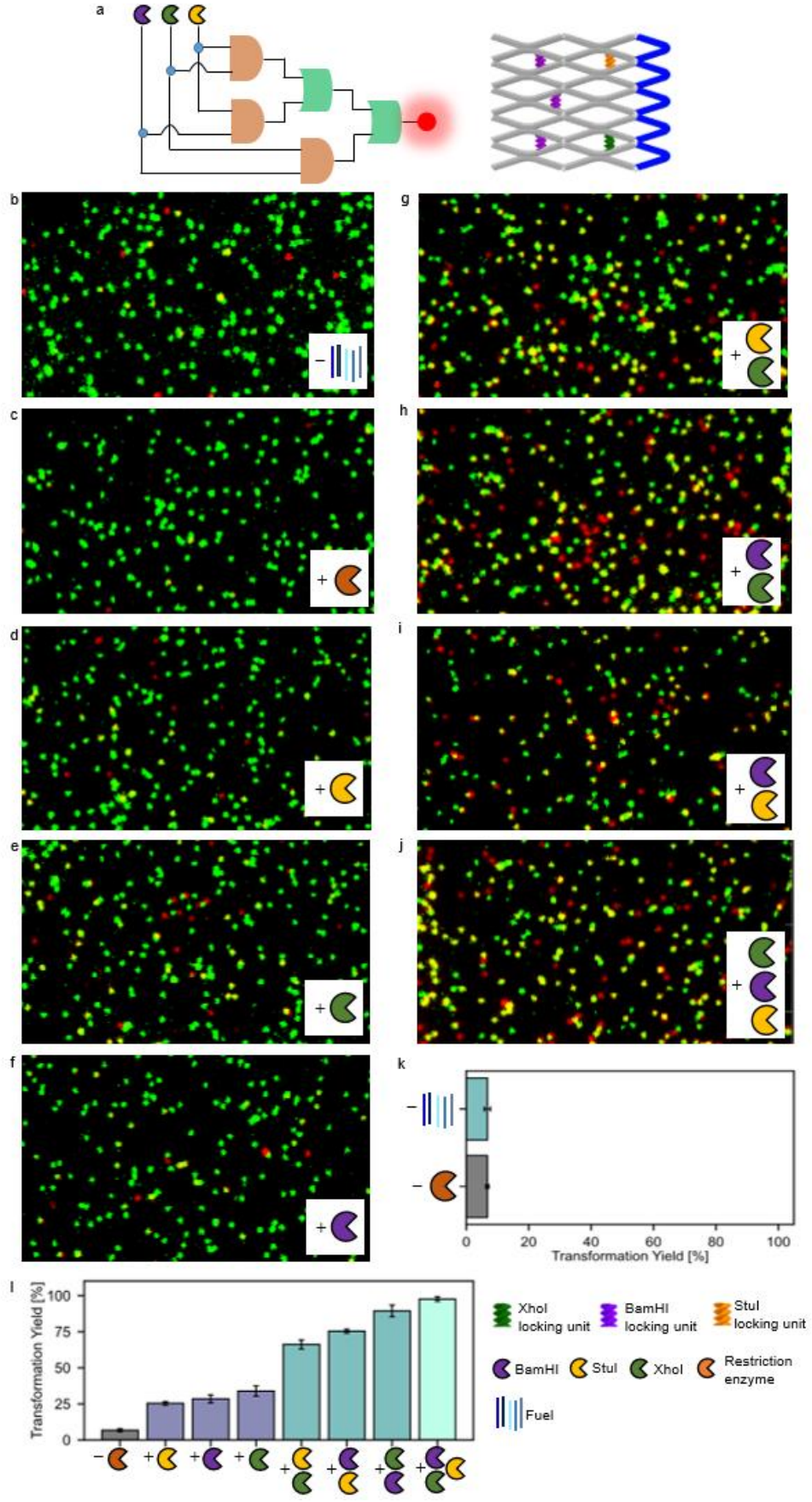

Figure S11. DNA origami array nanodevices processing a multi-level logic gate consisting of a series of three AND gates and two OR gates. (a) Schematic representation of DNA origami array structures with a multi-level logic gate responsive to combinations of StuI, XhoI and BamHI and (b-j)

exemplary TIRF images before and upon addition of different inputs. (k) Transformation yields obtained before and after incubation with fuel DNA strands but without restriction enzymes. (l) Transformation yields before and after incubation with fuel DNA strands and restriction enzymes. In addition to possible inputs, all DNA origami arrays were incubated with fuel DNA strands 1-5.

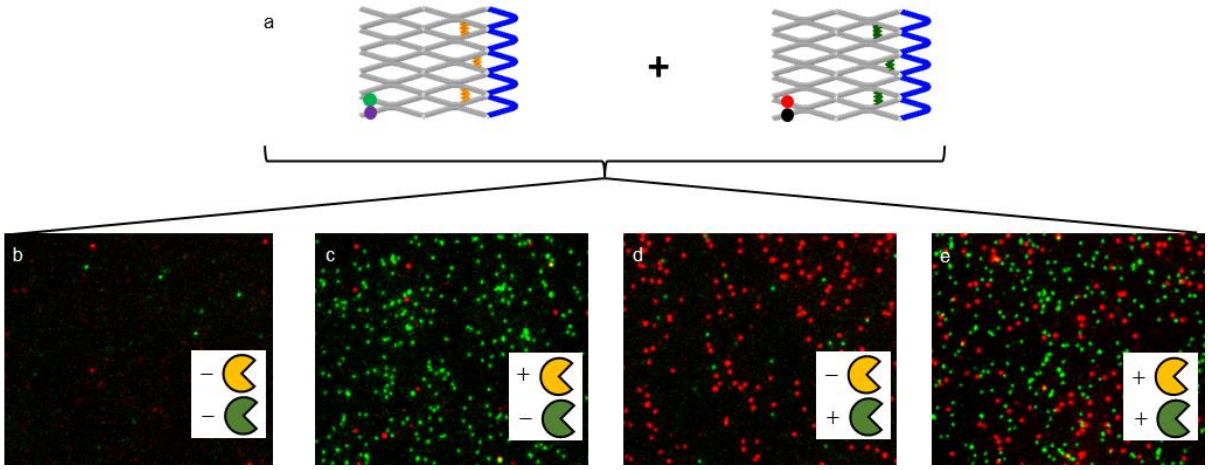

Figure S12. Multiplexing with DNA origami arrays. (a) Sketch of the two different DNA origami array designs used for multiplexing. The DNA origami array responsive to StuI restriction enzyme activity (left panel) carries a green fluorescence onset unit whereas the DNA origami array responsive to XhoI restriction enzyme activity (right panel) carries a red fluorescence onset unit. By immobilizing both DNA origami arrays on the same surface, multiplexing can be achieved by spectral separation. (b-e) Exemplary TIRF images of surfaces bearing both DNA origami array structures upon incubation with and without StuI (yellow) and XhoI (green) restriction enzymes. Only in the presence of the corresponding enzymes, green and/ or red spots appear. In addition to possible inputs, all DNA origami arrays were incubated with fuel DNA strands 1-5.

Supplementary Note 2. Cargo Release Unit

The cargo release unit is formed by two ssDNA strand protruding from domains of two neighboring antijunctions. The ssDNA strands are placed on the antijunction domains such that they are in close proximity in the untransformed conformation of the DNA array and further apart in its transformed conformation. They each contain a 10 nt non-complementary linker sequence followed by a 9 nt complementary sequence which – if both strands are in close proximity – forms a stem. The stem is followed by a 10 nt non-complementary sequence on each strand to which an ATTO542-labelled ssDNA strand containing a 20-nt complementary sequence is hybridized during DNA origami array folding.

Transformation of the antijunctions carrying the cargo release unit then results in the spatial separation of the two ssDNA strands forming the cargo release unit. The stem dehybridizes resulting in a weakened affinity of the cargo strand to the release unit and subsequently to its release.

During measurements also a certain degree of unspecific cargo release was observed. Both upon incubation with and without fuel DNA strands but without restriction enzyme, we noted a decrease in the fraction of structures carrying cargo. As this decrease occurred both upon incubation with and without fuel DNA strands, we do not attribute the unspecific cargo release mainly to the addition of fuel DNA strands but to the heightened incubation temperature of 37 °C (see Supplementary Fig. S13)

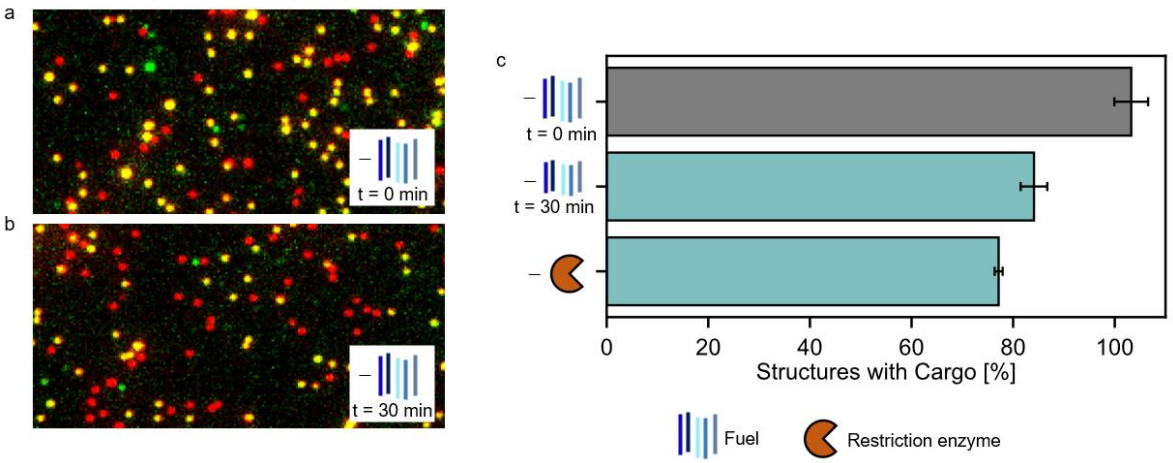

Figure S13. Unspecific release of a cargo DNA strand from DNA origami array structures upon incubation at 37°C and upon incubation without restriction enzyme. (a) Exemplary TIRF images of DNA origami array structures (a) before and (b) after 30 min incubation without fuel DNA strands at 37°C. (c) Corresponding fraction of structures with cargo DNA strand before and upon incubation without and with fuel DNA strands but without restriction enzyme. After incubation, we noted a decrease in the fraction of structures carrying cargo both without and with fuel DNA strands but without restriction enzyme. Thus, we do not attribute the unspecific cargo release mainly to the addition of the fuel DNA strands but to the heightened incubation temperature of 37 °C. In addition to possible inputs, all DNA origami arrays were incubated with fuel DNA strands 1-5.

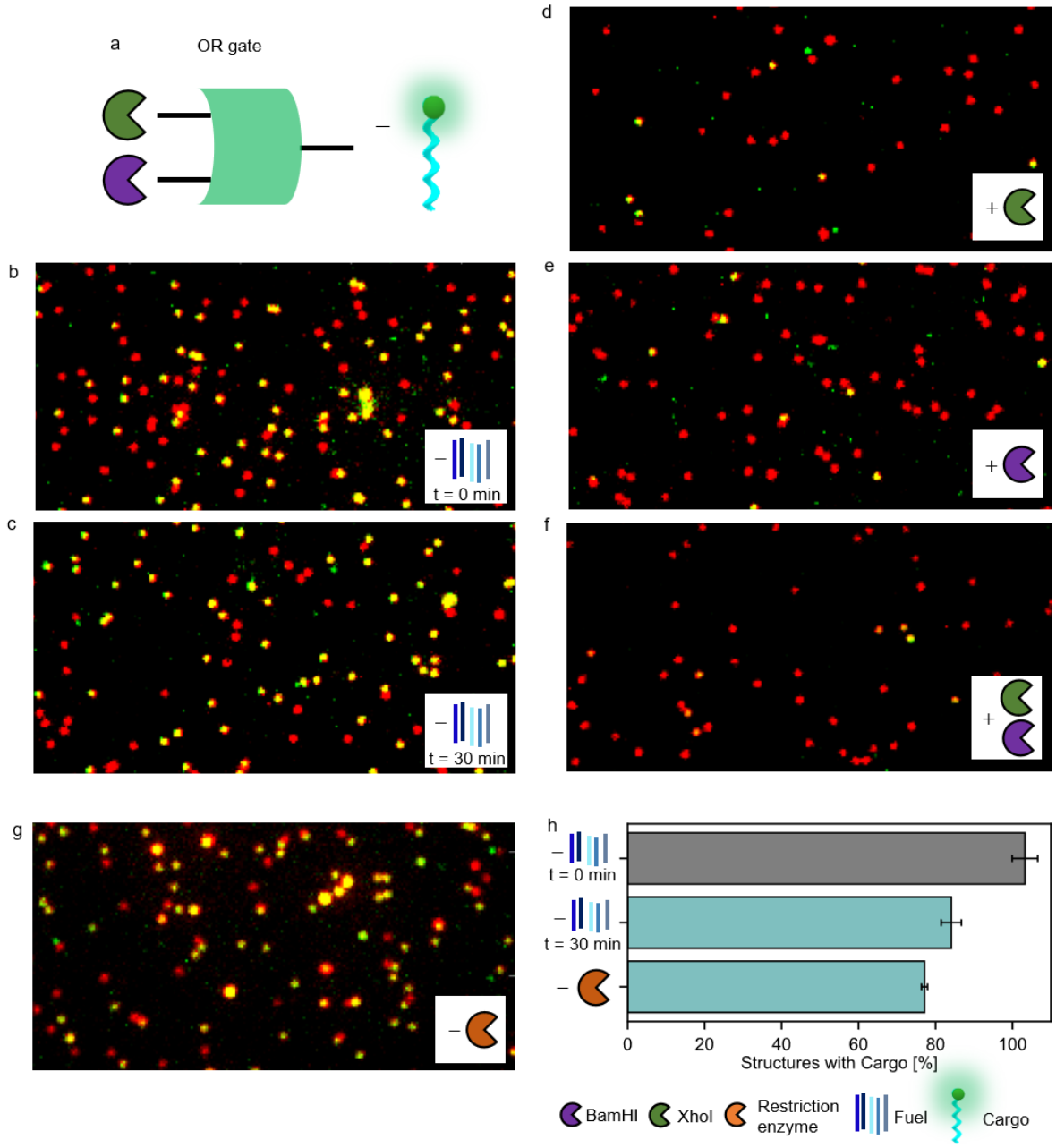

Figure S14. DNA origami arrays with AND logic gate releasing a cargo DNA strand in response to the combination of different restriction enzymes. (a) Schematic representation of a OR logic gate which releases a cargo DNA strand in response to the activity of BamHI and XhoI. (b-f) Exemplary TIRF images of DNA origami array structures before and after incubation with different inputs. (g) Fraction of structures with cargo before and after incubation without and with fuel DNA strand but without restriction enzymes. In addition to possible inputs, all DNA origami arrays were incubated with fuel DNA strands 1-5.

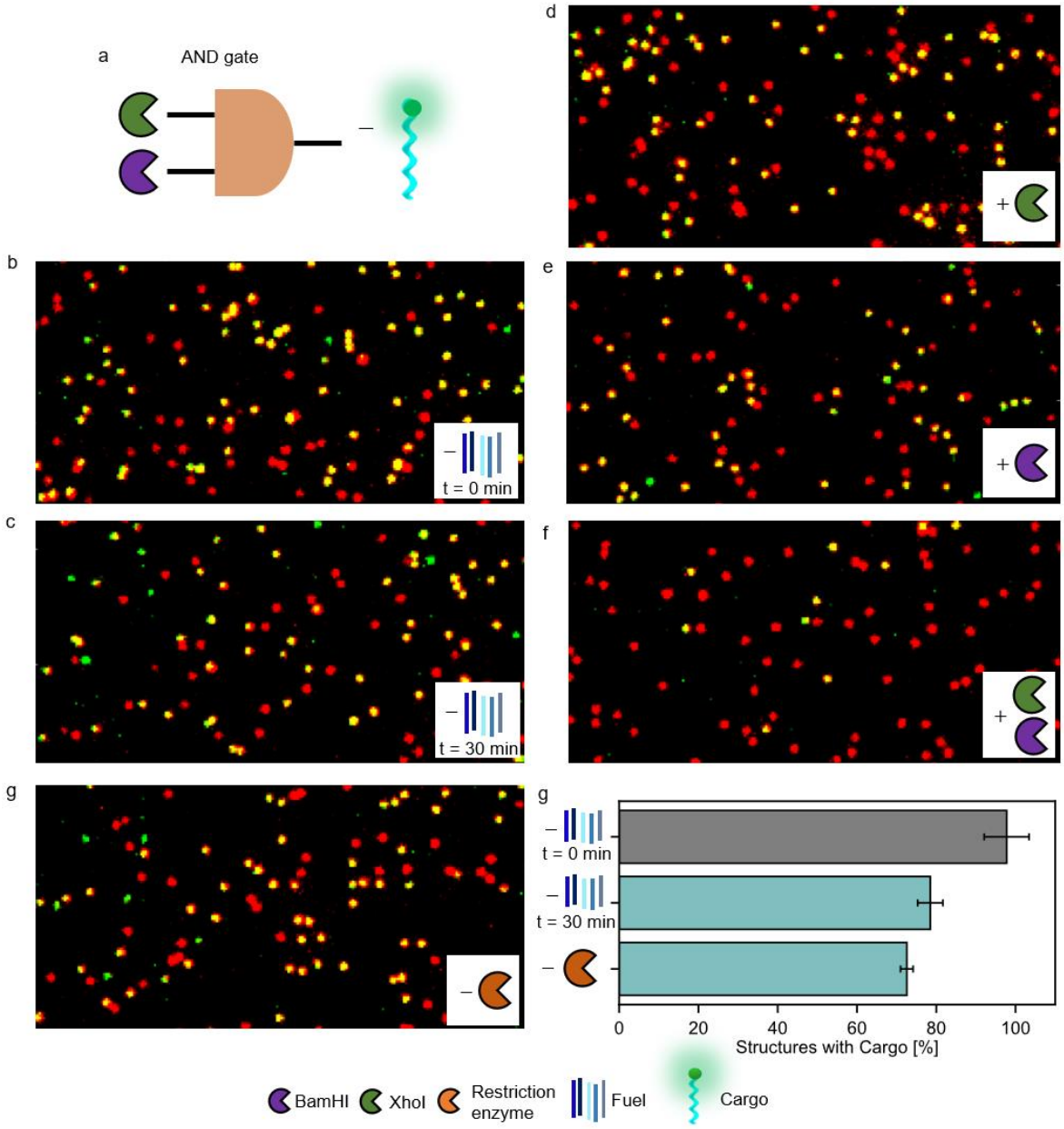

Figure S15. DNA origami arrays with OR logic gate releasing a cargo DNA strand in response to the combination of different restriction enzymes. (a) Schematic representation of a OR logic gate which releases a cargo DNA strand in response to the activity of BamHI and XhoI. (b-f) Exemplary TIRF images of DNA origami array structures before and after incubation with different inputs. (g) Fraction of structures with cargo before and after incubation with and without fuel DNA strand but without restriction enzymes. In addition to possible inputs, all DNA origami arrays were incubated with fuel DNA strands 1-5.

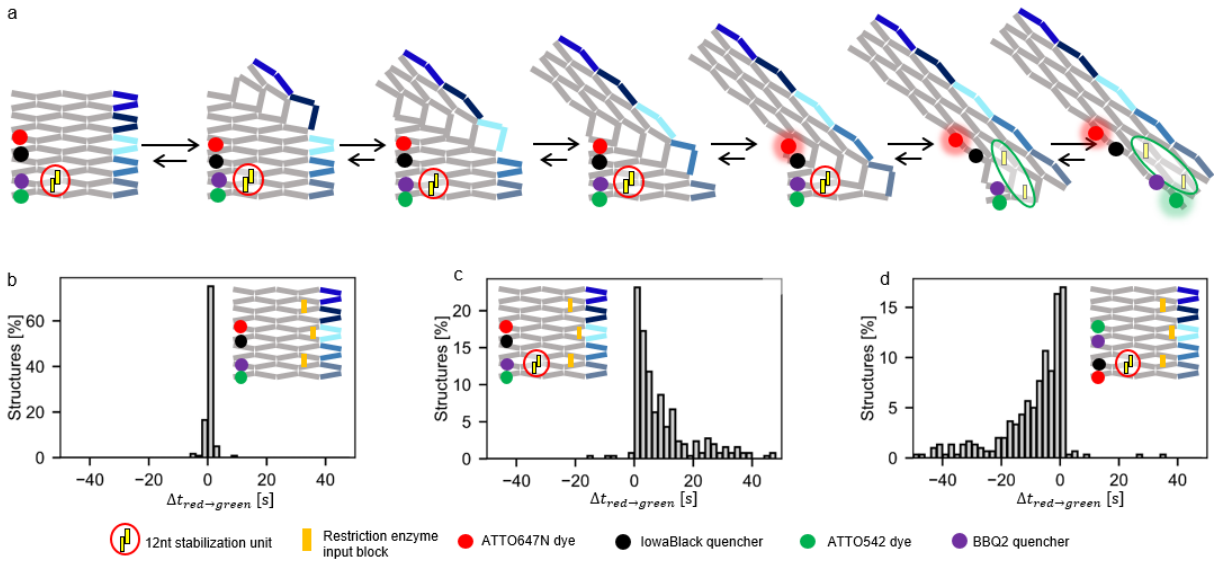

Figure S16. DNA origami array nanodevices to control the timing and the order between output operations. (a) A timing unit consisting of a 12 nt DNA lock is placed on antijunctions transforming before two red and green fluorescence onset units. (b-d) Distributions of the time difference between the fluorescence onset at the studied positions for a DNA origami array with BamHI-responsive input units (positions 1.1, 1.2, 1.3) obtained upon incubation with BamHI for DNA origamis (b) without and (c,d) with a timing unit incorporated. (b) Without the timing unit the red and green fluorescence onsets occurred simultaneously. (c,d) with the timing unit, the red and green fluorescence onsets occurred with a time delay between them. The order of fluorescence onsets hereby was controlled by the placement of the onset units with respect to the timing unit. In addition to BamHI, all DNA origami arrays were incubated with fuel DNA strands 1-5.

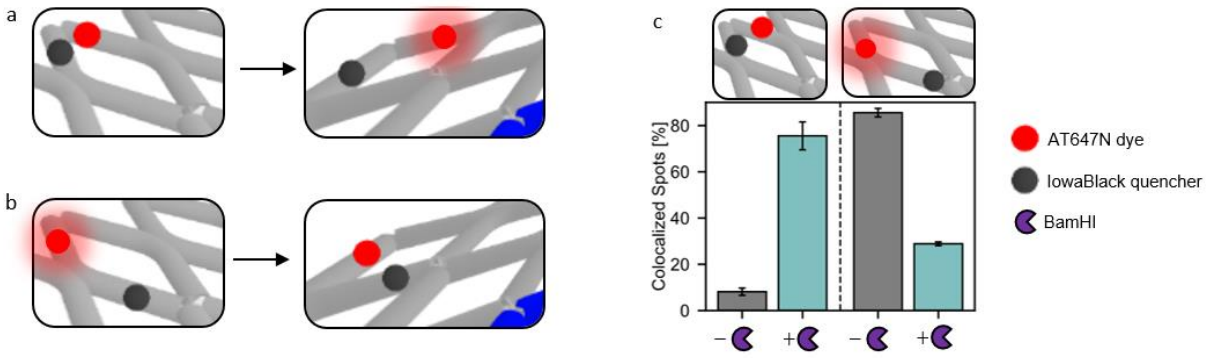

Figure S17. Concept of fluorescence onset and offset unit. (a,b) Sketch demonstrating the principle of a fluorescence onset (a) and a fluorescent offset (b) unit. (c) Fraction of red-green colocalized spots on dual-color TIRF images of DNA origami arrays with a fluorescence on-/offset unit and three restriction enzyme locking units responsive to BamHI incorporated before and upon incubation with BamHI. In addition to BamHI, all DNA origami arrays were incubated with fuel DNA strands 1-5.

Supplementary Note 3. Sequence of the p1800 scaffold used to fold the DNA origami array structure from 5’ to 3’ end:

TACGAAGAGTTCCAGCAGGGATTCCAAGAAATGGCCAATGAAGATTGGATCACC
TTTCGCACTAAGACCTACTTGTTTGAGGAGTGCCTGATGAATTGGCACGACCGC
CTCAGGAAAGTGGAGGAGCATTCTGTGATGACTGTCAAGCTCCAATCTGAGGTG
GGCAAATATAAGATTGTTATCCCTATCTAGAAGTACGTCCGCGGAGAACACCTG
CCACCCGATCACTGGCTGGATCTGTTACGCTTGCTGGGTCTGCCTCGCGGCAC
ATCTCTGGAGAAACTGCTGTTCGGTGACCTGCTGAGAGTTGCCGATACCATCGT
GGCCAAGGCTGCTAACCTGAAAGATCTGAACTCACGCGGCCAGGGTGAAGTGA
CCATCCGCGAATAACTCAGGGAACTGGATTTGTGGGGCGTGGGTGCTGTGTTC
ACACTGATCGGCTATGAGGACTCCCAGAGCCGCACCTAGAAGCTGATCAAGGA
TTGGAAGGAGCTCGTCAACCAGGTGGGCGACAATATATGCCTCCTGCAGTCCTT
GAAGGACTCACCATACTATAAAGGCTTTGAAGACAAGGTCAGCATCTGGGCAAG
GAAACTCGCCGAACTGGACGATAATTTGCAGAACCTCAACCATATTCGCAGAAA
GTGGGTTTACCTCGAACCATACTTTGGTCGCGGAGCCCTGCCCAAAGAGCAGA
CCAGATTCAACAGGGTGGGCGAAGATTTCCGCAGCATCATGACATATATCAAGA
AGGACAATCGCGTCACGCCCTTGACTACCCACGCAGGCATTCTAAACTCACTGC
TGACCATCCTGGACCAATTGCAGAGATGCCAGCGCAGCCTCAACGAGTTCCTG
GAGGCGAAGCGCAGCGCCTTCCCTCGCTTTAACTTCATCGGAGACGATGACCT
GCGCGAGATCTTGGGCCAGTCAACCAATTAATCCGTGATTCAGTCTCACCTCAA
GAAGCTGTTTGCTGGTATCAACTCTGGCTGTTTCGATGAGAAGTCTAAGCACTAT
ACTGCAATGAAGTCCTTGGAGGGGCAAGTTGTGCCATTCAAGAATAACGTACCC
TTGTCCAATAACGTCGAAACCTGGCTGAACGATCTGGCCCTGGAGATGAAGAAG
ACCCTGGAGGCGCTGCTGAAGGAGTGCGTGACAACTAGACGCAGCTCTCAGGG
AGCTGTGGGCCCTTCTCTGTTCCCATCACAGATCTAGTGCTTGGCCGAACAGAT
CAAGTTTACCGAAGATGTGGAGAACGCAATTAAAGATCACTCCCTGCACCAGAT
TGAGTAACAGCTGGTGAACAAATTGGAGCAGTATACTAACATCGACACATCTTC
CGTAGACCCAGGTAACACAGAGTCCGGTATTCTGGAGCTGAAACTGAAAGCACT
GATTCTCGACGGATCCACGCGCCCTGTAGCGGCGCATTAAGCGCGGCGGGTGT
GGTGGTTACGCGCAGCGTGACCGCTACACTTGCCAGCGCCCTAGCGCCCGCTC
CTTTCGCTTTCTTCCCTTCCTTTCTCGCCACGTTCGCCGGCTTTCCCCGTCAAGC
TCTAAATCGGGGGCTCCCTTTAGGGTTCCGATTTAGTGCTTTACGGCACCTCGA
CCCCAAAAAACTTGATTTGGGTGATGGTTCACGTAGTGGGCCATCGCCCTGATA
GACGGTTTTTCGCCCTTTGACGTTGGAGTCCACGTTCTTTAATAGTGGACTCTTG
TTCCAAACTGGAACAACACTCAACCCTATCTCGGGCTATTCTTTTGATTTATAAG
GGATTTTGCCGATTTCGGGGTACC

Table 1. Core staples from the 5‘ to the 3’ end for the DNA origami array structure.

ID	Sequence (5‘ to 3‘)	Function
C1	GGAGTCCTCATAGATGGTTCGAGGTAAACCCACTTTCTGATGT CATGATGCT	core
C2	GCGGAAATCTTCGAATTGGTTGACTGG CCCAAGATCTCGAGTGCTTAGACTT	core
C3	GTTGAGGCTGCGCGGTCCAGGATGGTCAGCAGTGAGTTTCCC AGATGCTGAC	core
C4	CTTGTCTTCAAAGAGTCCTTCAAGGACTGCAGGAGGCATCAAC TCTCAGCAG	core
C5	AATCTTATATTTGATTCGCGGATGGTCACTTCACCCTGGAGGT GCGGCTCTG	core
C6	GAGAGCTGCGTCTCCCCTCCAAG GACTTCATTGCAGTATCGCAGGT CATCGT	core
C7	AGTGATCGGGTGGAGCAGCCTTGGCCACGATGGTATCGGATA TTGTCGCCCA	core
C8	CCTGGTTGACGAGATCGTCCAGTTCGGCGAGTTTCCTTGAGA ATGCCTGCGT	core
C9	CTCATCGAAACAGAGATCTGTGATGGGAACAGAGAAGGGACT CAATCTGGTGCAGGGAGTGATCTTTTTT	core
C10	TTTTTGCGAAAGGTGATCCAATCTTCATTGGAACAGATCCAGC C	core
C11	ATGGCACAACTTGAGTTGTCACGCACTCCTTCAGCAGCGACG GAAGATGTGTCGATGTTAGTATATTTTT	core
C12	CTTCATCTCCAGGAGGTTTCGACGTTATTGGACAAGGGTCCTC CAGGAACTC	core
C13	GTCACCGAACAGCTGCCGCGAGGCAGACCCAGCAAGCGTCC ATTTCTTGGAATCCCTGCTGGAAC	core
C14	GGTTCTGCAAATTCTCCTTCCAATCCTTGATCAGCTTCTCCGC GTGAGTTCA	core
C15	GATCTTTCAGGTTCAGGTGTTCTCCGCGGACGTACTTCTCACT CCTCAAACAAGTAGGTCTTAGTTTTTT	core
C16	TTTTTTGAGGCGGTCGTGCCAATTCATCAGGAGATAGGGATAA C	core
C17	TACCGGACTCTGTGTTACCTGGGTCTCCTCCAGGGTCTT	core
C18	TTTTTCTGCTCCAATTTGTTCACCAGCTGTTCCCACAGCTCCCT	core
C19	CTCCGATGAAGTTCGTGACGCGATTGTCCTTCTTGATATCGAA TATGGTTGA	core
C20	GGGTAGTCAAGGGAAAGCGAGGGAAGGCGCTGCGCTTCGAC GTTATTCTTGA	core
X1	CCAAATCAAGTTTTTTGGGGTCGAGGTGCCGTAAAGCACTAA	loop
X2	AAACCGTCTATCAGGGCGATGGCCCACTACGTGAACCATCAC	loop
X3	GTCCACTATTAAAGAACGTGGACTCCAACGTCAAAGGGCGAA	loop
X4	GGTACCCCGAAATCGGCAAAATCCCTTATAAATCAAAAGAAT	loop
X5	AAGGAGCGGGCGCTAGGGCGCTGGCAAGTGTAGCGGTCACG C	loop
X6	AGCCCGAGATAGGGTTGAGTGTTGTTCCAGTTTGGAACAAGA	loop
X7	ATCGGAACCCTAAAGGGAGCCCCCGATTTAGAGCTTGACGGG	loop

X8	TGCGCGTAACCACCACACCCGCCGCGCTTAATGCGCCGCTAC	loop
X9	AGGGCGCGTGGATCCGTCGAGAATCAGTGCTTTCAGTTTCAG	loop
X10	GAAAGCCGGCGAACGTGGCGAGAAAGGAAGGGAAGAAAGCGA	loop

Table 2. Fuel staples from the 5‘ to the 3’ end used to transform the DNA origami array structure. Fuel staples are labelled according to the position they can bind to the DNA origami array structure, starting from the upper right corner to the lower right corner.

ID	**Sequence (5‘ to 3‘)**	**Function**
T1	AGTTCCCTGAGTTCCCACCTCAGATTGGAGCTTGACAGTCATCACAGAAGCTCCTCCACTTTCCTTTTT	fuel 1
T2	CCGCGACCAAAGTCCGATCAGTGTGAACACAGCACCCACGCCCCACAAACC	fuel 2
T3	TGAATCACGGATTCCCACCCTGTTGAATCTGGTCTGCTCTTTGGGCAGGGT	fuel 3
T4	TCGGCCAAGCACTCCAGAGTTGATACCAGCAAACAGCTTCTTGAGGTGAGAC	fuel 4
T5	TTTTTTTAATTGCGTTCTCCACATCTTCGGTAAACTTGATCTGT	fuel 5

Table 3. Staples from the 5‘ to the 3’ end for labelling the DNA origami array structure with biotin and fluorescent dye – quencher pairs. B1 is included in all DNA array structures for surface immobilization. For the upper and lower fluorescence onset units (U and D staples) either the green or the red dye-quencher pair is used. The staples of the lower fluorescence onset unit (D1-D6) are used to incorporate AT542 and AT647N dyes for co-localization in the DNA arrays. Here, the corresponding quencher-labeled oligonucleotides (D4/ D6) are replaced by their unlabeled alternatives. For the red fluorescence offset unit O2 is used in combination with the staples of the left fluorescence onset unit (L1-L4). Here, the quencher labelled oligonucleotide L4 is replaced by the corresponding unlabeled strand.

ID	Sequence (5‘ to 3‘)	Function	Replaces
B1	**Biotin-**GAAAGCCGGCGAACGTGGCGAGAAAGGAAGGGAAGAAAGCGA	biotin	X10
L1	CTGCAGGAGGCATCAACTCTCAGCAG	onset/ offset Left replacement	C3, C4
L2	CAGTGAGTTTCCCAGATGCT	onset/ offset Left replacement	
L3	GTTGAGGCTGCGCGGTCCAGGATGGTCAG-**ATTO647N**	onset/ offset Left red AT647N	
L4	**IowaBlack-**GACCTTGTCTTCAAAGAGTCCTTCAAGGA	onset Left red Iowa Black	
U1	CAGCAAGCGTCCATTTCTTG	onset Up replacement	C13
U2	**ATTO647N**-GAATCCCTGCTGGAAC	onset Up red AT647N	
U3	GTCACCGAACAGCTGCCGCGAGGCAGACC-**IowaBlack**	onset Up red Iowa Black	
U4	**ATTO542**-GAATCCCTGCTGGAAC	onset Up green AT542	
U5	GTCACCGAACAGCTGCCGCGAGGCAGACC-**BHQ2**	onset Up green BHQ2	
D1	ATTGGACAAGGGTCCTCCAGGAACTC	onset Low replacement	C12, C17
D2	ACCTGGGTCTCCTCCAGGGT	onset Low replacement	
D3	**ATTO647N-**CTTCTTCATCTCCAGGAGGTTTCGACGTT	onset Low red AT647N	
D4	TACCGGACTCTGTGTT-**IowaBlack**	onset Low red Iowa Black	
D5	**ATTO542-**CTTCTTCATCTCCAGGAGGTTTCGACGTT	onset Low green AT542	
D6	TACCGGACTCTGTGTT-**BHQ2**	onset Low green BHQ2	
O2	CCTGGTTGACGAGATCGTCCAGTTCGGCGAGTTTCCTTGAGAATGCCTG-**IowaBlack**	offset Left red Iowa Black	C8

Table 4. Staples from the 5‘ to the 3’ end for incorporation of activation input units responsive to restriction enzyme activity and light. Staples used to form locking units responsive to restriction enzyme activity (E-staples) and light of 300-350 nm (Li-staples). The part of the staples which is used to anker them into the core structure is shown in black wheras linker sections added for flexibility and the stems which form the DNA locks are shown in blue and red, respectively. For E-staples, the part of the stem which is designed to be responsive to restriction enzyme activity is highlighted with six bold red Xs. This section is to be replaced by the cutting sequence of the restriction enzyme the corresponding input unit is designed to be responsive to (see Table 5). In Li-1, a spacer photocleavable by light of 300-350 nm is included after the linker sequence as denoted in the sequence by PC in purple.

ID	Sequence (5‘ to 3‘)	Function	Replaces
E1	TGAGGCGGTCGTGCCAATTCATCAGGAGATAGGGATAA TTTT GCCT **XXXXXX** GTGATGTAGGTGGTAGAGG	1.1 Enzyme Unit 3'	C1, C2, C5, C9, C16
E2	CCTCTACCACCTACATCAC **XXXXXX** AGGC TTTT CACCCTGGAGGTGCGGCTCT	1.1 Enzyme Unit 5'	
E3	GGGAGTCCTCATAGATGGTTCGAG TTTT GCCT **XXXXXX** GTGATGTAGGTGGTAGAGG	1.2 Enzyme Unit 3'	
E4	CCTCTACCACCTACATCAC **XXXXXX** AGGC TTTT GCGGAAATCTTCGAATTGGTTGACTGGC	1.2 Enzyme Unit 5'	
E5	CCAAGATCTCGAGTGCTTAGACT TTTT GCCT **XXXXXX** GTGATGTAGGTGGTAGAGG	1.3 Enzyme Unit 3'	
E6	CCTCTACCACCTACATCAC **XXXXXX** AGGC TTTT GAGAAGGGACTCAATCTGGTGCAGGGAGTGATCT	1.3 Enzyme Unit 5'	
E7	TCTCATCGAAACAGAGATCTGTGATGGGAACA	1.x Enzyme Units Replacement	
E8	GTAAACCCACTTTCTGATGTCATGATGCT	1.x Enzyme Units Replacement	
E9	CAATCTTATATTTGATTCGCGGATGGTCACTT	1.x Enzyme Units Replacement	
E10	TTGATCAGCTTCTCCGCGTGAGTTCAG TTTT GCCT **XXXXXX** GTGATGTAGGTGGTAGAGG	2.1 Enzyme Unit 3'	C6, C14, C15, C18, C19
E11	CCTCTACCACCTACATCAC **XXXXXX** AGGC TTTT GACGTACTTCTCACTCCTCAAACAAGTAGGTCTTAGT	2.1 Enzyme Unit 5'	
E12	CTCCGATGAAGTTCGTGACGCGATTGTCCTTT TTTT GCCT **XXXXXX** GTGATGTAGGTGGTAGAGG	2.2 Enzyme Unit 3'	
E13	CCTCTACCACCTACATCAC **XXXXXX** AGGC TTTT TTTTCTGCAAATTCTCCTTCCAATCC	2.2 Enzyme Unit 5'	

E14	CTGCTCCAATTTGTTCACCAGCTGTTCCCACAGCTC CCTG TTTT GCCT **XXXXXX** GTGATGTAGGTGGTAGAGG	2.3 Enzyme Unit 3'	
E15	CCTCTACCACCTACATCAC **XXXXXX** AGGC TTTT CATTGCAGTATCGCAGGTCATCGT	2.3 Enzyme Unit 5'	
E16	AGAGCTGCGTCTCCCCTCCAAGGACTT	2.x Enzyme Units Replacement	
E17	TCTTGATATCGAATATGGTTGAGG	2.x Enzyme Units Replacement	
E18	ATCTTTCAGGTTCAGGTGTTCTCCGCG	2.x Enzyme Units Replacement	
E19	GCGAAAGGTGATCCAATCTTCATTGGAACAGATCCA G TTTTTT GCCT **XXXXXX** GTGATGTAGGTGGTAGAGG	3.1 Enzyme Unit 3'	C7, C8, C10, C11, C20
E20	CCTCTACCACCTACATCAC **XXXXXX** AGGC TTTTTT GCCACGATGGTATCGGATATTGTCGCC	3.1 Enzyme Unit 5'	
E21	CACCTGGTTGACGAGATCGTCCAGTT TTTTTT GCCT **XXXXXX** GTGATGTAGGTGGTAGAGG	3.2 Enzyme Unit 3'	
E22	CCTCTACCACCTACATCAC **XXXXXX** AGGC TTTTTT CGTGGGTAGTCAAGGGAAAGCGAGGGAAG	3.2 Enzyme Unit 5'	
E23	GCGCTGCGCTTCGACGTTATTCTT TTTTTT GCCT **XXXXXX** GTGATGTAGGTGGTAGAGG	3.3 Enzyme Unit 3'	
E24	CCTCTACCACCTACATCAC **XXXXXX** AGGC TTTTTT CACTCCTTCAGCAGCGACGGAAGATGTGTCGATGTT AGTATA	3.3 Enzyme Unit 5'	
E25	CCAGTGATCGGGTGGAGCAGCCTTG	3.x Enzyme Units Replacement	
E26	CGGCGAGTTTCCTTGAGAATGCCTG	3.x Enzyme Units Replacement	
E27	GAATGGCACAACTTGAGTTGTCACG	3.x Enzyme Units Replacement	

Li1	TGAGGCGGTCGTGCCAATTCATCAGGAGATAGGGATAA TTTT **PC** GCCTAAGCTTGTGATGTAGGTGGTAGAGG	1.1 Light Unit 3'	E1, E2
Li2	CCTCTACCACCTACATCACAAGCTTAGGC TTTT CACCCTGGAGGTGCGGCTCT	1.1 Light Unit 5'	

Table 5. Cutting sites of the used restriction enzymes from the 5‘ to the 3’ end. Sequences for the cut sites of the restriction enzymes BamHI, XhoI and StuI. Additionally, a fourth sequence is shown which is not cleavable by any of the aforementioned enzymes. Depending on which enzyme an input unit is designed to be responsive to, the sequences replace the red Xs for the corresponding E-staples in Table 4.

Restriction enzyme	Cut site (5‘ to 3‘)
BamHI	GGATCC
XhoI	CTCGAG
StuI	AGGCCT
not activatable	AAGCTT

Table 6. Staples from the 5‘ to the 3’ end for incorporation of an inhibition input units responsive to the anti-Dig antibody.

ID	Sequence (5‘ to 3‘)	Function	Replaces
A1	TGAGGCGGTCGTGCCAATTCATCAGGAGATAGGGATAAC-**Dig**	Antibody Unit - Antigen 1	C16
A2	TAACATTCCTAACTTCTCATACTCATCGAAACAGAGATCTGTG	Antibody Unit - Antigen 2 site	C9
A3	ATGGGAACAGAGAAGGGACTCAATCTGGTG	Antibody Unit - Antigen 2 Replacement	
A4	**Dig**-TTATGAGAAGTTAGGAATGTTA	Antibody Unit - Antigen 2	

Table 7. Staples from the 5‘ to the 3’ end for incorporation of activation and inhibition input units responsive to a 20 nt ssDNA input. The part of the staples which is used to anker them into the core structure is shown in black. Linker sections added for flexibility, stems and the ssDNA binding sites are shown in blue red and purple, respectively.

ID	Sequence (5‘ to 3‘)	Function	Replaces
Dna1	TGAGGCGGTCGTGCCAATTCATCAGGAGATAG GGATAA TT GTATCG CCTACATCAC	1.1 DNA Inhibition/ Activation Unit 3'	E1, E2
Dna2	TCCTCTACCA CGATAC TT CACCCTGGAGGTGCGGCTCT	1.1 DNA Inhibition Unit 5'	
Dna3	GGGAGTCCTCATAGATGGTTCGAG TT GTATCG CCTACATCAC	1.2 DNA Inhibition Unit 3'	E3, E4
Dna4	TCCTCTACCA CGATAC TT GCGGAAATCTTCGAATTGGTTGACTGGC	1.2 DNA Inhibition Unit 5'	
Dna5	TCCTCTACCA CGATAC TT GACGTACTTCTCACTCCTCAAACAAGTAGGTCT TAGT	1.1 DNA Activation Unit 5'	C15
Dna6	ATCTTTCAGGTTCAGGTG	1.1 DNA Activation Unit - Replacement	
Dna7	GTGATGTAGGTGGTAGAGGA	ssDNA Input	-

Table 8. Staples from the 5‘ to the 3’ end for incorporation of a cargo release output operation unit. The part of the staples which is used to anker them into the core structure is shown in black wheras linker sections added for flexibility and the stems which form the DNA locks are shown in blue and red, respectively. The part of the sequence to which the ATTO542-labelled cargo ssDNA strand which is to be released is hybridized is shown in purple.

ID	Sequence (5‘ to 3‘)	Function	Replaces
R1	TCCTCTACCA GTATCGTAG TTTTTTTTTT AGCAGTGAGTTTCCCAGATGCTGACCT	Cargo release - Catching unit 5'	C3, C4
R2	TGTCTTCAAAGAGTCCTTCAAGGACTGC TTTTTTTTTT CTACGATAC CCTACATCAC	Cargo release - Catching unit 3'	
R3	AGGAGGCATCAACTCTCAGCAG	Cargo release - Replacement	
R4	GTTGAGGCTGCGCGGTCCAGGATGGTC	Cargo release - Replacement	
R5	GTGATGTAGGTGGTAGAGGAT-**ATTO542**	Cargo strand	-

Table 9. Staples from the 5‘ to the 3’ end for incorporation of the timing unit used to retard the transformation at a specific position. The part of the staples which is used to anker them into the core structure is shown in black. Linker sections added for flexibility and the 12 nt long locking unit which forms a stem are shown in blue and red, respectively.

ID	**Sequence (5‘ to 3‘)**	**Function**	**Replaces**
T1	GGGTAGTCAAGGGAAAGCGAGGGAAGGCGCTG CGCTTCGACGTTATTCTTGAATG TTT CGACTACGATAC	Timing Unit - Locking unit 12bp	C11, C20
T2	GCACAACTTGAGTTGTCACGCACTCCTTCAGCA GCGACGGAAGATGTGTCGA T GTATCGTAGTCG	Timing Unit - Locking unit 12bp	

Table 10. DNA origami array designs used in this work. For each DNA origami design, the modified staples are listed. Staples which are used as given in Tables 3-9 are listed without additional notation. Staples which are used without their corresponding modification (either highlighted in color or in bold in Tables 3-9) are listed with the addition _um. For E-staples, the included cutting site of the corresponding enzyme (Table 5) is highlighted by the addition _Enzyme or _nonAct for the corresponding enzyme cutting site and the non-cleavable sequence, respectively. The modified staples replace staples of the core mix (C- and L-staples as highlighted in Tables 3-9). For DNA origami folding, in addition to the modified staples, all unreplaced core staples are added.

No.	Modified Staples	Description
1	B1, L1-4, D1-2, D5, D6_um, E1-6_BamHI, E7-9	BamHI Unit Introduction (Fig. 2)
2	B1, L1-4, D1-2, D5, D6_um, E1-6_XhoI, E7-9	XhoI Unit Introduction (Fig. 2)
3	B1, L1-4, D1-2, D5, D6_um, E1-6_StuI, E7-9	StuI Unit Introduction (Fig. 2)
4	B1, L1-4, D1-2, D5, D6_um, Li1-2, E3-4_um, E5-6_nonAct, E7-9	Light Unit Introduction (Fig. 2)
5	B1, L1-4, D1-2, D5, D6_um, A1-4	Dig Unit Introduction (Fig. 2)
6	B1, L1-4, D1-2, D5, D6_um, E1-6_StuI, E7-9, E10-15_XhoI, E16-18	AND gate (XhoI, StuI, Fig. 3)
7	B1, L1-4, D1-2, D5, D6_um, E1-2_StuI, E3-4_um, E5-6_XhoI, E7-9	OR gate (XhoI, StuI, Fig. 3)
8	B1, L1-4, D1-2, D5, D6_um, Li1-2, E3-4_um, E5-6_XhoI, E7-9	OR gate (XhoI, Light, Fig. 3)
9	B1, L1-4, D1-2, D5, D6_um, E1-2_nonAct, E3-4_StuI, E5-6_XhoI, E7-9, E19-24_BamHI, E25-27	3xAND gate (XhoI, StuI, BamHI, Fig. 3)
10	B1, L1-4, D1-2, D5, D6_um, E1-2_StuI, E3-4_um, E5-6_XhoI, E7-9, E19-24_BamHI, E25-27	2outOf3 gate (XhoI, StuI, BamHI, Fig.3)
11	B1, D1-3, D4_um, E1-6_BamHI, E7-9, R1-5	Cargo release by BamHI activity (Fig. 4)
12	B1, D1-3, D4_um, E1-2_nonAct, E3-4_BamHI, E5-6_XhoI, E7-9, R1-5	Cargo release by AND gate (BamHI, XhoI, Fig. 4)
13	B1, D1-3, D4_um, E1-2_BamHI, E3-4_um, E5-6_XhoI, E7-9, R1-5	Cargo release by OR gate (BamHI, XhoI, Fig. 4)
14	B1, L1-4, D1-2, D5, D6_um, Dna1, Dna5-6, E2-6_um, E7-9	DNA Activation Unit (Fig. S3)
15	B1, L1-4, D1-2, D5, D6_um, Dna1-4, E5-6_nonAct, E7-9	DNA Inhibition Unit (Fig. S3)
16	B1, L1-3, L4_um, O1, D1-2, D5, D6_um, E1-6_BamHI, E7-9	Fluorescence Offset Unit (activatable by BamHI, Fig. S3)
17	B1, L1-4, D1-2, D5, D6_um, E1-2_XhoI, E3-6_um, E7-9	1.1 XhoI Unit(Fig. S5)
18	B1, L1-4, D1-2, D5, D6_um, E1-2_um, E3-4_XhoI, E5-6_um, E7-9	1.2 XhoI Unit(Fig. S5)
19	B1, L1-4, D1-2, D5, D6_um, E1-4_um, E5-6_XhoI, E7-9	1.3 XhoI Unit (Fig. S5)
20	B1, L1-4, D1-2, D5, D6_um, E1-4_XhoI, E5-6_um, E7-9	1.1, 1.2 XhoI Unit (Fig. S5)

21	B1, L1-4, D1-2, D5, D6_um, E1-2_XhoI, E4-5_um, E5-6_XhoI, E7-9	1.1, 1.3 XhoI Unit (Fig. S5)
22	B1, L1-4, D1-2, D5, D6_um, E1-2_um, E3-6_XhoI, E7-9	1.2, 1.3 XhoI Unit (Fig. S5)
23	B1, L1-4, D1-2, D5, D6_um, E1-6_XhoI, E7-9	1.1, 1.2, 1.3 XhoI Unit (Fig. S5)
24	B1, L1-4, D1-2, D5, D6_um, E10-11_XhoI, E12-15_um, E16-18	2.1 XhoI Unit (Fig. S5)
25	B1, L1-4, D1-2, D5, D6_um, E10-11_um, E12-13_XhoI, E14-15_um, E16-18	2.2 XhoI Unit (Fig. S5)
26	B1, L1-4, D1-2, D5, D6_um, E10-13_um, E14-15_XhoI, E16-18	2.3 XhoI Unit (Fig. S5)
27	B1, L1-4, D1-2, D5, D6_um, E10-13_XhoI, E14-15_um, E16-18	2.1, 2.2 XhoI Unit (Fig. S5)
28	B1, L1-4, D1-2, D5, D6_um, E10-11_XhoI, E12-13_um, E14-15_XhoI, E16-18	2.1, 2.3 XhoI Unit (Fig. S5)
29	B1, L1-4, D1-2, D5, D6_um, E10-11_um, E12-15_XhoI, E16-18	2.2, 2.3 XhoI Unit (Fig. S5)
30	B1, L1-4, D1-2, D5, D6_um, E10-15_XhoI, E16-18	2.1, 2.2, 2.3 XhoI Unit (Fig. S5)
31	B1, L1-4, D1-2, D5, D6_um, E19-24_XhoI, E25-27	3.1, 3.2, 3.3 XhoI Unit (Fig. S5)
32	B1, L1-4, D1-2, D5, D6_um, E1-2_XhoI, E3-6_um, E7-9, E19-24_XhoI, E25-27	1.1, 3.1, 3.2, 3.3 XhoI Unit (Fig. S5)
33	B1, L1-4, D1-2, D5, D6_um, E1-2_um, E3-4_XhoI, E5-6_um, E7-9, E19-24_XhoI, E25-27	1.2, 3.1, 3.2, 3.3 XhoI Unit (Fig. S5)
34	B1, L1-4, D1-2, D5, D6_um, E1-4_um, E5-6_XhoI, E7-9, E19-24_XhoI, E25-27	1.3, 3.1, 3.2, 3.3 XhoI Unit (Fig. S5)
35	B1, L1-4, D1-2, D5, D6_um, E1-4_XhoI, E5-6_um, E7-9, E19-24_XhoI, E25-27	1.1, 1.2, 3.1, 3.2, 3.3 XhoI Unit (Fig. S5)
36	B1, L1-4, D1-2, D5, D6_um, E1-2_um, E3-6_XhoI, E7-9, E19-24_XhoI, E25-27	1.2, 1.3, 3.1, 3.2, 3.3 XhoI Unit (Fig. S5)
37	B1, L1-4, D1-2, D5, D6_um, E1-2_XhoI, E4-5_um, E5-6_XhoI, E7-9, E19-24_XhoI, E25-27	1.1, 1.3, 3.1, 3.2, 3.3 XhoI Unit (Fig. S5)
38	B1,	Fluorescence Onset - first green then red (Fig. S12)
39	B1,	Fluorescence Onset - first red then green (Fig. S12)
40	B1,	Fluorescence Onset - simultaneous (Fig. S13)
41	B1,	Fluorescence Onset - delayed with Timing unit (Fig. S13)

Sequence of the p1800 scaffold used to fold the DNA origami array structure from 5’ to 3’ end:

TACGAAGAGTTCCAGCAGGGATTCCAAGAAATGGCCAATGAAGATTGGATCACCTTTCG
CACTAAGACCTACTTGTTTGAGGAGTGCCTGATGAATTGGCACGACCGCCTCAGGAAAG
TGGAGGAGCATTCTGTGATGACTGTCAAGCTCCAATCTGAGGTGGGCAAATATAAGATT
GTTATCCCTATCTAGAAGTACGTCCGCGGAGAACACCTGCCACCCGATCACTGGCTGG
ATCTGTTACGCTTGCTGGGTCTGCCTCGCGGCACATCTCTGGAGAAACTGCTGTTCGGT
GACCTGCTGAGAGTTGCCGATACCATCGTGGCCAAGGCTGCTAACCTGAAAGATCTGA
ACTCACGCGGCCAGGGTGAAGTGACCATCCGCGAATAACTCAGGGAACTGGATTTGTG
GGGCGTGGGTGCTGTGTTCACACTGATCGGCTATGAGGACTCCCAGAGCCGCACCTAG
AAGCTGATCAAGGATTGGAAGGAGCTCGTCAACCAGGTGGGCGACAATATATGCCTCC
TGCAGTCCTTGAAGGACTCACCATACTATAAAGGCTTTGAAGACAAGGTCAGCATCTGG
GCAAGGAAACTCGCCGAACTGGACGATAATTTGCAGAACCTCAACCATATTCGCAGAAA
GTGGGTTTACCTCGAACCATACTTTGGTCGCGGAGCCCTGCCCAAAGAGCAGACCAGA
TTCAACAGGGTGGGCGAAGATTTCCGCAGCATCATGACATATATCAAGAAGGACAATCG
CGTCACGCCCTTGACTACCCACGCAGGCATTCTAAACTCACTGCTGACCATCCTGGACC
AATTGCAGAGATGCCAGCGCAGCCTCAACGAGTTCCTGGAGGCGAAGCGCAGCGCCTT
CCCTCGCTTTAACTTCATCGGAGACGATGACCTGCGCGAGATCTTGGGCCAGTCAACCA
ATTAATCCGTGATTCAGTCTCACCTCAAGAAGCTGTTTGCTGGTATCAACTCTGGCTGTT
TCGATGAGAAGTCTAAGCACTATACTGCAATGAAGTCCTTGGAGGGGCAAGTTGTGCCA
TTCAAGAATAACGTACCCTTGTCCAATAACGTCGAAACCTGGCTGAACGATCTGGCCCT
GGAGATGAAGAAGACCCTGGAGGCGCTGCTGAAGGAGTGCGTGACAACTAGACGCAG
CTCTCAGGGAGCTGTGGGCCCTTCTCTGTTCCCATCACAGATCTAGTGCTTGGCCGAAC
AGATCAAGTTTACCGAAGATGTGGAGAACGCAATTAAAGATCACTCCCTGCACCAGATT
GAGTAACAGCTGGTGAACAAATTGGAGCAGTATACTAACATCGACACATCTTCCGTAGA
CCCAGGTAACACAGAGTCCGGTATTCTGGAGCTGAAACTGAAAGCACTGATTCTCGACG
GATCCACGCGCCCTGTAGCGGCGCATTAAGCGCGGCGGGTGTGGTGGTTACGCGCAG
CGTGACCGCTACACTTGCCAGCGCCCTAGCGCCCGCTCCTTTCGCTTTCTTCCCTTCCT
TTCTCGCCACGTTCGCCGGCTTTCCCCGTCAAGCTCTAAATCGGGGGCTCCCTTTAGG
GTTCCGATTTAGTGCTTTACGGCACCTCGACCCCAAAAAACTTGATTTGGGTGATGGTT
CACGTAGTGGGCCATCGCCCTGATAGACGGTTTTTCGCCCTTTGACGTTGGAGTCCAC
GTTCTTTAATAGTGGACTCTTGTTCCAAACTGGAACAACACTCAACCCTATCTCGGGCTA
TTCTTTTGATTTATAAGGGATTTTGCCGATTTCGGGGTACC

Publication bibliography

Shaw, Alan; Hoffecker, Ian T.; Smyrlaki, Ioanna; Rosa, Joao; Grevys, Algirdas; Bratlie, Diane et al. (2019): Binding to nanopatterned antigens is dominated by the spatial tolerance of antibodies. In *Nature nanotechnology* 14 (2), pp. 184–190. DOI: 10.1038/s41565-018-0336-3.